Studies of the Technological Problems of Laser Driven Fusion Reactors – Annual Report I

R.W. Conn, S.I. Abdel-Khalik, G.A. Moses, E.T. Cheng, G. Cooper, J. Howard, G.L. Kulcinski, E. Larsen, E. Lovell, G. Magelssen, I.N. Sviatoslavsky, W. Wolfer, F. Beranek, S.K. Chang, R. Droll, N. Ghoniem, T. Hunter, M. Ortman, R.Spencer, G. Shuy, and M. Ragheb

December 1976

UWFDM-190

FUSION TECHNOLOGY INSTITUTE

UNIVERSITY OF WISCONSIN

MADISON WISCONSIN

"Legal Notice"

"This work was prepared by the University of Wisconsin as an account of work sponsored by the Electric Power Research Institute, Inc. ("EPRI"). Neither EPRI, members of EPRI, the University of Wisconsin, nor any person acting on behalf of either:

"a. Makes any warranty or representation, express or implied, with respect to the accuracy, completeness, or usefulness of the information contained in this report, or that the use of any information, apparatus, method, or process disclosed in this report may not infringe privately owned rights; or

"b. Assumes any liabilities with respect to the use of, or for damages resulting from the use of, any information, apparatus, method, or process disclosed in this report."

Studies of the Technological Problems of Laser Driven Fusion Reactors – Annual Report I

R.W. Conn, S.I. Abdel-Khalik, G.A. Moses, E.T. Cheng, G. Cooper, J. Howard, G.L. Kulcinski, E. Larsen, E. Lovell, G. Magelssen, I.N. Sviatoslavsky, W. Wolfer, F. Beranek, S.K. Chang, R. Droll, N. Ghoniem, T. Hunter, M. Ortman, R.Spencer, G. Shuy, and M. Ragheb

Fusion Technology Institute
University of Wisconsin
1500 Engineering Drive
Madison, WI 53706

http://fti.neep.wisc.edu

December 1976

UWFDM-190

Studies of the Technological Problems of Laser Driven Fusion Reactors*

ANNUAL REPORT-I

December 1976

R. W. Conn
S. Abdel-Khalik
G. A. Moses
E. T. Cheng
G. Cooper
J. Howard
G. L. Kulcinski
E. Larsen
E. Lovell
G. Magelssen
I. Sviatoslavsky
W. Wolfer
F. Beranek
S. K. Chang
R. Droll
N. Ghoniem
T. Hunter
M. Ortman
R. Spencer
G. Shuy
M. Ragheb

Fusion Technology Program
Nuclear Engineering Department
University of Wisconsin
1500 Johnson Drive
Madison, Wisconsin 53706

*Research supported by the Electric Power Research Institute under Contract RP237-3

Acknowledgment

This research is supported by the Electric Power Research Institute under grant RP237-3. We are grateful to the Institute for the support. Ms. Connie Linehan, Ms. Gail Herrington, and Ms. Bonnie Mack typed the manuscript and Mr. Richard Vacca coordinated production of the report. Their most cooperative efforts are deeply appreciated by all the members of the University of Wisconsin fusion research program.

Abstract

We report progress in inertial confinement fusion reactor research oriented over the past year towards pure laser fusion reactors for electric power production. Topics covered include laser-pellet modeling, target illumination and optics, lasers, cavity design and liner response, magnetic protection, blanket design and thermal hydraulics, steady state and time dependent neutronics analyses, materials behavior and neutron radiation damage, tritium cycle analysis, and power cycle design. Total system integration, plant design, optimization studies, and economic analyses are just beginning and no details are reported on these topics. Emphasis has been placed on the development of analytical tools for analysis in all areas and a pre-conceptual reactor design has been developed and used to focus the research. However, this design is preliminary and should be viewed as such. The analysis of most problems has been carried out parametrically so that a range of interest is covered rather than a specific set of performance characteristics. We have analyzed the neutron damage problem in considerable detail and find that through auspicious choice of operating temperature, first wall lifetime at high neutron wall loading ($\sim$7.5 MW/m^2) may be quite long. An overview is included to provide a general description of our work and extensive details are given in individual chapters.

TABLE OF CONTENTS

I. Introduction and Overview

Research on inertial confinement fusion has expanded dramatically over the past five years. The recent results on compression and neutron yields from laser illuminated targets and the possibility of thermonuclear neutron yields from electron beam illuminated targets are measures of rapid progress. It is still difficult to have a clear picture of how these results can be implemented in a practical reactor, but given the level of effort in experimental research, it is appropriate to begin developing the basis for understanding and analyzing the technological problems of inertial confinement fusion reactors.

Laser initiated thermonuclear fusion is currently receiving the greatest attention of all approaches to inertial confinement and we have, therefore, begun our studies of reactor technology problems by considering the laser fusion approach. The purpose of this research is to develop a greater understanding of the technological problems posed by laser fusion systems as reactors and to lay a foundation for future studies to make a more realistic assessment of the ultimate potential of such systems. In this first annual report, we discuss our efforts to develop models to analyze various aspects of laser fusion reactors and a preliminary attempt to combine these pieces into the start of a conceptual reactor design study. Our program is to begin with an analysis of laser fusion for central station electric power generation and to follow this with a study of laser fusion hybrid systems. Smaller but significant efforts will be devoted to an examination of advanced fuel cycles and a general comparison of inertial and magnetic confinement fusion technology problems. Our studies so far have concentrated on the first topic, namely, pure laser fusion systems applied to electric power generation. Studies have begun on advanced fuel cycles.

In the remainder of this first chapter, we summarize the questions we have asked, the methods we have developed to begin analyzing specific problems, the approaches we have taken to most of the problems uncovered, and the pre-conceptual reactor we have developed. Many specific analyses are, however, not summarized here but are included in the later chapters. In addition, all the details and many auxiliary results are given in the separate chapters. Thus, this overview is provided as an indication of our methodology and results so far, but it is not meant to be inclusive.

The questions which present themselves early in a laser fusion study can be divided as follows:

1. Laser Pellet Studies: What range of pellet gain is required? What yield should one choose? What value of laser energy is appropriate? What are the spectra associated with various forms of pellet debris? What degree of target illumination uniformity is required and how many laser beams do we need?

2. Laser Studies: What is the range of viable wavelengths? What is the laser energy? What is the laser pulse shape? How are beam lines designed and what are the problems with the last mirror? What repetition rate is required and how does this influence laser design, power supplies, and component lifetimes?

3. Cavity and Blanket Design: Do we need a protective liner for the first wall? Do we need magnetic fields to protect the liner? How does the liner respond to X-rays, ions, and reflected laser light? How does this vary as the spectra and fraction of energy in each category change? How will we design the first wall? How will we design the blanket and breed tritium?

4. Materials and Neutron Radiation Damage: Are there special rate effects in inertial confinement reactor systems? How does the damage vary with temperature? What structural material should we choose? What should we choose for the neutron wall loading? What are the dynamic stress problems and how do we treat them?

5. Tritium Systems and Power Cycle: What does the complete tritium cycle look like? How do we breed and recover tritium? How do we minimize leakage effects? How do we integrate the various forms of heat into an optimum power cycle? Do we need an intermediate loop?

It was clear to us that developing the tools to analyze the problems and questions outlined above would provide us with the basis necessary to develop an integrated reactor study. We have left for later analysis such areas as shield design, optical system layout, overall plant design, materials resource implications, optimization of the number of lasers, power supplies, chambers, and steam generators. We also felt that developing the appropriate tools of analysis would allow us to readily assess the influence of pellet design and output spectra as research continues and new results are put forth.

A pre-conceptual reactor design has been developed to help focus our analyses and keep our study integrated. We thus turn to a general description of this system. We will report some specific results here but again note that we have concentrated on developing tools of analysis and looking at problems parametrically. All this is reported in the separate chapters which follow.

A selected list of the main parameters characterizing our preliminary reactor system is given on Tables I-1 and I-2. The reactor has been named Solase-I* for future reference.

---

*Solase, as in "their solase in dorckaness, and splattering together joyously the plaps of their toppyhands as, with a cry of genuine distress, so prettly prattly pollylogue, they viewed him, the just one, their darling, away." Joyce, F.W. Laser fusion is a darling though many must now, with a cry of genuine distress, view it in dorckaness. For now, this must be "their solase".

The system has a pellet gain, defined as thermonuclear yield divided by incident laser energy, of 100. The relationship between target gain and system efficiency is an important one when there are several subsystems with low efficiency. In laser induced pellet fusion, the laser itself is a key subsystem which has a low anticipated efficiency. To determine the level of target gain required, we proceed by defining the gain of a pellet fusion target by

$$G = \frac{E_F}{E_{LAS}} \tag{1}$$

where E_F is the total thermonuclear energy produced and E_{LAS} is the incident energy onto the target. The energy absorbed by the target, E_A, is related to E_{LAS} by

$$E_A = \eta_c \, E_{LAS} \tag{2}$$

where η_c is the coupling efficiency, i.e., the fraction of incident laser light absorbed by the pellet. Let us define three additional efficiencies:

η_L = laser efficiency

η_{th} = gross plant thermal efficiency

η_p = net plant thermal efficiency.

Then the gain is given by

$$G = \left[\frac{1}{\eta_L \, (\eta_{th} - \eta_p)}\right] - 1 \tag{3}$$

while the net plant efficiency is given by

$$\eta_p = \eta_{th} - \frac{1}{\eta_L (G+1)} \quad . \tag{4}$$

Thus, we can determine the pellet gain required to achieve a certain net plant efficiency, η_p, for a system with a laser efficiency, η_L, and a gross

Table I-1

PARAMETERS OF PRE-SOLASE-I DESIGN

Pellet Parameters	
Pellet Gain	100
Pellet Yield	100 MJ
Minimum Pellet Mass	1 mg
Laser Parameters	
Laser Energy	1 MJ
Laser Wavelength	Open
Laser Type	Open, Gas
Number of Lasers	12
Rep Rate	30/S
Optical System Parameters	
Number of Beams on Target	6
Last Mirror Material	Cu
Distance From Target	~15 m
Aperture Diameter	2.5 m
Max. Energy Density	5 J/cm^2

Table I-2

PARAMETERS OF PRE-SOLASE-I DESIGN

Thermal Power (MW)	3170
Chamber Shape	Vertical Cylinder Spherical End Caps
Chamber Diameter	10 m
Chamber Height	20 m
Liner	Carbon Curtain
Structural Material	Stainless Steel
First Wall Temp.	300°C
Blanket and Breeder Li_2O Inlet Temp. Li_2O Outlet Temp.	Flowing Li_2O 450°C 550°C
Neutron Wall Loading Average Peak	 3.77 MW/m^2 7.65 MW/m^2

power cycle efficiency η_{th}. (This assumes the laser energy dominates the recycle power requirements).

The fraction of gross electrical power recycled to keep the laser operating is

$$F_R = \frac{1}{\eta_L \eta_{th} (G+1)} \quad . \tag{5}$$

An engineering breakeven condition can be defined as the value of gain, denoted $\bar{G}$, for which $F_R = 1$. $\bar{G}$ is given by

$$G = \left(\frac{1 - \eta_L}{\eta_L} \right) .$$

Scientific breakeven, on the other hand, is defined as $G \equiv G_S = 1$. Clearly, $\bar{G}$ can be substantially greater than G_S.

The gain required to achieve a given value of net plant efficiency, η_p, for various values of η_L is shown in Fig. I-1. Typically, $\eta_{th} - \eta_p$ is no larger than 0.3 since at this value η_{th} must be 60% to allow a net plant efficiency of only 30%. In general, η_{th} is between 35 and 50% so that we would consider $(\eta_{th} - \eta_p)$ values of 0.1 to 0.15 interesting with larger values quite difficult to achieve. The analysis shows clearly that for reasonable values of η_L like 10%, the gain required for engineering breakeven is 9 and the gain required to achieve $(\eta_{th} - \eta_p)$ of 0.1 to 0.15 is between 65 and 100. Close examination of these simple relationships shows clearly that for most cases of practical interest, pellet gain values in the range of 75-100 and higher will be required. Such gains have been reported in the literature. We see that in general gain increases with higher yield and that a gain of 75-100 is associated with yields of about 100 MJ, which is in the necessary range. However, some of these more optimistic results have been obtained from high aspect ratio shell targets and the feasibility of imploding such shells without suffering hydrodynamic instabilities is questionable.

FIGURE I-1

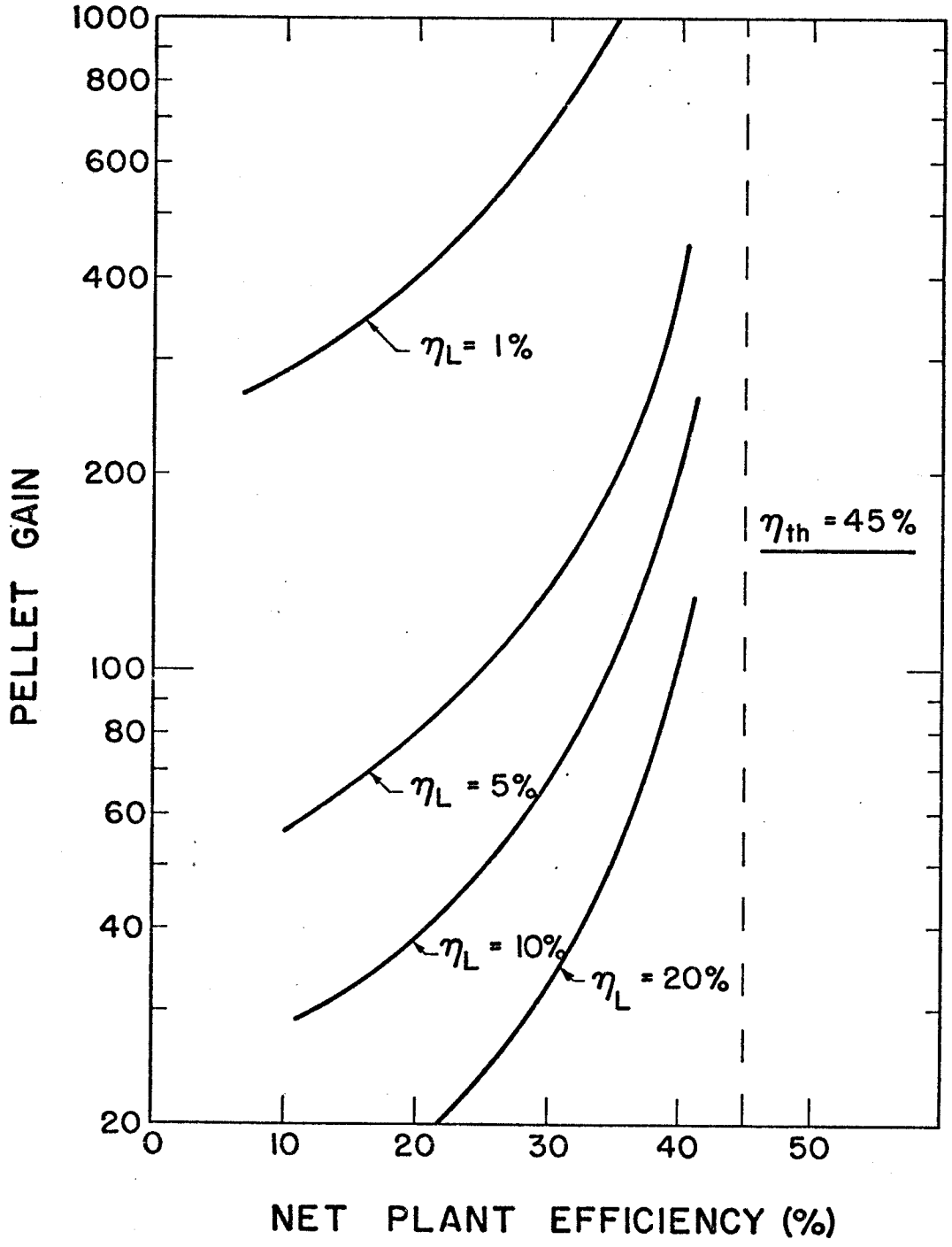
1000
800
600
400
200
100
80
60
40
20
PELLET GAIN
0
10
20
30
40
50
NET PLANT EFFICIENCY (%)
η_L = 1%
η_L = 5%
η_L = 10%
η_L = 20%
η_{th} = 45%

We have studied the question of pellet yield and gain to assess the prospects for achieving $G \geq 100$ using a one-dimensional, one fluid, two temperature plasma hydrodynamics code which includes a detailed treatment of burn dynamics. The code, PHD-IV, will also be used to study advanced fuel cycles. The most basic parameters that characterize the laser fusion pellet in the context of reactor design are thermonuclear yield and pellet gain. Each of these will depend on the fractional burnup of the fusion fuel, (that is the percentage of fuel compressed into the dense pellet core that ultimately burns). With the use of the PHD hydrodynamic - thermonuclear burn code such quantities can be computed as functions of pellet core mass, core ρR, microcore ρR, microcore temperature, and uncertainties in the physics of charged particle slowing down and plasma hydrodynamics. Table I-3 summarizes the results. Pellet core masses of 0.1 mg, .316 mg, and 1.0 mg were chosen to bound the estimated necessary mass required to give a thermonuclear yield of 100 MJ. In Fig. I-2 the yield is plotted as a function of ρR for the three different pellet masses. The yield rises sharply from $\rho R = 1$ to $\rho R = 3$ but beyond this point the yield flattens out. From these curves it would appear that $\rho R = 3$ g/cm^2 is about the optimum value regardless of the mass. It was also found that there is a linear dependence of the yield on pellet core mass (for this range of pellet mass) and that a plot of the yield vs. microcore ρR for a fixed core shows a threshold dependence. The ρR value of the microcore must exceed 0.38 g/cm^2 to provide significant yield. Above this value the yield is constant and below this value the yield is negligible. With this information the ρR and mass necessary to provide 100 MJ of energy can be identified.

To determine the optimim combination of all other pellet parameters, gain must be used. Maximizing gain for a fixed yield will minimize the necessary

Table I-3

Summary of Burn Parameter Study

MASS	ρR	$(\rho R_{\mu}) = .3$	$(\rho R_{\mu}) = .4$	$(\rho R_{\mu}) = .5$	$(\rho R_{\mu}) = .7$
.1	1	3.41-2*	.32	1.54	2.8
		7.99	37.4	99	68.8
				0	
.1	2			7.4	
				1804	
.1	3	2.27-3	7.7	10.22	10.2
		.626	2034	2525	2048
.1	5	1.18-3	12.8	13	13
		.2	2155	2168	2103
.1	7	3.55-2	14.5	14.6	14.6
		4.3	1756	1764	1749
.316	1	.109	.971	5.03	
		8.93	38.1	106	
.316	2	.019	.763	23.2	
		3.2	99	2220	
.316	3	.009	27.2	32.0	
		1.21	3369	3602	
.316	5	.012	40.55	40.83	
		.278	3313	3289	
.316	7	2.5-3	45.8	46.4	
		.147	2702	2649	
1.	1	.344	3.3	16.5	30
		9.5	41.3	110	74.8
1.	2			76.3	
				2649	
1.	3	2.2-2	83.6	104	101
		1.3	4292	4786	3415
1.	5	8.4-3	129	130	131
		.306	4641	4597	4303
1.	7	5.6-3	146	148	148
		.147	3795	3836	3754

* First number is yield in mega joules
Second number is the gain on core assuming perfect adiabatic compression from 1 ev.
Micro core temperature - 10 Kev

FIGURE I-2

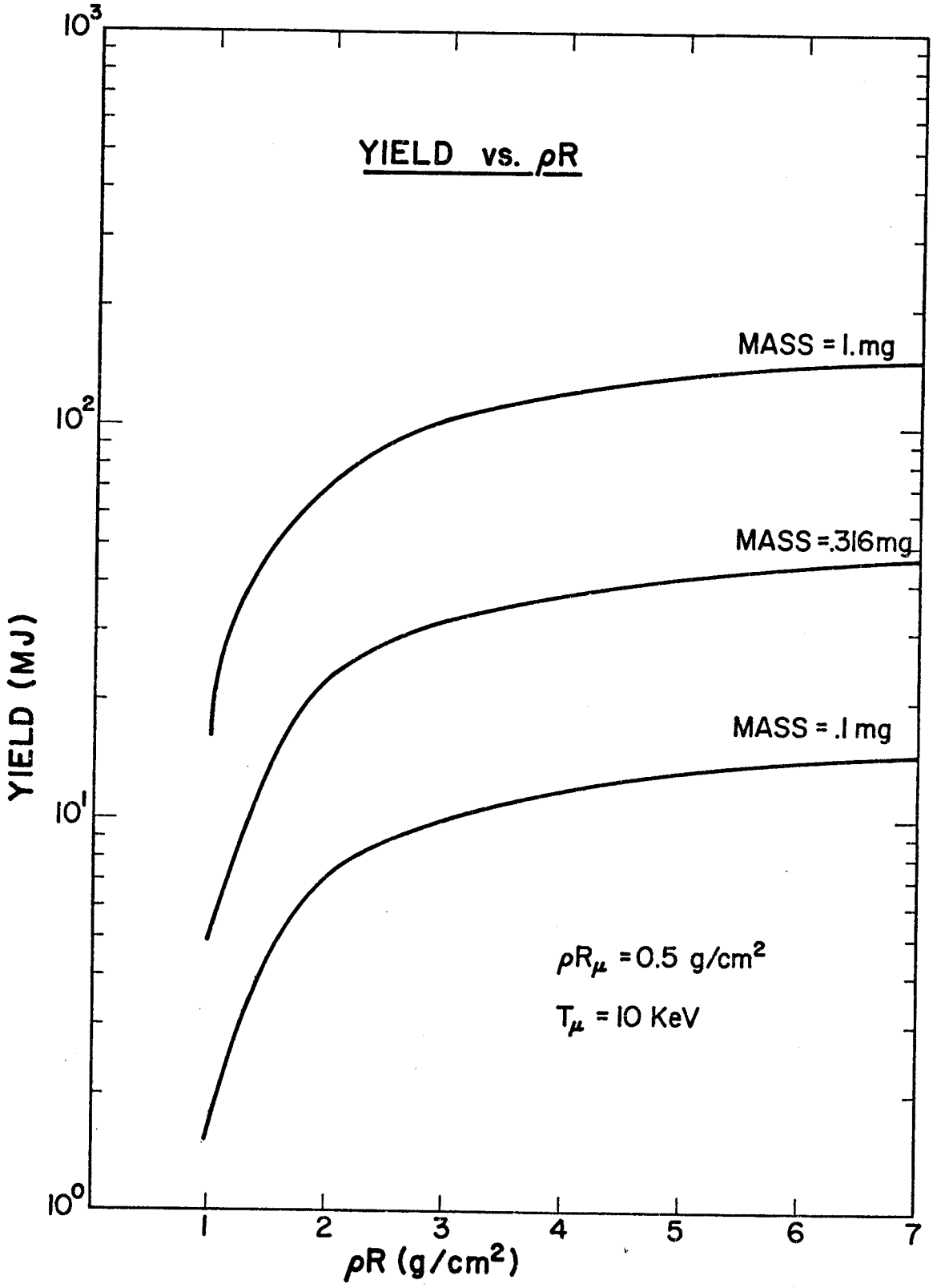
YIELD vs. ρR
MASS = 1. mg
MASS = .316mg
MASS = .1 mg
ρR$_\mu$ = 0.5 g/cm^2
T$_\mu$ = 10 KeV
YIELD (MJ)
ρR (g/cm^2)
10^3
10^2
10^1
10^0
1
2
3
4
5
6
7

input energy. The pellet core burn calculations, however, will only provide the gain on core (eg. thermonuclear yield/energy stored in the compressed core to be computed). The energy stored in the core is the sum of the microcore internal energy at 10 KeV and the energy in the remainder of the surrounding core. This latter energy is computed by assuming a temperature equal to that of an equivalent adiabatic compression of 1 eV plasma.

$$T = (1 \text{ ev}) \ (\rho/\rho_o)^{2/3}.$$

This will, in fact, over-estimate the gain because a perfect adiabatic compression is not possible; however, most interest here is in the ρR - mass combination at maximum gain rather than the absolute value of the gain at that point. Simple arguments indicate that the gain peaks around $\rho R = 3$ g/cm^2 and mass = 1 mg. The <u>total pellet gain</u> is, of course, the quantity that must be maximized and this might be sensitive to the particular implosion process giving a different optimum from the one indicated by gain on core. For the implosion of spherical ball or shell targets the coupling coefficient between the incident laser light and the internal energy stored in the core is predicted by sophisticated implosion calculations to be 5-10%. Using the 5% estimate and also assuming that the actual implosion process results in twice as much energy in the core as our adiabatic estimate, a gain on core of 4800 translates into an overall pellet gain of 120. This pellet gain will be adequate to compensate for a 10% efficient laser. Should laser efficiencies of 10% be unattainable, the laser core coupling efficiency must be increased to provide laser fusion power plant feasibility. The conceptual design of pellets with the necessary laser-core coupling will be discussed in Section II-F.

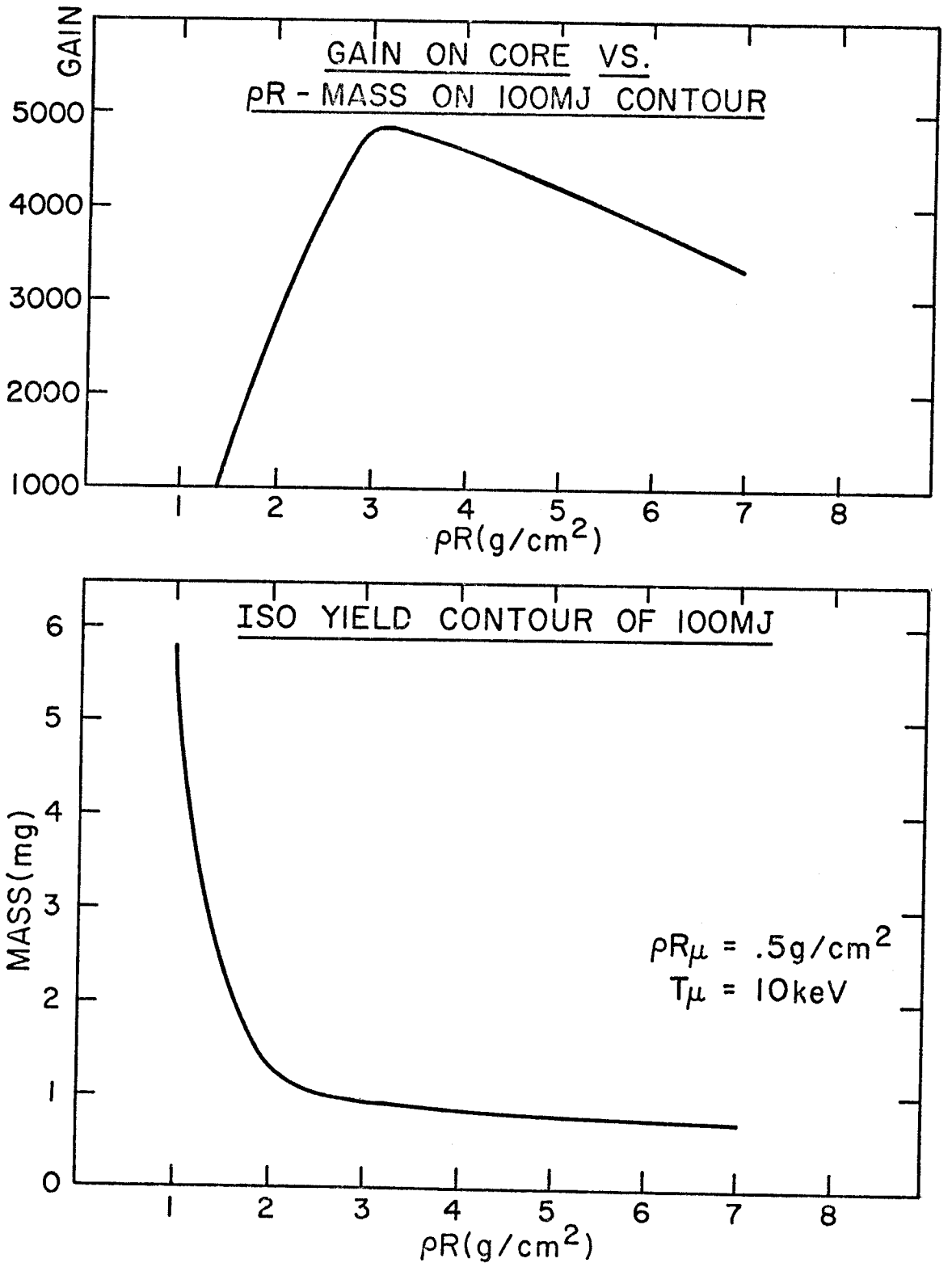
GAIN ON CORE VS.
ρR - MASS ON 100MJ CONTOUR
GAIN
5000
4000
3000
2000
1000
1
2
3
4
5
6
7
8
ρR(g/cm²)
ISO YIELD CONTOUR OF 100MJ
MASS(mg)
6
5
4
3
2
1
0
ρRμ = .5g/cm²
Tμ = 10keV
ρR(g/cm²)

FIGURE I-3

We have indicated in Table I-1 that aside from the laser energy of 1 MJ, we have not specified a particular wavelength or laser type except to indicate it would be a gas phase system. Instead, our study has started by surveying the various laser systems, analyzing their advantages and disadvantages, and comparing each against the potential requirements as summarized in Table I-4. The results are given on Table I-5 for "proven" lasers and on Table I-6 for potential lasers (systems that are yet to show lasing action). Today, there is no known or proposed system which obviously will meet the requirements for laser fusion. Which laser will prove optimum will depend much upon the ultimate wavelength, efficiency, and power requirements imposed by advanced pellet designs as well as developments in the lasers themselves. Thus, choosing the "right" specific laser for our design at this time is virtually impossible. In light of this, we have chosen the CO_2 laser for our design. This is not to be construed as an endorsement for CO_2, but rather a way to give a concrete basis to a generic design. It is felt that in order to meet the basic requirements for a laser-fusion laser (a flowing gas system, 1 MJ total energy out, and energy densities dictated by the optics and not the laser medium) that the ultimate laser's electrical, mechanical and optical parameters will not be dramatically different from those of the CO_2 design. Of course, each laser will have its own particular requirements for such things as optical components, possible chemical reprocessing and flash as opposed to discharge pumping which will not be specifically considered in our design. However, the total design should be quite similar and specific modifications readily made. (For example, flash pumped systems such as I*, O* or Nd^{+3} will likely use

Table I-4

REQUIREMENTS OF THE LASER FOR LASER FUSION

Performance Requirements

Energy	$\sim 10^5$ 10^6 J
Peak Power	~100-1000 TW
Pulse Width	0.1 - 1 nsec
Wavelength	3000 - 6000 Å (Perhaps, 0.3 - 10.6 μm)
Pulse Shape	$P(t) \sim \frac{P_o}{(1 - t/t_o)^2}$

Practical Considerations

Efficiency	$\geq$ 10% for G = 100; $\geq$ 1% for G = 1000
Pulse Repetition Rate	10 - 100 sec^{-1}
Small Signal Gain	0.001 - .01 cm^{-1}
Stored Energy Density	10^2 - 10^3 J/liter
Stimulated Emission cross section	10^{-19} - 10^{-20} cm^2
Low Capital Costs and Low Maintenance	

Table I-5

Lasers for Laser Fusion

Laser (Proven)	Wavelength	Advantages	Disadvantages
Iodine	1.315 μm	High Energy High Power Shortest λ of "Proven" Systems	Low Efficiency High Gain
HF	~2.7-3.0 μm	High Energy High Electrical Efficiency Reasonable Chemical Efficiency	High Gain Not a Storage Medium Relatively Long Pulses
CO_2	10.6-9.6 μm	High Energy High Power Reasonable Efficiency	Wavelength May Be Too Long High Gain

Table I-6

Lasers for Laser Fusion

Laser (Potential)	Wavelength	Advantages	Disadvantages
Oxygen Rare Gas Oxides	~557 nm	Wavelength Potential High Power High Energy Short Pulse	Low Efficiency (To Date)
Excimers Ar_2^*, Kr_2^*, Xe_2^*, ArF^*, KrF^*	~130-249 nm	High Power High Energy Potential High Efficiency	Wavelenghts Too Short for Optics
NF^*, HG_2^* $HgCd^*$	~335-800 nm	Wavelength Potential High Power High Energy High Efficiency	(Not Proven Systems)

electron-beam generated fluorescence to improve efficiencies and, thus, utilize the electron beam technology developed for CO_2). Thus, the CO_2 laser, which is relatively simple in operation, well understood, and apparently scalable should provide a good basic design for the laser system of our laser fusion reactor.

We have also given preliminary consideration to the number of laser beams required. Uniform target illumination has been shown (see Chapters II and III) to require a minimum of 12 beams and perhaps as many as 20. Each of these would be consistent with reasonable laser requirements of not having a single amplifier rated at more than 100 kJ. However, some reactor studies, such as those at Lawrence Livermore Laboratory and Los Alamos Scientific Laboratory, have used fewer than 12 beams on target, going as low as 6. If such an approach is ultimately feasible, the 12 laser beams can be combined following amplification and a schematic layout leading to six beam illumination is shown in Fig. I-4. Since it has been shown that six beams will not uniformly illuminate the target, it would not be necessary to locate such beams symmetrically around the chamber. We have not reduced the number of beams below 6 at 1 MJ total energy because of energy density limitations on optical elements and the desire to keep the largest laser amplifier unit below 100 kJ.

The reactor parameters listed on Table I-2 indicate the system generates 3170 MW(th). This is based on a laser energy of 1 MJ, a pellet gain of 100 based on 17.6 MeV per fusion and a total energy per fusion, including blanket multiplication of 18.6 MeV per fusion. The repetition rate is 30 pulses per second and a single chamber is currently employed. The overall cavity and blanket design shown in Fig. I-5 is oriented vertically because of the

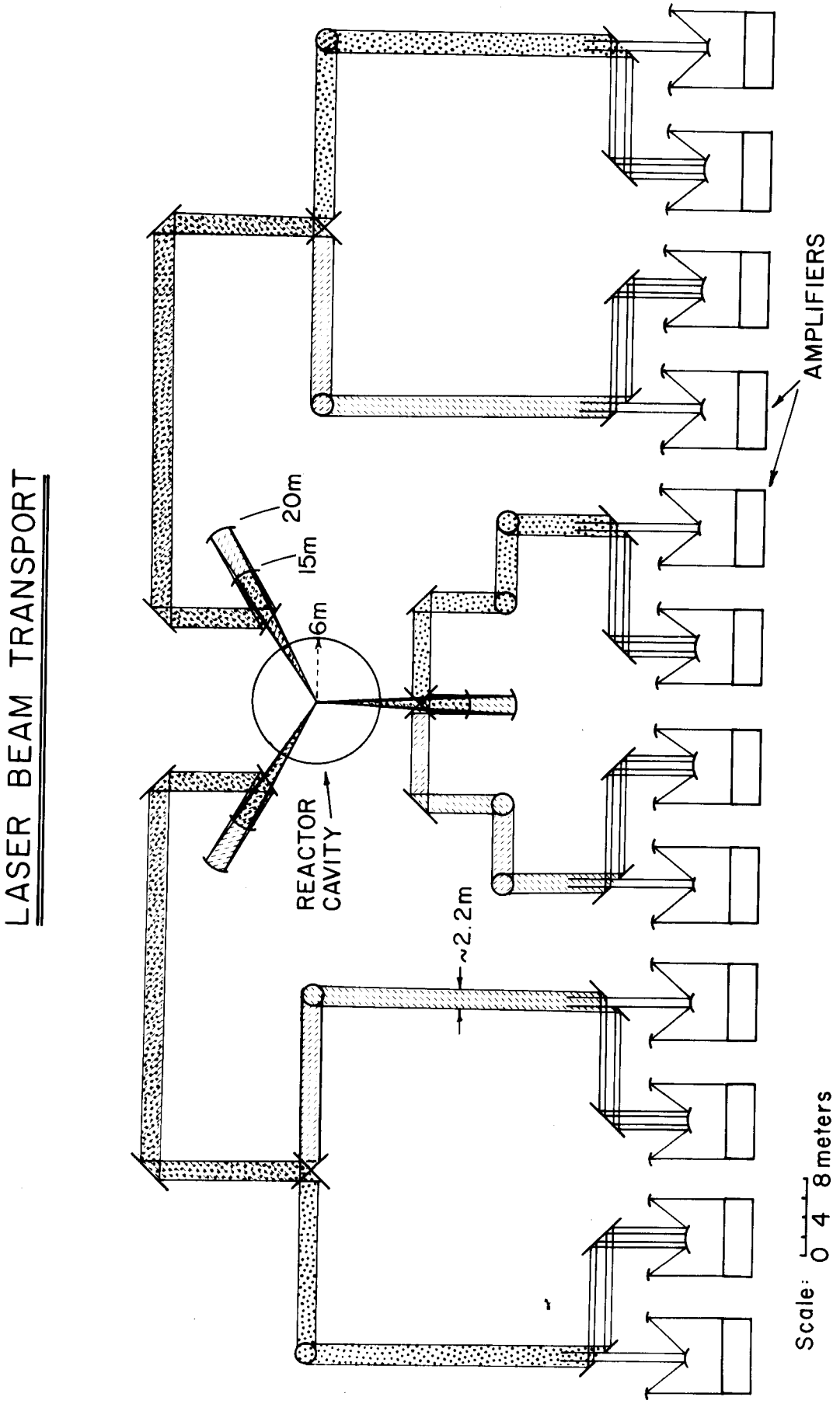
LASER BEAM TRANSPORT
20m
15m
6m
REACTOR CAVITY
~2.2m
AMPLIFIERS
Scale: 0 4 8 meters

FIGURE 1-4

Figure I-1

U W LASER FUSION REACTOR CAVITY

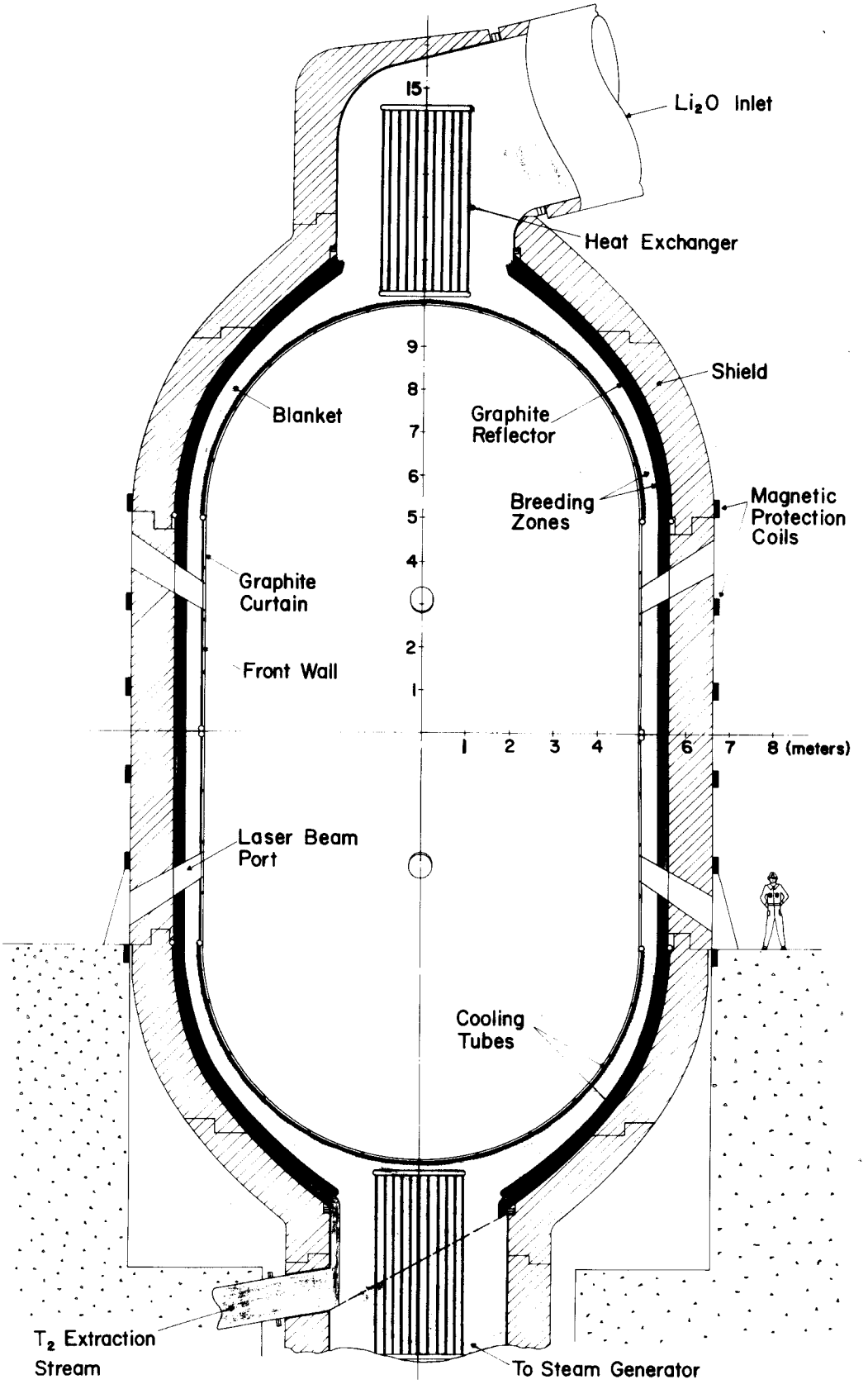

flowing Li_2O solid blanket design to be discussed shortly and described in Chapter VI. We will in future work study the trade-offs associated with multi-chamber systems.

The chamber uses the carbon curtain concept developed at Wisconsin in our tokamak studies to protect the first wall from impulsive heating by X-rays and charged particles. The performance of the liner has been studied parametrically as a function of the fraction of spectra of the X-rays and charged particles since the main performance parameter (liner surface temperature use) is linear in the amount of total amount of energy in X-rays or charged particles. The analysis is described in Chapter V. As an example, we show in Fig. I-6 the surface temperature rise on the carbon curtain as a function of the black-body temperature for a pellet yield of 100 MJ assuming the X-ray spectra can be so categorized. The surface ΔT is linear in the percentage of yield in X-rays and 1% is assumed on the figure. One can see that any spread in the arrival time of the X-rays is helpful and that the temperature rise is smaller the harder the X-ray spectrum. The case $\kappa = 0$ corresponds to instantaneous deposition of all X-ray energy.

We have also parametrically analyzed the influence of reflected laser light on the surface temperature rise of the liner. The results shown in Fig. I-7 are parametric in laser wavelength by the type of laser assuming 1 MJ of laser light incident on the target and 10% reflection. $\Delta T_{surface}$ is linear in the fraction of reflected light and small $\Delta T_{surfaces}$ require little reflection and/or long laser pulses.

An analysis of the temperature use due to ion bombardment based on spectra produced from PhD-IV indicate that the temperature rise could be as

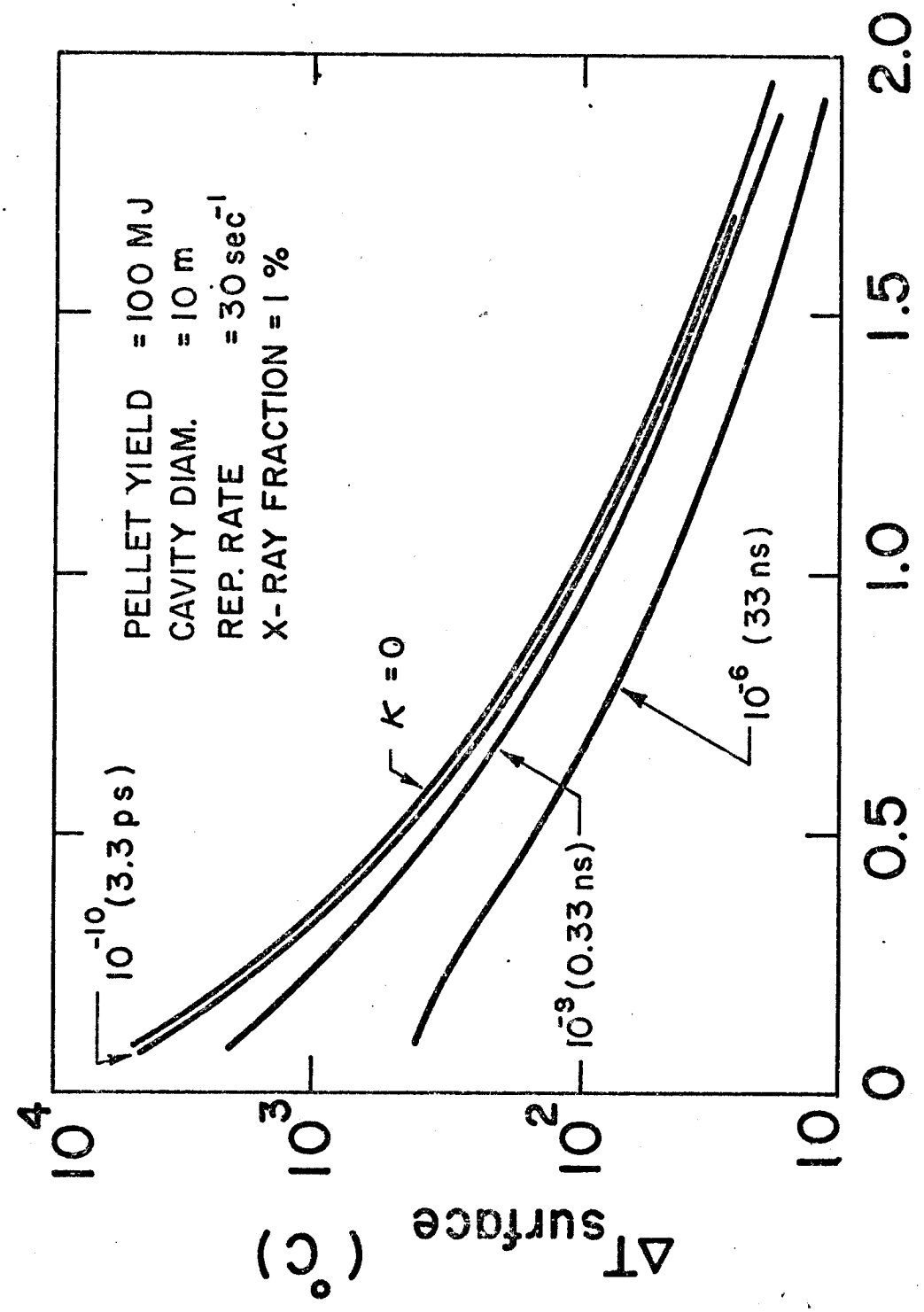
PELLET YIELD = 100 MJ
CAVITY DIAM. = 10 m
REP. RATE = 30 sec⁻¹
X-RAY FRACTION = 1 %
K = 0
10⁻¹⁰ (3.3 ps)
10⁻⁹ (0.33 ns)
10⁻⁶ (33 ns)
ΔT surface (°C)
10⁴
10³
10²
10
0
0.5
1.0
1.5
2.0
BLACK BODY TEMP. (keV)

FIGURE I-6

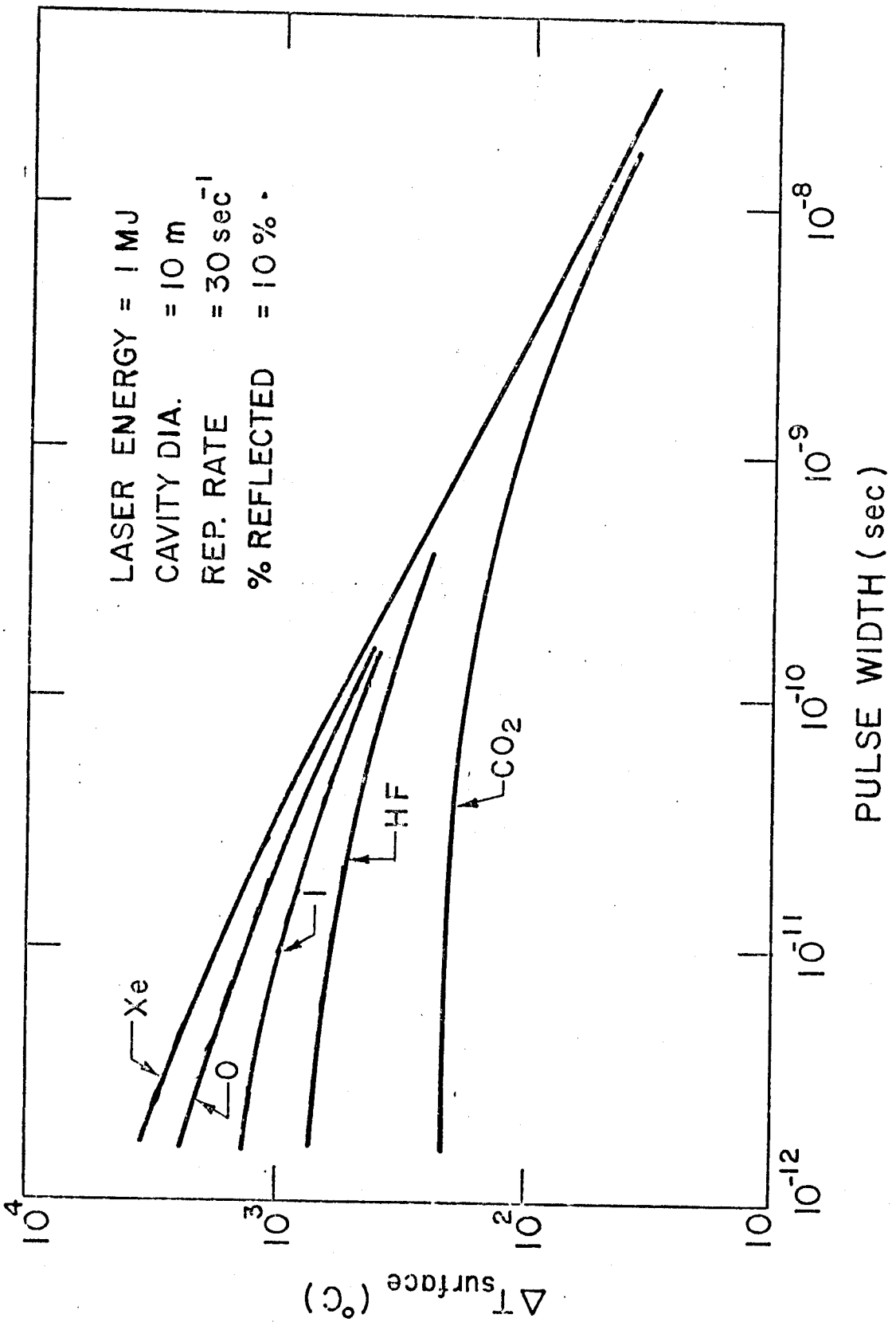
LASER ENERGY = 1 MJ
CAVITY DIA. = 10 m
REP. RATE = 30 sec^{-1}
% REFLECTED = 10 %
Xe
O
I
HF
CO_2
$\Delta T_{surface}$ (°C)
10^4
10^3
10^2
10
10^{-12}
10^{-11}
10^{-10}
10^{-9}
10^{-8}
PULSE WIDTH (sec)

FIGURE I-7.

high as $400^{o}C/J/cm^{2}$. Such large temperature rises would be intolerable and would require a different approach to cavity design. However, magnetic protection, as discussed by the Los Alamos group, may prove to help by directing particles away from the liner to energy sinks at the top and bottom of the chamber. This allows for fast pumping of the chamber and a spread, by time-of-flight, in the arrival time of energetic ions at the energy sinks.

We have performed a simple preliminary analysis here and found that a soloinoid field produced by coils described in Table I-7 is sufficient to stop the radial expansion in the horizontal direction at 0.9 r_w where r_w is the radius of the chamber wall. The vacuum field is 5 kG and the maximum field is 20 kG during the expansion.

The principal drawback to magnetic protection is that the exploding plasma is unstable to flute modes which give rise to transport across the restraining magnetic field. However, for this application confinement is not required. The relevant concern is that the growth rate for the flute modes be small enough to allow time for the debris to stream out the cylindrical chamber. (Note that this requirement makes it desirable for the energy sinks to be close to the explosion center, in opposition to the time-of-flight spreading condition mentioned above. Thus, some optimum distance must be determined). Previous studies at Los Alamos indicate that flute growth times may be roughly 5 times longer than transit times out the chamber. However, these results are based on rough estimates. In view of the critical nature of this problem, further study is required.

There are two groups of charged particles produced on explosion of simple targers, fast alphas and D-T debris. If we assume that both groups expand as hot plasmas then the helium plasma expands first, compressing the field until

Table I-7

Main Parameters Of Magnetic Protection System

Field Shape	Solenoid
Vacuum Field Strength	5 kG
Maximum Field	20 kG
Type of Coil	Cu
Coil Coolant	Water
Number of Coils	6
Coil Dimensions	20 cm x 50 cm
Overall Current Density	1250 A/cm^2
Power Dissipated	54 MW

the radial motion is stopped. This helium plasma continues its expansion along the axis, relieving the pressure, as the field begins to push the plasma back toward the axis. The D-T plasma then streams through the helium plasma and recompresses the field; then it too streams out the ends. If we assume that a particle's velocity component along the axis, v_z, is unchanged by the magnetic field (only approximately true) and that the explosion is isotropic, then the particles are uniformly distributed in v_z. An estimate of the time for an element of D-T plasma on the cylinder axis to reach the energy sink is 3×10^{-6} s, so in 3×10^{-5} s roughly 90% of the plasma has left the chamber.

The shape of the energy sinks at the end of the cylindrical chamber can be described by a function $z(r)$ with $z = 0$ at $r = 0$. The conditions that determine the shapes are:

(1) The surface is to be as far from the explosion center as possible (i.e. the surface is to be convex, as viewed from the source).

(2) The energy absorbed per unit area is to be constant over the surface. We derive the desired shape in terms of the radial distribution of the particles projected on a plane perpendicular to the cylinder axis. For purposes of illustration the simplifying assumption is made that this distribution is constant in time. This is approximately true if the conducting walls which compress the field are at a constant radius over the entire chamber, including the energy sinks. The radial distribution $f(r)$ is normalized by $2\pi \int_0^{R_{max}} f(r)rdr = 1$. An element of surface area at $z(r)$ is given by $dA = 2\pi r\sqrt{1 + (\frac{dz}{dr})^2}\, dr$, while the number of particles incident on this strip of area is $dN = \frac{N}{2}(2\pi r f(r)dr)$. If we require the energy per unit area to be some constant C we find

$$\frac{dz}{dr} = -\sqrt{\frac{N^2}{4C^2} f^2(r) - 1}\ .$$

We pick the negative sign for the square root to make the surface convex.

It is interesting to consider some special cases.

(a) Let f(r) be determined by a thin spherical shell of radius R projected on a plane perpendicular to the axis,

$$f(r) = \frac{1}{2\pi r^2 \sqrt{1-(r/R)^2}} \; ;$$

then the collector shapes are as illustrated in Fig. I-8.

(b) Let f(r) be determined by the projection of a solid sphere on a plane,

$$f(r) = \frac{3\sqrt{1-(r/R)^2}}{2\pi} \; ;$$

then the collector shapes are as illustrated in Fig. I-9.

The most critical problem at the moment is that of determining the growth rate of the flute instability. A detailed analysis of the exploding plasma as it is decelerated by the magnetic field in cylindrical geometry must be carried to see if the growth rate really is small enough to be neglected. In addition, some simulation capability needs to be developed, similar to that achieved by the Los Alamos group. Once this is in hand, optimization studies on shapes and sizes of energy sinks may be carried out.

The first metallic wall in the reactor is a membrane type stainless steel structure with built-in coolant channels. Typical membrane wall designs are shown in Fig. I-10. The design shown in Fig. I-10-B has been developed and successfully used by Babcock & Wilcox in their modern high pressure fossil boilers. Membrane walls can be easily manufactured; they have proven to be reliable, leak-free, and simple to install.

Boiling water is used to cool the first wall. The system is operated in a manner similar to recirculating boilers. Gaseous coolants were considered

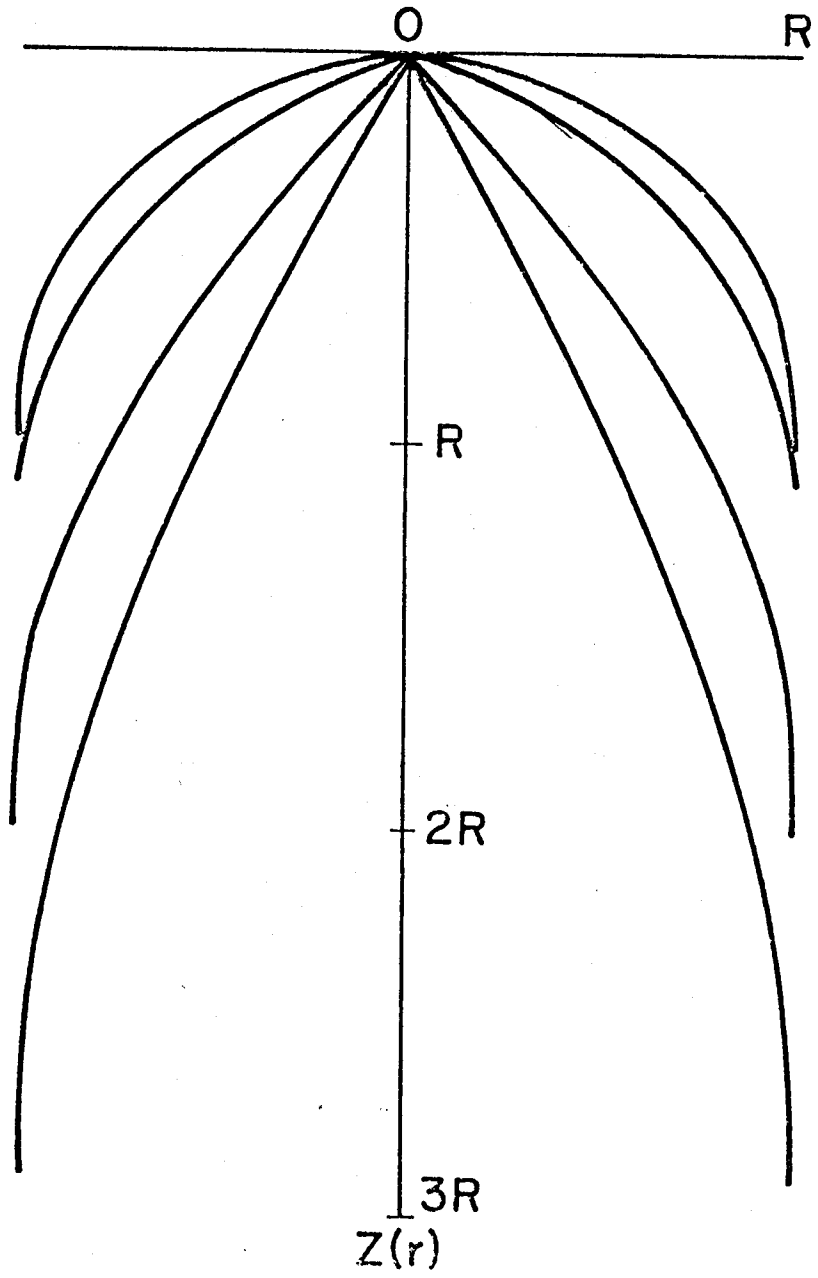

FIGURE I-8 ENERGY SINK SHAPE FOR A SHELL LIKE EXPLOSION. R = PLASMA RADIUS

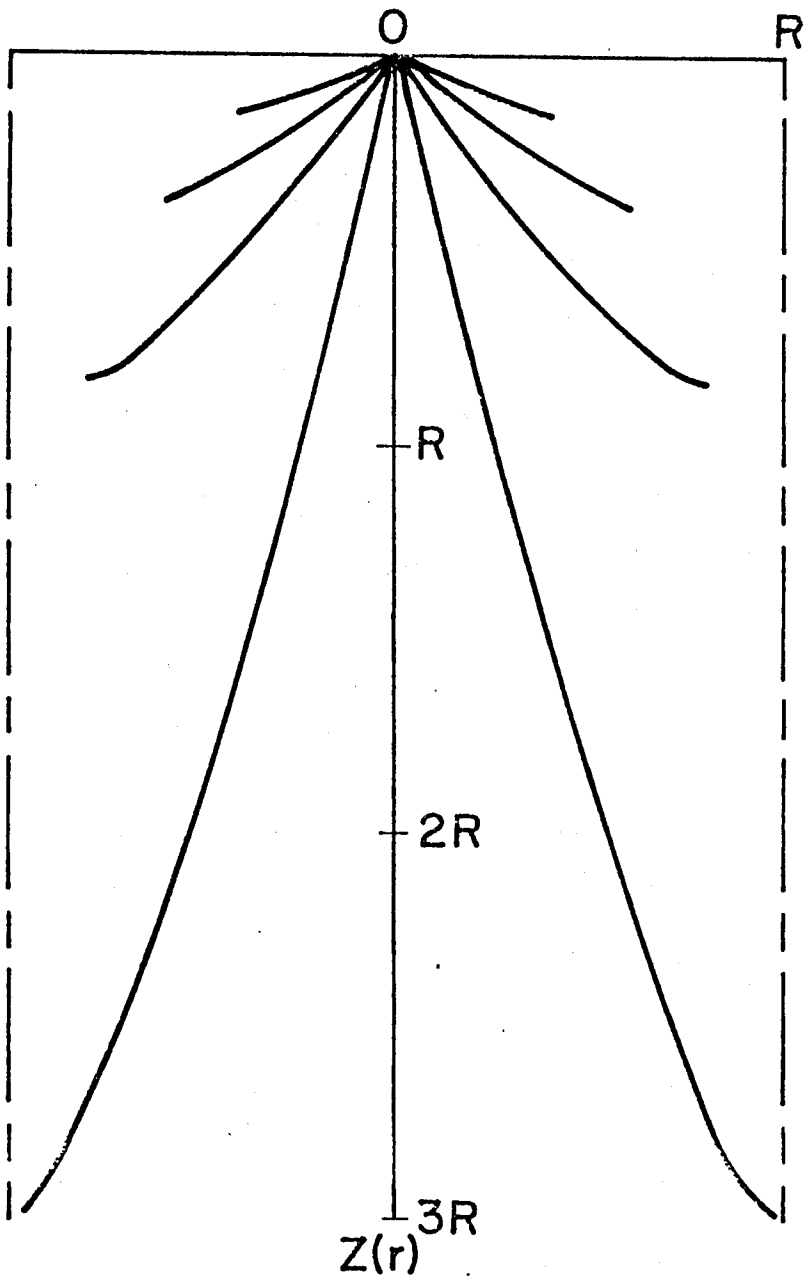

FIGURE I-9 ENERGY SINK SHAPE FOR A SOLID SPHERE EXPLOSION. R = PLASMA RADIUS

FIGURE I-10

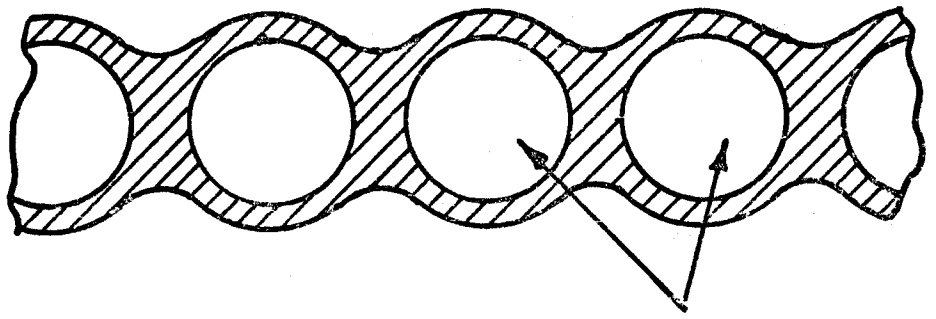

(A)

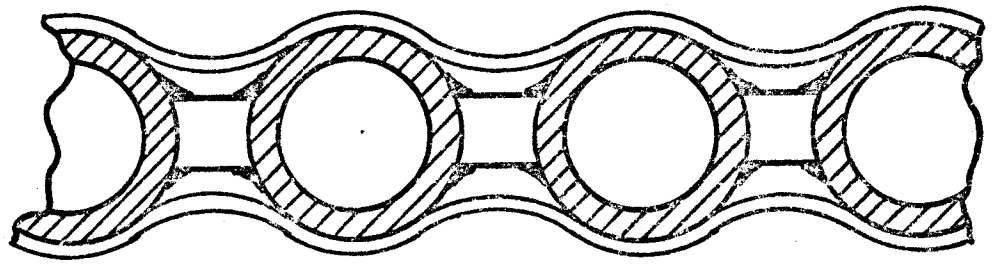

(B)

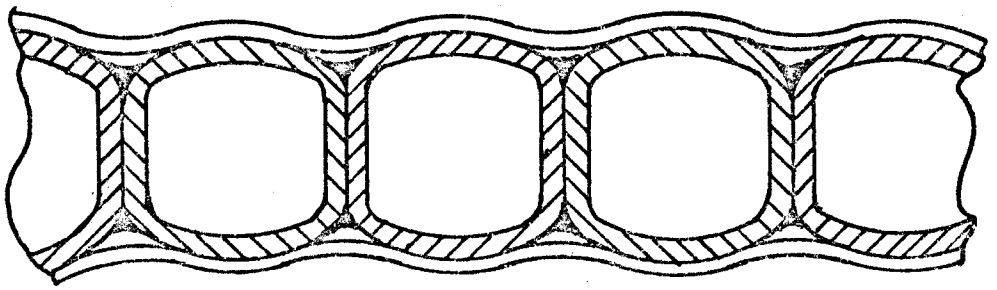

(C)

in great detail early on in the program and were abandoned in favor of the more efficient boiling mechanism. This is especially true in the end cap regions behind the collector plate of the charged particles where the heat flux is extremely high. The low-quality steam produced in the first wall is re-circulated via a steam drum. The saturated steam is used to cool the outer blanket surface where it is superheated before entering the intermediate pressure turbine. From the analysis presented in Chapter VI, the first wall is thus characterized by the parameters listed on Table I-8. One reason for utilizing boiling water is to produce an essentially isothermal system and the reasons for employing the 300°C temperature is related to neutron radiation damage and the desire for long first wall life at high wall loadings. This will be briefly discussed shortly but the more extensive treatment is given in Chapter VIII. Note here, however, the very important point that a 300°C first wall is possible in fusion systems because the blanket can be at higher temperatures. In fission reactors, a 300°C core temperature is unacceptable and those systems will have more severe radiation damage problems as a consequence.

A gravitational-flow lithium oxide blanket is used in our design and discussed in detail in Chapter VI. The merits of such a design for use in tokamak type reactors have been discussed by Sze, et al. of the University of Wisconsin. Here, approximately 75% of the total thermal power of the reactor is deposited in the blanket. The Li_2O microspheres serve the dual purpose of tritium breeding and heat transport. The particles enter the blanket from the top at 450°C. The stream is then divided into two breeding zones separated by a graphite reflector (Section VI.B). Approximately 98% of the Li_2O flows through the first breeding zone and leaves the blanket at an average temperature of

Table I-8

Parameters of First Wall

Material	Stainless Steel
Coolant	Boiling Water
Temperature	300°C
Coolant Flow Rate	~400 kg/s
Wall Thickness	1 mm
Pressure	1000 psia
Exit Quality	0.2
Exit Void Fraction	0.73
Maximum Heat Flux	39.4 W/cm^2
Thermal Stress	7.45 ksi
Hoop Stress	10 ksi

550°C. The remaining 2% flow through the second zone and are heated to 850°C; this high-temperature stream is used in the tritium extraction cycle (see Chapter IX).

The pressure within the blanket is kept at 1 atm; such low pressure allows the use of relatively thin structures to construct the blanket. Another advantage of this type of blanket is that Li_2O is a poor heat transfer medium. This allows the first wall to be operated at considerably lower temperatures than the Li_2O stream without transferring (i.e. degrading) too much heat to the first wall coolant. It also allows the steam-cooled back wall of the blanket to come in contact with the 850°C Li_2O in the second breeding zone without fear of the stainless steel wall ever exceeding the maximum safe temperature of 650°C.

The lithium oxide leaving the blanket is transported to the steam generator and back to the blanket. A gas-solid transport system is used to circulate the particles between the different components of the system.

The particle velocity distribution within the blanket is tailored to match the radial heat deposition curve determined from neutronics calculations and shown in Fig. I-11; faster flow is provided near the first wall where the volumetric heating is high. Higher velocities are also required near the graphite reflector to remove the heat generated within the graphite which is radiated and conducted to the Li_2O stream. The shaping of the velocity profile is accomplished by subdividing the blanket into different zones and maintaining the proper velocity within each zone by means of adjustable baffles at the exit. Other schemes for velocity shaping can be surmised.

A summary of the main thermal-hydraulic parameters of the blanket is given in Table I-9. The velocity distribution within the blanket and the

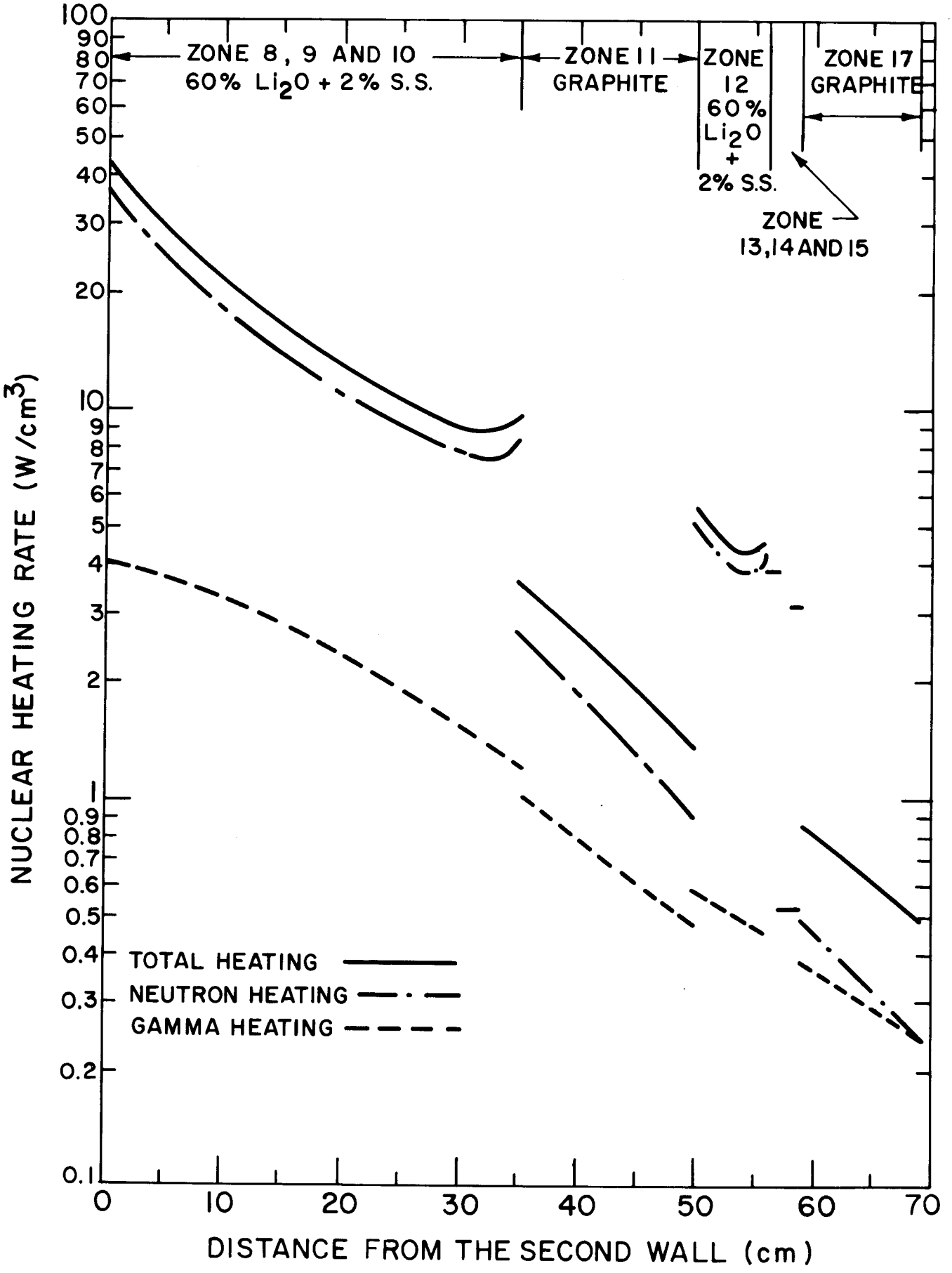
ZONE 8, 9 AND 10
60% Li_2O + 2% S.S.
ZONE 11
GRAPHITE
ZONE 12
60% Li_2O + 2% S.S.
ZONE 17
GRAPHITE
ZONE 13,14 AND 15
TOTAL HEATING
NEUTRON HEATING
GAMMA HEATING
NUCLEAR HEATING RATE (W/cm^3)
DISTANCE FROM THE SECOND WALL (cm)
100
90
80
70
60
50
40
30
20
10
9
8
7
6
5
4
3
2
1
0.9
0.8
0.7
0.6
0.5
0.4
0.3
0.2
0.1
0
10
20
30
40
50
60
70

Figure I-11

corresponding residence times have been determined. For the subregion immediately adjacent to the first wall, a trial and error solution is required to determine the necessary coolant velocity since the rate of heat transfer from that zone to the first wall coolant is dependent on the "effective" Reynolds number of the Li_2O stream. A viscosity of 1.5 cp is used to calculate Re for an equivalent continuum on the particles' side. The Dittus-Boelter correlation is used to determine the equivalent Nusselt number on the Li_2O side. The method of Deissler and Beogli is used to determine the effective thermal conductivity of the particles' stream and, hence, the heat transfer coefficient. Similar procedure is used to determine the rate of heat transfer from the second breeding zone to the steam-cooled back wall of the blanket. Heat transfer coefficients of 1.78 and 0.23 $kw/m^2\ ^oK$ are obtained at the front and back walls respectively.

The reasons for choosing the Li_2O gravitational flow blanket concept over other approaches are numerous but only a few reasons are given here. A summary of the advantages and areas of uncertainty are listed in Table I-10. The main advantages, particularly over the use of liquid metals, are a low tritium inventory, low chemical reactivity, and the potential for eliminating an intermediate loop. The advantages of Li_2O over other solid breeders include high temperature operating potential, adequate tritium breeding without a neutron multiplier like Be, and relatively simple tritium recovery.

The neutronics analysis of laser fusion reactor systems requires both time dependent and steady state methods of analysis. Steady state, or more accurately, time integrated neutronics are useful in providing integral parameters such as the tritium breeding ratio and the total energy produced per

Table I-9

Gravitational Flow Li_2O Blanket Design

Flow Parameters

Inlet Temperature	450°C
Outlet Temperature	550°C
Pressure	1 ATM
Flow Rate	
Average Flow Velocity	0.67 m/s
Void Fraction	0.40
Specific Heat	0.43 CAL/g°c
Equivalent Density	1.2 g/cm^3
Particle Size (Diameter)	0.1-0.2 mm

Table I-10

Advantages of Li_2O Flowing Blanket Concept

1. Low Tritium Inventory
2. Low Tritium Leakage
3. Adequate Breeding Without Be
4. Low Pressure Blanket
5. Low Structural Material Requirement
6. Reduced Thermal Fatigue
7. No Need for an IHX

Problem Areas Requiring Further Investigation

1. Li_2O Pellet Fabrication
2. Tritium Diffusion and Recovery
3. Thermodynamics of $Li_2O + H_2O$ System
4. Corrosion
5. Steam Generator Design
6. Solid Particle Circulation
7. Erosion and Attrition
8. Blanket Design for Abnormal Conditions

fusion neutron. Such an approach is also valuable for shield design and the analysis of leakage through ports in the system. On the other hand, effects that are rate dependent require a time dependent analysis of this basically pulsed neutron problem. This is especially true for materials radiation where displacement per atom rates can be the order of 1-10 dpa/s compared to 10^{-4} to 10^{-6} dpa/s in steady state magnetic confinement fusion devices and in fission reactors. Chapter VII contains the results of both steady state and time dependent neutronics analysis.

The schematic of the one-dimensional blanket model is shown in Table I-11. It consists of a 1.5 cm (50% dense) carbon liner (zone 3) two stainless steel walls of 0.1 cm each (zone 5 and 7) with a 1.8 cm thick, homogenized zone of 16% (volume) stainless steel and 84% (volume, 40% dense) water (zone 6) between a 35 cm cooling-breeding zone (zone 8, 9 and 10), a 15 cm graphite reflector (zone 11), and a 6 cm cooling-breeding zone (zone 12). The stainless steel zones are to approximate the water cooling tubes between the carbon liner and the first breeding zone as well as the second breeding zone and the graphite zone (zone 17). The cooling-breeding zones consist of Li_2O particles with 60% (volume) packing fraction and 2% (volume) stainless steel structure. The results of a time independent neutronics analysis are tabulated on Table I-12. The tritium breeding ratio in this design is 1.24 and the total nuclear energy per fusion is 15.07 MeV. Adding the 3.52 MeV alpha energy gives a total energy per fusion of 18.59 MeV. We have also begun to develop a Monte Carlo analysis capability to deal with inherently two-dimensional problems and the effects of laser beam ports. Preliminary results are reported in Chapter VII.

Table I-11

Neutronics Analysis - Material Composition

Zone Number	Thickness (cm)	Material Composition
1	0.1	Vacuum (Neutron Source)
2	499.9	Vacuum
3	1.5	Carbon Liner (50% dense)
4	1.0	Vacuum
5	0.1	Stainless Steel
6	1.8	16% Stainless Steel + 84% (40% dense) Water
7	0.1	Stainless Steel
8	15	60% Li_2O
9	10	+
10	10	2% Stainless Steel
11	15	Graphite
12	6	60% Li_2O + 2% Stainless Steel
13	1	Stainless Steel
14	1.8	16% Stainless Steel + 84% Water (Steam)
15	0.1	Stainless Steel
16	1	Vacuum
17	10	Graphite

Table I-12

Summary of Tritium Breeding, Radiation Damage Parameters and Nuclear Heating in the Laser Fusion Blanket

Tritium Breeding	
Tritium Production from $^{6}Li(n,\alpha)$	0.8228
Tritium Production from $^{7}Li(n,n'\alpha)$	0.4126
Tritium Breeding Ratio	1.2354
Atomic Displacement[a]	
Carbon Liner	1.2848×10^{-6}
Stainless Steel Wall	1.4580×10^{-6}
Helium Production[b]	
Carbon Liner	3.1164×10^{-4}
Stainless Steel Wall	2.9695×10^{-5}
Hydrogen Production[b]	
Stainless Steel Wall	8.2616×10^{-5}
Nuclear Heating[c]	
Neutron Heating	12.35
Gamma Heating	2.72
Total Heating	15.07

a. dpa per unit time interval (total number of neutrons produced equivalent to a fusion energy of 3×10^{3} MJ)

b. appm per unit time interval (total number of neutrons produced equivalent to a fusion energy of 3×10^{3} MJ)

c. in units of MeV per incoming 14.1 MeV neutron

Since laser fusion is a pulsed neutron system in which the neutron source duration is much less than the slowing down time of the neutrons, it is also necessary to examine the rate effects which may occur. The analysis of the blanket is carried out using the multigroup discrete ordinates computer code Time Dependent ANISN (TDA). This code was chosen over one using a Monte Carlo technique since a simple one-dimensional geometry is used and the main reason for using a Monte Carlo code is its capability of handling complex or multidimensional geometries. A spherical geometry is used to simulate the midplane of the cylindrical vessel which is the region receiving the highest flux and thus incurring the most damage. A sphere also allows the use of a point source. This is the most realistic source for this calculation since the flux from a pellet explosion falls as $1/r^2$ as it approaches the wall. If a cylindrical geometry was chosen, a line source must be used which decays as $1/r$. An analysis of time of flight spreading of the neutron arrival time at the first wall has been derived based on the fact that the average 14 MeV neutron pulse has an energy spread of about 1.7 MeV fwhm. Thus, the neutrons arrive at r = 5m spread in time over about 10 ns. This is quite important since the neutron production time is only about 10 ps. Using this time dependent neutron source, time dependent neutron transport calculations were performed to provide input for radiation damage. The detailed results are given in Chapter VII and the radiation damage analysis is given in Chapter VIII. The neutron radiation environment for the first wall and all other structural materials between the liner and the blanket differs in two distinct ways from the neutron radiation in fission reactors: a major part of the neutron spectrum consist of 14 MeV neutrons, and this component is pulsed. Therefore, during a very short time interval of 10 nsec displacements are produced at a very fast rate, i.e. 2.6 dpa/sec in the first wall. The form of the damage

produced by 14 MeV neutrons consists of larger cascades compared to those generated by fast neutrons in a breeder reactor. Furthermore, the gas production rate via (n,α) reactions is also substantially higher than in a breeder reactor.

Since there are no data available at this time on irradiation effects of pulsed 14 MeV neutrons, a theoretical assessment of possible radiation effects was made in conjunction with experimental data which cover some aspect of this particular irradiation environment. It should be noted at the outset that we have an incomplete understanding and only a sketchy theoretical description of the radiation damage even for steady-state neutron irradiations in fission reactors. The various attempts described in Chapter VIII to assess the radiation effects in inertially confined fusion reactors only delineate the possibilities and limitations that may exist for the design of these future reactors. Furthermore, the various attempts were not designed to be mutually consistent, but rather to approach the problems from different viewpoints. We have nevertheless discovered some striking indications that damage at low temperatures ($< 350^{o}C$) may be much less severe than at higher temperatures (> 400-$450^{o}C$). These findings are applicable to both inertial and magnetic confinement systems and thus holds out the possibility of high wall loadings and long wall lifetimes. It is these findings which have governed the choices of first wall and blanket temperatures and since the results may have such a strong impact on ultimate economic feasibility, we describe them here and more extensively in Chapter VIII.

Based on details discussed on Chapter VIII, it is found that the release of vacancies from radiation produced cascades is so slow that one should not expect any difference in pulsed or steady-state irradiations for processes which are controlled by the vacancy kinetics. The swelling rate when averaged over many

pulses is expected to be very similar to steady state irradiations. Accordingly, we adopted the viewpoint with regard to swelling at low temperatures ($T < 550°C$), that its rate is independent of the pulsed nature and the gas production rate and is determined by the average point defect production rate, P, and the irradiation temperature, T.

The incubation dose for swelling is strongly dependent upon the gas production rate. This viewpoint is also suggested by the extensive observations on the variability in the swelling behavior of type 316 stainless steel. Differences in heat treatment and cold-working in the reactor environment (and even in the irradiation source) primarily affect the incubation dose for swelling. However, the steady-state swelling rate is changed little by these variables. It has also been observed that the microstructure (i.e. in particular, the dislocation density) becomes very similar in the steady-state swelling regime although it may have been different initially. The steady-state density of the microstructure is a strong function of the temperature. Based on the observations of Brager and Straalsund, the total sink density (i.e. dislocations, loop, and voids) is assumed to be given by

$$L[cm^{-2}] = \{1.35 \times 10^{-9} \exp(-E_1/kT) + 6.67 \times 10^{-3} \exp(-E_v^m/kT)\}^{-1} \quad (1)$$

where $E_1 = 0.3$ eV and $E_v^m = 1.4$ eV is the vacancy migration energy. Fig. I-12 shows the total sink density L as a function of temperature.

If N_o is the void concentration and r the average radius, then the swelling rate is given by

$$4\pi N_o r^2 \frac{dr}{dt} = \Omega \left(\frac{1}{4\pi N_o r} + \frac{1}{\rho}\right)^{-1} \{\delta Z \Psi - D_v (C_v^o - C_v^{eq})\} . \quad (2)$$

FIGURE I-12

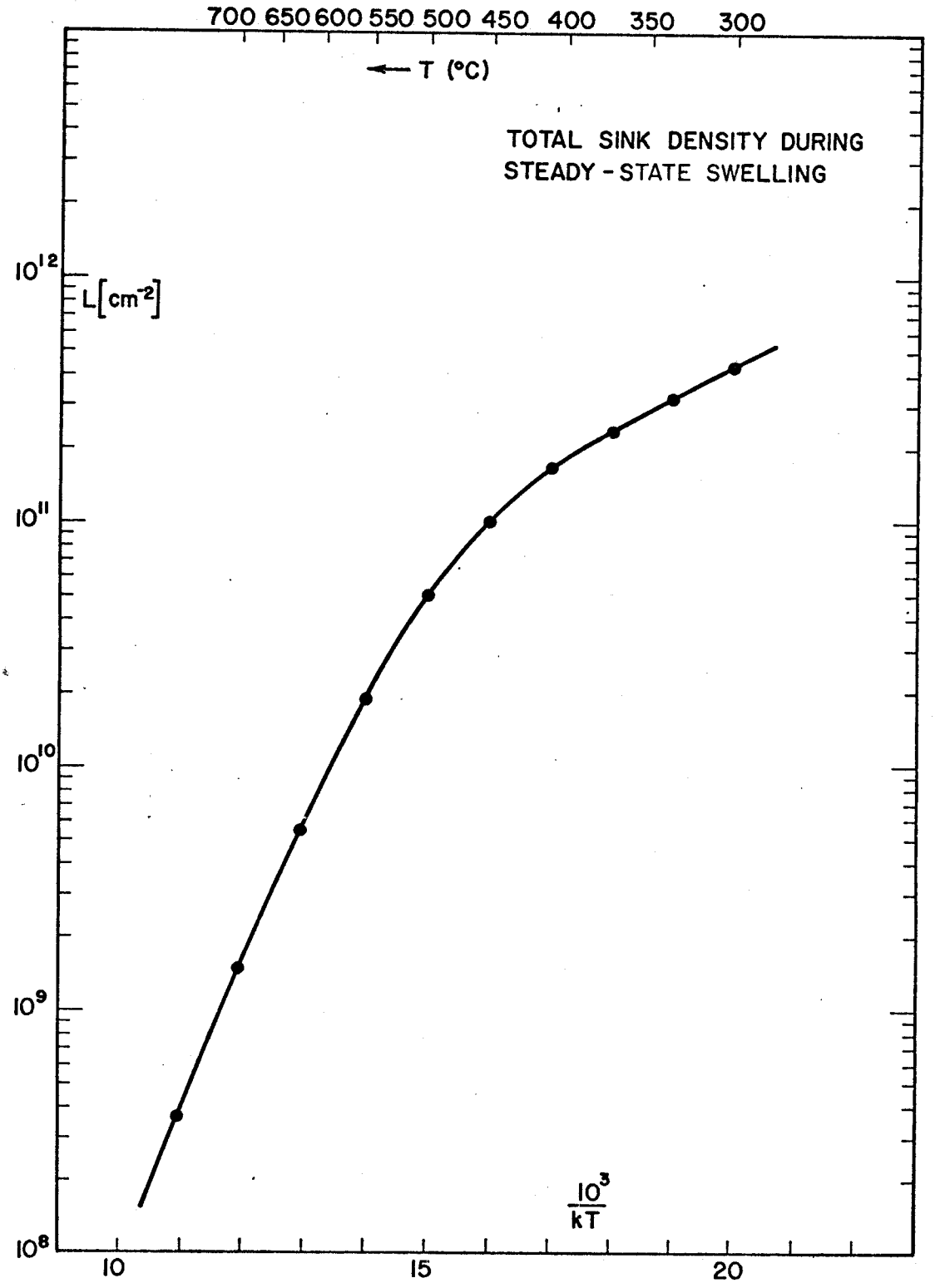
700 650 600 550 500 450 400 350 300
T (°C)
TOTAL SINK DENSITY DURING
STEADY - STATE SWELLING
10^{12}
L[cm^{-2}]
10^{11}
10^{10}
10^{9}
10^{8}
$\frac{10^3}{kT}$
10
15
20

Here, ρ is the dislocation density (including loops), i.e.,

$$L = 4\pi N_o r + \rho \ , \tag{3}$$

and

$$C_v^o = C_v^{eq} \exp \{(\frac{2\gamma}{r} - pg) \frac{\Omega}{kT}\} \tag{4}$$

is the vacancy concentration in equilibrium with the voids. γ is the surface energy, pg the gas pressure, Ω the atomic volume, δZ the bias. Ψ is given by

$$\Psi = \frac{L}{2\kappa} \{[(1 + \frac{\kappa}{L} D_v C_v^{eq})^2 + 4P \frac{\kappa}{L^2}]^{1/2} - (1 + \frac{\kappa}{L} D_v C_v^{eq})\} \tag{5}$$

and

$$\kappa = 10^3 \ \Omega^{-2/3}/D_v \tag{6}$$

is the recombination coefficient. To fix the bias, δZ, and the void density N_o, we assume that $4\pi N_o r = 10^{10}$ cm^{-2} at T = 500°C when steady-state swelling is reached. The steady-state swelling rate of SS 316 in EBR-II at this temperature is about 1% per $\phi t = 10^{22}$ n/cm^2/sec. The point defect production rate is estimated to be $P = 10^{16}$ Frenkel pairs/cm^3/sec or 5.6×10^{-7} dpa/sec. At this temperature we may neglect the annealing term in Eq. (2). Then, δZ was determined to be 0.033 or 3.3%.

Next, we assume that $4\pi N_o r$ remains the same for steady-state swelling at all temperatures and computed the swelling rate for T below 500°C. The results are given in the second column of Table I-13, and the rates are in good agreement with the observed rates for CW 316 stainless steels irradiated in EBR-II. In fact, the selection of the temperature dependence of L is

made to achieve this agreement over the temperature range from about 370°C up to 550°C, where sufficient data are available. This particular fitting of a swelling rate model to the data is adopted in order to predict swelling at temperatures below 370°C. It is felt that an uncritical use of the swelling correlation used for fast reactors is inappropriate here, since the incubation dose for swelling in EBR-II is rather large, i.e. around 40 dpa. However, the irradiation results from HFIR already give substantial swelling at 40 to 50 dpa. Indeed, in order to predict the swelling of 20% CW 316 at T = 380°C as observed in HFIR based on the rates listed in the second column of Table I-13, a zero incubation dose must be assumed. However, the irradiation results at 450°C in HFIR indicate that an incubation dose of 40 dpa is needed just as in ERB-II. It should be noted that this is coincidental since the particular material used in HFIR irradiations has a much larger incubation dose if irradiated in EBR-II.

A rather pessimistic estimate of the swelling rate at low temperatures can be made by assuming that the void sink density, $4\pi N_o r$, is always equal to the dislocation density ρ. It is easy to show that Eq. (2) then gives the maximum swelling rate, i.e.

$$\dot{S} \leq \frac{\Omega L}{4} \delta Z \Psi \ . \qquad (7)$$

Although this condition may prevail at the temperature for peak swelling (~500°C), it is usually not observed at lower temperatures for 316 stainless steel. Nevertheless, using this assumption and Eq. (1) for L, swelling rates as listed in the third column of Table I-13 were computed.

In the forth and fifth column are listed the estimated nominal and maximum swelling rate for the midplane of the first wall in SOLASE-I. Note that the EBR-II damage rate is 5.6×10^{-7} dpa/sec, whereas the dose rate here is 1.614×10^{-6} dpa/sec; therefore, the recombination is higher for a larger dose rate and the swelling rate per dpa correspondingly lower.

The swelling in % per year for the midplane of the first wall is given in Table I-14 computed from the swelling rates. It is assumed that no incubation period exists and that swelling is linear with dose. For a first-wall temperature of 300°C the nominal swelling is expected to be around 10% for a plant-life of 30 years. The maximum swelling could be expected to reach 30%. Since the maximum wall loading is 7.65 MW/m^2, this would correspond to a material lifetime of about 230 $MW\text{-}yr/m^2$, an obviously very large value. Note, however, that earlier estimates made at Wisconsin and elsewhere of wall lifetimes of 2-6 $MW\text{-}yr/m^2$ were for operating temperatures of 500°C and above. The results shown in Table I-14 are consistent with these earlier estimates and show the strong motivation to operate components in high fluxes at low temperatures.

The large amounts of helium atoms produced by the fusion neutrons raises the possibility that helium alone could lead to large volume changes even if it were not contained in gas bubbles but was incorporated only in the crystalline lattice. The distortion of the lattice around the helium atoms changes the lattice parameter and hence the volume of the crystal.

To evaluate this, we used the recent calculations by Johnson et al. on the relaxation volume of helium atoms in bcc metals. Their results are summarized in Table I-15.

Table I-13

Swelling Rates in %/dpa

	In EBR-II		In Solase-I	
T(°C)	nominal	maximum	nominal	maximum
250	0.003	0.016	0.0017	0.0095
300	0.010	0.035	0.0063	0.0205
350	0.027	0.066	0.0182	0.0392
400	0.059	0.113	0.0424	0.0666
450	0.109	0.167	0.0844	0.0994
500	0.195	0.212	0.1248	0.1576

Table I-14

Swelling in %/yr in Solase-I

T(°C)	nominal	maximum
250	0.086	0.484
300	0.323	1.040
350	0.925	1.994
400	2.156	3.389
450	4.297	5.061
500	6.352	8.024

Table I-15

Volume Changes for He Atoms in bcc Metal in Units of the Atomic Volume of the Host Metal

Metal	V	Fe	Mo	Ta	W
Substitutional	0.88	1.21	0.93	0.74	0.85
Interstitial	0.39	0.93	0.46	0.44	0.56

The helium production in the first wall is 7.82×10^{-4} He atoms/year/host atom. Assuming that all He atoms are in substitutional positions and that each occupies the volume of 1.21 host atoms, the volumetric expansion rate is

$$\frac{d}{dt} (\Delta v/v)_{SHe} = 9.46 \times 10^{-4}/\text{year} . \quad (8)$$

For a 30 year operation time with a plant availability of 75%, we obtain

$$(\Delta v/v)_{SHe} = 2.13\% . \quad (9)$$

It should be noted that although a helium concentration of 1.76% is large, it is still an order of magnitude lower than the critical concentration at which blistering takes place in He-ion bombardments of metals. There, a critical He fluence of 10^{18} He/cm^2 is needed before blistering or gas-release is observed. For an ion energy of 300 keV the penetration depth is about 10^{-4} cm. Hence, the critical concentration of He in the bombarded layer is of the order of 10^{22} He atoms/cm^3 or about one helium atom for every ten target atoms. As a result, it appears that even over 30 years at 7.65 MW/m^2, the swelling due to He buildup for steel operating at 300^{o}C will be about 2% and less than that due to displacement damage. Thus, the results on extended wall life remain strikingly positive. Clearly, more experimental work on low temperature irradiations is needed to confirm this analysis.

In summary:

1) Simple considerations of the mobility of interstitials and vacancies show that vacancies remain in their collision cascades for many pulses. Hence, time-averaged displacement rates can be used to make an assessment of swelling rates and irradiation creep rates at low temperatures.

2) Nominal swelling predictions indicate that the first wall could be run at an operating temperature of 300°C and only swell about 10% during the plant's life.

3) The upper estimate of swelling at 300°C gives a total swelling of 30%.

4) For comparison, if the first wall were operated at 500°C, a nominal swelling of about 12% would be reached within about 2 years.

5) The low-temperature embrittlement of the first wall due to radiation hardening results in a low fracture toughness. To prevent rupture of the tubes in the first wall, surface flaws must be smaller than about 5×10^{-3} cm.

Finally, we have begun to consider the tritium and power cycle integration problems and these are discussed in Chapters IX and X. The pathways of tritium in the entire plant have been identified including tritium breeding, extraction, recycle and loss to the environment. These are shown in Fig. I-13. The exact construction of the D-T pellet and its method of insertion into the reactor with the required accuracy and frequency is unknown at this time. The data in Table I-15 on the deuterium and tritium mass requirements for fueling this plant are based on an energy yield/pellet of 150×10^{6} joules and an energy yield/fusion event of 2.93×10^{-12} joules (18.3 MeV). The number of fusion events/pellet is then 5.1×10^{19} and since the D and T are consumed one for one, this is also the number of D and T atoms consumed per shot. The mass of fuel atoms consumed and recycled per day is based on a rep rate of 20/sec and a fusion efficiency of 6%. These calculations do not take into account misfirings which would add to the recycle burden and the total mass of D and T fabricated as pellets/day.

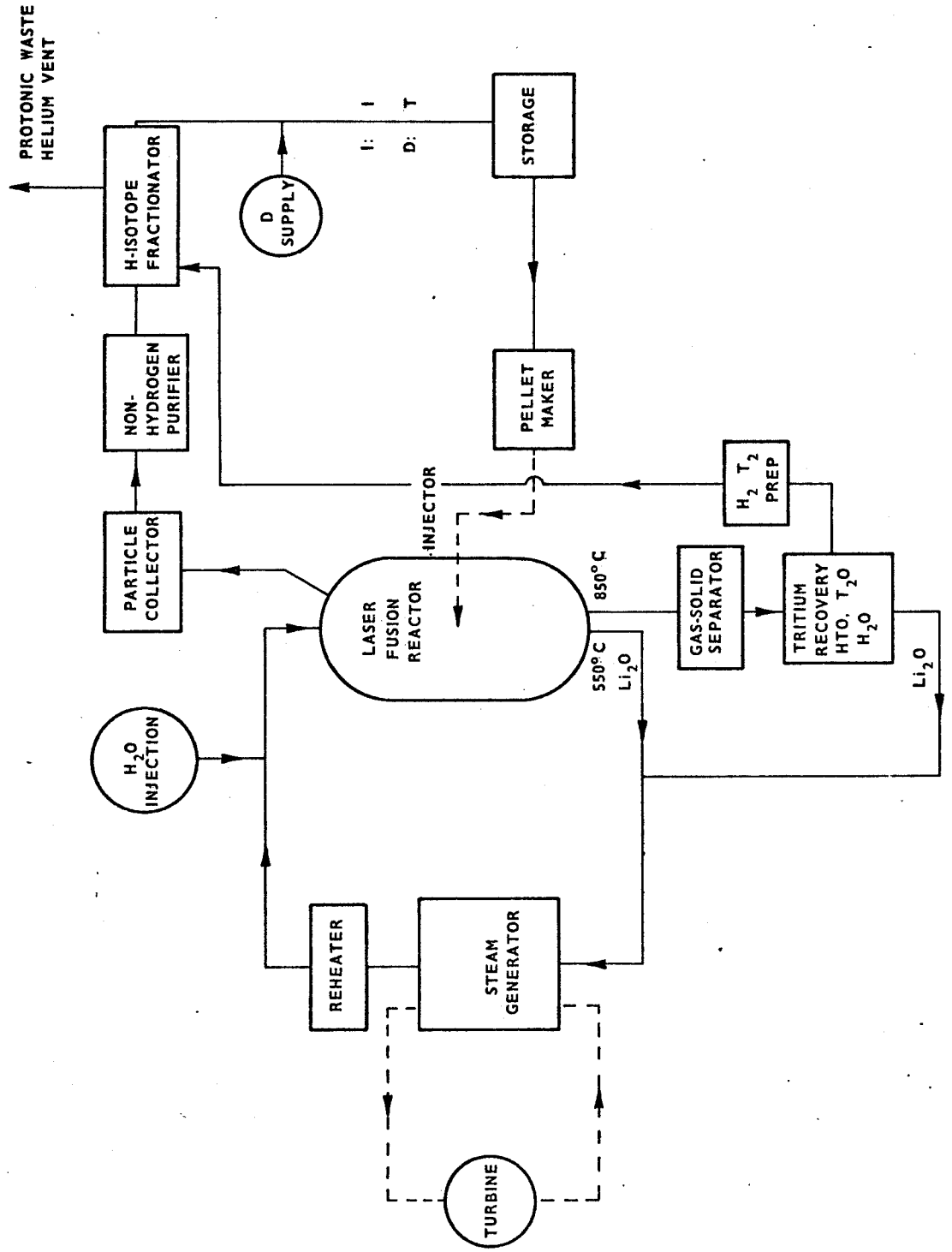

FIGURE I-13

TRITIUM PATHWAYS IN LASER FUSION PLANT

Table I-15

Deuterium-Tritium Fuel Requirements

	D	T
Moles consumed/day	145	145
kg consumed/day	0.290	0.435
kg recycled/day	4.83	7.25
kg fabricated/day	5.12	7.685

This completes a broad overview of work reported in the following chapters. Many topics were not mentioned or mentioned but not described in detail so the reader is encouraged to read specific chapters for details on topics of interest.

II. Laser Fusion Physics

II-A. Pedagogy

II-A-1. Introduction to General Ideas of Inertial Confinement

The laser driven fusion concept of CTR[1-3] relies on the inertia of the fuel itself to provide confinement while laser beams supply the energy to bring the fusion fuel to thermonuclear conditions. The confinement time is dictated by the disassembly time of the fuel which in turn is determined by the size of the fuel assembly. For fuel in the form of a sphere the disassembly time is approximately

$$\tau_d = R/C_s$$

where R is the radius of the sphere and C_s is the isothermal sound speed (which is independent of density). The necessary energy required to achieve thermonuclear conditions (10 keV ion temperature) is determined by the amount of fuel mass in the spherical assembly. It will be demonstrated later that these two criteria for successful inertial confinement fusion (fuel size and fuel mass) are intimately related.

The most meaningful figure of merit for inertial confinement fuel assemblies is the product of fuel density and fuel radius, ρR, rather than the customary density-energy confinement time product, $n\tau$. The density-radius product can be interpreted in several equivalent ways. If thermonuclear burn efficiency of a fuel pellet is expressed as the ratio of characteristic dissassembly time to thermonuclear burn time, then this ratio is proportional to ρR, namely

$$\tau_b = \frac{1}{(\overline{\sigma v})\ \rho/m_i}$$

and

$$\tau_d/\tau_b = \rho R\ \overline{\sigma v}/C_s m_i \ .$$

For deuterium-tritium fuel (the most reactive fusion fuel) at 20 KeV $\overline{\sigma v}/C_s m_i \approx 1$ so that the ρR product should exceed 1 to provide good efficiency. To sustain the burn the fuel temperature must be maintained at 20 KeV or greater by redeposition of energy from the thermonuclear reaction products. In the case of DT fuel this is a 3.5 MeV alpha particle. Thus the fuel must be characterized by a "size" that is in excess of the range of a 3.5 MeV alpha particle. The density independent range of a 3.5 MeV alpha particle in a 20 KeV DT plasma is about 0.3 gram/cm^2. Hence the ρR value of the fuel must exceed 0.3 g/cm^2 and computer calculations show that ρR = 3 g/cm^2 is about the optimum value for the fusion fuel.

The density-radius product can be related to the original mass and radius criteria by

$$\rho R = \frac{M}{\frac{4}{3}\pi R^3} R = \frac{3}{4\pi} \frac{M}{R^2} \ .$$

The pellet heating requirements can be relaxed from the above analysis by thermonuclear burn propagation.[4] Only the central pellet core corresponding to ρR = .3 g/cm^2 need be heated to 10 KeV. The remainder of the pellet may be compressed at a cold temperature. The thermonuclear burning will start in the inner hot micro core, quickly self heat the micro core to 20 KeV and then burn outward in a wave consuming the remainder of the core. This burn wave can greatly reduce the laser energy necessary to achieve a fixed yield as will be demonstrated in the following section.

II-A-1-a. Laser Requirements for Laser Fusion

The necessary conditions to promote efficient thermonuclear burning have been established and now the energy necessary to achieve these conditions must

now be obtained and related to the thermonuclear energy yield to determine under what conditions inertial confinement fusion becomes attractive from an energy gain point of view. This can be done by relating the input (laser) energy to the plasma thermal energy via an efficiency ε and by also relating the thermonuclear yield energy to the plasma thermal energy by a multiplication factor β that accounts for thermonuclear burn propagation[5]. Define

$$G_p \equiv E_{fusion}/E_{laser}$$

$$\varepsilon \equiv E_{plasma}/E_{laser}$$

$$E_{fusion} = \beta \frac{4}{3}\pi R^3 n^2 \overline{\sigma v} \tau_d$$

$$\tau_d = R/C_s$$

n = plasma density

C_s = isothermal sound speed

R = plasma radius

$\overline{\sigma v}$ = fusion reaction rate

Combining these terms gives an expression for the laser energy as a function of pellet energy gain, coupling efficiencies and the volumetric compression of the fuel[3,5].

$$E_{laser} = \frac{G_p^3}{(\varepsilon\beta)^4} \frac{1}{\eta^2} (x)\ 1.6\ MJ$$

$\eta = n/n_{solid}$ - compression factor

To reach energy breakeven ($G_p = 1$) at solid DT density ($\eta = 1$) assuming $\varepsilon\beta = 1$ requires a laser energy of 1.6 MJ. For reactor applications the gain must be about 100 to compensate for power plant inefficiencies so that in this

case $E_{laser} = 1.6 \times 10^6$ MJ. This laser energy is far in excess of any conceivable laser system. If, however, the pellet can be compressed to ten thousand times solid density ($\eta = 10^4$) then the necessary laser energy for a reactor is 16 kilojoules.

$$E_{laser} = \frac{(100)^3}{(1)^4} \frac{1}{(10^4)^2} \times 1.6 \text{ MJ} = 16 \text{ KJ}$$

This laser energy is within reach of lasers in the planning stage today. However, more detailed analysis will show that this simple argument is too optimistic by probably an order of magnitude or more because η and ε are in fact not independent parameters. Two observations should be made about this formula.

(i) Increasing the value of η has implicitly reduced the amount of mass being compressed. In other words, the same ρR value is achieved by compressing a smaller amount of fuel. Hence, with the gain held fixed at 100 the lower laser energy requirement really is the result of less fuel mass.

(ii) The laser-plasma coupling efficiency is typically 5% with the remaining 95% of the laser energy used to compress the fuel pellet. The multiplication factor (β) accounting for thermonuclear burn propagation must then be 20 to give $\varepsilon\beta = 1$. Such multiplication is only feasible for fuel masses greater than or equal to one milligram.

These additional constraints must be satisfied when defining fuel pellet requirements for power plant applications. This will be done in section II-A-2.

II-A-1-b. Implosion Scenario

The next step is to identify how laser beams can, in fact, compress and heat a pellet of fusion fuel by following through an implosion scenario.

A small (one millimeter), spherical drop of liquid deuterium-tritium fusion fuel is irradiated uniformly over its surface with light from a high power

laser source. The outer surface of the droplet heats, ionizes and ablates outward. The electrons in this cloud of plasma continue to absorb more laser radiation via inverse bremsstrahlung. The laser radiation is only able to penetrate into the plasma up to the "critical density" where the electron plasma frequency is equal to the incident laser frequency. The transport of energy from the critical density inward occurs via the mechanisms of thermal conduction and hydrodynamic motion. As the plasma surface is heated and ablates outward (blow-off) a shock front is formed that converges (implodes) inward toward the center, pushing cold D-T fuel ahead of it to higher and higher densities along a Fermi degenerate adiabat (Figure 1). Figure 1 distinguishes three regions in the plasma during the implosion process. Beyond the critical density (Region III) the underdense plasma absorbs the laser energy and expands outward. Between the shock front and the critical density (Region II), electron thermal conduction is the dominant mechanism transporting energy from Region III in to the ablation surface. Inside the ablation surface (Region I) the D-T fuel is compressed along a low adiabat ($\sim$ 1 ev) to very high densities. When the shock fronts finally converge together at the center of the pellet, the central part of the dense pellet core is shock-heated to thermonuclear temperatures (Figure 2). This central hot spot or microcore must have a density-radius product of 0.4 g/cm^2 to initiate bootstrap heating and the entire core must have ρR = 3 g/cm^2 to provide significant yield and gain. The μ core will then self-heat to 20 KeV or more and the alpha particle reaction products will heat the next thin layer of surrounding plasma, raising its temperature to thermonuclear values. As this process continues a burn wave will propagate outward, consuming the dense pellet core. The idea is thus to adiabatically compress the D-T fuel to ρR = 3 g/cm^2 and then ignite the central microcore. Detailed calculations indicate that such a scenario might be possible utilizing a very precisely

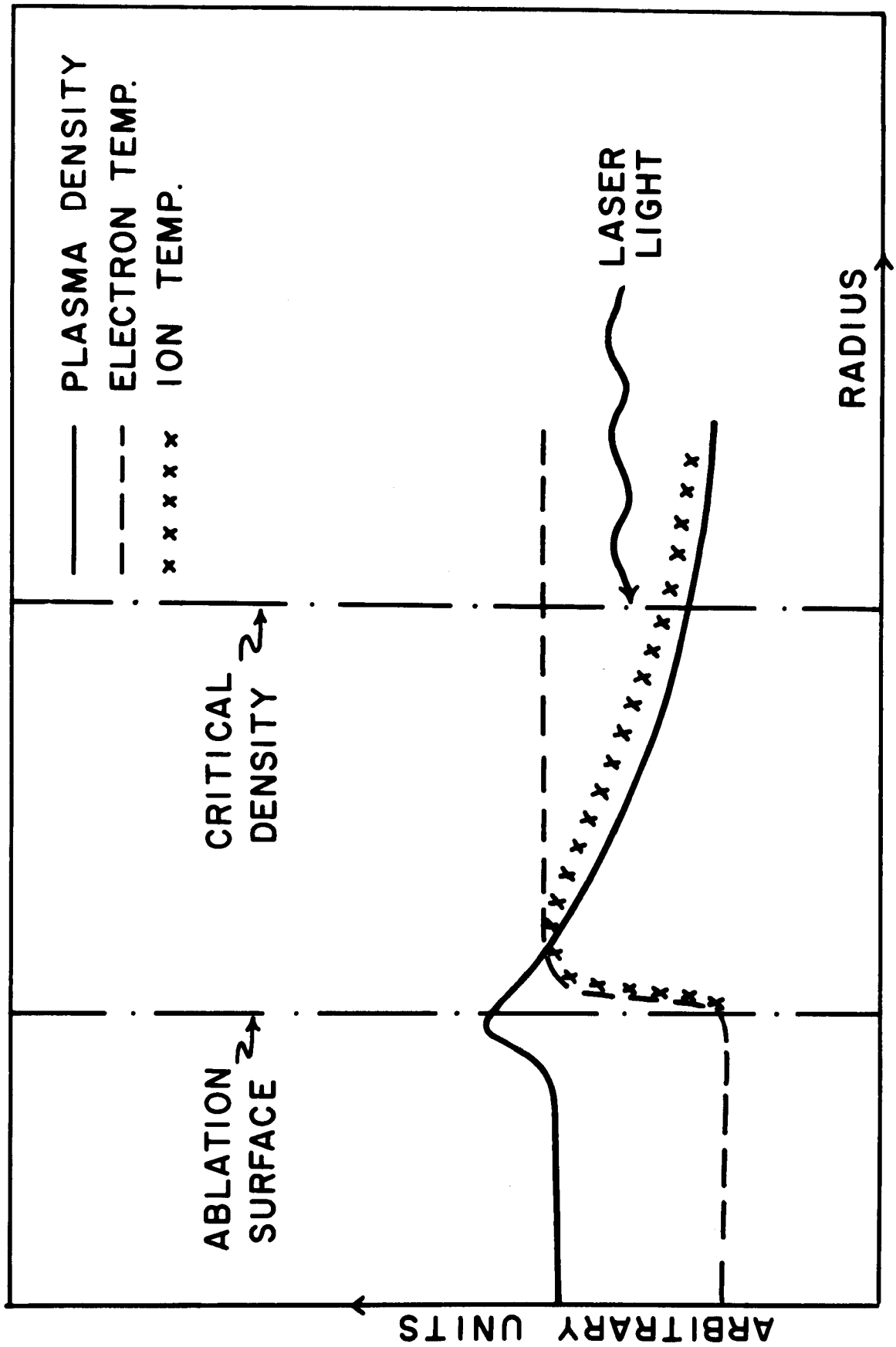

LASER-PELLET INTERACTION SCENARIO

FIGURE II-A-1-1

FIGURE II-A-1-2

PROPAGATING BURN FROM 10keV MICROCORE

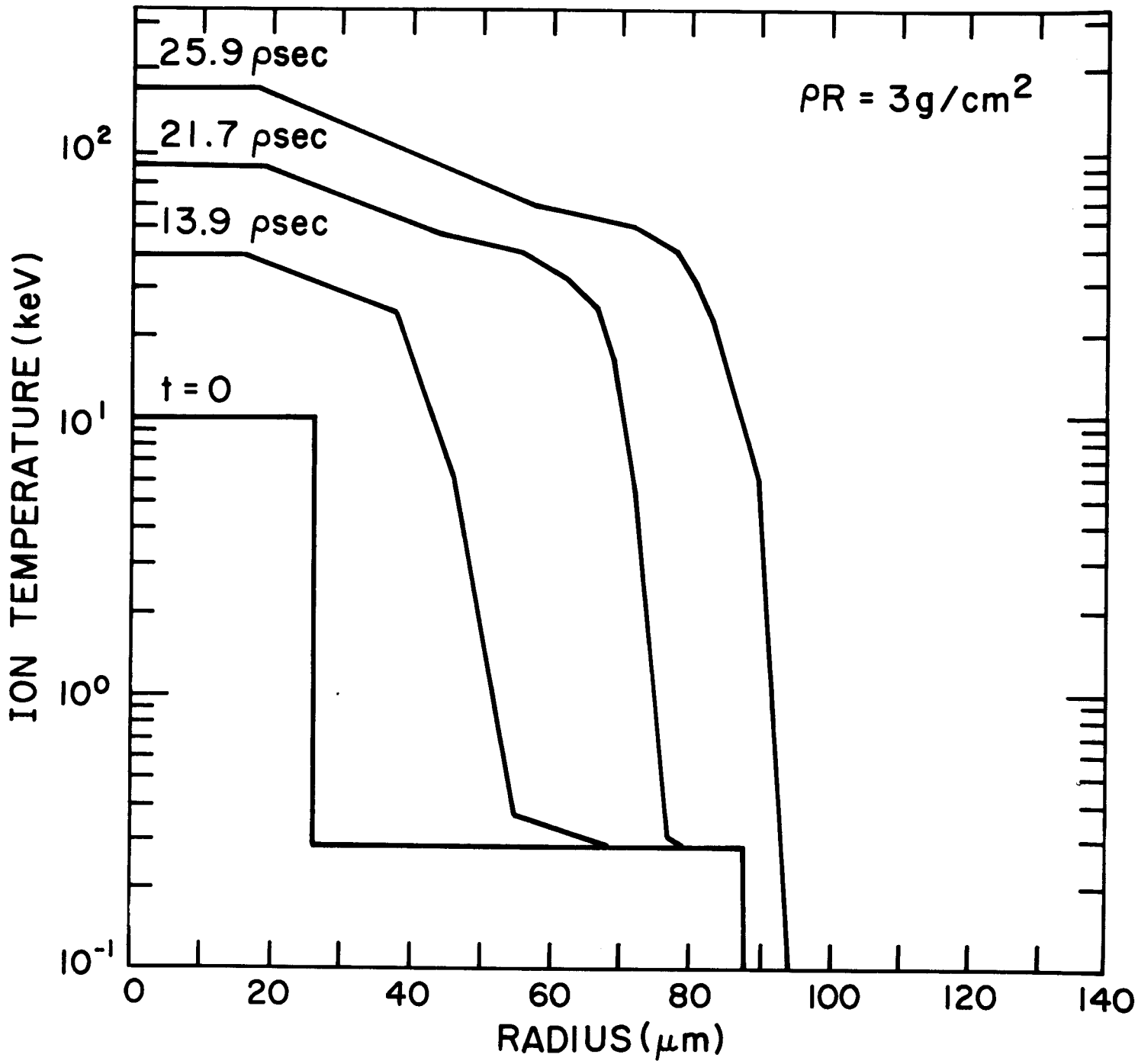

programmed laser pulse. The simple theory of homogeneous isentropic compression[6,7] shows that the laser pulse should take the general form

$$P_L(t) = P_L(o)\ [1 - t/t_o]^{-p}$$

where t_o is approximately the collapse time of the shock front and $p \simeq 2$. The detailed calculations show that this pulse is in fact nearly the ideal form[8]. The laser pulse must deliver energy to the plasma at the proper rate to preserve the delicate relation between the electron temperature front and the converging shock front (see Figure 1). The temperature front must propagate inward at the proper speed to drive the shock front ahead of it. Should energy be added too quickly the electron temperature front will race ahead of the shock, preheat the core, and degrade or destroy the implosion. Should energy not be delivered at a high enough rate the shock front will not have sufficient strength to compress the plasma to high densities.

The proper laser pulse shape is thus very dependent on plasma properties such as thermal conductivity, laser light absorption, and equation of state. The physical models used to describe the laser-pellet implosion and burn will be discussed in sections II-A-3 to II-A-6.

References II-A-1

1. J. Nuckolls, L. Wood, A. Thiessen, and G. Zimmerman, Nature 239, 139 (1972).

2. J. Clarke, H. Fisher, and R. Mason, Phys. Rev. Lett. 30, 89 (1973).

3. K. Brueckner and S. Jorna, Rev. Mod. Phys. 46, 325 (1974).

4. G. Fraley, E. Linnebur, R. Mason, and R. Morse, Phys. Fl. 17, 474 (1974).

5. R. Kidder, in Fundamental and Applied Laser Physics, (Wiley, New York, 1973).

6. R. Kidder, Nuc. Fus. 14, 797 (1974).

7. R. Kidder, Nuc. Fus. 16, 3 (1976).

8. A. Thiessen, G. Zimmerman, T. Weaver, J. Emmett, J. Nuckolls, and L. Wood, UCRL-74802, 1973.

II-A-2-a. Efficiencies and Pellet Gain Requirements for Laser Fusion Reactors

The relationship between target gain and system efficiency is an important one when there are several subsystems with low efficiency. In laser-induced pellet fusion, the laser itself is a key subsystem which has a low anticipated efficiency. To determine the level of target gain required, we proceed by defining the gain of a pellet fusion target by

$$G = \frac{E_F}{E_{LAS}} \quad , \tag{1}$$

where E_F is the total thermonuclear energy produced and E_{LAS} is the incident energy onto the target. The energy absorbed by the target, E_A, is related to E_{LAS} by

$$E_A = \eta_c \, E_{LAS} \tag{2}$$

where η_c is the coupling efficiency, i.e., the fraction of incident laser light absorbed by the pellet. Let us define three additional efficiencies:

η_L = laser efficiency

n_{th} = gross plant thermal efficiency

n_p = net plant thermal efficiency.

Then the gain is given by

$$G = \left[\frac{1}{\eta_L \, (\eta_{th} - \eta_p)} \right] - 1 \, , \tag{3}$$

while the net plan efficiency is given by

$$\eta_p = \eta_{th} - \frac{1}{\eta_L (G+1)} \, . \tag{4}$$

Thus, we can determine the pellet gain required to achieve a certain net plant efficiency, η_p, for a system with a laser efficiency, η_L, and a gross power cycle efficiency η_{th}. (This assumes the laser energy dominates the recycle power requirements.)

The fraction of gross electrical power recycled to keep the laser operating is

$$F_R = \frac{1}{\eta_L \, \eta_{th} \, (G + 1)} \quad . \tag{5}$$

An engineering breakeven condition can be defined as the value of gain, denoted $\bar{G}$, for which $F_R = 1$. $\bar{G}$ is given by

$$\bar{G} = \left(\frac{1 - \eta_L}{\eta_L} \right) \quad .$$

Scientific breakeven, on the other hand, is defined as $G \equiv G_S = 1$. Clearly, $\bar{G}$ can be substantially greater than G_S.

The gain required to achieve a given value of $(\eta_{th} - \eta_p)$ for various values of η_L is shown in Fig. 1. Typically, $\eta_{th} - \eta_p$ is no larger than 0.3 since at this value, η_{th} must be 60% to allow a net plant efficiency of only 30%. In general, η_{th} is between 35 and 50% so that we would consider $(\eta_{th} - \eta_p)$ values of 0.1 to 0.15 interesting with larger values quite difficult to achieve. The analysis shows clearly that for reasonable values of η_L like 10%, the gain required for engineering breakeven is 9 and the gain required to achieve $(\eta_{th} - \eta_p)$ of 0.1 to 0.15 is between 65 and 100. Close examination of these simple relationships shows clearly that for most cases of practical interest, pellet gain values in the range of 75-100 and higher will be required. Such gains have been reported in the literature (Figure 2). We see that in general gain increases with higher yield and that a gain of 75-100 is associated with yields of about 100 MJ, which is in the necessary range. However, some of these more optimistic results have been obtained from high aspect ratio shell targets and the feasibility of imploding such shells without suffering hydrodynamic instabilities is questionable.

FIGURE 1

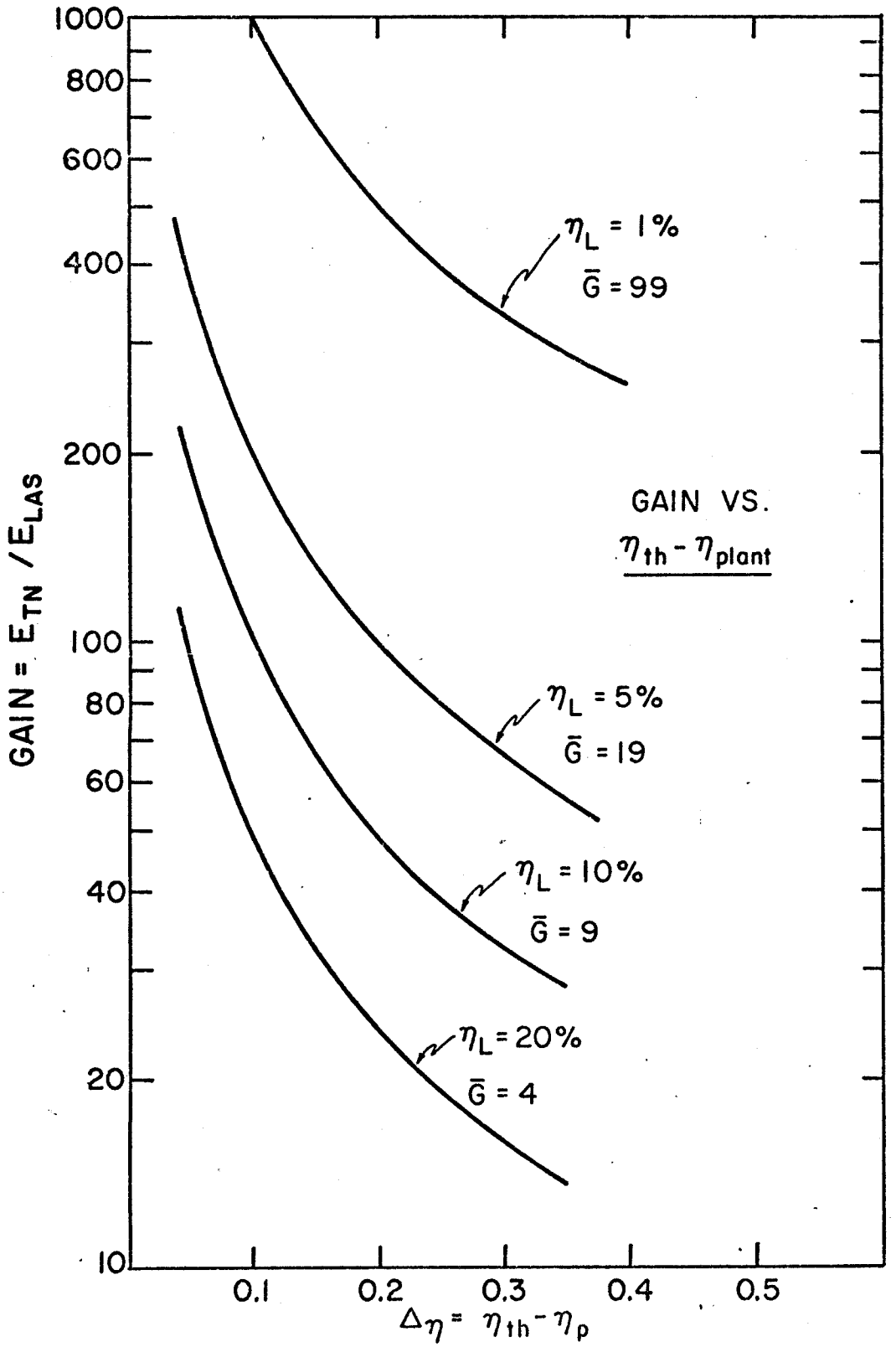
1000
800
600
400
200
100
80
60
40
20
10
GAIN = E_{TN} / E_{LAS}
0.1
0.2
0.3
0.4
0.5
$\Delta\eta = \eta_{th} - \eta_p$
η_L = 1%
$\bar{G}$ = 99
η_L = 5%
$\bar{G}$ = 19
η_L = 10%
$\bar{G}$ = 9
η_L = 20%
$\bar{G}$ = 4
GAIN VS.
$\eta_{th} - \eta_{plant}$

YIELD VS. LASER ENERGY INPUT

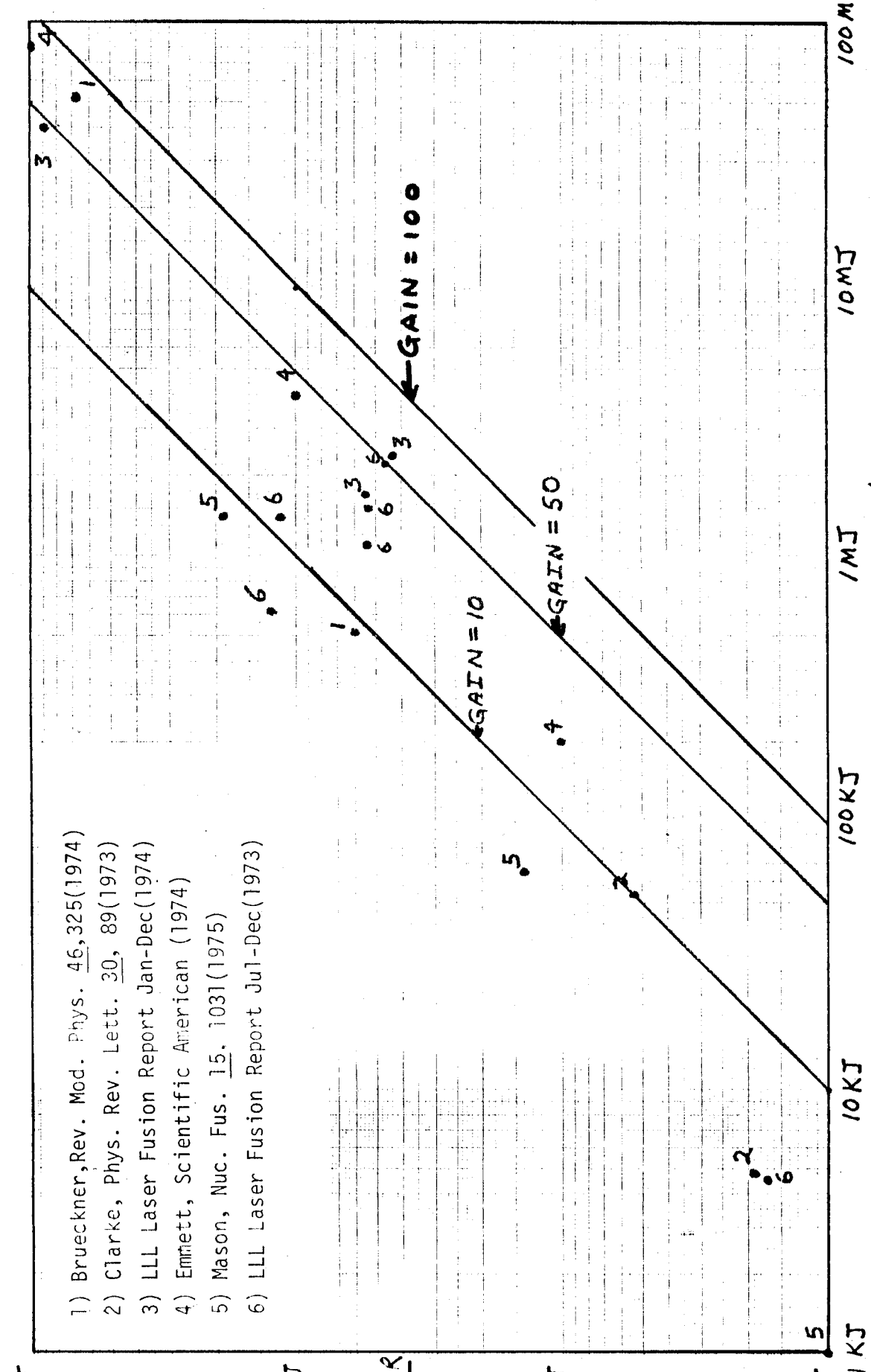

FIGURE 2

II-A-2-b. Pellet Implications

From the viewpoint of reactor design, pellet gain of 100 is necessary to make a pure laser fusion reactor feasible and a yield of 100 MJ is consistent with a full scale reactor power system. The 100 MJ yield will determine the amount of fuel in the pellet (i.e. the mass of the compressed core) and the gain of 100 implies that this fuel must reach thermonuclear conditions using a one megajoule laser.

The mass of fuel is calculated by assuming the DT fusion reaction Q value is 17.6 MeV. Then a mass of 0.297 milligrams (mg) of DT must react to produce 100 MJ of energy.

$$N = \frac{Y(MJ)}{Q(MeV)(1.6 \times 10^{-19}\ MJ/MeV)} = 3.55 \times 10^{19}\ \text{reactions}$$

Each reaction requires one deuterium and one tritium nucleus.

$$M_b = N^*[M_D + M_T]$$

$$= 0.297\ \text{mg}.$$

To determine the necessary total mass of the core, the fractional burn-up must be determined. For $\rho R = 3\ g/cm^2$ and a $T = 10$ KeV microcore of $0.5\ g/cm^2$, the fractional burnup is $f_B = 0.31$. This gives the total core mass as 0.958 (mg). This mass of DT compressed to $\rho R = 3\ g/cm^2$ implies a compression of $\eta = 1315.7$. So for $\varepsilon\beta = 1$, the necessary laser energy is found to be 0.92 MJ.

$$E_L = \frac{(100)^3}{(1)^4}\ \frac{1.6\ MJ}{(1315.7)^2} = 0.92\ MJ.$$

Therefore, the yield and gain found necessary for a pure laser fusion power plant derived from purely electrical output and plant efficiency arguments fall very close to those values considered achievable from only pellet physics arguments.

If it is rather arbitrarily assumed at this point that the fraction of total pellet mass remaining in the core after implosion is 30% then the total pellet mass must be M_p = 3.19 mg.

II-A-3. Hydrodynamics

II-A-3-a. Introduction

In this section, we present a rather pragmatic discussion of laser fusion physics with no attempt to derive the results from the more detailed kinetic theory. The emphasis is on what is currently used rather than what should be used.

To understand in detail the dynamics and interaction of laser light heating, heat transfer, ablation-implosion, and thermonuclear burn, the laser fusion plasma is typically modeled using the hydrodynamic description along with laser-plasma interaction physics and rate equations to predict thermonuclear yield.[1] Solution of the hydrodynamics equations generally requires that the plasma be in local thermodynamic equilibrium (LTE) where equations of state and transport coefficients can be defined to close the set of equations.[2] This is generally valid for the collision dominated dense plasma, although there are important exceptions that can strongly alter the results given by the purely hydrodynamic description. These effects are treated through corrections to the transport coeffcients.

Non-thermal particles such as thermonuclear reaction product charged particles,photons and non-thermal electrons are treated as particle species separate from the "thermal background plasma" described by the hydrodynamic treatment. These non-thermal particles have mean free paths much longer than the hydrodynamic scale lengths and must be treated using kinetic theory.

These will be described in later sections. This section will deal with the purely hydrodynamic description.

II-A-3-b. One Fluid-Two Temperature Model

For the purposes of modeling pellet implosions as well as interpreting current experiments, the one fluid-two temperature plasma hydrodynamic model is typically used. In this model, the electrons and ions are assumed to move together as a single fluid (with the same velocity $\underline{U}(\underline{r},t)$) implying charge neutrality over lengths of hydrodynamic interest. This approximation is verified by comparing the plasma Debye length with the hydrodynamic scale of about one micron over the temperature and density range relevant to laser fusion plasmas.

Table 1

Debye Length (cm)

Temp (eV) \ Density (cm^{-3})	10^{18}	10^{20}	10^{22}	10^{24}
10	2.35×10^{-6}	2.35×10^{-7}	2.35×10^{-8}	2.35×10^{-9}
10^2	7.43×10^{-6}	7.43×10^{-7}	7.43×10^{-8}	7.43×10^{-9}
10^3	2.35×10^{-5}	2.35×10^{-6}	2.35×10^{-7}	2.35×10^{-8}
10^4	7.43×10^{-5}	7.43×10^{-6}	7.43×10^{-7}	7.43×10^{-8}

For purposes of energy transfer, the electrons and ions are treated as separate species, each in local thermodynamic equilibrium at different temperatures, $T_e(\underline{r}, t)$ and $T_i(\underline{r}, t)$. The necessity of the two temperature model is demonstrated by comparison of the electron-electron, ion-ion, and electron-ion energy equilibration times in Table 2.

Table 2

Electron-Electron, Ion-Ion, Electron-Ion Collision Times

Temperature (ev)	Density (cm^{-3}) 10^{19}			10^{21}			10^{23}		
	t_{ee}	t_{ii}	t_{ei}	t_{ee}	t_{ii}	t_{ei}	t_{ee}	t_{ii}	t_{ei}
10	10^{-13}	7×10^{-12}	2×10^{-10}	10^{-15}	7×10^{-12}	2×10^{-12}	10^{-17}	7×10^{-16}	2×10^{-14}
100	10^{-12}	2×10^{-10}	6×10^{-9}	10^{-14}	2×10^{-12}	6×10^{-11}	10^{-16}	2×10^{-14}	6×10^{-13}
1000	10^{-10}	7×10^{-9}	2×10^{-7}	10^{-12}	7×10^{-11}	2×10^{-9}	10^{-14}	7×10^{-13}	2×10^{-11}
10000	10^{-9}	2×10^{-7}	6×10^{-6}	10^{-11}	2×10^{-9}	6×10^{-8}	10^{-13}	2×10^{-11}	6×10^{-10}

t (seconds)

Since typical time scales in an implosion are less than 10^{-9} seconds, it is clear that energy will diffuse through electron and ion populations before the electrons and ions can equilibrate.

Momentarily treating the plasma an an inviscid fluid, the one fluid-two temperature hydrodynamics equations can be written:

$$\frac{\partial \rho}{\partial t} + \nabla \cdot (\rho \underline{u}) = 0 \qquad \text{(Continuity)}$$

$$\rho\left[\frac{\partial \underline{u}}{\partial t} + \underline{u} \cdot \nabla \underline{u}\right] = -\nabla(P_e + P_i) \qquad \text{(Momentum)}$$

$$\rho C_{v_e}\left[\frac{\partial T_e}{\partial t} + \underline{u} \cdot \nabla T_e\right] = \nabla \cdot K_e \nabla T_e - P_e(\nabla \cdot \underline{u}) - \omega_{ei}(T_e - T_i) + S_e \qquad \text{(Energy)}$$

$$\rho C_{v_i}\left[\frac{\partial T_i}{\partial t} + \underline{u} \cdot \nabla T_i\right] = \nabla \cdot K_i \nabla T_i - P_i(\nabla \cdot \underline{u}) + \omega_{ei}(T_e - T_i) + S_i$$

$$\rho = n_e m_e + n_i m_i$$

One must have equations of state to close this set of equations.

$$P_e = P_e(n_e, T_e) \quad ; \; P_i = P_i(n_i, T_i)$$
$$C_{v_e} = C_{v_e}(n_e, T_e) \quad ; \; C_{v_i} = C_{v_i}(n_i, T_i) \; .$$

The transport law for the heat fluxes $\underline{q}_e$ and $\underline{q}_i$ has already been specified in the form of Fourier's Law:

$$\underline{q}_e = -K_e \nabla T_e \quad \& \quad \underline{q}_i = -K_i \nabla T_i \; ,$$

so that expressions must also be supplied for the transport coefficients:

K_e - electron thermal conductivity

K_i - ion thermal conductivity

ω_{ei} - electron-ion temperature equilibration coefficient .

The exact forms of these terms will be discussed in the next two sections. Along with the convection, conduction, work and equilibration terms, each temperature equation has an external source term. The electron source term will account for temporal and spatial electron energy gain and loss with the non thermal radiation field; energy gain from the absorption of laser light; and gain from the redeposition of energy by non-thermal thermonuclear reaction products. The ion source must account for gain from thermonuclear reaction product energy redeposition.

With the annihilation of ions by fusion reactions and the treatment of the resultant reaction products as separate non-hydrodynamic species, the right hand side of the continuity equation must strictly be replaced by annihilation and creation terms to account for fusion reactions and rethermalization of the reaction products.

III-A-3-c. Equation of State

The equations of state for a relatively hot, fully ionized plasma can be adequately approximated by the ideal gas laws.

$$P_e = n_e k_B T_e \quad , \quad P_i = n_i k_B T_i$$

$$C_{v_e} = \frac{3}{2} k_B Z/m_i \quad , \quad C_{v_i} = \frac{3}{2} k_B/m_i \quad .$$

Unfortunately, the cold, highly compressed DT plasma ahead of the converging shock fronts during implosion does not obey this law. The electrons are Fermions and strictly obey Fermi-Dirac rather than Boltzmann statistics. In their highly compressed, cold state they begin to fill all the available low energy states and equations of state must be derived from Fermi-Dirac distribution functions[3]. In addition, the energy associated with different solid phases, the liquid phase, dissociation and ionization of real materials must be treated in order to correctly predict the electron pressure[4]. For

higher Z materials the differing ionization states must also be treated, even at high temperatures, through models such as Saha equilibrium or by solving the non-equilibrium ionization rate equations. These complications require different theories and approximations for each temperature and density range and for every different material. A great amount of theoretical and experimental work has been invested in accurate equations of state in support of the nuclear weapons program, and more recently directly in support of the needs of the laser fusion effort. Equations of state for purposes of computation are usually in the form of tables of pressure values or tables of fitting parameters that are evaluated to obtain pressure values as functions of density or compressibility and temperature.

Equations of state are most important in correctly predicting the adiabatic compression of the dense pellet ore. Further discussion of specific equations of state is found in section II-B-2-d.

III-A-3-d. Transport Coefficients

Whereas the accuracy of equation of state values is most important in the cold, dense pellet core, the transport coefficients are dominant in the hot, ablating pellet corona. Classical (Spitzer) values for the transport coefficients are[5]

$$K_e = 20\left(\frac{2}{\pi}\right)^{3/2} \frac{k_B\,(k_B T_e)^{5/2}}{m_e^{1/2}\, e^4\, Z\, \ln\Lambda_{ei}}$$

$$K_i = 20\left(\frac{2}{\pi}\right)^{3/2} \frac{k_B\,(k_B T_i)^{5/2}}{m_i^{1/2}\, e^4\, Z^4\, \ln\Lambda_{ii}}$$

$$\omega_{ei} = \frac{8(2\pi)^{1/2}\, n_e Z^2 e^4 \ln\Lambda_{ei}}{3 m_e m_i\, k_B^{3/2}} \left(\frac{T_e}{M_e} + \frac{T_i}{M_i}\right)^{-3/2}$$

The coefficients all depend strongly on T_e or T_i, making the electron and ion temperature diffusion equations highly non-linear. If non-parallel temperature and density gradients exist, (due to non symmetric implosion), self-generated magnetic fields arise, and the transport coefficients must be corrected for conduction perpendicular to the B-field[6].

$$K_e \rightarrow \frac{Ke}{1 + \omega_c^2 \tau^2}$$

In addition to these purely magneto hydrodynamic effects, the electron heat flux is often poorly described by a Fourier transport law. Because the laser heats the electrons, the electron heat flux can be very strong, resulting in very steep temperature gradients that apparently violate the hydrodynamic criteria

$$Te/\nabla T_e < \lambda_e$$

where λ_e is the electron mean free path.

The result of this breakdown of the transport law is an electron thermal wave propagation speed far in excess of the electron thermal velocity; a clearly nonphysical result. To alleviate this troublesome problem, (and in effect to model non hydrodynamic behavior with hydrodynamic equations) an electron thermal flux limiter is often added to the temperature equations[7]

$$q_e = - K_e \nabla T_e \rightarrow - \frac{K_e \nabla T_e}{1 + \left| \frac{K_e \nabla T_e}{q_{MAX}} \right|}$$

where q_{MAX} is an upper limit on the physically achievable heat flux which is usually dependent on local electron density and temperature. Just as for the pressure, these transport coefficients must be derived using Fermi-Dirac statistics for the dense cold pellet core plasma[8,9].

Comparison of calculational hydrodynamic models with results of current experiments indicate that the classical values of these transport coefficients may be in error by a significant amount[10,11]. They generally overestimate thermal conductivity by as much as a factor of ten! Explanations of this reduced thermal conduction include: the effect of self generated magnetic fields and effective enhancement of the electron collision frequency by plasma turbulence[11].

In all of the previous discussion, the other major transport coefficient, viscosity, has been ignored. Laser fusion plasmas are generally treated as an inviscid fluid although the equation of motion for such a fluid becomes purely hyperbolic and admits discontinuous solutions such as shocks. Such discontinuities are very difficult to treat numerically so an artificial viscosity[12] is empirically introduced into the hydrodynamics equations in the form of an additional ion pressure

$$P_i \rightarrow P_i + q$$

that is zero everywhere except in the vicinity of a shock, where it adds dissipation. Its form is necessarily such that the jump conditions (Heugoniot relations) across the shock are preserved. This clever "fudge" greatly facilitates the numerical solution of the coupled, non-linear, partial differential equations of hydrodynamics.

References II-A-3

1. K. Brueckner and S. Jorna, Rev. Mod. Phys. 46, 325 (1974).

2. S. Chapman and T. Cowling, The Mathematical Theory of Non-uniform Gases, (Cambridge University Press, Cambridge, 1953).

3. Landau and Liftsitz, Statistical Physics, 2nd Ed., (Addison-Wesley, Reading, Mass., 1969).

4. S. G. Brush, in Progress in High Temperature Physics and Chemistry, Vol. I, Ed. C. A. Rouse (Pergamon Press, London, 1967).

5. L. Spitzer, Physics of Fully Ionized Gases, (Wiley, New York, 1965).

6. S. I. Braginskii, in Review of Plasma Physics, Vol. I, (Consultants Bureau, New York, 1965).

7. J. Shearer, UCID-15745, 1970.

8. H. Brysk, P. Campbell, and P. Hammerling, Plasma Phys. 17, 473 (1975).

9. H. Brysk, Plasma Phys. 16, 927 (1974).

10. R. Malone, R. Mc Crory, and R. Morse, Phys. Rev. Lett. 34, 721 (1975).

11. Mount Lassen Conference on Transport Processes in Laser Fusion Plasmas (1976).

12. J. Von Neumann, J. Appl. Phys. 21, 232 (1950).

II-A-4 Burn Dynamics

II-A-4-a. Reaction Rates

The basic goal of laser driven fusion is of course to produce a net energy gain via fusion reactions. We first consider the most reactive fusion fuel, a 50-50 atomic percent mixture of deuterium and tritium, the two heavy isotopes of hydrogen. They fuse to form a helium nucleus (alpha particle) and a neutron.

$$ {}_1D^2 + {}_1T^3 \longrightarrow {}_2He^4\ (3.5\ MeV) + {}_0n^1\ (14.1\ MeV) $$

The energy released in this reaction (Q-value) is approximately 17.6 MeV with 3.5 MeV going to the charged alpha particle. The reaction rate for thermonuclear D-T fusion $(\overline{\sigma v})_{DT}$ is plotted in Figure 1. Note that it has a broad maximum between ion temperatures of 20 KeV and 80 KeV. The next most probable reaction is between two deuterium nuclei.

$$ {}_1D^2 + {}_1D^2 \xrightarrow{50\%} {}_2He^3\ (.82\ MeV) + {}_0n^1\ (2.45\ MeV) $$

$$ \xrightarrow{50\%} {}_1T^3\ (1.01\ MeV) + {}_1p^1\ (3.02\ MeV) $$

The average Q-value is 3.15 MeV while the average energy going into charged particles is 1.925 MeV. The D-D fusion reaction rate $(\overline{\sigma v})_{DD}$ is also plotted in Figure 1. The D-T reaction is favored over the D-D reaction by about two orders of magnitude. The rate equations for thermal deuterium and tritium concentrations are

FIGURE II-A-4-1
FUSION REACTION PARAMETER

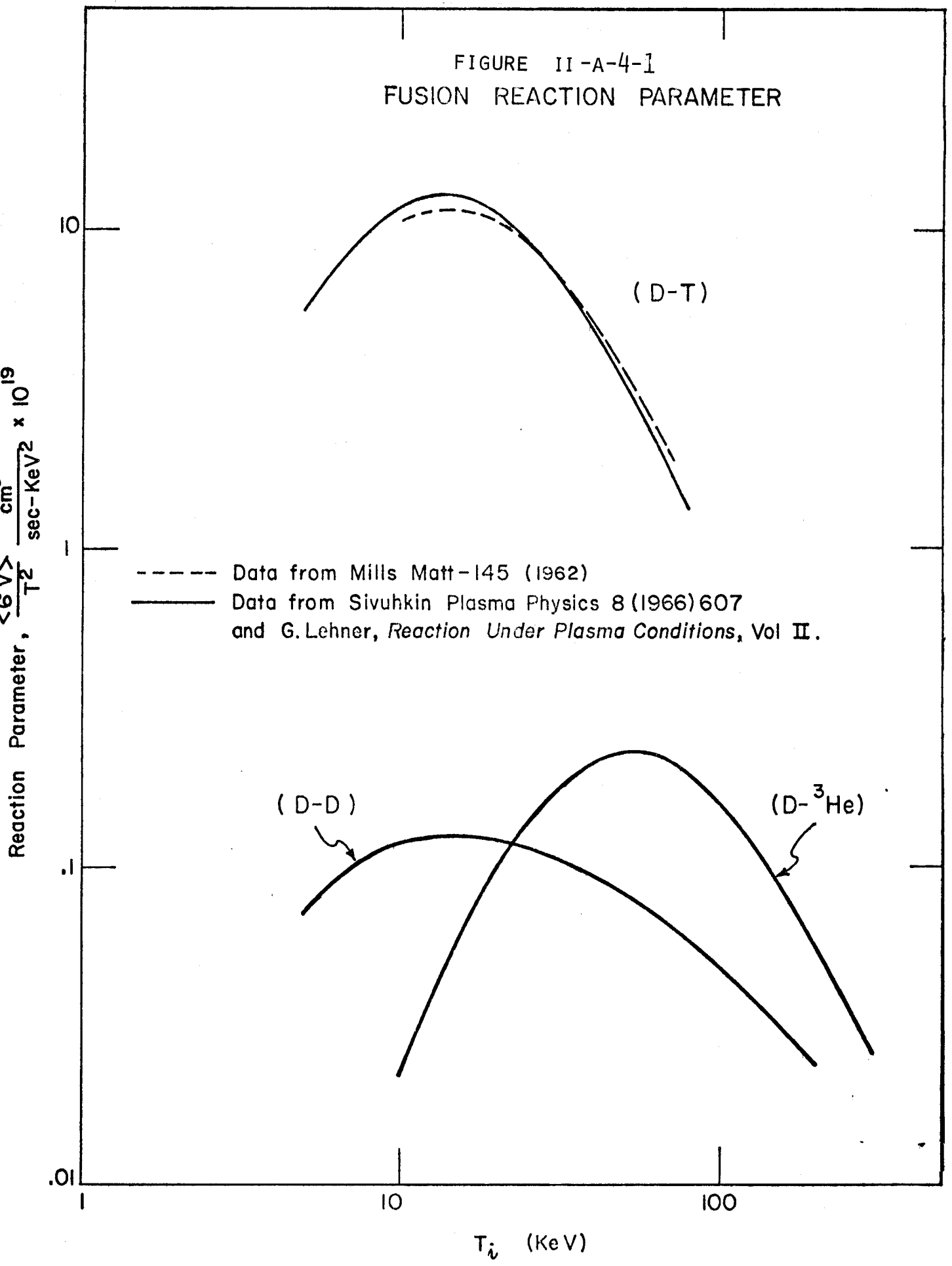

$$\frac{dn_D}{dt} = - n_D n_T \, (\overline{\sigma v})_{DT} - n_D^2 \, (\overline{\sigma v})_{DD}$$

$$\frac{dn_T}{dt} = - n_D n_T \, (\overline{\sigma v})_{DT} \, .$$

Since the D-D reaction produces a tritium ion for every two fusions it would seem that the equation for n_T should contain a positive term proportional to $n_D^2 \, (\overline{\sigma v})_{DD}$. The tritium ion reaction product is not thermal however, and must be treated separately since its "beam plasma" reaction rate will be much greater than the Maxwellian averaged thermal reaction rate.

II-A-4-b. Charged Particle Transport

Particular attention has been drawn to the energy of the charged particle reaction products. The requirement for efficient thermonuclear burning is that the range of the charged particle reaction products is a small fraction of the radius of the dense pellet core. If this is true then the reaction products will slow down and further heat the core. In this way, only a small central hot spot (microcore) need be heated to an ignition temperature, 4-10 keV. Once burning starts, the reaction product energy redeposition will quickly "bootstrap" heat the microcore to greater than 20 keV where the D-T reaction rate is greatest. As the hot microcore becomes transparent to the reaction products they stream out and are rapidly thermalized in the surrounding colder plasma. In this way a thermonuclear detonation wave propagates outward from the microcore, Figure 2. To accurately describe this process one must not only solve the rate equations but

FIG. 2 PROPAGATING BURN FROM 10keV MICROCORE

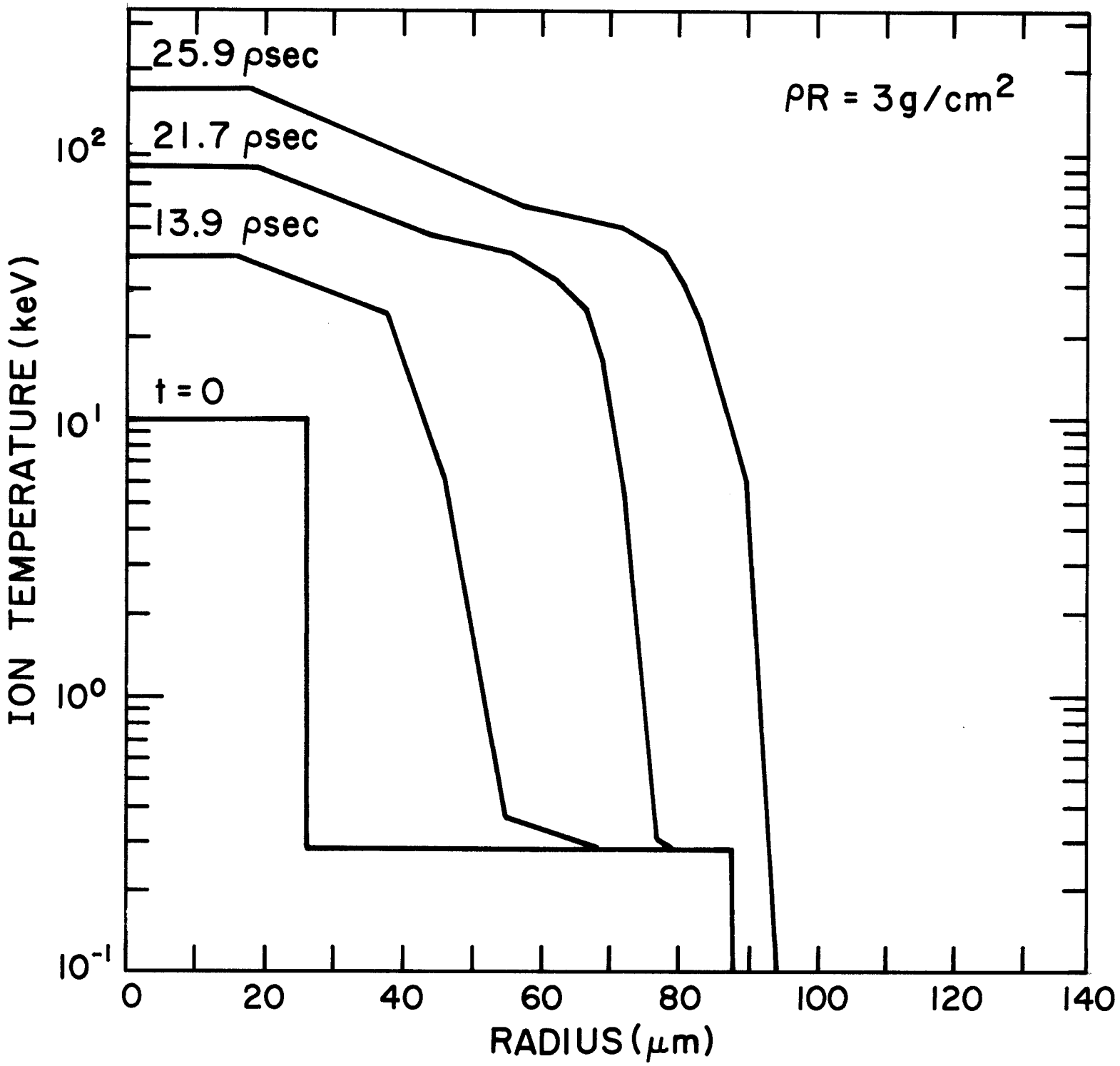

must treat the transport and thermalization of the reaction products. To do this the Fokker-Planck equation is solved for a fast test particle in a thermal background plasma to obtain a range-energy relation.[1]

$$\frac{dv}{ds} = - 4\pi r_o^2 m_e^2 n_i Z_i^2 Z^2 \ell n\Lambda_i / m_i m v^3 - 4(2\pi)^{1/2} r_o^2 m_e^{5/2} n_e Z^2 \ell n\Lambda_e / 3m(k_B T_e)^{3/2}$$

where r_o is the classical electron radius, and the unsubscripted variables apply to the fast charged particle. The two terms for slowing down in electrons and ions are plotted in Figure 3. The energy loss rate to electrons is independent of the fast particle velocity; however, the energy loss rate to ions increases as the fast particle velocity decreases. Thus the particles lose most of their energy to electrons along the first part of their path and to the ions near the end of their flight. Fast ions lose half of their energy to electrons and half to ions at an electron temperature of about 30 KeV. Actual transport of the charged particles can be modelled to varying degrees of accuracy by any of the standard linear transport techniques (discrete ordinates S_N,[2] flux limited diffusion,[3] time dependent particle tracking,[4] no transport-local energy deposition[5]). A more detailed discussion of particle transport is found in the Numerical Modelling section.

The range-energy equation implies that the density independent range of a 3.5 MeV alpha particle in a 10 KeV D-T plasma is about .3-.4 g/cm^2. This, therefore, defines the minimum size of the microcore (it must have a density-radius product of at least .4 g/cm^2).

FIGURE 3

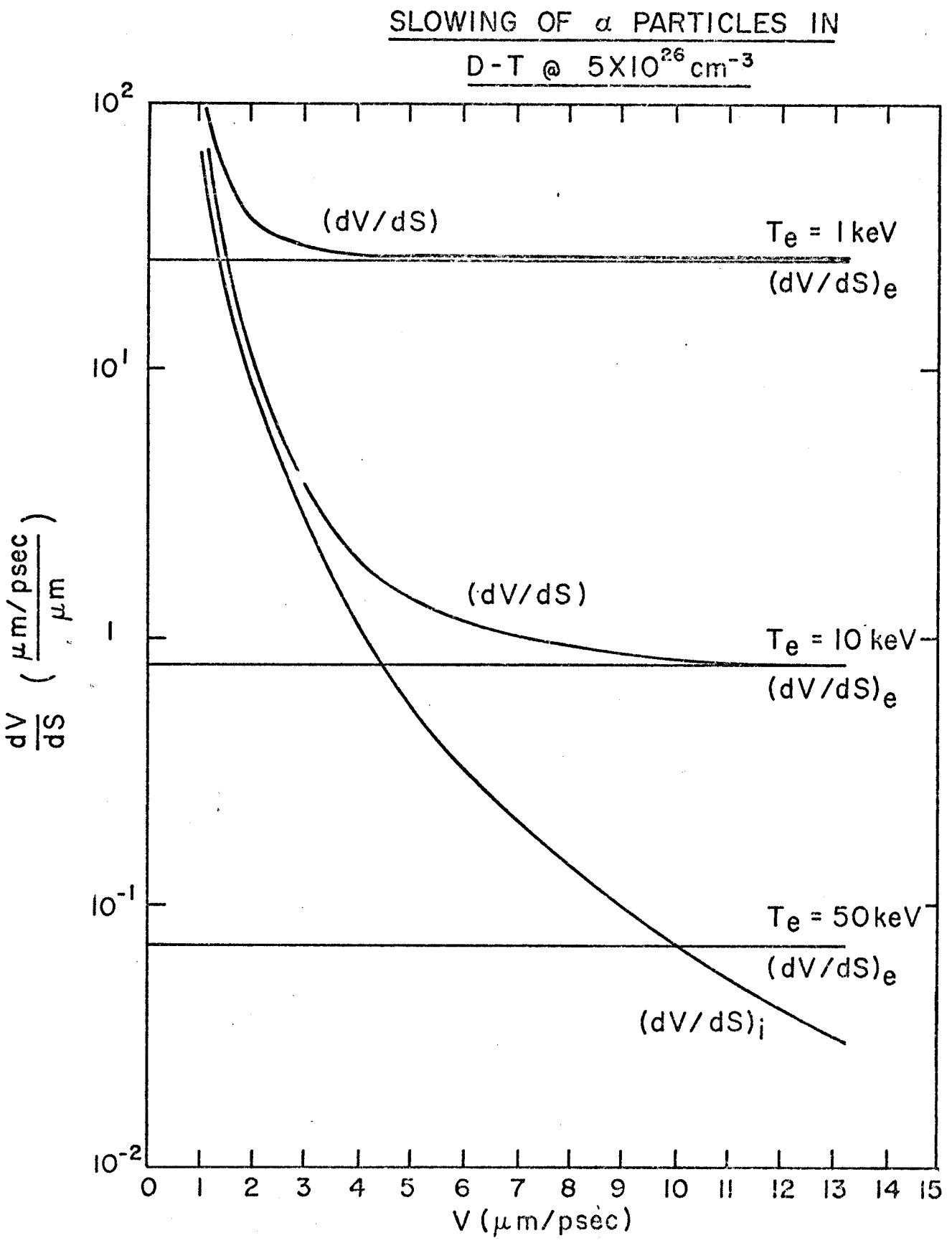
SLOWING OF α PARTICLES IN
D-T @ 5X10^26 cm^-3
10^2
10^1
1
10^-1
10^-2
dV/dS (μm/psec / μm)
(dV/dS)
Te = 1 keV
(dV/dS)e
(dV/dS)
Te = 10 keV
(dV/dS)e
Te = 50 keV
(dV/dS)e
(dV/dS)i
0 1 2 3 4 5 6 7 8 9 10 11 12 13 14 15
V (μm/psec)

The charged particles slowing down in the background plasma act as a source of both energy and momentum and as such they affect the hydrodynamic behavior of the plasma. The hydrodynamics in turn affects the temperature and density so that the hydrodynamics and burn dynamics must be treated as coupled processes.

References for Section II-A-4

1. K. Brueckner and H. Brysk, J. Plasma Phys. 10, 141 (1973).

2. M. Antal and C. Lee, LA-UR-75-726.

3. Corman, Nuc. Fus. 15, 377 (1975).

4. See Section II-B-2-C.

5. R. Kidder and Barnes, UCRL-50583.

II.A.5 Laser Light Absorption

II.A.5.a Introduction

In order to achieve a high overall plant efficiency, it is essential that the pellet absorb most of the laser energy delivered to it. The theory of laser-plasma coupling is rapidly developing, with some major points still in dispute. First of all there is the question of whether or not classical absorption (inverse bremsstrahlung) can account for the measured values in current experiments on small (100 μm diameter) pellets. While Rochester and KMS have claimed that collisional absorption adequately explains their data[1], LASL and LLL say that some additional process, probably resonance absorption, is called for to explain the amount of absorption observed in their experiments,[2] performed under similar conditions. Self-steepening certainly plays a role in this controversy; recent experiments[3] report scale heights as small as one micron, in which case collisional absorption would be negligible. There is also new evidence for polarization-dependent absorption and reflection indicative of resonance absorption[2]. In one elegant experiment using gaseous targets,[4] electrons associated with resonance absorption have been seen for the first time. Certainly, as more powerful laser systems come on line and corona temperatures go up, collisional absorption will fall off. Resonance absorption can then absorb up to 50% of the remaining energy. It is worthy of note that back-reflection due to stimulated Brillouin scattering[5] has <u>not</u> been as severe as anticipated,[6] due probably to complex time-dependent processes associated with ponderamotive forces in the corona.

Another very important question is the dependence of absorption on laser wavelength. First, since collisional absorption $\sim \lambda^{-2}$, shorter wavelengths are favored. Further, the critical density $\sim \lambda^{-2}$, with the result that

shorter wavelength light is absorbed closer to the ablation front, reducing the conduction length. Thus, shorter wavelengths (3000-5000 Å) are favored for increased pellet gain. Until recently, experimental evidence indicated that, at flux densities of 10^{14} W/cm^2, most of the incident energy at 10.6 μm would be lost to fast ion motion. However, a recent experiment[7] finds that 1.06 μm and 10.6 μm radiation both yield about the same suprathermal electron energy at flux densities of 10^{15} W/cm^2. Whether or not this surprising result is borne out by further experiments is of vital importance to the laser fusion program. As will be seen in section III, longer wavelengths are much easier to deal with in designing a beam transport system.

It should be noted that most of today's theory is motivated by the need to interpret current experiments using small targets. Reactor-grade pellets are much more massive with the consequence that corona temperatures will be highly non-isothermal. Most of present-day analysis of parametric instabilities ignore temperature gradients. In particular, stimulated Brillouin scattering may be strong for more massive pellets.

II.A.5.b Classical Absorption

In the classical picture, individual electrons gain energy by absorbing photons in the coulomb field of a nearby ion. For this reason, inverse bremsstrahlung is often referred to as "collisional," or "free-free" absorption. At low intensities, the classical and quantum-mechanical results are comparable, in which case the latter treatment might be termed "semiclassical". Both, however, are linear. The important nonlinear effects that come into play at intensities greater than about 10^{13} W/cm^2 will be discussed later.

In this section we shall study linear collisional absorption by means of geometrical optics, which is admissable whenever the refractive index of the

plasma does not change appreciably in a distance of one wavelength. Even at normal incidence, when the ray penetrates to the critical surface, it can be shown that geometric optics gives the correct absorption to within a few percent, except for long laser wavelengths and high-Z materials.[8] For spherically symmetric isothermal plasmas the absorption integral along a ray path can be reduced to a simple radial integral depending only on the density scale height and angle of incidence. This integral is performed in closed form in slab geometry, and asymptotically for small scale heights and angles of incidence in the spherical case. Lateral refractive transport of laser energy, while a dominant effect in two-beam illumination systems[9] is of lesser importance for many-beam systems, and will not be treated in detail here.

Consider laser radiation obliquely incident on a spherically symmetric plasma, as illustrated in Fig. 1. The intensity along a ray path is given by

$$\Phi = \Phi_{IN} \exp\left(-\int_0^{\ell} \kappa(\ell)d\ell\right) \quad W/cm^2 \qquad (1)$$

where Φ_{IN} is the flux incident on the pellet and ℓ is distance measured along a ray. The quantum mechanical free-free absorption coefficient, corrected for spontaneous emission, can be written[10]

$$\kappa = \frac{4}{3}\left(\frac{2}{\pi m}\right)^{1/2}\left(\frac{e^6}{mc^3}\right)\lambda_L^2 \frac{Z_{eff}\, n_e^2}{N\theta_e^{3/2}} f(x)\ cm^{-1}, \qquad (2)$$

where, for a multi-species plasma,

$$Z_{eff} \equiv \frac{\langle Z^2\rangle}{\langle Z\rangle} \qquad (3)$$

$\theta_e = k\,T_e$, λ_L is the vacuum laser wavelength, N is the refractive index, and

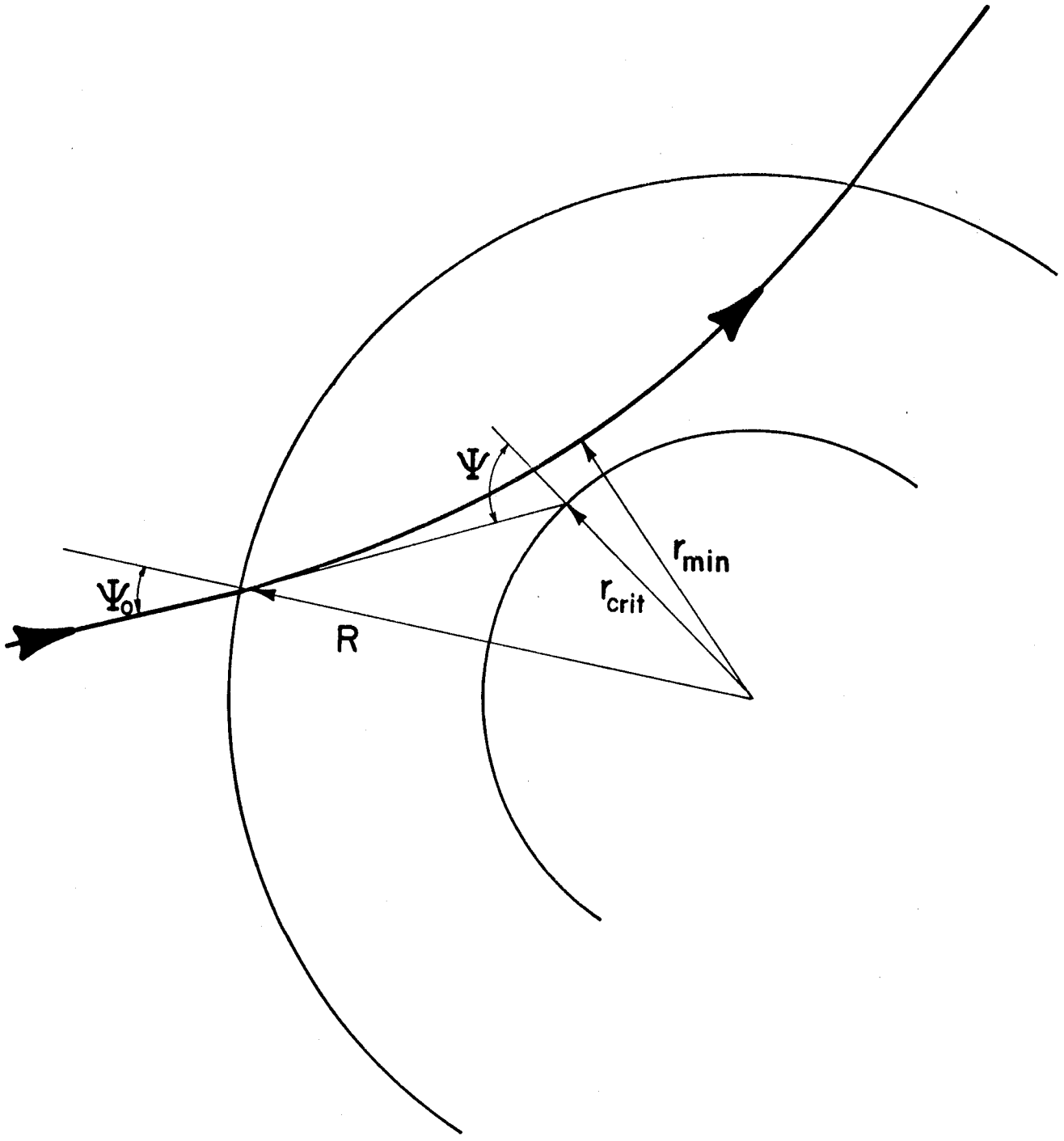

FIGURE 1

$$f(x) \equiv \frac{\sinh x}{x} K_o(x), \tag{4}$$

where $K_o(x)$ is the modified Bessel function of the second kind, and

$$x \equiv \frac{h\nu}{2\theta_e} \tag{5}$$

Typically $\lambda_L = 1$ μm and $\theta_e = 1$ keV, so that we may take $x << 1$ in Eq. (4) and write

$$\lim_{x \to o} f(x) = \ell n \frac{2}{x} - .5772 = \ell n\ (2.25\ \theta_e/h\nu). \tag{6}$$

In a purely classical treatment of collisional absorption, $f(x)$ is replaced by $\ell n\Lambda$. The present discussion would more appropriately be labelled "linear" absorption.

When the electron-ion collision frequency $\nu_{ei} << \omega$, the refractive index of the underdense plasma is simply

$$N = \sqrt{1 - \omega_p^2/\omega^2} = \sqrt{1 - n_e/n_c}, \quad \omega_p < \omega \tag{7}$$

Thus, inverse bremsstrahlung absorption is most effective for high Z materials at relatively low electron temperatures. Restricting our attention to an isothermal plasma, let us write

$$\kappa = \kappa_o(\theta_e) \frac{n_e^2}{N} \tag{8}$$

The total absorption suffered by a ray as it passes in and out of the corona is then given by

$$\Phi_{ABS} = \Phi_{IN}\ (1 - e^{-\kappa_o A}). \tag{9}$$

The quantity $p = \kappa_o A/2$ is known as the optical thickness.

We shall refer to

$$A = 2 \int_0^\infty \frac{n_e^2}{N} \, d\ell \tag{10}$$

as the absorption integral.

The phase and group velocities are given by

$$v_p = \frac{c}{\sqrt{1 - \omega_p^2/\omega^2}} \tag{11}$$

$$v_G = c^2/v_p = c\sqrt{1 - \omega_p^2/\omega^2} \, , \tag{12}$$

showing clearly that the laser energy spends most of its time near the critical surface where the bulk of the absorption takes place. A relevant quantity of interest is the <u>energy transit time</u> (in and out):

$$t_T = 2 \int \frac{d\ell}{v_G} = \frac{2}{c} \int \frac{d\ell}{\sqrt{1 - \omega_p^2/\omega^2}} \, . \tag{13}$$

In order for ray tracing studies to make sense, t_T must be much less than the laser pulse length. Even more restrictedly, there must not be significant changes in the intensity in a time t_T. To evaluate the transit time integral (13), let us assume an exponential density profile

$$n_e = n_c e^{-x/L}, \tag{14}$$

where x is distance measured from the critical surface and L is the scale height. This profile is fairly accurate for isothermal atmospheres at relatively low laser intensities.[11] Then, at normal incidence,

$$t_T = \frac{2}{c} \int_0^X \frac{dx}{\sqrt{1 - e^{-x/L}}} \quad , \tag{15}$$

where X is chosen where the plasma density becomes negligibly tenuous. Carrying out the integral, we find

$$t_T = \frac{2X}{c} + \frac{4L}{c} \ln \left(1+\sqrt{1 - e^{-X/L}}\right). \tag{16}$$

Let us choose X large enough that $e^{-X/L} << 1$. Then

$$t_T \approx \frac{2X}{c} + (4\ln 2) \frac{L}{c}. \tag{17}$$

Since 2X/c is just the vacuum travel time, we see that the energy lag time is simply

$$\Delta t_T \approx 4\ln 2 \frac{L}{c} = 2.773 \frac{L}{c} . \tag{18}$$

For small pellets, L ≈ 100 μm, so that $\Delta t_T \approx 0.9$ psec. If X = 300 μm, the total transit time through the plasma is about 3.0 psec, still a very short time, even for 40 psec pulses. For very steeply rising pulses there is the possibility of some pulse shape distortion by the time the laser energy reaches the critical surface, due to the time dependence of L.

Another approximation made in deriving the linear absorption coefficient is the transparency condition,

$$\nu_c/\omega_L << 1, \tag{19}$$

where ν_c is the electron-ion collision frequency. The full classical absorption coefficient may be written

$$\kappa = \frac{2\omega_L}{c} \left[- \frac{\beta}{2} + \frac{1}{2} \sqrt{\beta^2 + (1 - \beta)^2 (\nu_c/\omega_L)^2} \right]^{1/2} , \tag{20}$$

where

$$\beta \equiv 1 - \frac{\omega_p^2}{\omega_L^2 + \nu_c^2} \tag{21}$$

When (19) is satisfied this simplifies to

$$\kappa^{(o)} = \left(\frac{\omega_p}{\omega_L}\right)^2 \left(\frac{\nu_c}{v_G}\right) . \tag{22}$$

As a sufficient condition for transparency let us evaluate (22) at the critical surface where the absorption is strongest:

$$v_G \kappa_c^{(o)} = \nu_c << \omega_L . \tag{23}$$

Kidder shows that, for $\lambda_L = 1.06$ μm,

$$v_G \kappa_c^{(o)} = \frac{3 \ell n\Lambda \; c Z_{eff}}{\theta_e^{3/2}} \text{ cm}^{-1}, \tag{24}$$

with θ_e in KeV. Using (24) in (23) then gives the result,

$$\frac{Z_{eff} \ell n\Lambda}{\theta_e^{3/2}} << 2 \times 10^4 \tag{25}$$

Since $\ell n\Lambda$ lies in the range 5-10 for kilovolt temperatures, we see that the transparency condition is well met for DT or glass, but might be violated for higher Z materials.

The classical absorption coefficient (2) is subject to several restrictions. First of all, at normal incidence, when the ray penetrates to the critical surface, the geometrical optics approximation breaks down. Dawson, Kaw and Green[12] show that consideration of the full wave equation gives an <u>increase</u> in absorption over that predicted by (2).

A veritable host of pronounced nonlinear effects come into play at higher laser intensities, perhaps the most important being density profile modification due to ponderamotive forces,[13] and resonance absorption.[14] Other effects include self-focusing in the plasma itself,[13] stimulated Brillouin and Raman scattering,[5] and parametric instabilities.[14] We are currently considering 1 MJ of 5000 Å laser radiation with a peak power of 1000 TW incident on pure DT shells of radius 1 mm. These parameters imply intensities of about 10^{16} W/cm^2 and electron temperatures in the 10 KeV range. Thus, we can expect relatively small collisional absorption in highly non-isothermal atmospheres, strong density steepening, and (hopefully) enhanced resonance absorption.

With these caveats, let us as a first step evaluate the absorption integral (10) under the very simplified conditions of an isothermal exponential density profile.

II-A-5-c. Absorption at Oblique Incidence

In Section III-A-1., it will be shown that at least 12 and probably 20 beams would be required to yield acceptably uniform irradiance over the pellet surface. Both theoretical studies[15] and numerical simulations[16] show that if catastrophic growth of the Rayleigh-Taylor instability is to be avoided, about 90% optical uniformity must be maintained at early times, the exact growth rate of the most unstable mode depending somewhat on the number of beams employed. However, a price must be paid for such high uniformity in the form of non-normal incidence and consequent refractive losses. The primary aim of this section is to estimate the magnitude of these losses in a conceptual laser fusion reactor.

Generally we find that for physically realistic spatial beam profiles, the integrated absorption does not depend strongly on the maximum angle of incidence, due to the concentration of beam power near the optical axis. However, the weighted average ("effective") angle of incidence usually turns out to exceed the range ($7\text{-}10^{o}$) where resonant absorption is expected to be strongest. It should be emphasized that the present work takes no account of such nonlinear effects as self-steepening[13] of the density profile, due to the substantial ponderamotive forces generated at high laser intensities. In such cases the resulting pressure can greatly reduce the scale height to the point where collisional absorption becomes quite negligible.

Slab Geometry

Consider a ray incident at angle Ψ on an infinite isothermal slab of plasma, as illustrated in Figure 2. Assuming the density profile[17]

$$n_e = \begin{cases} n_c e^{-x/L} & x < X \\ 0 & x > X \end{cases}, \tag{26}$$

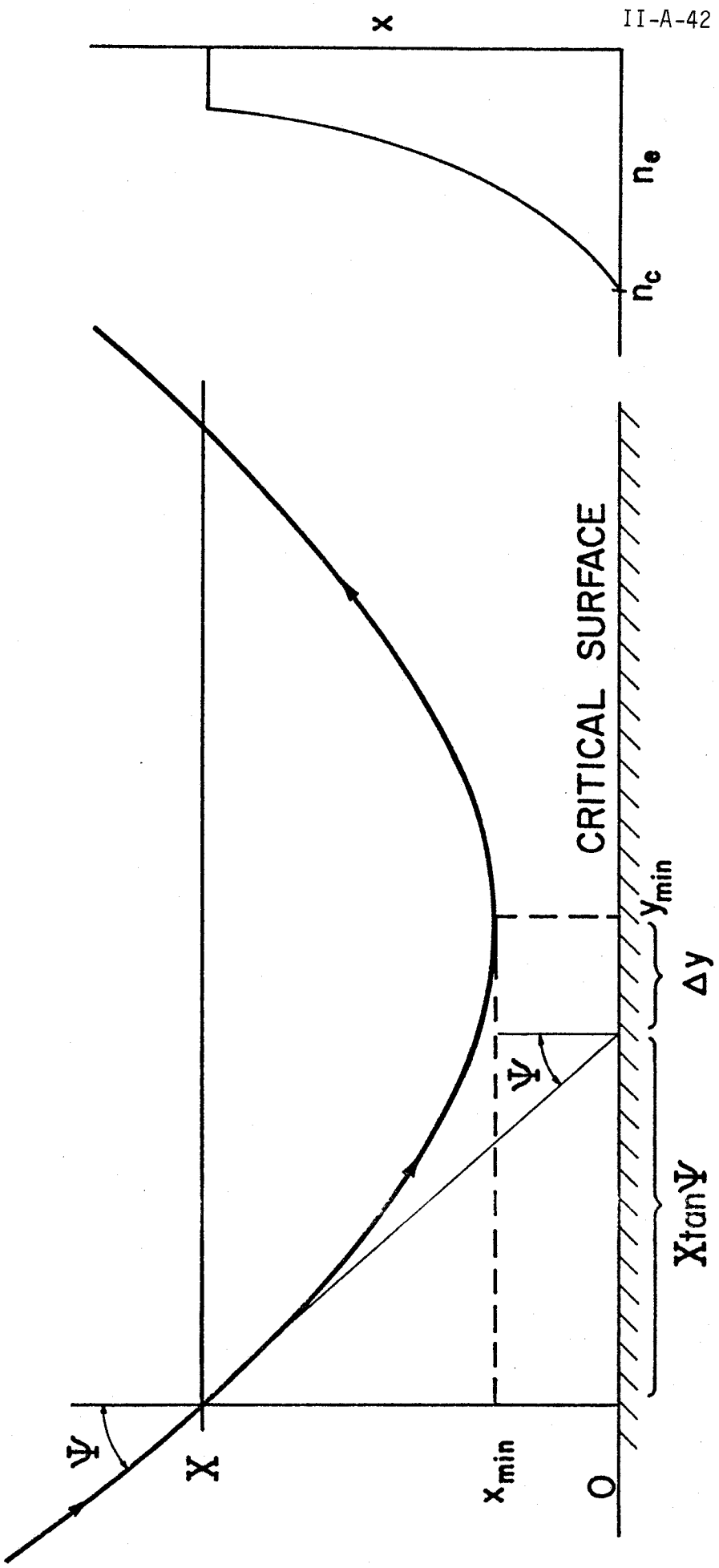

FIGURE 2

we can find the ray path in the x-y plane as follows. From the invariant

$$N(x)\,\sin\theta = \sin\Psi\ , \tag{27}$$

where θ is the angle between the normal and the local tangent, we find

$$N(x_{min}) = \sin\Psi \tag{28}$$

$$y_{min} = \sin\Psi \int_{x_m}^{X} \frac{dx}{\sqrt{N^2 - \sin^2\Psi}}\ . \tag{29}$$

Since

$$N = \sqrt{1 - e^{-x/L}}\ , \tag{30}$$

we have

$$x_{min} = 2L\ \ell n\ \sec\Psi \tag{31}$$

and

$$y_{min} = X\tan\Psi + 2L\tan\Psi\ \ell n\ (\cos\Psi + \sqrt{\cos^2\Psi - e^{-X/L}}\ )\ . \tag{32}$$

A quantity useful for computing the uniformity of energy deposited near the critical surface is the net displacement

$$\Delta y = y_{min} - X\tan\Psi \tag{33}$$

or

$$\Delta y = 2L\tan\Psi\ \ell n\ (\cos\Psi + \sqrt{\cos^2\Psi - e^{-X/L}}\ )\ . \tag{34}$$

When Ψ is small, this reduces to

$$\Delta y \approx 2L\ \Psi\ \ell n\ (1 + \sqrt{1 - e^{-X/L}}\ )\ , \tag{35}$$

and when $X >> L$, Eq. (34) reduces to

$$\Delta y \approx 2L\tan\Psi\ \ell n\ (2\cos\Psi)\ . \tag{36}$$

Note that Δy reaches a maximum for some value of Ψ, as Fig. 3 shows for the case $X >> L$.

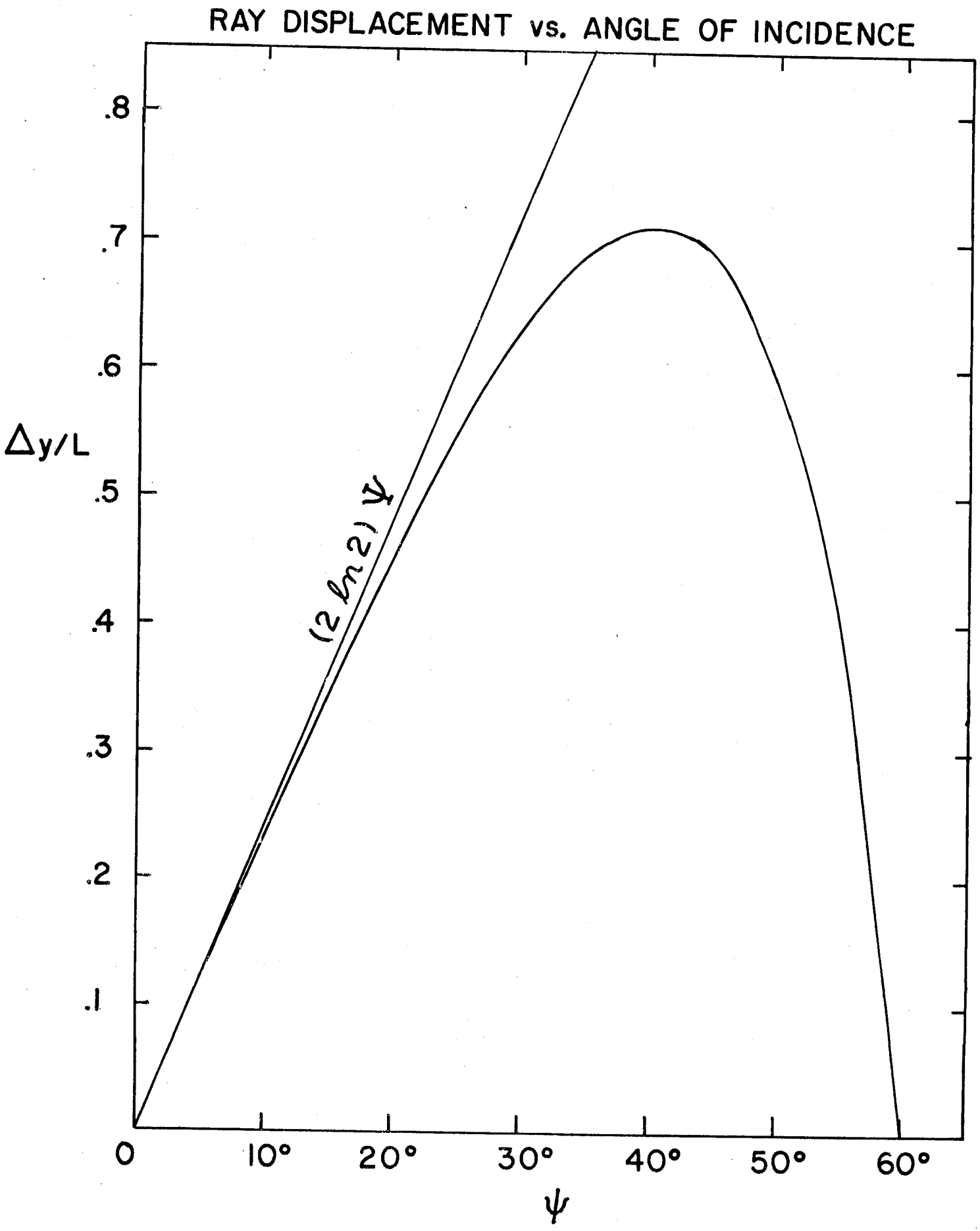
RAY DISPLACEMENT vs. ANGLE OF INCIDENCE
Δy/L
.8
.7
.6
.5
.4
.3
.2
.1
0
10°
20°
30°
40°
50°
60°
ψ
(2 tan 2) ψ

The absorption integral (10) becomes

$$A = 2 \int_{x_m}^{X} \frac{n_e^2}{N} \frac{d\ell}{dx} dx = 2 \int_{x_m}^{X} \frac{n_e^2 \, dx}{\sqrt{1 - n_e/n_c} \cos\theta} \quad . \tag{37}$$

For the exponential profile (26), this may be written

$$A = 4L \int_{\sin\Psi}^{N_1} \frac{N (1 - N^2) \, dN}{\sqrt{N^2 - \sin^2\Psi}} \quad , \tag{38}$$

where $N_1^2 = 1 - e^{-X/L}$. Thus,

$$A = \frac{8L}{3} \sqrt{\cos^2\Psi - e^{-X/L}} \quad (\cos^2\Psi + \frac{1}{2} e^{-X/L}) \quad . \tag{39}$$

When $X >> L$,

$$A = \frac{8L}{3} \cos^3\Psi \quad . \tag{40}$$

This formula is widely used in estimating the effect of oblique incidence on absorption. In the next section, we shall derive the analogue in spherical geometry as an asymptotic series in L. A case of interest is $\Psi << 1$, but $e^{-X/L}$ not small. We find

$$A = \frac{8L}{3} (1 + \frac{1}{2}\gamma) \sqrt{1 - \gamma} \left[1 - \frac{3 (2 - \gamma)}{2 (1 - \gamma) (2 + \gamma)} \Psi^2\right] , \tag{41}$$

where $\gamma \equiv e^{-X/L}$. Equations (36) and (40) have been previously derived by Brueckner.[18] Shearer[19] obtains a $\cos^5\Psi$ law for linear density profiles.

Spherical Geometry

Figure 1 shows a ray impinging on a spherically symmetric isothermal plasma. Note that in this case the projected angle of incidence at

r_{crit}, Ψ, differs from the exterior angle Ψ_o. When N = N(r), an invariant exists, known as Bouger's Law,[20]

$$rN(r)\sin\theta = r_c \sin\Psi = r_m N(r_m) = R\sin\Psi_o. \tag{42}$$

For small Ψ, (42) yields

$$r_{min} \approx r_c + \frac{n_c}{|n_c'|}\sin^2\Psi \ . \tag{43}$$

For larger Ψ, this is a good starting point for an iterative solution of (42). For an exponential density profile,

$$r_m \approx r_c + L\sin^2\Psi \ . \tag{44}$$

While the angular displacement θ_{min} is readily calculated, we shall omit it here, since for multibeam systems, uniformity is of interest only at early times, when the scale height is short enough for the slab result (34) to apply. The absorption is

$$A = 2\int_{r_m}^{\infty} \frac{n_e^2}{N}\frac{d\ell}{dr}\,dr \ , \tag{45}$$

where we have taken $r \to \infty$ for simplicity. From Fig. 1

$$d\ell = dr\sec\theta \ . \tag{46}$$

Thus,

$$A(\Psi,L) = 2\int_{r_m}^{\infty} \frac{rn_e^2 dr}{\sqrt{r^2N^2 - \sin^2\Psi}} \ , \tag{47}$$

where r_c has been scaled out. Note that A depends on Ψ and L through the lower limit of integration as well as the integrand itself. Numerical evaluation of (47) is complicated by the singularity at r_m, even though N(r) doesn't vanish for $\Psi \neq 0$. At normal incidence, (47) reduces to

$$A_\perp = 2 \int_{r_c}^{\infty} \frac{n_e^2 \, dr}{\sqrt{1 - n_e/n_c}} \quad . \tag{48}$$

On this case the integrand is singular at r_c because N = 0. For the exponential density profile we again obtain

$$A_\perp = \frac{8L}{3} \quad . \tag{49}$$

At oblique incidence, closed form expressions for A do not seem to exist. However, two limiting cases may be treated analytically; (a) small incident angles, for arbitrary L; and (b) small L, for which the slab geometry results apply.

Before proceeding to these special cases, let us ask wherever L can be predicted <u>a priori</u>. In slab geometry, the "isothermal blowoff model" gives

$$L = v_s t \tag{50}$$

where

$$v_s = \left(\frac{n_i \theta_i + n_e \theta_e}{m_i} \right)^{1/2} \approx \left(\frac{n_e \theta_e}{m_i} \right)^{1/2} \tag{51}$$

is the isothermal sound speed.

In spherical geometry, numerical studies and experiments suggest that a better model may be

$$n_e = n_c \left(\frac{r_c}{r} \right)^2 e^{-(r - r_c)/L} \quad . \tag{52}$$

The effective scale height at r_c is therefore

$$L_{true} = -\frac{n_c}{n_c'} = \frac{L}{1 + 2L/r_c} \quad . \tag{53}$$

At early times the slab result is recovered, but at later times,

$$L_{true} \to r_c/2 \quad . \tag{54}$$

In most cases of interest we may let $R \to \infty$ in the absorption integrals, the expansion front typically extending to about three scale heights or so. Figure 4 shows the normalized absorption integral $A/A_\perp$ as a function of Ψ for various scale heights for the exponential density profile (26). As one would expect, the slab result,

$$A/A_\perp = \cos^3\Psi \tag{55}$$

is recovered as $L \to 0$. In fact, due to the fact that the curves cross near $\Psi = 30^o$, eq. (55) fits to within 5% for $L < 1$, $\Psi \leq 30^o$. Thus, curvature <u>decreases</u> absorption slightly at small angles of incidence, but substantially <u>increases</u> absorption at larger Ψ due to the increased path length in the plasma.

An asymptotic expansion of $A(\Psi,L)$ for $\Psi << 1$ may be carried out as follows. Taking

$$z^2 = N^2 - \frac{\sin^2\Psi}{r^2} \tag{56}$$

eq. (47) may be manipulated into the (exact) form

$$A/A_\perp = 1 - \frac{3}{2}(I_1 + I_2)\sin^2\Psi, \tag{57}$$

where

$$I_1 = \int_0^1 \frac{dz}{r^2} \tag{58}$$

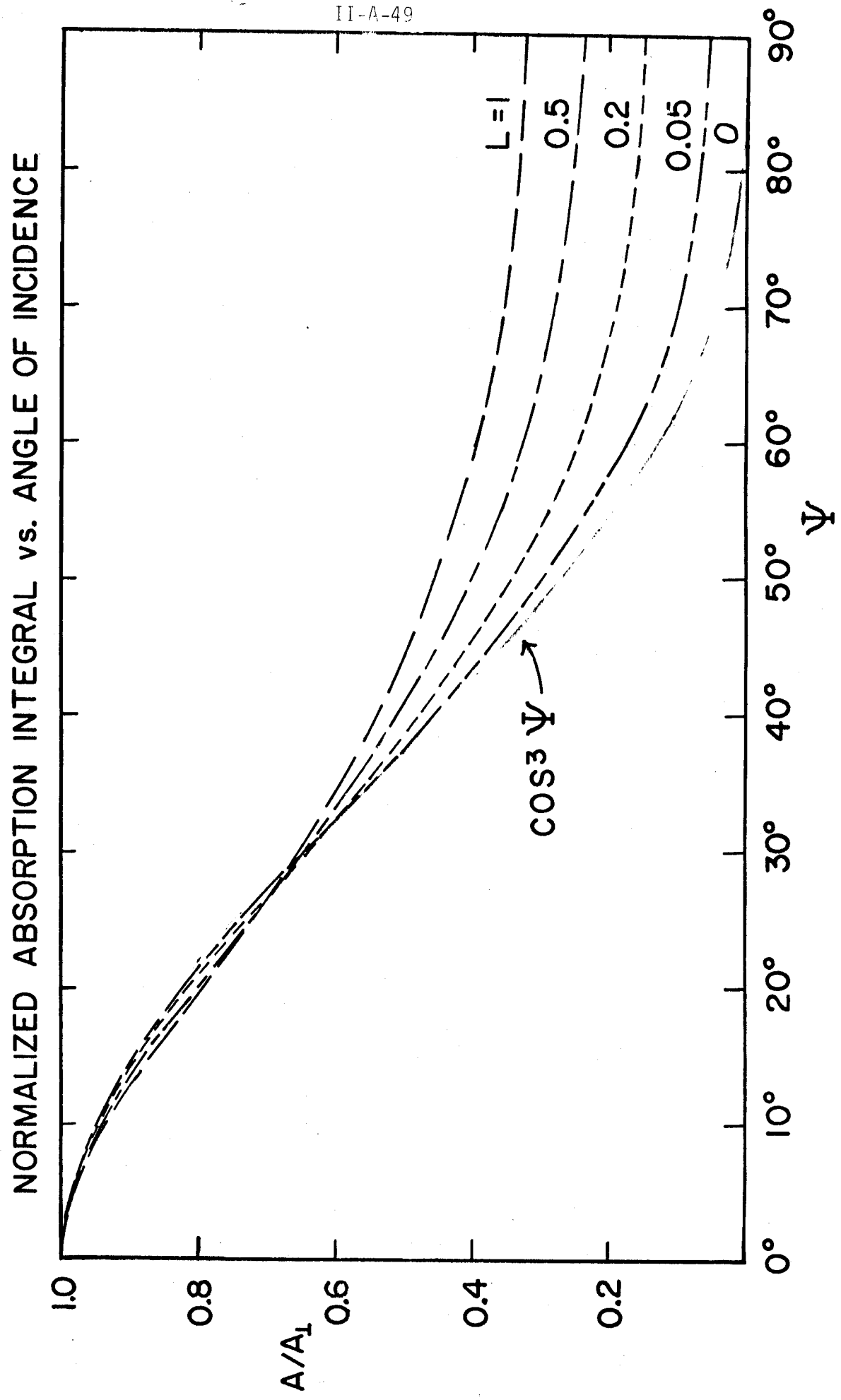
NORMALIZED ABSORPTION INTEGRAL vs. ANGLE OF INCIDENCE
A/A⊥
1.0
0.8
0.6
0.4
0.2
0°
10°
20°
30°
40°
50°
60°
70°
80°
90°
Ψ
L=1
0.5
0.2
0.05
0
COS³ Ψ

FIGURE 4

$$I_2 = \int_{r_m}^{\infty} \frac{e^{-x/L}}{r^3 z}\, dr \ , \tag{59}$$

where $x = r-1$, all distances being measured in units of r_c. For small Ψ,

$$I_1' = \tilde{I}_1 + I_1' \sin^2\Psi \tag{60}$$

$$I_2 = \tilde{I}_2 + I_2' \sin^2\Psi, \tag{61}$$

where

$$\tilde{I}_1 = 2\int_0^{\infty} \frac{\sqrt{1 - e^{-x/L}}}{(1+x)^3}\, dx \sim 1 - 1.227L + 6.522L^2 - \ldots \tag{62}$$

$$\tilde{I}_2 = 6L\int_0^{\infty} \frac{\sqrt{1 - e^{-x/L}}}{(1+x)^4}\, dx \sim 2L - 3.681L^2 + 13.04L^3 - \ldots \tag{63}$$

and

$$I_1' = -\int_0^{\infty} \frac{dx}{(1+x)^5 \sqrt{1 - e^{-x/L}}} \tag{64}$$

$$I_2' = -5L\int_0^{\infty} \frac{dx}{(1+x)^6 \sqrt{1 - e^{-x/L}}} \ . \tag{65}$$

This gives the desired expansion

$$A/A_{\perp} \sim 1 - \frac{3}{2}(\tilde{I}_1 + \tilde{I}_2)\sin^2\Psi + \frac{3}{2}(I_1' + I_2')\sin^4\Psi \ , \tag{66}$$

from which

$$\lim_{\Psi \to 0} A/A_{\perp} = 1 - \frac{3}{2}(\tilde{I}_1 + \tilde{I}_2)\Psi^2 \ . \tag{67}$$

This formula is very accurate for $L \leq 1$ and $\Psi < 10^{\circ}$. From the asymptotic expansions (62) and (63) we see

UNIFORMITY

EACH BEAM: $\Phi(\theta) = \Phi_L(r)\left(\frac{f}{R_T}\right)^2 \frac{1 + \delta\cos\theta}{(\cos\theta + \delta)^3}$ W/cm^2

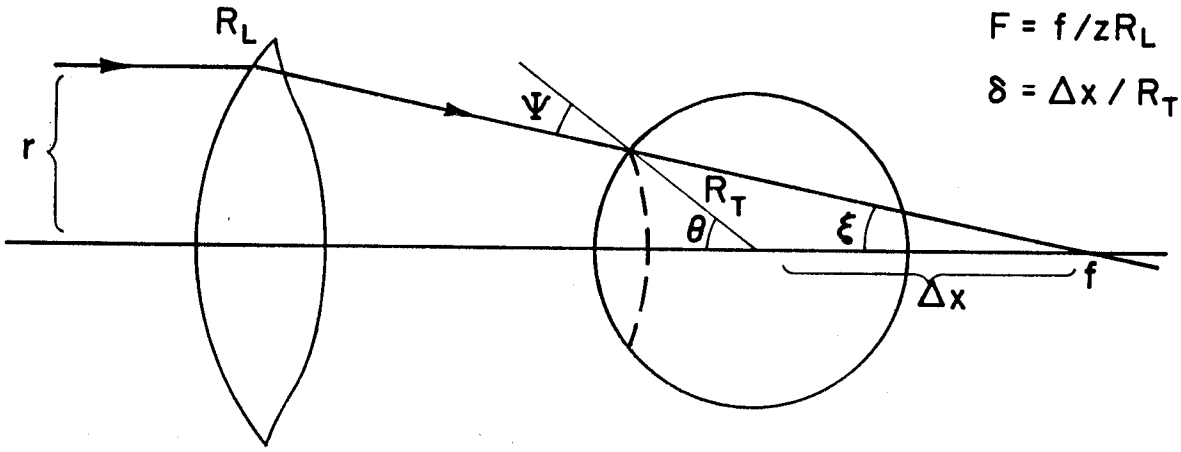

FIGURE 5

$$\lim_{\substack{\Psi \to 0 \\ L \to 0}} A/A_{\perp} = 1 - \frac{3}{2}\Psi^2 (1 + 0.773\, L) \quad . \tag{68}$$

In agreement with the slab result as $L \to 0$ and accurate to 0.1% for $L < .2$, $\Psi < 10^{0}$.

In general, our attempts to improve on the $\cos^3\Psi$ approximation to $A/A_{\perp}$ were disappointing, only modest improvements resulting for $L < 0.2$, $\Psi < 40^{0}$ or for $L < 1.0$, $\Psi < 10^{0}$.

II-A-5-d. Total Power Absorbed at Oblique Incidence

In estimating the total laser power absorbed by a pellet we must take into account the distribution of angles of incident due to

(1) The specific optical element (lens or mirror) employed

(2) The spatial beam profile incident on that element

Consider then an annular flux tube incident on a spherical target whose center is located a distance Δx inside the focus f, as depicted in Fig. 5 (assuming lenses for concreteness). The plasma corona is assumed to extend to an outer radius R, outside of which negligible absorption and refraction occur. The projected angle of incidence Ψ and lens angle ξ are related by

$$\sin\Psi = \frac{\Delta x}{r_c} \sin\xi \quad , \tag{69}$$

where

$$\tan\xi = \frac{r_L}{f} \quad . \tag{70}$$

Recall that the f/no. is

$$F = f/2R_L \quad . \tag{71}$$

In eq. (69) we assume that the critical radius remains near the original pellet radius, so that Ψ is a known function of the lens radius r_L. In reality r_c usually expands by about 50%, which enhances absorption, as will be seen in the next section.

The flux Φ_{in} (w/cm^2) incident on the pellet at r = R is related to the flux on the lens $\Phi_L(r_L)$ by

$$\Phi_L \, dA_L = \Phi_{in} \, dA_{in} \, , \tag{72}$$

which yields an expression for the target irradiance

$$\Phi_{in} = \Phi_L(r_L) \left(\frac{f}{R}\right)^2 \frac{1 + \frac{\Delta x}{R} \cos\theta}{\left(\cos\theta + \frac{\Delta x}{R}\right)^3} \, . \tag{73}$$

To calculate the total absorption, we first observe that in the presence of focusing, the exponential law, eq. (1) must be replaced by

$$\frac{\partial \Phi}{\partial \ell} = -\kappa\Phi + \left(\frac{\partial \Phi}{\partial \ell}\right)_{foc} \, . \tag{74}$$

An infinitesimal flux tube of cross sectional area δa encloses a power

$$\delta P = \Phi \delta a. \tag{75}$$

Along this flux tube,

$$\left(\frac{\partial \Phi}{\partial \ell}\right)_{foc} = - \frac{\Phi}{\delta a} \frac{\partial}{\partial \ell} \delta a. \tag{76}$$

Using this expression in eq. (74) and integrating then yields

$$\delta P_{out} = \delta P_{in} e^{-\int_o^{\ell} \kappa d\ell} \, . \tag{77}$$

Thus, it is <u>power</u>, not flux, that obeys an exponential absorption law.

To apply eq. (77) to the problem at hand, let us integrate over all flux tubes incident on the pellet

$$P_{out} = \int e^{-\int \kappa d\ell} dP_{in} = \int e^{-\int \kappa d\ell} dP_L. \tag{78}$$

The total power incident on the lens is

$$P_{in} = P_L = \int \Phi_L(r_L) dA_L. \tag{79}$$

The fractional absorption is therefore

$$n_{AB} = 1 - \frac{P_{out}}{P_L} = 1 - \frac{\int_o^{R_L} \Phi_L \, e^{-\kappa_o A_\perp \cos^3\psi} \, r_L dr_L}{\int_o^{R_L} \Phi_L r_L dr_L} \, , \tag{80}$$

where $\Psi(r)$ is given by (69) and (70). Finally we may define an "effective angle of incidence" by

$$P_u = P_L \, e^{-\kappa_o A_\perp \cos^3 \Psi_{eff}} \quad . \tag{81}$$

As a specific example let us take

$$\Phi_L(r_L) = \Phi_o \, e^{-(r_L/a)^3} \quad , \tag{82}$$

with a = 0.70. This beam profile, depicted in Fig. 6, gives good uniformity[21] for 20 f/1.5 lenses and a beam overlap $\theta_{max} \gtrsim 50°$. To complete the necessary algebra we have, from Fig. 5,

$$\delta = \Delta x / r_c = 2F \sin\theta_{max} - \cos\theta_{max} \tag{83}$$

$$\sin\theta_{max} = \frac{2F\delta + \sqrt{1 + 4F^2 - \delta^2}}{1 + 4F^2} \quad . \tag{84}$$

The integrated absorption and Ψ_{eff} are shown in Figures 7 and 8 for several values of $\kappa_o L$, with L in cm and, for λ_L = 1.06 μm,

$$\kappa_o = \frac{3 \, \ell n \Lambda \, Z_{eff}}{\theta_e^{3/2}} \ cm^{-1} \quad .$$

Thus, if θ_e = 1 keV and Z_{eff} = 1, L = 10^{-2} cm, $\kappa_o L$ = .25 and $\eta_{ab} \simeq 45\%$. η_{ab} reaches a maximum and Ψ_{eff} vanishes at $\theta_{max} = \xi = 18.4^o$, as they should. Due to the concentration of energy near the beam axis, the refractive loss at oblique incidence is quite moderate, amounting to only a few percent at $\theta_{max} = 50^o$.

For reference, Fig. 8 also shows the maximum angle of incidence, assuming f/1.5 lenses. Thus, at $\theta_{max} = 50^o$ most of the beam energy is

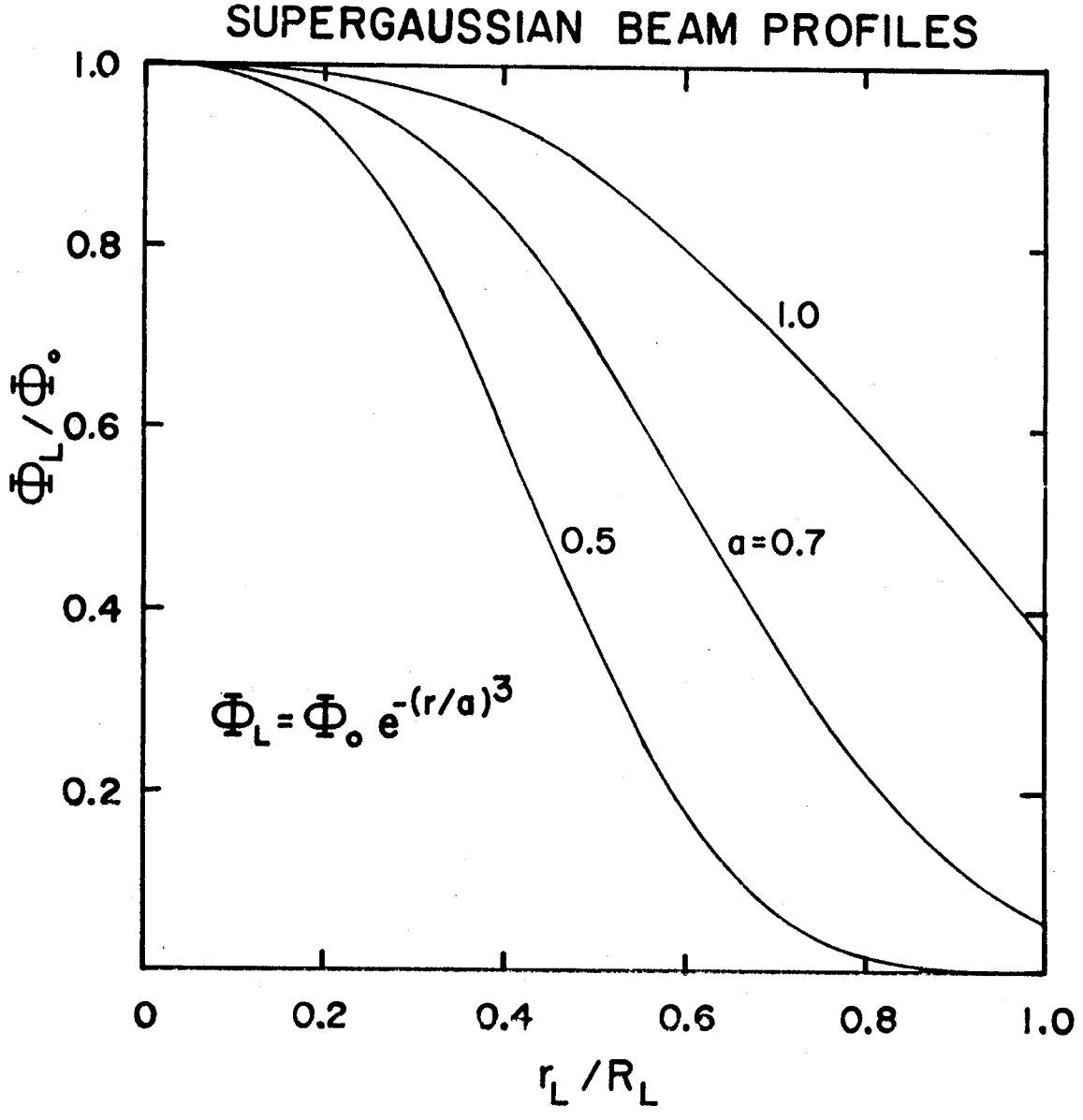
SUPERGAUSSIAN BEAM PROFILES
1.0
0.8
0.6
0.4
0.2
0
0.2
0.4
0.6
0.8
1.0
Φ_L/Φ_o
r_L/R_L
1.0
a=0.7
0.5
$\Phi_L = \Phi_o\, e^{-(r/a)^3}$

FIGURE 6

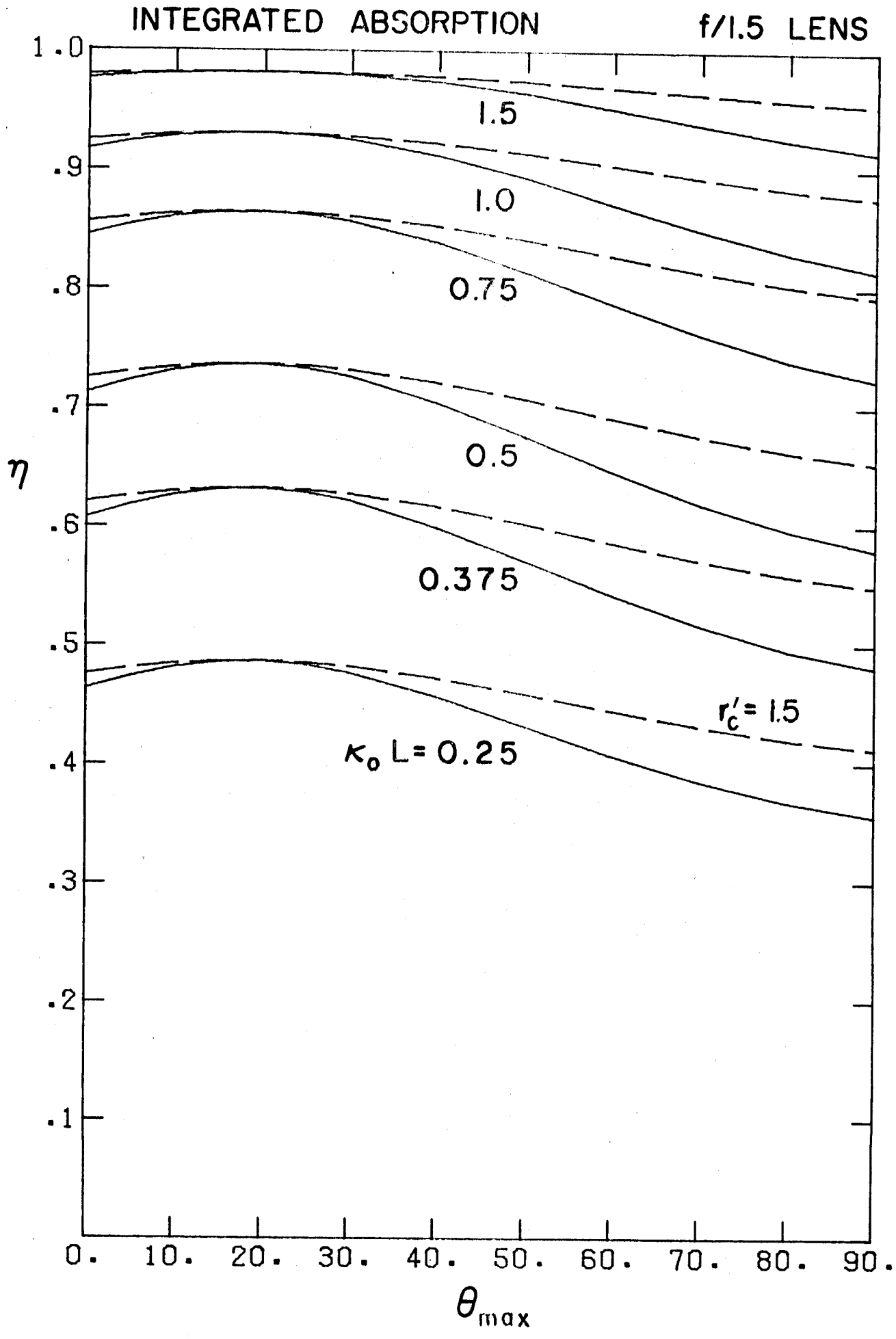
INTEGRATED ABSORPTION
f/1.5 LENS
1.0
.9
.8
.7
.6
.5
.4
.3
.2
.1
η
1.5
1.0
0.75
0.5
0.375
$r_c' = 1.5$
$\kappa_o L = 0.25$
0.
10.
20.
30.
40.
50.
60.
70.
80.
90.
θ_{max}

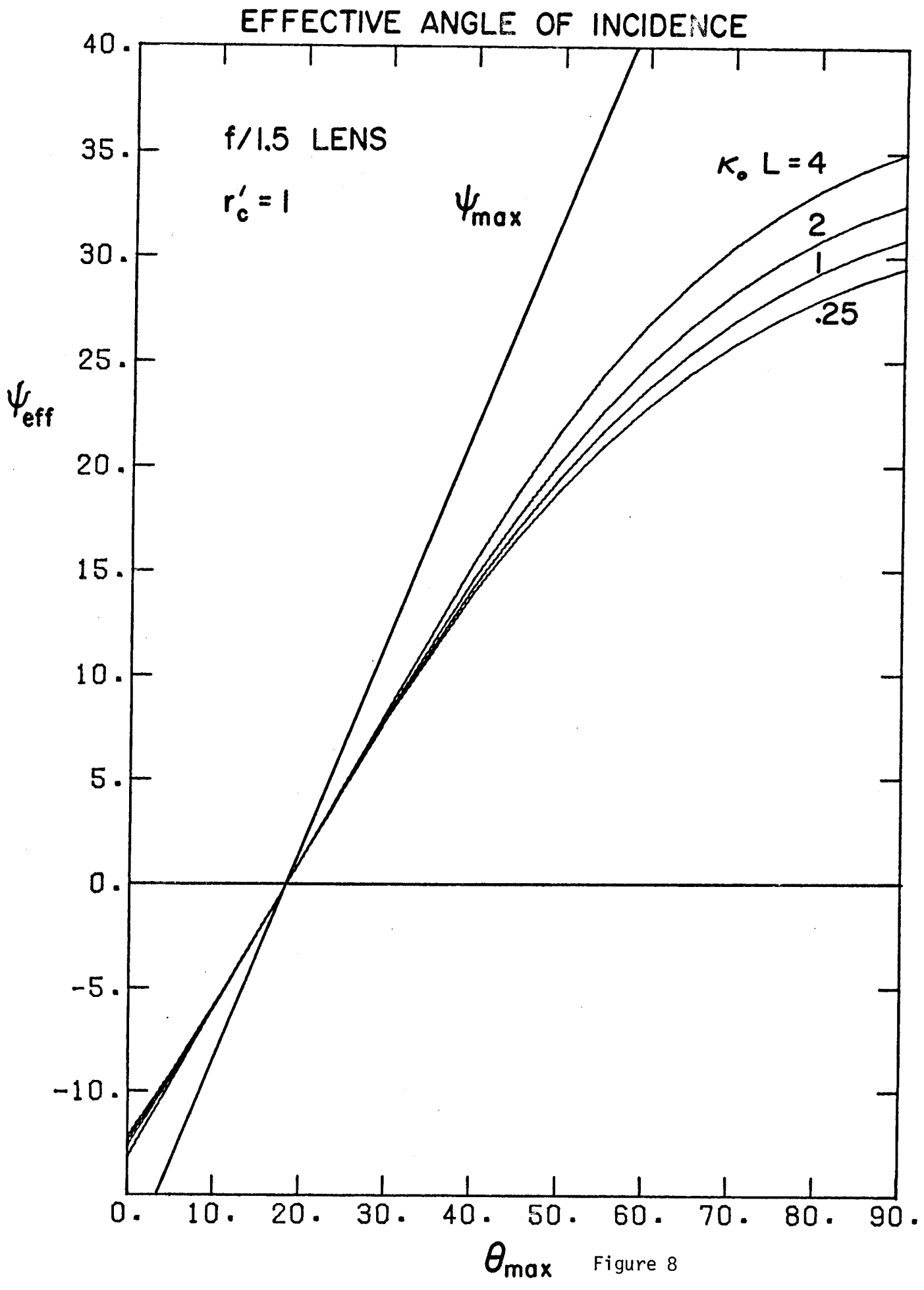
EFFECTIVE ANGLE OF INCIDENCE
f/1.5 LENS
$r_c' = 1$
ψ_{max}
$\kappa_o L = 4$
2
1
.25
ψ_{eff}
40.
35.
30.
25.
20.
15.
10.
5.
0.
-5.
-10.
0.
10.
20.
30.
40.
50.
60.
70.
80.
90.
θ_{max}

Figure 8

incident near $\Psi_{eff} \simeq 20^{o}$, considerably less than $\Psi_{max} = 31.5^{o}$, but still above the range for effective resonant absorption.

II-A-5-e. Effect of Expanding Critical Radius

When r_c increases in time, the projected angle of incidence Ψ decreases, enhancing absorption. Suppose that r_c has moved out to a position r_c'. The new angle of incidence is given by

$$\sin\Psi' = \frac{r_c}{r_c'} \sin\Psi \ . \tag{85}$$

Thus

$$\sin\Psi'(r_L) = \frac{r_L \left(\frac{r_c}{r_c'}\right)^{\delta}}{\sqrt{r_L^2 + 4F^2}} \ . \tag{86}$$

Using (86) in (80) and (81) we readily define a new absorption η_{ab}' and effective angle of incidence Ψ_{eff}'.

Since $\theta' < \theta$, the effective spot size is also reduced as r_c increases. The resulting degraded uniformity of illumination is of no consequence at later times, where a substantial hot corona has been established. While it is straightforward to calculate θ'_{max}, we shall plot η_{ab}' and Ψ_{eff}' vs. θ_{max}, as this is our reference value. The integrated absorption is shown as the dashed curves in Fig. 7 for $r_c' = 1.5\ r_c$ and in Fig. 9 for $r_c' = 2.0\ r_c$. Clearly, the effect of these (quite typical) expansions is to reduce refractive losses due to nonnormal illumination to entirely negligible levels. The burden then falls on resonant absorption to absorb the remaining energy. As Figs. 10 and 11 show, the expansion

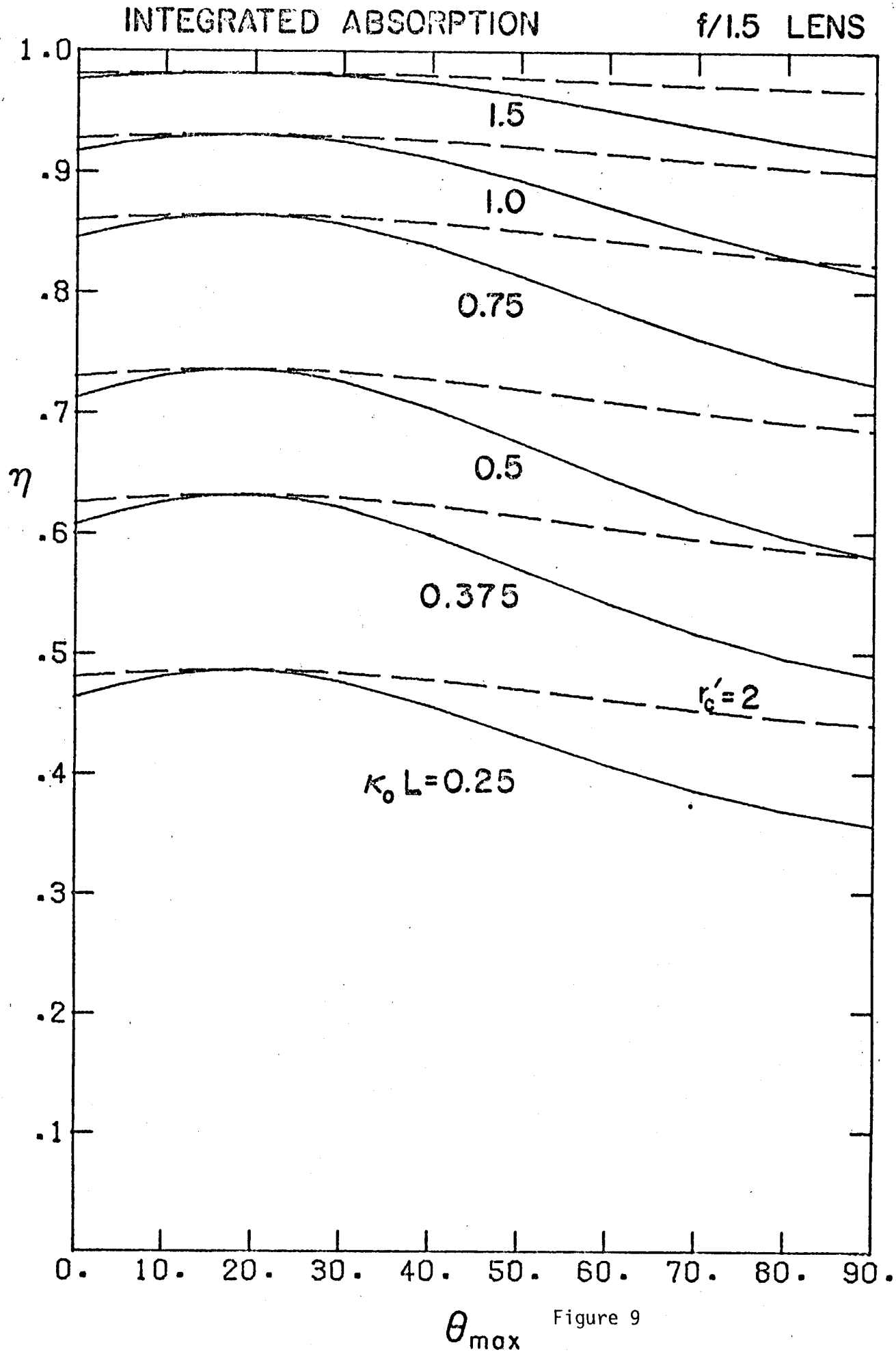
INTEGRATED ABSORPTION
f/1.5 LENS
1.0
.9
.8
.7
.6
.5
.4
.3
.2
.1
η
1.5
1.0
0.75
0.5
0.375
$r_c' = 2$
$\kappa_0 L = 0.25$
0.
10.
20.
30.
40.
50.
60.
70.
80.
90.
θ_{max}

Figure 9

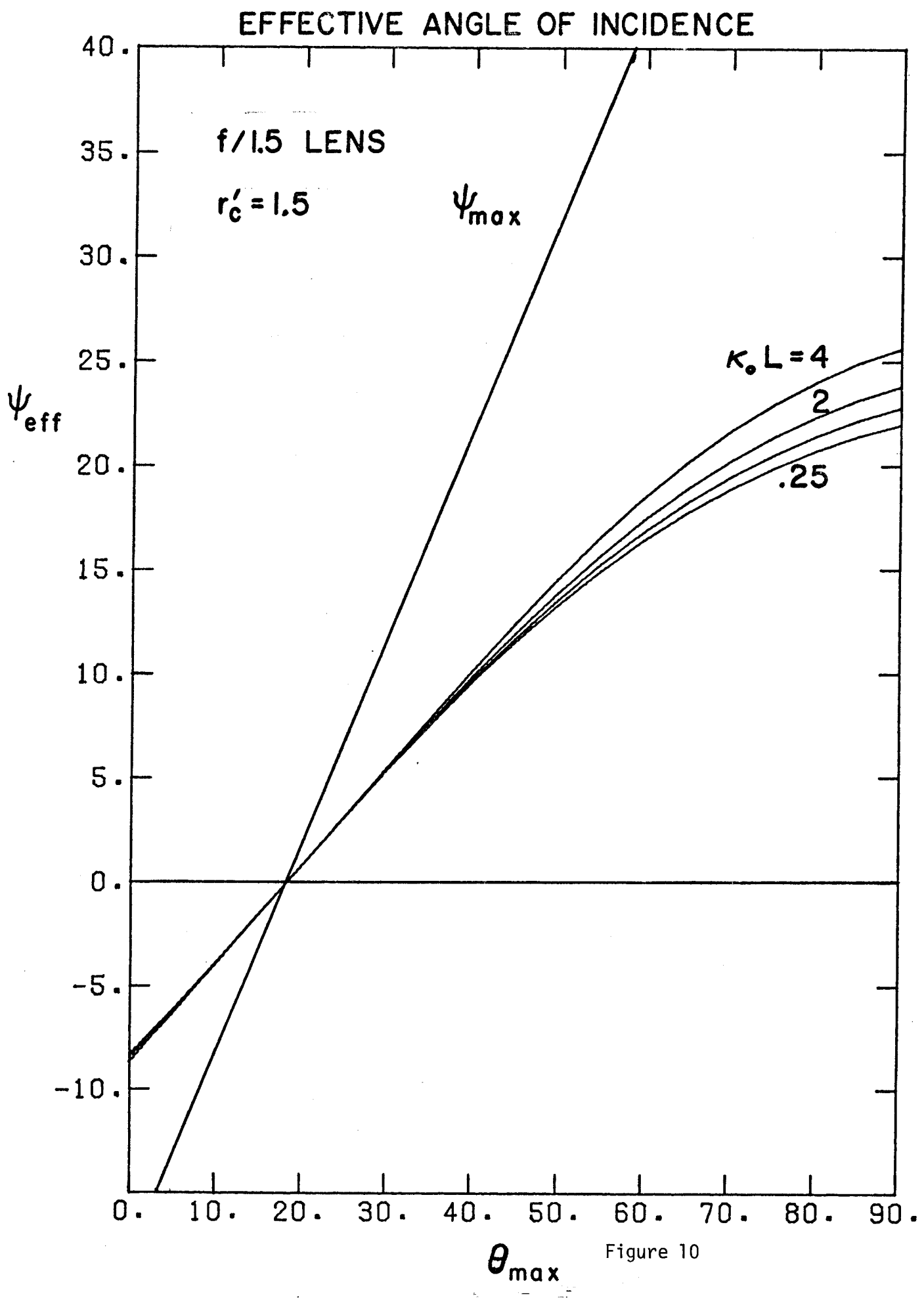
EFFECTIVE ANGLE OF INCIDENCE
f/1.5 LENS
$r_c' = 1.5$
ψ_{max}
$\kappa_o L = 4$
2
.25
ψ_{eff}
θ_{max}
40.
35.
30.
25.
20.
15.
10.
5.
0.
-5.
-10.
0.
10.
20.
30.
40.
50.
60.
70.
80.
90.

Figure 10

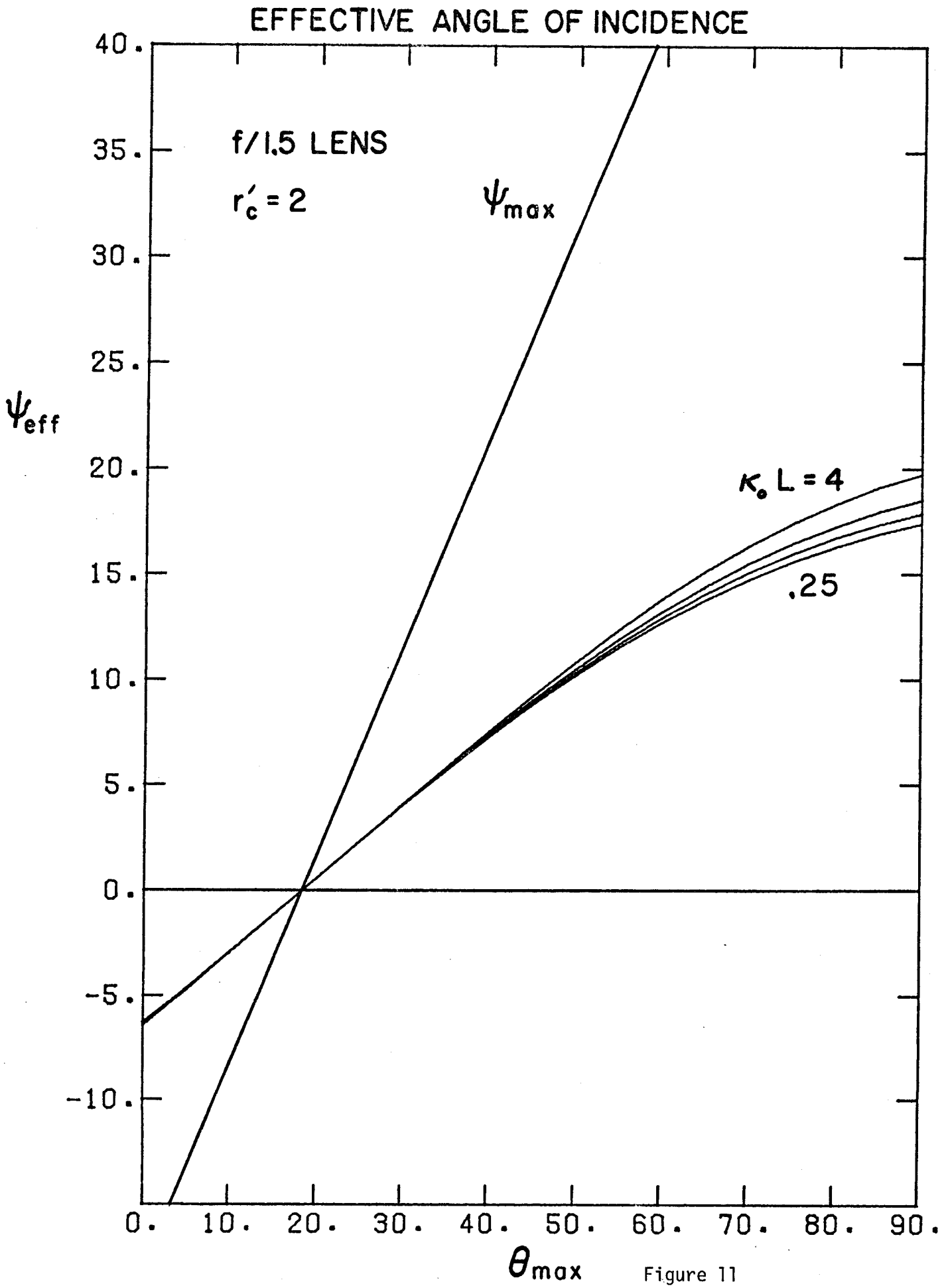
EFFECTIVE ANGLE OF INCIDENCE
f/1.5 LENS
$r_c' = 2$
ψ_{max}
$\kappa_o L = 4$
.25
ψ_{eff}
θ_{max}
40.
35.
30.
25.
20.
15.
10.
5.
0.
-5.
-10.
0. 10. 20. 30. 40. 50. 60. 70. 80. 90.

Figure 11

of r_c can dramatically reduce Ψ_{eff}. For example, if $\theta_{max} = 50^o$, $\Psi_{eff} = 14^o$ for $r_c' = 1.5\ r_c$, and $\Psi_{eff} \simeq 10^o$ for $r_c' = 2.0\ r_c$.

We have also calculated η_{ab} and Ψ_{eff} for f/3.5 lenses. An illumination system composed of 20 f/3.5 lenses takes up only 10% of the target solid angle as opposed to 50% for 20 f/1.5 lenses. As Figure 13 indicates, the absorption again does not depart significantly from that at normal incidence, the net absorption at $\theta_{max} = 50^o$ being only slightly inferior to that using f/1.5 lenses. On the other hand, the effective angles of incidence are significantly larger using f/3.5 lenses, as shown in Figs. 13-15. This time the values at $r_c' = 1$, 1.5 and 2.0 are about 25^o, 17.5^o and 12.5^o, resp., all at $\theta_{max} = 50^o$. Since resonant absorption is expected to be strongest for $\Psi = 7\text{-}10^o$, it is apparent that f/3.5 optics are above this range, even for large expansions of r_c, while f/1.5 optics are marginal, and then only if r_c doubles by the time the bulk of the laser pulse arrives.

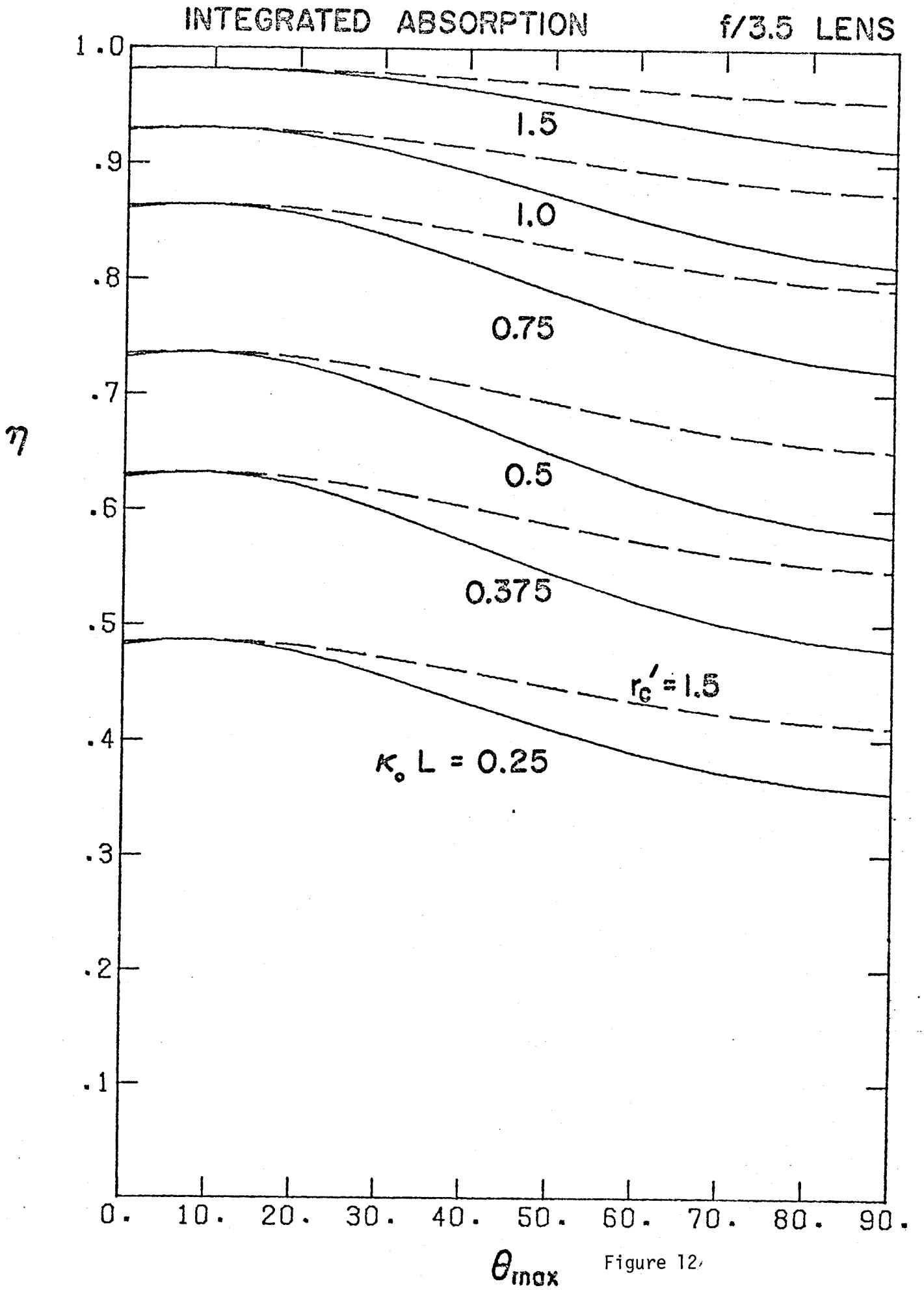
INTEGRATED ABSORPTION
f/3.5 LENS
1.0
.9
.8
.7
.6
.5
.4
.3
.2
.1
η
1.5
1.0
0.75
0.5
0.375
$r_c' = 1.5$
$K_o L = 0.25$
0.
10.
20.
30.
40.
50.
60.
70.
80.
90.
θ_{max}

Figure 12.

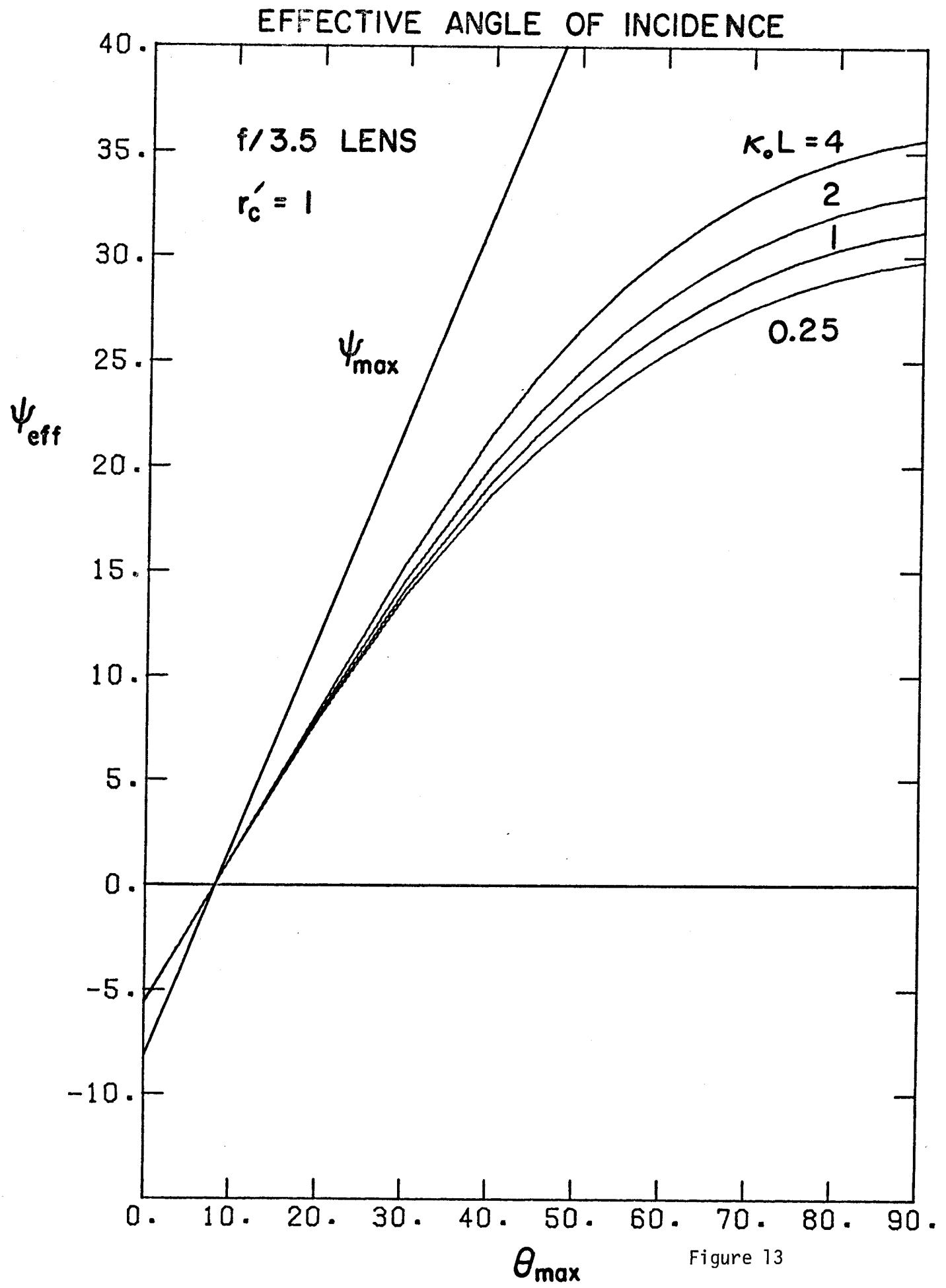
EFFECTIVE ANGLE OF INCIDENCE
f/3.5 LENS
$r_c' = 1$
$\kappa_o L = 4$
2
1
0.25
ψ_{max}
ψ_{eff}
θ_{max}
40.
35.
30.
25.
20.
15.
10.
5.
0.
-5.
-10.
0.
10.
20.
30.
40.
50.
60.
70.
80.
90.

Figure 13

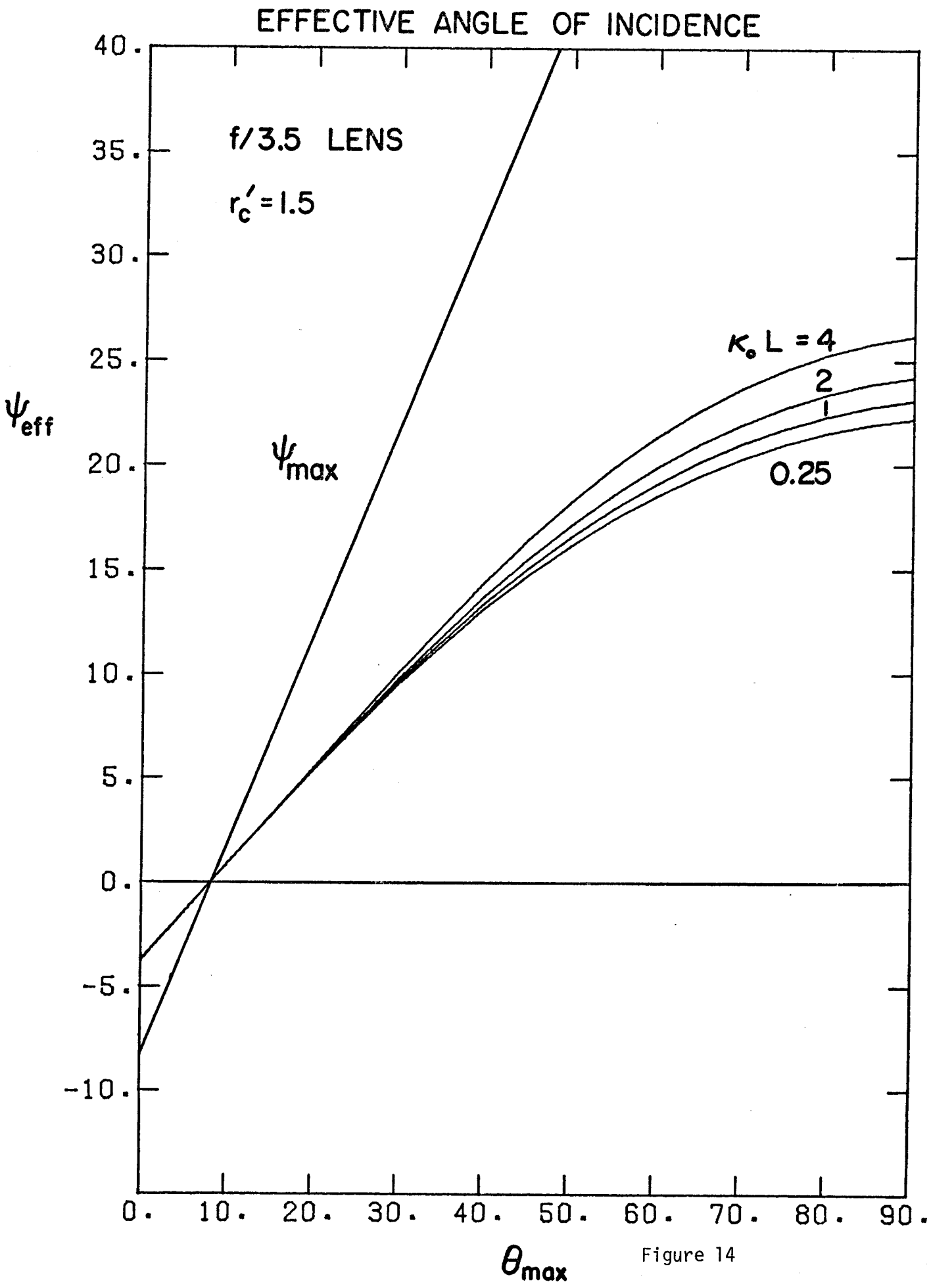
EFFECTIVE ANGLE OF INCIDENCE
f/3.5 LENS
$r_c' = 1.5$
ψ_{max}
$\kappa_o L = 4$
2
1
0.25
ψ_{eff}
θ_{max}
40.
35.
30.
25.
20.
15.
10.
5.
0.
-5.
-10.
0.
10.
20.
30.
40.
50.
60.
70.
80.
90.

Figure 14

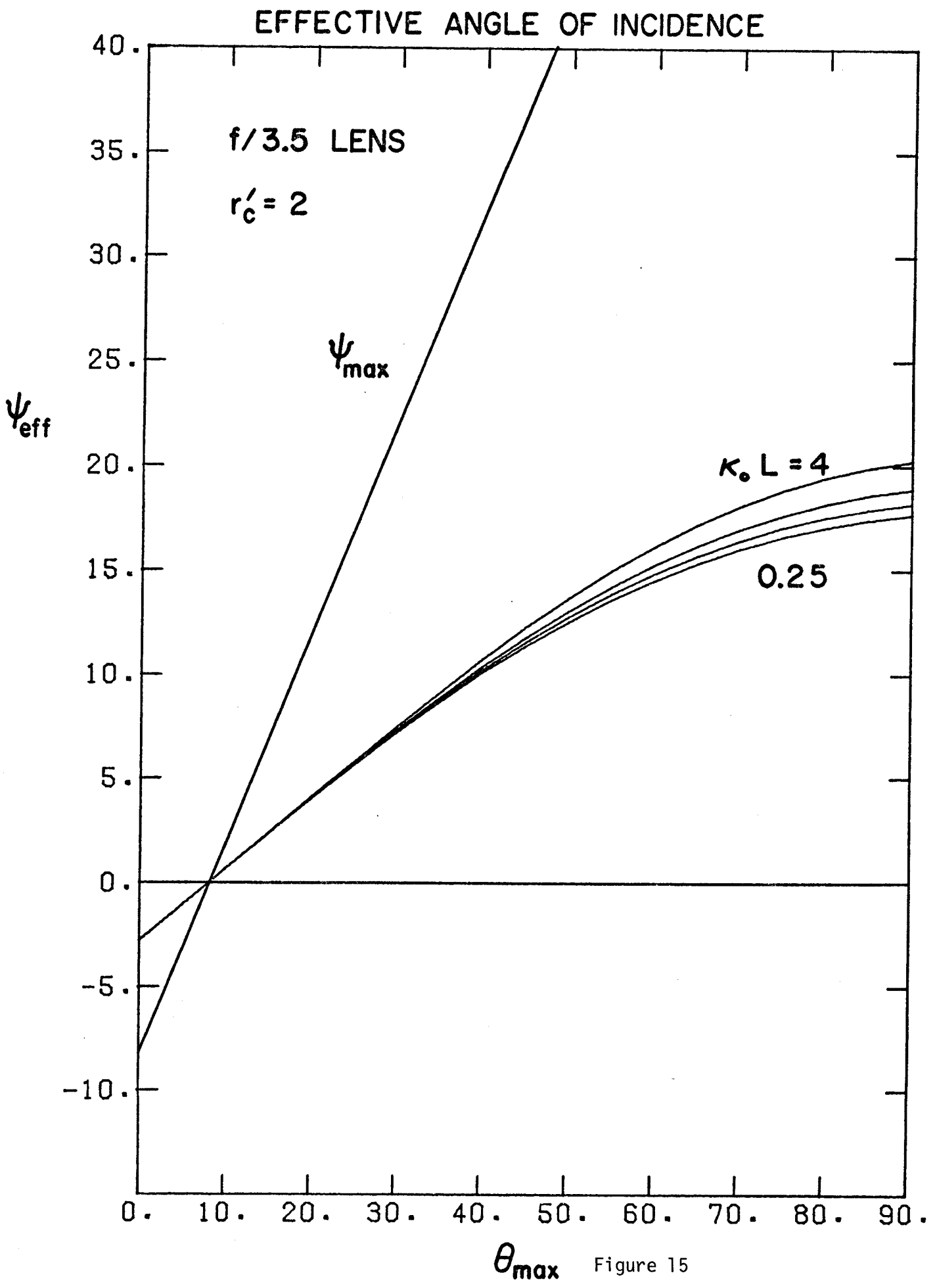
EFFECTIVE ANGLE OF INCIDENCE
f/3.5 LENS
$r_c' = 2$
ψ_{max}
$\kappa_o L = 4$
0.25
ψ_{eff}
θ_{max}
40.
35.
30.
25.
20.
15.
10.
5.
0.
-5.
-10.
0.
10.
20.
30.
40.
50.
60.
70.
80.
90.

Figure 15

II.A.5.f Resonance Absorption and Density Profile Steepening.

It is well known that collisional absorption decreases rapidly with increasing electron temperature and that nonclassical processes must be invoked to explain the amount of absorption observed in current experiments and required for projected reactor-grade implosions. The prevailing view is that resonance absorption[14] plays a dominant role, the p-polarized component of $\vec{E}$ driving plasma oscillations at the critical surface.

Resonance absorption is maximized when

$$L\sin^3\theta_o = \lambda/10.6, \tag{87}$$

where θ_o is the angle of incidence (our Ψ) and L is the density scale height at the critical surface. In the absence of any density profile steepening, strong absorption is confined to a rather narrow range of θ_o. Typical values are 30-50% absorption. Figure 16 shows L as a function of θ_o for λ = 0.53μm, 1.06μm and 10.6μm. For current experiments on small targets (L = 50-100μm) with λ = 1.06μm, the optimal angle of incidence is seen to be 6-7°, but reactor-grade pellets (L $\tilde{=}$ 1000μm) would require $\theta_o \approx 3°$. It is difficult to see how such small angles of incidence could be produced under conditions of uniform illumination.

Fortunately, density profile steepening due to radiation pressure, as well as by the resonance absorption process itself[13], broadens the effective range of incident angles. Extensive numerical studies have been carried out for small pellets, for which scale heights as small as 1μm have been measured. Further numerical simulation is needed to estimate the degree of self-steepening and resonance absorption in the larger pellets envisioned for use in a laser fusion reactor such as SOLASE I.

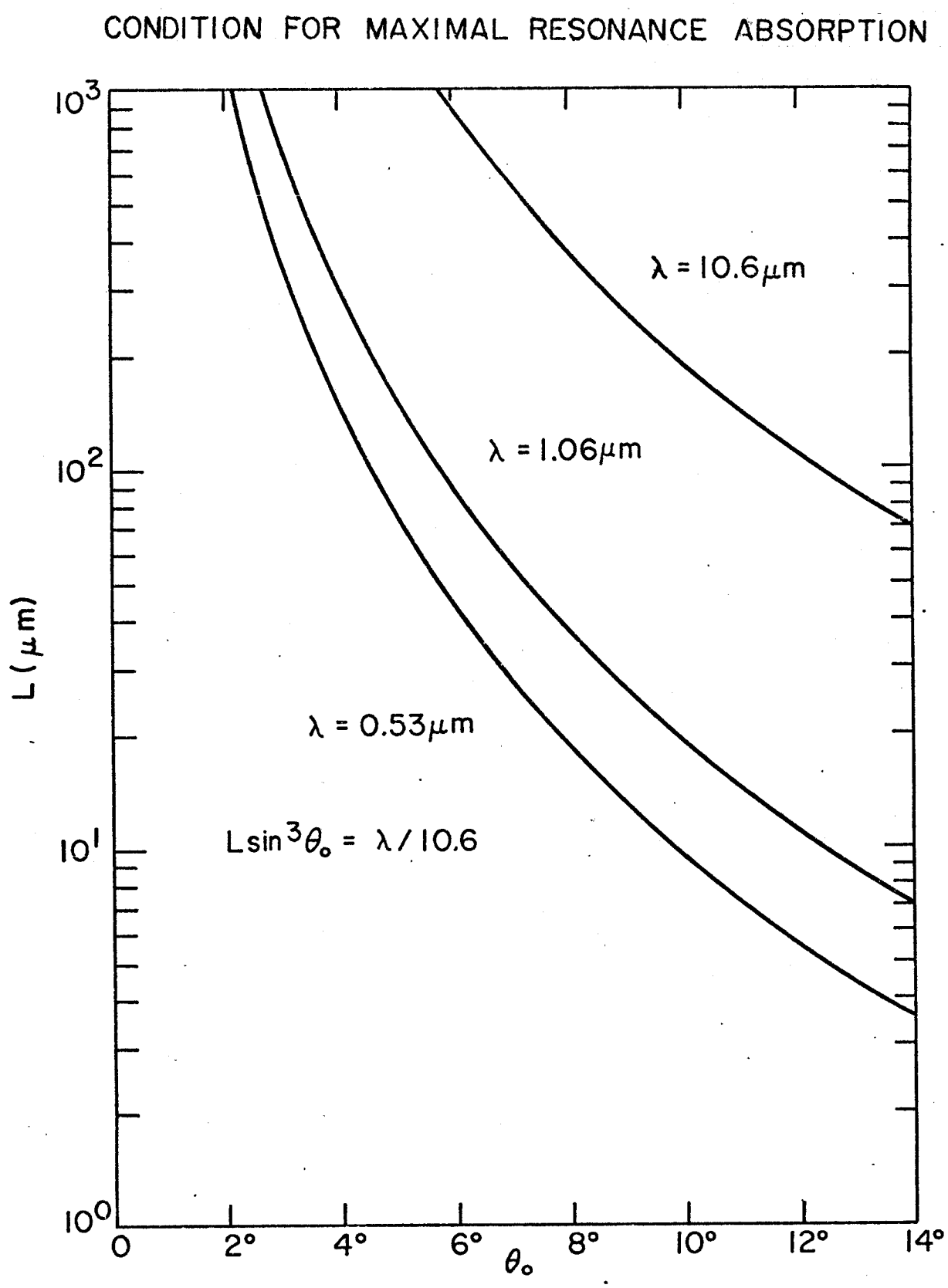
CONDITION FOR MAXIMAL RESONANCE ABSORPTION
10^3
10^2
10^1
10^0
L (μm)
λ = 10.6μm
λ = 1.06μm
λ = 0.53μm
$L\sin^3\theta_o = \lambda / 10.6$
0
2°
4°
6°
8°
10°
12°
14°
θ_o

FIGURE 16

References for Section II-A-5.

1. J. G. Downward, R. A. Grandey, F. J. Mayer and D. Mitrovitch, Bull. Am. Phys. Soc. 20, 1247 (1975).

2. H. G. Ahlstron et al., Bull. Am. Phys. Soc. 21, 1046 (1976).

3. D. W. Phillion and R. L. Lerche, Bull. Am. Phys. Soc. 21, 1046 (1976).

4. P. Kolodner and E. Yablonovitch, Bull. Am. Phys. Soc. 21, 1083 (1976).

5. D. W. Forslund, J. M. Kindel and E. L. Lindman, Phys. Fluids 18, 1002 (1975).

6. LLL Laser Program Annual Report 1975, UCRL 50021-75, p. 311.

7. D. V. Gionvanielli, Bull. Am. Phys. Soc. 21, 1047 (1976).

8. R. E. Kidder, Proc. Int. School of Physics, Enrico Fermi Course 45 (1971).

9. J. E. Howard, R. A. Cover and S. Jorna, Bull. Am. Phys. Soc. 18, 1346 (1973).

10. J. W. Shearer and W. S. Barnes, in Laser Interaction and Related Phenomena, Ed. H. Hora and H. Schwartz, Plenum Press(New York), 1971.

11. K. A. Brueckner and S. Jorna, Rev. Mod. Phys. 46, 325 (1974).

12. J. Dawson, P. Kaw and B. Green, Phys. Fluids 12, 875 (1969).

13. K. G. Estabrook, E. J. Valeo and W. L. Kruer, Phys. Fluids 18, 1151 (1975).

14. J. P. Freidberg, R. W. Mitchell, R. L. Morse and L. I. Rudsinski, Phys. Rev. Lett. 28, 795 (1972).

15. R. E. Kidder, Nucl. Fusion 16, 3 (1976).

16. LLL Laser Program Annual Report-1974, UCRL-50021-74, p. 392.

17. E. Cojacaru and P. Mulser, Plasma Phys. 17, 393 (1975).

18. K. A. Brueckner, private communication.

19. J. W. Shearer, Phys. Fluids 14, 183 (1971).

20. M. Born and W. Wolf, Principles of Optics, 2nd ed., Pergamon Press (Oxford) 1964, p. 123.

21. J. E. Howard, Univ. of Wisconsin Nuclear Engineering Department Report UWFDM-172, 1976.

II-A-6. Radiation

II-A-6-a. Introduction

Radiative processes and transport can play an important role in the compression and heating of the pellet and in the design of the laser fusion reactor. In order to achieve densities high enough for efficient thermonuclear burn, the fusion pellet must be compressed along a low adiabat.[1] This will not be possible if the compressed region of the pellet is significantly preheated by X-rays originating in the hot outer regions.[2] In addition, radiation flow and energy loss during implosion and burn can effect the ion and electron fluid motion and energy and, therefore, the implosion and burn process. The X-ray spectra and X-ray energy escaping a fusion pellet will depend upon its design. The radiation transport within a pellet with a high Z outer shell will not be the same as the transport within a bare DT pellet. For example, the X-ray spectra escaping the pellet, the X-ray diffusion time to the walls of the reactor and the X-ray energy content will be different for the two designs. The type of surface damage caused by an intense X-ray flux depends upon the X-ray spectra and total energy. A satisfactory model of compression and thermonuclear burn must, therefore, include a comprehensive treatment of radiation and radiation transport.

II-A-6-b. The Radiation Transport Equation

To solve the radiation transport problem we will need to know the relationship between radiative specific intensity and other physically meaningful quantities. In terms of the specific intensity we can obtain the energy density at a given frequency

$$E(\underline{r},\gamma,t) = 1/c \int_{4\pi} d\underline{\Omega}\ I(\underline{r},\gamma,\underline{\Omega},t) \qquad (1)$$

the i-th component of the radiative flux vector

$$F_i(\underline{r},\gamma,t) = \int_{4\pi} d\underline{\Omega}\ \Omega_i\ I(\underline{r},\gamma,\underline{\Omega},t) \qquad (2)$$

and the ij-th component of the radiative pressure tensor

$$P_{ij}(\underline{r},\gamma,t) = \int_{4\pi} d\underline{\Omega}\ \Omega_i\Omega_j\ I(\underline{r},\gamma,\underline{\Omega},t) \qquad (3)$$

These are the variables we will use in our radiation transport model.

After making certain assumptions about the radiation and its interaction with matter, the radiative specific intensity can be shown to satisfy a continuity equation of the form[3]

$$1/c\ \frac{\partial}{\partial t}\ I(\gamma,\underline{\Omega}) = -\underline{\Omega}\cdot\underline{\nabla}\ I(\gamma,\underline{\Omega})$$

$$- \sigma_a(\gamma)\ I(\gamma,\underline{\Omega}) + J(\gamma)(1 + c^2 I(\gamma,\underline{\Omega})/2h\gamma^3)$$

$$- \int\int d\gamma' d\underline{\Omega}'\ \sigma_s(\gamma \to \gamma',\ \underline{\Omega}\cdot\underline{\Omega}')\ I(\gamma,\underline{\Omega})\left(1 + \frac{c^2 I(\gamma',\underline{\Omega}')}{ch\gamma'^3}\right)$$

$$+ \int\int d\gamma' d\underline{\Omega}'\ \sigma_s(\gamma' \to \gamma,\ \underline{\Omega}\cdot\underline{\Omega}')\ \frac{\gamma}{\gamma'}\ I(\gamma',\underline{\Omega}')\left(1 + \frac{c^2 I(\gamma,\underline{\Omega})}{2h\gamma^3}\right) \qquad (4)$$

where the first term on the right hand side of the equation is due to photon streaming, the second to photon absorption, the third to photon emission, the fourth to photon outscattering ($\gamma \to \gamma'$ and $\underline{\Omega} \to \underline{\Omega}'$) and the last to photon inscattering ($\gamma \to \gamma'$ and $\underline{\Omega}' \to \underline{\Omega}$).

A discussion of the variable Eddington method, the method we have used to solve the transport equation, is given in Section II-B-2-g. This method is based on the expansion of the angular moments $\int I\mu^k d\mu$ for one dimensional planar or spherical symmetric problems. The expansion is truncated after the second moment and a semiempirical expression is used to determine the pressure tensor.

II-A-6-c. Radiation Processes in a Laser-Fusion Plasma

II-A-6-c-i. Introduction

Figure 1 illustrates a typical plasma configuration which results when a target pellet consisting of a relatively high density spherical shell containing DT fuel in gaseous form is compressed by an intense laser pulse.[2] Region I is the compressed fuel. Region II is the compressed inner layer of the tamper shell, and region III and region IV are the expanding outer layers of the tamper shell. The laser energy is deposited in region IV, just outside the critical density surface.

Each of the last three regions represents a different atomic modeling problem. Since region II is relatively cold and highly compressed, it is opaque to most of the X-ray radiation and can be described by an LTE equation of state. Conversely, regions III and IV are transparent to most of the radiation. Region III can, in general, be represented by a steady state coronal equation of state, but the coronal model breaks down in region IV and must be replaced by a time-dependent solution to the rate equations.

Bremsstrahlung radiation in the region of the critical density surface, region IV, must be corrected for forced oscillations of the electrons in the laser electric field. Suprathermal electrons created by plasma instabilities in region IV radiate a hard bremsstrahlung spectrum when they undergo scattering as they propagate inward toward region II.

This section is concerned with developing an atomic plasma model and the corresponding radiation emission and absorption coefficients, including nonthermal processes.

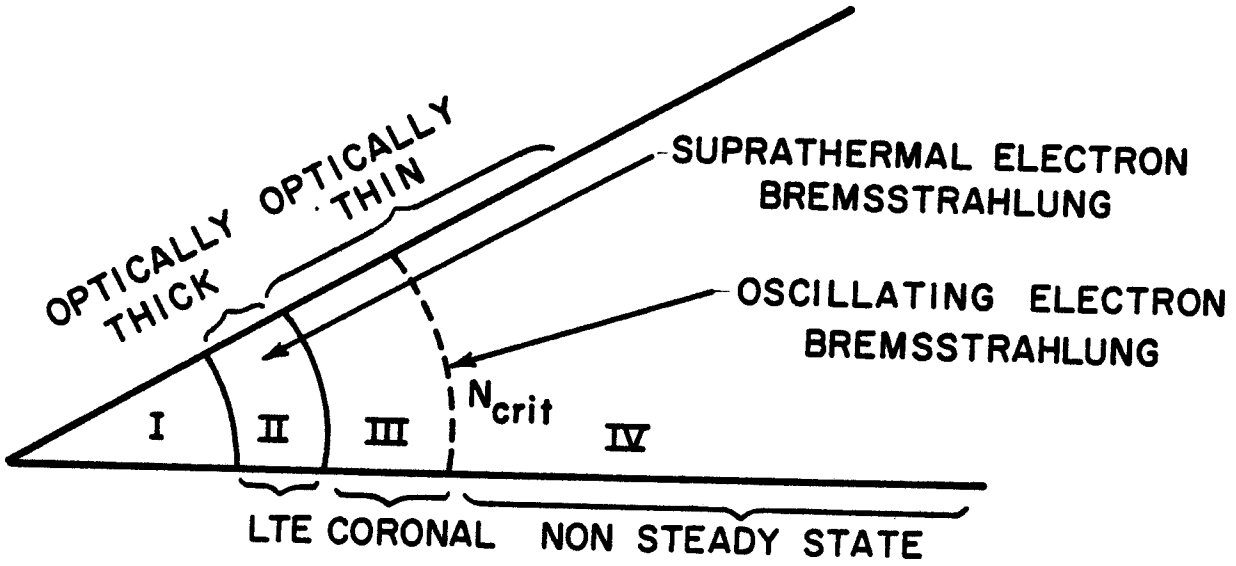

TYPICAL PLASMA CONFIGURATION OCCURRING IN LASER HEATED FUSION TARGETS SHOWING THE DIFFERENT REGIONS PERTINENT TO THE RADIATION TRANSPORT PROBLEM.

FIGURE I

II-A-6-c-ii. Description of the Atomic State of a Plasma

To describe radiative processes occurring in a laser-fusion plasma, a model of the atomic state of a partially ionized mixture of chemical elements is needed. The model should be able to calculate the charge state and the electron configuration state of any ion in the plasma.

Let the concentration of atoms of atomic number Z be specified by C_Z. The number density of atoms of type Z is

$$N_Z = C_Z N_i \ ,$$

where N_i is the number density of atoms of all types given by

$$N_i = \rho \frac{N_o}{\overline{A}}$$

In the above expression, N_o is Avogadro's number, ρ is the density and $\overline{A} = \Sigma\, C_Z A_Z$, where A_Z is the atomic weight of element Z.

An atom of atomic number Z can exist in various ionic charge states. We define $f_{Z,S}$ as the fraction of atoms of element Z that exist in charge state S. Therefore, the population of ions in a chemical mixture at any time is given by C_Z and $f_{Z,S}$.

The electron configuration of an ion is specified by the occupation numbers for each energy level. We define $n_{Z,S,j}$ as the number of bound electrons in level j of an ion of element Z in charge state S.

When $f_{Z,S}$ and $n_{Z,S,j}$ are known, the radiation emission and absorption coefficients for the plasma can be obtained. In the model presented, a mean ion configuration is first obtained from $f_{Z,S}$ for each element and the radiation properties are then determined for a mixture of mean ions of concentration C_Z.

II-A-6-c-iii. The Distribution of Ion States

Local Thermal Equilibrium (LTE)

In general, both collisional and radiative transition rates determine the distribution of electrons among the various energy states. In high density plasmas dominated by collisional processes, the ion population is said to be in local thermal equilibrium (LTE) at the material temperature T. In LTE the distribution of energy states can be obtained from the law of equipartition without requiring a specific knowledge of transition rates.

Three-body recombination is a radiationless interaction involving one ion and two electrons in which one electron is captured by the ion and the other is scattered away while conserving energy and momentum. The processes of ionization by two-body electron-ion collisions and three-body recombination are statistical inverses of one another, and LTE is a condition of statistical equilibrium. Thus, for LTE plasmas, ionization states can be determined by equations (the Saha equations) which result from a balance between collisional ionization by two-body electron-ion collisions and three-body recombination.

The state of a LTE plasma is described by the following equations which are given for Fermi-Dirac statistics in order to be applicable for any degree of degeneracy. The density of free electrons in the velocity range $dv = dp/m$ is[2]

$$N_e(p)dp = \frac{8\pi}{h^3} \frac{p^2 dp}{e^{-n + p^2/2mkT} + 1} \qquad (5)$$

where p is the electron momentum, m the electron mass and n is the degeneracy parameter. The degeneracy parameter is obtained in terms of the density and temperature by normalization,

$$N_e = \frac{4\pi}{h^3} (2mkT)^{3/2} F_{1/2}(\eta) \qquad (6)$$

where $F_{1/2}(\eta)$ is the Fermi-Dirac integral of order 1/2.

The distribution of ions of element Z in the ground state is given by the Saha equation

$$\frac{f_{Z,S+1}}{f_{Z,S}} = \frac{w_{S+1}}{w_S} e^{-n-X_{Z,S}/kT} \qquad (7)$$

where w_S is the statistical weight and $X_{Z,S}$ is the ionization energy of state S. If each ion is assumed to exist in the ground state only, the Saha equation for small degeneracy becomes[4]

$$\frac{f_{Z,S+1}}{f_{Z,S}} = \frac{2}{N_e} \left(\frac{2\pi mkT}{h^2}\right)^{3/2} e^{-X_{Z,S}/kT} \qquad (8)$$

Steady State Coronal Region

In an optically thin plasma, the photon emission process is not balanced by its inverse process. As a result, the population distribution departs from that of equipartition and LTE ceases to be valid.

At moderately low densities, the ion population can exist in a quasi-steady state where collisional ionization is balanced by radiative recombination. A plasma in this condition is described by the steady state coronal model. In this model the ion population is given by the expression[4]

$$\frac{f_{Z,S+1}}{f_{Z,S}} = 3.3 \times 10^{-16} \frac{\Delta_{S,Z}}{1+d} \frac{(kT)^{3/4}}{X_{Z,S}^{11/4}} e^{-X_{Z,S}/kT} \text{ cgs units} \qquad (9)$$

where $\Delta_{Z,S}$ is the number of electrons in the last occupied shell of the ion S, and d is the correction for dielectric recombination.

Dielectric recombination is a process whereby a free electron is captured by an ion which is left in a doubly excited state.[5] The doubly excited ion subsequently decays to a singly excited state with the emission of a photon. Consequently, this process requires detailed knowledge of the

excited states.

Nonsteady State Region

So far it has been assumed that atomic processes occur quickly enough that the population densities adjust almost instantaneosly to external changes in the plasma. Because transition rates are density dependent, the quasi-steady state assumption will break down at sufficiently low denisty. For a coronal model plasma, the atomic relaxation time τ is almost independent of temperature and given approximately by[4] $\tau = 10^{12} N_e^{-1}$. Atomic relaxation times for different electron densities are given in Table I.[2] When hydrodynamic work or thermal conduction rates are comparable to those represented by Table I, the quasi-steady state model breaks down and rate equations must be solved to obtain the ionic populations.

Table I

Atomic Relaxation Times for Corona Model Plasmas

N_e	10^{21}	10^{22}	10^{23}	10^{24}
τ(sec)	10^{-9}	10^{-10}	10^{-11}	10^{-12}

Occupation Numbers for Ions - Ground State Model

Each ion will be assumed to exist in the ground state only. Occupation numbers for ions in the ground state are obtained as follows.[2]

Let the maximum number of bound electrons per shell be $A_j = 2j^2$ and let the cummulative number of bound electrons out to and including shell j be

$$B_j = \sum_{k=1}^{j} 2k^2 .$$

Define j′ as the quantum number at the last full shell j, i.e. $B_{j'} \leq Z\text{-}S$, where $Z - S = n_{BE}$ is the total number of bound electrons. The occupation number of each level j for the ionic state S of element Z is given by:

if $n_{BE} \leq 2$, $j' = 0$ and $n_{Z,S,1} = n_{BE}$

$$n_{Z,S,j} = 0, \quad j > j'$$

if $n_{BE} > 2$, $j' > 0$ and $n_{Z,S,j} = A_j$, $j = 1,2 \ldots, j'$

$$n_{Z,S,j'+1} = n_{BE} - B_{j'}$$

$$n_{Z,S,j} = 0, \quad j > j' + 1$$

A Model for the LTE and Steady State Coronal Regions of the Plasma

The model presented here is based on the idea that collisional ionization is balanced by three-body recombination at high densities and by radiative recombination at low densities.[2] Thus, the model assumes that radiative excitation is negligible compared with collisional excitation in determining populations of energy states. The steady state model is determined by

$$R_{CI} = R_{RR} + R_{CR} \tag{10}$$

where the collisional ionization rate neglecting degeneracy, R_{CI}, is given by[4]

$$R_{CI} = f_{Z,S} N_e S_s,$$

$$S_s = 4.9 \cdot 10^{-24} \frac{\Delta_{Z,S} (kT)^{1/4}}{X_{Z,S}^{7/4}} e^{-X_{Z,S}/kT} \tag{11}$$

the radiative recombination rate, R_{RR}, is given by[4]

$$R_{RR} = f_{Z,S+1} N_e \alpha_{S+1} \tag{12}$$

$$\alpha_{S+1} = 1.5 \cdot 10^{-8}(1 + d) \frac{X_{Z,S}}{(kT)^{1/2}}$$

and the collisional recombination rate, R_{CR}, is given by[6]

$$R_{CR} = f_{Z,S+1} N_e^2 B_{S+1},$$

$$B_{S+1} = 1.6 \cdot 10^{-63} \frac{\Delta_{Z,S}}{X_{Z,S}^{7/4}(kT)^{5/4}} \qquad (13)$$

The balance of rates, equation (10) then gives for the ratio of ion fraction

$$\frac{f_{Z,S+1}}{f_{Z,S}} = \frac{S_s}{\alpha_{S+1} + N_e B_{S+1}} \qquad (14)$$

which in regions of high density, $\alpha >> N_e B$, reduces to the Saha equation (8) and in regions of low density, $\alpha << N_e B$, reduces to the coronal equation (9).

II-A-6-c-iv. A Mean Ion Representation for Computing Radiative Properties

Once the ionization energies are known, the ion distribution can be obtained for a wide range of temperatures and densities from equation (14). Ionization energies can be computed using the Mayer method.[7,8]

Because the number of possible charge states and energy levels for mixtures of several moderately high Z elements is large, the model used to calculate these levels and states needs to be computationally inexpensive. Ion distributions are usually clustered rather closely about the mean. We make use of this behavior and define a mean ion configuration for each element in the plasma. These mean values are then used to calculate radiation emission and absorption.[9]

We define the mean ion configuration in terms of the distribution of ionic states,[2]

$$n_{Z,j} = \Sigma f_{Z,S} n_{Z,S,j} \qquad (15)$$

The mean ion defined by (15) will have a charge given by

$$Z' = Z - \sum_j n_{Z,j} \tag{16}$$

Once the occupation numbers of the mean ion are known, the screened nuclear charge can be determined by

$$Z^*_{Z,j} = Z - \sum_{k \neq j} n_{Z,K}\, \sigma_{jK} - n_{Z,j}(1 - 1/d_j)\sigma_{jj}, \tag{17}$$

where σ_{jK} are the Slater screening constants and where

$$d_j = \min[2_j^2,\ n_{BE} - \sum_{k=1}^{j-1} n_{Z,K}]$$

The mean ion ionization energy in electron volts can be written as

$$X_{Z,j} = 13.6\left(\frac{Z^*_{Z,j}}{j}\right)^2 - \frac{Z'e^2}{2a_{Z'}}\left[3 - \frac{\langle r^2_{Z,j}\rangle}{a^2_{Z'}}\right] - E_o \tag{18}$$

where

$$E_o = 13.6 \cdot \frac{3}{5} \cdot \frac{N_i}{N_e} \sum_Z C_Z \sum_S f_{Z,S}\, S^2 \left(\frac{a_o}{a_s}\right) ,$$

$$a_{Z'} = \left(\frac{3}{4\pi}\frac{Z'}{N_e}\right)^{1/3} ,$$

$$\langle r^2_{Z,j}\rangle = a_o^2\, \frac{2j^4}{(Z^*_{Z,j})^2}\left[1 + \frac{1}{2j^2}\right] ,$$

and a_o is the Bohr radius.

II-A-6-c-v. Emission Processes

Thermal Bremsstrahlung Emission

The bremsstrahlung emission into 4π steradians is given by[10]

$$J^{\gamma}_{ff}\, d\gamma = 8.05 \cdot 10^{-46} \frac{N_e N_i}{\sqrt{kT}} \sum C_Z Z'^2 e^{-\frac{h\gamma}{kT}}\, \bar{g}_{ff} d\gamma \tag{19}$$

ergs/cm^3-sec

where C_Z is the concentration of atomic element Z, Z' is the mean ion charge of element Z, N_e and N_i are the electron and ion number densities and $\bar{g}_{ff}$ is the Gaunt factor averaged over a Maxwellian velocity distribution. In the Born approximation, the Gaunt factor is written[11]

$$\bar{g}_{ff} = \frac{\sqrt{3}}{\pi} K_o(x)e^x$$

$$x = \frac{1}{2}\frac{h\gamma}{kT}$$

where $K_o(x)$ is given in terms of the modified Bessel function of imaginary argument

$$K_o(x) = \pi/2\ [i\ H_o(ix)]$$

When the electrons are degenerate, the Gaunt factor must be averaged over a Fermi distribution and must include a factor which limits the availability of free states in the continuum. These corrections can be expressed in terms of an average Gaunt factor,

$$\frac{8\pi mkT}{h^3}\ \bar{g}_o\ \ln\ (1 + e^n)$$

when $\bar{g}_o$ contains the limitation on the availability of states and has been tabulated by Greene.[12]

Recombination Emission

The recombination emission into 4π steradians is given by[10]

$$J_{fb}\ d\gamma = 1.75 \cdot 10^{-56}\ \frac{N_e N_i}{(kT)^{3/2}}\ \sum_Z C_Z \sum_j \Delta_j \cdot$$

$$\frac{Z^{*4}}{j^5}\ \bar{g}_j\ H(h\gamma - X_j)\ e^{-(h\gamma - X_j)/kT} d\gamma \qquad (20)$$

$$\text{ergs/cm}^3\text{-sec}$$

where Δ_j gives the number of vacancies in level j of the mean ion of element Z, X_j is the ionization energy of level j of the mean ion, and g_j is the Gaunt factor. The recombination spectrum into the state j does not extend to energies smaller than X_j, a property which is insured by the step function H(x), where

$$H(x) = 0, \quad x < 0$$

$$H(x) = 1, \quad x \geq 0$$

The Gaunt corrections are taken only in the vicinity of the edge and are averages obtained from Karzas and Latter.[13]

The correction for the availability of free states in the continuum under degenerate conditions is handled in a way similar to that for bremsstrahlung where the probability of finding an electron in a free state which will recombine to the level j with the emission of a photon of energy $h\gamma$ is

$$q_j = \frac{1}{e^{n-(h\gamma-X_j)/kT} + 1}$$

Degeneracy corrections can, therefore, be included by means of a modified Gaunt factor for each level.

Line Emission

The treatment of line emission divides itself naturally into LTE and non-LTE regions. In the high density region there are many ion states, each with a different distribution of energy levels creating a large number of lines, the positions of which shift with changes in the temperature and density.

The model described here does not provide a detailed treatment of excited states and populations. We assume that the lines are completely smeared together from the position of each edge X_j to the position of the transition to the nearest level $(X_j - X_{j+1})$.[8]

This approximation probably yields an overestimate of the line emission, but in regions which are opaque to the radiation the method is not critical.(2) The criterion for the validity of the smearing approximation is that the wing-spreads of the lines should be on the order of the separation between the lines. This is often the case in high density regions where collisional broadening dominates.

In the LTE region, the line emission into 4π steradians in the smearing approximation can be written(14)

$$J_{bb}\, d\gamma = \frac{8\pi^2 e^2}{mh^2 c^3}\, N_i \sum_Z C_Z \sum_j f_j \frac{n_{Z,j}}{\Delta X_{Z,j}} \cdot$$

$$[H(h\gamma - X_{Z,j} + \Delta X_{Z,j}) - H(h\gamma - X_{z,j})].$$

$$e^{-h\gamma/kT}\, (h\gamma)^3\, d(h\gamma) \qquad \text{ergs/cm}^3\text{-sec} \qquad (21)$$

where $n_{Z,j}$ is the occupation number for level j, f_j is the sum of the oscillator strengths corresponding to transitions from level j to all higher levels averaged over all possible angular momenta and $\Delta X_{Z,j} = X_{Z,j}$

$- (X_{Z,j} - X_{Z,j+1})$ is the width of the region of smeared lines. The f numbers can be obtained from tables.(7)

In the non-LTE region, we use an expression for line emission given by Griem which is derived for electron impact ionization and radiation decay.(15) The total line radiation into 4π steradians from transitions to the ground state from all excited states is

$$J_{bb} d\gamma = 4.35 \cdot 10^{-24} \frac{N_e N_i}{\sqrt{kT}} \sum C_s \frac{1}{\Delta X_{Z,1}} e^{-\Delta E_Z/kT}$$

$$[H(h\gamma - X_{Z,1} + \Delta X_{Z,1}) - H(h\gamma - X_{Z,1})]\, d(h\gamma) \qquad (22)$$

$$\text{ergs/cm}^3\text{-sec}$$

where $\Delta E_Z = X_{Z,1} - X_{Z,2}$ is the excitation energy of the resonance line, and the emission is assumed to be smeared over the energy range $\Delta X_{Z,1}$ as previously described.

Nonthermal Emission

Two additional radiation processes should be included in the laser-heated plasma problem. Both processes are associated with nonthermal electron distributions resulting from the electric field of the laser beam.

The first process results from forced electron oscillations created by the laser electric field near the critical density surface.[16] The inclusion of this forced oscillation into the Maxwellian distribution results in a bremsstrahlung spectrum which is harder than the purely thermal spectrum.

The velocity distribution can be assumed to be a Maxwellian displaced by the instantaneous oscillation velocity

$$f(\underline{v}) = \left(\frac{m}{2\pi kT}\right)^{3/2} e^{-\frac{m}{2kT}(\underline{v} - \underline{v}_{osc})^2} \qquad (23)$$

where

$$v_{osc} = \frac{e\varepsilon}{mw_L} \cos\ell$$

$$\ell = w_L t$$

In these expressions, ε is the peak electric field strength, and w_L is the angular frequency of the laser beam. Equation (23) is only valid if the electron-ion collision time is greater than the laser oscillation time in the region of the critical density. This will be the case for 1.06 μm laser radiation.

The bremsstrahlung emission into 4π steradians is given by

$$J\, d\gamma = 4\pi N_e N_i \int d\sigma(\gamma)\, v\, f(\underline{v})\, d^3\underline{v} \tag{24}$$

where the differential cross section is[17]

$$d\sigma(\gamma) = 8/3\, Z^2\, \frac{e^6}{m^2c^3}\, \ln\Lambda\, v^{-2}\, d\gamma\ .$$

The $\ln\Lambda$ factor is approximately 0 for $v < v_o = \sqrt{2h\gamma/m}$ and $\ln\Lambda_o$ for $\underline{v} \geq v_o$.

The time average of the instantaneous emission rate is

$$J_{oe}\, d\gamma = \frac{16\sqrt{2}}{3}\, \frac{e^6 \ln\Lambda_o}{(mc^2)^{3/2}}\, \Sigma\, C_Z\, Z'^2\, \frac{N_e N_i}{\sqrt{kT}}\ \cdot$$

$$\int_0^{\pi/2} \frac{\operatorname{erfc}(\rho_\gamma - \varepsilon\cos\ell) - \operatorname{erfc}(\rho_\gamma + \varepsilon\cos\ell)}{\varepsilon\cos\ell}\, d\ell\, d\gamma \qquad \text{ergs/cm}^3\text{-sec} \tag{25}$$

where

$$\rho_\gamma = \sqrt{\frac{h\gamma}{kT}}$$

$$\varepsilon = \sqrt{\frac{m}{2kT}}\, \frac{e\varepsilon}{mw_L}$$

The second nonthermal radiation process is bremsstrahlung emission caused by suprathermal electrons which are thought to be created by plasma instabilities near the region of the critical density surface. If we assume a suprathermal electron distribution of the form[18]

$$f_{st}(v) = \frac{2\pi}{3}\, \left(\frac{m}{2\pi\alpha kT}\right)^{5/2} v^2\, e^{-\frac{mv^2}{2\alpha kT}} \tag{26}$$

which is normalized to unity and where α is a free parameter, the bremsstrahlung emission into 4π steradians is given by

$$J_{st}d\gamma = \frac{64}{9}\, \left(\frac{e^6}{hm^2c^4}\right)\, \Sigma\, C_Z Z'^2\, N_{st} N_i$$

$$\sqrt{2\pi \frac{mc^2}{\alpha kT}}\ \ln\Lambda_o\ (1 + \frac{h\gamma}{\alpha kT})\ e^{-h\gamma/\alpha kT}\ d(h\gamma) \qquad (27)$$

$$\text{ergs/cm}^3\text{-sec}$$

Matches to recent experimental data indicate values of α in the range from 4 to 6.[18] The suprathermal electron density N_{St} must be determined by an electron transport calculation.

II-A-6-c-vi. Absorption Coefficients

In the LTE region absorption coefficients corrected for induced emission are obtained from the emission functions by Kirchhoff's law,

$$\sigma(\gamma) = \frac{J(\gamma)}{B(\gamma)} = \frac{(hc)^2}{2}\ \frac{J(\gamma)}{(h\gamma)^3}\ (e^{\frac{h\gamma}{kT}} - 1) \qquad (28)$$

where $J(\gamma) = J_{ff} + J_{fb} + J_{bb}$.

In the non-LTE regions, Kirchhoff's law is not valid, but since the plasma is always transparent there, the form of the absorption coefficient is immaterial.

References for Section II-A-6

1. J. Nuckolls, et al., "Laser Compression of Matter to Super-High Densities: Thermonuclear Applications," Nature 239, 139-142 (1972).

2. P. M. Campbell, et al., "Radiation Processes in a Laser-Fusion Plasma," KMSF-U457 (1976).

3. G. C. Pomraning, Radiation Hydrodynamics, Pergamon Press, Oxford (1973).

4. R. McWhirter, Spectral Intensities, Ed. R. H. Huddlestone and S. L. Leonard, Academic Press (1965).

5. A Burgess, "Dielectric Recombination and the Temperature of the Solar Corona," Astrophys. J. 139, 776-780 (1964).

6. P. J. Mallozzi, et al., "X-Ray Emission from Laser Generated Plasmas," Battelle Columbus Laboratories, Final Report on Contract DAAH01-71-C-0550 (1972).

7. H. M. Mayer, "Methods of Opacity Calculations," Los Alamos Scientific Laboratory Report, LA-647 (1947).

8. B. Kivel and H. Mayer, "Opacity of Highly Ionized Air," J. Quant. Spectr. and Radiation Transfer 5, 13-38 (1965).

9. A. N. Cox, Stellar Absorption Coefficients and Opacities, Ed. D. McLaughlin, University of Chicago Press (1965).

10. T. F. Stratton, X-Ray Spectroscopy, Ed. R. H. Huddlestone and S. L. Leonard, Academic Press (1965).

11. J. Shearer and W. Barnes, "Numerical Calculations of Plasma Heating by Means of Sub-Nanosecond Laser Pulses," in Laser Interaction and Related Phenomena, Ed. H. Hora and H. Schwartz, Plenum Press (1971).

12. J. M. Greene,"Fermi-Dirac Averages of the Free-Free Hydrogenic Gaunt Factor," Rand Corp. Report RM-2580-AEC (1960).

13. W. Karzas and R. Latter, "Radiation Transitions in a Coulomb Field," Astrophys. J. Suppl. 6, 167-212 (1961).

14. R. Woolley and S. Stibbs, The Outer Layers of a Star, Oxford University Press (1953).

15. H. R. Griem, Plasma Spectroscopy, McGraw Hill (1964).

16. D. Mitrovich, K. Brueckner and S. Segall, "Bremsstrahlung Radiation from Forced Oscillation of Thermal Electrons in a Laser Electric Field," KMS Document KMSF-U361 (1975).

References (cont.)

17. J. D. Jackson, Classical Electrodynamics, John Wiley and Sons (1962).

18. J. Nuckolls, "Laser Fusion," Chapter 6 in Laser Fusion Program Semiannual Report - July-December 1973, Lawrence Livermore Laboratory Report UCRL-50021-73-2 (1974).

II-A-7 HYDRODYNAMIC STABILITY

The hydrodynamic stability of spherical laser driven implosions is one of the most important unanswered experimental questions facing laser fusion feasibility. The ablation front in the implosion process as described in section II-A-1-a experiences an acceleration characteristic of the classical Rayleigh-Taylor instability.[1,2] The situation is not exactly analogous however because there are a strong temperature gradient and ablative effects in the laser driven implosion. Early arguments[3] claimed that the ablation process would convect instabilities away from the ablation surface before they could grow to large amplitudes. This thinking was further re-enforced by the results of numerical three dimensional perturbation calculations[4] where the fluid variables were expanded in spherical harmonics. Another early study[5] using a similar numerical treatment showed, however, that the instability was not stablized and infact low mode numbers grew at a rate greater than the classic Rayleigh-Taylor rate. This discrepancy was resolved[6,7] with the discovery that one must distinguish between truly ablatively driven, isentropic implosions and the very fast non isentropic, "exploding pusher" implosion, characteristic of the computer calculations in Ref. 4 and also characteristic of the glass micro balloon targets used in laser fusion experiments today.[11] In these implosions the shell target is heated isothermally very quickly and then it explodes, both inward and outward. This different nonisentropic implosion mechanism explains the absence of instabilities in target implosions to date and in the Ref. 4 calculations. The major laser fusion experimental groups today generally agree that the results of full two dimensional hydrodynamic simulations,[7] the perturbation approach,[6] and analytic estimates,[8] indicate that the isentropic implosion of thin shells (high aspect ratio $R/\Delta R=8$) will be impossible because

of the excessive Rayleigh-Taylor growth rates. Thin shells quickly break up when the perturbation amplitude becomes comparable to the shell thickness. Since the implosion of a thin shell is over a much longer distance the perturbation has a greater chance to grow. This is a very serious problem because thin shells offered the opportunity to reduce the laser power and wavelength requirements over those for a solid DT ball.[9] Less power is required because a smaller force is acting through a longer distance and the wavelength requirement is reduced because the scale heights at large radii in a shell implosion are greater than in an equivalent sphere implosion. The pulse shape is also not as critical. With aspect ratios limited to less than 8, the advantages of shells over spheres disappears. Two dimensional simulations of a 400 μm sphere with a carefully shaped 50 KJ laser pulse indicates that a good implosion can be achieved with ±10% variation in the laser uniformity provided that a low density atmosphere is initially created with a pre-pulse and that long wavelength light (2um) is used in the first part of the pulse.[10] This rather ideal case seems at this point to be unattainable for laser fusion power plant applications because of the exacting laser parameters that are required (spatial profile, pulse shape, variable wavelength, excessive power).

The conclusion at this point must be that theoretical estimates of Rayleigh-Taylor instability growth during the implosion of shells will limit the aspect ratio to less than 8. This gives these thick shells very little advantage over solid balls which require enormous laser powers and very exacting pulse shapes to achieve isentropic compression to densities and temperatures requisite for yields and gains of 100 MJ and 100 respectively. Hence the implosion scenario necessary to achieve proper core conditions (see section II-E) has not yet been discovered or reported.

II-A-7. References

1. Lord Rayleigh, Scientific Papers, II, p 200-207, Cambridge, England (1900).
2. G. Taylor, Proc. Roy. Soc. A 201, 192 (1950).
3. J. Nuckolls, L. Wood, A. Thiessen, and G. Zimmerman, Nature 239, 193 (1972).
4. D. Henderson, and R. Morse, Phys. Rev. Lett. 32, 355 (1974).
5. J. Shiau, E. Goldman, and C. Weng, Phys. Rev. Lett 32, 352 (1974).
6. G. Fraley, W. Gula, D. Henderson, R. McCrory, R. Malone, R. Mason, and R. Morse, IAEA Conf. on Plasma Physics and Controlled Nuclear Fusion Research (1974), paper IAEA-CN - 33/F 5-5.
7. J. Lindl and W. Mead, Phys. Rev. Lett. 34, 1273 (1975).
8. R. Kidder, Nuc. Fus. 16, 3 (1976).
9. J. Nuckolls, J. Lindl, W. Mead, A. Thiessen, L. Wood and G. Zimmerman, IAEA Conf. on Plasma Physics and Controlled Nuclear Fusion Research (1974), paper DAEA-CN - 33/F 5-4.
10. LLL Laser Fusion Annual Report, 392 (1974).
11. G. Charatis, et al, IAEA Conf. on Plasma Physics and Controlled Nuclear Fusion Research (1974), paper IAEA-CN - 33/F 1.

II-A-8 Hot Electrons

II-A-8-a Introduction

Efficient thermonuclear burn requires compression along a low adiabat.[1] If nearly adiabatic compression is to be achieved, there must be strong coupling, in the form of thermal conduction, between the electrons heated by the laser and electrons inside the critical radius. One possible coupling problem is the formation of high energy tails on the electron distribution function due to resonance absorption of the laser light near the critical density surface.[2-4] Numerous experiments and simulations have detected these hot electrons;[5-10] i.e., they are evidenced by hard X-ray spectra in experimental studies. Very energetic electrons might deposit their energy deep inside the pellet ahead of the ablation front and this energy deposition would result in a continually rising adiabat. A higher adiabat means that a higher driving pressure would be required to achieve a given compression.[11] In addition, suprathermal electrons could give rise to a lower ablation pressure for a given laser power. This would occur if the energy coupling rate between hot and cold electrons decreased as the energy of the hot electrons increased. Clearly, a comprehensive model of hot electron creation and propagation is necessary if current and future laser-plasma experiments are to be understood.

II-A-8-b Creation

Several theories have been proposed to explain the creation of a suprathermal electron tail caused by the laser-plasma interaction. These theories fall into two broad categories, the incoherent[12-14] production of energetic electrons by a broad wave spectrum, or the coherent[15] production of energetic electrons by a single wave. The fundamental assumption of these theories is that one can calculate the rate at which the source of free

energy, the laser light, couples energy and momentum into a plasma fluctuation.[15] For example, in Raman backscatter, the incident and backscattered waves exert a ponderomotive force on the electrons and, thereby, produce an electron current. Since this current is in phase with the electric field of an electron plasma oscillation, one has an energy input into the plasma. The energy dissipation mechanism is another question. If the plasma wave has small amplitude, one can show that the laser light momentum and energy are fed into the plasma wave causing it to grow exponentially at a linear growth rate.[15] When the wave reaches a sufficient amplitude, the energy input is dissipated nonlinearly, for instance, by trapping or by mode coupling and diffusion through wave number space. If the plasma wave grows to sufficient amplitude to trap electrons, the energy is dissipated by pulling electrons into an energetic nonthermal tail of the distribution function. If mode coupling occurs, diffusion through wave number space results in dissipation through Landau damping on the electrons. This damping also generates an energetic tail.

II-A-8-c Propagation

The theory of hot electron transport is just beginning to be developed. Lawrence Livermore Laboratory uses a multigroup flux-limited diffusion model.[11] In this model the electrons lose energy to radiation by bremsstrahlung and to the background electrons by Coulomb collisions. In addition, relative to the ions, the net current of all electrons is assumed to be zero and the electric field required to enforce this condition is calculated. The ohmic work done by the electrons against this electric field is transferred between electron groups and provides an additional coupling between thermal and suprathermal electrons.

The role of magnetic fields, turbulence, electrostatic sheaths, and collisions on hot electron transport will all have to be understood before a comprehensive theory is developed. We consider some of the difficulties in developing such a theory. Near the critical density surface the plasma is collisionless. A spatially localized high energy electron tail can become two stream unstable as the electrons propagate inward toward the center of the pellet.[16] As a result they may lose considerable energy to langmuir turbulence. This streaming behavior will also induce a background electron return current which may create ion-acoustic turbulence. These processes will decrease the hot electron energy deposited in the pellet interior. In addition, the langmuir and ion-acoustic turbulence will act as energy sources for the background ions and electrons, and ion-acoustic turbulence and laser generated magnetic fields will reduce thermal conduction.[17-19] A reduced thermal conduction will result in slower transport of heated electrons from the laser-absorbing region into the interior of the pellet and, therefore, will decouple the temperature of the pellet surface and the interior.

This high surface energy poses at least two problems. Higher electron temperatures will mean larger radiation losses by bremsstrahlung and a greater likelihood of core preheat by radiation. It also means that relatively few ions, those which initially lay close to the pellet surface, will carry off a relatively larger fraction of the absorbed laser energy as they expand into the vacuum than if the thermal conduction was classical.[20] The general result of this hot ion creation is that for a given laser power, one achieves a lower ablation pressure than the classical result would suggest.

Besides the processes discussed above one would also need to understand the effects of collisions in the pellet interior and the effects of the electrostatic sheath[20] which forms when hot electrons move toward the vacuum.

References for Section II-A-8

1. J. Nuckolls, L. Wood, R. Thiessen and G. Zimmerman, Nature 239,139 (1972).
2. J. S. DeGroot and J. E. Tull, Phys. Fluids 18,672 (1975).
3. K. G. Estrabrook, E. J. Valeo and L. Kruer, Phys. Fluids 18,1151 (1975).
4. J. P. Freidberg, R. W. Mitchell, R. L. Morse and L. I. Rudsinski, Phys. Rev. Lett. 28,795 (1972).
5. J. W. Shearer, S. W. Mead, J. Petruzzi, F. Rainer, J. E. Swain and C. E. Violet, Phys. Rev. A6,764 (1972).
6. H. Dreicer, D. B. Henderson and J. C. Ingraham, Phys. Rev. Lett. 26,1616 (1971).
7. H. Dreicer, D. B. Henderson and J. C. Ingraham, Phys. Rev. Lett 31,426 (1973).
8. D. Forslund, J. Kindel and E. Lindman, Phys. Rev. Lett. 30,739 (1973).
9. J. S. DeGroot and J. I. Katz, Phys. Fluids 16,401 (1973).
10. W. L. Kruer and J. M. Dawson, Phys. Fluids 15,446 (1972).
11. J. D. Lindl, Nuclear Fusion 14,511 (1974).
12. J. I. Katz, J. Weinstock, W. L. Kruer, J. S. DeGroot, and R. J. Faehl, Phys. Fluids 12,1951 (1973).
13. J. J. Thompson, R. J. Faehl and W. L. Kruer, Phys. Rev. Lett. 31,918 (1973).
14. M. Z. Caponi and R. C. Davidson, Phys. Rev. Lett. 31,86 (1973).
15. W. M. Manheimer and H. H. Klein, Phys. Fluids 17,1889 (1974).
16. G. Magelssen, N.C.A.R. Cooperative Thesis No. 37 (1976).
17. D. W. Forslund, J. Geophys. Res. 75,17 (1970).
18. R. J. Bickerton, Nuclear Fusion 13,457 (1973).
19. K. G. Estrabrook, "Plasma Physics", Chapter 6 in Laser Fusion Program Annual Report - January - December 1975, Lawrence Livermore Laboratory Report UCRL-50021-75.
20. F. Skoberne, LA-5739-PR (1974).

II-B-1 Numerical Modelling

II-B-1-a. Introduction and Survey of Computer Codes

Laser driven fusion feasibility has only been demonstrated through the results of hydrodynamic simulation computer codes. Such codes first indicated that sufficient pellet gain might be possible to make laser driven fusion a candidate for power plant applications[1,2]. Currently these codes are being used to study and unfold the results of laser-plasma interaction experiments and the compression of D-T fuel by laser driven implosion.

A survey of laser fusion computer codes is given with all information taken from the literature. It is understood that such codes are under constant development so in fact this survey may not include all aspects of each code.

The most notable of the laser fusion hydrodynamics codes is LASNEX[3], which was developed at Lawrence Livermore Lab (LLL) but is currently also used at Los Alamos Scientific Laboratory (LASL). LASNEX is described as a laser fusion target design code. It is a two dimensional (r,z), one fluid, two temperature Lagrangian hydrodynamics code, that treats the nonthermal radiation field and nonthermal electrons using multi-group flux limited diffusion theory. It solves for the magnetic field in cases where self-generated fields arise and uses Braginskii's, B-field corrected, transport coefficients. It contains a ray trace option to follow the paths of laser light rays in the environment of complex electron density gradients, and by virtue of its home it has available sophisticated tables of equation of state and radiation opacity values. This sophistication allows LASNEX to simulate the experiments performed currently and to analyze the diagnostics (mostly X-rays) that come from these experiments. Such experiments may be fundamentally two dimensional, such as ball on disk targets, or the fluid motion may develop into two dimensional flow, such as a laser focussed to a small spot on a slab, and these require a two dimensional

computer simulation to correctly predict the effects of self-generated magnetic fields and laser light refraction. The nonthermal X-ray spectrum measured in the laboratory must be analyzed by accounting for the numerous bound-bound and free-bound transitions of high Z materials as well as the free-free bremsstrahlung radiation from thermal and non-thermal electrons. This radiation must be transported in a multi-group calculation to reproduce the measured X-ray spectrum.

LASNEX uses multi-group flux limited diffusion to describe the transport of DT and DD reaction products.

Another two dimensional laser plasma hydrodynamics code has been developed at the Naval Research Laboratory (NRL). This code is a two dimensional (r,z) one fluid, two temperature Eulerian code with sophisticated treatments of the self generated magnetic field equations and radiative processes. It uses Braginskii transport coefficients but does not contain any treatment of thermonuclear burn.

KMS Fusion, Incorporated uses a rather sophisticated one dimensional hydrodynamics code called TRYHD[5] that has one-fluid, two temperature hydrodynamics with a multi-frequency variable Eddington treatment of radiation transport and a particle tracking method of calculating charged particle reaction product transport. The burn dynamics capability of this code suffers from the time independent approximation for the transport which deviates somewhat from a time dependent calculation as will be seen in a later section.

The University of Rochester has developed a one dimensional, one fluid two temperature code called SUPER[6]. This code uses a very simple local deposition approximation of burn dynamics but is in the process of being upgraded to accurately account for charged particle slowing down, using the time dependent particle tracking algorithm that is described in section II-B-2-C.

A sophisticated thermonuclear burn code is the one dimensional, one fluid, three temperature code used at LASL[7]. Again it has elaborate equations of state and opacity tables. This code uses the S_N discrete ordinates transport approximation to transport both charged particle and neutron reaction products in the laser fusion pellet.

None of the computer codes described above are available for distribution due to either proprietary or security classification reasons. Only a few laser fusion hydrodynamics codes are available to the general scientific community and none of these has a good thermonuclear burn capability[8,9].

For the purposes of studying laser fusion power plant feasibility the ability to estimate pellet yield, fractional burn up, and gain is essential. Also, since many of these estimates rely on physical parameters whose values are not well known it is important to test the sensitivity of yield, fractional burn up, and gain to uncertainties in these parameters. This requires a hydrodynamic-thermonuclear burn modeling code. Such a code has been developed at the University of Wisconsin, ultimately for general distribution, and currently for use in the laser fusion power plant feasibility study.

References II-B-1

1. J. Nuckolls, L. Wood, A. Thiessen, and G. Zimmerman, Nature 239, 139 (1972).

2. J. Clarke, H. Fisher, and R. Mason, Phys. Rev. Lett. 30, 89 (1973).

3. G. Zimmerman, in Comments on Modern Physics, Part E, Vol. II, No. 2 (1975).

4. D. Colombant, K. Whitney, D. Tidman, N. Winsor, and J. Davis, Phys. Fl. 18, 1687 (1975).

5. K. Brueckner and S. Jorna, Rev. Mod. Phys. 46, 325 (1974).

6. E. Goldman, Univ. of Rochester Lab. for Laser Energetics Report #16, 1973.

7. G. Fraley, E. Linnebur, R. Mason, and R. Morse, Phys. Fl. 17, 474 (1974).

8. J. Christiansen, D. Ashby, and K. Roberts, Comp. Phys. Comm. 7, 271 (1974).

9. G. Moses and J. Duderstadt, Transactions of the ANS Meeting, Toronto, p. 50 (1976).

II-B-2 PHD IV - A Laser-Plasma Hydrodynamics - Thermonuclear Burn - Radiative Transfer - Computer Code

II-B-2-a. Introduction

PHD-IV is a one dimensional (planar, cylindrical, or spherical) one fluid, two temperature (electron and ion) plasma hydrodynamics computer code. In addition to the hydrodynamics equations it solves rate equations for thermonuclear reactions (DT and DD) with proper local depletion of the reacting ions and transports the charged particle reaction products using an accurate and efficient time dependent particle tracking technique. Energy is redeposited along the particle path to the thermal electrons and ions and momentum transfer to the plasma fluid is

also included. Hydrodynamic transport coefficients are classical with electron heat flux limitation. Tabulated equations of state accounting for solid and liquid phases, dissociation, and ionization for deuterium and tritium and for glass (SiO_2) are used along with tabulated Thomas-Fermi-Dirac equations of state for intermediate Z materials(*). Ideal gas laws are used at high temperature. Only radiation emission and absorption from free-free transitions is currently calculated and this radiation is transported using a multi-frequency group, time dependent variable Eddington technique. Laser light absorption is treated by inverse bremsstrahlung attenuation from the outer plasma boundary to the critical density where a specified fraction is dumped and the remainder is reflected and attenuated on its way back out.

The PHD-IV computer code is about 6000 card images in length and was developed on a UNIVAC 1110 computer using IBM FORTRAN IV. With minor modifications it should run on CDC 6600 and 7600 computers.

II-B-2-b. Plasma Hydrodynamics

PHD-IV uses very conventional techniques for solving the one dimensional equations of hydrodyanmics. The plasma is divided into JMAX zones with zone boundaries tied to the fluid in the Lagrangian formulation. Velocities are evaluated at zone boundaries (j = 0, ... JMAX) and the equation of motion is solved using an explicit finite difference technique.(6)

$$\frac{\partial u}{\partial t} = - \frac{1}{\rho} \nabla (P_e + P_i + P_r + q) + \Delta u_{TN}$$

u = fluid velocity

ρ = fluid density

P_e = electron pressure

P_i = ion pressure

*TFD-EOS obtained from UR-LLE under stipulation that they not be released with the code.

P_r = radiation pressure

q = Von Neumann artificial viscosity

Δu_{TN} = rate of change of fluid velocity due to momentum transfer from non thermal reaction products

Temperatures are evaluated at the zone centers (j = 1/2, ... JMAX - 1/2) and the coupled nonlinear temperature equations are solved simultaneously using an implicit finite difference scheme.(6)

$$\rho C_{ve} \frac{\partial T_e}{\partial t} = \nabla \cdot K_e \nabla T_e - P_e (\nabla \cdot u) - \omega_{ei} (T_e - T_i) + S_e$$

$$\rho C_{vi} \frac{\partial T_i}{\partial t} = \nabla \cdot K_e \nabla T_i - (P_i + q) (\nabla \cdot u) + \omega_{ei} (T_e - T_i) + S_i$$

T_e = electron temperature

T_i = ion temperature

C_{ve} = electron specific heat

C_{vi} = ion specific heat

K_e = electron thermal conductivity

K_i = ion thermal conductivity

ω_{ei} = electron-ion equilibration coefficient

S_e = energy source to the electrons

S_i = energy source to the ions

The nonlinear coefficients are evaluated using either a temperature extrapolation technique or the equations are iterated to convergence. The equation of motion and the temperature equations are out of phase by one half time step with the first solved from $t^{n-1/2}$ to $t^{n+1/2}$ and the temperature equations solved from t^n to t^{n+1}. The spatial derivatives are parameterized to allow for solution in planer, cylindrical or spherical geometry. A time dependent pressure boundary condition can be specified on the outer boundary and the temperature outer

boundary condition can be either

$$T = T_{bc} \text{ or } \left.\frac{\partial T}{\partial r}\right|_{r = r_{outer}} = 0$$

The zero flux condition is usually the most applicable. The inner boundary is treated as either an immovable reflection point (for a sphere for instance) or as an inner surface adjacent to a vacuum (for a hollow shell). Upon collapse of the center void of a hollow shell to a point the inner boundary is pinned to the center for the remainder of the simulation. The energy sources for the electron and ion temperature equations include laser energy absorbed by the electrons, thermonuclear reaction product redeposition to the electrons and ions, and electron energy gain or loss from the radiation field.

Numerical stability and accuracy are maintained by automatic calculation of the next time step using the most severe limitation imposed by the Courant condition, percent change in temperature and percent change in density.

II-B-2-c. Thermonuclear Burn

PHD-IV solves the rate equations for DT and DD thermonuclear reactions using standard finite difference solutions of first order differential equations in those spatial zones containing D and/or T at the necessary densities and temperatures.

$$\frac{d\, n_D}{dt} = - n_D n_T \, (\overline{\sigma v})_{DT} - n_D^2 \, (\overline{\sigma v})_{DD}$$

$$\frac{d\, n_T}{dt} = - n_D n_T \, (\overline{\sigma v})_{DT}$$

The reaction rates are obtained by interpolation in tables of $(\overline{\sigma v})_{DT}$ and $(\overline{\sigma v})_{DD}$.

The charged particle reaction products are transported and slowed down using time dependent particle tracking methods. The basic approximation in this scheme is straight line particle trajectories from particle birth to

thermalization or escape. The reaction products from each zone are divided into a number of directions (typically 3-9) and the range energy relation is numerically integrated along each path, accounting for temperature and density changes in all zones that the path crosses.

$$\frac{dv}{ds} = A + B/v^3$$

$$A = 8.35 \times 10^{-46} \, (Z^2/m) \, \ell n \Lambda_e n_e / T_e^{3/2}$$

$$B = 6.67 \times 10^{-69} \, (Z^2/m) \ell n \Lambda_i \, \langle Z_i^2 \rangle \, n_i^2/\rho$$

This is shown schematically in Figure 1. The velocity lost to the electrons and ions is tallied for all zones and the final sum of all charged particle deposition is fed as a source term to the temperature equations. Momentum deposition is fed to the equation of motion. Another important feature is that particles are allowed to travel only as far as they can move on the current time step. They are then "remembered" by the code and are picked up and moved along their path again on the next time step, along with the newly born particles. In this way a time dependent transport treatment is used. The number of time levels that particles may be remembered is only limited by the amount of computer storage available. Typically 30-50 levels provide good results, with efficient computer storage utilization coming from a data structure design that allows inward directed particles ($\mu \leq 0$) to travel for more time levels than outward directed particles ($\mu > 0$).

Code test results and results relevant to the laser fusion reactor design are given in section II-E.

II-B-2-d. Equation of State

The following equation of state quantities are required to close the set of hydrodynamics equations.

PARTICLE TRACKING

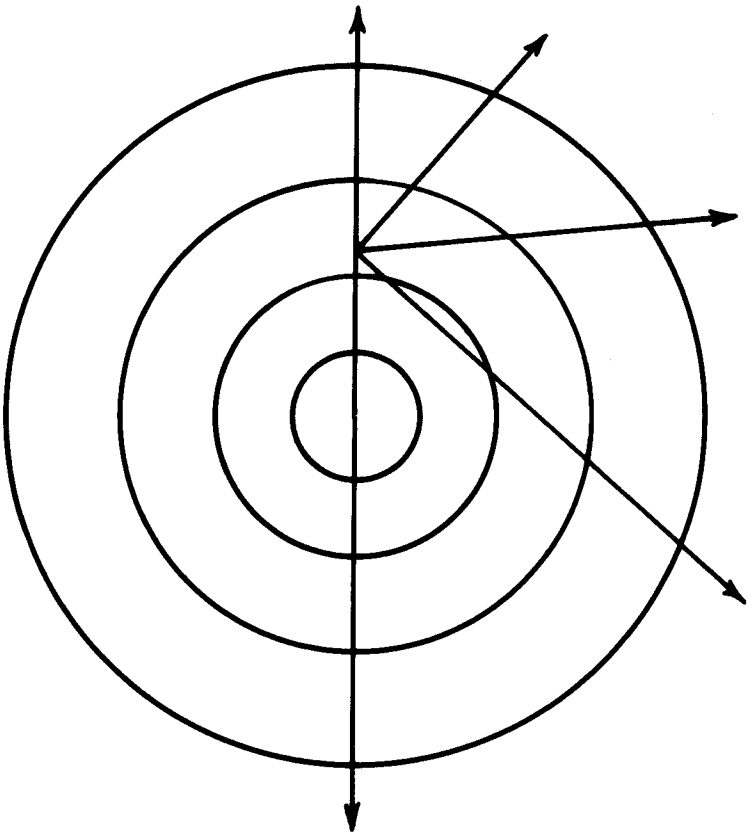

$\frac{dV}{dS}$ INTEGRATED ALONG EACH RAY

FIGURE 1

$P_e(n_e,T_e)$	electron pressure
$P_i(n_i,T_i)$	ion pressure
$E_e(n_e,T_e)$	electron specific internal energy
$E_i(n_i,T_i)$	ion specific internal energy
$(P_e)_T = \frac{\partial P_e}{\partial T_e}$	derivative of electron pressure
$(P_i)_T = \frac{\partial P_i}{\partial T_i}$	derivative of ion pressure
$C_{ve} = \frac{\partial E_e}{\partial T_e}$	electron specific heat
$C_{vi} = \frac{\partial E_i}{\partial T_i}$	ion specific heat

The ion equations of state are evaluated using ideal gas laws.

$$P_i = n_i\, k_B\, T_i \qquad E_i = 3/2\; n_i\, k_B\, T_i/m_i$$

The electron equations of state are evaluated at high temperatures by ideal gas laws. At low temperatures and high densities characteristic of the imploded pellet core, tabulated values for P_e and E_e for deuterium and tritium that account for different phases, dissociation and ionization are used.[8] The "raw" values of pressure and energy as functions of temperature and compressibility are fitted with bicubic splines. The fitting coefficients are then tabulated rather than the pressure/energy values themselves. The cubic polynomial fit allows for easy evaluation of the derivatives of pressure and energy. Also available in the same form is an equation of state for SiO_2 glass.

II-B-2-e. Transport Coefficients

The electron and ion thermal conductivities are evaluated at the zone boundaries using average temperatures from the two surrounding zones. Classical values are used[9]

$$K_e = \frac{4.923 \times 10^{-4}\, T_e^{5/2}}{(4 + Z)\, \ln\Lambda_{ei}} \qquad \frac{\text{Jerks}}{\text{Cm}\cdot\text{Shake}\cdot\text{Kev}}$$

$$K_i = \frac{2.444 \times 10^{-5} T_i^{5/2}}{A^{1/2} Z^4 \ln\Lambda_{ii}} \quad \frac{\text{Jerks}}{\text{Cm}\cdot\text{Shake}\cdot\text{Kev}}$$

with the electron heat flux limited by the value

$$q_{MAX} = 3.445 \times 10^{-25} N_e T_e^{3/2} \frac{\text{.Jerks}}{\text{Cm}^2\text{.Shake}}$$

1 Jerk = 10^{16} ergs

1 Shake = 10^{-8} seconds

The electron-ion coupling coefficient is evaluated in each zone using the expression

$$\omega_{ei} = 605.9\ \rho \left(\frac{Z}{A}\right)^2 \frac{\ln\Lambda_{ei}}{T_e^{3/2}} C_{ve} \frac{\text{Jerks}}{\text{Kev}\cdot\text{Shake}\cdot\text{gram}}$$

All leading numerical constants can be changed through code input to test the effect of uncertainties in these transport coefficients.

II-B-2-f. Laser Absorption

Laser intensity or power is given at the outer plasma boundary as a function of time $P_L(t)$. This power is classically attenuated through all zones between the outer boundary and the zone containing the critical density. Here a specified fraction ($0 \leq f \leq 1$) of the unattenuated energy is dumped and the remainder is reflected and attenuated on its path back out. The energy deposition rate in the electrons in each zone is

$$S_e = \frac{(\psi^+_{j-1} - \psi^+_j) + (\psi^-_j - \psi^-_{j-1})}{\Delta m_{j-1/2}} \quad \frac{\text{Jerks}}{\text{Shake}\cdot\text{Gram}}$$

for a spherical calculation where

ψ^- is the incident power and

ψ^+ is the reflected power.

The inverse bremsstrahlung attenuation coefficient is

$$K_{IB} = \frac{4.9 \times 10^{-31} (n_e \lambda)^2 \langle Z^2 \rangle \ln \Lambda_{ei}}{(1 + 5.4 \sqrt{T_e})(1 + 558 T_e) \langle Z \rangle \sqrt{1 - n_e/n_{e_c}}} \quad cm^{-1}$$

where λ - laser wavelength

n_{e_c} - critical electron density

References II-B-2

1. G. Fraley, E. Linnebur, R. Mason, and R. Morse, Phys. Fl. 17, 474 (1974).

2. Longmire, Elementary Plasma Physics, (Wiley, New York, 1967).

3. E. Corman, W. Loewe, and G. Cooper, Nuc. Fus. 15, 377 (1975).

II-B-2-g Radiation

II-B-2-g-i Introduction

The following describes the technique developed to study radiation transport within an imploding, burning pellet. Ideally, the radiation transport calculation should satisfy the following criteria. The transfer technique should be capable of giving energy and spectral X-ray information. This information is necessary for the design of the reactor -- the type of wall damage depending upon the amount of X-ray energy and its spectra. The technique should be able to treat plasmas with both large and small opacities. This requirement is necessary because radiative mean free paths can be much larger or much smaller than pellet size -- the path length depending upon the pellets density and temperature coordinate structure and upon the pellet's chemical content. The transfer equations should limit to the correct physical equations. Photons with large mean free paths should be described by a free streaming form of the transport equation. Conversely, a diffusion form of the transport equation should be used for photons with short mean free paths. The technique must satisfy some appropriate cost requirement. Because the transfer problem is solved numerically and because the number of time iterations for a hydrodynamical burn calculation is large, the technique should not require an excessive amount of cost per time cycle.

The variable Eddington method described in this report satisfies the cost requirements and is capable of providing the needed X-ray spectra while treating the radiation transport problem adequately.

II-B-2-g-ii Variable Eddington Method

The equation of radiation transport can be written in terms of the specific intensity $I(\nu, \underline{r}, \underline{\Omega}, t)$, which gives the distribution of radiant energy of a given frequency in position, time and direction. For problems with one

dimensional symmetry the specific intensity at a given frequency can be defined in terms of its position r, its direction cosine with respect to r, μ, and the time t. Knowing the specific intensity the radiation energy density, flux and pressure can be obtained. The radiation energy density at a given frequency is

$$E(\nu, r, t) = \frac{2\pi}{c} \int_{-1}^{1} I(\nu, r, \mu, t)\, d\mu \qquad (1)$$

The r component of the radiative flux is

$$F(\nu, r, t) = 2\pi \int_{-1}^{1} I(\nu, r, \mu, t)\, d\mu \qquad (2)$$

and the rr component of the radiation pressure is

$$P(\nu, r, t) = \frac{2\pi}{c} \int_{-1}^{1} I(\nu, r, \mu, t)\, d\mu \qquad (3)$$

As seen in section II-A-G the specific intensity satisfies a continuity equation. For planar or spherical symmetry the continuity equation can be written as [1]

$$\frac{1}{c}\frac{\partial I}{\partial t} + \mu\frac{\partial I}{\partial r} + 1/2\ (\alpha - 1)\ \frac{(1 - \mu^2)}{r}\frac{\partial I}{\partial \mu} +$$

$$(\sigma_a + \sigma_s)\ I = J/4\pi + S \qquad (4)$$

where $\alpha = 1$ for plane geometry and $\alpha = 3$ for spherical geometry. Notice that in writing this equation coherent scattering is assumed. If there is no change in frequency upon scattering (coherent scattering) induced inscattering and outscattering terms cancel. The functional structure of the absorption and scattering cross sections (σ_a and σ_s) and the emission and scattering source functions (J and S) depend on the atomic model and the chemical content of the plasma. For the plasmas we will consider, low temperature (several

kilovolts) and fluid velocities much less than the speed of light, we have

$$S(\nu, r, \mu, t) = \sigma_s \int_{-1}^{1} K(\mu,\mu') \, I(\nu, r, \mu', t) \, d\mu' \qquad (5)$$

We assume $K(\mu,\mu')$ is the Thomson scattering kernal for free electrons at rest.[2] Thus,

$$K(\mu,\mu') = 1/2 \, [1 + (3\mu^2 - 1) \, (3\mu'^2 - 1)]$$

Even though we have considerably reduced the complexity of the transport equation, it is still extremely difficult to solve in its present form - equation (4). Our approach is to assume that the angular distribution of the radiation is not a critical quantity. The transport problem can then be simplified by eliminating the direction cosine. The variable Eddington method is based on an expansion of the angular moments $\int I(\nu, r, \mu, t) \, \mu^k \, d\mu$.[3] Using equation (4), for the first two moments we obtain

$$\frac{\partial E}{\partial t} + \frac{1}{r^{\alpha - 1}} \frac{\partial}{\partial r} (r^{\alpha - 1} F) + c \, \sigma_a \, E = J \qquad (6)$$

$$\frac{1}{c} \frac{\partial F}{\partial t} + c \left[\frac{\partial P}{\partial r} + \frac{\alpha-1}{r} (3P - E)\right] +$$

$$(\sigma_a + \sigma_s) \, F = 0 \qquad (7)$$

Notice that μ has been eliminated and that the frequency appears only as a parameter. Notice also, however, that there are three dependent variables and only two equations. In a moment representation each equation contains at least one higher order moment. In the variable Eddington technique we keep only the first two equations of the moment expansion and develop a semi-empirical expression for the pressure tensor,

$$P = f \, E \qquad (8)$$

where $f = f(v, r, t)$ is called the Eddington factor. If the correct form of the Eddington factor were known this method would be equivalent to the full transport equation. In practice we use only approximate expressions for f which are based on a simple physical model. The primary requirement on f is that it should limit to a value of 1/3 in regions with large opacities (isotropic radiation) and to a value of 1 in regions with small opacities (streaming radiation).

II-B-2-g-iii Diffusion and Streaming Limits

The variable Eddington technique has the necessary property of limiting to wave propagation in optically thin regions and to diffusion transport in optically thick regions. To see this consider the plane geometry case.

For plane geometry equations (6) and (7) become

$$\frac{\partial E}{\partial t} + \frac{\partial F}{\partial r} + c\,\sigma_a\,E = J$$

$$1/c\,\frac{\partial F}{\partial t} + c\frac{\partial}{\partial r}\,(fE) + (\sigma_a + \sigma_s)\,F = 0$$

For an optically thick region

$$1/c\,\frac{\partial F}{\partial t} \ll (\sigma_s + \sigma_a)\,F$$

This implies that

$$F \simeq -\,c/(\sigma_a + \sigma_s)\,\frac{\partial\,(fE)}{\partial r}$$

In addition, for an optically thick region $f \to 1/3$; therefore

$$F \simeq -\,c/3(\sigma_a + \sigma_s)\,\frac{\partial E}{\partial r}$$

This expression is the familiar form for the flux in a diffusive medium. Using this expression for the flux and using the energy equation, the diffusion form of the transport equations can be written as

$$\frac{\partial E}{\partial t} - \frac{\partial}{\partial r}\left(\frac{c}{3(\sigma_a + \sigma_s)}\frac{\partial E}{\partial r}\right) + c\,\sigma_a E = J$$

This is the nonLTE diffusion form of the radiation transport equation.

For optically thin regions $\sigma \to 0$. In this limit equations (6) and (7) become

$$\frac{\partial E}{\partial t} + \frac{\partial F}{\partial r} \simeq 0$$

$$1/c\,\frac{\partial F}{\partial t} + c\,\frac{\partial E}{\partial r} \simeq 0$$

Notice that the Eddington factor has been set equal to one, its free streaming value. If we now eliminate F we find

$$\frac{\partial^2 E}{\partial t^2} + c^2\,\frac{\partial^2 E}{\partial r^2} = 0$$

which is just the wave equation for photons.

II-B-2-g-iv The Eddington Factor

We have chosen a simple physical model to determine the Eddington factor. A model only for the spherically symmetric case is available at this time. As we gain experience with the code and with different transport problems, we will develop models for other geometries and probably improve our method for determining the spherically symmetric form for f. The primary criterion on f is that it limit to the correct physical values. For example, f must limit to 1/3 for optically thick and to 1 for optically thin regions of the plasma.

To determine f we calculate the radiation pressure, energy density and flux between two concentric and uniform temperature spherical bodies.[2] Consider the vacuum region, the annular region between the two radiating concentric spheres shown in Figure 1. The sphere near the origin is denoted by 1 while the outer sphere is denoted by 2.

Figure 1

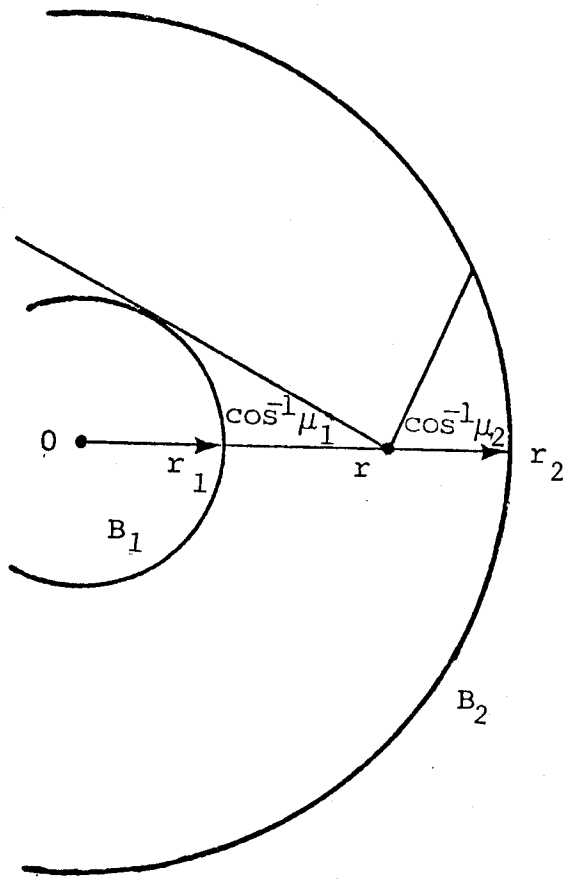

Eddington Factor Model of Vacuum Region
between Two Concentric Radiating Spheres

We use geometry to calculate μ_1 and radiation retardation to calculate μ_2.

The expressions for E, F and P are

$\mu_2 < 0$

$$E = \frac{2\pi}{c}\left[B_1(1 - \mu,) + B_2(1 + \mu_2)\right] \tag{8}$$

$$F = \pi\left[B_1(1 - \mu_1^2) - B_2(1 - \mu_2^2)\right] \tag{9}$$

$$P = \frac{2\pi}{3c}\left[B_1(1 - \mu_1^3) + B_2(1 + \mu_2^3)\right] \tag{10}$$

where B_1 is the radiation source for sphere 1 while B_2 is the source for sphere 2. Therefore, we can write f as

$$f = P/E = 1/3\left[1 + \frac{2F}{cE}(\mu_1 + \mu_2) - \frac{2\pi\,\mu_1\,\mu_2}{cE}\left[\frac{B_1}{\mu_1}(1 - \mu_1^2) - \frac{B_2}{\mu_2}(1 - \mu_2^2)\right]\right] \tag{11}$$

If the problem is geometry limited and $\mu_1 = \mu_2$

$$f = \frac{1}{3}\left[1 + \frac{2F}{cE}\mu_1\right] \tag{12}$$

This is the form of the Eddington factor that we use in our code where E and F are the local energy density and flux, respectively. For the spherically symmetric imploding, burning pellet problem the material vacuum interface is not well defined. The radiation opacities vary much more slowly as a function of radius. Thus, we can not define μ_1 in a unique way. We assume that the source function at the surface of the radiating sphere is a linear function

of the optical depth -- the Milne-Eddington model. For a sphere[4]

$$B_\tau = B_o\ (1 + 1.5\ \tau).$$

Consequently, at a point r, u_1 is determined by the tangent drawn from r to a sphere, centered at the origin, and whose surface passes through a point two-thirds of a mean free path back along the radius from the point of interest, r.[2] Notice that as the mean free path becomes very large $F \to cE$ and $\mu \to 1$ and as the mean free path becomes very small $\mu_1 \to 0$. Thus, f limits to the correct physical values.

II-B-2-g-v Multifrequency Group Averaging

Because the radiative mean free path is frequency dependent the first step in developing a numerical technique for solving the transport equation is to develop equations for frequency groups. To do this we first determine the range of frequencies we need to consider. We then divide this range into a number of frequency groups (v_m, v_{m+1}) which can be changed to fit the conditions of the problem. To determine the transport equations for a given group we integrate the equation over the groups frequency range. For example, the transport equations for group (v_m, v_{m+1}) becomes

$$\frac{\partial E}{\partial t}(v_m) + \frac{1}{r^{\alpha}-1}\frac{\partial}{\partial r}\left(r^{\alpha-1}\ F(v_m)\right)$$

$$+ c\ \bar{\sigma}_p(v_m)\ E(v_m) = J(v_m) \qquad (12)$$

$$\frac{1}{c}\frac{\partial F}{\partial t}(v_m) + c\left[\frac{\partial}{\partial r}\ f(v_m)\ E(v_m) + \frac{\alpha-1}{2r}\ (3f(v_m) - 1)\ E(v_m)\right]$$

$$+ \bar{\sigma}_R(v_m)\ F(v_m) = 0$$

where

$$E(v_m) = \int_{v_m}^{v_{m+1}} E(v)\ dv$$

$$F(v_m) = \int_{v_m}^{v_{m+1}} F(v)\ dv$$

$$f(v_m) = 1/3 \left[1 + \frac{2\ F(v_m)}{c\ E(v_m)}\ \mu(v_m) \right]$$

and

$$J(v_m) = \int_{v_m}^{v_{m+1}} J(v)\ dv$$

Notice that in order to do the frequency average of σ_a and $\sigma_a + \sigma_s$ we need to know F(v) and E(v), functions which are not known. Our approach is to assume we can use a local Planck average in the energy equation,

$$\bar{\sigma}_p(v_m) = \frac{\int_{v_m}^{v_{m+1}} B(v, T)\ \sigma_a(v)\ dv}{\int_{v_m}^{v_{m+1}} B(v, T)\ dv}$$

where T is the local electron temperature in the plasma and a local Rosseland average in the flux equation,

$$\frac{1}{\bar{\sigma}_R(v_m)} = \frac{\int_{v_m}^{v_{m+1}} \frac{1}{(\sigma_a(v) + \sigma_s)}\ \frac{\partial B}{\partial T}\ (v, T)\ dv}{\int_{v_m}^{v_{m+1}} \frac{\partial B}{\partial T}\ (v, T)\ dv}$$

II-B-2-g-vi Boundary Conditions

For the case of a spherically symmetric burning, imploding pellet the outer boundary of the plasma is optically thin. At the outer surface we can divide the radiation into an outgoing part I_+ which is determined by the transport model and an incoming part I_- which is determined by external conditions. Using these definitions we can write the specific intensity for streaming radiation as

$$I(\mu) = I_+ \, \delta(\mu - 1) \qquad \mu \geq 0$$

$$I(\mu) = 0 \qquad \mu < 0$$

or $I(\mu) = 0 \quad \mu \geq 0$, $I(\mu) = I_- \, \delta(\mu+1) \quad \mu < 0$ which gives for the total outer boundary flux

$$F = cE - 2F_-$$

where F_- is the incoming flux.

The flux at the inner boundary is assumed to be isotropic and, thus, $F = 0$. These are the two boundary conditions used in our code.

II-B-2-g-vii Radiation Coupling to the Ions and Electrons

In modeling the time evolution of a imploding, burning pellet, it is necessary to solve the coupled ion, electron and radiation equations. We are using a two-temperature, one-fluid hydrodynamical model for the ion and electron motion. In this model the electron internal energy equation is given by

$$\frac{d\varepsilon_e}{dt} = - P_e \frac{dv}{dt} - \frac{c_v^i}{\tau} (T_e - T_i)$$

$$+ \frac{1}{\rho \, r^{\alpha-1}} \frac{\partial}{\partial r} \left(K_e \, r^{\alpha-1} \frac{\partial Te}{\partial r} \right) +$$

$$1/\rho \sum_k (c\,\sigma_p(v_k)\,E(v_k) - J(v_k)) + \dot{S}_e \qquad (14)$$

where ε_e is the electron internal energy per unit mass, P_e is the electron partial pressure, C_v^i is the ion specific heat, K_e is the electron thermal conductivity, τ is the electron -- ion collision exchange time, $1/\rho \sum_k (c\,\sigma_p(v_k)\,E(v_k) - J(v_k))$ are the radiation energy emission and absorption terms and $\dot{S}_e$ is the energy source term due to laser coupling and thermonuclear burn. Radiation is also coupled to the electron and ion fluid motion through the radiation pressure.

We have developed the computer code in such a way that we can do any one of three different treatments of the radiation transport problem. We can do a time independent frequency dependent calculation. For example, to do this calculation we ignore the time derivatives in the multifrequency equations and use the absorption and emission terms given on the hydrodynamic time scale. We can do a frequency independent time dependent calculation, i.e., the one frequency group case. We can do a frequency dependent time dependent calculation which doesn't require the solution to the coupled set of ion, electron and multifrequency radiation equations.[2] We accomplish this by first doing a frequency dependent time independent calculation for the energy density, flux and pressure. Using these calculated values we find frequency-averaged values of the absorption coefficients and the Eddington factors. These calculated averaged values are then used to do a frequency averaged time dependent calculation of the energy and flux. The averaged energy density and flux are then coupled to the ion and electron energy and the fluid motion. By doing this we replace the coupled multigroup radiation, ion and electron energy equations with coupled one group radiation, ion and electron equations. This fact could greatly reduce the computer cost.[2]

II-B-2-g-viii Spectral Information

To make the hydro-burn calculation with radiation transport economic we use as few frequency groups as possible -- the number of groups being determined by whether or not we can find the temperature and density history of the plasma accurately enough. On the other hand, we would like to know the x-ray spectral structure. To meet the latter requirement a post-processing large multifrequency time independent radiation calculation can be done. For example, this time independent calculation could be done with 20 to 40 frequency groups whereas the implosion and burn calculation would be done with as few as 10 groups.

II-B-2-g-ix Comparison Of Our Radiation Transport Calculations To Published Results

To insure that the radiation transport code was numerically debugged we compared our transport calculations and the results of J. P. Apruzese and J. Davis[5] for simple test problems. They use three different methods for solving the transport problem. They are the Variable Eddington, the Strict Eddington and the Ray Tracing methods (see Figure 2). In Figure 2,J is the mean radiation intensity defined as

$$J = 1/2 \int_{-1}^{1} I(\mu)\, d\mu$$

where $I(\mu)$ is the specific intensity and where μ is the angle between the direction of radiation flow and the radial direction -- spherical symmetry is assumed. There are three different problems considered. For these problems the source function defined as the emission coefficient divided by the absorption coefficient is constant throughout the sphere. The three cases considered are $kR_0 = 1.3$, $kR_0 = 4.9$, and $kR_0 = 100$ where k is the absorption coefficient and where R_0 is the radius of the sphere. Our results, dotted lines in the graph, compare quite well with their calculations

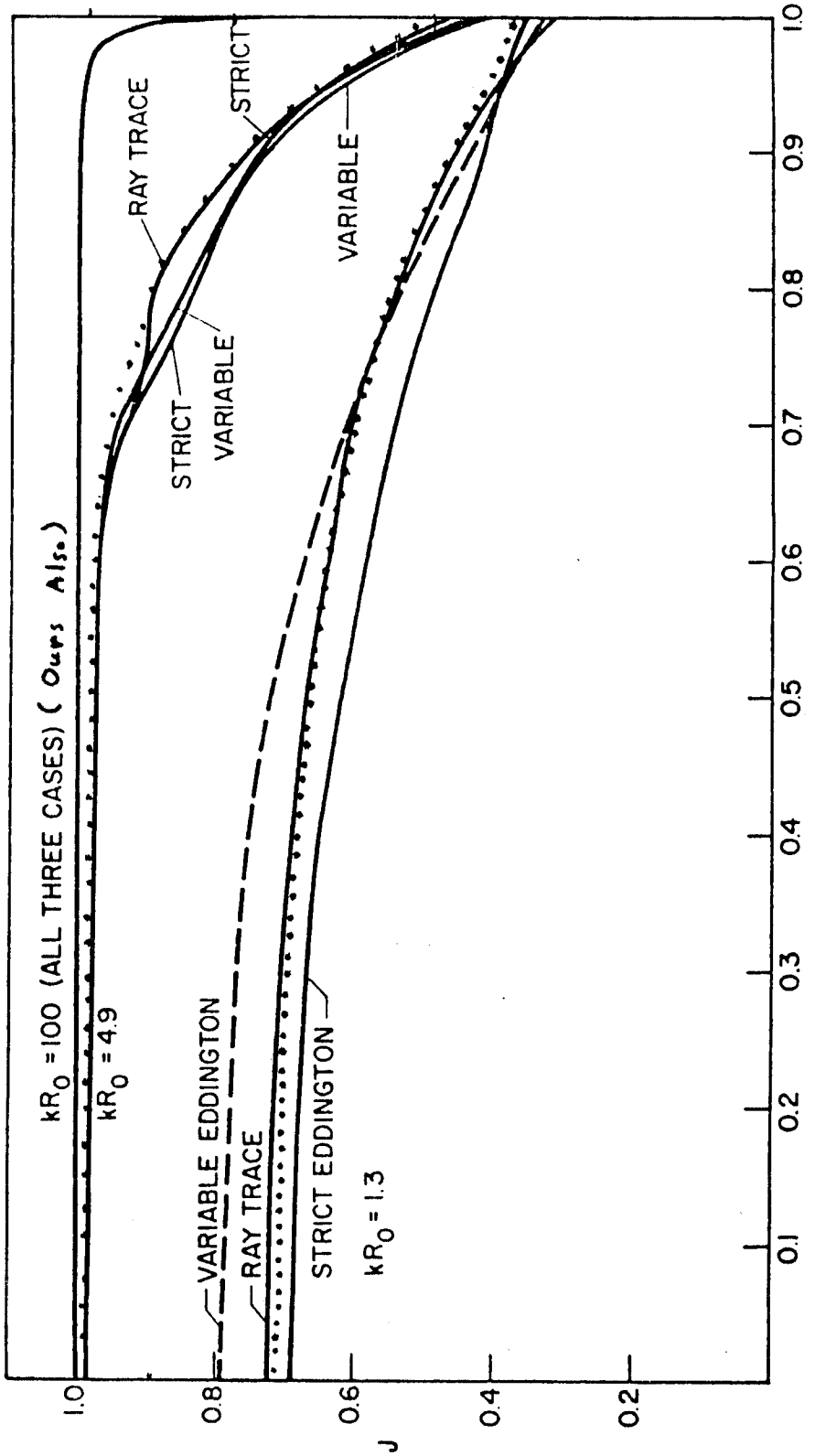

Figure 2 Mean intensity J vs. radius r for optical depths of 1.3, 4.9, and 100 for ray-trace, strict Eddington, and variable Eddington transport calculations (dotted lines give our calculations)

II-B-2 - References

1. S. I. Pai, Radiation Gas Dynamics, Springer-Verlag (1966).

2. P. M. Campbell and J. J. Kubis, "A Variable Eddington Method for Radiation Transport in Dense Fusion Plasmas," KMSF-U458 (1976).

3. P. M. Campbell, "A Numerical Method for Discrete Ordinate and Moment Equations in Radiation Transfer," Int. J. Heat Mass Transfer 12, 497 (1969).

4. V. Kourganoff, Basic Methods in Transfer Problems, Dover (1963).

5. J. P. Apruzese and J. Davis, "Evaluation of the Radiation Field in a Spherically Symmetric Plasma," NRL Memorandum Report 3277 (1976).

6. R. Richtmyer and K. Morton, Different Methods for Initial-Value Problems, (Wiley, New York, 1967).

7. H. Brysk, KMSF Report U275 (1975).

8. G. Kerley, LA-4776, (1972).

9. L. Spitzer, Physics of Fully Ionized Gases, (Wiley, New York, 1965).

II-C Advanced Fuels

All fusion fuels except the deuterium-tritium mixture are called advanced fuels. These are listed along with DT in Table 1. Each of these other fuels requires higher temperatures and densities or mass than DT to reach the same thermonuclear yield. Peaking of the reaction rates at higher temperatures necessitates the higher burn temperature to promote the most efficient burning. The lower absolute magnitudes of advanced fuel reaction rates in comparison to DT along with the possible smaller Q value requires higher fractional burn up and thus higher ρR for advanced fuel cores to reach the same yield. This might also be accomplished at reduced ρR and low fractional burn up but with increased core mass. With this approach the gain on core is likely to suffer however. The laser requirements necessary to achieve greater ρR, temperature and possibly mass seem to be formidable. In the near term, therefore, it is assumed that DT will be utilized as the fusion fuel.

Within the context of this laser fusion study we are interested in advanced fuels as a somewhat separate issue from the power plant feasibility. With the PHD burn code as a tool we are in a good position to estimate the values of fuel core parameters necessary to promote high yield burning, therefore the study of advanced fuels for inertial confinement fusion seems well justified. This analysis has not been done at this time, however, it should be completed within the next few months.

One advanced fuel of interest is of course pure deuterium. This has a reaction rate closest to the most reactive DT and as such it might require the smallest increase in temperature and ρR requirements. The advantage of DD is the elimination of tritium breeding in the blanket and at first glance the conspicuous absence of 14 Mev neutrons (there is one 2.45 Mev neutron for every two reactions however).

$$_1D^2 + {}_1D^2 \xrightarrow{50\%} {}_1T^3\ (1.01\ \text{Mev}) + {}_1P^1\ (3.02\ \text{Mev})$$

$$50\%\ {}_2He^3\ (.82\ \text{Mev}) + {}_0N^1\ (2.45\ \text{Mev})$$

14 MeV neutrons are not totally absent, however, for a triton is produced for every two DD reactions and it must slow down in the deuterium plasma. The probability of causing a DT reaction while slowing down could be quite large. If all of the tritons fused with deuterium while slowing down there would be an equal number of 14 MeV and 2.45 MeV neutrons and the DD advanced fuel loses some of its attractiveness from the materials damage point of view. These calculations will be done to determine the fraction of tritons fusing while slowing down and also the fuel core parameters necessary to promote pure DD fusion. These will serve as a guide for defining the laser characteristics necessary to achieve DD fusion.

Another fuel of interest is a mixture of hydrogen and Boron-11.

$$_1P^1 + B^{11} \rightarrow 3\,{}_2He^4\ (8.682\ \text{Mev})$$

This advanced fuel has the advantage of no neutron reaction products at all. Only 3 alpha particles are the result of a P-B^{11} fusion (or fission if you like) with a Q value of 8.682 MeV. The alpha particles are emitted in some continuous spectrum (as in β decay). The PHD burn code will be modified to calculate the necessary ρR and temperature requirements for P-B^{11} fusion. To do this the energy spectra of the alphas particles must be determined (the code will use either an average energy or some statistical sampling of this distribution). The transport will be straight forward because the charged particle reaction products are the same as for DT. With all of the energy in charged particles the reactor design might be substantially different.

With the peak in the reaction rate at about 300 KeV it will be difficult to bring P-B^{11} to ignition conditions. This might be relieved by using a

small amount of DT to get the burn started. This would again involve 14 MeV neutrons, though many fewer in number than in pure DT fuel. We hope to determine the optimum combination of DT, P-B^{11}, temperature and ρR for this advanced fuel pellet.

Another problem with the P-B^{11} reaction is the uncertainty in the fusion cross section and hence in the reaction rate, $\langle\sigma v\rangle$. We have computed[1] our own reaction rate based on the most up to date data[2] and have compared our results with earlier calculations.[3-7] We find substantial differences with some previous calculations[3] and are ducking the relationship to other analyses.[4-7]

Our code calculates the reaction rate, $\langle\sigma v\rangle$, assuming that both species have Maxwellian distributions. The integral[8] is evaluated numerically using a number of different techniques (Laguerre integration, Trapazoidal Rule, etc.), all of which give consistent results. The cross-section data is in tabular form in increments of 25 KeV lab. energy. Linear interpolation is also used.

Many values of the fusion cross section for the P-B^{11} reactions are in existence and yet they differ dramatically.[2-3, 9-11] For example, the resonance at ~650 KeV has a cross section which lies somewhere between the low of ~550 mb to a high of ~850 mb! Clearly, with such confusion in the data, reaction rates will vary. We are currently pursuing this matter further with Tombrello and Fowler at Cal Tech and should resolve remaining differences in the near future.

Table 1

Advanced Fuels

Fuel	Reaction Products (Mev)	Q-Value (Mev)
(D,T)	$_2He^4(3.5)$, $_0n^1(14.1)$	17.6
(D,D)	$_2He^3(.82)$, $_0n^1(2.45)$	3.65
	$_1T^3(1.01)$, $_1H^1(3.02)$	
(D,He^3)	$_2He^4(3.6)$, $_1H^1(14.7)$	18.3
(D,Li^6)	$2_2He^4(22.4)$	22.4
(P,Li^7)	$2_2He^4(22.4)$	22.4
(P,B^{11})	$3_2He^4(8.682)$	8.682

References II-C

1. M. Gordinier, R. Conn, Univ. of Wisconsin-Madison (Private Communication) (10/76).

2. T. Tombrello, Cal-Tech, (Private Communication) (10/76).

3. G. Miley, H. Towner, and N. Ivich, "Fusion Cross Sections and Reactivities," Univ. of Illinois Nuclear Engr. Program Report COO-2218-17.

4. W. A. Fowler, G. Caughlin and B. Zimmerman, "Thermonuclear Reaction Rates, II", Annual Review of Astronomy and Astrophysics, 13, 69, 1975.

5. D. C. Moreau, "Potentiality of the Proton-Boron Fuel for Controlled Thermonuclear Fusion," Princeton University Engineering Masters Thesis, May 1976.

6. T. Weaver, G. Zimmerman, L. Woods, "Prospects for Exotic Fuel Usuage in CTR Systems I. "$B(P,2\alpha)He^4$: A Clean High Performance CTR Fuel" Lawrence Livermore Reports UCRL-74191 and 74352.

7. J. M. Dawson, "CTF Using the P-B" Reaction" (Private Communication).

8. See Ref. #3 for explicit form of the integral.

9. I. D. Proctor, H. F. Lutz, W. Bartolini (10 June 1974).

10. Segel, Hanna, Allis; Phys. Rev., 139, B818 (1965).

11. Symons, Treacy; Nuclear Physics, 46, 93, (1963).

II-D. Implosion Studies

The implosion of the laser fusion fuel pellet can be decoupled from the subsequent thermonuclear burn phase of the pellet dynamics. From the instant that thermonuclear ignition occurs, the dynamics of the implosion process will be irrelevant to the final energy yield. Therefore, the implosion process can be viewed as ending at the instant of ignition. This greatly simplifies calculations, for the implosion and burn can be done in separate calculations and the two processes can be separately studied in detail. At this time, much more effort has been invested in the thermonuclear burn problem than in the implosion process. Several reasons have accounted for this. 1) The expected yield from a given amount of fuel and the energy gain of the pellet are fundamental to the design of a laser fusion power plant. 2) Thermonuclear calculations can be done in a somewhat generic nature with a one dimensional hydrodynamics code. Regardless of geometry, the idea of a hot microcore surrounded by cold fuel promoting a thermonuclear burn wave seems to be fundamental to good yield and energy gain. 3) Burn calculations define the necessary ρR value for the core and the temperature of the hot microcore. The implosion must, therefore, be of sufficient strength to attain the required ρR and the final collapse velocity must be sufficiently high to shock heat the microcore to the desired temperature. 4) The implosion process is sensitive to equations of state and adequate equations of state have only recently been added to the PHD code. 5) The implosion process can be sensitive to two dimensional effects which are not modelled by a one dimensional code and finally 6) it has been suggested that specific target designs outside the scope of this study are actually necessary to achieve the ρR and temperature values required for significant yield and gain.

With all of these problems in mind a limited number of numerical implosion studies have been conducted using admittedly over-simplified physical modelling, and more will be done in the future using more sophisticated models as they are developed. These will be used as a guide for identifying the weakest links in the implosion process. The details of the pellet design studied most completely at this time are given in Table 1. This pellet has an aspect ratio of 2.07 to provide zeroth order insurance that it can be stably imploded. This is below the maximum aspect ratio deemed allowable from Rayleigh-Taylor instability considerations. The ideal gas equations of state provide much too optimistic results and this point is emphasized here. The laser pulse shape was the optimized power law form.

$$P_L(t) = P_L(o) \,/\, [1 - t/t_o]^P \qquad P_L(t) < P_L(max)$$

$$= 0 \qquad\qquad\qquad\qquad P_L(t) > P_L(max)$$

Nearly 100 implosion calculations were performed using different combinations of $P_L(o)$, $P_L(max)$, t_o, and p, with all unattenuated laser energy dumped at the critical density. Probably the most significant information gained from the simulations is the sensitivity of the implosion results to the laser pulse parameters. Private correspondence with researchers at the Lawrence Livermore Laboratory has confirmed that this sensitivity is also present in LASNEX simulations of similar pellets. We therefore have assurance that these first, simple calculations are not over estimating the sensitivity. There is particular sensitivity to the $P_L(o)$ parameter which says that the

Table 1

Summary of Implosion-Burn Calculations

Pellet initial conditions:

Mass (g)	2.964(-3)
Outer radius (cm)	.16615
Inner radius (cm)	.1016
Aspect ratio ($R/\Delta R$)	2.07
Composition	50% D/50% T
Initial temperature (KeV)	.0001
Initial density (g/cm^3)	.2

Laser pulse parameters:

$P_2(o)$(TW)	.17
P_L(MAX)(TW)	2000
p	2.3
t_o(nsec)	50
λ_L(Å)	5300
$n_c(cm^{-3})$	3.98(+21)
All unattenuated energy dumped at n_c	
E_L(MJ)	1.3

power level early in the pulse is very important. This initial shocking of the pellet will determine the adiabat along which the core will be ultimately compressed. A low temperature adiabat is crucial to the successful implosion of the core.

The maximum laser power necessary to achieve an appreciable microcore temperature was 2000 TW. This value is far too high for several reasons.

1) It is doubtful that lasers and optics can be designed to deliver powers of this magnitude onto pellets at the rate of 20-30 times per second. (See also (3)).
2) With the laser energy "dump" approximation, this power level raises the temperature at the critical density to 10 Kev where inverse bremsstrahlung absorption is negligible. In light of current experimental evidence, this result can be considered totally unrealistic because problems of scale height steepening and supra thermal electron generation are not accounted for and these would certainly dominate the energy absorption process.
3) Since the ideal gas equations of state predict implosion results far too optimistically, the actual laser power necessary to reach ignition temperature is <u>even greater</u> by a factor of 2 to 10.

Several general conclusions can be drawn from this study, however. Large ρR values are obtained at the sacrifice of microcore temperature, and vice versa. Adequate ρR seems to be a function of the incident laser energy; however, ignition temperature is dependent on the maximum laser power. Therefore, analytic estimates of energy and power required to reach a given ρR will not necessarily be those necessary to reach ignition conditions (higher power will be required).

With the laser energy dump in use, these calculations really are an indication of implosion performance for a given energy absorption time profile since laser absorption physics is really not dominant. This would indicate that no matter how this energy is delivered, the implosion of these low aspect ratio, Rayleigh-Taylor stable shells is very sensitive to the temporal energy deposition profile. Sensitivity can be reduced by defining more robust laser characteristics; however, then pellet gain suffers and this is unacceptable for a pure laser fusion power plant. Indications are that multi-layered targets might reduce the sensitivity; however, again at the expense of pellet gain. It should also be noted that no attempt has yet been made to assess the problems due to uncertainty in the electron thermal conduction process but this will certainly have its own effect on implosion performance.

The final conclusion of this particular pellet study must be that simple low aspect ratio shells do not have the fundamental characteristics to allow them to reach adequate ρR and ignition temperatures, for laser energy and power within maximum conceivable limits. The only alternative at this point is to increase the aspect ratio to large values to test ρR/ignition temperature characteristics of thin shells and for the moment ignore the instability problem. These calculations will be performed in the future.

References II-D

1. R. Kidder, Nucl. Fus. 16, 3 (1976).

II-E. Thermonuclear Burn Studies

II-E-1. Comparison of PHD Results with other Published Results

With little experimental data available on alpha particle slowing down in dense plasmas, the best test of our calculations comes from comparison with the results of others. Favorable comparison of our results with other results derived from a similar transport and slowing down model coupled to a hydrodynamics calculation indicates that we are correctly treating the problem within the restrictions of our model. Favorable comparison with a more exact Monte Carlo collisional slowing down calculation indicates that our time dependent particle tracking model is in fact quite accurate within the restrictions of collisional slowing down theory. By arbitrarily scaling the slowing down terms in our model we simulate the possible effect of enhanced slowing down from collective interactions with the plasma. These calculations will be discussed in section II-E-3.

Our first comparison is with a propagating burn calculation published by Fraley, et al.,[1] where a 10 μg DT pellet compressed to a density of 6000 g/cm^3 (ρR = 4.4 g/cm^2) with the inner 10% of the pellet mass raised to 20 KeV is allowed to burn and disassemble. Temperature and density "snap shots" of the Fraley calculation and the PHD calculation are shown in Figure 1. Notice that the absolute magnitudes of the temperature and density are often different but that the general nature of the hydrodynamics is very similar. The temperature of the center zone is too large in the PHD results because the μ = -1 inward direction of the alpha particles from each zone pass through the center zone along its diameter. This is an inaccurate average path length through the center zone, the average will of course always be less than this. Methods for correcting this without going to a larger number of directions is being investigated. For the strongly burning pellets that we are currently

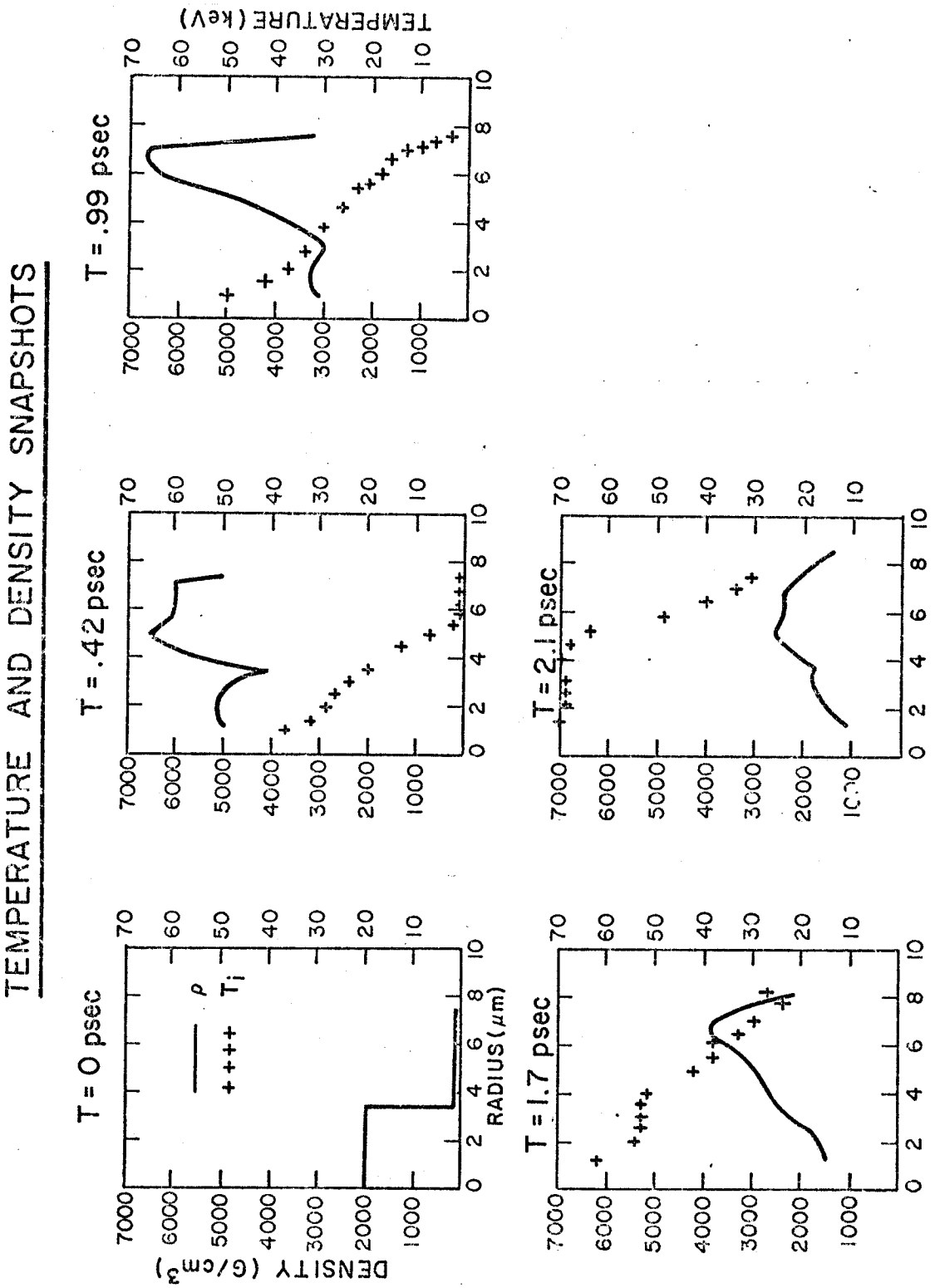
TEMPERATURE AND DENSITY SNAPSHOTS
T = 0 psec
T = .42 psec
T = .99 psec
T = 1.7 psec
T = 2.1 psec
DENSITY (G/cm³)
TEMPERATURE (keV)
RADIUS (μm)
ρ
Ti

FIGURE 1

Temperature and Density Snapshots

(from: G. Fraley, et. al., Phys. Fluids 17, 474 (1974))

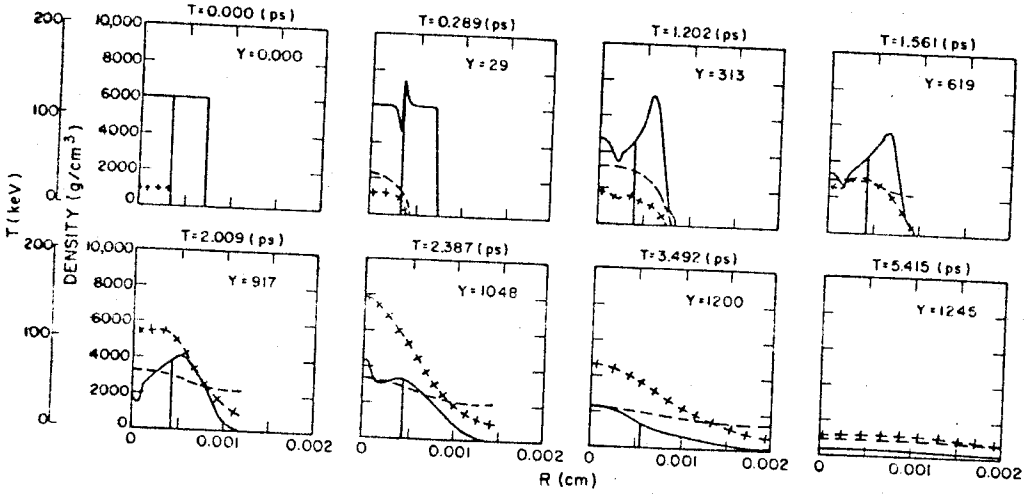

FIG. 6. Propagating burn in a 10-μg sphere; free outer boundary. Inner 10% of the mass $T = 20$ keV; remaining mass $T = 1$ keV.

investigating this is not a serious problem. Due to the broad peak in the DT reaction rate the thermonuclear energy output vs. time for the two calculations shown in Figure 2 is similar, with the final yield differing by 18%. Such results should be considered as acceptable agreement considering that no attempt was made to normalize our calculations to this or any other similar hydrodynamics calculation.

The Fraley, et al. model uses one dimensional, one fluid, 3 temperature lagrangian hydrodynamics coupled to an S_N transport treatment of the alpha particles using the slowing down formulation of Longmire[2]. The PHD model, as explained in section II-B-2-C, uses one dimensional, one fluid, two temperature Lagrangian hydrodynamics coupled to a time dependent particle tracking transport treatment of the alpha particles. It also uses the classical coulomb collision slowing down model. As such, we must consider our relatively good agreement with the results of the LASL calculations as confirmation of the correctness of the PHD computer program, within the approximation of the transport technique. In the case of alpha particle transport where most of the energy loss is through small angle scattering, the time dependent tracking technique and S_N transport are quite similar.

In the next test we compare the particle tracking technique (with straight line trajectories) to the more accurate Monte Carlo calculation of Corman, et al[3]. In Figure 3 we look in detail at the fractional energy redeposition into the electrons and ions vs. the distance from the source of 3.5 MeV alphas measured in units of slowing down mean free path on the electrons alone. Also plotted are the results of 100 group flux limited multi group diffusion of the alphas. We first note that the spatial scale is considerably less than one mean free path on electrons alone so one would expect that a transport calculation is necessary. This is confirmed by the multigroup diffusion results where we see a gross error in the details of redeposition to the ions.

FIG. 2 YIELD VS. TIME - A COMPARISON WITH S_N

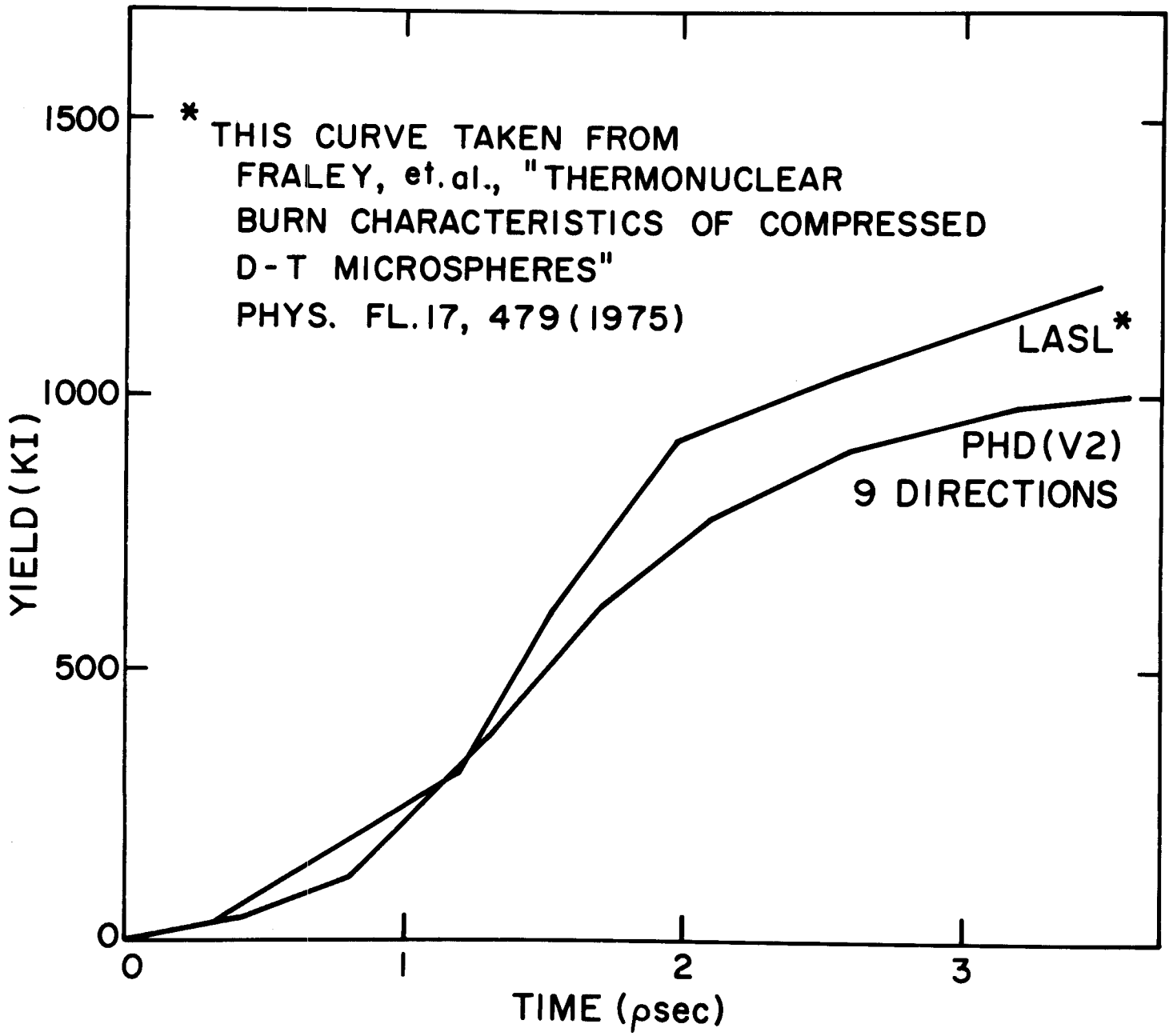

FIGURE 3 COMPARISON OF STRAIGHT LINE PARTICLE TRACKING AND MONTE CARLO

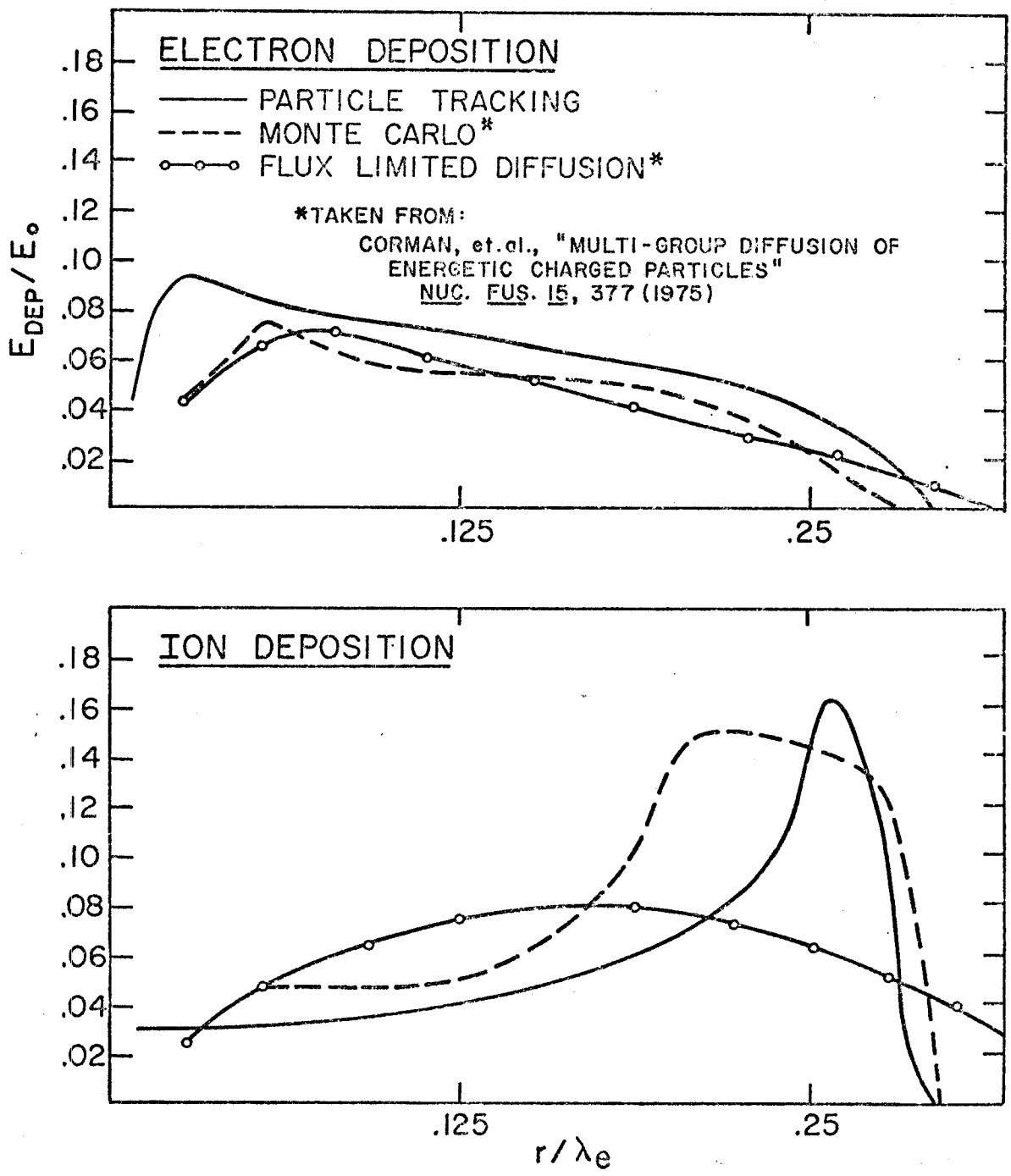

Fast alphas lose most of their energy to electrons along straight line trajectories until they slow down past a certain velocity after which they lose the largest share of their energy to the ions in larger angle collisions. This explains the broad peak in the Monte Carlo ion redeposition curve near the end of the alpha range. This peak is totally missed by the diffusion calculation although the total energy partitioning between electrons and ions is correct. The particle tracking method compares very well with both the electron and ion Monte Carlo redeposition, again, considering that no normalization is attempted. Slight adjustment of the slowing down term reproduces the Monte Carlo electron curve. The particle tracking method also predicts a peak in the ion redeposition however its peak is not as broad as the Monte Carlo peak and has its centroid farther from the origin. This discrepancy can be explained by recalling that the particle tracking method only allows straight line trajectories and this approximation will break down when scattering on the ions becomes appreciable. This method will therefore not account for back scattered alphas and will predict a peak that is narrower and further from the origin than would be expected. Techniques for distributing the energy at the end of range to broaden the peak are being investigated. It should also be noted that this is a rather severe test of the straight line approximation because the electron temperature in this problem is 50 KeV and Figure 4 shows that at this temperature a large fraction of the alpha energy is lost to the ions (rather than to electrons along straight lines). For electron temperatures less than 50 KeV the particle tracking method should be even more valid and for temperatures greater than 50 KeV the actual mean free path of the alpha particle is long compared to typical pellet dimensions, thus little energy is deposited and the error is again small. We therefore interpret these two results as confirmation that the

FIGURE 4

SLOWING OF α PARTICLES IN D-T @ $5 \times 10^{26}\ cm^{-3}$

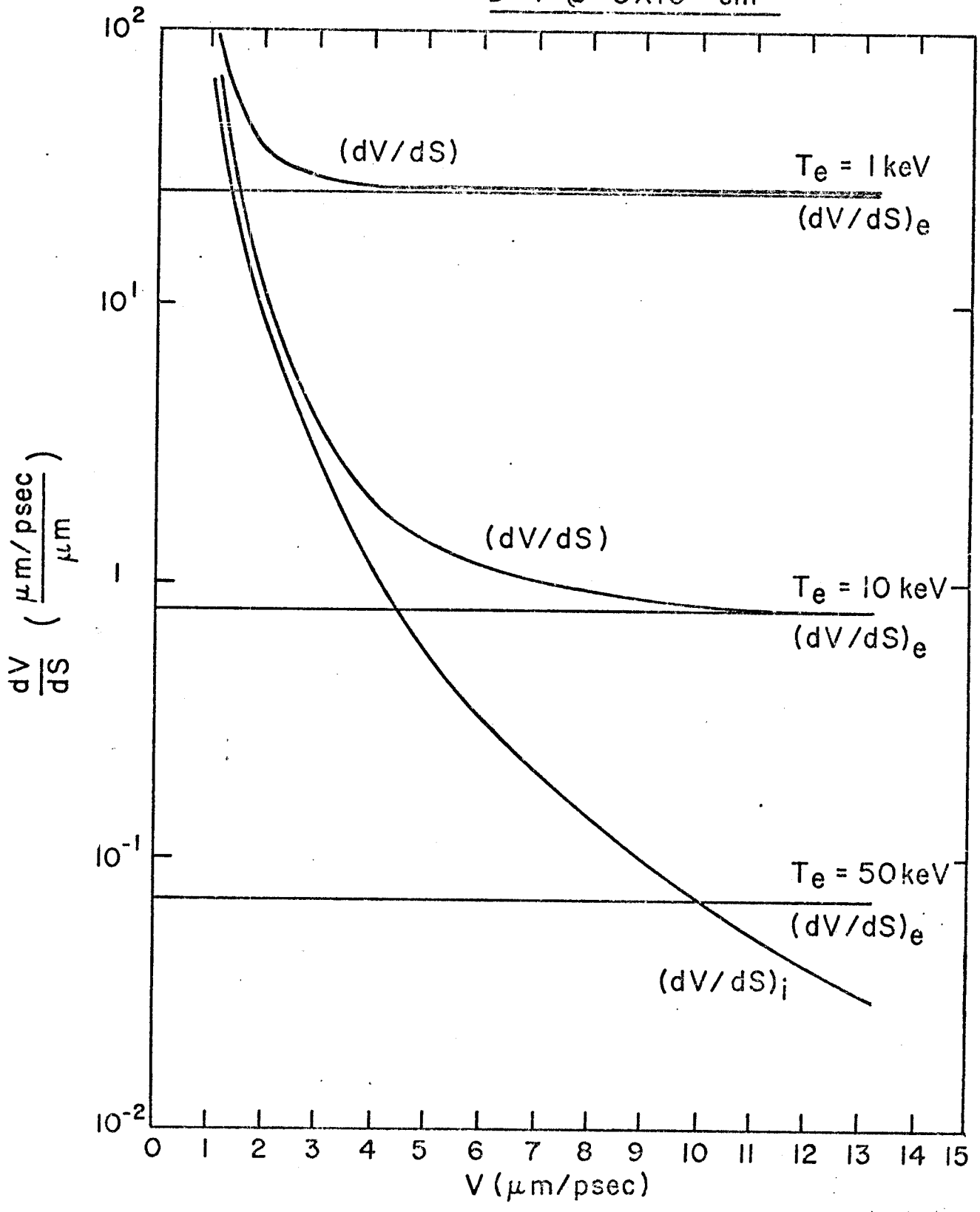

particle tracking model does remarkable well in predicting the coulomb collisional slowing down of the charged particle thermonuclear reaction products, and that when coupled to a Lagrangian hydrodynamics calculation it reproduces the hydrodynamic and burn results of a similar, presumably well tested, hydrodynamics code.

II-E-2. Sensitivity of PHD Results to Parameters Characterizing the Time Dependent Particle Tracking Model

The results of numerical simulations will always depend to some extent on the parameters used in the calculation (eg. number of mesh points, number of time steps, etc.) It is hoped that the calculations can be done using parameters that do not sensitively effect the results. The most relevant parameters in this regard for the time dependent particle tracking technique are the number of directions in which particles are allowed to move, the number of time levels that they are "remembered" and the minimum time step allowed for the thermonuclear calculation. In the PHD code the hydrodynamic time step is set by the Courant or percent change in temperature and/or density conditions and the thermonuclear burn time step need not be the same. It may be equal to or longer than the hydrodynamic time step. In Figure 5 are plotted the DT neutron yield and the number of alpha particles escaping the pellet as a function of these parameters for a 1 mg, ρR = 3 g/cm^2, ρR_μ = .8 g/cm^2, T_μ = 10 Kev, compressed pellet core. Notice that the neutron yield is insensitive to all of these parameters for this high yield pellet.

Once the transport calculation runs out of time levels for remembering the particles it simply forces the particles to slow down or escape by doing a time independent calculation after the last remembered level. Thus when the number of outward levels = 1 we are really doing a time independent transport calculation on each thermonuclear time step. Quite remarkably, Figure 5

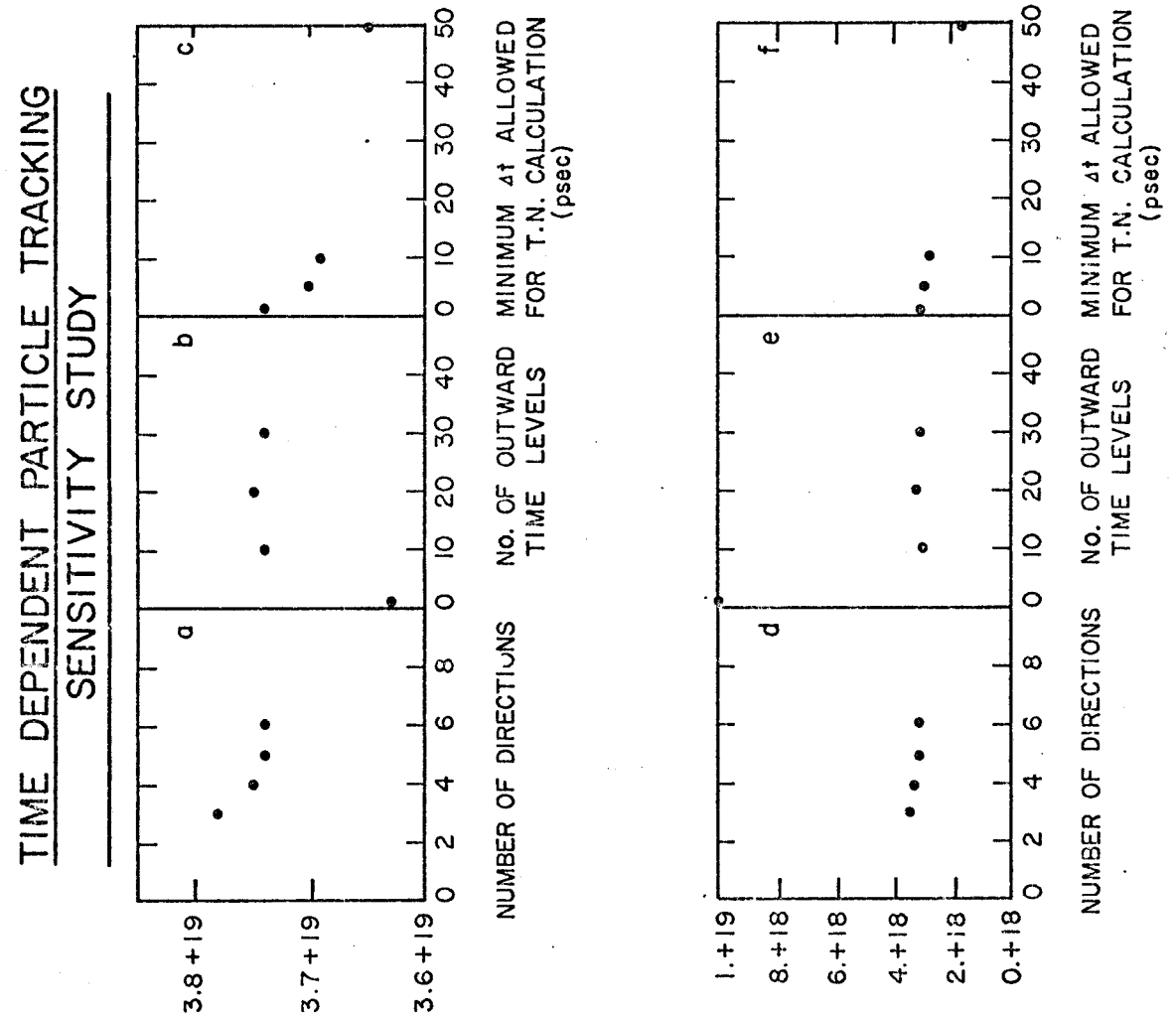
TIME DEPENDENT PARTICLE TRACKING
SENSITIVITY STUDY
NEUTRON YIELD
3.8+19
3.7+19
3.6+19
a
b
c
ALPHA PARTICLES ESCAPED
1.+19
8.+18
6.+18
4.+18
2.+18
0.+18
d
e
f
0 2 4 6 8 0 10 20 30 40 0 10 20 30 40 50
NUMBER OF DIRECTIONS
No. OF OUTWARD TIME LEVELS
MINIMUM Δt ALLOWED FOR T.N. CALCULATION (psec)

FIGURE 5

indicates that this gross transport inaccuracy does not have a large effect on the predicted yield and this fact can be utilized to reduce the cost of the calculation. However, the more transport dependent alpha particle leakage is in considerable error for the time independent case as indicated in part (e) of Figure 5. In light of this fact the insensitivity of the yield in this problem can again be attributed to the broad plateau in the DT reaction rate above 20 KeV. So long as enough alpha particle energy redeposition is available to raise temperatures above 20 KeV, the yield is determined by the hydrodynamic disassembly rather than the DT reaction rate. One cannot ignore the error in leakage however because the number of these alpha particles and their energy spectrum will be important to the reactor cavity designer.

In the case of each different parameter the yield and escaped particle number seem to be approaching asymptotic values. In the results that follow the transport calculations were done using sufficiently stringent parameters to insure that we were operating in the asymptotic range. Typically, 5 directions, 30 outward time levels, 60 inward time levels, and a minimum time step of 0.1 picoseconds were used in the calculations.

II-E-3. Pellet Core Burn Calculations

II-E-3-a. Yield, Gain on Core, Fractional Burn-up

The most basic parameters that characterize the laser fusion pellet in the context of reactor design are thermonuclear yield and pellet gain. Each of these will depend on the fractional burn-up of the fusion fuel, (that is the percentage of fuel compressed into the dense pellet core that ultimately burns). With the use of the PHD hydrodynamic - thermonuclear burn code such quantities can be computed as functions of pellet core mass, core ρR, micro-core ρR, micro core temperature, and uncertainties in the physics of charged particle slowing down and plasma hydrodynamics. Table 1 summarizes the results.

Table I

Summary of Burn Parameter Study

MASS	ρR	$(\rho R_{\mu}) = .3$	$(\rho R_{\mu}) = .4$	$(\rho R_{\mu}) = .5$	$(\rho R_{\mu}) = .7$
.1	1	3.41-2*	.32	1.54	2.8
		7.99	37.4	99	68.8
				0	
.1	2			7.4	
				1804	
.1	3	2.27-3	7.7	10.22	10.2
		.626	2034	2525	2048
.1	5	1.18-3	12.8	13	13
		.2	2155	2168	2103
.1	7	3.55-2	14.5	14.6	14.6
		4.3	1756	1764	1749
.316	1	.109	.971	5.03	
		8.93	38.1	106	
.316	2	.019	.763	23.2	
		3.2	99	2220	
.316	3	.009	27.2	32.0	
		1.21	3369	3602	
.316	5	.012	40.55	40.83	
		.278	3313	3289	
.316	7	2.5-3	45.8	46.4	
		.147	2702	2649	
1.	1	.344	3.3	16.5	30
		9.5	41.3	110	74.8
1.	2			76.3	
				2649	
1.	3	2.2-2	83.6	104	101
		1.3	4292	4786	3415
1.	5	8.4-3	129	130	131
		.306	4641	4597	4303
1.	7	5.6-3	146	148	148
		.147	3795	3836	3754

* First number is yield in mega joules
Second number is the gain on core assuming perfect adiabatic compression from 1 ev.
Micro core temperature - 10 Kev

Pellet core masses of 0.1 mg, .316 and 1.0 mg were chosen to bound the estimated necessary mass required to give a thermonuclear yield of 100 MJ. In Figure 6, the yield is plotted as a function of ρR for the three different pellet masses. The yield rises sharply from $\rho R = 1$ to $\rho R = 3$ but beyond this point the yield flattens out. From these curves it would appear that $\rho R = 3$ g/cm^2 is about the optimum value regardless of the mass. We also note the very linear dependence of the yield on pellet core mass (for this range of pellet mass). Figure 7 plots the yield vs. micro-core ρR for a fixed core ρR. The dependence is of a threshold nature. The ρR value of the micro-core must exceed 0.38 g/cm^2 to provide significant yield. Above this value the yield is constant and below this value the yield is negligible. With this information, the ρR and mass necessary to provide 100 MJ of energy can be identified. To determine the optimim combination the other pellet characteristic, gain must be used. Maximizing gain for a fixed yield will mimimize the necessary input energy. The pellet core burn calculations however will only allow the gain on core (eg. thermonuclear yield/energy stored in the compressed core) to be computed. The energy stored in the core is the sum of the micro-core internal energy at 10 KeV and the energy in the remainder of the surrounding core. This latter energy is computed by assuming a temperature equal to that of an equivalent adiabatic compression of a 1 eV plasma.

$$T = (1 \text{ ev}) \, (\rho/\rho_0)^{2/3}$$

This will in fact over-estimate the gain because a perfect adiabatic compression is not possible, however, most interest here is in the ρR - mass combination

FIGURE 6

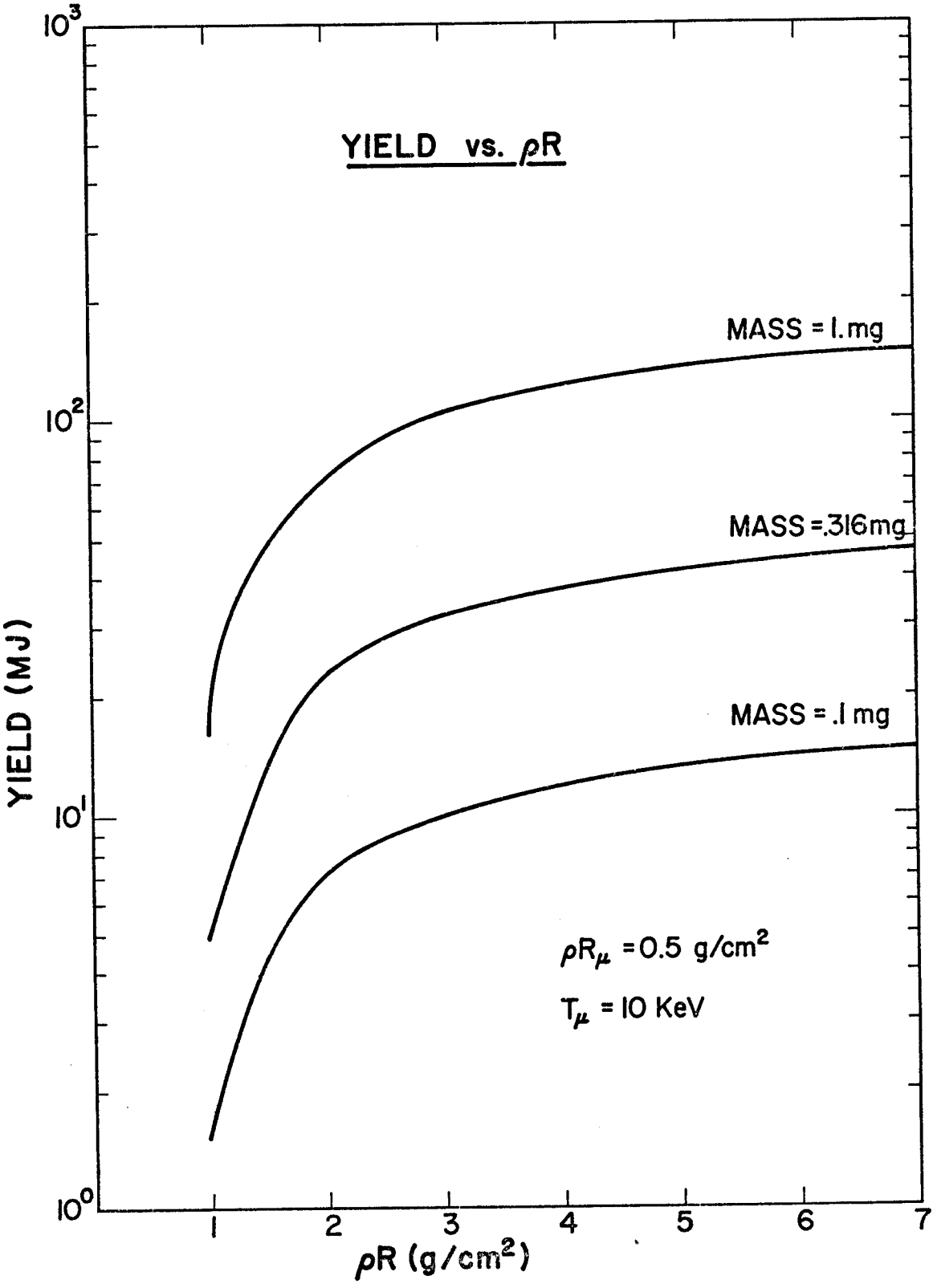
YIELD vs. ρR
MASS = 1. mg
MASS = .316mg
MASS = .1 mg
ρR_μ = 0.5 g/cm^2
T_μ = 10 KeV
YIELD (MJ)
10^3
10^2
10^1
10^0
1
2
3
4
5
6
7
ρR (g/cm^2)

FIGURE 7

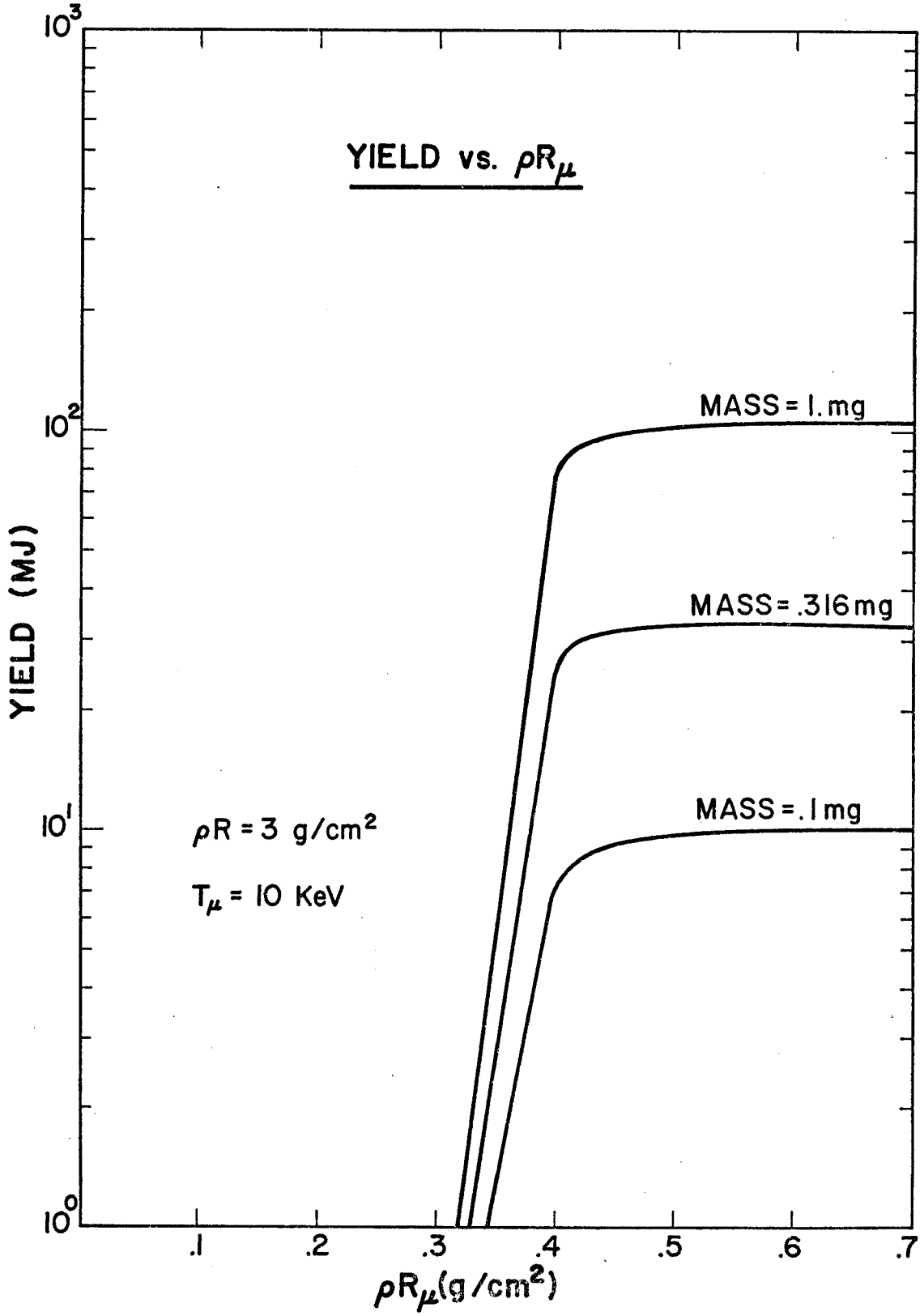
YIELD vs. ρR_μ
YIELD (MJ)
10^3
10^2
10^1
10^0
MASS = 1. mg
MASS = .316 mg
MASS = .1 mg
$\rho R = 3$ g/cm^2
$T_\mu = 10$ KeV
.1
.2
.3
.4
.5
.6
.7
ρR_μ(g/cm^2)

at maximum gain rather than the absolute value of the gain at that point. The yield in Fig. 6 can be fitted to within a few percent by the expression

$$Y = 10^3 \, m \, H \, (\rho R_\mu - 0.38) \begin{cases} [16 + 60(\rho R - 1)\ .585] & 1 < \rho < 3 \\ [71 + 11\ \rho R] & 3 \leq \rho R \leq 7 \end{cases}$$

and the internal energy invested in the core is

$$E_c = (.32)\left(\frac{4\pi}{3}\right)^{1/3} m^{2/3}\, \rho R + (38.3)\left(\frac{4\pi}{3}\right)^{1/2} \frac{(\rho R_\mu)^{3/2}}{m_\mu^{1/2}}\, T_\mu$$

where Y is the yield in MJ, m is the core mass in grams, H is a step function, ρR is the density-radius product in g/cm^2, E_c is the core internal energy in MJ, ρR_μ is the density-radius product of the micro-core in g/cm^2, m_μ is the microcore mass in grams and T_μ is the microcore temperature in keV. In Fig. 9, the first equation is used to plot a 100 MJ isoyield contour for combinations of ρR and mass and in Fig. 8 the ratio of these two equations gives the gain on core. Figure 8 indicates that the gain peaks around $\rho R = 3\ g/cm^2$ and mass = 1 mg. The <u>total pellet gain</u> is of course the quantity that must be maximized and this might be sensitive to the particular implosion process giving a different optimim from the one indicated by gain on core. For the implosion of spherical ball or shell targets, the coupling coefficient between the incident laser light and the internal energy stored in the core is predicted by sophisticated implosion calculations to be 5-10%. Using the 5% estimate and also assuming that the actual implosion process results in twice as much energy in the core as our adiabatic estimate, the gain on core of 4800 translates into an overall pellet gain of 120. This pellet gain will be adequate to compensate for a 10% efficient laser. Should laser efficiencies of 10% be unattainable, the laser-core coupling efficiency must be increased to provide laser fusion power plant feasibility. The conceptual design of pellets with the necessary laser-core coupling will be discussed in section II-F.

Fractional burn-up vs. ρR for a fixed mass of course takes the same form as the yield and is shown in Figure 10. The fractional burn-up of the optimum pellet core is 31%.

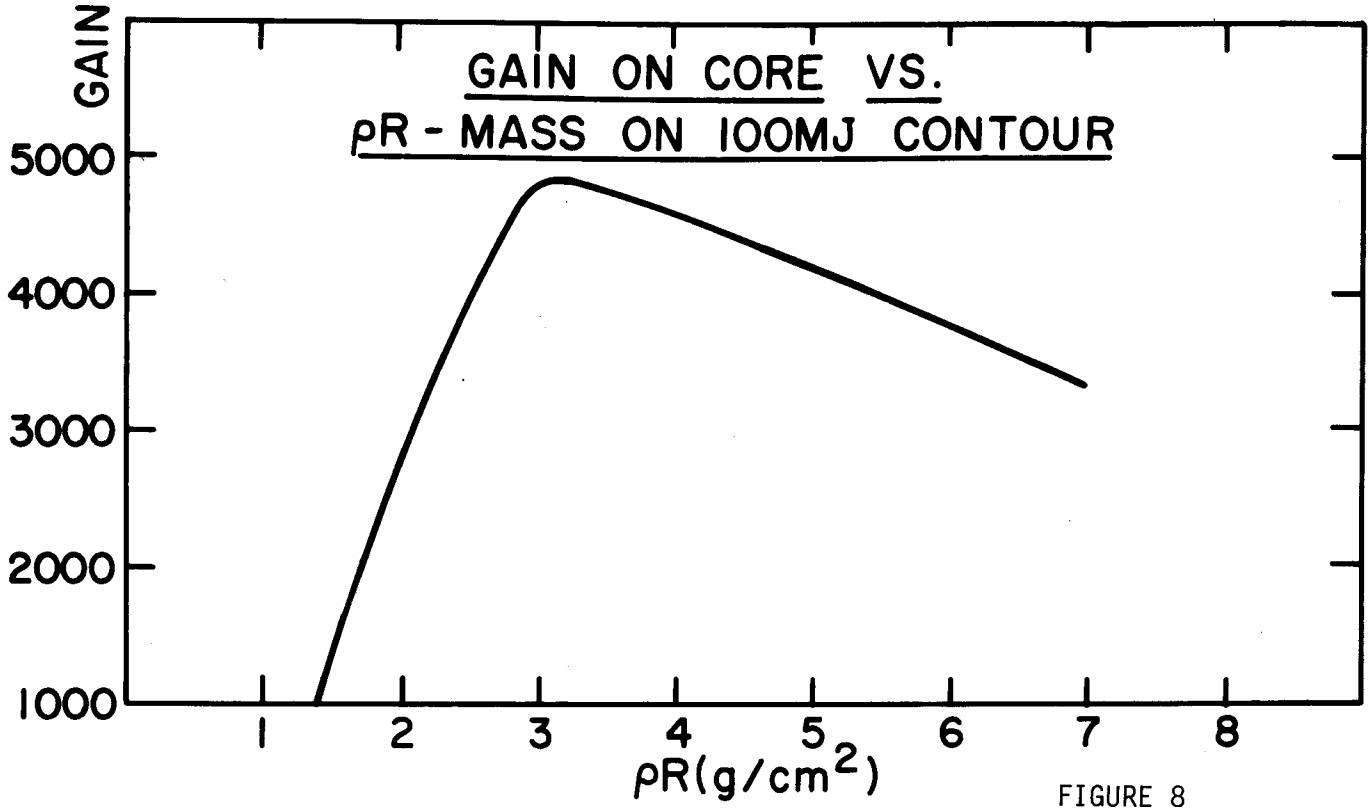

FIGURE 8

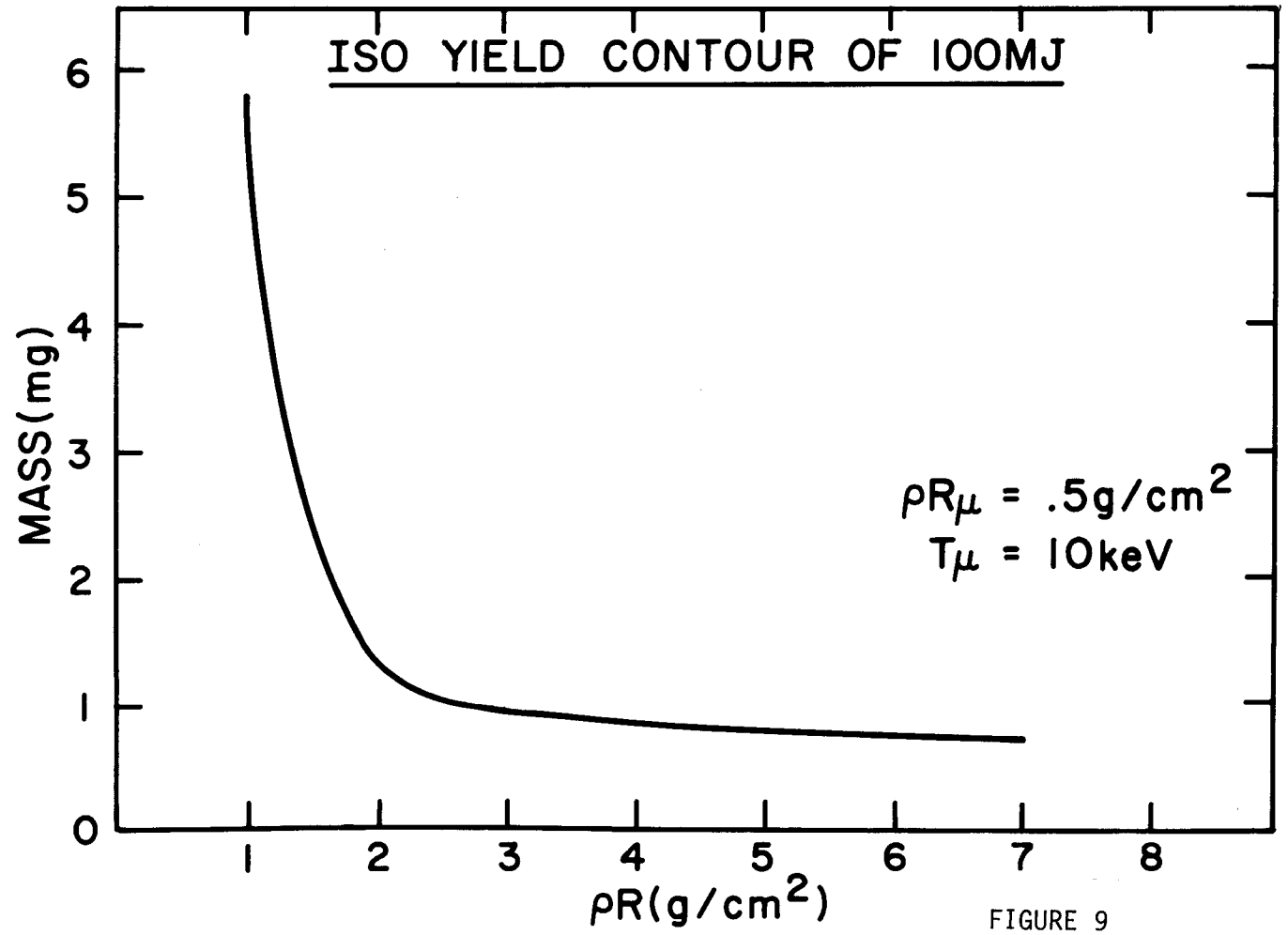

FIGURE 9

FIGURE 10

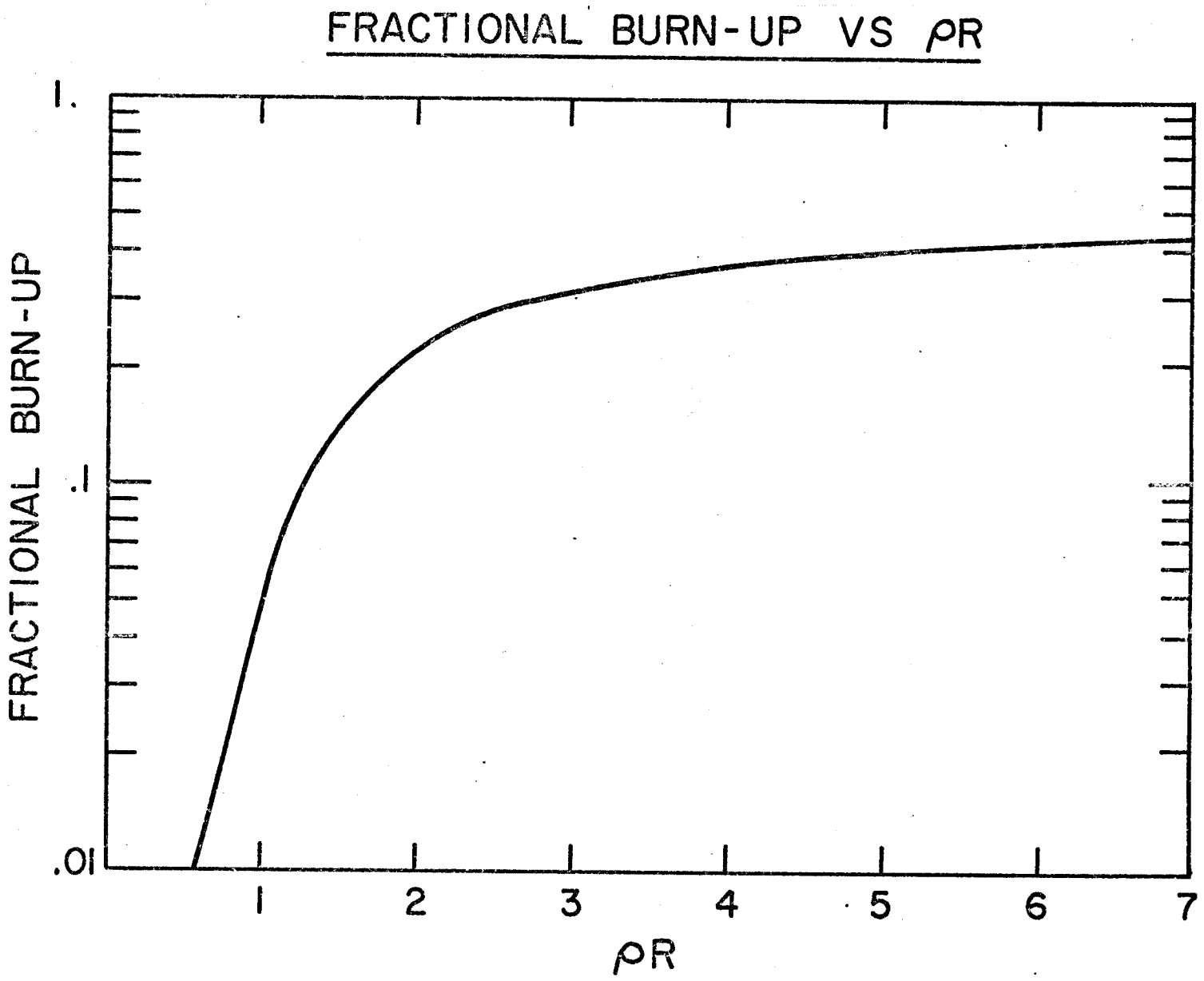

A chronology of the burn dynamics for the $\rho R = 3\ g/cm^2$, mass = 1 mg, $(\rho R)_\mu = .5\ g/cm^2$, $T_\mu = 10$ Kev pellet core is shown as temperature and density "snap shots" in Figures (11) through (15). The same core uniformly heated to 10 KeV is shown in Figures (16) through (20). The total and differential yield as a function of time for the two pellets are shown in Figures (21) and (22). These figures show that the uniform temperature core burns to its depletion limit about 25 pico seconds sooner than the hot micro core pellet, but they both produce essentially the same total yield. The energy invested in the uniform temperature core is however, 55 times the energy invested in the pellet with a hot micro core. In the micro core case there were 3.6×10^{19} 14 Mev neutrons produced and 1.28×10^{17} 2.45 Mev neutrons. These neutrons are assumed to escape the pellet, however future studies will investigate the effect of neutron heating of the pellet. This will presumably not have much effect for the pellet of interest here because we obtained identical yields for the micro core and uniformly heated core. For other more complex pellet designs this may not be the case.

II-E-3-b. Charged Particle Spectra of Pellet

Energy from the pellet will come in three forms: neutrons, charged particles, and x-rays. About 76% of the energy will come in the neutrons and the other 24% will be divided between charged particles and x-rays. For bare targets it is estimated that 23% of the energy will be in charged particles. These charged particles will be both thermal plasma ions and fast thermonuclear reaction products that have escaped the pellet ahead of the ablating outer boundary. PHD calculations indicate that for the $\rho R = 3\ g/cm^2$, mass = 1 mg, pellet core, 33% of the reaction product charged particles escape the pellet and they carry 19% of the total charged particle energy. The remaining energy is in the thermal expanding plasma. The time integrated spectra of the

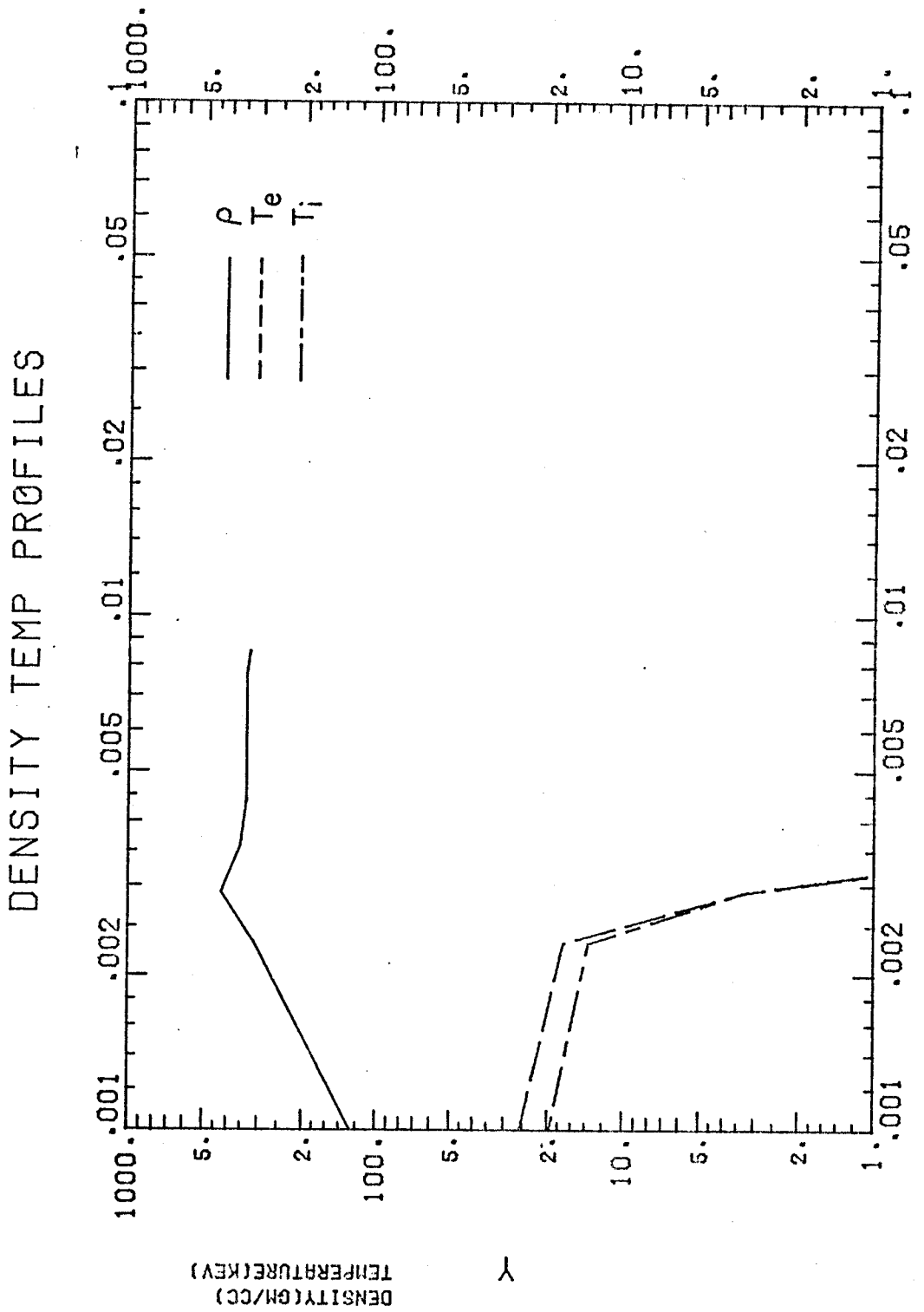
DENSITY TEMP PROFILES
ρ
Te
Ti
1000.
100.
10.
1.
.001
.002
.005
.01
.02
.05
.1
RADIUS(CM)
HOT CORE TEMP
TIME(NS) .0121
DENSITY(GM/CC)
TEMPERATURE(KEV)

FIGURE 11

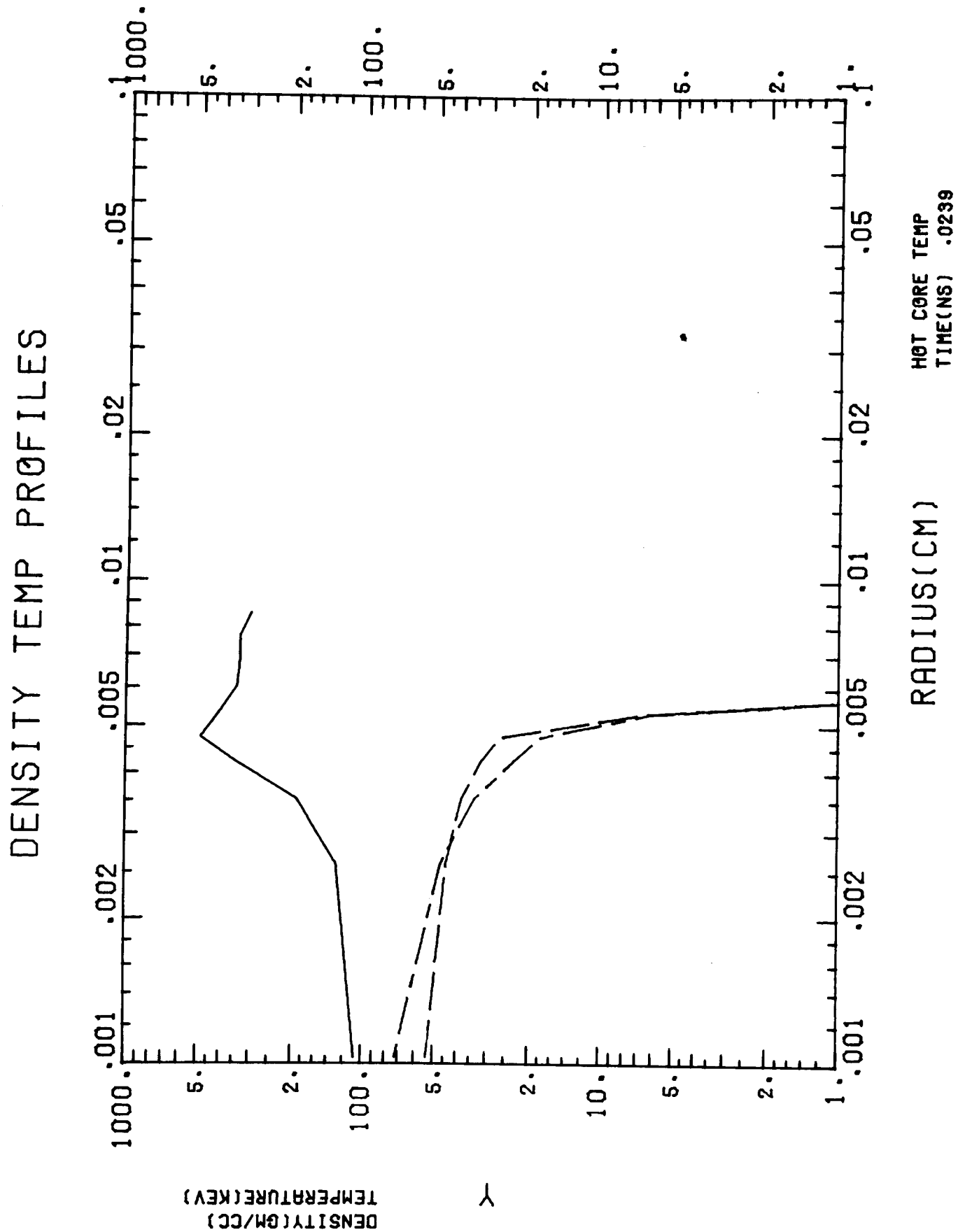
DENSITY TEMP PROFILES
HOT CORE TEMP
TIME(NS) .0239
RADIUS(CM)
DENSITY(GM/CC)
TEMPERATURE(KEV)
1000.
100.
10.
1.
.1
.05
.02
.01
.005
.002
.001
5.
2.

FIGURE 12

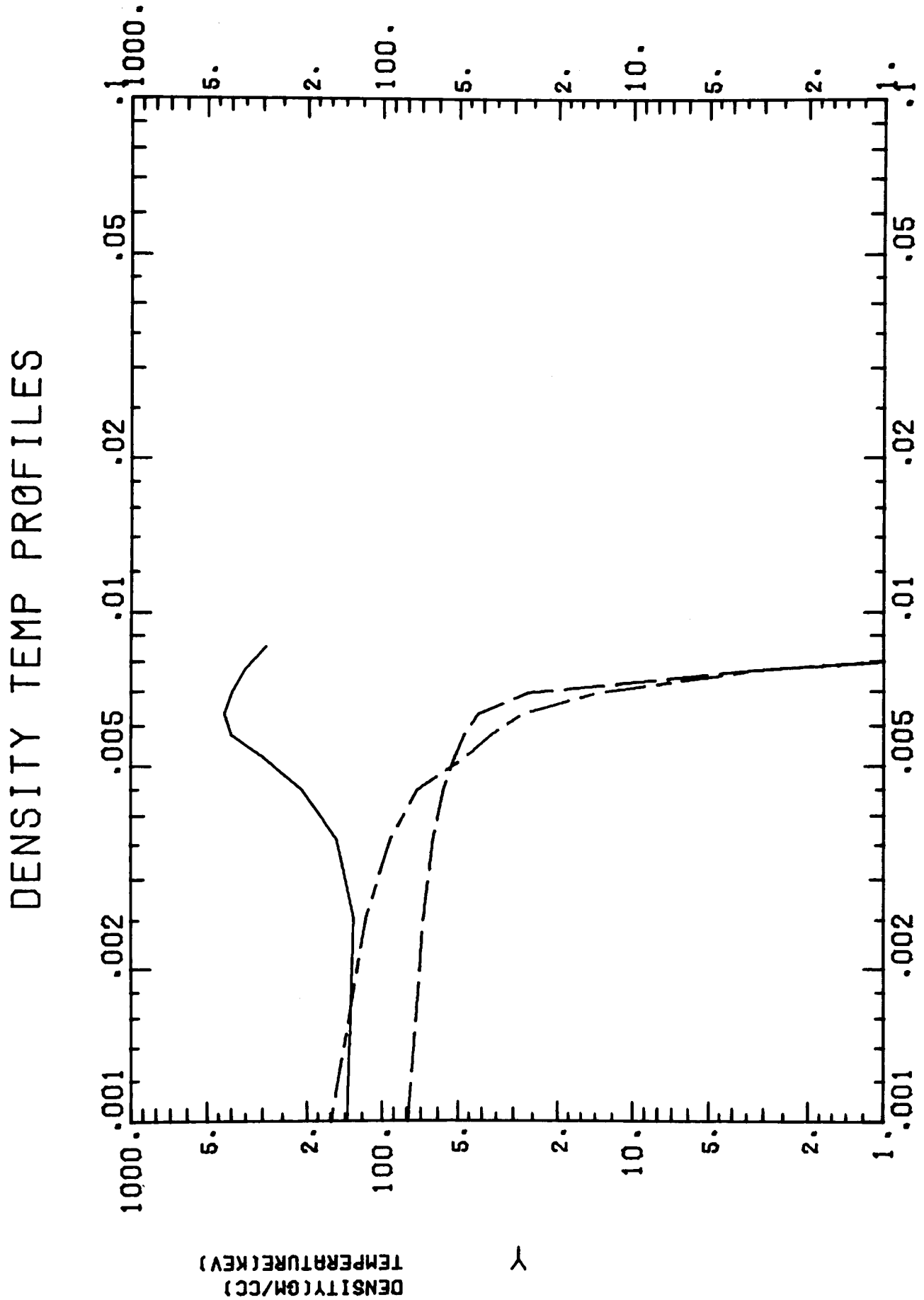
DENSITY TEMP PROFILES
1000.
5.
2.
100.
5.
2.
10.
5.
2.
1.
.1
.05
.02
.01
.005
.002
.001
RADIUS(CM)
HOT CORE TEMP
TIME(NS) .0200
DENSITY(GM/CC)
TEMPERATURE(KEV)

FIGURE 13

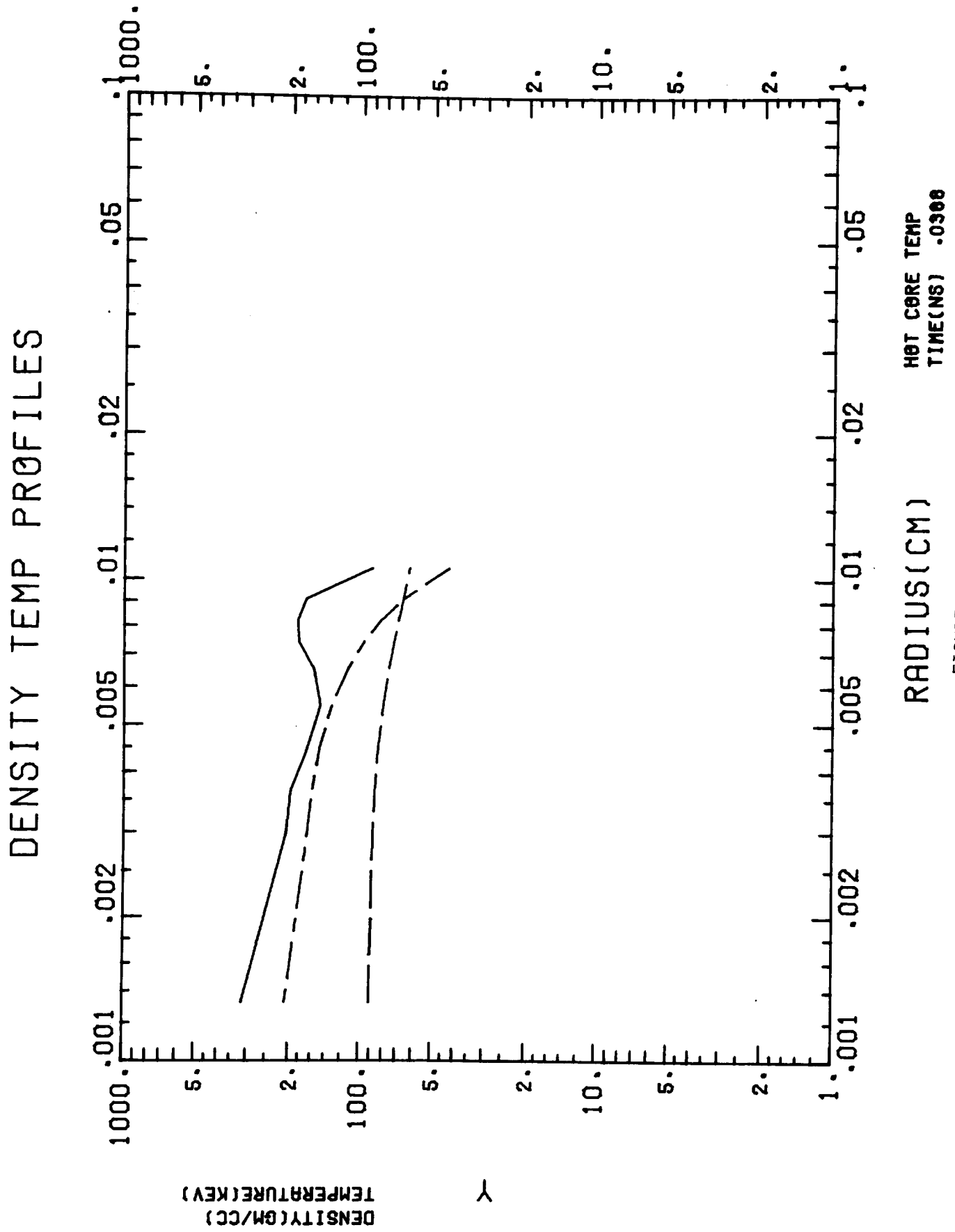
DENSITY TEMP PROFILES
1000.
5.
2.
100.
5.
2.
10.
5.
2.
1.
.05
.02
.01
.005
.002
.001
1000.
5.
2.
100.
5.
2.
10.
5.
2.
1.
.001
.002
.005
.01
.02
.05
RADIUS(CM)
HOT CORE TEMP
TIME(NS) .0300
DENSITY(GM/CC)
TEMPERATURE(KEV)

FIGURE 14

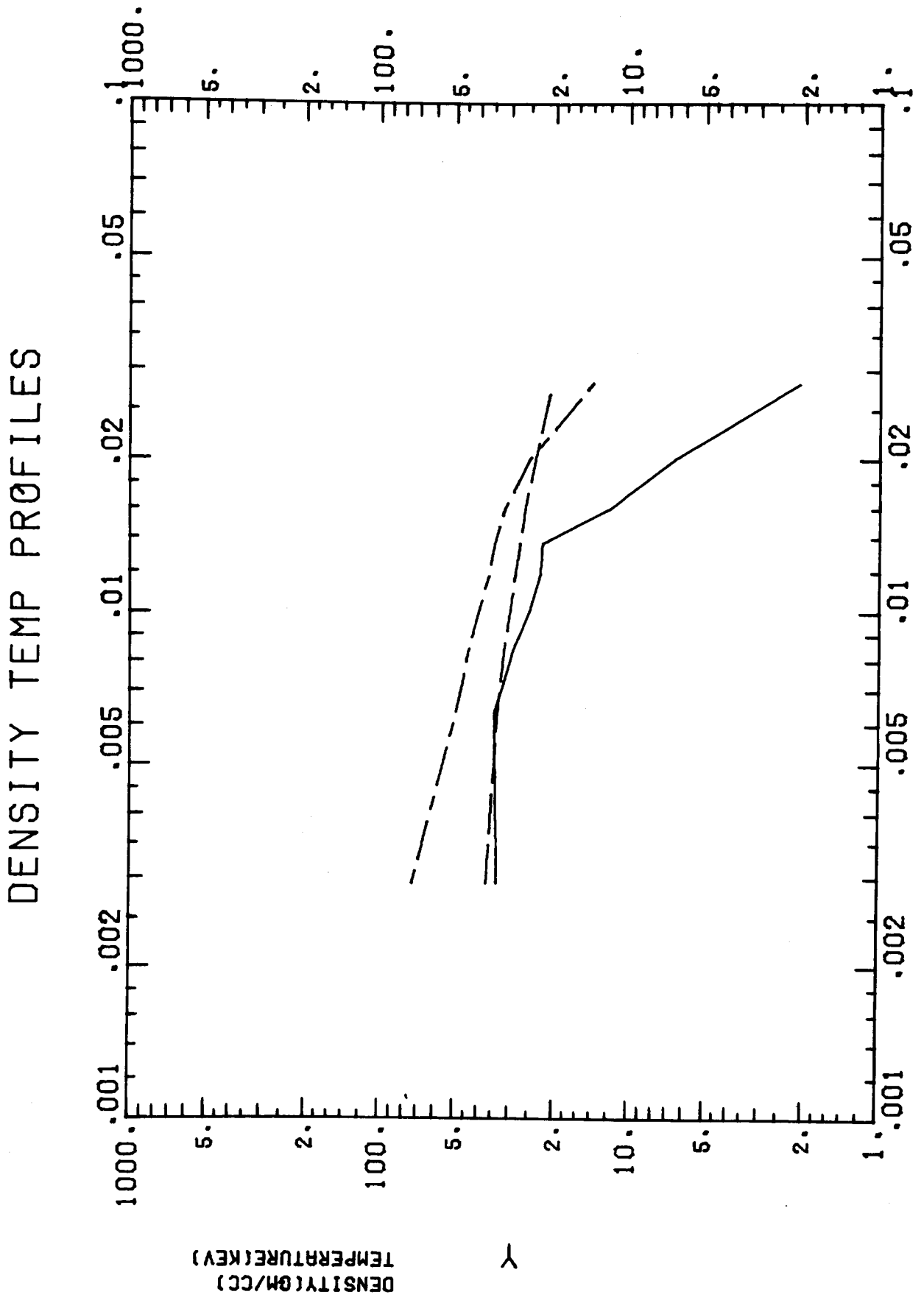
DENSITY TEMP PROFILES
1000.
5.
2.
100.
5.
2.
10.
5.
2.
1.
.05
.02
.01
.005
.002
.001
1000.
5.
2.
100.
5.
2.
10.
5.
2.
1.
.001
.002
.005
.01
.02
.05
RADIUS(CM)
HOT CORE TEMP
TIME(NS) .0645
DENSITY(GM/CC)
TEMPERATURE(KEV)

FIGURE 15

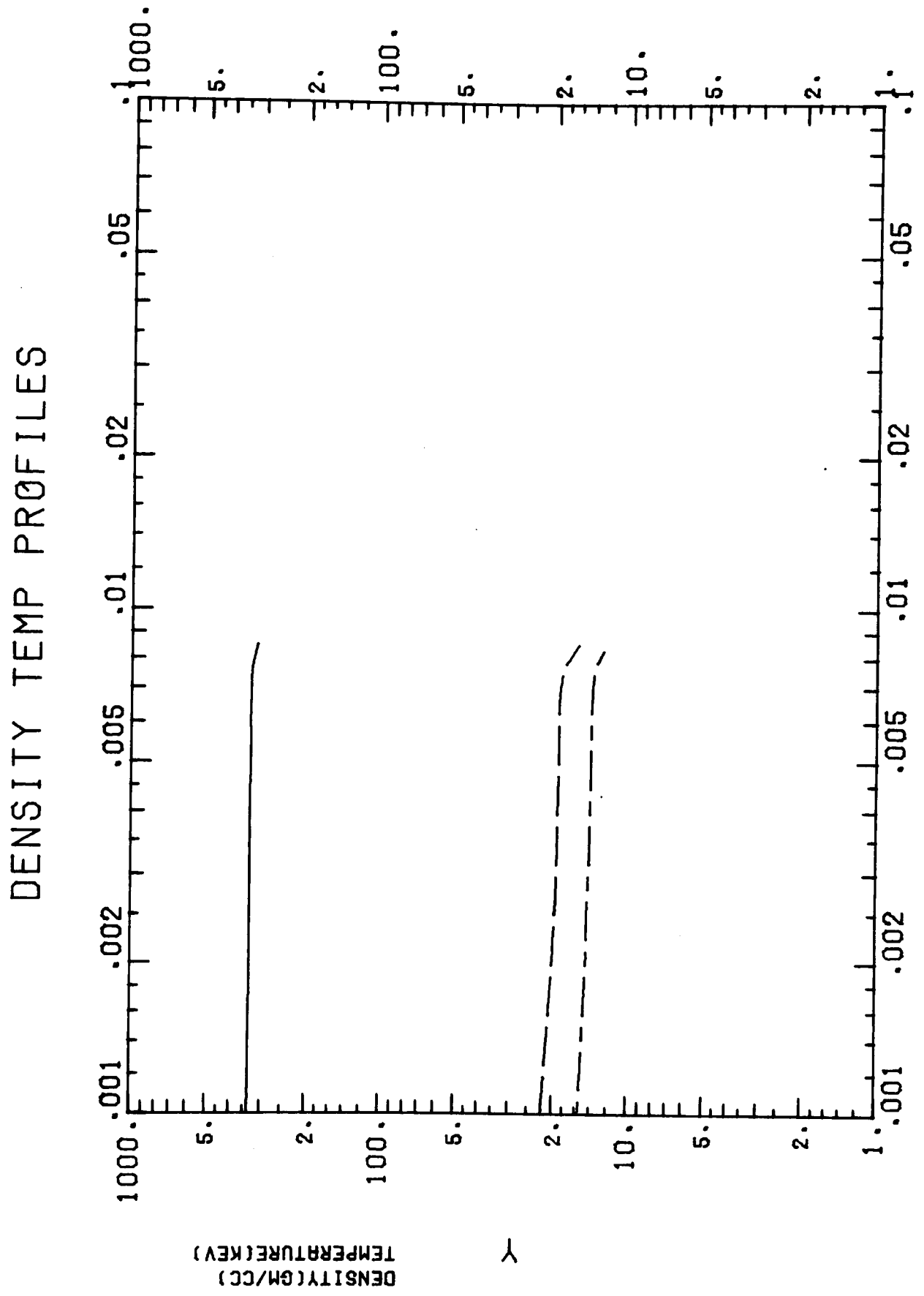
DENSITY TEMP PROFILES
1000.
5.
2.
100.
5.
2.
10.
5.
2.
1.
.001
.002
.005
.01
.02
.05
.1
DENSITY(GM/CC)
TEMPERATURE(KEV)
RADIUS(CM)
UNIFORM TEMP
TIME(NS) .0010

FIGURE 16

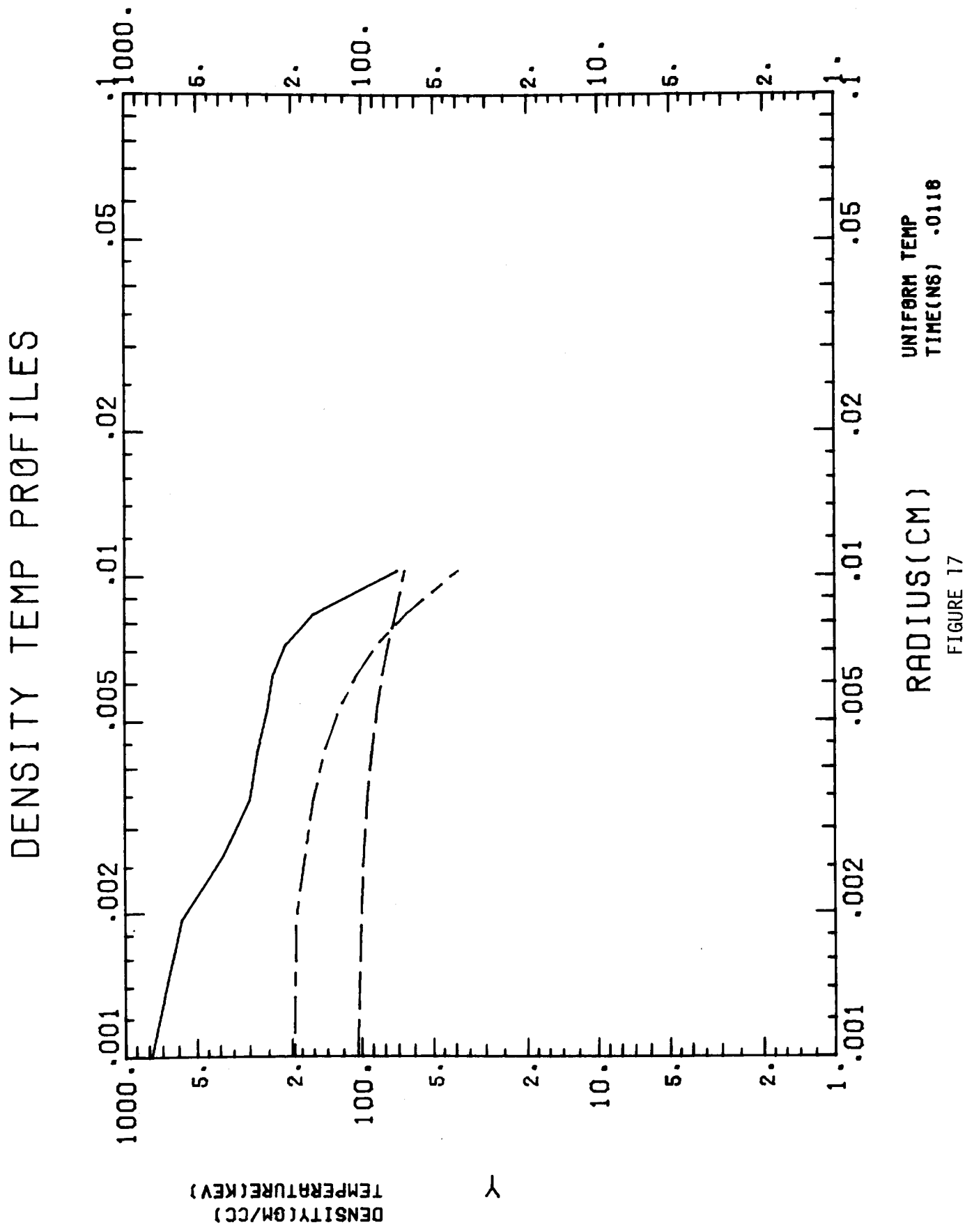
DENSITY TEMP PROFILES
1000.
5.
2.
100.
5.
2.
10.
5.
2.
1.
.001
.002
.005
.01
.02
.05
.1
RADIUS(CM)
UNIFORM TEMP
TIME(NS) .0110
DENSITY(GM/CC)
TEMPERATURE(KEV)

FIGURE 17

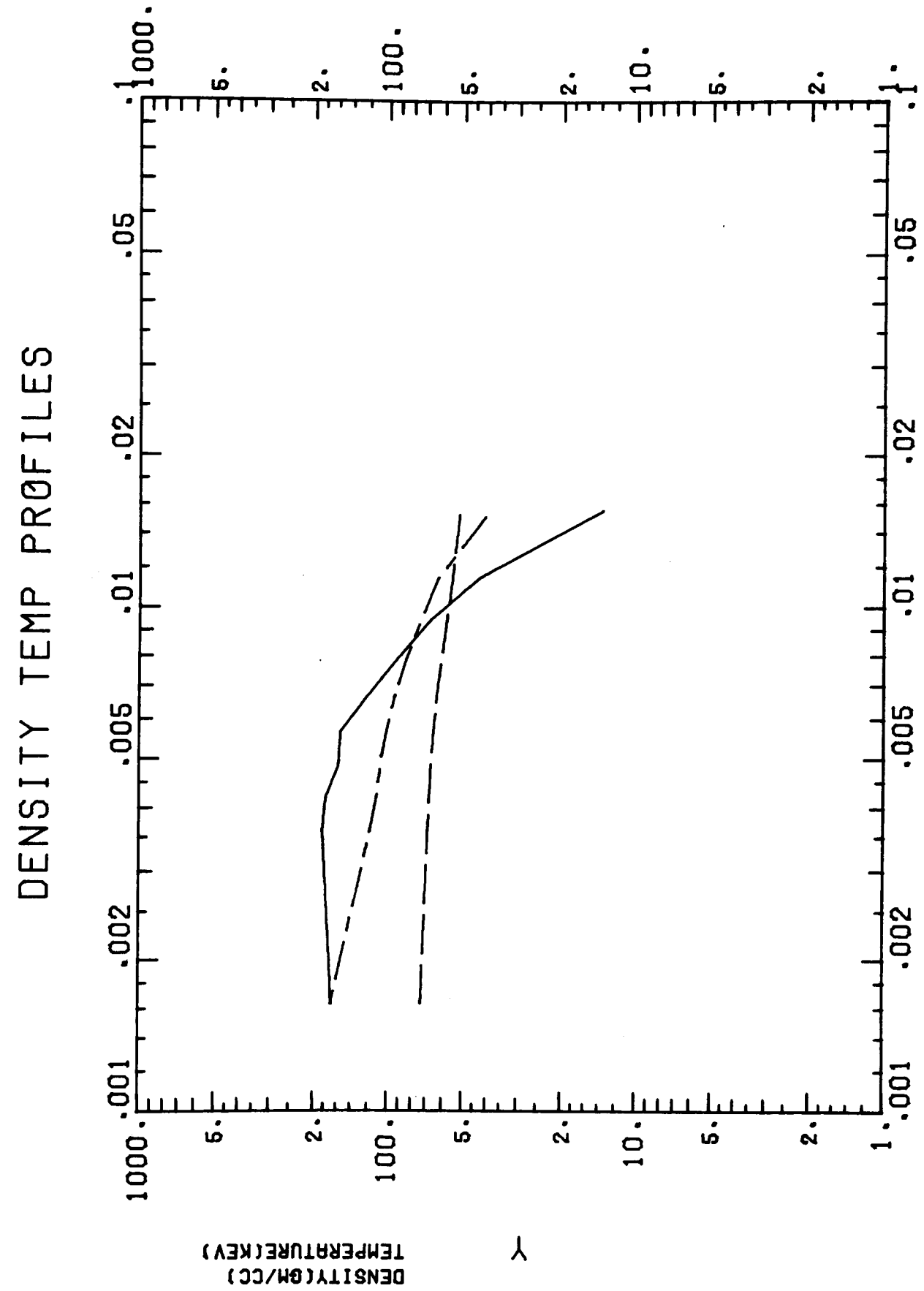
DENSITY TEMP PROFILES
1000.
5.
2.
100.
5.
2.
10.
5.
2.
1.
.1
.05
.02
.01
.005
.002
.001
RADIUS(CM)
UNIFORM TEMP
TIME(NS) .0220
DENSITY(GM/CC)
TEMPERATURE(KEV)

FIGURE 18

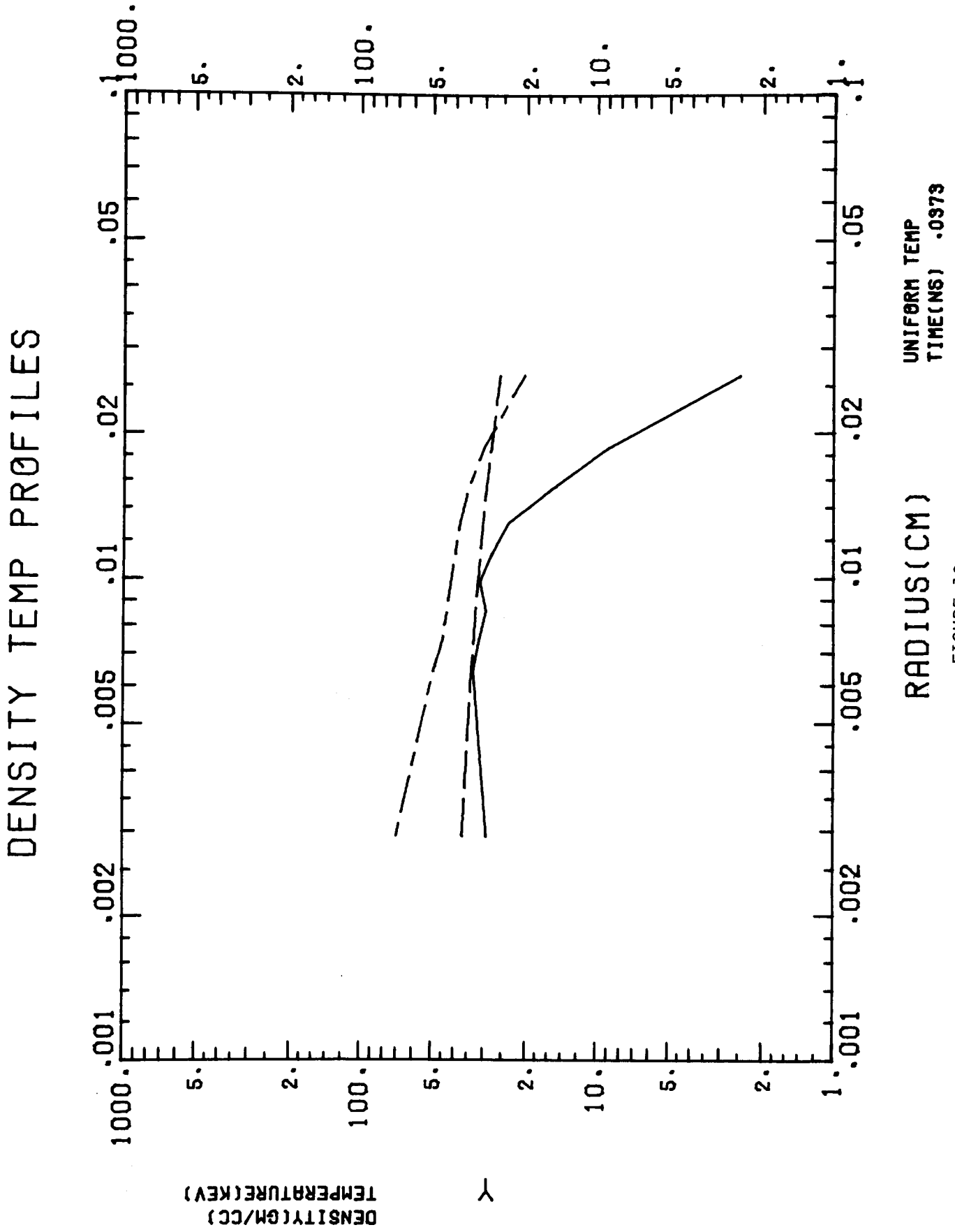
DENSITY TEMP PROFILES
1000.
5.
2.
100.
5.
2.
10.
5.
2.
1.
.1
.05
.02
.01
.005
.002
.001
1000.
5.
2.
100.
5.
2.
10.
5.
2.
1.
.001
.002
.005
.01
.02
.05
.1
RADIUS(CM)
UNIFORM TEMP
TIME(NS) .0373
DENSITY(GM/CC)
TEMPERATURE(KEV)

FIGURE 19

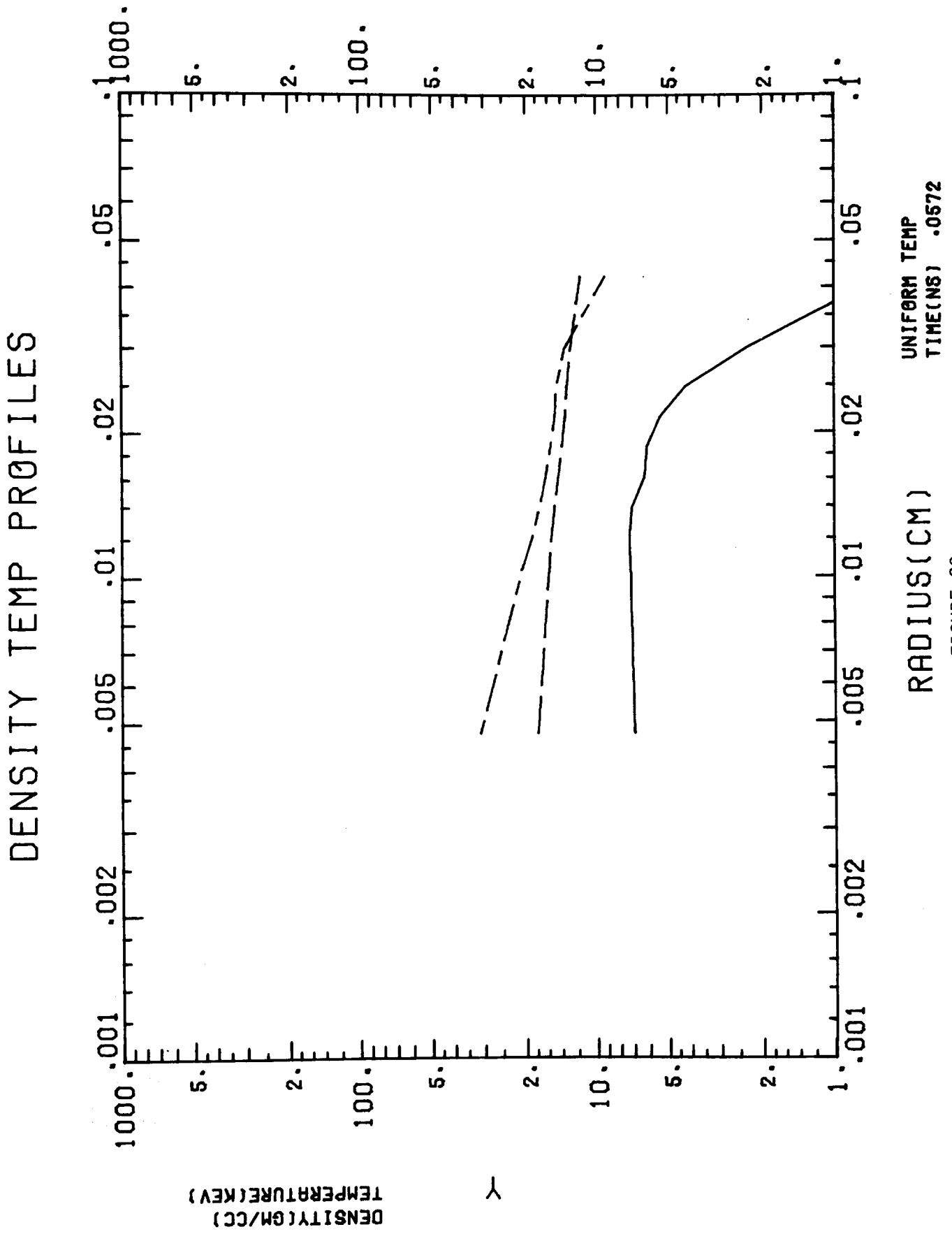
DENSITY TEMP PROFILES
1000.
100.
10.
1.
.1
.05
.02
.01
.005
.002
.001
5.
2.
RADIUS(CM)
UNIFORM TEMP
TIME(NS) .0572
DENSITY(GM/CC)
TEMPERATURE(KEV)

FIGURE 20

FIGURE 21

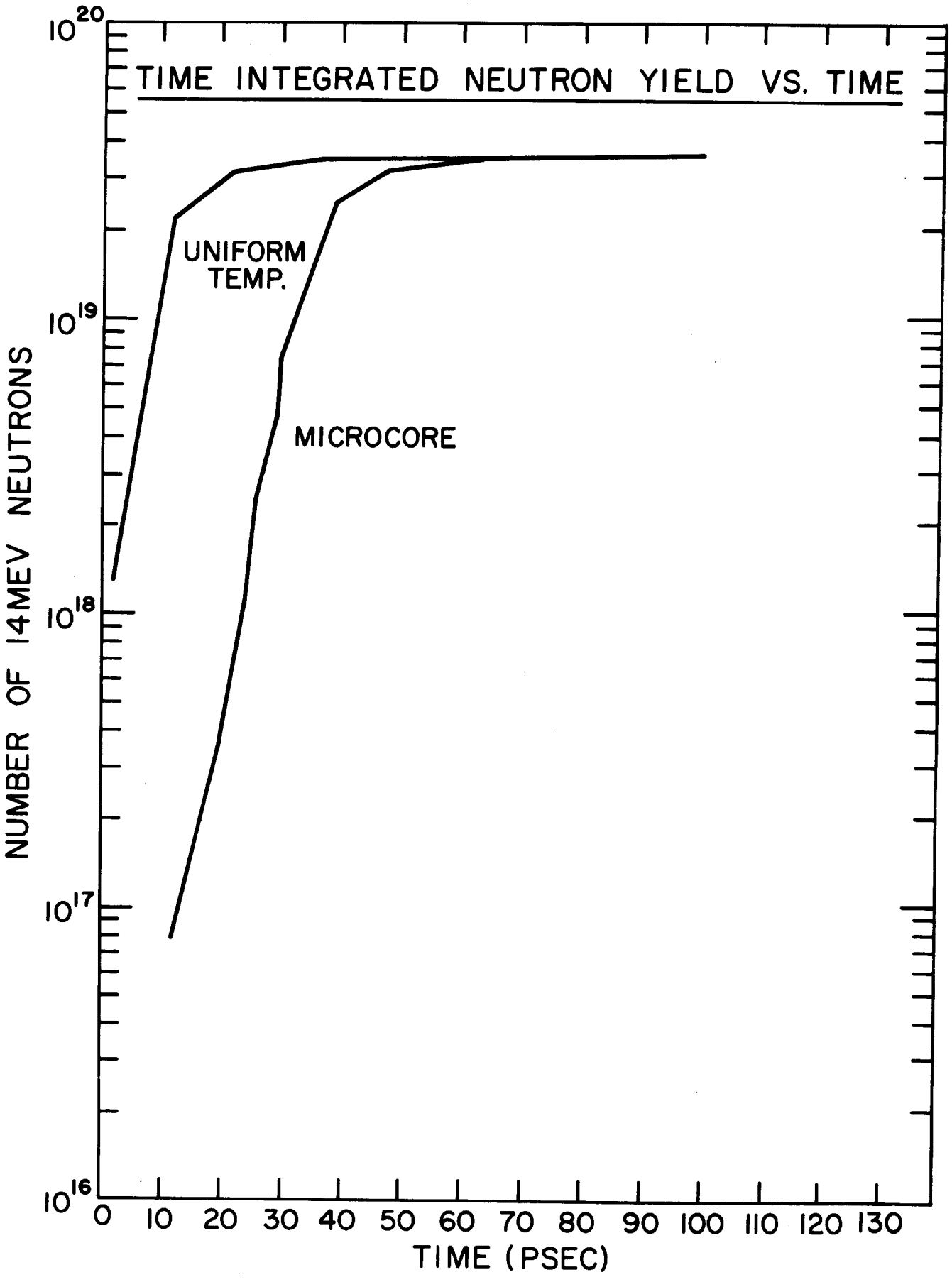
TIME INTEGRATED NEUTRON YIELD VS. TIME
UNIFORM TEMP.
MICROCORE
NUMBER OF 14MEV NEUTRONS
10^{20}
10^{19}
10^{18}
10^{17}
10^{16}
0 10 20 30 40 50 60 70 80 90 100 110 120 130
TIME (PSEC)

FIGURE 22

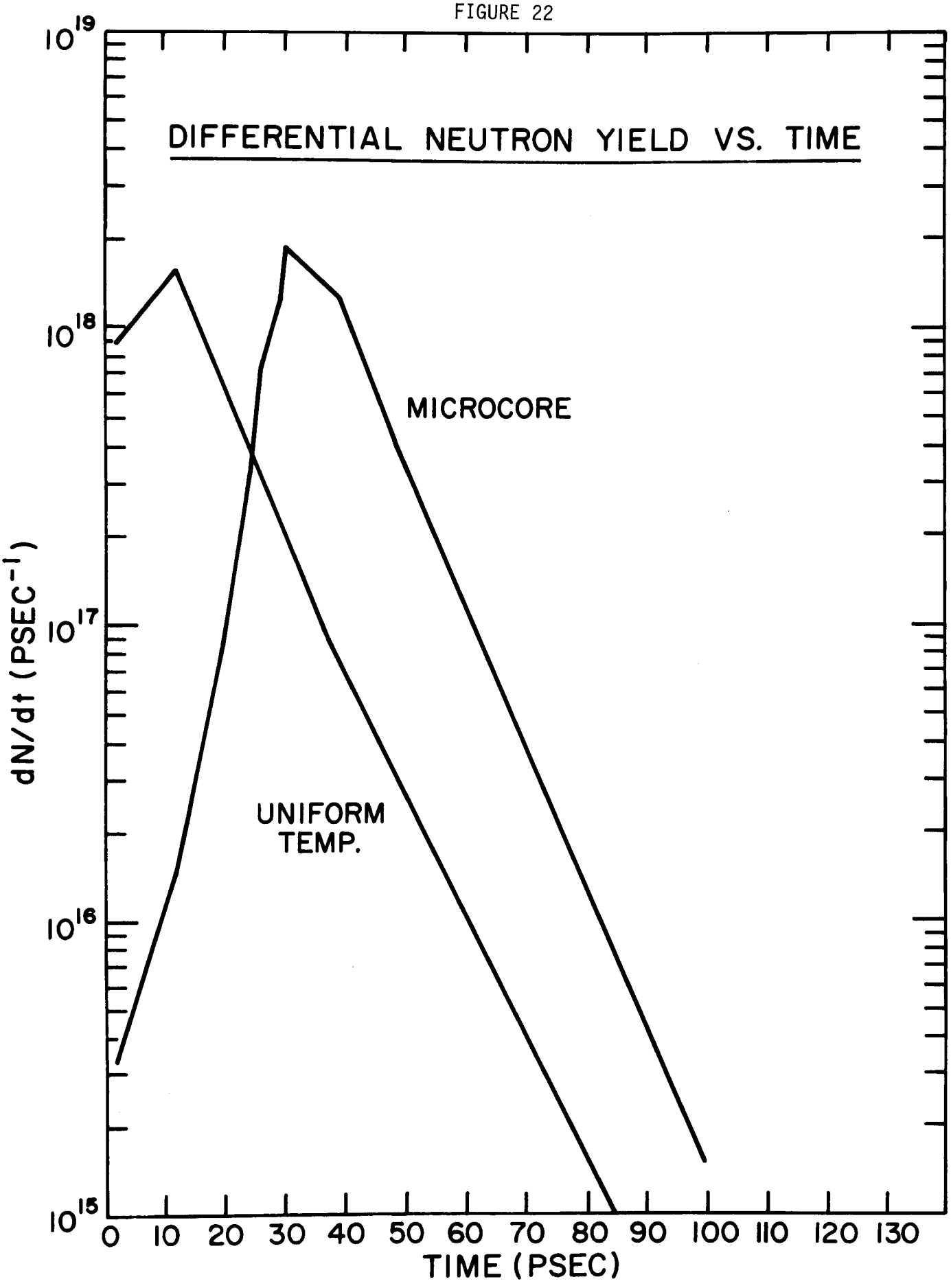
DIFFERENTIAL NEUTRON YIELD VS. TIME
MICROCORE
UNIFORM TEMP.
dN/dt (PSEC⁻¹)
10¹⁹
10¹⁸
10¹⁷
10¹⁶
10¹⁵
0 10 20 30 40 50 60 70 80 90 100 110 120 130
TIME (PSEC)

$_2He^4$, $_1H^1$, $_1H^3$, $_2He^3$ DT and DD reaction products are plotted in Figures 23 to 26. The average alpha particle energy is 1.84 Mev in the laboratory frame of reference.

II-E-3-c. Sensitivity to Uncertainties in the Charged Particle Slowing Down Theory

A quick test is made of the effect of uncertainty in the collisional theory of charged particle slowing down. The electron and ion slowing down terms are each scaled up by a factor of ten to simulate possible energy loss through self generated plasma turbulence. If this were infact a large effect then it would reduce the ρR requirements of the pellet core. Plotted in Figure 27 are yield vs. ρR for the unenhanced and enhanced slowing down. For pellets of 1 mg mass, better alpha energy recapture does not seem to be a very important effect with the increase in yield at $\rho R = 1$ g/cm^2 only 60%. At $\rho R = 3$ g/cm^2 the effect is almost negligible.

Further studies including variations in thermal conduction and electron ion equilibration will also be done.

FIGURE 23

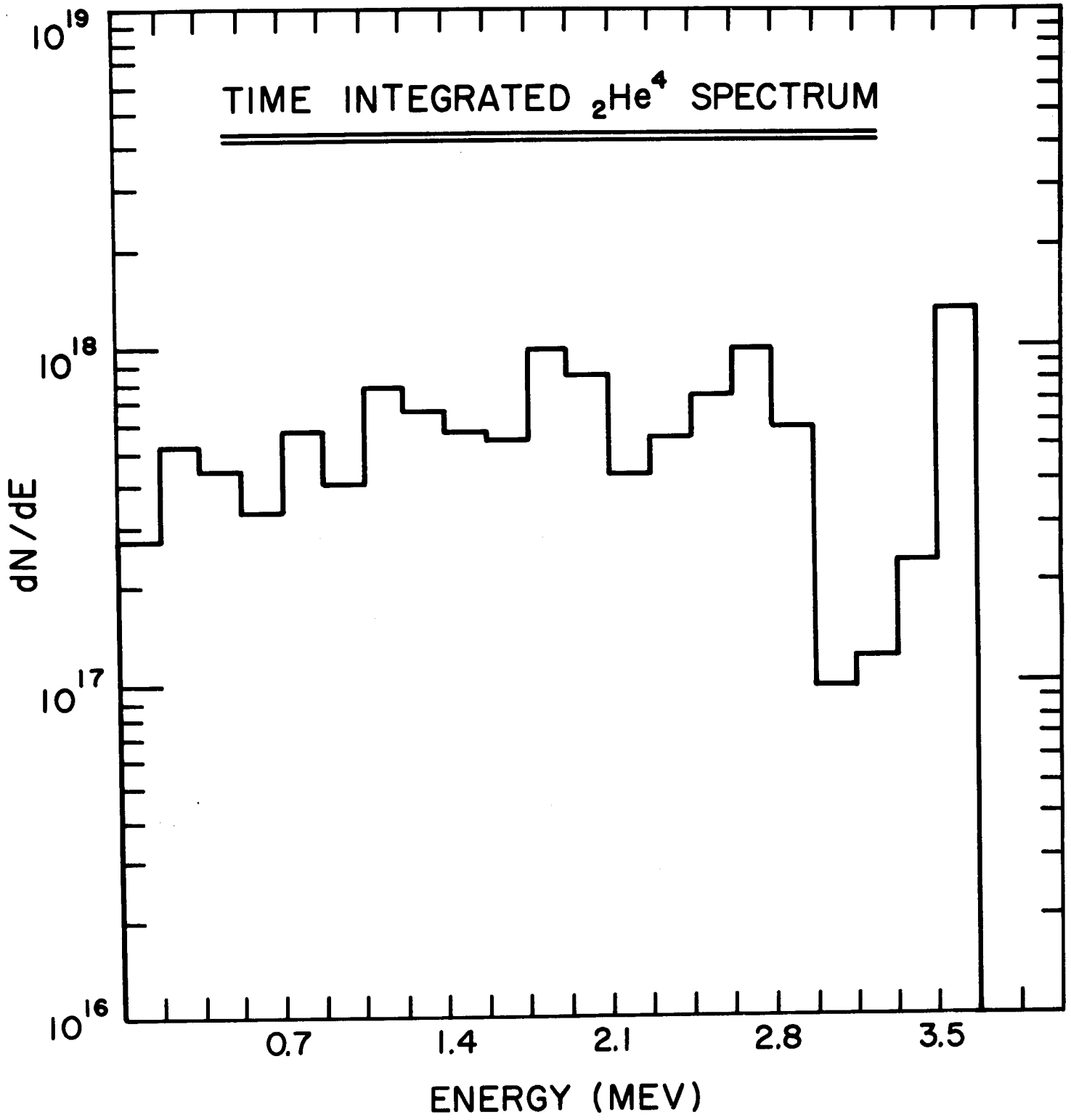
TIME INTEGRATED $_2He^4$ SPECTRUM
10^{19}
10^{18}
10^{17}
10^{16}
dN/dE
0.7
1.4
2.1
2.8
3.5
ENERGY (MEV)

FIGURE 24

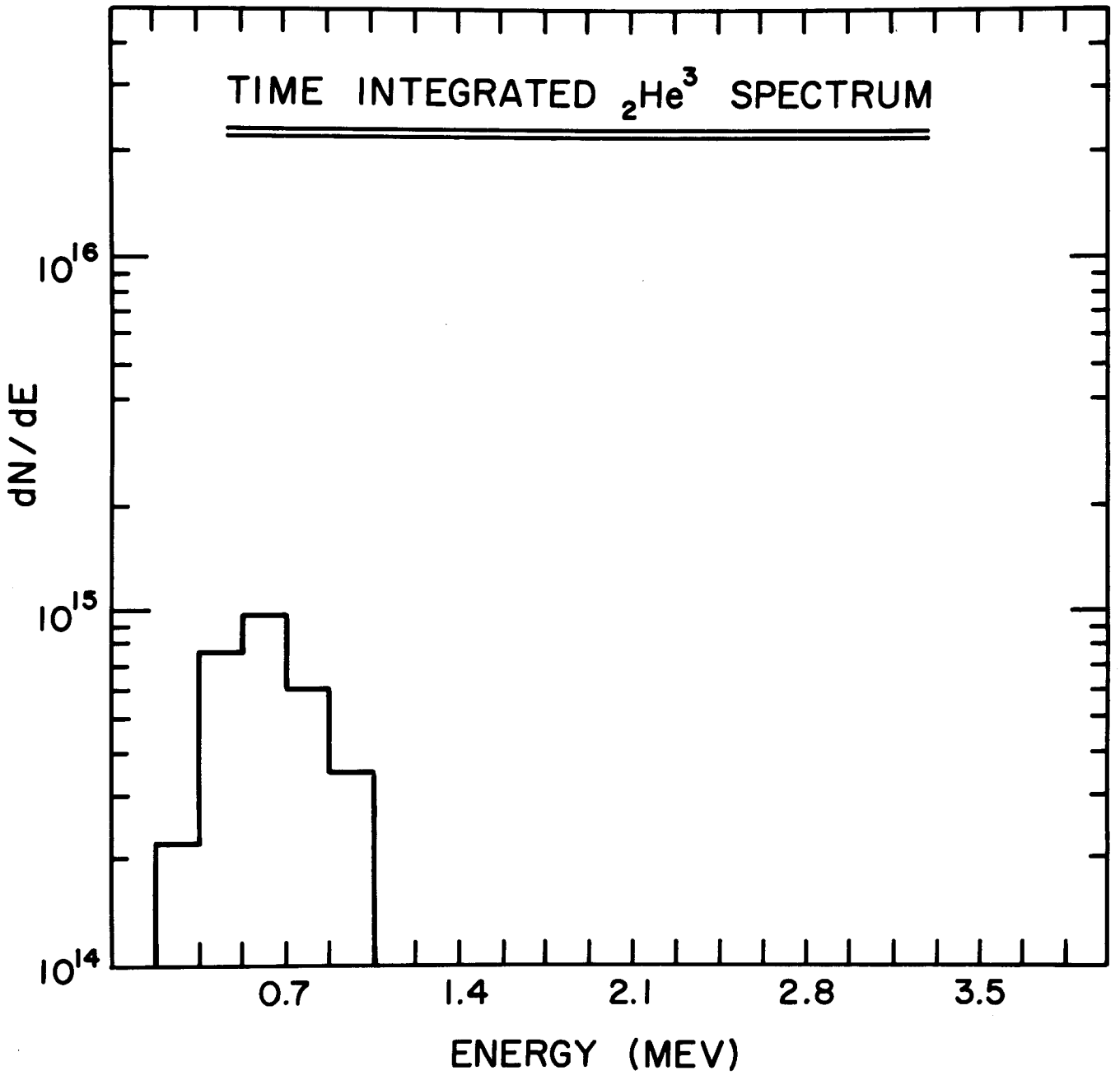
TIME INTEGRATED $_2He^3$ SPECTRUM
10^{16}
10^{15}
10^{14}
dN/dE
0.7
1.4
2.1
2.8
3.5
ENERGY (MEV)

FIGURE 25

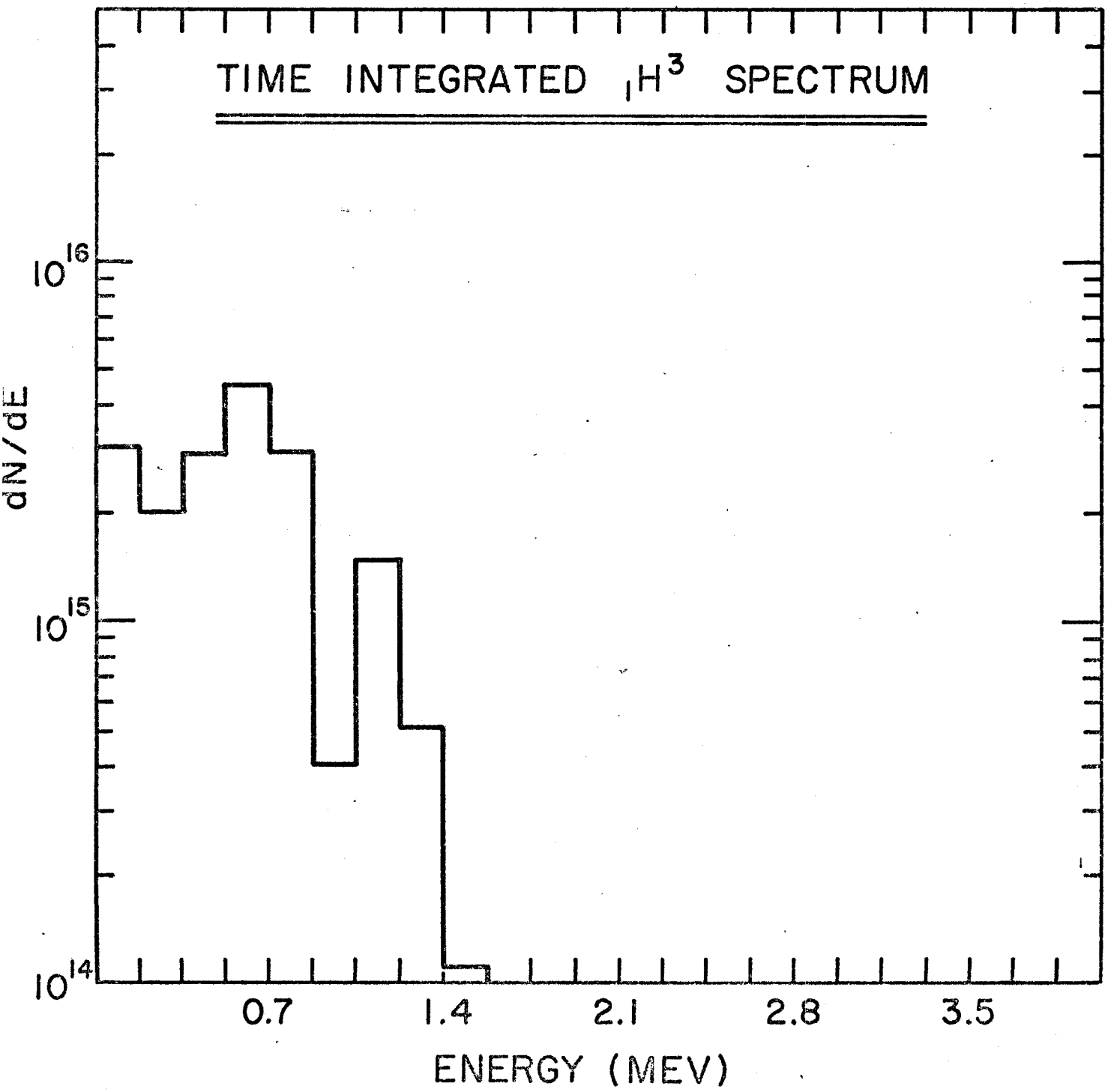
TIME INTEGRATED $_1H^3$ SPECTRUM
10^{16}
10^{15}
10^{14}
dN/dE
0.7
1.4
2.1
2.8
3.5
ENERGY (MEV)

FIGURE 26

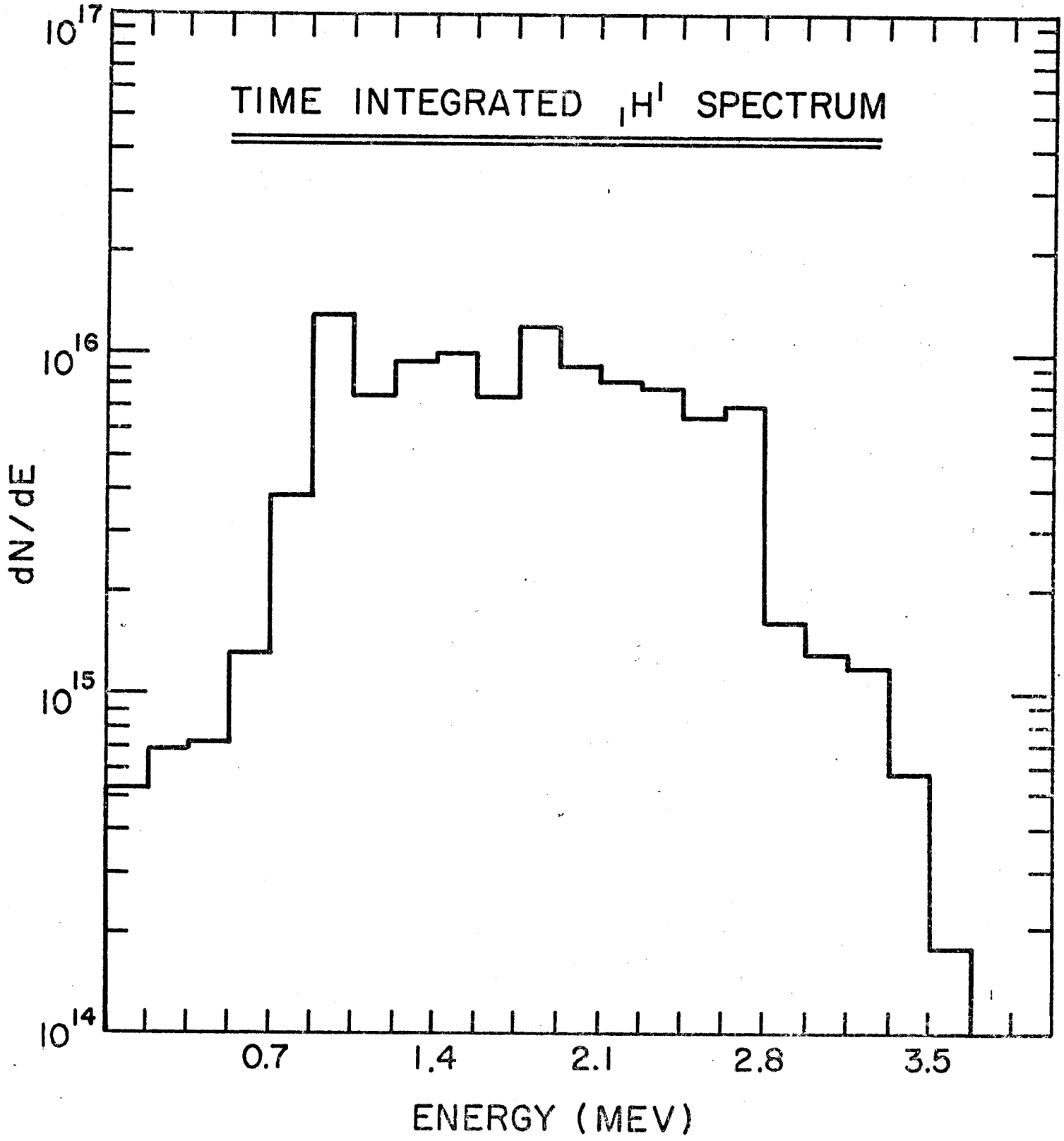
TIME INTEGRATED $_1H^1$ SPECTRUM
10^{17}
10^{16}
10^{15}
10^{14}
dN / dE
0.7
1.4
2.1
2.8
3.5
ENERGY (MEV)

FIGURE 27

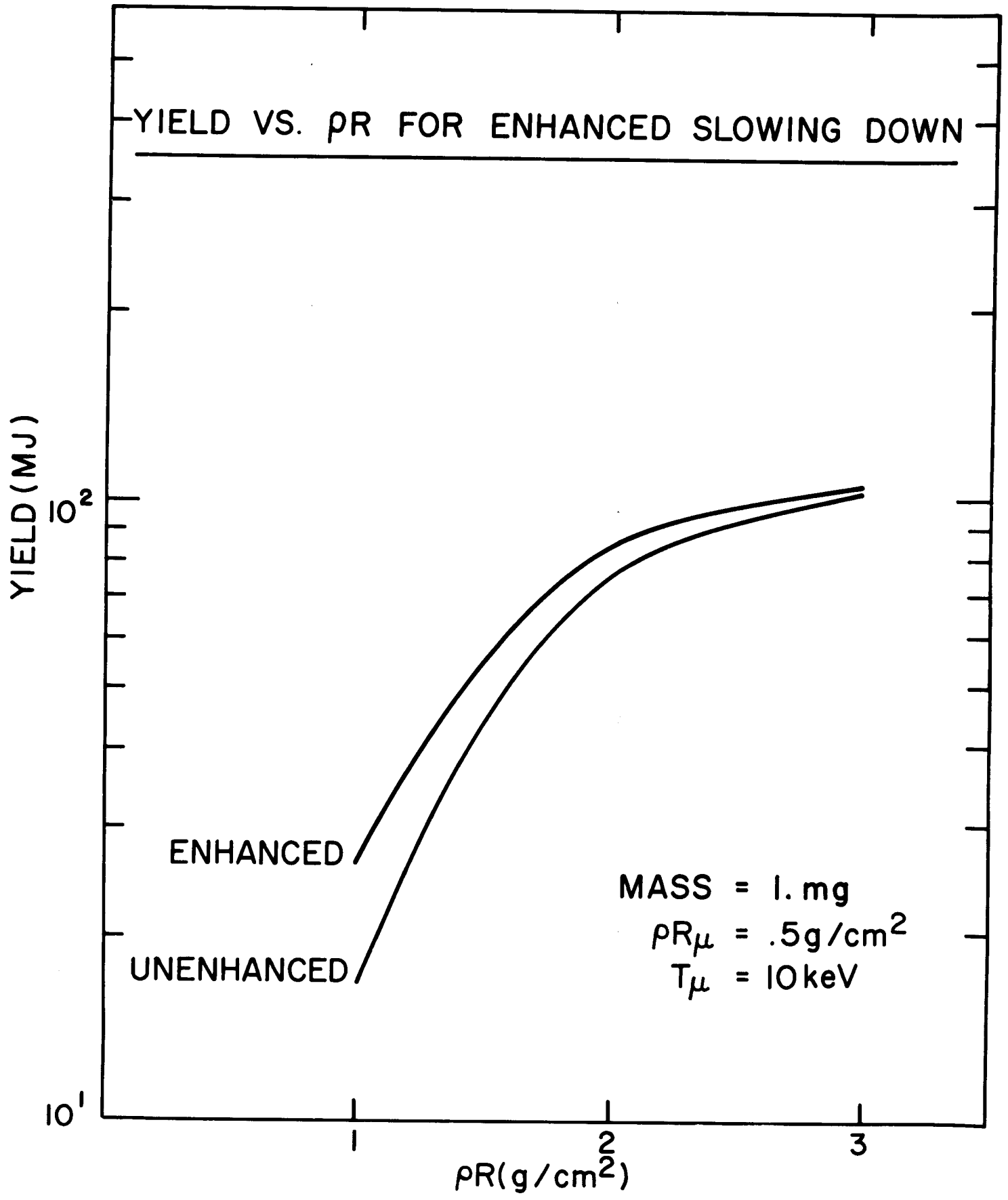
YIELD VS. ρR FOR ENHANCED SLOWING DOWN
YIELD (MJ)
10²
10¹
ENHANCED
UNENHANCED
MASS = 1. mg
ρRμ = .5g/cm²
Tμ = 10keV
1
2
3
ρR(g/cm²)

II-E References

1. G. Fraley, E. Linnebur, R. Mason and R. Morse, Phys. Fl. 17, 474 (1974).

2. Longmire, Elementary Plasma Physics, (Wiley, New York, 1967).

3. E. Corman, W. Loewe, and G. Cooper, Nuc. Fus. 15, 377 (1975).

II-F. Prospects for High Gain Pellets

Pellet gains of G = 100 are necessary for laser fusion power plant feasibility assuming a laser efficiency of $\eta_L = .1$. For a laser efficiency of $\eta_L = .01$ the necessary pellet gain must be 1000. Since laser efficiencies of 10% appear to be very difficult to attain it is logical to investigate the possibility of increasing the pellet gain. Pellet gain can be expressed as the product of gain on core and hydrodynamic efficiency.

$$G = G_C \, \eta_H$$

$$G_C = Y/W_T$$

$$\eta_H = W/E_L$$

Y = thermonuclear yield

W_T = internal energy of the compressed core

E_L = incident laser energy

Obviously the pellet gain can be increased by increasing either G_C or η_H. Since η_H is intimately related to the very complex light absorption and implosion mechanisms we choose to analyze the simpler gain on core.

To analyze the gain on core we attempt to define the most optimum core configuration possible without treating the problem of how such a configuration might be created. The core configuration that is usually used to demonstrate the principles of ignition and thermonuclear burn is shown in Fig. 1. This is a uniformly compressed core of $\rho R = 3$ g/cm^2 and $\rho R_\mu = .5$ g/cm^2 with $T_\mu = 10$ Kev. In Fig. 1 we also postulate a more optimum configuration. Here the core is not uniformly compressed but has a density variation of

$$\rho(r) = .5/r$$

This density profile has the property that if any particular radius (r^*) is chosen and the density inside this radius is held constant at $\rho = .5/r^*$ then

FIGURE 1

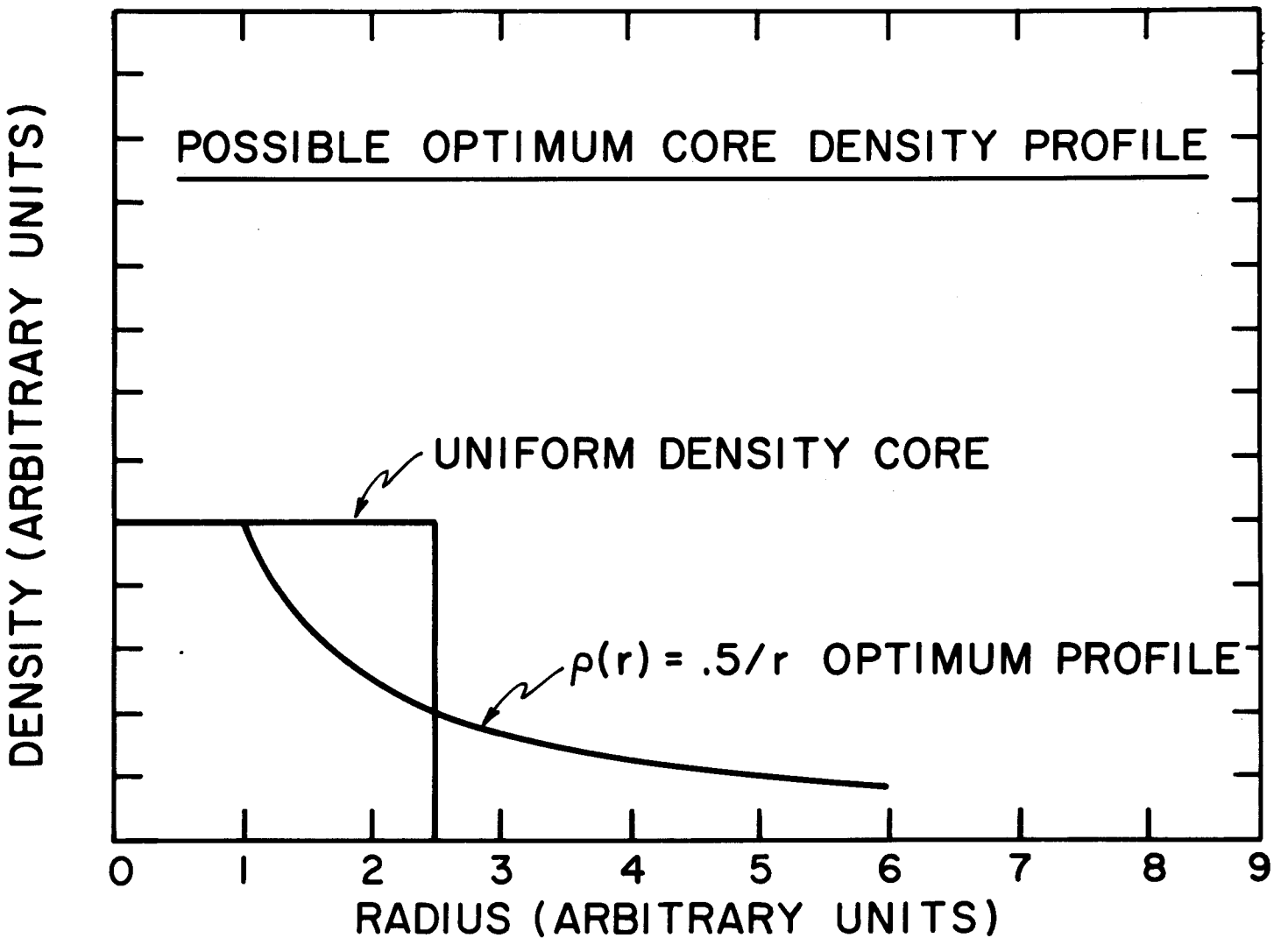
POSSIBLE OPTIMUM CORE DENSITY PROFILE
UNIFORM DENSITY CORE
ρ(r) = .5/r OPTIMUM PROFILE
DENSITY (ARBITRARY UNITS)
0
1
2
3
4
5
6
7
8
9
RADIUS (ARBITRARY UNITS)

the sphere inside this radius will have $\rho r^* = .5$ g/cm^2, the necessary micro core value. On the other hand the remainder of the core will have a density falling from this value. Therefore more mass will be necessary to achieve a given total ρR value. Assuming that fractional burn up is independent of mass, and only depends on ρR, this increased mass will provide greater yield. It remains to be determined of course whether W_T will be greater for this greater mass and thus cut down the gain on core. Another consideration in choosing the density profile is the necessity of promoting thermonuclear burn. This profile will have no trouble in this regard. Simple analysis shows

$$W_c \ (J/cm^3) = 3.225 \times 10^5 \ \rho^{5/3}$$

$$W_\mu \ (J/cm^3) = 3.83 \times 10^7 \ \rho_\mu \ T_\mu \ (Kev)$$

where W_c is the energy/cm^3 necessary to compress the core to its density ρ from solid density and W_μ is the energy/cm^3 necessary to heat the micro core to temperature T_μ. The total energy input is then

$$W_T = 4\pi \int_o^{R_\mu} T_\mu \ 3.83 \times 10^7 \left[\frac{.5}{R_\mu}\right] r^2 dr + 4\pi \int_{R_\mu}^{R} 3.225 \times 10^5 \left[\frac{.5}{r}\right]^{5/3} r^2 \ dr$$

$$+ 4\pi \int_o^{R_\mu} 3.225 \times 10^5 \left[\frac{.5}{R_\mu}\right]^{5/3} r^2 \ dr$$

$$W_T = 8 \times 10^7 \ R_\mu^2 \ T_\mu + 1.9 \times 10^5 \ R_\mu^{4/3} + 9.6 \times 10^5 \ R^{4/3} \ (Joules)$$

The value of total ρR is

$$\rho R = \int_o^{R_\mu} \rho_\mu \ dr + \int_{R_\mu}^{R} \rho(r) \ dr$$

$$= \frac{1}{2} \left[1 + \ln \left(R/R_\mu\right)\right]$$

and the total mass is

$$M = \pi (R^2 - R_\mu^2/3)$$

Fractional burn up is estimated from computer calculations for uniformly compressed cores as (see section II-E-3-a)

$$f_B = \begin{cases} .05\ \rho R & 0<\rho R<1 \\ .05 + .1875\ (\rho R - 1)^{.585} & 1<\rho R<3 \\ .21 + .033\ \rho R & 3<\rho R<7 \end{cases}$$

and the yield is given by

$$Y = 3.37 \times 10^{11}\ f_B\ M \quad \text{(Joules)}$$

We have now expressed ρ_μ, M, W_T, ρR, f_B, Y, and G_c as functions of R_μ and R. We investigate two different cases:

(I) $y \simeq 100$ MJ and $G_c \simeq 20000$

(II) $y \simeq 1000$ MJ and $G_c \simeq 20000$

If the hydrodynamic efficiency were $\eta_H = .05$ then these cases would imply pellet gains of 1000 with input laser energies of 100 KJ and 1 MJ. Table 1 summarizes the results for case I. With a microcore radius of 10 microns, implying a compression of 2347 times solid density, the necessary conditions were met. They were also met at microcore radii of 20 μ and 30 μ but not greater than this. This implies that a compression of the micro core of at least 782 times solid density is necessary to achieve gains of 1000 <u>if the incident laser energy is 100 KJ</u>. In Table 2 the results of case II are given and we see that the necessary conditions are still achievable with a compression of only 235 times solid density <u>if the incident energy is 1 MJ</u>. As the microcore radius gets larger, the total core radius must also increase to provide the same yield, thus implying that the fractional burn up goes down, due to the increased mass. An economy of scale can be observed in Table 3 where the results for different radii and a fixed microcore radius are given. As the available energy W_T goes up,

Table 1

Summary of Case I - 100 KJ Yield

μ-Radius (cm)	μ-Compression	Radius (cm)	Mass (g)	ρR (g/cm^2)	Fractional Burnup	Internal Energy (J)	Yield (J)	Gain on Core
1.-3	2347	2.-2	1.3-3	2.	.24	5.3+3	1.+8	1.9+4
2.-3	1174	3.-2	2.8-3	1.85	.22	9.3+3	2.1+8	2.26+4
3.-3	782	3.-2	2.8-3	1.65	.19	9.7+3	1.9+8	1.9+4

Table 2

Summary of Case II - 1 MJ Field

μ-Radius (cm)	μ-Compression	Radius (cm)	Mass (g)	ρR (g/cm^2)	Fractional Burnup	Internal Energy (J)	Yield (J)	Gain on Core
1.-3	2347	6.-2	1.1-2	2.55	.29	2.27+4	1.1+9	4.9+4
2.-3	1174	6.-2	1.1-2	2.2	.26	2.3+4	9.9+8	4.3+4
3.-3	782	6.-2	1.1-2	2.0	.24	2.3+4	9.0+8	3.9+4
4.-3	587	7.-2	1.5-2	1.93	.23	2.9+4	1.2+9	4.1+4
5.-3	465	7.-2	1.5-2	1.82	.22	3.0+4	1.1+9	3.8+4
6.-3	391	7.-2	1.5-2	1.73	.21	3.1+4	1.1+9	3.5+4
7.-3	335	7.-2	1.5-2	1.65	.20	3.2+4	1.0+9	3.2+4
8.-3	293	7.-2	1.5-2	1.58	.19	3.3+4	9.7+8	2.9+4
9.-3	261	7.-2	1.5-2	1.53	.18	3.5+4	9.2+8	2.7+4
10.-3	235	8.-2	2.-3	1.54	.18	4.2+4	1.2+9	2.9+4

Table 3

Summary of Different Core Radii at Fixed μ-Core Radius

μ-Radius = 3.-3 cm Compression = 782

Radius (cm)	Mass (g)	ρR (g/cm^2)	Fractional Burnup	Internal Energy (J)	Yield (J)	Gain on Core
1.-2	3.-4	1.1	.1	2.9+3	1.0+7	3.6+3
2.2-2	1.2-3	1.45	.17	6.0+3	7.0+7	1.2+4
3.-2	2.8-3	1.65	.20	9.8+3	1.9+8	1.9+4
4.-2	5.0-3	1.80	.21	1.4+4	3.6+8	2.6+4
6.-2	1.1-2	2.0	.24	2.3+4	9.0+8	3.9+4
8.-2	2.0-3	2.14	.25	3.4+4	1.7+9	5.0+4
10.-2	3.1-2	2.25	.26	4.5+4	2.8+9	6.2+4

the yield goes up but so does the gain on core. The yields, however, become unmanageably large as more energy is added. How this analysis translates into a laser pulse shape is impossible to predict since the implosion process is not specified. The laser energy is of course fixed once a value for the hydrodynamic efficiency is chosen and the maximum laser power might be crudely estimated because this will depend on the maximum compression of the pellet. With this in mind, the lowest microcore density which will still provide the yield and gain is desirable. For the case of 100 KJ of laser energy this will be a compression of about 782. With 1 MJ of laser energy incident the compression can be less than 235 thus the maximum laser power for the 1 MJ case will be less than for the 100 KJ case.

This analysis will be developed further in the future, but for now several conclusions can be made.

1) Density profiles can be defined that give gain on core in excess of 20000 which might imply total pellet gains of 1000 for incident laser energies of 100 KJ to 1 MJ.
2) As laser energy is reduced, the necessary compression to reach $G_c \geq$ 20000 is increased, implying greater maximum laser power.
3) Yield increases more than linearly as input laser energy increases, thus there is an economy of scale however the yield quickly reaches unmanageably large values for laser energies in excess of 1 MJ.
4) With 100 KJ of laser light (assuming $\eta_H = .05$) a maximum compression of only 782 times solid density is necessary to produce a yield 100 MJ.
5) This analysis is <u>very</u> schematic in nature and is only an attempt to define the best that can be done under the most ideal circumstances. No attempt has yet been made to investigate how such a compressed core could actually be obtained.

III. Optics Studies

III-A. Optimal Illumination Studies

III-A-1. Introduction

This section describes the calculation of irradiance profiles on a spherical surface due to N overlapping beams, where N = 4,6,8,12 or 20, corresponding to the symmetry of the five Platonic solids. Program PLATO computes $I(\theta,\phi)$ in the neighborhood of one spot, including overlap from its nearest neighbors. Provision is currently made for the following spatial beam profiles; flat, Gaussian and "supergaussian". Others will be tried as we think of them.

Basically, our task is to provide a specified uniformity of illumination over the entire pellet surface, keeping the rays as normal to the surface as possible. The required degree of uniformity is determined chiefly by its effect on growth of the Rayleigh-Taylor instability,[1] while the angles of incidence must be held down in order to maximize inverse bremsstrahlung absorption, and also to minimize refraction in the blowoff layer.[2]

To control pellet irradiance, we have at our disposal four independent quantities; N, the number of beams; δ, the shift of the beam focus relative to the pellet center; F, the f/no. of the focused beam; and the beam profile $I_o(r)$, where r is the beam radius on the last optical element (lens or mirror.) The beam profile may depend on 2-3 parameters, so it would seem we have a formidable parameter space to deal with. In practice, however, only a few values of N are considered, F then being determined by the maximum solid angle alloted to optics. Of course, the optics must be sufficiently distant from the target so that the beam aperture is adequate to handle the energy and power per beam as well as the radiation and debris from the target. The total aperture area is determined in practice by material damage constraints on the beam energy, rather than self-focusing constraints on the beam power.

A more complete treatment of the uniformity problem would entail following the energy deposition in the early phases of the corona expansion, taking into account refraction and lessened energy absorption near the beam edges where the angles of incidence are largest.

III-A-2. The Platonic Solids

A sphere may be partitioned into N equal-solid-angle wedges by means of the five platonic solids, illustrated in Fig. 1.

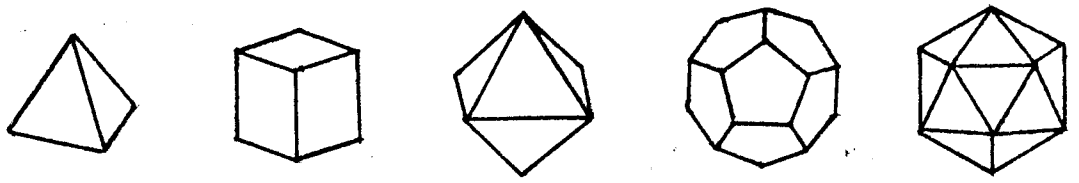

Figure 1

A sphere may also be divided into two equal solid angle portions by means of a plane cut through its center.* Other partitions are possible. For example, beams placed at each of the 12 vertices of an icosahedron allows symmetric placement of 32 beams. The Ω-10 facility at Rochester is designed for 24 beams.

Each Platonic solid being made up of N regular polygonal faces, it is customary to classify them according to the number of sides (p) of the polygons and the number of adjacent faces (q) at a vertex. Given the number of faces N_S, it is easy to show that the number of edges and vertices are given by

$$N_E = 1/2\ p\ N_S \tag{1}$$

$$N_V = \frac{p}{q} N_S . \tag{2}$$

These numbers are related by Euler's formula,[3]

$$N_V + N_S - N_E = 2 . \tag{3}$$

---

* I have recently learned of the existence of a sixth platonic solid, the "dihedron," a double plane polygon enclosing no volume.[6]

We shall also need the dihedral angle α and the wedge angle β, as depicted in Fig. 2.

$$\sin \frac{\alpha}{2} = \cos \frac{\beta}{2} = \frac{\cos(\pi/q)}{\sin(\pi/p)} \tag{4}$$

$$\beta = \pi - \alpha \tag{4a}$$

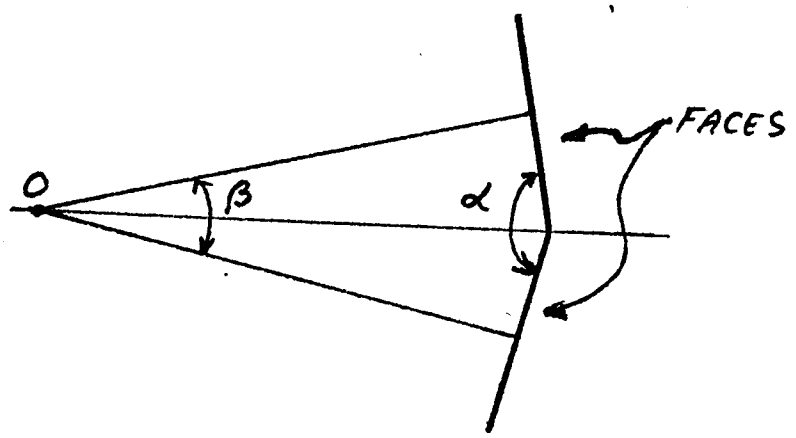

Figure 2

Table 1 summarizes these parameters for all of the Platonic solids.

	N_S	N_E	N_V	p	q	α	β
Tetrahedron	4	6	4	3	3	70.53	109.47°
Hexahedron	6	12	8	4	3	90°	90°
Octahedron	8	12	6	3	4	109.467°	70.53°
Dodecahedron	12	30	20	5	3	116.567°	63.43°
Icosahedron	20	30	12	3	5	138.18°	41.82°

Table 1

Since laser beams are circular rather than prismatic, it is necessary to overlap them in order to cover the entire pellet surface, as illustrated in Fig. 3.

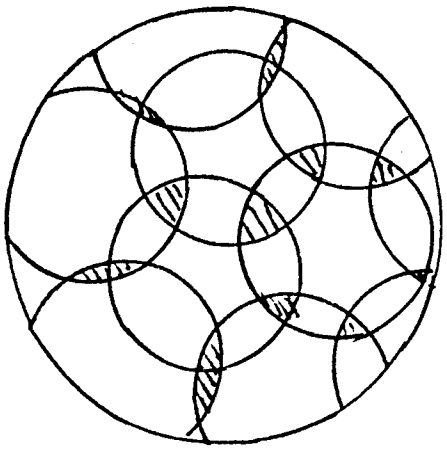

Figure 3

III-A-3. Intensity Profiles

Each beam contributes an irradiance[4]

$$I(\theta) = I_o(r)\left(\frac{f_L}{R_T}\right)^2 \frac{1 + \frac{\Delta x}{R_T}\cos\theta}{\left(\cos\theta + \frac{\Delta x}{R_T}\right)^3} \quad W/cm^2, \tag{5}$$

as illustrated in Fig. 4

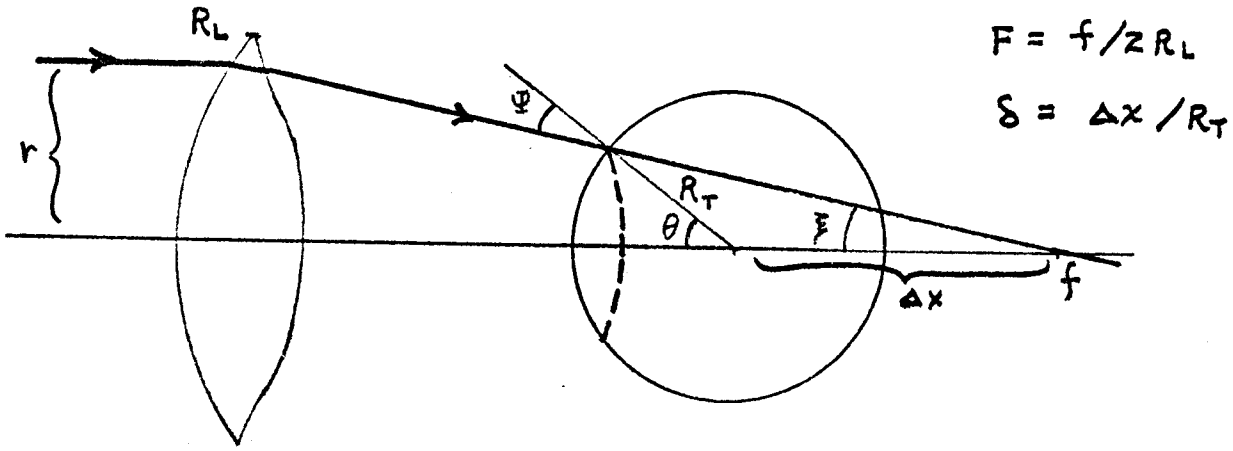

Figure 4

Here f_L is the focal length of the lens or mirror, R_T is the target radius, r is the beam radius, and Δx is the focal shift. The angle of incidence Ψ is given in terms of the beam half-angle ξ and the focal shift Δx by

$$\sin\Psi = \frac{\Delta x}{R_T}\sin\xi \ . \tag{6}$$

The beam half-angle is related to the f/no. by

$$\cot \xi = 2\ F, \tag{7}$$

so that

$$\sin\Psi_{max} = \frac{\delta}{\sqrt{1 + 4F^2}}\ , \tag{8}$$

where

$$\delta \equiv \Delta x/R_T\ . \tag{9}$$

It is essential that Ψ_{max} be made as small as possible in order to minimize laser energy lost through refraction. This important effect is treated in detail in Section II.A.

Now when we come to optimize pellet illumination uniformity, the outcome will be a certain spot size as measured by the pellet central angle θ_{max}. From Fig. 4, the corresponding focal shift is given by

$$\delta = 2F\ \sin\theta_{max} - \cos\theta_{max}. \tag{10}$$

So the price we pay for uniformity is given by combining eqs. (8) and (9):

$$\sin\Psi_{max} = \frac{2F\ \sin\theta_{max} - \cos\theta_{max}}{\sqrt{1 + 4F^2}}\ , \tag{11}$$

which is just another way of writing

$$\Psi_{max} = \theta_{max} - \xi. \tag{12}$$

Equation (1) shows that if θ_{max} is large, then ξ must also be large in order to keep Ψ_{max} small. From eq. (7), we see that large ξ naturally translates into small f/no.

Unlike a research facility like SHIVA, the beam transport system in a laser fusion reactor (LFR) can only take up a small fraction of the solid angle

subtended to the target. Whereas SHIVA has about 50% of its solid angle devoted to beams, an LFR is limited to about 10% for economic reasons. Since each beam occupies a solid angle

$$\Delta\Omega = 2\pi(1 - \cos\xi), \tag{13}$$

the total fractional solid angle taken up by N beams is, using eq. (7),

$$\gamma = \frac{N\Delta\Omega}{4\pi} = \frac{N}{2}\left[1 - \frac{2F}{\sqrt{1 + 4F^2}}\right]. \tag{14}$$

Solving for F, we find, for $\gamma << 1$,

$$F_{min} = \frac{\frac{1}{2}(1 - \frac{2\gamma}{N})}{\sqrt{1 - (1 - \frac{2\gamma}{N})^2}} \approx \frac{1}{4}\sqrt{\frac{N}{\gamma}} \tag{15}$$

This important relation tells us we need to use as few beams as possible in order to minimize the f/no. Table 2 lists F_{min} for a few values with $\gamma = 0.1$ and 0.2.

N	$\gamma = 0.1$	$\gamma = 0.2$
4	1.58	1.12
8	2.24	1.58
12	2.74	1.94
20	3.54	2.50

Table 2

The maximum angle of incidence is related to θ_{max} and N from eqs. (11) and (15):

$$\sin\Psi_{max} \approx \sin\theta_{max} - 2\sqrt{\frac{\gamma}{N}}\cos\theta_{max}. \tag{16}$$

Alternatively, eq. (12) gives

$$\Psi_{max} \approx \theta_{max} - \tan^{-1}(2\sqrt{\frac{\gamma}{N}}). \tag{17}$$

We are now in a position to design a pellet illumination scheme, proceeding as follows:

1. Choose a definite fractional solid angle γ, say 10%.
2. Choose the no. of beams, say N = 12 or 20.
3. This fixes the minimum f/no. by eq. (15).
4. Next choose a beam profile, say gaussian.
5. Vary δ until the uniformity exceeds the desired value, say 90%. This number directly affects the Rayleigh-Taylor growth rate.[1]
6. The optimum δ and F determines θ_{max} from eq. (10):

$$\sin\theta_{max} = \frac{2F\delta + \sqrt{1 + 4F^2 - \delta^2}}{1 + 4F^2} . \tag{18}$$

7. Eq. (16) or (17) determines Ψ_{max}.
8. Ψ_{max} determines the amount of laser energy lost due to refraction
9. If Ψ_{max} is too large, one has two main options:
   - 9.1 relax the uniformity requirement (5)
   - 9.2 relax the solid angle requirement (1).

III-A-4. Calculating Beam Overlap

Before carrying out the above optimization procedure, we have to learn how to calculate the intensity due to a number of overlapping spots. We shall consider here only the cases N = 8, 12, and 20; octahedral, dodecahedral and icosahedral.

First of all, by symmetry we need only consider a single pie-slice-shaped region, as depicted in Fig. 5 for the icosahedron (only 3 nearest neighbor spots are shown).

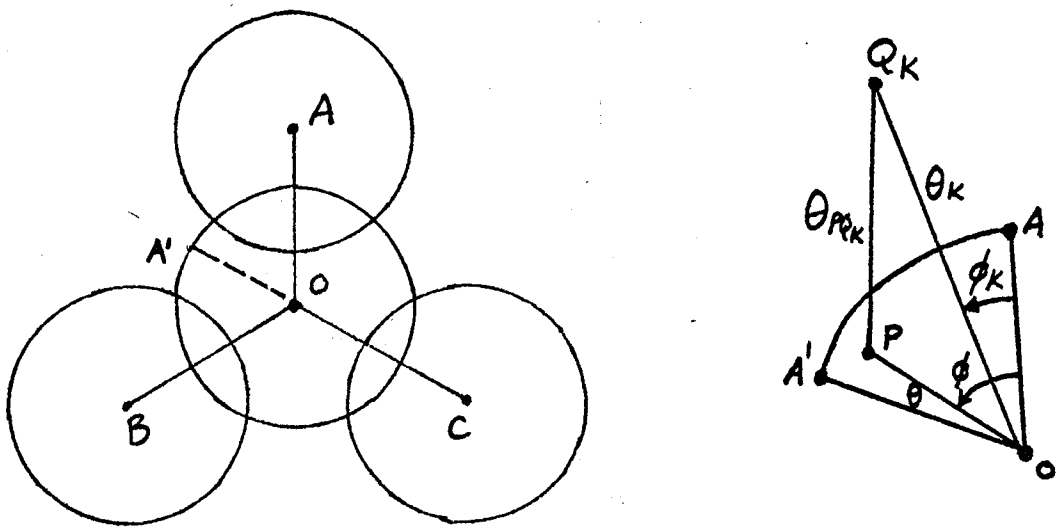

Figure 5

In this case, only spots 0 and A need be considered. In general however, several spots may contribute to the intensity at point P according to eq. (5) with θ_{PQ_k} given by

$$\cos\theta_{PQ_k} = \cos\theta\ \cos\theta_k + \sin\theta\ \sin\theta_k\ \cos(\phi - \phi_k) \qquad (19)$$

as shown in Fig. 6.

The coordinates of the neighboring beams are conveniently found by means of the Schlegel diagram.[3] This is simply a two-dimensional perspective of the polyhedron gotten by bringing one face up to the eye.

III-A-4-a. Octahedron - 6 Nearest Neighbors

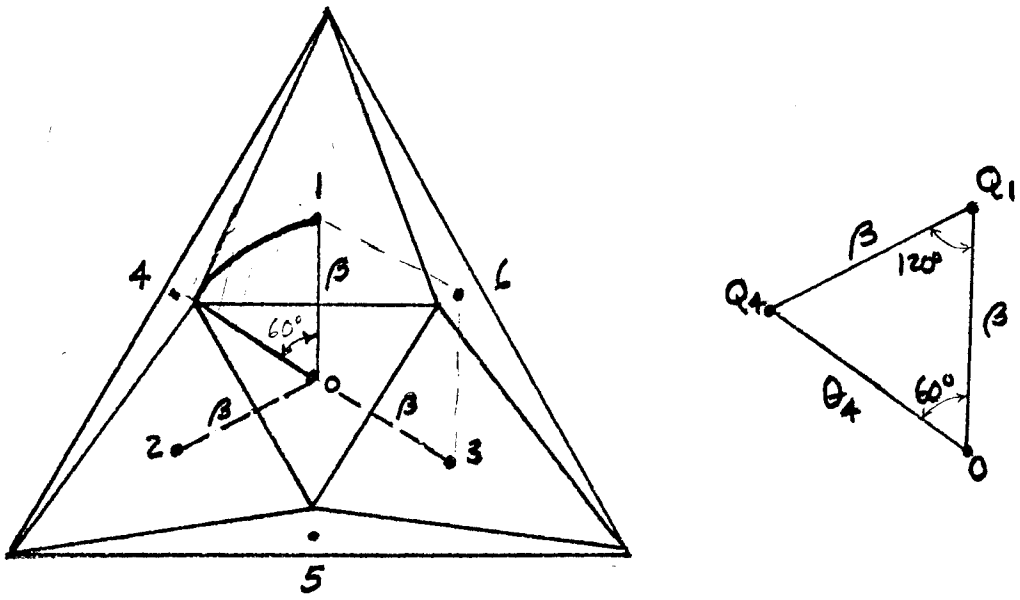

Figure 6

We wish to locate points Q_k, k = 1,6 w. r. t. point 0, using the above Schlegel diagram. The 8th (opposite) point will be ignored. The fundamental pie-slice has its 60° wedge at point 0, with one side along the OQ_k. From Table 1, the angular side $\beta = 70.53°$. We want to solve the spherical triangle OQ_1Q_4 for the angular side θ_4. By the cosine law, $\cos\theta_4 = -1/3$, so that $\theta_4 = \pi - \beta$. Thus,

$\phi_1 = 0$	$\theta_1 = \beta = 70.53°$
$\phi_2 = 120°$	$\theta_2 = \beta$
$\phi_3 = 240°$	$\theta_3 = \beta$
$\phi_4 = 60°$	$\theta_4 = 180° - \beta = 109.47°$
$\phi_5 = 180°$	$\theta_5 = \theta_4$
$\phi_6 = 300°$	$\theta_6 = \theta_4$

III-A-4-b. Dodecahedron - 10 Nearest Neighbors

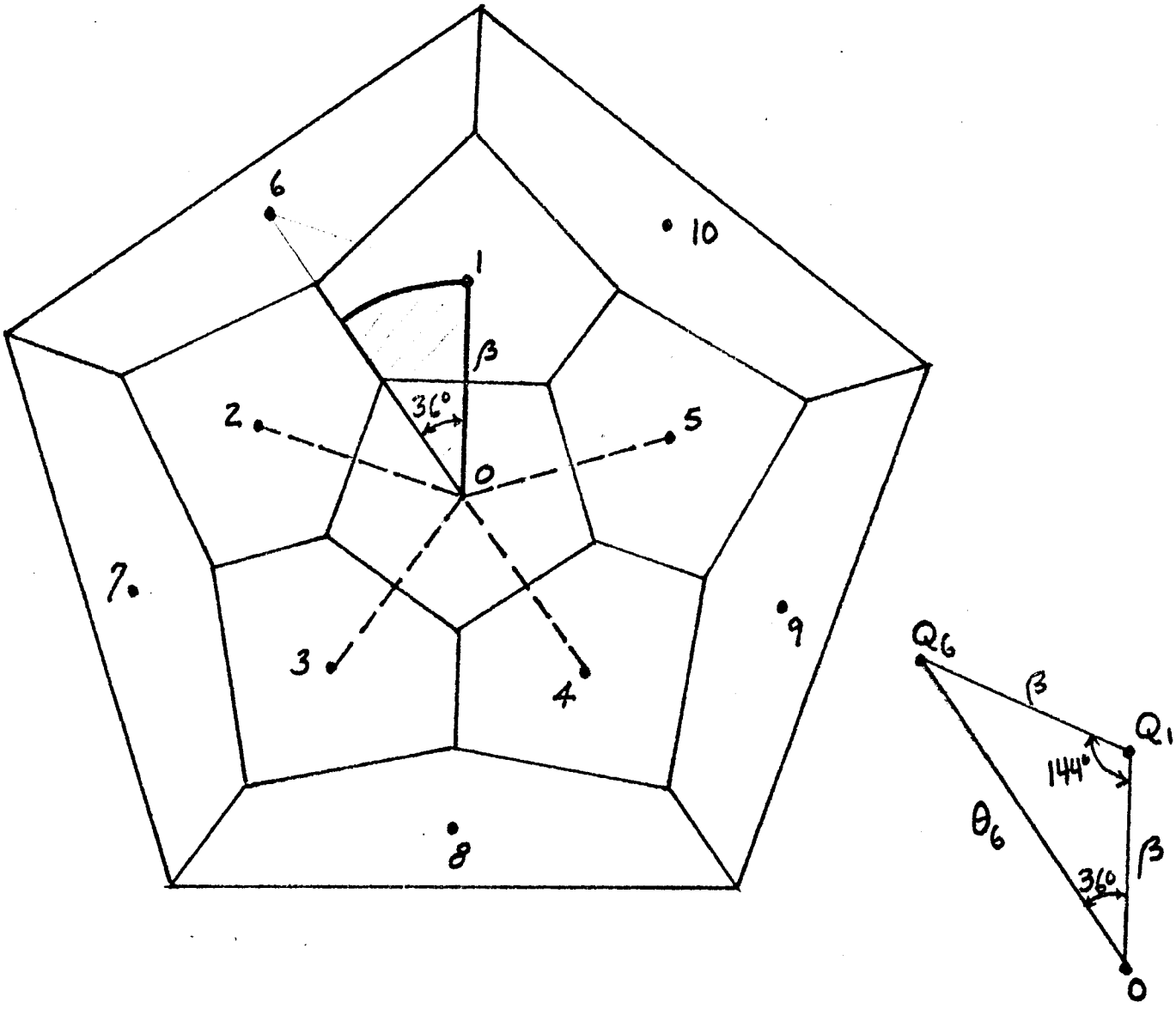

Figure 7

Figure 7 shows the Schlegel diagram; again the opposite 12th face is ignored. In this case, the fundamental pie-slice subtends a 36° angle. From Table 1, $\beta = 63.43°$. Solving the spherical triangle OQ_1Q_6 for the angle θ_6, we find that $\theta_6 = \pi - \beta$.

Thus,

$\phi_1 = 0$	$\theta_1 = \beta = 63.43°$
$\phi_2 = 72°$	$\theta_2 = \beta$
$\phi_3 = 144°$	$\theta_3 = \beta$
$\phi_4 = 216°$	$\theta_4 = \beta$
$\phi_5 = 288°$	$\theta_5 = \beta$
$\phi_6 = 36°$	$\theta_6 = \pi - \beta = 116.57°$
$\phi_7 = 108°$	$\theta_7 = \theta_6$
$\phi_8 = 180°$	$\theta_8 = \theta_6$
$\phi_9 = 252°$	$\theta_9 = \theta_6$
$\phi_{10} = 324°$	$\theta_{10} = \theta_6$

III-A-4-c. Icosahedron - 18 Nearest Neighbors

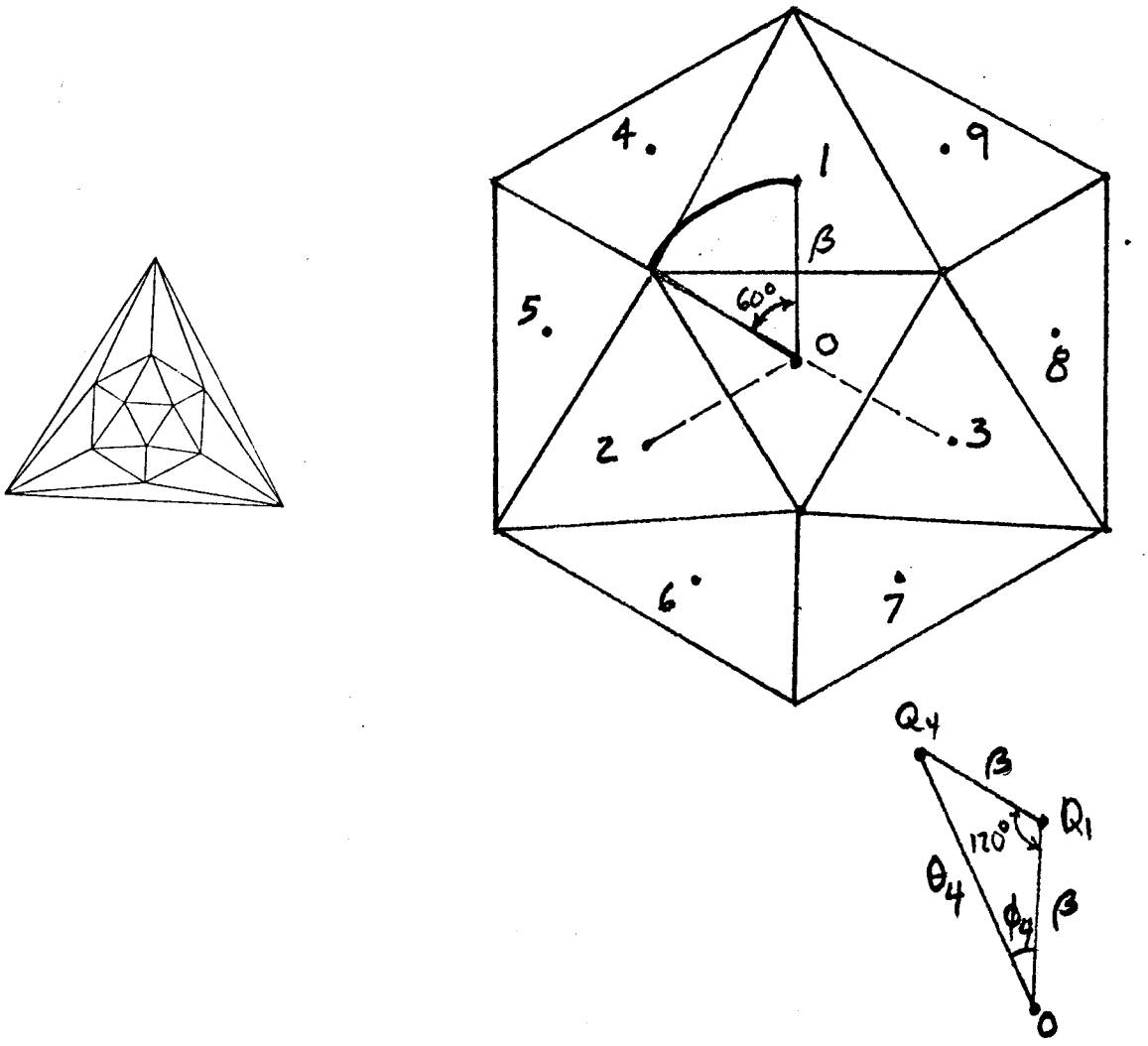

Figure 8

Figure 8 shows the Schlegel diagram and a restricted portion containing the 9 nearest neighbors we intend to include. It is doubtful that we would need to consider more beams. From Table 1, $\beta = 41.82°$. Solving the spherical triangle OQ_1Q_4 for θ_4, we find

$$\cos\theta_4 = 1 - \frac{3}{2}\sin^2\beta.$$

Since $\sin\beta = 2/3$, it follows that $\cos\theta_4 = 1/3$, so that $\theta_4 = 70.53°$, which is just the octahedron wedge angle!

In this case, we also have to solve for the angle ϕ_4. By the sine law,

$$\sin\phi_4 = \frac{\sin\beta \sin 60°}{\sin\theta_4} = \frac{\sqrt{3}}{2\sqrt{2}} \quad ,$$

so that $\phi_4 = 37.76°$. Referring to Fig. 8, we see that the coordinates of the 9 nearest neighbors are

$$\begin{aligned}
\phi_1 &= 0 & \theta_1 &= \beta = 41.82° \\
\phi_2 &= 120° & \theta_2 &= \beta \\
\phi_3 &= 240° & \theta_3 &= \beta \\
\phi_4 &= 37.76° & \theta_4 &= 70.53° \\
\phi_5 &= 120° - \phi_4 = 82.24° & \theta_5 &= \theta_4 \\
\phi_6 &= 120° + \phi_4 = 157.76° & \theta_6 &= \theta_4 \\
\phi_7 &= 240° - \phi_4 = 202.24° & \theta_7 &= \theta_4 \\
\phi_8 &= 240° + \phi_4 = 277.76° & \theta_8 &= \theta_4 \\
\phi_9 &= 360° - \phi_4 = 322.24° & \theta_9 &= \theta_4
\end{aligned}$$

We have recently found that more beams are needed when $\theta_{max} \gtrsim 72°$. The complete Schlegel diagram is revealed in all its arcane glory in Fig. 8a. The coordinates of points 10-18 may be found by solving spherical triangles 0-4-11 and 0-1-18. The details are left as an exercise to the reader . The results are found on the following page.

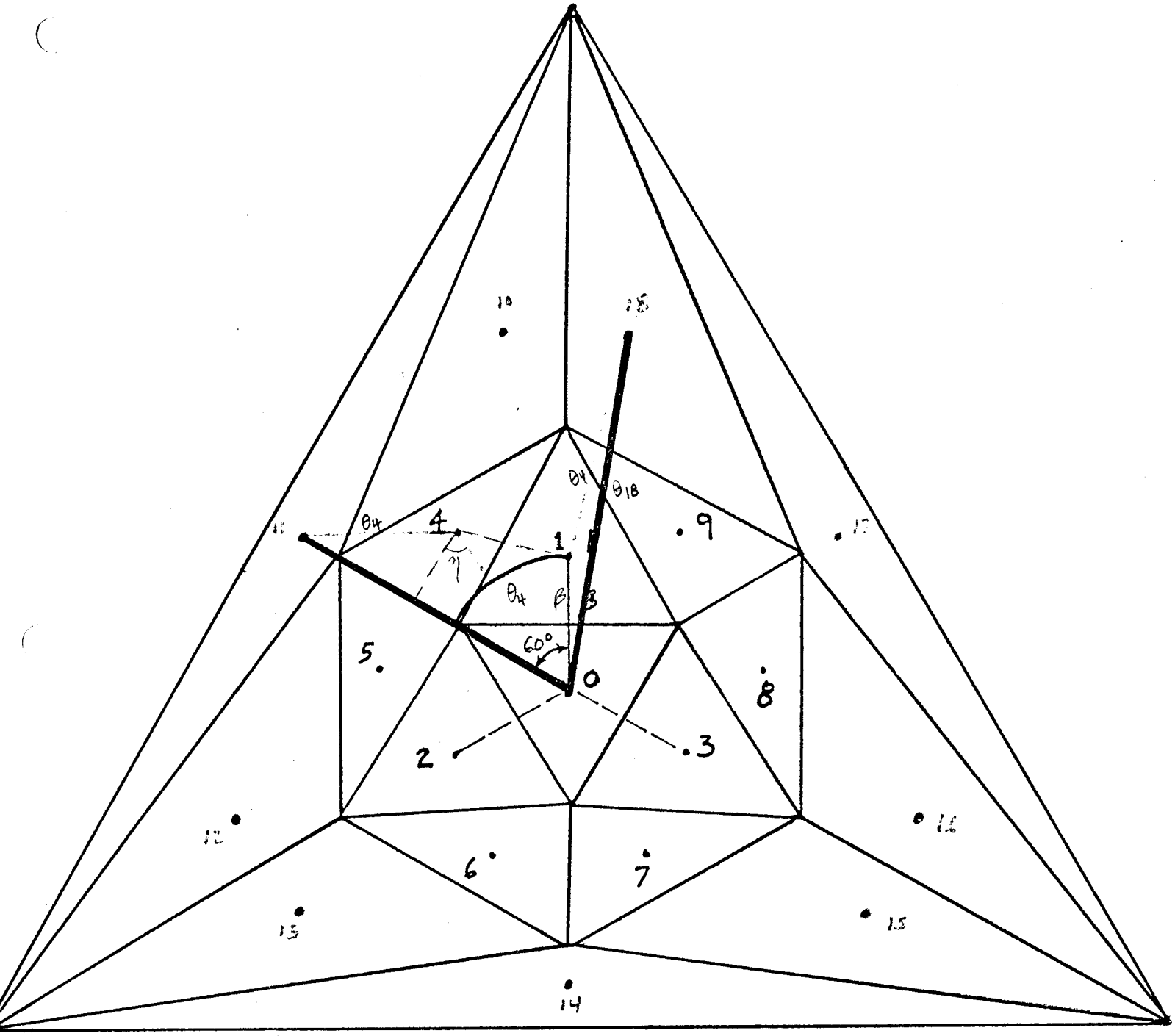

Figure 8a

$$\phi_{10} = 60°-\phi_4 \qquad \theta_{10} = 180° - \theta_4$$
$$\phi_{11} = 60° \qquad \theta_{11} = 180° - \beta$$
$$\phi_{12} = 60° + \phi_4 \qquad \theta_{12} = 180° - \theta_4$$
$$\phi_{13} = 180° - \phi_4 \qquad \theta_{13} = 180° - \theta_4$$
$$\phi_{14} = 180° \qquad \theta_{14} = 180° - \beta$$
$$\phi_{15} = 180° + \phi_4 \qquad \theta_{15} = 180° - \theta_4$$
$$\phi_{16} = 300° - \phi_4 \qquad \theta_{16} = 180° - \theta_4$$
$$\phi_{17} = 300° \qquad \theta_{17} = 180° - \beta$$
$$\phi_{18} = 300° + \phi_4 \qquad \theta_{18} = 180° - \theta_4$$

Minimum Value of θ_{max} for Overlap

We have located a sufficient number of nearest neighbors to calculate the irradiance on a sphere with a considerable amount of overlap. From Fig. 5, we see that the condition for the spots to just touch is

$$\theta_{max} = \beta/2 \ . \tag{20}$$

Thus, we know we need a focal shift of at least

$$\delta_{min} = 2F \sin\beta/2 - \cos\beta/2 \tag{21}$$

in order to achieve uniform irradiance.

III-A-4-d. Minimum Value of θ_{max} for Total Coverage

When the nearest neighbor spots overlap sufficiently, there will be no unilluminated areas on the pellet. To calculate θ_{max} for 100% coverage, we must look at each case individually.

Octahedron

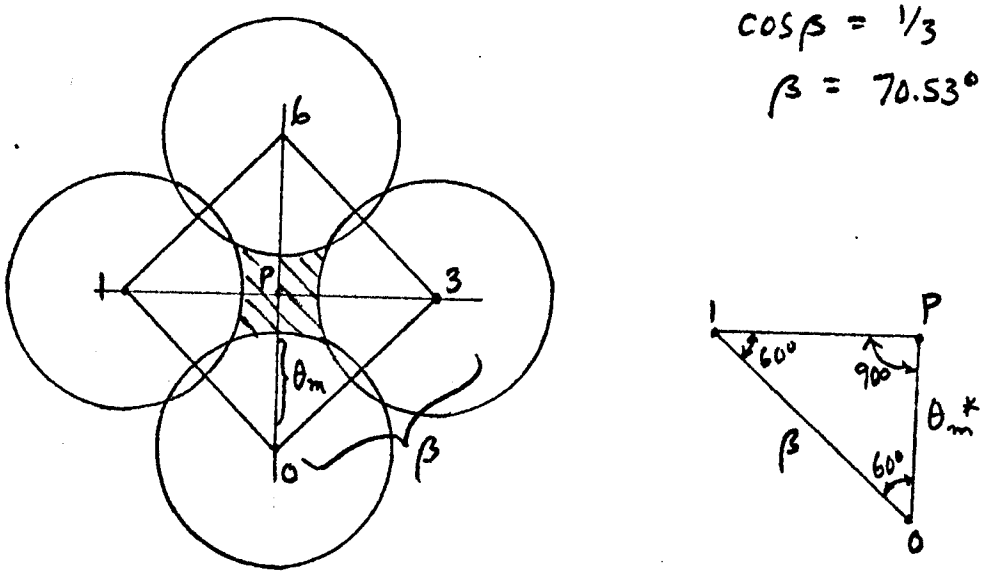

Figure 9

Figure 9 depicts the four nearest neighbor beams. In order to wipe out the small rectangular area in the center, we solve the triangle 01P. The law of sines gives

$$\sin\theta_m^* = \sin 60° \sin\beta = (\tfrac{1}{2}\sqrt{3})(\tfrac{2}{3}\sqrt{2}) = \sqrt{2/3}\ , \qquad (22)$$

or

$$\theta_m^* = \tan^{-1}\sqrt{2} = 54.74°.$$

Dodecahedron

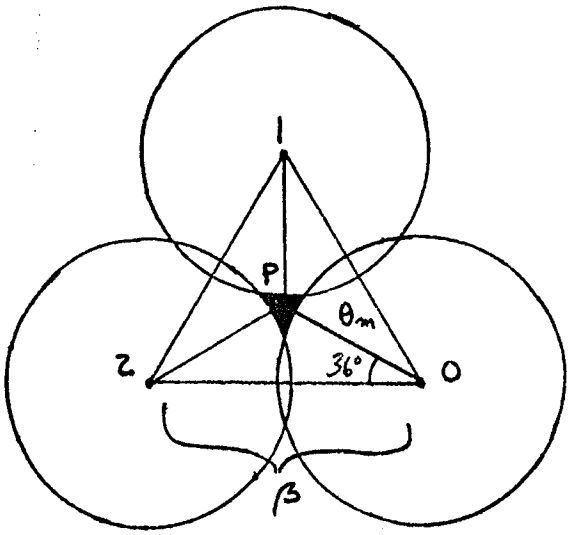

$\beta = 63.43°$

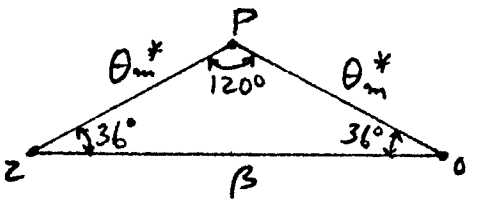

Figure 10

Figure 10 shows the three nearest neighbor spots. To wipe out the triangular hole in the center, we solve the spherical triangle OP2 and find

$$\sin\theta_m^* = \frac{\sin 36°}{\sin 60°} \sin\beta = 0.606,$$

so that

$$\theta_m^* = 37.3°$$

Isocahedron

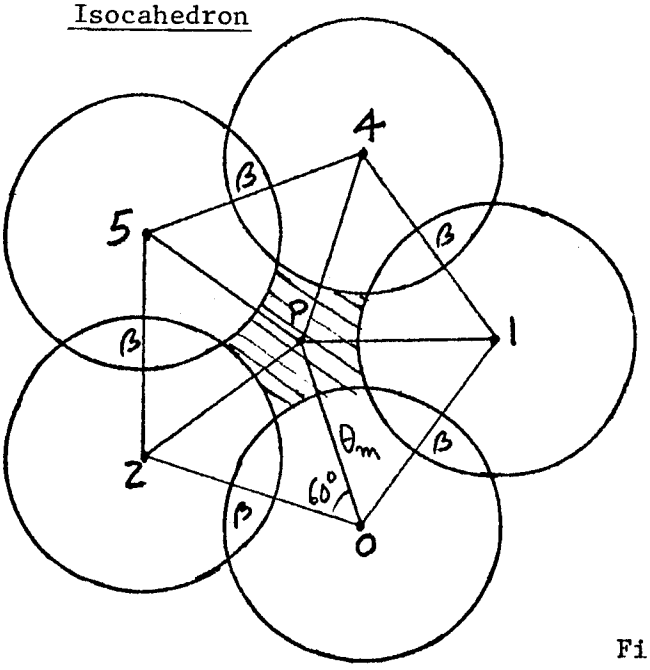

$\beta = 41.82°$

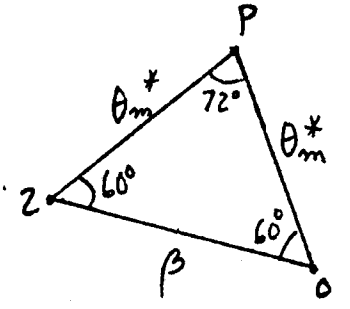

Figure 11

Figure 11 shows the five nearest neighbor spots. Solving the spherical triangle OP2 gives

$$\sin\Theta^*_m = \frac{\sin 60^\circ \sin\beta}{\sin 72^\circ} = .606 \qquad (24)$$

Thus, $\Theta^*_{max} = 37.3^\circ$, the same value as for the N = 12 case!

III-A-5. Numerical Results

Having debugged program PLATO, the first thing we set out to do was to try to duplicate as far as possible Livermore's optimal illumination curves for SHIVA published in their 1974 Annual Report. This is a good way to check out the program, as well as gain an independent view of the problem. Of course, SHIVA was never intended to resemble a reactor; its 20 beams take up 51% of the total solid angle subtended by the target!

Next we look at a reactor-type configuration, limiting optics to 10 or 20% of the total solid angle. This yields respectably uniform illumination for 12 or 20 beams, with 8 beams running a poor third. However, good uniformity for these high f/no. configurations can only be achieved at the expense of rakishly large angles of incidence, and the consequent loss of laser energy through refraction in the plasma corona. The questions of refraction and energy absorption in the corona are dealt with in section II.A.5.

III-A-5-a. Optimization

This pilot study differs from the LLL studies in two important respects. First of all, they employ aplanatic coma-free lenses, whereas we use ideal thin lenses. This difference probably does not greatly alter most of our results; however, aplanatic lenses are certainly preferable from a

practical standpoint, and we may decide to use them in our conceptual design studies. More realistic studies will have to assume parabolic mirrors, an entirely different story.

More important is the choice of beam profile. Livermore specifies a beam profile as a function of the angle θ, whereas we work with the beam radius r. Further, they have done exhaustive studies with more complicated functions than our simple gaussian shapes. Thus, our uniformity curves are generally a bit lower than theirs.

Our first study assumes a gaussian beam profile incident on f/1.5 lenses;

$$I_o(r) = e^{-r^2/a^2}, \tag{25}$$

with a = 0.5, 0.75 and 1.0, for N = 8, 12 and 20 beams. Figures 12-14 show the uniformity η as a function of central angle θ_{max}, where

$$\eta \equiv 1 - \left(\frac{I_{max} - I_{min}}{I_{max} + I_{min}} \right) . \tag{26}$$

This criterion is different from Livermore's $\eta_L = I_{min}/I_{max}$ and we need to justify our choice. To do this, consider a sinusoidal ripple of amplitude A superimposed on a D.C. signal of magnitude B.

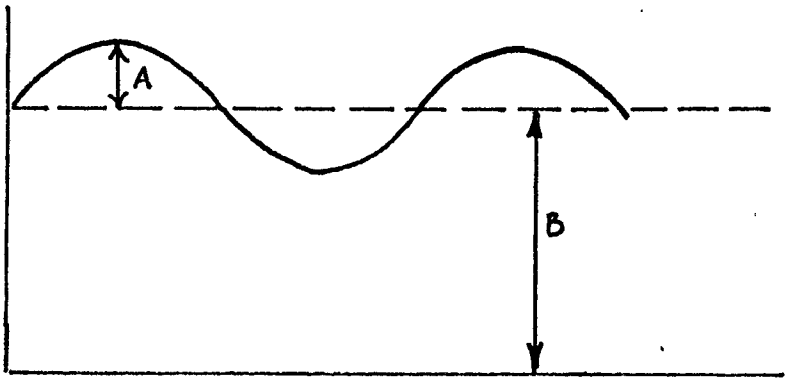

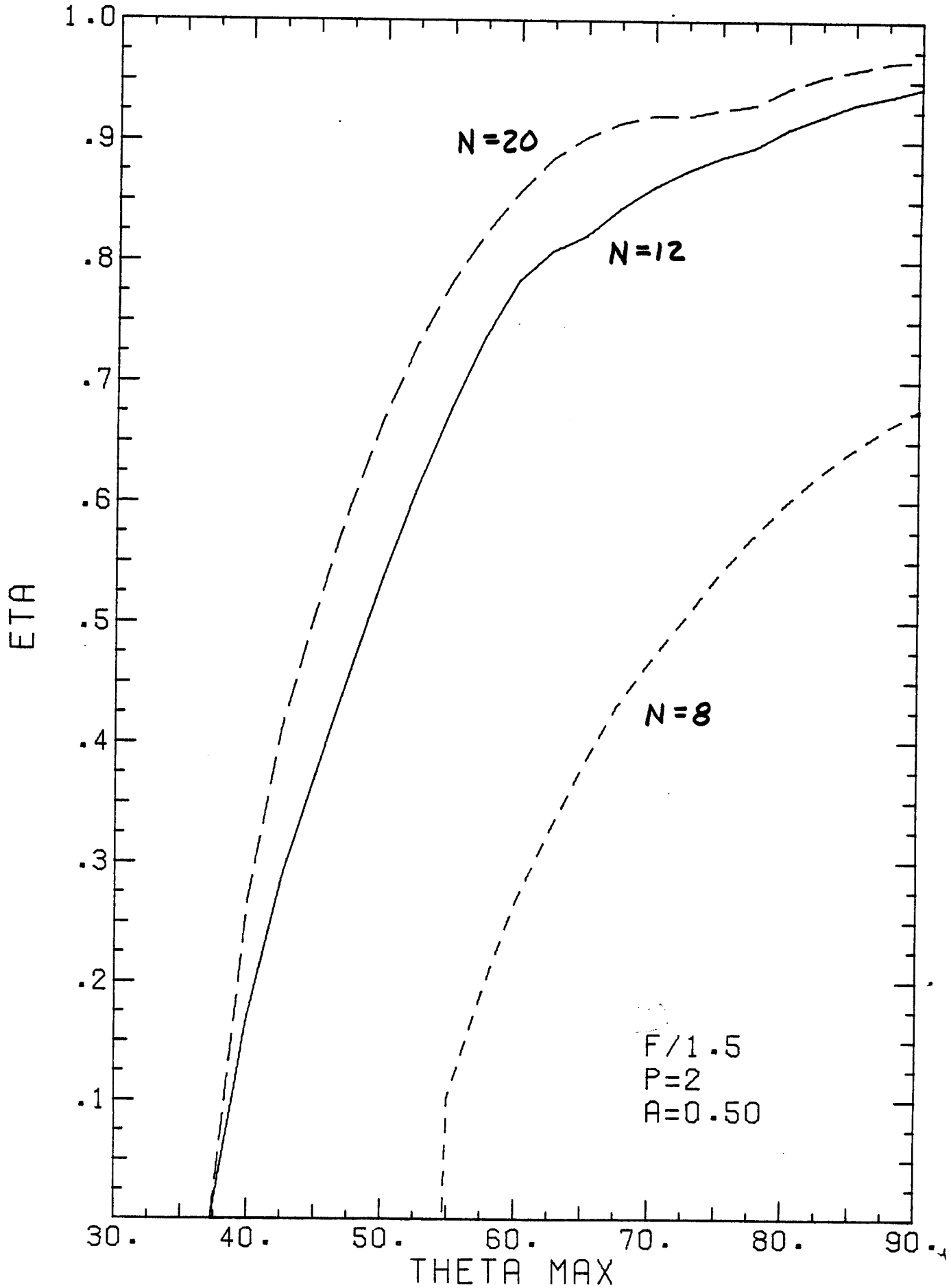
1.0
.9
.8
.7
.6
.5
.4
.3
.2
.1
ETA
N=20
N=12
N=8
F/1.5
P=2
A=0.50
30.
40.
50.
60.
70.
80.
90.
THETA MAX

Figure 12

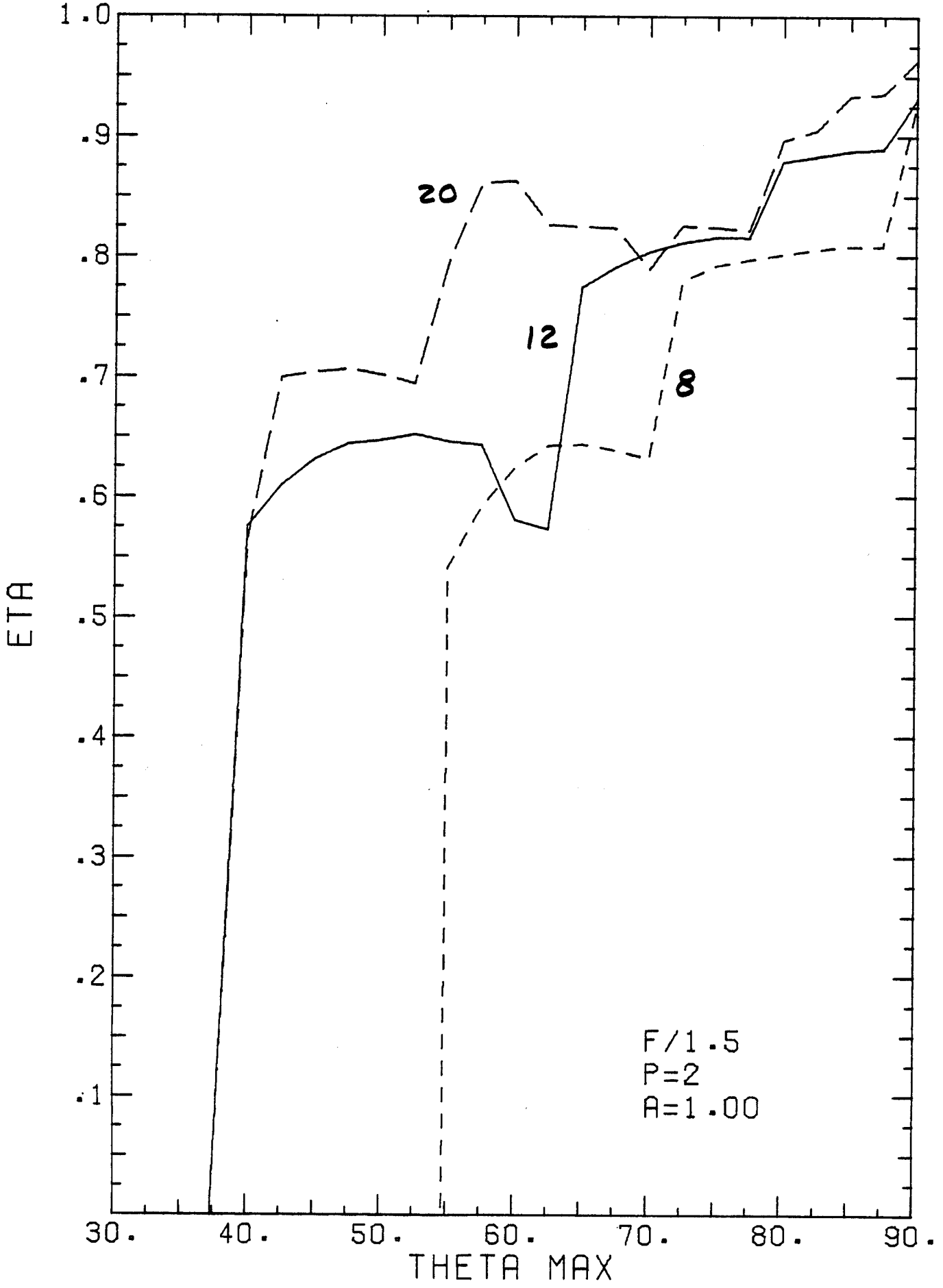
1.0
.9
.8
.7
.6
.5
.4
.3
.2
.1
ETA
20
12
8
F/1.5
P=2
A=1.00
30.
40.
50.
60.
70.
80.
90.
THETA MAX

Figure 13

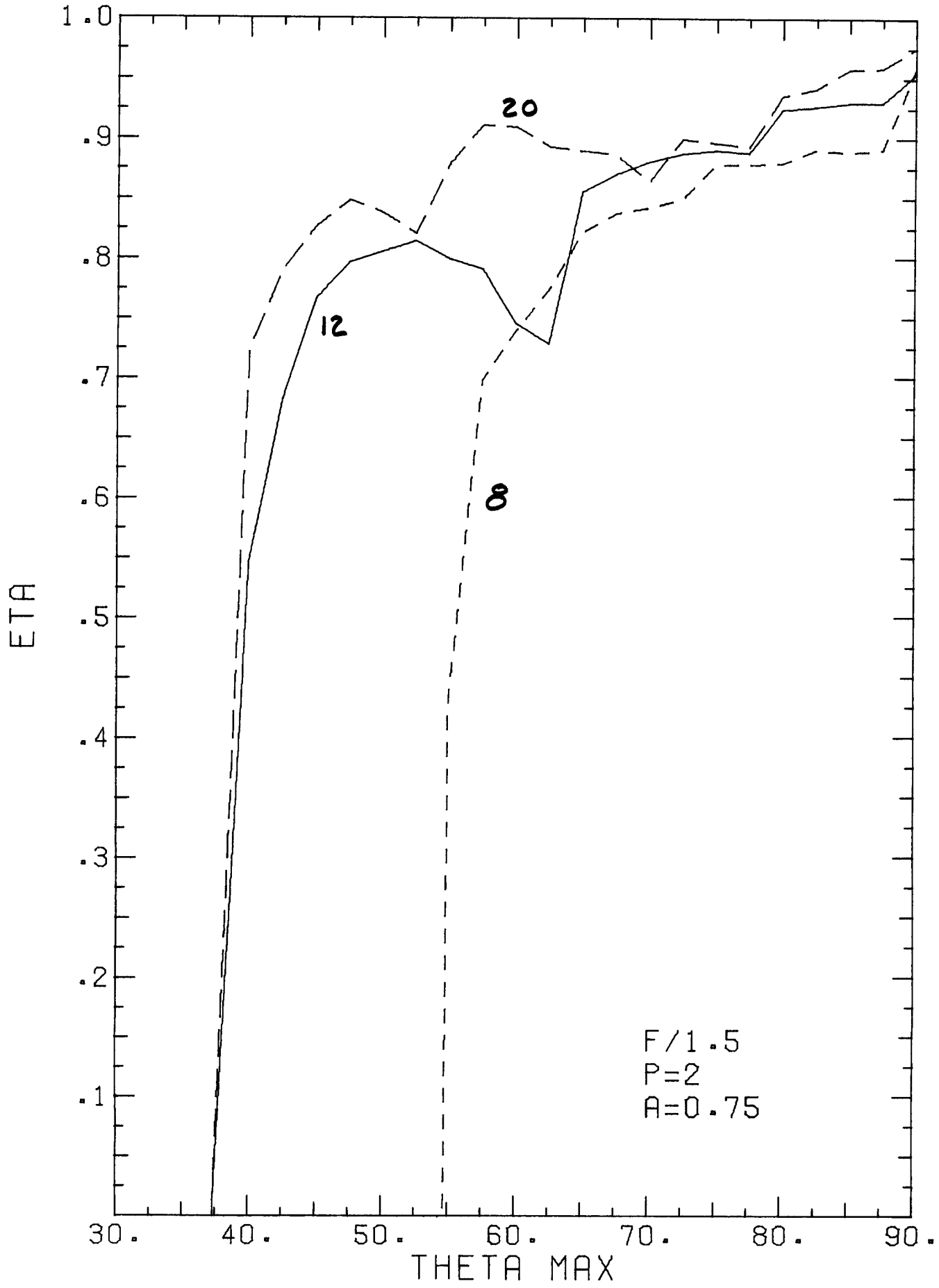
1.0
.9
.8
.7
.6
.5
.4
.3
.2
.1
ETA
20
12
8
F/1.5
P=2
A=0.75
30.
40.
50.
60.
70.
80.
90.
THETA MAX

Figure 14

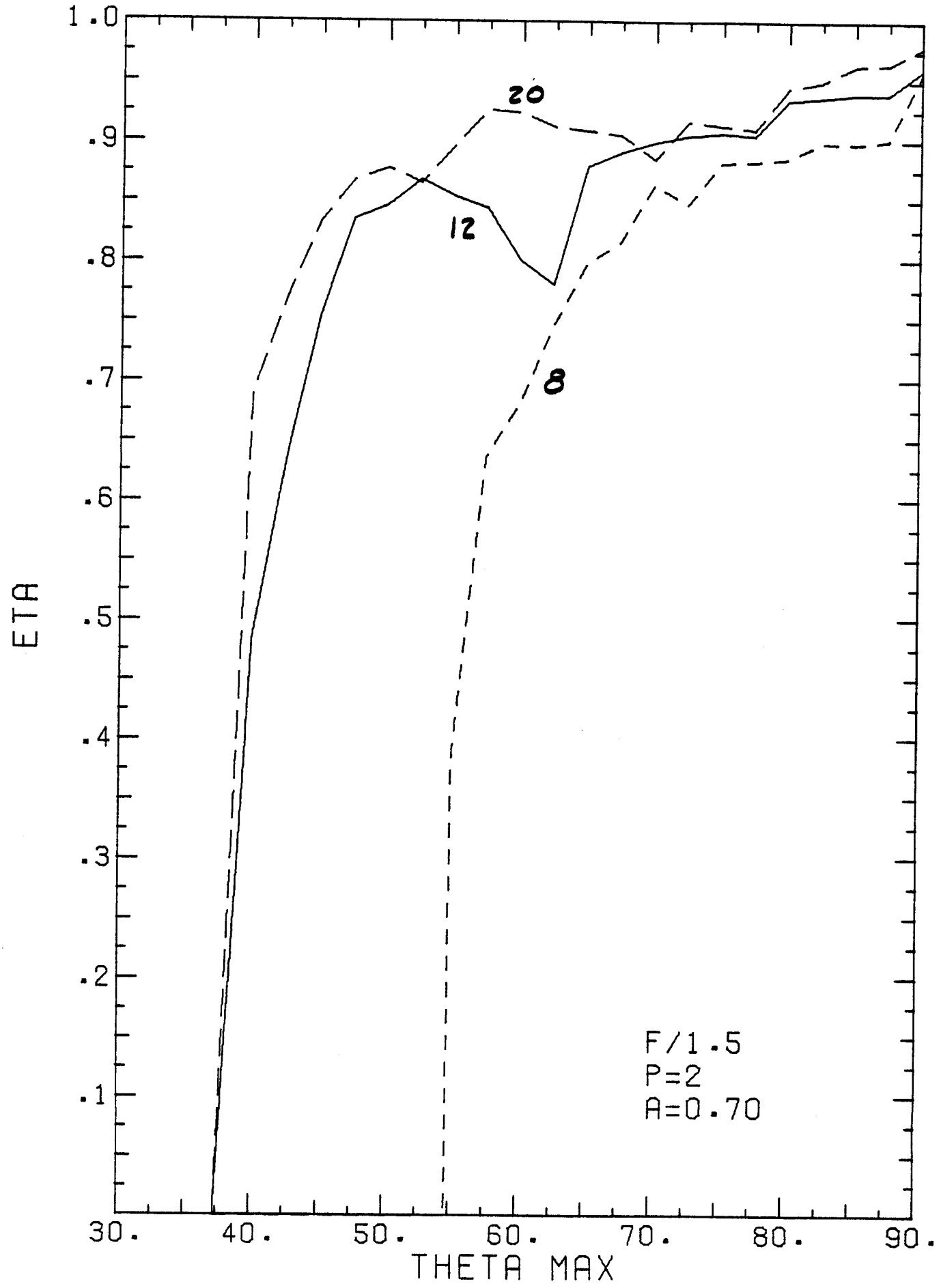
1.0
.9
.8
.7
.6
.5
.4
.3
.2
.1
ETA
20
12
8
F/1.5
P=2
A=0.70
30.
40.
50.
60.
70.
80.
90.
THETA MAX

Figure 15

It is natural to express the deviation fron constancy as A/B and the "uniformity" as 1 - A/B, which is identical to our criterion (26). Both η and η_L have the happy property of varying between 0 and 1.

Note that $\eta = 0$ at $\theta_{max} = 54.7°$ for 8 beams and $\eta = 0$ at $\theta_{max} = 37.3°$ for 12 of 20 beams, as predicted in section 4.5. Clearly the best uniformity is obtained for $a = 0.75$. Somewhat better uniformity results for $a = 0.70$, as shown in Fig. 15. Also note the great improvement in going from 8 to 12 beams, and the smaller, but non-negligible improvement in going from 12 to 20 beams. Indeed, the curves sometimes cross! The 12 and 20 beam cases always seem to improve (or worsen) together.

We have also carried out a limited number of optimization studies using "supergaussian" beam profiles of the form*

$$I_o(r) = e^{-(r/a)^p}, \tag{27}$$

with $p = 3,4$ and 5. Generally, the results were poor for $p = 4$ and 5. For $p = 3$, best results were again obtained for $a = 0.70$, as Figs. 16-19 illustrate. Better than 95% uniformity was obtained for 20 beams and better than 93% uniformity using 12 beams, both at $\theta_{max} \tilde{=} 50°$, where $\Psi_{max} \tilde{=} 32°$. Unfortunately, while the 20 beam peak has a broad maximum, the 12 beam peak is characteristically narrow, indicating a sensitivity to optical misalignment.

Figures 20 and 21 illustrate the gaussian and supergaussian beam profiles for $a = 0.5$, 0.7, and 1.0. We have also computed fill factors, defined as

$$ff = \frac{1}{\pi r_L^2} \int_o^{r_L} I_o(r) 2\pi r dr \tag{28}$$

for a number of supergaussian profiles, as recorded in Table 3.

* The half-width at half maximum is $x_{1/2} = a\,(\ln 2)^{1/n}$.

Fill Factors

p \ a	.5	.70	.75	1.0
2	.2454	.4263	.4674	.6321
3	.2257	.4310	.4841	.6998
4	.2216	.4326	.4926	.7468
5	.2218	.4346	.4978	.7813

Table 3

Note that for a Gaussian profile,

$$ff = a^2 \left(1 - e^{-1/a^2}\right) . \tag{29}$$

Now we see that there is something special about our optimum a = 0.70; it is practically a stationary point for the variation of fill factor with the index p. There is less than a 2% change in ff as p varies from 2 to 5. Table 3 also points up the fact that considerable energy can be wasted in beam-tailoring.

Better uniformity is doubtless realizable for slightly different beam profiles; however, such fine tuning is not our objective here. We are merely interested in investigating the gross differences between competing illumination schemes at this point. By careful shaping of the beam profile, the uniformity may be made to exceed 95% at a fairly low value of θ_{max}. If the Rayleigh-Taylor

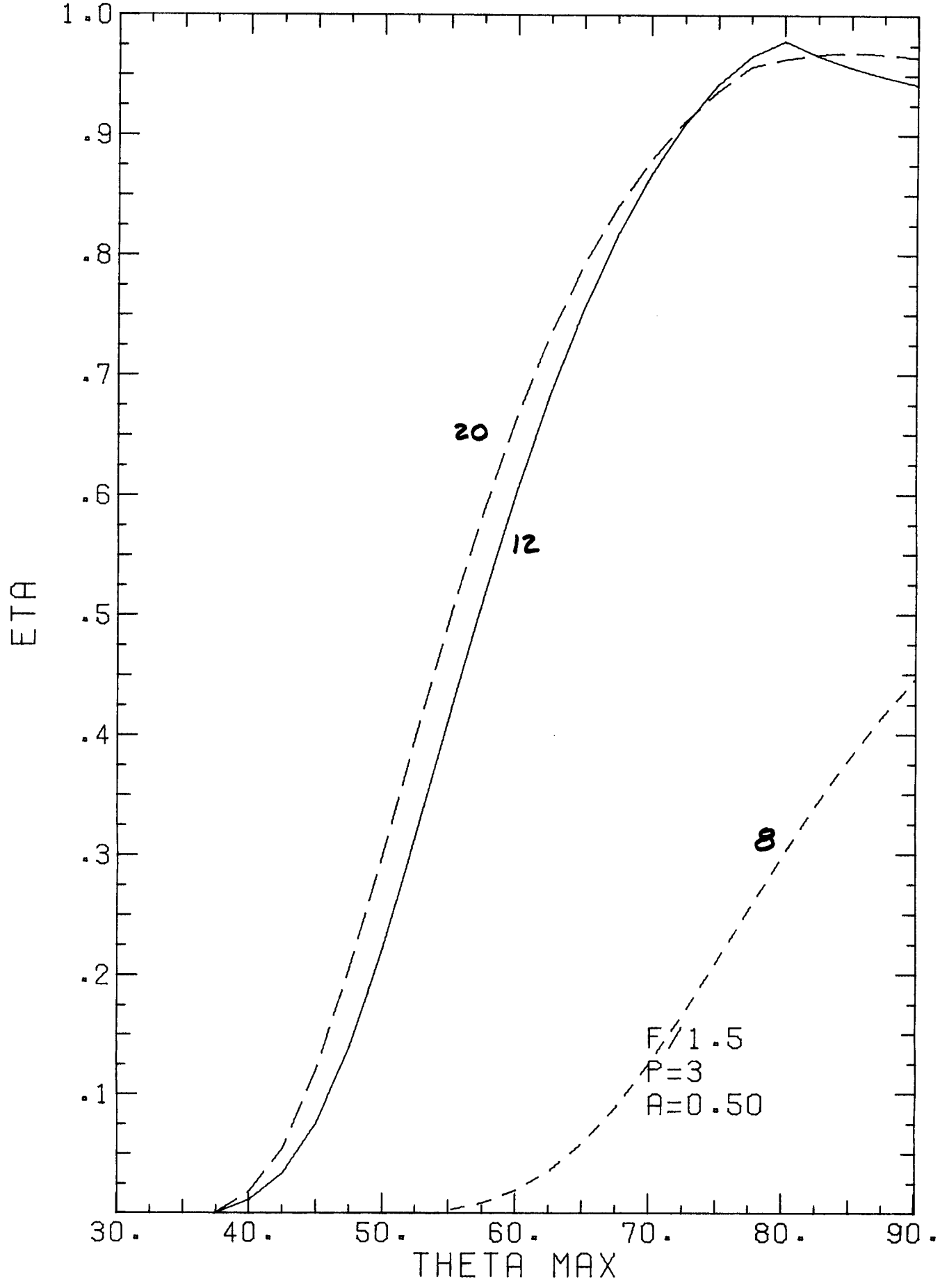
1.0
.9
.8
.7
.6
.5
.4
.3
.2
.1
ETA
20
12
8
F/1.5
P=3
A=0.50
30.
40.
50.
60.
70.
80.
90.
THETA MAX

Figure 16

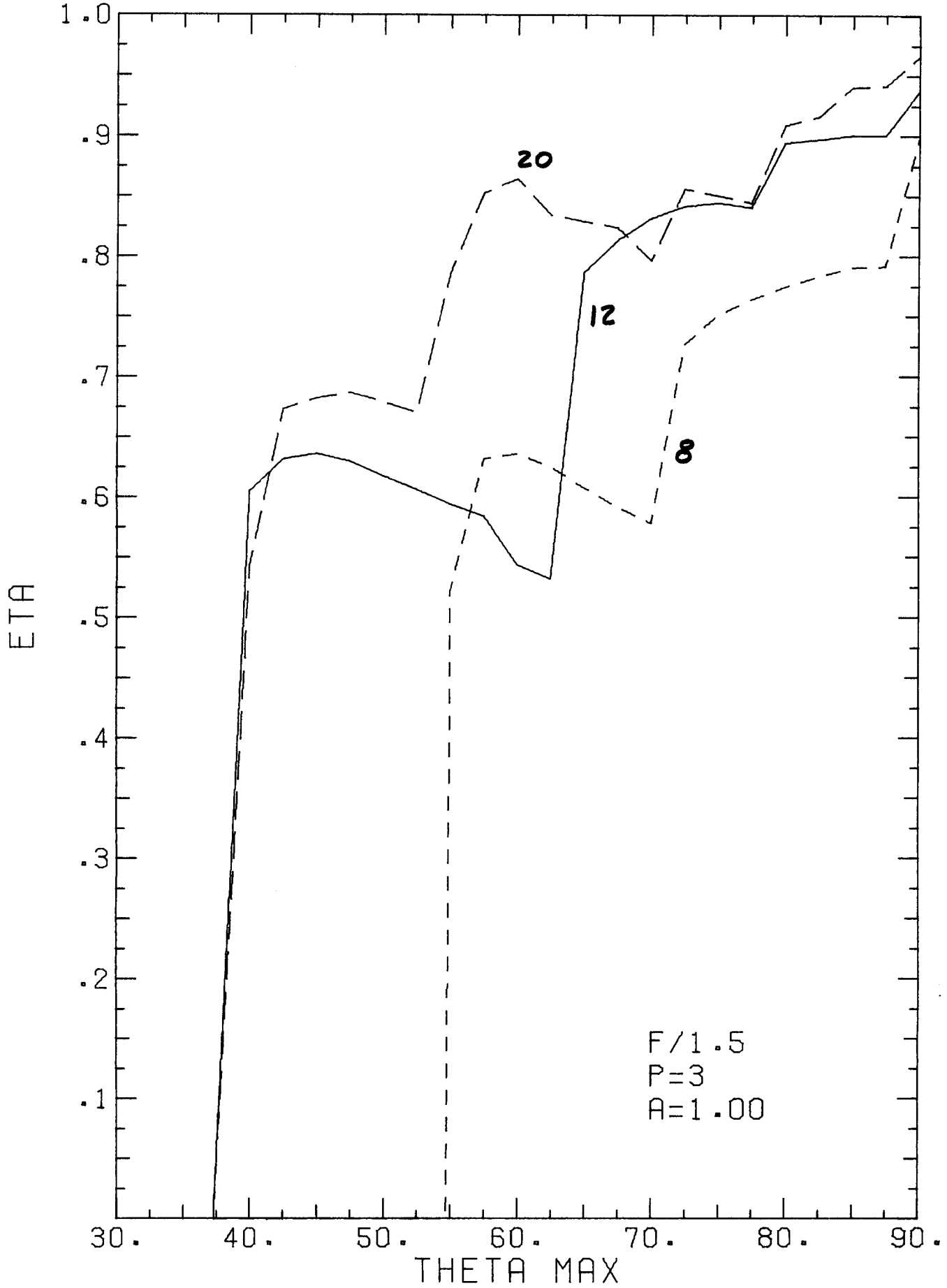
1.0
.9
.8
.7
.6
.5
.4
.3
.2
.1
ETA
20
12
8
F/1.5
P=3
A=1.00
30.
40.
50.
60.
70.
80.
90.
THETA MAX

Figure 17

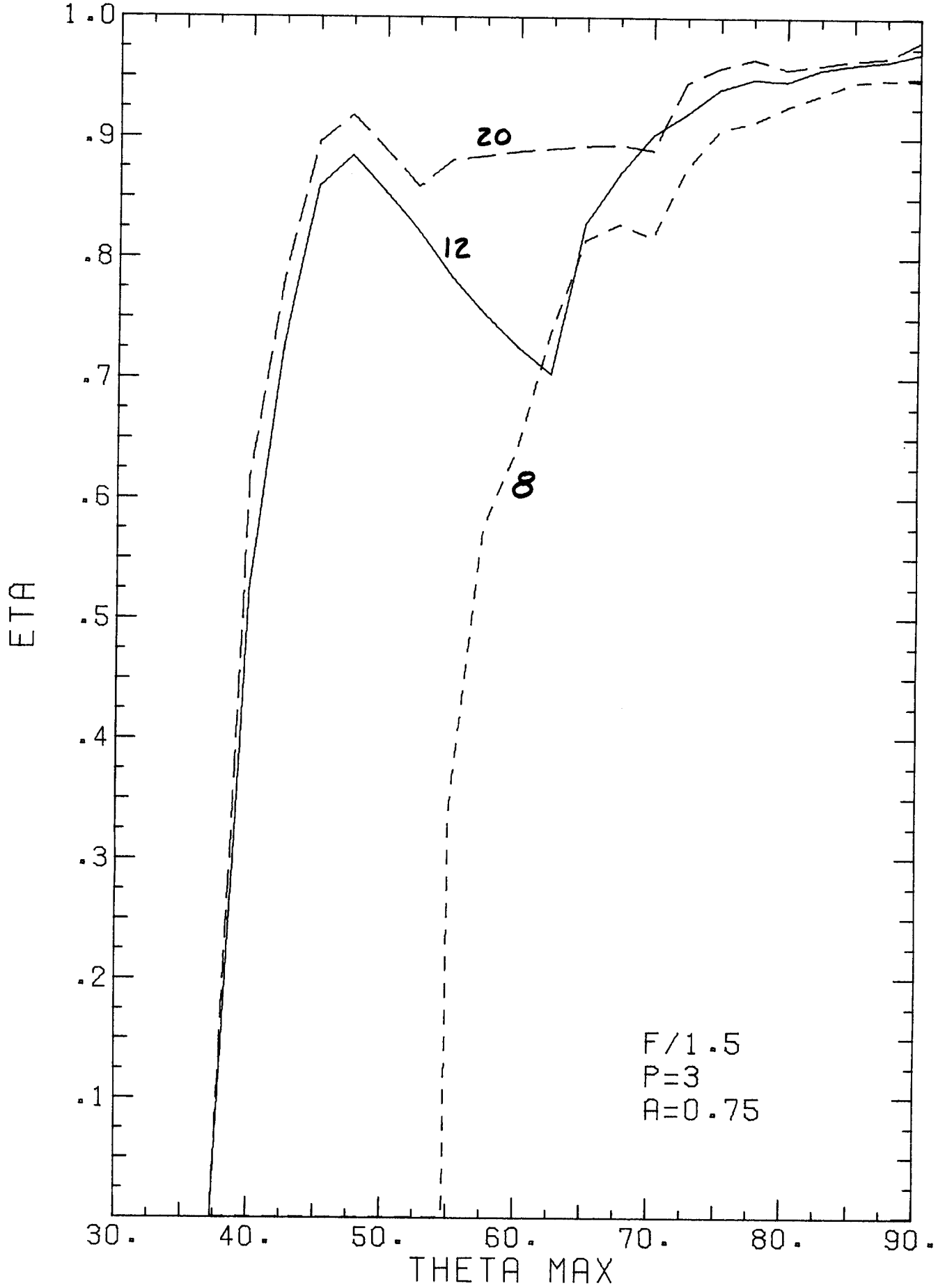
1.0
.9
.8
.7
.6
.5
.4
.3
.2
.1
ETA
20
12
8
F/1.5
P=3
A=0.75
30.
40.
50.
60.
70.
80.
90.
THETA MAX

Figure 18

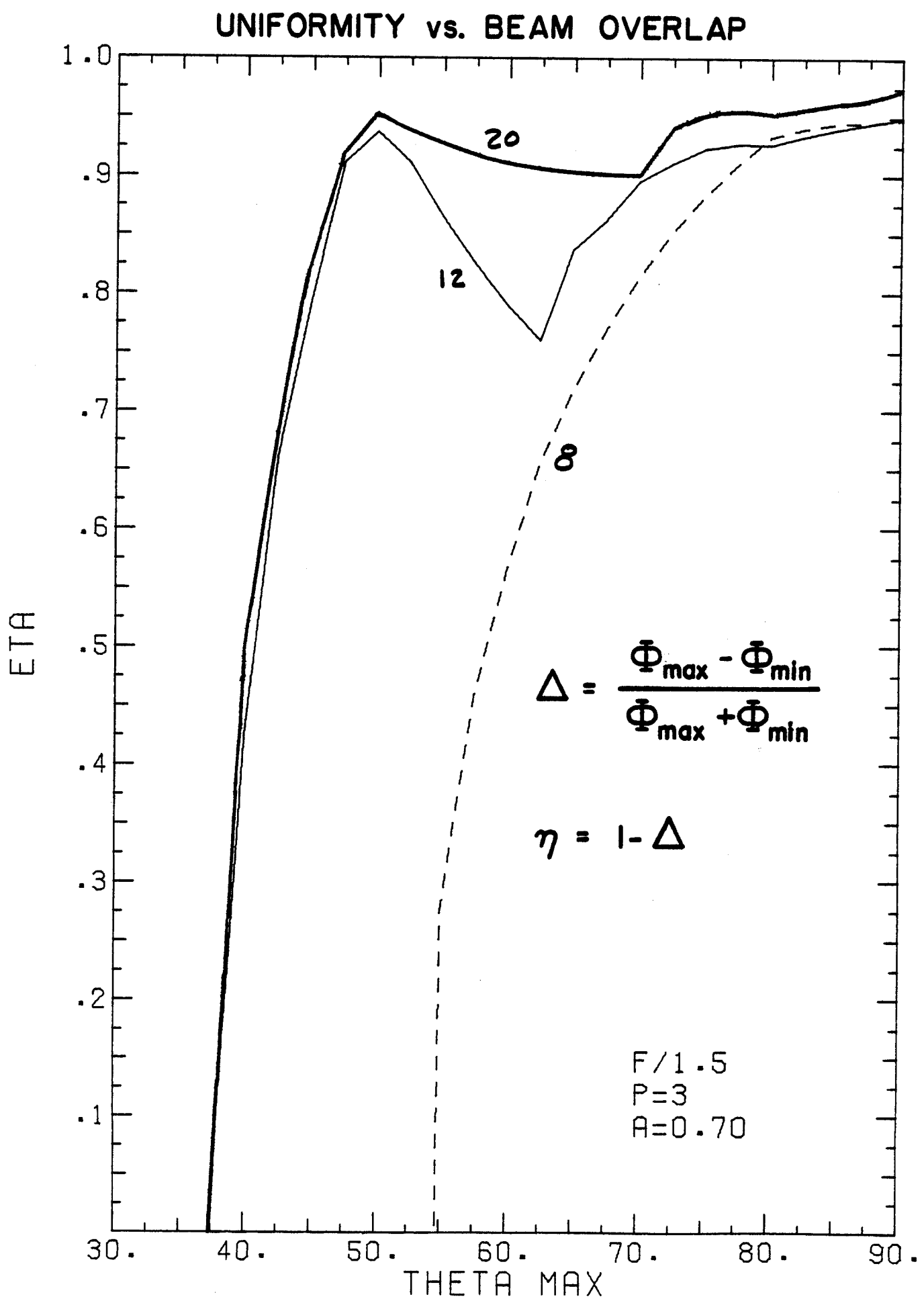
UNIFORMITY vs. BEAM OVERLAP
1.0
.9
.8
.7
.6
.5
.4
.3
.2
.1
ETA
20
12
8
$\Delta = \frac{\Phi_{max} - \Phi_{min}}{\Phi_{max} + \Phi_{min}}$
$\eta = 1 - \Delta$
F/1.5
P=3
A=0.70
30.
40.
50.
60.
70.
80.
90.
THETA MAX

Figure 19

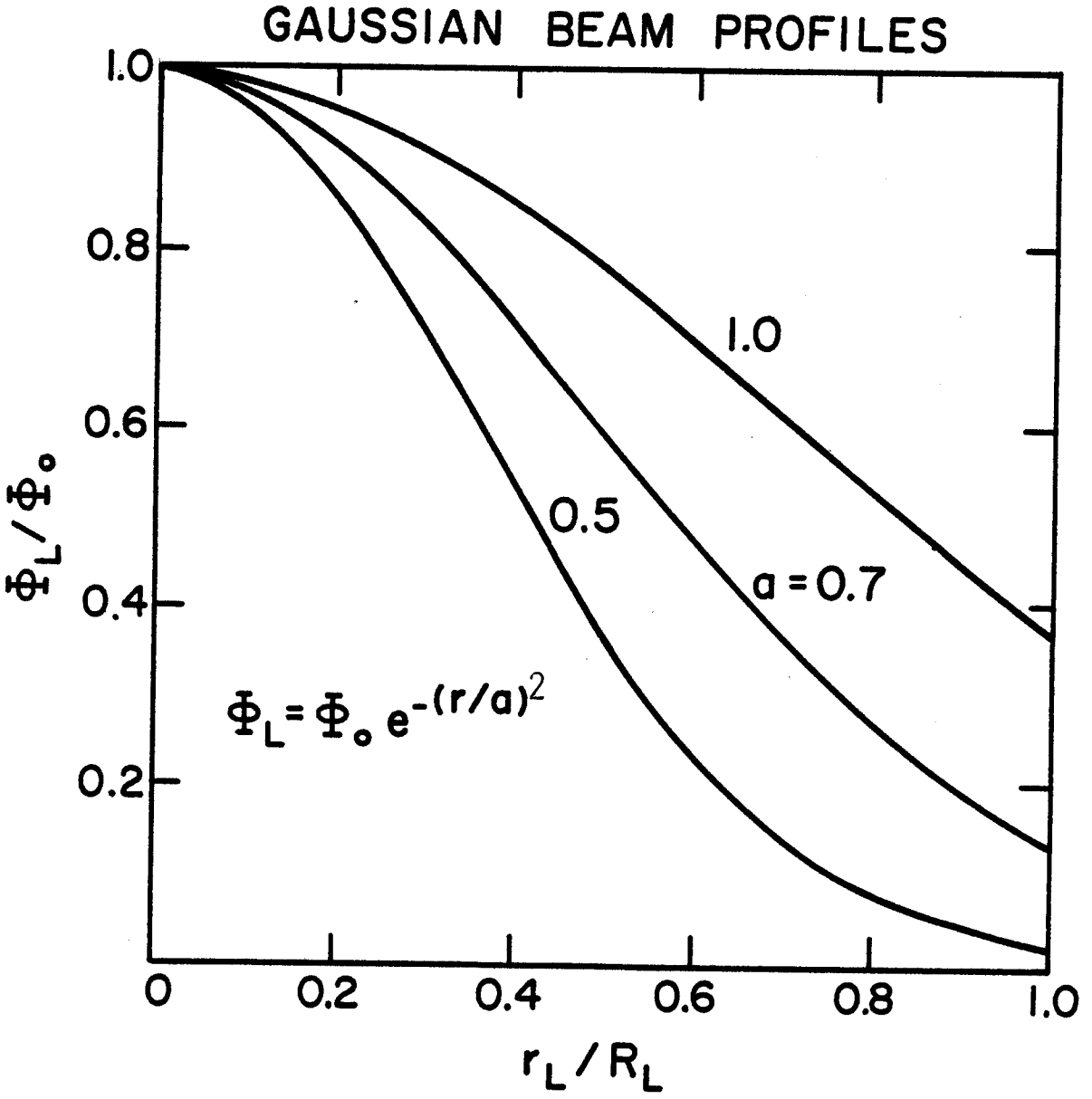
GAUSSIAN BEAM PROFILES
1.0
0.8
0.6
0.4
0.2
0
0.2
0.4
0.6
0.8
1.0
Φ_L / Φ_o
r_L / R_L
1.0
0.5
a = 0.7
$\Phi_L = \Phi_o e^{-(r/a)^2}$

Figure 20

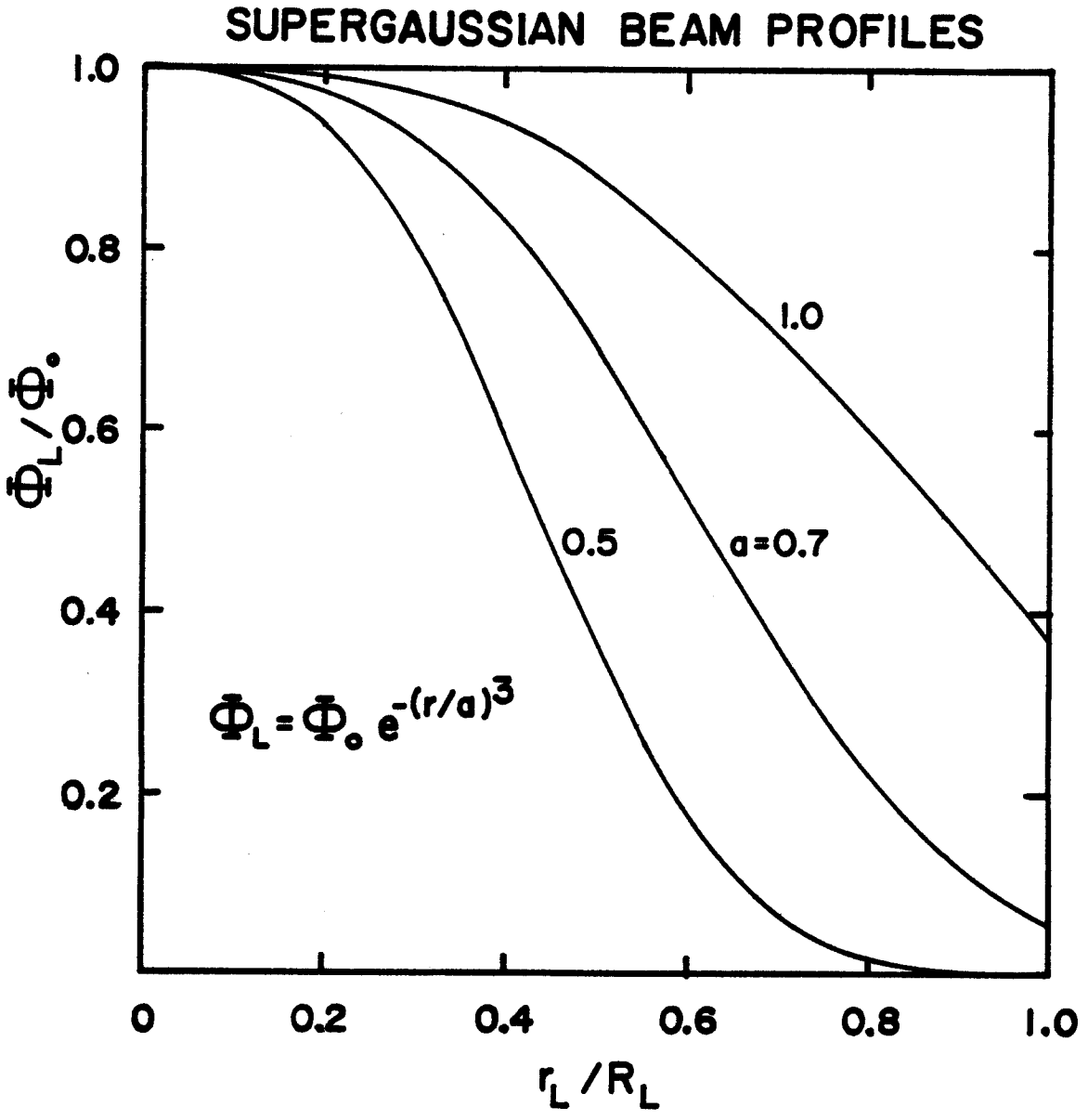
SUPERGAUSSIAN BEAM PROFILES
1.0
0.8
0.6
0.4
0.2
Φ_L/Φ_o
1.0
0.5
a=0.7
$\Phi_L = \Phi_o\, e^{-(r/a)^3}$
0
0.2
0.4
0.6
0.8
1.0
r_L/R_L

Figure 21

instability proves to be as critical as theoretical studies imply, then such high uniformity would indeed be required. Even if this does not turn out to be the case, 12 beams would still offer clear advantages over 8.

The clinker to all of this is the fact that the angle of incidence generally increases with increasing uniformity. This is pointed out in Fig. 22, which plots Ψ_{max} vs θ_{max} for different f/nos. For example, at F = 1.5, the smallest possible Ψ_{max} is 18° for N = 12 or 20. This problem may be alleviated by the fact that the critical surface usually expands appreciably in time, which decreases the effective angle of incidence.

Figure 23, excerpted from the LLL 74 Annual Report,[5] shows η_L vs θ_{max} for a parabolic beam profile. Based on the LLL and the present studies, optimal illumination using f/1.5 lenses may be expected to occur around $\theta_{max} = 50°$ at the least, for which Fig. 22 gives $\Psi_{max} \approx 32°$.

III-A-5-b. Solid Angle-Limited Designs

Finally we turn to the reactor-type cases where the f/nos. are limited by the fractional solid angle alloted to optics, as listed in Table 2. As before, we consider 8, 12 and 20 beams, but we use only one beam profile, the "optimal" supergaussian, with a = 0.70 and p = 3. Figs. 24 and 25 show the results for $\gamma = \Delta\Omega/4\pi = 0.1$ and 0.2. Again the 8 beam configuration runs a poor third. What is perhaps surprising is that the curves are almost identical for N = 20, with only a few percent difference in the N = 12 curves. Of course,the angles of incidence are somewhat worse for the $\gamma = 0.1$ cases. For example, for N = 20 at $\theta_{max} = 50°$, $\Psi_{max} = 38.5°$ and 42°, for $\gamma = 0.2$ and 0.1, resp. For N = 12, $\Psi_{max} = 36°$ and 39.5°. That is, decreasing γ by a factor of 2 only increases Ψ_{max} (and hence Ψ_{eff}) by 10%! While Ψ_{eff} depends on N, F, θ_{max} and the beam profile, among other things, we expect it to be proportional to Ψ_{max}. A detailed study of refraction and energy absorption is under way.

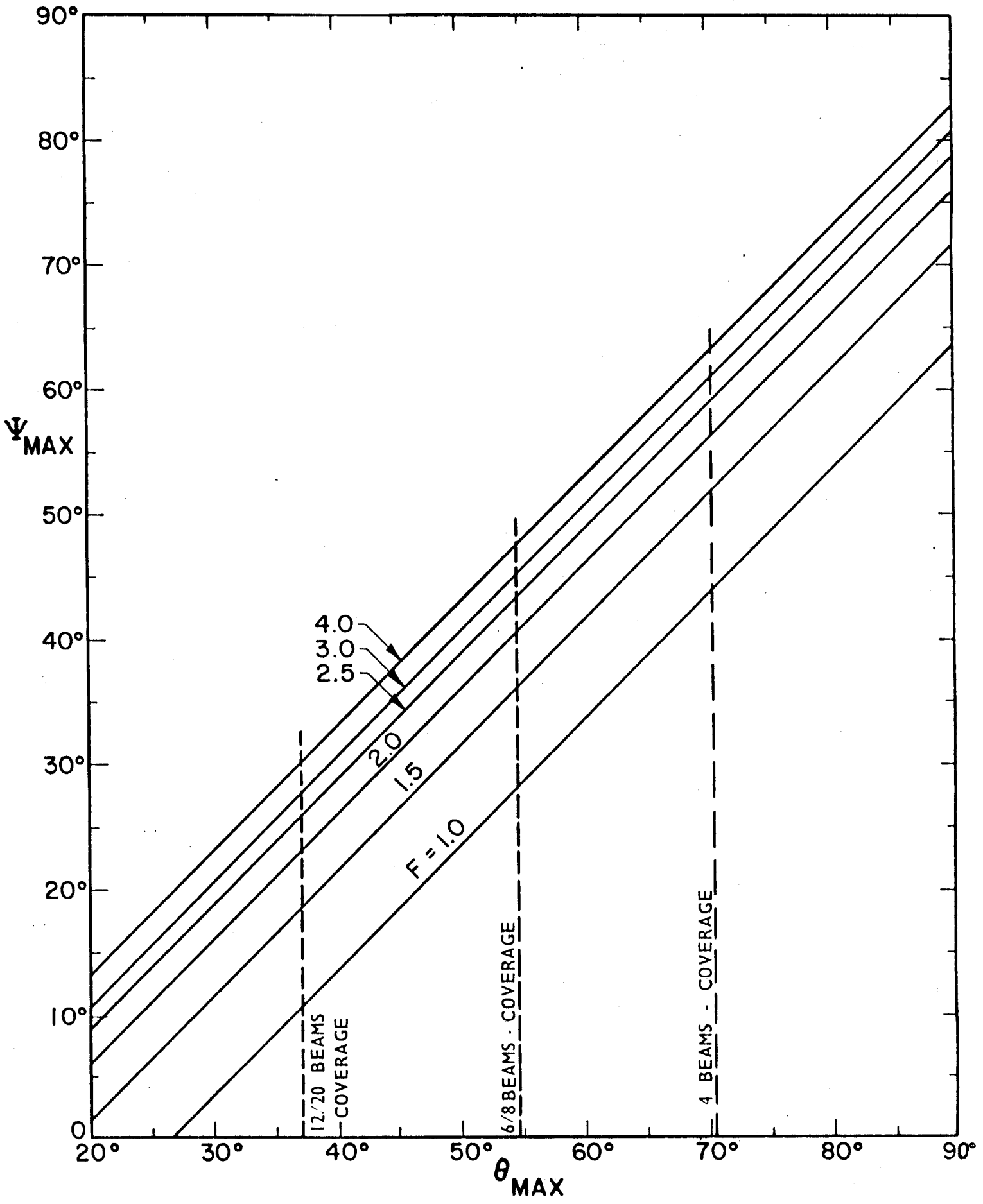

Figure 22 - Maximum Angle of Incidence vs. Maximum Central Angle

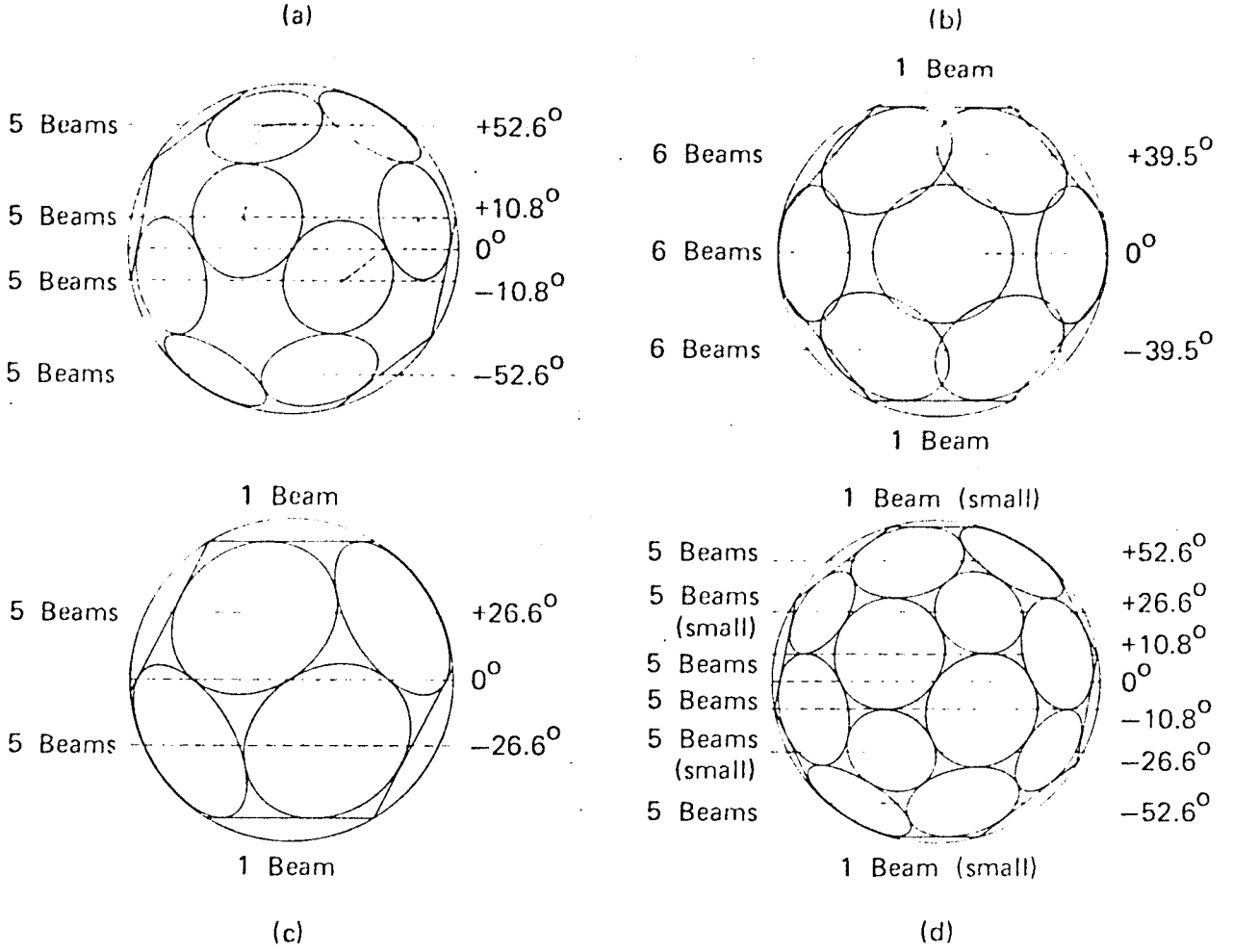

Fig. 3-32. Illumination design configurations: (a) icosahedron (20 beams); (b) Sommargren LUXOR-hedron (20 beams); (c) dodecahedron (12 beams); (d) truncated icosahedron (32 beams).

The illumination uniformity described by the ratio of minimum to maximum intensity for the simple quadratic profile is shown in Fig. 3-33 as a function of the beam angular radius measured from the target center. Although neither geometry satisfies the normality criterion for moderately fast lenses, the icosahedral geometry gives ±8% with a 45° beam radius. In order to improve the normality, either faster lenses or more beams are required. The improvement available with faster lenses is limited by the edge-to-edge crowding of 20 apertures on a sphere at f/1.3 allowing for minimal flanges. An f/1.5 illumination system is a good compromise between speed and crowding.

Illumination Design: Interference. The interference of adjacent beams has been examined. Sheets of interference maxima and minima simultaneously tangent to two adjacent beams at their intersection run parallel to the beam edge deep into the target surface. If the beam edges are not normally incident on the target

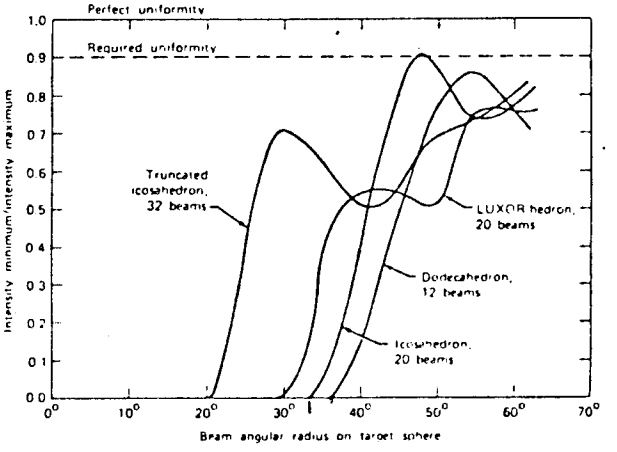

Fig. 3-33. Illumination uniformity for four configurations as a function of beam angular radius measured from target center.

Figure 23

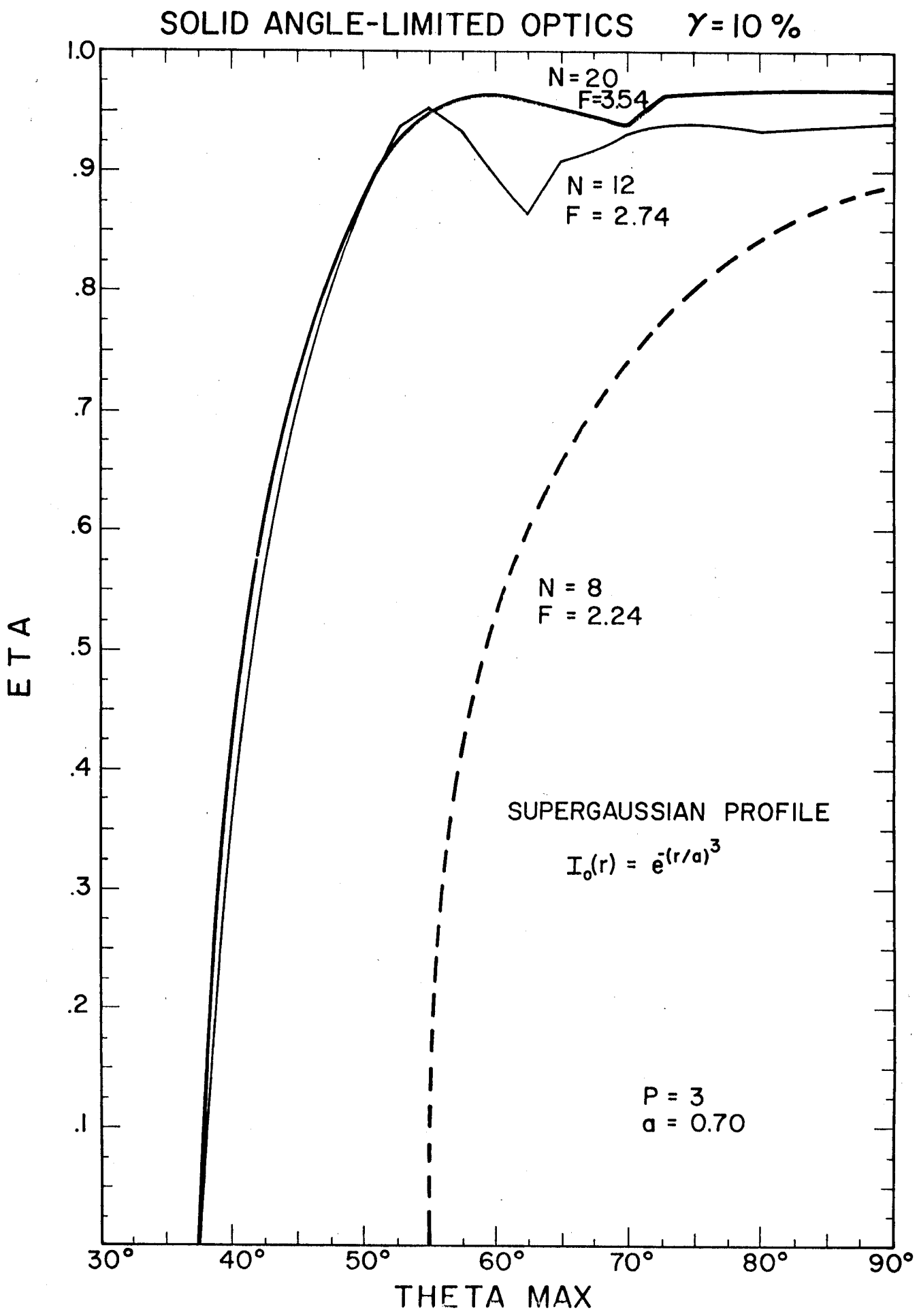
SOLID ANGLE-LIMITED OPTICS γ = 10 %
N = 20
F = 3.54
N = 12
F = 2.74
N = 8
F = 2.24
SUPERGAUSSIAN PROFILE
$I_o(r) = e^{-(r/a)^3}$
P = 3
a = 0.70
ETA
THETA MAX
1.0
.9
.8
.7
.6
.5
.4
.3
.2
.1
30°
40°
50°
60°
70°
80°
90°

FIGURE 24

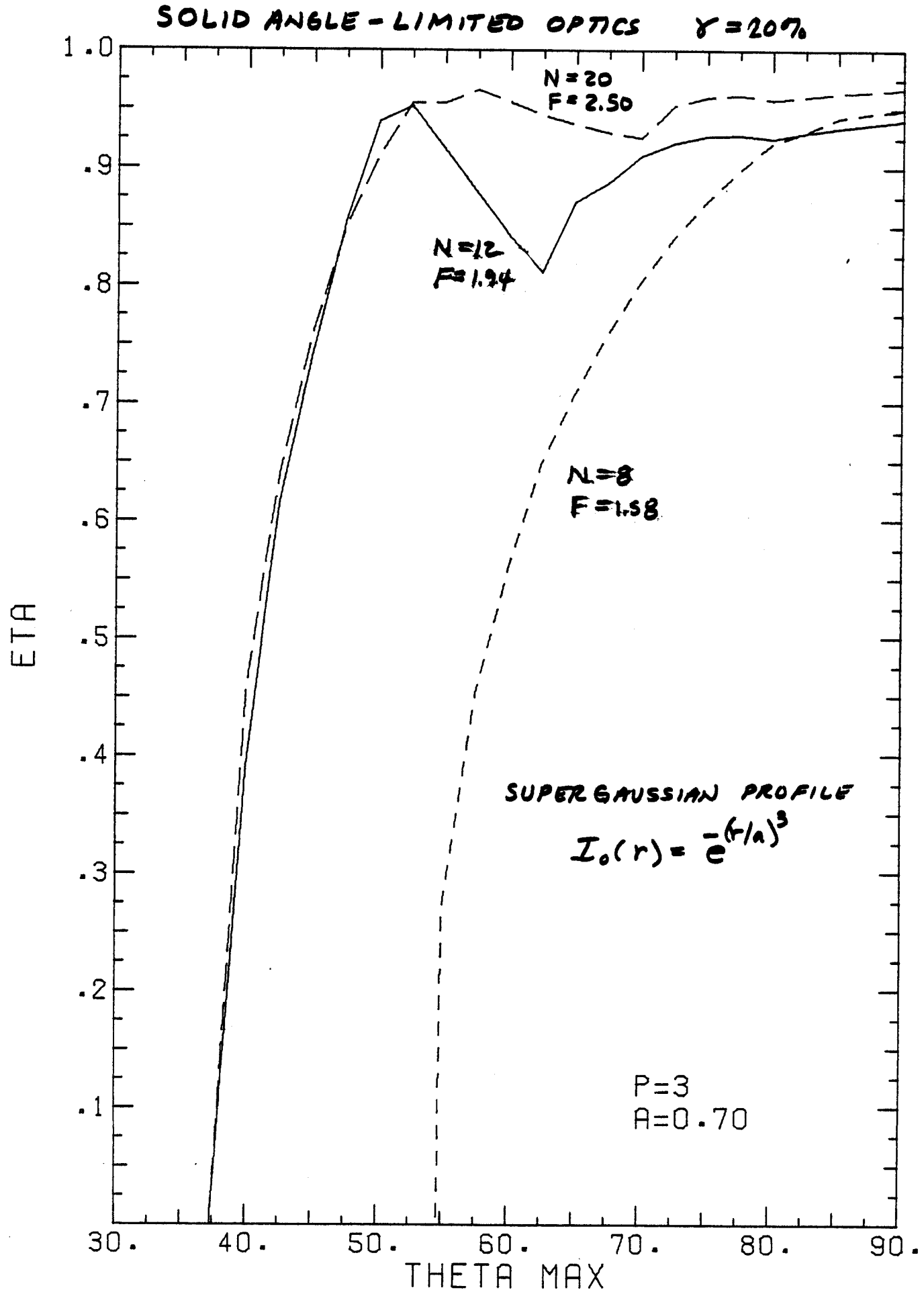
SOLID ANGLE - LIMITED OPTICS γ = 20%
N = 20
F = 2.50
N = 12
F = 1.94
N = 8
F = 1.58
SUPER GAUSSIAN PROFILE
$I_o(r) = e^{-(r/a)^3}$
P = 3
A = 0.70
ETA
THETA MAX
1.0
.9
.8
.7
.6
.5
.4
.3
.2
.1
30.
40.
50.
60.
70.
80.
90.

Figure 25

III-A-6. Discussion

We have described the calculation of illumination uniformity on spherical targets for 8, 12 and 20 overlapping beams arranged according to the symmetry of the Platonic solids with ideal thin lenses as the final optical elements. Due to the extreme symmetry of these configurations, only a small pie-shaped region had to be examined. Other, less symmetrical, illumination schemes would require looking at a larger portion of the sphere and therefore entail more programming. On the other hand, it would be easy to modify PLATO to employ aplanatic lenses, or parabolic mirrors. Further, spatial beam profiles of arbitrary complexity may be used in place of the present family of supergaussians.

Optimization studies were made using f/1.5 lenses in each of the 8, 12 and 20 beam configurations. Generally, the best uniformity was obtained for a cubic supergaussian having a width parameter $a \approx 0.70$. While the maximum uniformity was found to be comparable for 12 or 20 beams, the 12 beam case seemed vulnerable to misalignment. Eight beam illumination was always found to run a poor third. Typical angles of incidence were $\approx 32°$, indicating considerable loss of energy through refraction. In an attempt to reduce this loss, we have also studied 12 beam illumination with f/1.14 lenses, which take up the same total solid angle as 20 f/1.5 lenses. The result is the rather sharply peaked curve shown in Fig. 26. Good uniformity is obtained near $\theta_{max} = 50°$, where $\Psi_{max} \approx 25°$, reducing refraction losses somewhat.

Figure 26

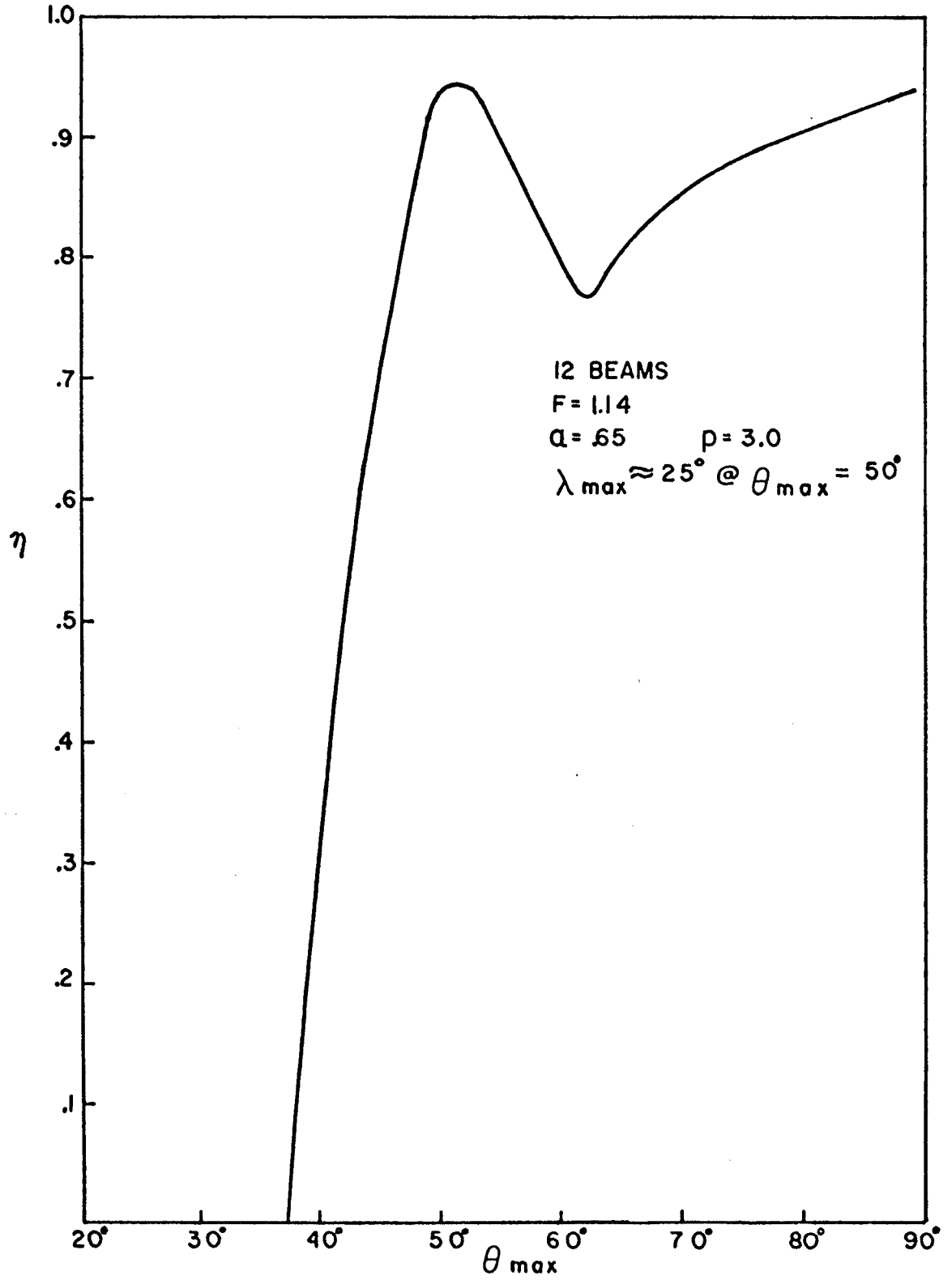
1.0
.9
.8
.7
.6
.5
.4
.3
.2
.1
η
12 BEAMS
F = 1.14
a = .65
p = 3.0
λ max ≈ 25° @ θ max = 50°
20°
30°
40°
50°
60°
70°
80°
90°
θ max

References for Section III-A

1. R. E. Kidder, Nucl. Fusion 16, (1976).

2. J. E. Howard, S. Jorna and R. A. Cover, Bull. Am. Phys. Soc. 18, 1346 (1973).

3. H. S. M. Coxeter, Introduction to Geometry, 2nd ed. (Wiley, New York) 1969, p. 152.

4. C. E. Thomas, Appl. Optics 14, 1267 (1975).

5. Lawrence Livermore Laboratory Annual Report (1974) p. 88.

6. F. Klein, Lectures on the Icosahedron, Dover (N.Y.), 1956.

III.B. Beam Transport Requirements

III.B.1 Introduction

The design of a laser beam transport system entails a large number of interrelated decisions. Plasma physics studies of the laser-pellet interaction tell us that about 1 MJ of laser energy and a peak power of perhaps 1000 TW are needed to achieve a respectable gain.[1] Estimates of the ideal laser wavelength for efficient laser-plasma coupling vary from 3000 Å to 1 μm or more.[2] Some recent experiments suggest that 10.6 μm radiation may be as effective as 1 μm radiation.[3] Although these uncertainties sometimes give the impression that one is erecting glass castles on quicksand, nevertheless one may explore the advantages and disadvantages of long/short wavelengths from a practical point of view. As concrete values we have chosen 5000 Å, 1.0 μm and 10 μm for our numerical examples.

Some of the questions we shall address in this section are

- Are mirrors preferrable to lenses?
- How large do the beam apertures have to be?
- How far away may we place the final optical element?
- How many beams are needed?

The principal determining factors we shall have to weigh in answering these questions are uniformity of illumination, damage to optical components, beam quality, diffraction and positioning errors, besides the usual considerations of cost and reliability. In general, we shall find that optical components are cheaper and less susceptible to damage at longer wavelengths, but there is some disadvantage due to diffraction.

Uniform and Non-Uniform Illumination

The implications of uniform illumination vis-a-vis F number and number of beams were described earlier. Non-uniform illumination eases many of these constraints and it is worthwhile considering this as an alternate case. The laser energy and peak power are about the same in both cases. However, the differing illumination uniformities have a significant effect on the reactor design, so that most of our conclusions will come in pairs.

III.B.2 Mirrors or Lenses?

Several limitations dictate against the use of lenses as the final optical elements of a laser fusion reactor. The first of these is the large aperture size demanded by self-focusing and material damage thresholds. While glasses are inherently tougher than metals with respect to surface damage (low absorption), the dielectric coatings needed to reduce the natural 4% surface reflectance of glass are about as vulnerable as metallic surfaces. Also, large aperture ($r \approx 1m$) aspheric lenses are more expensive than mirrors of comparable size. On the other hand, large aperture diamond-turned mirrors are now routinely fabricated without hand polishing, at moderate cost.[4,5] At present diamond-turning looks very favorable for 10.6 μm radiation, and is well under development for 1.06 μm radiation. A more drastic drawback exists with the CO_2 laser, wherein two transitions are simultaneously pumped (to increase the efficiency), so that refractive optics is out of the question. This is of course the exception rather than the rule for gas lasers.

But by far the most serious objection to the use of lenses is self-focusing. At the anticipated peak powers, the nonlinear optical effects would result in intolerable distortions of the focal region.[6] Mirrors are entirely free of such effects.

Two other possibly serious effects which we know little of at present are consequences of the intense neutron flux on glass. While surface corrosion

may be minimal, several months of neutron bombardment can produce swelling and materially change the refractive index. Further research is needed to determine the effects of high neutron fluences on glasses.

We are fairly certain that if laser fusion works at all, it will utilize some sort of gas phase laser, this being the only kind of laser expected to achieve an efficiency of 10% or better. Limitations on the size of the electric field needed to produce a discharge may then necessitate annular apertures. Since annular apertures make annular beams, we are led to consider toric optics, which may be either reflective or refractive ("catoptric"). Again reflective optics is preferable, due to ease of fabrication and freedom from self-focusing. We are just beginning to look at toric optics.

III.B.3 Aperture Size

Depending on the particular design parameters, the aperture area may be constrained by the need to avoid surface damage due to large energy fluxes, or by various destructive nonlinear optical effects loosely termed "self-focusing," which occur at large beam power densities.

III.B.3.a Damage Thresholds

In a typical laser fusion experiment one finds scores of dielectric coatings, which currently constitute the weak link in transporting high laser energy fluxes[7]. The lowest damage thresholds seem to occur in polarizers, with AR coatings the next most vulnerable. Damage mechanisms in dielectric films seem to be quite complex, and are presently under intensive investigation[8]. Gross failure is caused by avalanche ionization, with multiphoton processes becoming important at smaller λ. Dielectric films suffer deformation due to residual stress and thermal cycling, while the degree of damage depends on various parameters such as substrate roughness, interlayer roughness, residual stress, and standing wave intensity. Lack of quality control in the manu-

facturing process often leaves impurities, particulate inclusions and defects in a highly variable degree. Although controlled experimentation is difficult, progress is being made and we shall be following new fabrication techniques as they develop.

It turns out that uncoated micromachined mirror surfaces have about the same damage thresholds as coated conventional surfaces, Φ_{max} = 5-10 J/cm^2 for 100 psec-1nsec pulse widths. In general, $\Phi_{max} \sim \sqrt{\text{pulse width}}$ and increases somewhat with wavelength, due to the concentration of unreflected energy within about one skin depth. Based on a modest extrapolation from present experience we assume a working energy density,

$$\Phi_{max} = 5 \text{ J/cm}^2 \tag{1}$$

for both uncoated mirrors and dielectric surfaces. This figure would be somewhat larger for longer pulse widths.

Defining a fill factor

$$ff = \frac{\langle\Phi\rangle}{\Phi_{max}} \tag{2}$$

we can calculate the total beam area needed to handle a given total laser energy E_L:

$$A_{TOT} = \frac{E_L}{\langle\Phi\rangle} = \frac{E_L}{ff\ \Phi_{max}} \ . \tag{3}$$

Uniform Illumination

The illumination studies described in section III-A show that uniformity is optimal for the cubic exponential beam profile

$$\Phi_L = \Phi_o\ \bar{e}^{(r/a)^3} \tag{4}$$

with a = 0.7. Here the beam radius r is measured in units of the maximum beam radius and Φ_o is the value on axis. The resulting fill factor is ff = 0.43,

which for E_L = 1 MJ yields a total aperture area $A_{TOT} = 4.66 \times 10^5$ cm^2. Setting $A_{TOT} = N\pi R_M^2$ (N beams) we obtain the following table:

	uniform	nonuniform
N	R_M(cm)	R_M(cm)
6	158	115
8	136	99.7
10	122	89.2
12	111	81.4
16	96.5	70.5
20	86.3	63.1
24	78.8	57.6

Table 1

Now our optimal illumination studies suggest that at least 12 and possibly 20 beams are needed to achieve 90% uniformity on target, indicating beam radii in the range 86-111 cm. (The actual beam radius will be somewhat smaller since it strikes the mirror at an angle). The complexities of cost and convenience of large aperture optics will be treated briefly in the next section.

Nonuniform Illumination

In this mode, precise beam tailoring in not necessary. We want instead to maximize the fill factor. Using the "top-hat" profile

$$\Phi_L = \Phi_0 \, e^{-(r/a)^p} \qquad (5)$$

with p = 5 and a = 1, we find ff = 0.8. An 80% fill factor seems a reasonable goal in the presence of beam loss due to Fresnel diffraction and nonlinear effects in whatever glass is present in the system. Again taking E_L = 1 MJ and Φ_{max} = 5 J/cm^2 we find $A_{TOT} = 2.5 \times 10^5$ cm^2. The resulting aperture sizes are listed in Table 1 alongside the values for uniform illumination. Here we

see an immediate advantage to non-uniform illumination; many fewer beams can be used (6 or 8) at the same aperture area. How many beams should we use?

III.B.3.b Cost Considerations

For a fixed total aperture area, many combinations of beam number and aperture size are within the realm of possibility. Copper mirrors of one meter radius or larger are available off-the-shelf, both diamond-turned and conventional. Naturally one would prefer to use as few mirrors as possible, but not at an impossible cost. Figure 1 depicts cost vs. radius for conventional coated Cu mirrors[9] suitable for λ = 10.6 μm, with a surface figure of $\lambda/20$. Extrapolating from the cost data we find that each 80 cm radius mirror would cost at least $20,000. Twenty of these mirrors would then cost about $400,000, a small fraction of the total cost of a reactor. From Figure 1 we also see that cost ~ area for R_M > 15 cm. Other useful rules of thumb are, cost ~ λ^{-1} and that paraboloids cost approximately ten times as much as flats and spheroids. Thus, 20 flats suitable for λ = 1.06 μm @ $\lambda/10$ could run as much as $2,000,000 with proportionally longer delivery times. While diamond-turned paraboloids are expected to be cheaper than their conventional counterparts, we have no definite cost data on them at present. For shorter wavelengths copper becomes absorbing and must be plated with aluminum, which is reflective down to λ = 3000 Å.

III.B.3.c Self-Focusing

Most amorphous materials suffer an increase in refractive index with increasing laser intensity, so that a plane wave whose intensity decreases radially will eventually collapse on itself, as shown in Fig. 2. This is called whole-beam self-focusing[6], and occurs in Nd:glass at about 10^{10} W/cm^2. In general, the onset of whole beam self-focusing may be anticipated by means of the "**B**-integral",

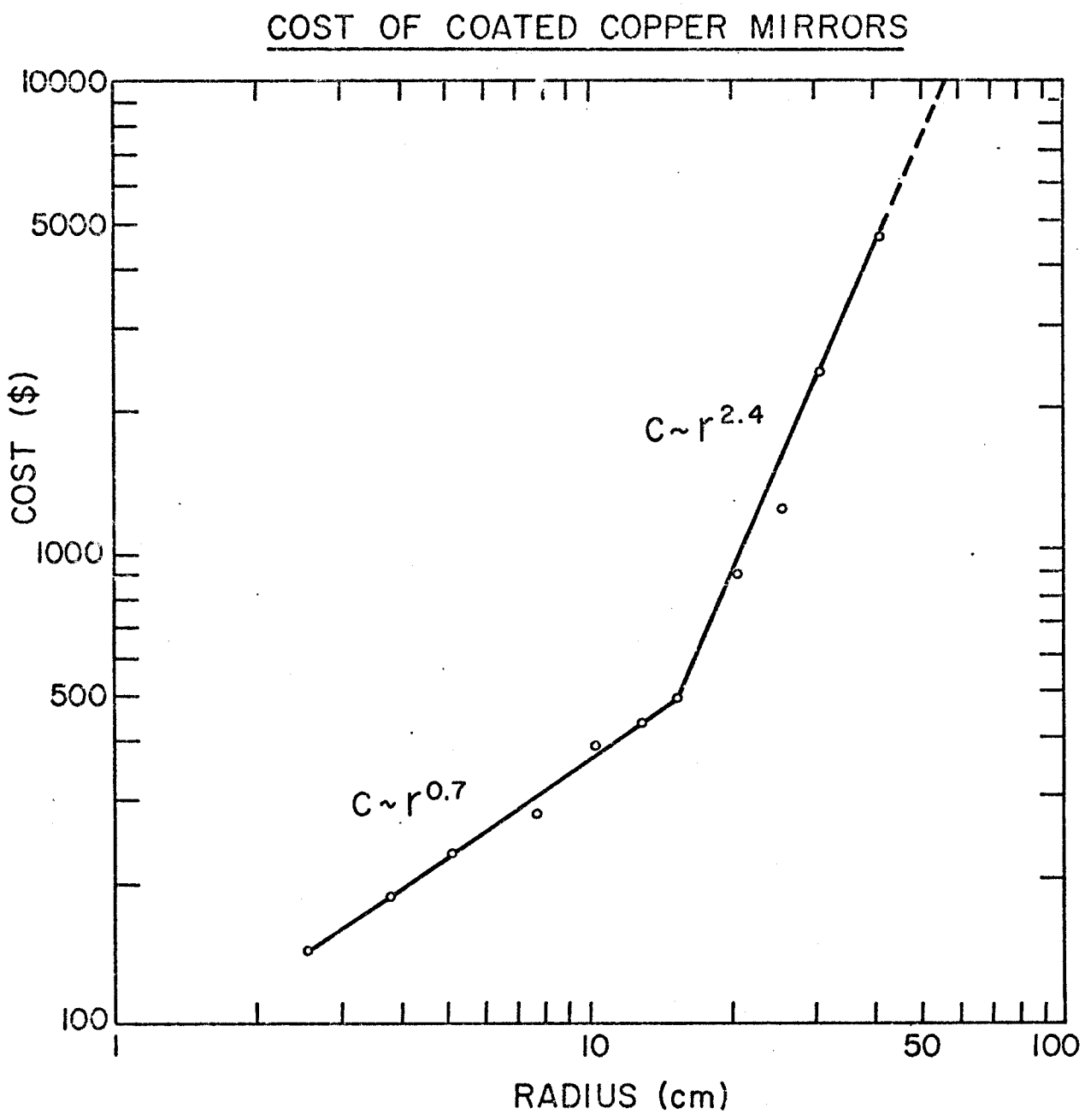
COST OF COATED COPPER MIRRORS
10000
5000
1000
500
100
COST ($)
C ~ r^2.4
C ~ r^0.7
1
10
50
100
RADIUS (cm)

FIGURE 1

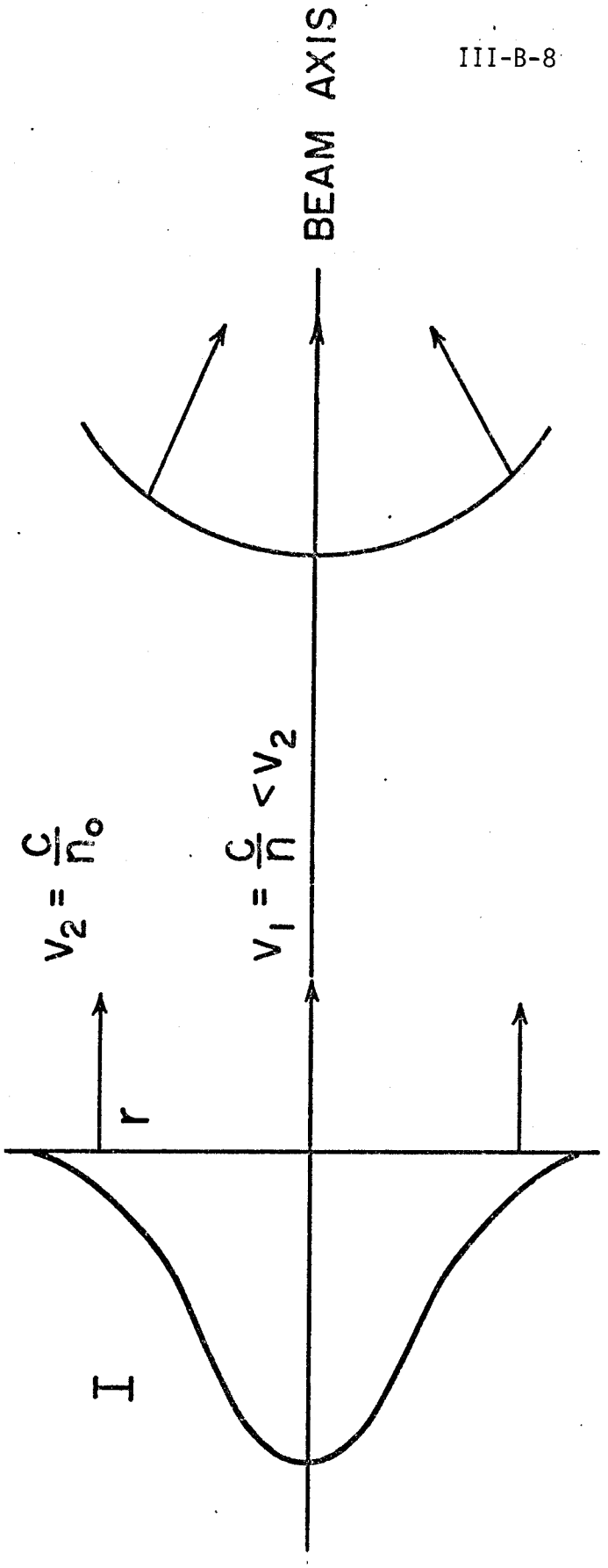

FIGURE 2

$$B = \frac{2\pi}{\lambda} \int \frac{n_2}{n} \langle E^2 \rangle \, d\ell \qquad (6)$$

where λ is the vacuum wavelength, and n_2 is the nonlinear part of the refractive index

$$n = n_0 + n_2 \langle E_2 \rangle \, . \qquad (7)$$

The time averaged field is related to the beam intensity via

$$\langle E^2 \rangle = \frac{4\pi\Phi}{nc} \, . \qquad (8)$$

A related nasty phenomenon is small-scale self-focusing[6], which is the exponential growth of tiny ripples into fiercely intense filaments. While the mathematical theory is more complicated in this case, it turns out that the growth rate of the most unstable (spatial) mode is given by eq. (6). In practice one finds damage due to small-scale self-focusing for beam fluctuations of 5-10 GW/cm^2. Such ripples may arise from Fresnel diffraction at any of the many apertures in a laser chain, from dust on optical surfaces, or particulate inclusions. Self-focusing can also produce serious nonlinear beam divergence, with attendant loss of beam energy. Diffraction rings may be minimized by the use of semi-opaque "soft apertures", as well as by pinhole filters, at the expense of some energy loss. Both large- and small-scale self focusing are now well understood theoretically; such calculations form an essential part of the design of any high-power laser system. While most present-day systems are limited to about a terrawatt per beam, larger peak powers can be handled by means of larger apertures.

Even in a gas laser a certain amount of refractive material is unavoidable, for example in windows, spatial filters and Faraday rotators. In this case we can use the B-integral to derive an upper bound for the maximum length of refractive material in the system.

To avoid whole-beam self-focusing it is required that

$$B < 4\pi \ , \tag{9}$$

and to avoid small-scale self-focusing the more stringent condition

$$B < 2\pi \tag{10}$$

must be obeyed.[6] Suppose we have a peak power P_{max} and a total aperture area A_{TOT}. Then

$$\Phi = \frac{P_{max}}{A_{TOT}} = \frac{nc\,\langle E^2 \rangle}{4\pi} \ . \tag{11}$$

Thus, to avoid small-scale focusing, we require as an upper bound (ignoring gain and changing beam area as we proceed down the laser chain),

$$\frac{8\pi^2 n_2 \ell P_{max}}{\lambda N c A_{TOT}} < 2\pi \ . \tag{12}$$

Taking $n = 1.5$, $n_2 = 5 \times 10^{-14}$ esu, $\lambda = 1$ μm and $P_{max} = 10^{15}$ W $= 10^{22}$ ergs/sec gives

$$\ell/A_{TOT} < 7.2 \times 10^{-4} \text{ cm}^{-1} \ . \tag{13}$$

Thus, if $A_{TOT} = 2.5 \times 10^5$ cm^2 (nonuniform illumination),

$$\ell_{max} = 179 \text{ cm} \tag{14}$$

and if $A_{TOT} = 4.7 \times 10^5$ cm^2 (uniform illumination),

$$\ell_{max} = 336 \text{ cm} \tag{15}$$

These are to be interpreted as absolute upper bounds on ℓ. As a check, note that Φ at the exit aperture is 4 GW/cm^2 and 2.15 GW/cm^2, for nonuniform and uniform illumination, resp., just below the "threshold" of 10 GW/cm^2. These numbers show that in this case, providing an aperture large enough to prevent surface damage automatically takes care of self-focusing problems, allowing up to a few meters of low-n_2 glass in the system.

III.B.3.d Thermal Distortion

A temperature rise of only a few tenths of a degree can result in several fringes deformation of a copper or molybdenum mirror.[10] One way to combat this problem is by actively cooling the mirror, i.e. passing a fluid through the body of the mirror. The present state of the art can hold thermal distortion to less than one micron at a laser flux of 150 KW/cm^2, about 5 orders of magnitude less than the envisioned flux at 10^{10} W/cm^2. Further research in this area is indicated.

III.B.4 Location and Protection of Final Mirrors

High quality bare metal mirrors are so delicate that they can be rendered useless[10] by breathing on them! This statement graphically illustrates the point that protection of the final mirrors in a reactor environment is a nontrivial problem deserving considerable thought. Our first impulse is to put them as far away from the action as possible. Figure 3 depicts one possible scheme.[11] This is more readily accomplished in the case of nonuniform illumination, the distance being limited only by diffraction and pointing errors. Uniform illumination places constraints on the f/no. so that apertures must go up proportionally as distance is increased. Cost and manufacturing difficulty of large aperture mirrors then become the limiting factors. There is only one 5m mirror in existence.

The final mirror surfaces will be directly exposed to X-rays, charged particles, neutrons, charge-exchange neutrals, and possibly macroscopic debri from imperfect implosions, besides the laser itself. X-rays fluences can be held to innocuous levels by keeping the minimum distance above 10 meters.

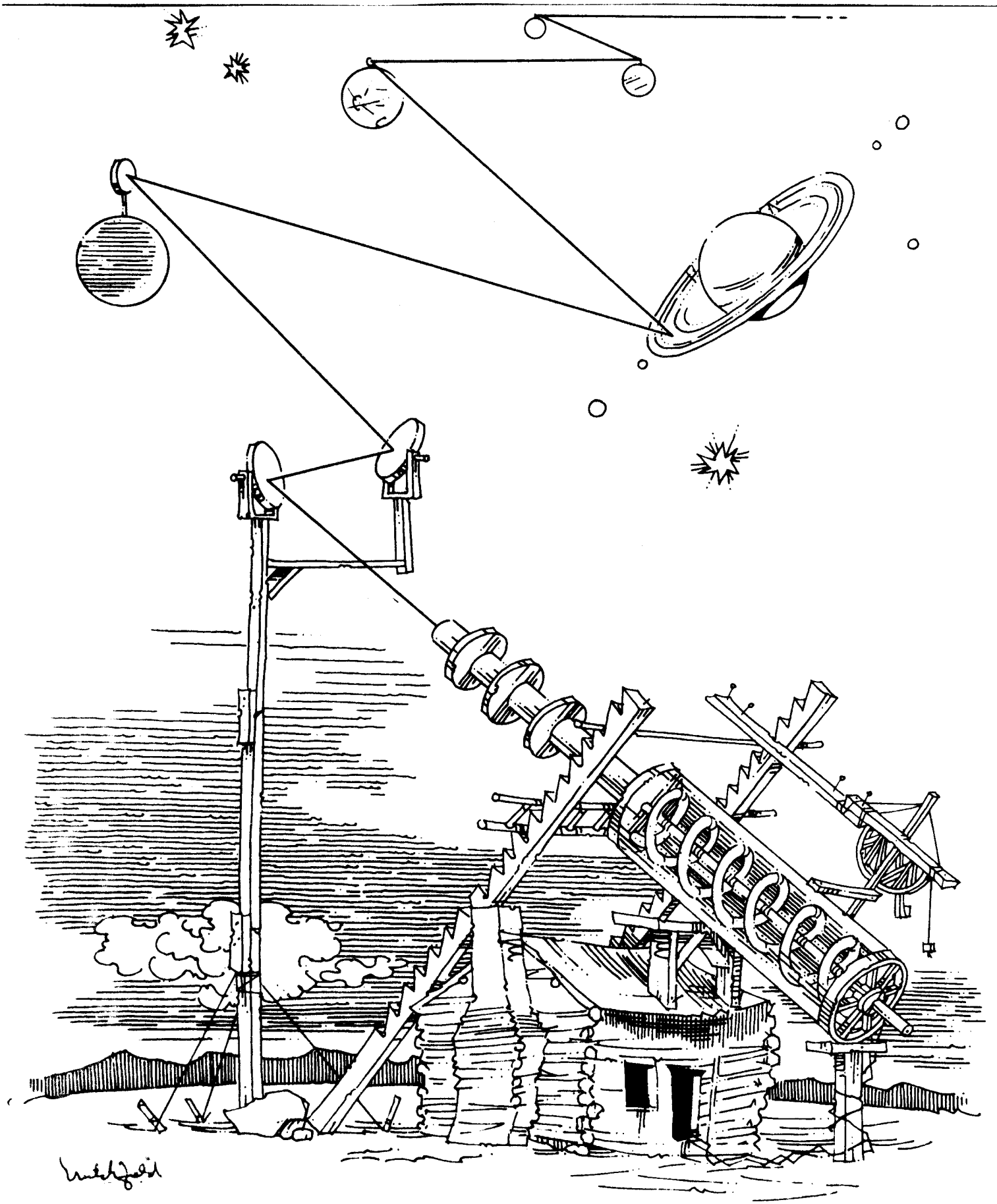

FIGURE 3

(Surface melting can be further discouraged by actively cooling the mirrors). Charged particles can probably be diverted by magnetic fields. Individual macroscopic particles may be caught by a disposable cover plate. It may also be desirable to blow jets of neutral gas across the mirror surfaces to remove dust particles. This leaves only the neutrons.

Since 14 MeV neutrons will strike the final mirrors, it behooves us to understand quantitatively the various processes that contribute to swelling, such as point defect accumulation, growth of voids and helium formation via (n,α) reactions. The amount of swelling (and therefore the mirror lifetime) may then be optimized by controlling the mirror substrate material, distance from the target, and ambient temperature. This problem is presently under active investigation.

III.B.4.a Role of Diffraction

The spot radius produced by an ideal lens or mirror is

$$\rho = 1.22\ \lambda\ (\text{f/no.})\ .$$

This is the location of the first minimum of the familiar far field Airy pattern, containing 84% of the total beam intensity. In particular, we easily obtain the following tabulated values:

λ \ F	2.5	5	10
1 μm	3	6	12
10 μm	30	60	120

Table 2. Spot size in microns

These numbers show that there is no difficulty in hitting a 1 mm radius target in any expected case, but that uniform illumination ($F \approx 3.5$) might prove difficult at longer wavelengths.

Diffraction can be a serious problem for annular beams, if the inner radius is close to the outer radius. Detailed treatment of this problem is underway.

III.B.4.b Pointing Errors

If the final mirror is tilted a small angle ϕ, the axis will be displaced a vertical distance $\Delta = f\phi$, where f is the focal length. Assuming f = 10 m, it follows that maintaining $\Delta < 10$ μm requires the ability to control the tilt angle ϕ to within 1 μ rad. The SHIVA experiment at LLL should be instructive in exploring the limits of our ability to simultaneously control the positioning of many optical elements. The sum total (in some statistical sense) of all of the positioning errors and optical aberrations is termed the "error budget," and must be monitored as carefully as the cumulative B-integral in designing an optical system.

References for Section III-B

1. R. E. Kidder, Nucl. Fusion 16, 3 (1976).

2. R. L. McCrory and R. L. Morse, LA-6420-MS, July 1976.

3. D. V. Giovanielli, Bull. Am. Phys. Soc. 21, 1047 (1976).

4. T. T. Saito and L. B. Simmons, Appl. Optics 13, 2647 (1974).

5. T. T. Saito, Appl. Optics 14, 1773 (1975).

6. L^3 1974 Annual Report, UCRL-50021-74, p. 200, et. seq.

7. A. J. Glass and A. H. Guenther, Electro-Optics Systems Design, June 1976, p. 28.

8. A. J. Glass and A. H. Guenther, Laser Induced Damage in Optical Materials, 7th ASTM Symposium Proceedings, 1975.

9. Spawr Optical Research, Inc., Corona, Ca., Data Sheet #110, February 1976.

10. W. J. Spawr and R. L. Pierce, "Metal Mirror Selection Guide," SOR Report No. 74-004, Spawr Optical Research, Corona, Ca., May 1976.

11. Drawing by William Crutchfield, from M. Tuchman, Art and Technology, Viking Press (N.Y.) 1971, p. 20, reproduced by permission of the artist.

12. H. E. Bennett, in Laser Induced Damage in Optical Materials: 1976, A. J. Glass and A. H. Guenther, eds. (NBS Special Publication 462, 1977) p. 11.

13. M. Sparks, J. Appl. Phys. 42, 5029 (1971).

14. M. Monsler, Optical Engineering 15, 158 (1976).

IV. Lasers for Laser Fusion

A. Introduction

In any laser fusion scheme, the laser is, of course, of primary importance. Its performance (or lack thereof) could be the difference between the success or failure of a reactor system. Due to the combined lack of experimental results and a lack of a complete physical understanding of the laser-pellet interaction, the exact requirements needed for the ideal laser are still in question. However, for simple shell targets the necessary characteristics are generally known[1,2] and are summarized in Table I. These characteristics have been divided into two classes: those that are necessary to implode a pellet and those necessary to make a practical and economic reactor system. It is quite probable that these requirements could be relaxed considerably for a hybrid reactor system.

From the requirements listed in Table I, one can infer a number of properties that would be exhibited by the ideal laser. First, the wavelength range of 3000-6000 Å implies an electronic transition. The wavelength range is desirable to efficiently couple laser energy into the pellet. The lower cutoff at 3000 Å is dictated by two-photon absorption damage suffered by optical components at shorter wavelengths and the lack of efficient reflectors. Recent experiments, however, indicate less wavelength dependence than originally thought and may allow wavelengths of at least 2-3 μm and possibly even 10 μm.

The short pulse widths of 0.1-1 nsec are necessary to obtain a satisfactory implosion and imply two things of the laser. The first is that the energy must be stored directly in the upper laser level as collisional processes are too slow to repopulate the level during the pulse. This again suggests an electronic transition. The second is that the upper laser level should have

TABLE I

REQUIREMENTS OF THE LASER FOR LASER FUSION

Performance Requirements

Energy	$\sim 10^5 - 10^6$
Peak Power	~100 - 1000 TW
Pulse Width	0.1 - 1 nsec
Wavelength	3000 - 6000 Å (0.3 - 10 μm)
Pulse Shape	$P(t) \sim \frac{P_o}{(1 - t/t_o)^2}$

Practical Considerations

Efficiency	≥10%
Pulse Repetition Rate	10 - 100 sec^{-1}
Small Signal Gain	0.001 - .01 cm^{-1}
Stored Energy Density	$10^2 - 10^3$ J/liter
Stimulated Emission Cross Section	$10^{-19} - 10^{-20}$ cm^2
Low Capital Costs and Low Maintenance	

a long lifetime (at least several microseconds) in order that energy can be transferred over a "long" period of time instead of the technologically difficult nanosecond time scales.

The high repetition rates that will be necessary dictate that the laser medium be in the gas phase in order that waste heat can be removed by convection. A gas medium also eliminates permanent optical damage that can result in solid systems. Finally, gas systems tend to have lower costs and maintenance.

The gain of the system must be relatively low. This helps to minimize both parasitic oscillations which will reduce the energy available to the main pulse and prepulsing which can destroy a pellet before the primary pulse arrives. A low gain also serves to relax the requirements on the isolation components of the optical system.

The efficiency, of course, should be as high as possible since the laser input power will constitute a major portion of the plant's recirculating power. The minimum efficiency required will depend on a number of factors, but one desires about 10% for a practical system. This implies saturated operation of the amplifiers which gives the most efficient extraction. This in turn implies that the beam flux should saturate near the limits imposed by the optics (1-10 J/cm^2). Since the saturation energy flux is equal to $h\nu/\sigma$, the stimulated emission cross section, σ, should be $\sim 10^{-19}$-10^{-20} cm^2 for a 5000 Å laser.

Obviously, there is no existing laser which satisfies all these requirements and there may never be such an ideal laser. Therefore, one must evaluate each and decide on the laser which optimizes the system. The next section evaluates both "proven" laser systems and potential systems in light of these requirements.

IV-B. Survey of Lasers for Laser Fusion

IV-B-1. The Iodine Laser

The iodine laser is based on the photodissociation of any of many different perfluoroalkyl iodides[3,4] which yield excited atomic iodine. The two compounds giving the best results to date[4] are i-C_3F_7I and n-C_3F_7I with C_2F_5I, CF_3I and CD_3I also giving reasonable results. A typical reaction would then be

$$i\text{-}C_3F_7I + h\nu \rightarrow C_3F_7 + I^*$$

which results in lasing on the $^2P_{1/2} \rightarrow {}^2P_{3/2}$ transition (1.315 μm) of iodine. The absorption band for the photodissociation process in C_3F_7I peaks at 270 nm, has a bandwidth of ~36 nm and has an average absorption coefficient of 1.14×10^{-2} $(Torr\text{-}cm)^{-1}$.[5]

The lasing levels actually have a hyperfine structure[4] as shown in Fig. 1. In addition, these levels can be further split by the magnetic fields generated by the flashlamps. This leads to complications in energy extraction. It has been determined that the lower levels mix rapidly enough on subnanosecond time scales that they may be considered as one state but that the upper levels do not.[6] Thus, in order to extract the maximum energy, both transitions must be amplified which gives a maximum extraction efficiency of 66%.[6] If only the transition with the higher gain ($F = 3 \rightarrow F = 4$) were to be amplified, the efficiency would drop to 46%.[6]

A list of important parameters of the iodine laser is given in Table II. To date, the laser has been pulsed to 300J with pulse widths ranging from 1-3 nsec.[6]

IV-B-2. Advantages of Iodine Lasers

The primary advantage of the iodine laser is that its wavelength is the shortest of the "proven" high-power gas lasers, although at 1.315 μm it still may be longer than desirable.

FIGURE 1

THE IODINE LASER

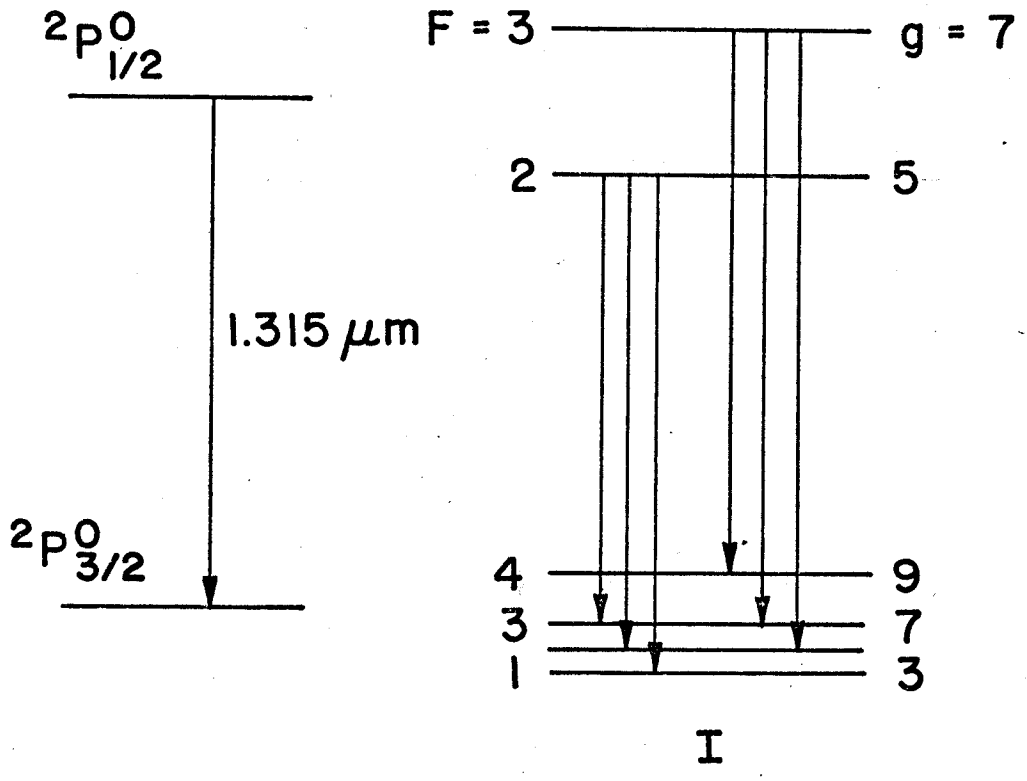

$$C_3F_7I + h\nu \longrightarrow C_3F_7 + I^*$$

I^* → LASES AT 1.315 μm

TABLE II

PROPERTIES OF THE IODINE LASER

Wavelength	1.315 μm
Small Signal Gain	~ 0.1 cm^{-1}
Stimulated Emission cross section	$1.37 \times 10^{-16}/P_{tot}$ ~ 1.37×10^{-19} at 1000 torr
Pulse Width	0.1 - 1 nsec
Extractable Energy	0.72 J/l-Torr (C_3F_7I)
Efficiency	~ 0.5%

A second great advantage is that pulse lengths as short as 0.1 nsec can be effectively extracted. An additional advantage is that iodine is flash pumped. This allows one to go to very large apertures in order to increase the total energy out without increasing the energy density. This is an advantage over discharge pumped lasers whose apertures are limited by the electric field that can be applied. Finally, the iodine laser has shown that it is capable of producing high energy pulses.

IV-B-3. Disadvantages of the Iodine Laser

Although an attractive system, the iodine laser suffers from a serious drawback, its efficiency. If standard flashlamps are used to pump the laser, this efficiency will be limited from about 1/2% to 1%, which seems low for a pure laser fusion reactor. Another problem is that of regeneration of the laser medium as not all the gas recombines to form the original molecule after having been dissociated. Thus, some chemical reprocessing must be done which will reduce the net efficiency even further. A potential problem could result from the use of flashlamps. State-of-the-art flashlamps are simply not adequate. There appears to be no insurmountable problem in designing lamps which can be pulsed at the necessary repetition rates but a serious question to consider is the failure rate. If this rate is too high, it could lead to excessive maintenance requirements.

IV-B-4. Possible Improvements

The question to be asked now is whether these disadvantages can be alleviated. The poor efficiency observed is not something inherent to the system (~20% quantum efficiency) but is the result of using flashlamps, since only a small fraction of their output lies in the proper absorption band. Thus a method of improving the efficiency is to utilize non-equilibrium flash sources such as electron-beam generated fluorescence of molecules like XeBr* which

exhibit strong spontaneous emission in the absorption band of C_3F_7I. It is thought that use of such a source could increase the efficiency, but only to ~1 or 2%.[7] This might also help to eliminate the possible drawbacks of flashlamps. The flashlamps themselves can probably be improved by such methods as doping to yield net efficiencies of 1-1 1/2%. There appears to be little one can do to improve the regeneration problem. Fortunately, the molecule which gives the best laser response (i-C_3F_7I) also seems to have the best regeneration properties. It is thought that shortening the pump time would improve the regeneration. Perhaps a catalyst could be found which would improve regeneration without adversely affecting the laser.

An alternative approach which should probably be more thoroughly explored than it has been to date is the dissociation of the iodine by direct electron impact. Pumping by this method has been demonstrated[8] but it has not been demonstrated whether a substantial increase in the possible efficiency could actually be realized with electron pumping. Nor has it has been demonstrated that an electron pumped laser can be effectively scaled to the required size. Because of the basic attractiveness of the iodine laser, it would seem very worthwhile to pursue electron pumping because of the possibility of improving the efficiency. The use of electron pumping would result in a tradeoff of advantages with a flash pumped system. One would lose the advantage of being able to go to large apertures of the flash system but would gain a more compact system which would possibly be more reliable.

IV-B-5. Summary of Iodine Lasers

To summarize, the iodine laser is a very attractive system except for the fundamental problem of efficiency. This drawback would appear to eliminate this laser from any practical pure laser-fusion reactor scheme. However, when

considering some form of hybrid system in which the efficiency requirement could be greatly relaxed, the iodine laser becomes quite promising. Also if shorter wavelengths should prove to be essential, this would work greatly to the advantage of the iodine laser as opposed to a CO_2 laser, for example.

IV-B-6. The HF Chemical Laser

The hydrogen fluoride chemical laser, as the name implies, is based on any of a large number of chemical reactions which yield HF in an excited state. Thus, it is actually the chemical reaction that pumps the laser, creating a population inversion on many vibrational-rotational transitions of HF. A simplified potential energy diagram is shown in Fig. 2. Lasing occurs on transitions with wavelengths varying from approximately 2.7-3.2 μm.

Although a number of reactants yield a laser, the ones which promise the greatest electrical efficiency are F_2 and H_2 because they can undergo the following chain reaction:

$$F + H_2 \rightarrow (HF)^* + H \qquad (1)$$

$$H + F_2 \rightarrow (HF)^* + F \qquad (2)$$

in which the products of each reaction feed the other. Reaction (2) has the most energy available and populates higher vibrational levels ($v \leq 6$) of HF than does reaction (1) ($v \leq 3$) but unfortunately distributes the energy relatively uniformly[9] which minimizes the inversion. Reaction (1) on the other hand, preferentially populates the upper levels ($v = 3,2$) and contributes most to the inversion.[9] Generally, the proposed high power HF lasers would utilize an electron beam initiated chain reaction between H_2 and F_2. In addition to H_2 and F_2, these gas mixtures will usually contain a small percent of oxygen to stabilize the mixture,[10] some SF_6 to both increase the electron beam's energy deposition in the gas and increase the initial

The Hydrogen-Fluoride Chemical Laser

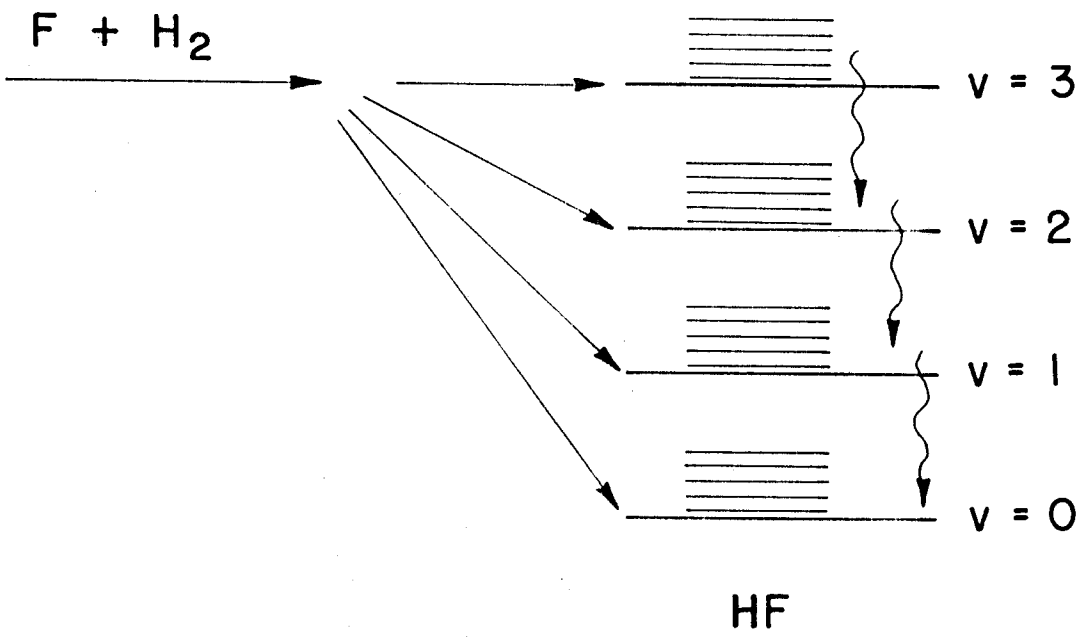

$$H + F_2 \longrightarrow (HF)^* + F$$

$$F + H_2 \longrightarrow (HF)^* + H$$

LASES AT ~2.7 - 3.0 μm

FIGURE 2

atomic flourine concentration,[11] and sometimes a diluent such as He, Ar, or N_2. Other systems using SF_6 instead of F_2 may also be used. This would have the disadvantages of lower electrical efficiency and probably higher costs, but a higher chemical efficiency would make the net efficiency about the same and the difficulties of gas handling would be greatly reduced.

The general characteristics of the HF laser are shown in Table III. The performance to date has been most impressive as far as total energy out at 4 kJ but the pulse width was rather long, being 26 nsec.[12]

IV-B-7. Advantages of the HF Laser

The primary advantage of the HF laser is the very large energies that can be extracted. The second primary advantage is the relatively high efficiency of the system. The electrical efficiency should be at least 10%[13] for SF_6 and C_2H_6 mixtures, and probably about 100% for H_2 and F_2 mixtures.[14,15] The chemical efficiency should be about 10-15%.[12,15] Thus, the total efficiency is quite reasonable. However, the cost of regeneration of the gasses will reduce the net efficiency to about 3-5%. The high electrical efficiency is also advantageous from the standpoint of relaxing the requirements on the power supplies.

IV-B-8. Disadvantages of the HF Laser

The wavelength of HF at 2.7-3.0 μm is not ideal but it is still in the range of iodine and because of the high efficiency there is the possibility of up conversion. The major difficulties with HF are its high gain and the fast relaxation of the lasing levels. The high gain means that there will be problems with prepulsing which both reduces the energy available to the main pulse and can destroy the pellet before the main pulse arrives, and parasitic oscillations which also reduce the energy available to the main pulse. The fast relaxation means that HF is not a storage medium - one must

TABLE III

PROPERTIES OF THE HF LASER

Wavelength	~ 2.7 - 3.0 μm
Small Signal Gain	0.1 - 1.0 cm^{-1}
Stimulated Emission cross section	$4.4 \times 10^{-7}/\Delta\nu$ cm^2
	~ 2.5×10^{-17} at 1 atm HF
Pulse Width	26 nsec (~ 1 nsec)
Extractable Energy	150 - 185 J/l
Efficiency (Electrical)	~ 100%
Efficiency (Chemical)	10 - 15%

extract the energy as it is generated. Thus, one loses a primary advantage of lasers, their pulse compressing capability. Because of this, the pulse lengths of HF tend to be of the order of the pumping rate which is coupled to both the pressure and electron-beam pulse lengths. With state-of-the-art systems this results in unacceptably long pulses.

A final problem is the need for safe and controlled handling of multi-atmospheres of H_2 and F_2. Of particular difficulty will be the rapid mixing and burning that will be required for the high repetition rates necessary.

IV-B-9. Possible Improvements

The problem that HF is not a storage medium can be effectively eliminated if the rate of reaction can be increased enough that the instantaneous energy available is sufficient to meet fusion requirements. There are two ways of increasing the reaction rate. The first is to increase the pressure which increases both the rate of reaction and the total energy available. Calculations by Jensen[15] indicate that by increasing the pressure to 13 atm. of F_2 and 3 atm. of H_2 that a power level of 1 TW/liter can be achieved with state-of-the-art electron beams. Of course, handling such high pressure mixtures would be extremely difficult. The second approach is to increase the rate of production of atomic fluorine. This could be done be decreasing the time interval over which the electron beam energy is dumped into the gas and by using additives such as SF_6 which improve fluorine production. However, at best the burn time will still be a few nanoseconds long.

Since such high powers can apparently be extracted without energy storage, it has been suggested that prepulsing can be eliminated by running an off target beam through the amplifier until the primary beam arrives.[16] Since no energy is stored, no energy is lost to the amplified beams. Such a scheme has been demonstrated at low energies.[16] It was found that problems of parasitics can be eliminated if a beam is amplified during the entire pumping

time and if the amplified beam fills the entire amplifier volume. A 4 nsec beam has been successfully switched from a 30 nsec pulse by changing the plane of polarization of the incoming beam by 90° for 4 nsec and passing the outgoing amplified beam through a dielectric set at the Brewster angle so that the original beam was passed but the 4 nsec pulse was reflected. It has yet to be demonstrated that this method will work effectively at the much higher energies required. Even if successful, this method will decrease the net efficiency as much of the energy is wasted. An alternative is to successively pass several short, smaller beams in varying directions through different regions of the amplifier (see Fig. 3). It is thought that a sufficient amount of the amplifier volume will be filled with each beam to suppress parasitics. In such a manner, much more usuable energy could be extracted in several short pulses.

It should be pointed out that since the pulse width of HF is related to the reaction rate[12], increasing the pressure not only increases the total power but also decreases the pulse width. However, to efficiently take advantage of this the electron beam pulse widths must be reduced to the same time scale which implies 1 to 2 nsec electron beam pulses, which may not be practical. This, coupled with the development of short pulse, multiline oscillators, could yield pulses at least as short as 5 nsec.

Two other suggestions have been made which should be mentioned.[17] The first is to utilize a traveling wave excitation scheme in which instead of exciting the entire volume of the amplifier simultaneously, one excites only a small portion of the volume, sweeping this excitation pulse along in front of the beam to be amplified. In this manner, one does not allow time for the parasitics to build up or relaxation to occur. The second idea is to suppress oscillation on $\Delta v = 1$ transitions and force oscillations on the $\Delta v = 2$

MULTIBEAM EXTRACTION FOR HF AMPLIFIER

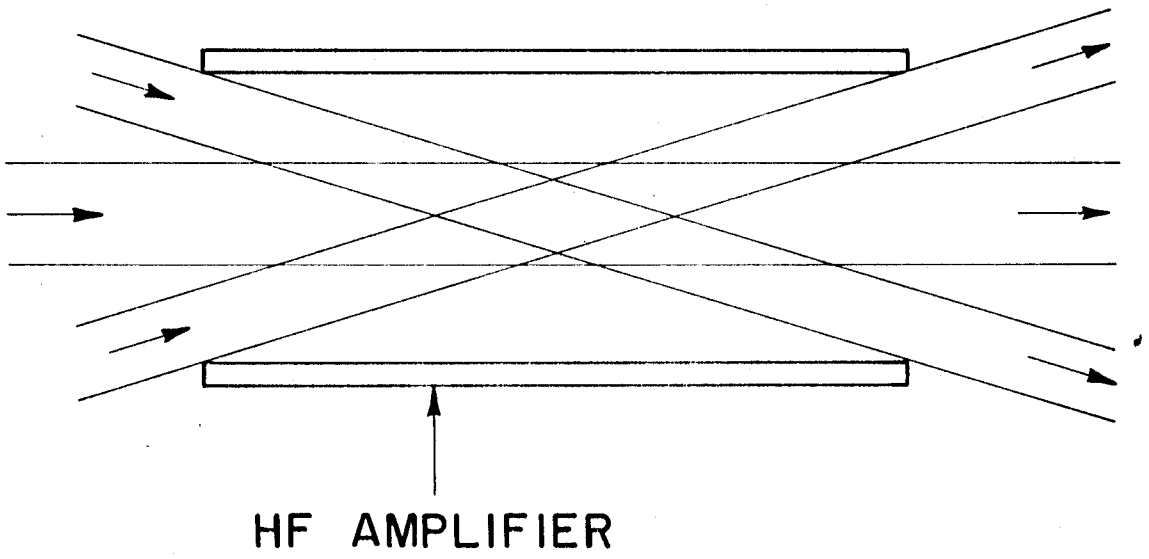

FIGURE 3

transitions, as has been observed in DF.[18] This would accomplish two things. First, it would effectively double the frequency and secondly, it would reduce the gain since $\Delta v = 2$ transitions have smaller stimulated emission coefficients. Thus, it would help to alleviate a couple of the problems associated with HF.

Finally, to help minimize the effects of the regeneration of HF into H_2 and F_2, it has been suggested that the heat generated by the chemical reaction be used to generate electricity.[15] This could substantially reduce the net energy cost of the electrolysis of the HF. Utilizing such a scheme, Jensen[15] has claimed a net efficiency of approximately 8% could be obtained for a large optimized system.

IV-B-10. Summary of the HF Laser

To summarize, the HF chemical laser has several serious problems in view of the requirements of laser fusion. How successful any of the proposed solutions will be remains to be seen. However, given that it has a high potential efficiency and a wavelength that is not too unreasonable, it would seem that a search for solutions would certainly be worthwhile. The possible 100% electrical efficiency would also greatly relax the requirements on the power supplies as compared to a 10% efficient system. Thus, even in light of its difficulties, the HF laser is an attractive system to consider for laser fusion applications.

IV-B-11. The CO_2 Laser

Unlike either the iodine or HF lasers, the CO_2 laser is not a chemical laser but is pumped directly by electron impact or by vibrational excitation transfer from excited nitrogen molecules. A simplified potential energy diagram of the CO_2 system is shown in Fig. 4. Lasing generally occurs on the vibrational-rotational transitions between the (001) and (100) levels of CO_2 (~10.6μm) but can also occur between the (001) and (020) levels (9.6μm)

The CO_2 Laser

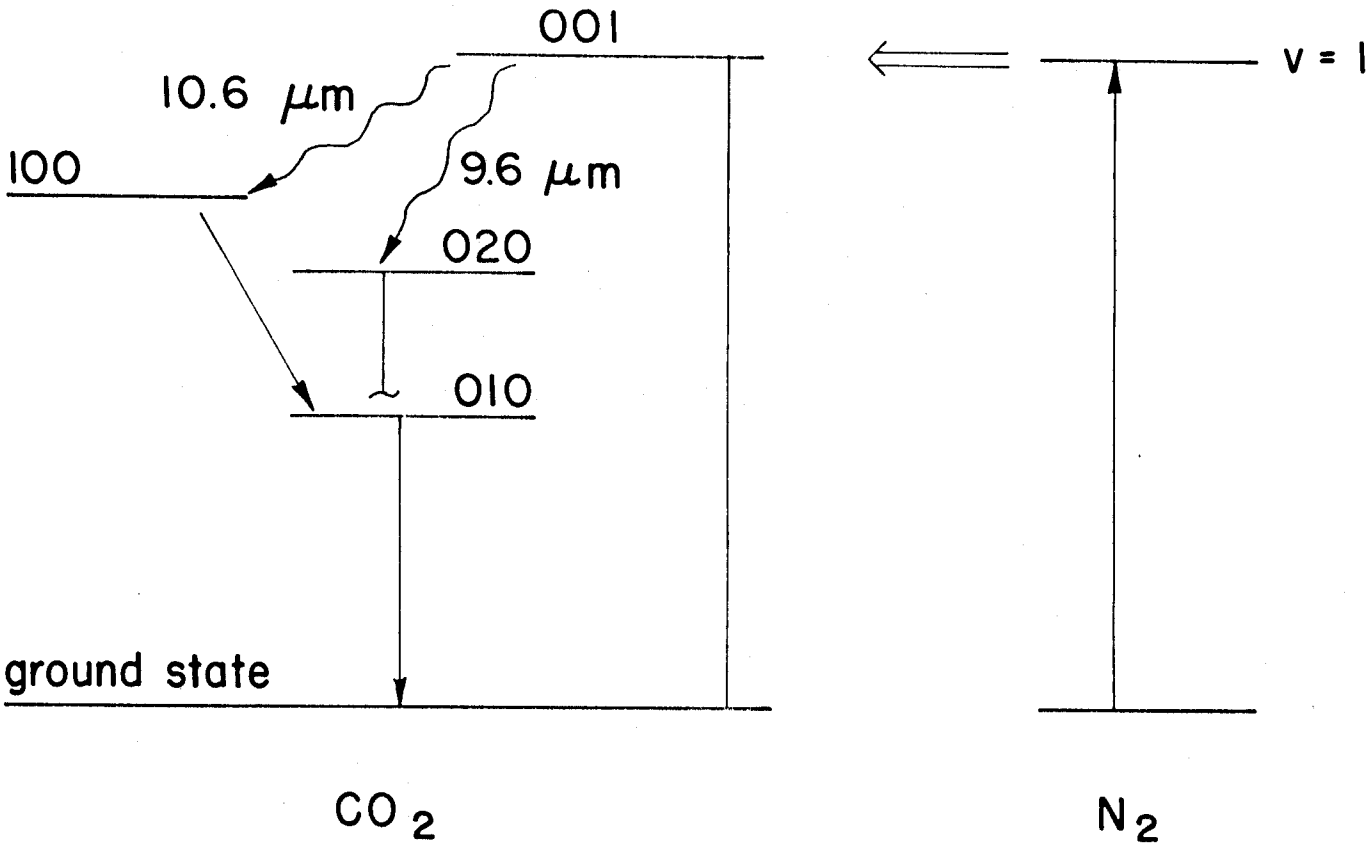

$$CO_2 + e \longrightarrow CO_2^* + e$$

$$CO_2 + N_2^* \longrightarrow CO_2^* + N_2$$

$$\downarrow$$

LASES AT 10.6, 9.6 μm

FIGURE 4

which becomes quite important for short pulse extraction.[19] The three numbers identifying the levels refer to the various vibrational modes of the CO_2 molecule. The upper laser level (001) is the first asymmetric stretch mode, while the lower (100) level is the first symmetric stretch mode and the (020) level is the second bending mode.

The CO_2 laser is potentially very efficient having a quantum efficiency of over 40%. Also a substantial percentage of the direct electron impact energy into the CO_2 molecule is eventually channeled into the upper laser level. In addition, much of the energy going into the N_2 is channeled into its first vibrational state which is rapidly transferred directly to the CO_2's upper laser level. As a result, overall efficiencies of about 30% can be obtained. Unfortunately, in the nanosecond time scales required, all the advantageous collisional processes become insignificant - the short pulse will interact only with those rotational levels which are directly connected to transitions in the incoming pulse. This greatly reduces the efficiency of the CO_2 laser. In order to obtain the maximum energy available, one must amplify as many rotational transitions as possible on both the 10.4 and 9.4 μm bands. Even this will limit the effeciency to about 2-5% unless one can successfully develop multipass amplifiers.

The general characteristics of the CO_2 laser are given in Table IV. The performance to date for CO_2 is ~600 J in 1.4 nsec[20] (250J in 1 nsec).

IV-B-12. Advantages of the CO_2 Laser

The most fundamental advantage of CO_2 is that it is capable of high energy output in relatively short pulses (.25-1 nsec). Also, the efficiency at 2-5% is not too unreasonable. Finally, it is a very well understood system and relatively simple in design (as compared to handling high-pressure HF for example).

TABLE IV

PROPERTIES OF THE CO_2 LASER

Wavelength	10.6 μm, 9.6 μm
Small Signal Gain	0.05 cm^{-1}
Stimulated Emission cross section (single line)	$\frac{1.5 \times 10^{-18}}{P(atm)}$ cm^2
Pulse Width	0.25 - 1 nsec
Extractable Energy	5 J/l
Efficiency	~ 2 - 5%

IV-B-13. Disadvantages of the CO_2 Laser

The principal disadvantage of the CO_2 laser appears to be its wavelength. Just how serious this is has not been fully determined but for simple shell targets, having a wavelength of 10.6 μm appears to be a decided disadvantage. Another problem is a gain which is higher than desirable which leads to problems of parasitic oscillations, prepulsing, and isolation of the amplifiers.

IV-B-14. Possible Improvements

If shorter wavelengths prove to be essential, the CO_2 laser's potential will be greatly reduced since up conversion to even 2.5 μm would be very costly in terms of the net efficiency of the system.

The problem of high gain can be solved in part by developing better isolating components. Also calculations indicate that there is an inherent buildup time for parasitic oscillations of about 1/2 μsec.[21] Therefore, if pumping can be accomplished in less than this time, the effects of parasitics can be minimized. Calculations also indicate that 95% of maximum gain can be reached by discharge pumping[21] in the 1/2 μsec allowed.

A second approach to alleviating the gain problem is to eliminate He from the laser mix. It has been found that relatively more energy can be extracted for a given gain and energy input in a heliumless mixture than with the usual laser mix.[20] By doing this one not only reduces the gain problem but increases the efficiency. Unfortunately, much higher voltages are required for a heliumless mixture putting an added burden on the power supplies although for a given energy input the current requirements would be greatly reduced.

IV-B-15. Summary of the CO_2 Laser

The CO_2 laser appears to be an attractive system with apparently no insurmountable problems in scaling to the required power levels. Also the

efficiency, while not ideal, is not too unreasonable. The main question is whether 10.6 μm will prove too long to effectively couple energy into the targets.

IV-B-16. Brand X Lasers

As can be easily concluded from the above, no known laser is ideal for laser fusion, particularly if wavelengths in the range of 3000-6000 Å prove to be essential. Therefore, a major search continues for the brand X laser.

Much effort has concentrated on atomic oxygen and, to a lesser extent, the other group VI elements, sulfur, seleniun and tellurium and elements with similar properties to these, nitrogen, carbon, lead and tin. These elements are characterized by having low lying electronic transitions which have small stimulated emission cross sections and relatively long lifetimes.[22] The fact that these states lie close to the ground state means that the quantum efficiencies are quite reasonable. Also since all the energy is stored in a single state, this energy can be readily extracted in short pulses. As an example, a potential energy diagram of oxygen is shown in Fig. 5 and its characteristics are listed in Table V. Such characteristics make these systems near ideal candidates for laser fusion lasers.

To date, atomic oxygen itself has not been observed to lase. However, the rare-gas oxides ArO, KrO and XeO have lased.[23,24] The oxides have the disadvantages of greatly reduced lifetimes ($\sim 10^{-6}$ sec) as compared to atomic oxygen itself (~1 sec) and reduced beam quality due to the high pressures required. The oxide lasers have used electron beams to excite mixtures of either O_2 or N_2O and the rare gas. The exact pumping mechanism is still in question. It has also been proposed that the atomic oxygen be pumped by the photodissociation of N_2O by Kr_2^* or Ar_2^* superfluorescence.[25] This is advantageous since there is near unity probability of dissociating $O(^1S_0)$ state

The Oxygen System

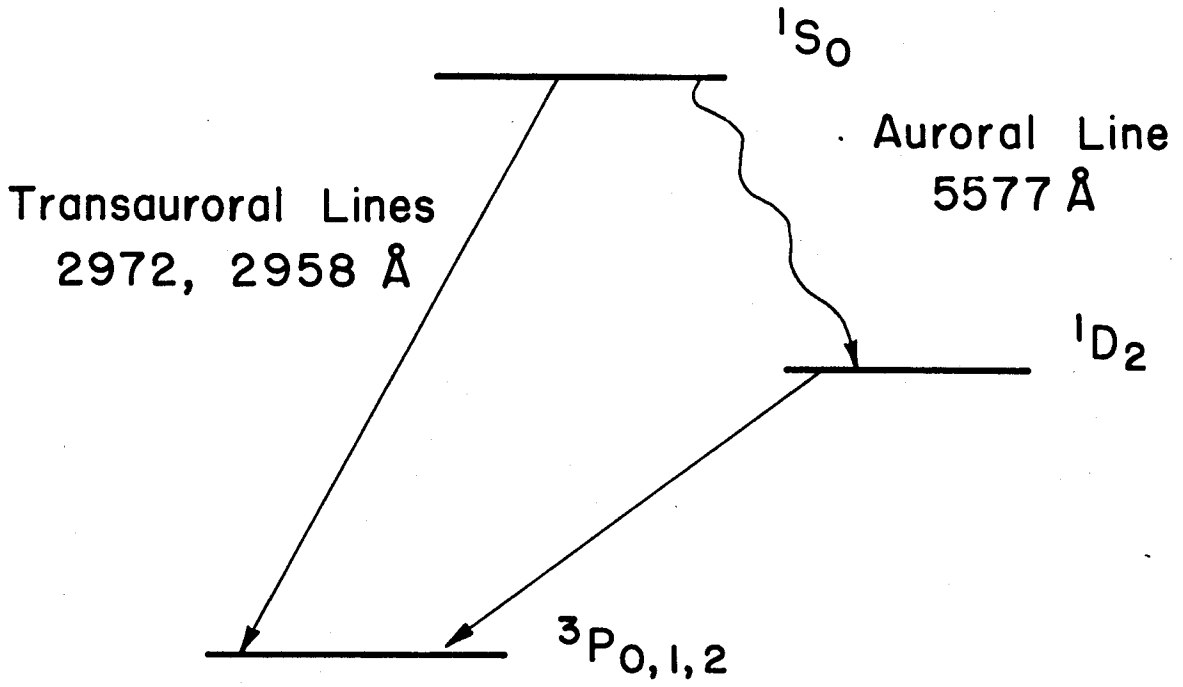

$$XO + \Delta E \longrightarrow X + O^*$$

$$\downarrow$$

LASES AT 5577 Å

FIGURE 5

TABLE V

PROPERTIES OF ATOMIC OXYGEN

Wavelength	5577 Å
Small Signal Gain	0.005 cm^{-1}
Stimulated Emission cross section	8.7×10^{-20} cm^2
Extractable Energy	5 J/l

PROPERTIES OF THE RARE-GAS OXIDES

	ArO	KrO	XeO
Wavelength (Å)	5576	5578	5300-5500
Stimulated Emission cross section (cm^2)	$\frac{3 \times 10^{-21}}{P(atm)}$	$\frac{1 \times 10^{-20}}{P(atm)}$	$\frac{2.9 \times 10^{-19}}{P(atm)}$

atoms from N_2O for wavelengths of approximately 1250-1400 Å. Gain has been observed using this method[26] with Ar fluorescence.

The main problem with oxygen appears to be the difficulty in developing an efficiently pumped system. The lack of a detailed understanding of the system makes it difficult to predict whether an efficient pumping scheme can be found. However, it is thought that efficiencies of 1 or 2% may be realistically obtainable.

Another group of lasers that have received great attention are the various excimer systems. Such systems have great potential and are extremely attractive for several reasons. First, the efficiencies by which the upper states are formed can be very high (as much as 30-50% of the energy deposited in the gas goes to form excited states). Secondly, excimers of interest exist only in the excited states, having dissociative ground states. Thus, essentially all the energy in the upper states can be extracted. Thirdly, due to the dissociative ground states (see Fig. 6) the excimers lase over a continium, resulting in broad bandwidths which allows very short pulse extraction.

Several excimer lasers have been developed. The Kr_2^*, Xe_2^*, KrF*, and ArF* lasers are all potentially efficient, high-power systems. However, their wavelengths are much too short and would cause severe two-photon damage to optical components and in addition there is a lack of efficient reflectors at these wavelengths. The XeF* laser's wavelength at 3540 Å is more reasonable but this laser suffers from a bound ground state. A number of metal vapor-rare gas excimers have been proposed but none have been proven and many suffer from strong self absorption. The search continues, however, with work being done on systems such as Hg_2* and HgCd*.

Schematic of a Typical Excimer System

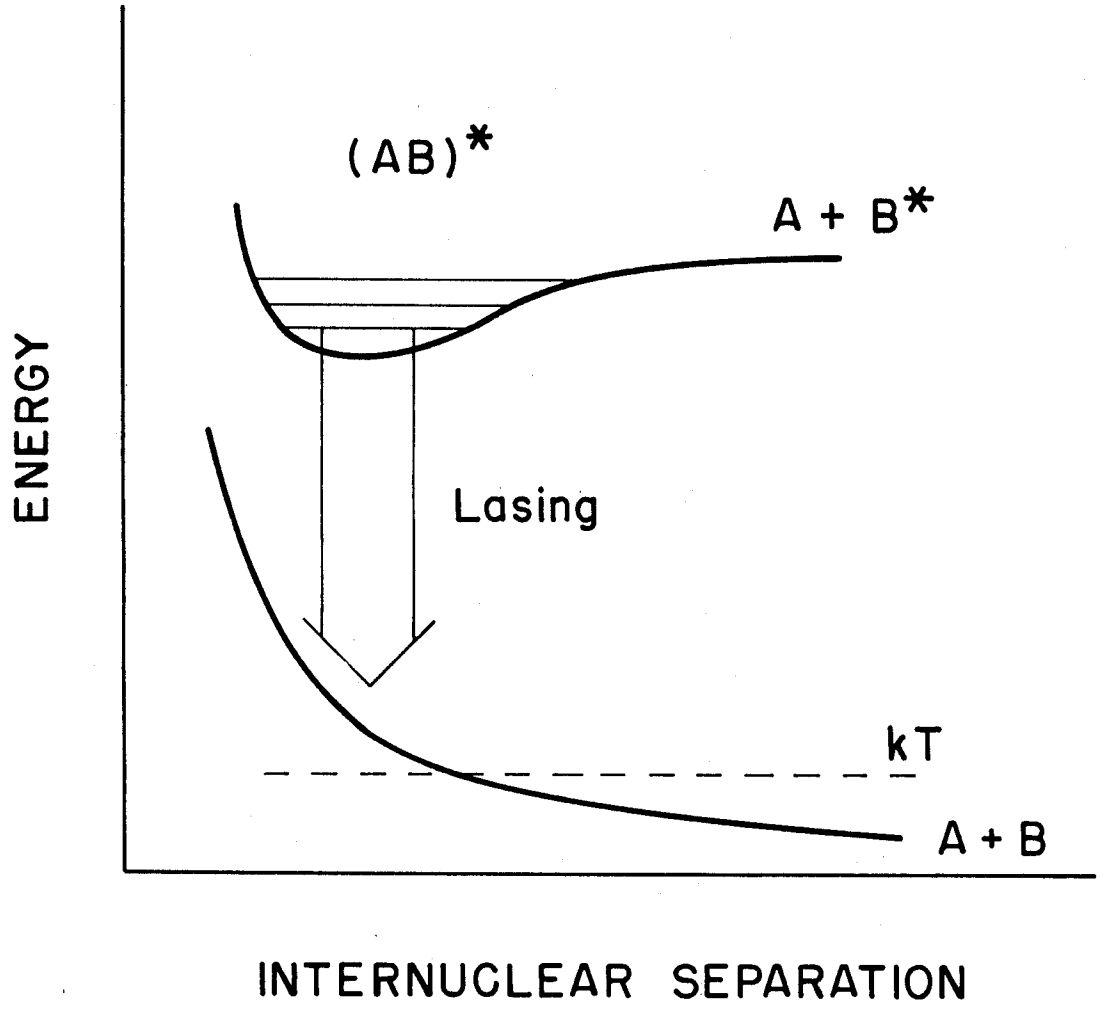

FIGURE 6

Another system that has been proposed is a gaseous phase neodymium or other rare earth laser. If successful, this would eliminate the problems associated with the glass such as heat removal, but if the laser were still flash pumped, the efficiency would probably not be greatly improved.

To summarize, there is no laser candidate that obviously will meet the ideal requirements for laser fusion. Oxygen appears to have all the makings, but it has yet to be shown that it can be pumped efficiently. It is clear that the development of these systems, as well as the search for new candidates, must continue if a more suitable laser is to be found.

IV-C. Design Study System

As stated above, there is no known or proposed system which obviously will meet the requirements for laser fusion. Which laser will prove optimum will depend much upon the ultimate wavelength, efficiency, and power requirements imposed by the physics of the laser pellet interaction as well as developments in the lasers themselves. Thus, choosing the "right" specific laser for our design at this time is virtually impossible, the choice thus becoming somewhat arbitrary. In light of this, we have chosen the CO_2 laser for our design. This is not to be construed as an endorsement for CO_2, but rather as a way to give a concrete basis to a generic design. It was felt that in order to meet the basic requirements for a laser fusion laser (a flowing gas system, 1 MJ total energy out, and energy densities dictated by the optics and not the laser medium) that the ultimate laser's electrical, mechanical and optical parameters will not be dramatically different from those of the CO_2 design. Of course, each laser will have its own particular requirements for such things as optical components, possible chemical reprocessing and flash as opposed to discharge pumping which will not be specifically considered in our design. However, the total design should be quite

similar and specific modifications readily made. (For example, flash pumped systems such as I*, O*, or Nd^{+3} will likely use electron-beam generated fluorescence to improve efficiencies and, thus, utilize the electron beam technology developed for CO_2.) Thus, the CO_2 laser, which is relatively simple in operation, well understood, and apparently scalable, should provide a good basic design for the laser system of our laser fusion reactor.

References for Section IV

1. W. Krupke and C. Rhodes, "Ideal Laser Characteristics for Fusion," LLL Laser Program Annual Report (1974), 446-447. (UCRL-50021-74).

2. J. Wilson and D. O. Ham, "Specifications for a Fusion Laser," Laser Focus, 12 no. 11, 38-41 (1976).

3. J. V. V. Kasper and G. C. Pimentel, "Atomic Iodine Photodissociation Laser," Appl. Phy. Lett. 5, 231-233 (1964).

4. C. C. Davis, R. J. Pirkle, R. A. McFarlane, and G. J. Wolga, "Output Mode Spectra, Comparative Parametric Operation, Quenching, Photolytic Reversibility, and Short Pulse Generation in Atomic Iodine Photodissociation Lasers," IEEE J. Quantum Electron. QE-12, 334-352 (1976).

5. R. W. F. Gross, "High Power Iodine Lasers for Laser Fusion," in Laser Induced Fusion and X-Ray Laser Studies ed. S. F. Jacobs, M. O. Scully, M. Sargent III and C. D. Caatrell III (Addison-Wesley Pub. Co. Pon Mills, Ontario 1976)Chap. 7, 311-368.

6. G. Brederlow, K. J. Witte, E. Fill, K. Hohla and R. Volk, "The Astrix III Pulsed High-Power Iodine Laser," IEEE J. Quantum. Electron. QE-12 152-155 (1976).

7. J. C. Swingle, C. E. Turner, Jr., J. R. Murray, E. V. George and W. F. Krupke, "Photolytic Pumping of the Iodine Laser by XeBr*," Appl. Phys. Lett 28, 387-388 (1976).

8. L. D. Pleasance and L. A. Weaver, "Laser emission at 1.32 μm from Atomic Iodine Produced by Electrical Dissociation of CF_3I," Appl. Phys. Lett. 27 407-409 (1975).

9. G. Emanuel, N. Cohen and T. A. Jacobs, "Theoretical Performance of a HF Chemical CW Laser," J. Quant. Spectrose. Radiat. Transfer. 13 1365-1393 (1973).

10. F. K. Truby, "Stability of Multiatmosphere H_2-F_2-O_2 Mixtures for HF Laser Studies," Appl. Phys. Lett. 29,247-249 (1976).

11. R. A. Gerber, E. L. Patterson, L. S. Blari and N. R. Greiner , "Multi-kilojoule HF Laser Using Intense-Electron-Beam Initiation of H_2-F_2 Mixtures," Appl. Phys. Lett. 25 281-283 (1974).

12. Laser Focus, 12, no. 6,24-28 (1975).

13. E. L. Patterson and R. A. Gerber, "Characteristics of a High-Energy Hydrogen Fluoride (HF) Laser Initiated by an Intense Electron Beam" IEEE J. Quantum Electron. QE-11, 642-647 (1975).

14. J. A. Mangano, R. L. Limpaecher, J. D. Dougherty and F. Russell, "Efficient Electrical Initiation of a HF Chemical Laser," Appl. Phys. Lett. 27 293-295 (1975).

15. R. J. Jensen, "HF Chemical Lasers," in Progress in Lasers and Laser Fusion, ed. A. Perlmutter and S. M. Wildmayer (Plenum Press, New York, 1975) p. 53-70.

16. R. W. Getzinger, N. R. Greiner, K. D. Ware, J. P. Carpenter, and R. G. Wenzel, "Controlled Energy Extraction and Sharp Nanosecond Pulses from a HF Amplifier," IEEE J. Quantum Electron. QE-12, 556-558 (1976).

17. K. L. Kompa, "High Power Chemical Lasers: Problems and Perspectives," in Laser Interaction and Related Phenomena ed. H. J. Schwarz and H. Hora (Plenum Press, New York, 1974) p. 115-132.

18. S. N. Sucherd, and G. C. Pimentel, "Denterium Fluoride Vibrational Overtone Chemical Laser," Appl. Phys. Lett. 18 530-531 (1971).

19. B. J. Feldman, "Short-Pulse Multiline and Multiband Energy Extraction in High-Pressure CO_2-Laser Amplifiers," IEEE J. Quantum Electron. QE-9, 1070-1078 (1973).

20. F. Skoberne, Laser Fusion Program Progress Report (LA-6245-PR) July 1976, p. 11.

21. L. J. Denes, L. H. Taylor, L. E. Kline, R. J. Spreadburg and R. V. Babcock, "Pumping Characteristics of Multiatmosphere CO_2 Amplifiers," 29th Annual Gaseous electronics Conference, Cleveland, Ohio 1976.

22. J. E. Murray, "Group VI Elements As Potential High-Energy Visible-Laser Sources", LLL, Laser Program Annual Report (1974) 448-450 (UCRL-50021-74).

23. H. T. Powell, J. R. Murray and C. K. Rhodes, "Laser Oscillation on the Green Bands of XeO and KrO," Appl. Phys. Lett. 12, 730-732 (1974).

24. H. T. Powell, "Rare Gas-Oxygen Excimer Lasers," LLL, Laser Program Annual Report (1974), 451-456 (UCRL-50021-74).

25. J. R. Murray and C. K. Rhodes, "The Possibility of a High-Energy-Storage Visible Laser on the Anroral Line of Oxygen," LLL Report UCRL-51455 (1973).

26. W. M. Hughes, N. T. Olson and R. Hunter, "Experiments on 558 nm Argon Oxide Laser System," Appl. Phys. Lett. 28, 81-83 (1976).

V. Cavity and Chamber Design

V-A. Pedagogy

The energy release from the exploding pellets of inertially-confined fusion systems consists of energetic neutrons, photons, and charged particles which eventually dissipate their kinetic energies in the walls surrounding the reactor cavity. The X-rays and charged particles emanating from the microexplosion and the reflected laser light from the pellet have a relatively short range and, as a result, severe surface-heating problems may arise in the first wall. Protection of the first wall from damage due to these irradiations poses many interesting and challenging engineering problems. The energy deposition densities in cavity walls due to neutrons and gamma rays are not large and do not pose significant heat transfer problems. In this and the following sections, the main problems associated with cavity and chamber design for laser fusion reactors are discussed.

Calculations of the implosion of bare D-T pellets indicate that approximately 1% of the energy yield is in the form of X-rays.[1-5] Structured pellets produce higher X-ray fractions with considerably softer spectra. This tends to exasperate the surface-heating problem since softer X-rays have a shorter range. Typical X-ray spectrum for a pure DT microexplosion is shown in Fig. 1. The bulk of these X-rays are produced during the thermonuclear burn, which typically lasts about 10 ps. For structured pellets, the X and gamma radiation occurs over a somewhat longer time interval.[4]

Approximately 76% of the thermonuclear energy yield is carried away by the neutrons. The neutron energy spectrum closely resembles a 14 MeV mono-energetic source (Fig. 2). These neutrons are released during the burn time of 10 ps. Depending on the cavity diameter (a few meters), they arrive at the first wall approximately 100 ns after the X-rays. The energy deposition by the neutrons occurs primarily in the blanket regions in neutron-slowing-down times,

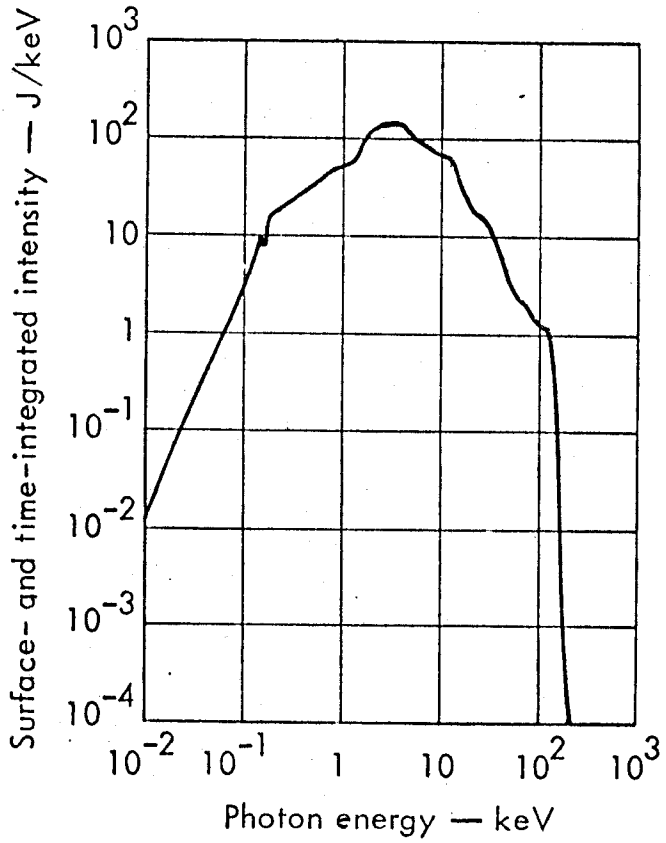

Figure 1

Typical X-Ray Pulse Spectrum of a Megajoule DT Fusion Microexplosion [from (1)]

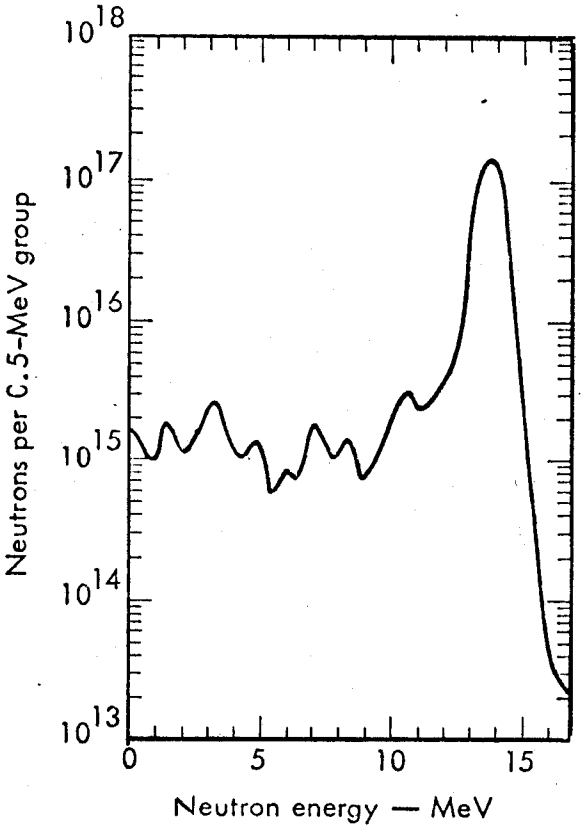

Figure 2

Neutron Pulse Spectrum of a Megajoule DT Fusion Micro-explosion [from (1)]

a few microseconds for 14 MeV neutrons in lithium.

A significant portion (~23%) of the energy yield from the microexplosion is released in the form of energetic charged particles. The 2 MeV alpha particles excaping from the pellet carry approximately one-third of that energy. The remaining two-thirds are associated with the pellet debris. These include the unburned deuterons, tritons and trapped alphas. The arrival times at the first wall of free-streaming charged particles and of the debris plasma depend on chamber geometry and dimensions, and on the kinetic energy and spectra of the particles. These times are also affected by the presence of a magnetic field or significant amounts of residual gas in the chamber. The energy spectrum of the debris is nearly Maxwellian with the average energy equal to the energy deposited in the pellet from the laser and burn divided by the number of particles. For earlier reactor chamber concepts, time intervals for energy deposition by charged particles of the order of a few microseconds have been reported.[4] Much shorter times are associated with the 2 MeV alphas.[6]

A significant fraction of the incident laser light can be reflected from the DT plasma surrounding the pellet by such processes as Brillouin and Raman instabilities before it reaches the critical plasma density.[1] This reflection may persist for time periods of the order of 100 ps. The reflectivity increases for plasmas with longer density gradients. The reflected photon energy will be deposited in the first wall in a series of pulses with diminishing amplitudes which depend on the wall surface absorptivity. Like the X-rays and charged particles, the reflected laser light will result in rapid surface heating in the first wall because of its short range.

The rapid surface heating of the first wall results in high stress levels due to the thermal gradients in the material. The coupling between the energy equation and the equation of motion makes the problem difficult to solve. For X-rays, the characteristic thermal time for energy deposition, $\tau_T \equiv 1/\mu^2\alpha$, is considerably larger than the characteristic mechanical time, $\tau_m \equiv 1/\mu c$, which, in turn, in larger than the energy deposition period τ (See Table 1). Here μ is the energy attenuation coefficient, α is the thermal diffusivity, and c is the wave velocity in the first wall material. This means that for X-rays the time variation effects produced by heat conduction are small compared with the time variation effects in the pressure wave. Hence, a simple instantaneous heat deposition model can be used to determine the temperature rise. Also, the approximate theory of uncoupled dynamic thermoelasticity and viscoelasticity can be used to determine the moving stress pulse produced by the X-rays.[1] Similar conclusions can be made for neutron energy deposition.

For the reflected laser light, the three time constant, τ, τ_T, and τ_m are of the same order and the simple uncoupled models will yield conservative estimates of both temperature and stress. Therefore, complex codes for coupled radiation diffusion and hydrodynamic motion, such as CHART D, are needed for realistic estimates of these effects.

For the ion loading, τ_m is considerably less than both τ_T and τ. Therefore, the stress due to the charged particle energy deposition can be determined by quasi-static thermoelastic or viscoelastic theory while the temperature history can be determined using classical diffusion theory.

The analytical tools for assessing the surface-heating and stress problems are difficult but, nevertheless, can be developed. The main issue, however, is to develop an economical cavity design which would be able to accommodate

and protect against these severe conditions. Three different designs have been proposed, viz. a dry wall, a wet wall, and a magnetically-protected wall. These are compared and critically evaluated in the following section.

Table 1

Energy Attenuation Factors and the Pulse Time, and Mechanical and Thermal Characteristic Times for Laser Fusion Reaction Products in Typical First Wall Materials (from Ref. [1])

	Photons	Soft X-Rays	Charged Particles	Neutrons
μ, m^{-1}	10^{8}	10^{5}-10^{6}	10^{5}-10^{6}	1-10
τ,s	10^{-10}	10^{-11}	10^{-6}	10^{-11}
τ_m,s	10^{-11}	10^{-9}-10^{-8}	10^{-9}-10^{-8}	10^{-4}-10^{-3}
τ_T, s	10^{-11}	10^{-7}-10^{-5}	10^{-7}-10^{-5}	10^{3}-10^{5}

References for Section V-A.

1. A. J. Glass and K. L. Cummings (Eds.), "Laser Program Annual Report", Lawrence Livermore Laboratory (1975).

2. L. A. Booth (Compiler), "Central Station Power Generation by Laser-Driven Fusion," Los Alamos Scientific Laboratory Report LA-4858-MS, Vol. I (1972).

3. J. M. Williams, et al., "Engineering Design for Laser Controlled Thermonuclear Reactors," Proc. 5th Symposium on Engineering Problems of Fusion Research, Princeton, NJ (1973).

4. T. G. Frank, et al., "Heat Transfer Problems Associated with Laser Fusion," Proc. 6th National Heat Transfer Conference, St. Louis (1976).

5. J. Hovingh, et al., "The Preliminary Design of a Suppressed Ablation Laser-Induced Fusion Reactor," Proc. 1st Topical Meeting on the Technology of Controlled Nuclear Fusion, CONF-740402-P1, San Diego (1974).

6. J. Hovingh, "First Wall Studies of a Laser-Fusion Hybrid Reactor Design," Proc. 2nd Topical Meeting on the Technology of Controlled Nuclear Fusion, Richland, Washington (1976).

V-B. Cavity Design Concepts

The microexplosion in inertially-confined fusion systems must be contained in an economically viable manner which assures the integrity of the different reactor components and permits efficient utilization of the different energy forms emanating from the microexplosion. The energy deposition by the soft X-rays, charged particles, and reflected laser light takes place in an extremely thin surface layer causing rapid surface heating of the first wall.

Protection of the first wall from damage due to these irradiations is the main objective of the designer. The energy from the 14 MeV neutrons and high energy gammas is deposited in relatively large volumes and do not pose significant heat transfer problems.

One obvious solution to the surface-heating problem is to make the cavity sufficiently large to reduce the wall loading, and hence, the corresponding temperature rise. The temperatures and stresses produced in the first wall are roughly proportional to the inverse of the cavity diameter squared while the cost of the reactor and blanket varies as the diameter squared. Therefore, there is an economic incentive for developing technologically viable systems which do not merely depend on size alone. Three different first wall designs have been proposed, viz. a wet wall, a dry wall and a magnetically-protected wall. These are discussed below.

The wet wall concept developed by LASL[1,2] features a thin liquid film of lithium over a niobium first wall. The lithium film protects the metallic first wall from the soft X-rays, photons, and charged particles. While it appears to be a clever way of protecting the first wall, the wet wall design suffers from

several drawbacks which makes it less attractive for power producing systems. The repetition rate is limited because of the large amount of ablated lithium which has to be pumped out of the cavity after each microexplosion. The vacuum pumping power required is excessive because of the high vapor pressure of lithium. Another disadvantage of the wet wall design is the relatively complex first wall design needed to allow the film to be replenished after each microexplosion. It is also doubtful that a stable thin liquid film can be established over the entire first wall. If unstabilities occur, the liquid may flow in rivulets causing dry hot regions in the first wall.

The suppressed ablation system developed by LLL is a modification of the wet wall design.[3] Lithium ablation is suppressed by using a liner consisting of pyramidal elements to effectively increase a given cavity diameter. This niobium liner lowers energy fluxes to a level where excessive lithium ablation does not occur. At any rate, the suppressed ablation system suffers from the same disadvantages as the wetted-wall design.

In dry wall designs, an unprotected wall is used as a first barrier between the microexplosion cavity and the blanket. This wall may be metallic, e.g. niobium or stainless steel, or it may be fabricated from graphite or carbon curtain over a metallic wall.[4] Advantages of metallic walls are the ease of fabrication and the low vapor pressures which result in lower vacuum pumping requirements. The main disadvantage, however, is that helium from the thermonuclear burn is deposited in the wall and tends to accumulate forming bubbles which fracture and spall the first wall. Chemical ablation of graphite liners by the hydrogen isotopes in the debris may be significant.[5] These form methane and acetylene which are more difficult to vacuum pump and recover tritium from than the inorganic pellet debris.

A magnetically-protected first wall design has been recommended.[6] A solenoid surrounding the cylindrical cavity is used to divert the charged particles away from a dry niobium first wall. The energy of the charged particles debris is collected on some externally-cooled surfaces at both ends of the cylinder. The magnetic protection will not protect the first wall from the photons or soft X-rays. However, it is quite effective in protecting the first wall since ions are the main surface-heating culprits. It has also been suggested that the ion energy be converted to electricity by exhausting the debris into an MHD duct;[7] the efficacy of this concept remains to be shown. Magnetic protection has two minor disadvantages. The first is that the blanket modules and first wall are less accessible than in dry wall designs. The second disadvantage is that if a liquid metal is selected as a coolant, the pumping power required to move the coolant will increase if movement occurs across the magnetic field. These disadvantages can be side stepped by proper design and use of other equally effective coolants such as boiling water.

References V-B

[1] L. A. Booth (compiler), "Central Station Power Generation by Laser-Driven Fusion", Los Alamos Scientific Laboratory, LA-4858-MS (1872).

[2] J. M. Williams, et al., "A Conceptual Laser Controlled Thermonuclear Reactor Power Plant", Proc. 1st Topical Meeting on the Technology of Controlled Nuclear Fusion, San Diego (1974).

[3] J. Hovingh, et al., "The Preliminary Design of a Suppressed Laser Induced Fusion Reactor", ibid (1974).

[4] J. M. Williams, et al., "Engineering Design Considerations for Laser Controlled Thermonuclear Reactors", Proc. Fifth Symp. Eng. Problems of Fusion Research, Princeton, N. J. (1973).

[5] M. Balooch and D. R. Olander, "Hydrogen Attack of Fusion Reactor First Walls Made of Graphite", Trans ANS Winter Meeting, San Francisco (1975).

[6] T. Brank, et al., "A Laser Fusion Reactor Concept Utilizing Magnetic Fields for Cavity Protection", Proc. 1st Topical Meeting on the Technology of Controlled Nuclear Fusion, San Diego (1974).

[7] J. Nuckolls, J. Emmett and L. Wood, "Laser-Induced Thermonuclear Fusion", Physics Today, (August 1974).

V-C. Magnetic Protection

To analyze magnetic protection of laser fusion cavities, we consider a cylindrical cavity impressed with a solenoidal magnetic field.[1] The field acts to hinder expansion perpendicular to the axis of the cylinder while allowing the expansion along this axis to proceed unimpeded. The explosion debris is thus channeled to the ends of the cylinder where it is absorbed by energy sinks. Absorbing the charged particles on the surfaces at the ends of the cylinder rather than on the cylinder walls has several advantages:

(1) The energy sinks may be designed to equalize the incident energy flux at the surface of the sink, thus reducing the problem of thermal stress in this structure.

(2) Compared to the cavity wall, the sinks are relatively far away from the explosion center. Since the particles must travel farther, there can be more time-of-flight spreading of their spatial distribution, allowing the rate of thermal conduction from the surface layer to compete with the energy deposition rate. This can lead to a lower surface temperature.

(3) Energy sinks at the ends are much easier to maintain and replace than the cavity walls.[2]

The principal drawback to magnetic protection is that the exploding plasma is unstable to flute modes, which give rise to transport across the restraining magnetic field. However, for this application confinement is not required. The relevant concern is that the growth rate for the flute modes be small enough to allow time for the debris to stream out the cylindrical chamber. (Note that this requirement makes it desirable for the energy sinks

to be close to the explosion center, in opposition to the time-of-flight spreading condition mentioned above. Thus, some optimum distance must be determined). Previous studies indicate that flute growth times may be roughly 5 times longer than transit times out the chamber.[3,4] However, these results are based on rough estimates and in view of the critical nature of this problem, further study is required.

Astrophysical interests and recent work on filling mirror machines with laser produced plasmas have led to a fairly extensive literature on the problem of plasmas exploding into magnetic fields. Bernstein and Fader[5] discuss a resistive plasma expanding into a uniform magnetic field, the results of which are carried further in a paper by Haught, Polk and Fader[6] where results are discussed in relation to experiments. Poukey[7] discusses the expansion of a plasma shell into a uniform background magnetic field, and he includes the change of shape of the shell. It is important to note that none of these papers consider a magnetic field compressed against a conducting wall, and care must be taken in applying these results to the present problem. References 1-4 and 8 contain some of the work of the magnetic protection group at Los Alamos which has been particularly useful in defining the directions of our study.

We now proceed to discuss some preliminary results. Taking as a test case the explosion of a 0.4 mg D-T pellet with a fractional burn-up of 30% and a yield of 150 MJ, we find from the burn dynamics (Section II) that the charged particles are distributed as follows:

Fast alpha particles: There are approximately 2×10^{18} alphas with an average energy of 2 MeV.

Debris plasma: The debris forms initially a D-T plasma with 260 KeV of radial kinetic energy and 26 KeV of thermal energy (values at a radius of 2 cm).

If we assume that both groups expand as hot plasmas (see reference 3), then the helium plasma expands first, compressing the field until the radial motion is stopped. This helium plasma continues its expansion along the axis, relieving the pressure, as the field begins to push the plasma back toward the axis. The D-T plasma then streams through the helium plasma and recompresses the field; it too then streams out the ends.[4] If we assume that a particle's velocity component along the axis, v_z, is unchanged by the magnetic field (only approximately true) and that the explosion is isotropic, then the particles are uniformly distributed in v_z. An estimate of the time for an element of D-T plasma on the cylinder axis to reach the energy sink is 3×10^{-6} s, so in 3×10^{-5} s roughly 90% of the plasma has left the chamber. We will now take this characteristic time and investigate some of the relevant processes which occur.

a. Diffusion of the Magnetic Field into the Conducting Wall

If we assume that the field is suddenly compressed against the conducting wall with the helium plasma expansion time, $\tau = 5 \times 10^{-7}$ s, then the diffusion problem can be approximated by a one dimensional problem in which there is a jump in the magnetic diffusion coefficient

at a point, and B is held constant to the left of the jump point. Solving this problem by matching classical solutions in the two regions gives for the current distribution in the wall (as a function of depth x and time t),

$$j(x,t) \propto \frac{e^{-x^2/4kt}}{\sqrt{4\pi kt}} \text{ , where } k = \frac{c^2}{4\pi\sigma}$$

and σ is the electrical conductivity of the wall material. The half width of this profile is

$$\Delta x = \left(\frac{c^2}{\pi\sigma} \ell n 2\right) t \ .$$

Setting $t = 3 \times 10^{-5}$ s, we find that a copper shell ($\sigma \simeq 5 \times 10^{17}$ s) would give $\Delta x \simeq .01$ cm, and a stainless steel shell ($\sigma \simeq 10^{16}$ s) would give 0.6 cm. Hence, several millimeters of conducting metal shell should allow the field to be compressed and protect the copper coils from large voltage pulses caused by the expanding plasma.

b. Diffusion of the Magnetic Field into the Plasma

Since hot plasmas have high conductivities and correspondingly small skin depths, we expect the above analysis also to apply here. Indeed, a 200 eV D-T plasma has a conductivity like that of stainless steel. Since the electrons start out at 20 KeV (thermal) at a radius of 2 cm, for at least radii not too much larger than 2 cm, the field will be excluded because of the high conductivity. At larger radii, we might expect some field penetration due to lower electron temperatures. In addition, if any high Z materials get swept up in the plasma, the conductivity would be further decreased. As the skin depths begin

to be of the same size of the radius, the 1-dimensional analysis is no longer applicable. The details of the time evolution of the electron temperature must also be known more exactly to predict the amount of field penetration into the plasma. This problem requires further study.

c. Time-of-flight Spreading of the Particles

If we assume that the 26 KeV temperature given by the hydrodynamics has meaning in terms of a local maxwellian in a frame moving with the plasma, we may estimate how much the particles are spread in time when they reach the energy sinks. As an illustration we consider 260 KeV deuterons with a 26 KeV thermal spread, interpreted to mean that their distribution function is proportional to $e^{-\frac{1}{2}m\frac{(v-v_o)^2}{kT}}$. The particles then arrive at a distance z from the source spread in time according to the factor,

$$e^{\left[-\frac{1}{2}\frac{mv_o^2}{kT}\left(1-\frac{z}{v_o t}\right)^2\right.} .$$

In the present case, we find a spread of about 0.3×10^{-6}s. This is enough to help reduce the ablation rate at the sinks.

We now turn to a preliminary analysis of the problem of designing the shape of the energy collecting surfaces at the cylinder ends. This surface can be described by a function z(r) with z = 0 at r = 0. The conditions that determine the shapes are:

(1) The surface is to be as far from the explosion center as possible (i.e. the surface is to be convex, as viewed from the source).

(2) The energy absorbed per unit area is to be constant over the surface. We derive the desired shape in terms of the radial distribution of the particles projected on a plane perpendicular to the cylinder axis.

For purposes of illustration we make the simplifying assumption that this distribution is constant in time which is approximately true if the conducting walls which compress the field are at a constant radius over the entire chamber, including the energy sinks. The radial distribution $f(r)$ is normalized by $2\pi \int_0^{R_{max}} f(r) r dr = 1$. An element of surface area at $z(r)$ is given by $dA = 2\pi r\sqrt{1 + (\frac{dz}{dr})^2}\, dr$, while the number of particles incident on this strip is $dN = \frac{N}{2}(2\pi r f(r) dr)$. If we require the energy per unit area to be some constant C we find

$$\frac{dz}{dr} = -\sqrt{\frac{N^2}{4C^2} f^2(r) - 1} \ .$$

We pick the negative sign for the square root to make the surface convex.

It is interesting to consider some special cases.

(a) Let $f(r)$ be determined by a thin spherical shell of radius R projected on a plane perpendicular to the axis,

$$f(r) = \frac{1}{2\pi R^2 \sqrt{1-(r/R)^2}} \ ;$$

Then the collector shapes are as illustrated in Figure 1.

(b) Let $f(r)$ be determined by the projection of a solid sphere on a plane,

$$f(r) = \frac{3\sqrt{1-(r/R)^2}}{2\pi} \ ;$$

Then the collector shapes are as illustrated in Figure 2. Note that solutions do not exist for this last case all the way to R. This occurs because at some $r < R$, $\frac{dN}{dA}$ tends to 0 independent of the collector shape, making it impossible to maintain constant energy deposition

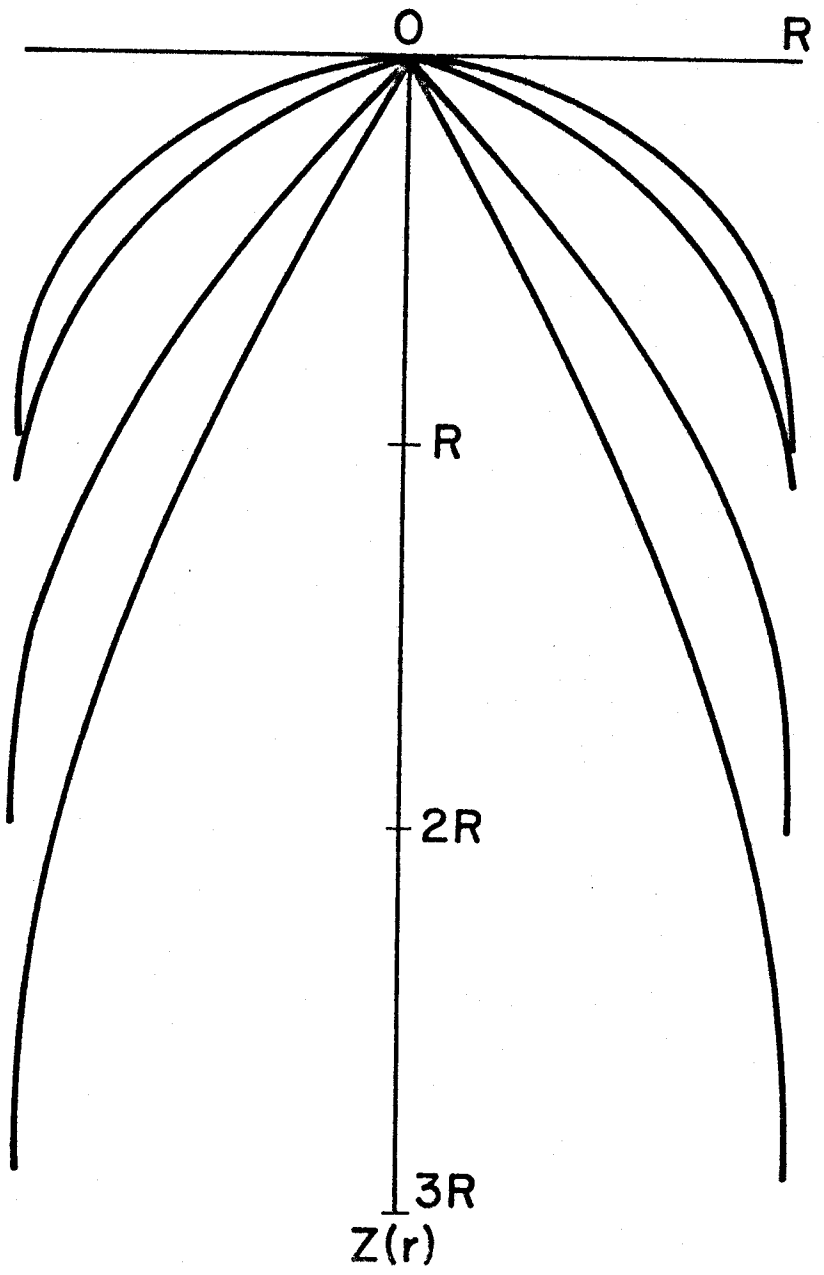

Fig. I ENERGY SINK SHAPE FOR A SHELL LIKE EXPLOSION.
R = PLASMA RADIUS

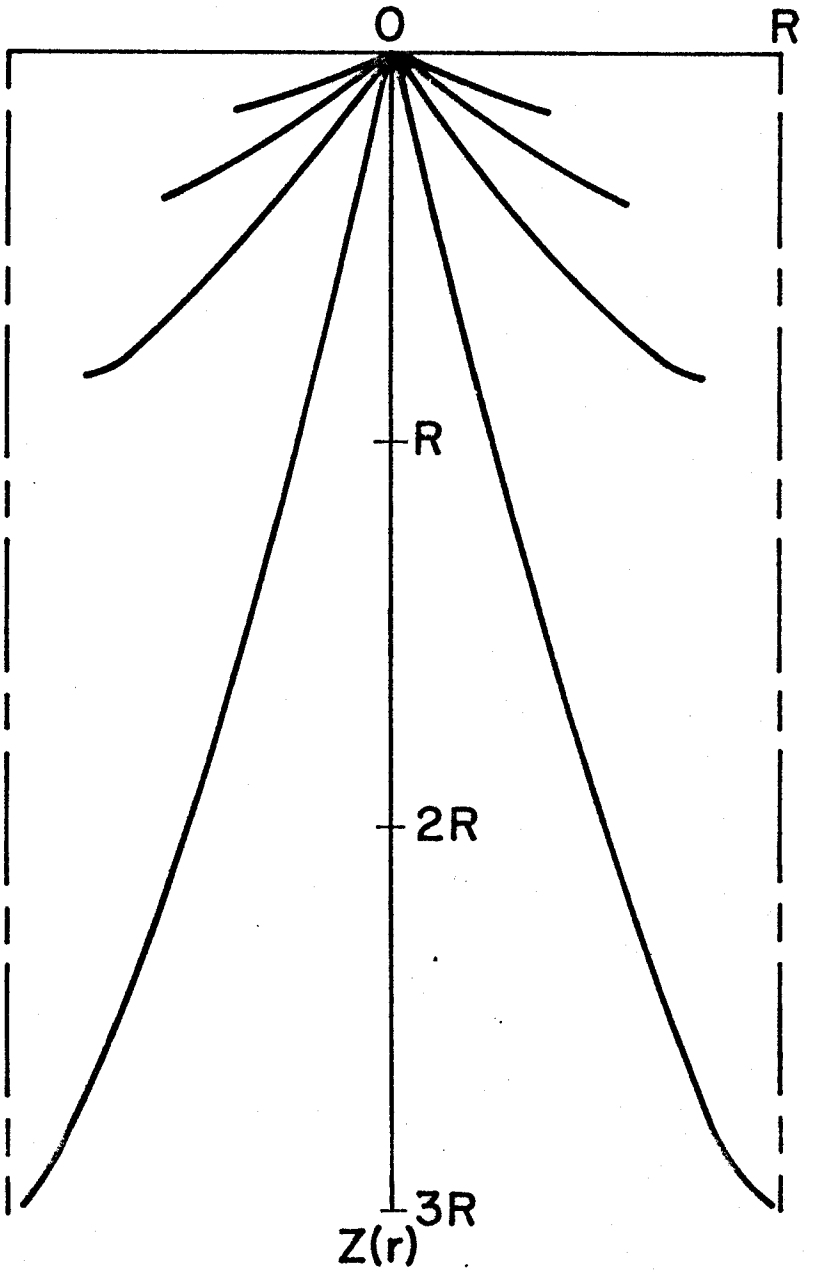

Fig. 2 ENERGY SINK SHAPE FOR A SOLID SPHERE EXPLOSION.
R = PLASMA RADIUS

per unit area. We see that the problem of finding the right collector shape may not have a solution, and it may be necessary to settle for some non-uniformity in the energy per unit area on the collector.

There is another variable in the problem, however, which we ignored in making these simplifying assumptions. The radius of the conducting wall against which the field is compressed may be varied. In particular, it may be held constant along the cylinder, and then be allowed to increase in the energy sink region. As the plasma enters this region, the restraining magnetic pressure will drop, allowing the plasma to expand radially as it traverses the sink region. By varying both the collector shape and the conducting wall radius, it may be possible to achieve uniform wall loading for a wider variety of radial distributions, f(r). A good example of the effect mentioned above is contained in reference 5.

Future Directions

The most critical problem at the moment is to determine the growth rate of the flute instability. A detailed analysis of the exploding plasma as it is decelerated by the magnetic field in cylindrical geometry is needed to see if the growth rate is small enough.
In addition, some simulation capability needs to be developed, similar to that achieved by the Los Alamos group. Once this is in hand, optimization studies on shapes and sizes of energy sinks may be carried out.

References for Section V-C

1. L. A. Booth and T. G. Frank, "A Technology Assessment of Laser-Fusion Power Development," Los Alamos Scientific Laboratory Report LA-UR-76-2060, presented at the Second ANS Topical Meeting on The Technology of Controlled Nuclear Fusion, September 21-23, 1976; Richland, Washington.

2. D. A. Freiwald, T. G. Frank, E. A. Kern, and L. A. Booth, "Laser Fusion Generating Stations Based on the Magnetically Protected Reactor Cavity," Los Alamos Scientific Laboratory Report LA-UR-75-2035, presented at the ANS 1975 Winter Meeting, San Francisco, California, November 17-21, 1975.

3. J. J. Devaney, "Magnetically Protected First Wall for a Laser Induced Thermonuclear Reactor."

4. T. Frank, D. Freiwald, T. Merson, J. Devaney, "A Laser Fusion Reactor Concept Utilizing Magnetic Fields for Cavity Wall Protection, Los Alamos Scientific Laboratory Report LA-UR-74-495, presented at the First Topical Meeting on the Technology of Controlled Nuclear Fusion (ANS), San Diego, California, April 16-18, 1974.

5. I. B. Bernstein and W. J. Fader, Phys. Fluids 11, 2209 (1968).

6. A. F. Haught, D. H. Polk, and W. J. Fader, Phys. Fluids 13, 2842 (1970).

7. J. W. Poukey, Phys. Fluids 12, 1452 (1969).

8. J. C. Goldstein, I. O. Bohackevsky, and D. O. Dickman, "Ion Motion in Laser Fusion Reactor Vessel Studies," Los Alamos Scientific Laboratory Report LA-UR-76-2381, presented at the APS Plasma Division Annual Meeting in San Francisco, California, November 15-19, 1976.

V.D. Liner Design

In dry-wall type cavities, a liner is provided to protect the metallic first wall from the X-rays and charged particles emanating from the pellet and from the reflected laser light. Without the liner, the surface temperature of the wall may rise sharply after each pulse and exceed allowable limits since these photons and charged particles have a relatively short range. Hence, the surface heating and ablation of the first wall (or its protective liner) may be the limiting factors in determining the necessary cavity size to contain the microexplosion.

Aside from directly protecting the first wall, the liner will also rectify the pulsating surface heating loads and radiate a steady heat flux to it. This will depend on the ratio between the thermal time constant of the liner and the time between pulses. When this ratio is greater than $\sim$ 100, the liner should be able to dampen these variations effectively.[1,2] This criterion, along with the structural and ablation requirements, may dictate the necessary liner thickness.

A preliminary assessment of the surface heating problems caused by these pulsating photon and ion sources show carbon to be the best candidate for liner material. It can be operated at relatively high temperatures since its sublimation temperature is quite high and its vapor pressure at lower temperatures is sufficiently low. A 1.5 cm thick graphite liner is selected, which for a repetition rate of 30 sec^{-1} would readily satisfy the time constant criterion.

In this section, general analytical models for predicting the thermal response of the liner and its stress levels as a result of these pulsed

irradiations are developed. Generalized charts for predicting the surface temperature rise as a function of the different design and operational parameters of the system as well as the nature of incident irradiations are given. Most of the analyses presented herein are done in a parametric fashion in order to maintain generality and understand the effects of the different variables. Specific examples pertaining to our design are also given.

V.D.1 Liner Temperature History

(i) Theory: In the following, an analytical model for evaluating the transient temperature distribution in the liner is presented. This model is used to determine the periodic surface temperature rise caused by the reflected laser light and the X-rays emanating from the micro-explosion. A pulsating source of monoenergetic photons resulting in an exponential heat deposition curve is first considered. The resulting solution is then used, along with superposition techniques, to determine the temperature history produced by a pulsating source of black body radiation.

Reactor cavities are either spherical or cylindrical with diameters considerably larger than the liner thickness. Hence, the liner can be represented by a plane wall as shown in Fig. (1.1a). Radiative heat exchange between different parts of the liner and convective heat transfer at its inner surface can be ignored. This corresponds to an insulated boundary at x = o (Fig. (1.1a)). The outside surface of the liner is assumed to remain at a constant temperature T_o throughout the transient. This condition can be physically realized if the time constant of the liner is considerably larger than the time between pulses. Under these

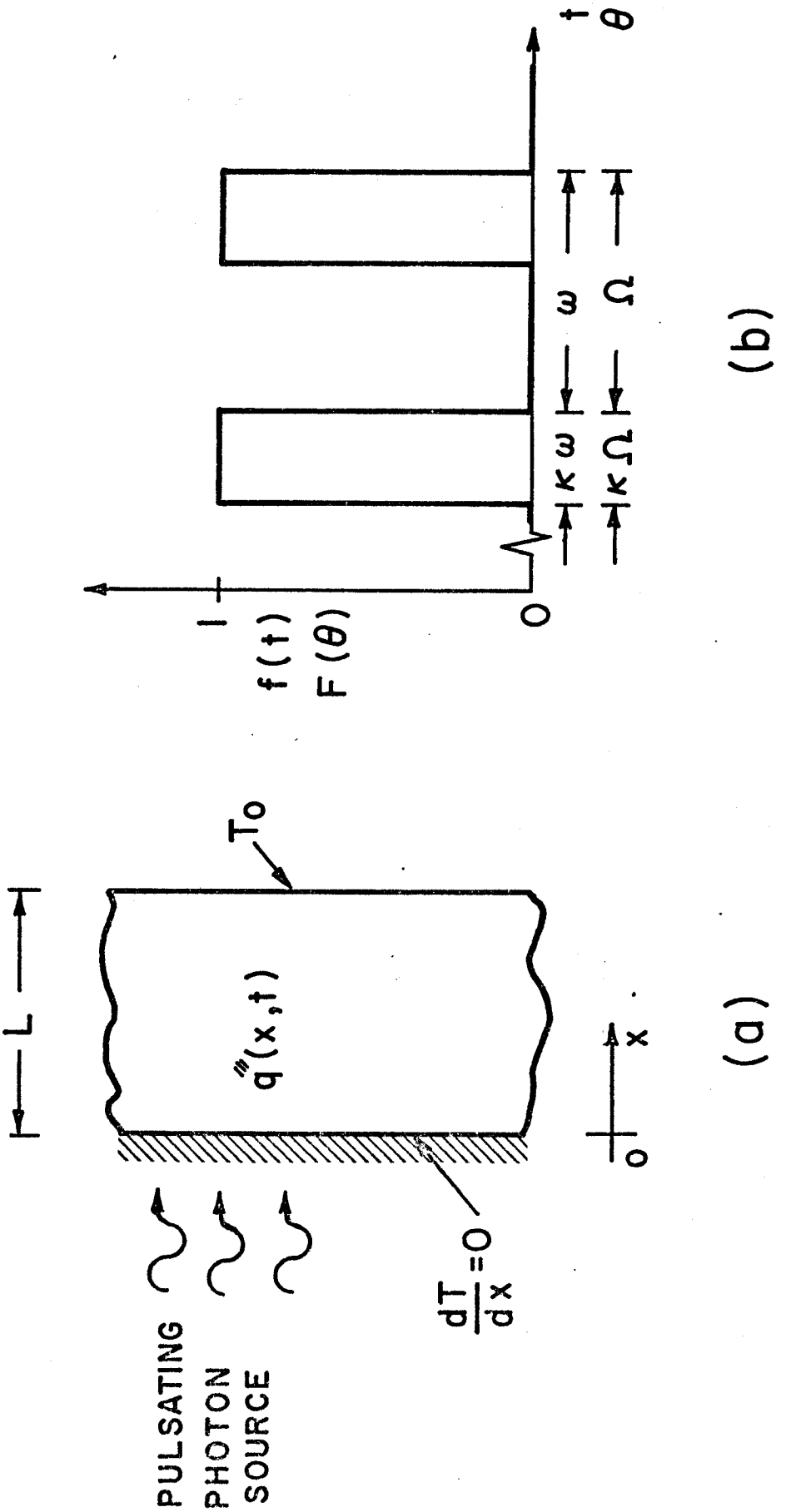

Figure 1.1

Schematic representation of the liner and time dependence of the volumetric heat generation function f(t)

conditions, the pulsating surface-heating loads are rectified and a constant heat flux is radiated from the liner to the isothermal first wall. The initial temperature distribution in the liner is assumed to be uniform and equal to T_o. This assumption should not affect the sustained transient solution in which we are interested.

The heat conduction equation, boundary conditions, and initial condition for the above stated problem are:

$$\frac{\partial^2 T}{\partial x^2} + \frac{q'''}{k} = \frac{1}{\alpha}\frac{\partial T}{\partial t} \tag{1.1}$$

$$\left.\begin{aligned} \frac{\partial T}{\partial x}(o,t) &= o \\ T(L,t) &= T_o \end{aligned}\right\} \tag{1.2}$$

$$T(x,o) = T_o \, . \tag{1.3}$$

Here, the thermal conductivity k and diffusivity α are assumed to be constant, $q'''(x,t)$ is the volumetric heat generation rate whose spatial and temporal distributions depend on the characterization of the incident irradiations. For a pulsating flux of monoenergetic photons, q''' can be represented by:

$$q'''(x,t) = (q'''_o \bar{e}^{\mu x})\, f(t) \tag{1.4}$$

where q'''_o is the volumetric heat generation rate at the surface, μ is the absorption coefficient, and f(t) is the on/off control function shown in Fig. (1.1b). The time between pulses and the pulse width are assumed to be constant and equal to ω and $\kappa\omega$ respectively. The surface heat

generation rate q_o''' is related to the incident flux ϕ_o, absorption coefficient μ, and photon energy ($h\nu$) by the relation: $q_o''' = \phi_o \mu\ (h\nu)$. The incident flux ϕ_o is assumed to remain constant during the "on" period so that q_o''' is not a function of time. It is a straightforward matter, however, to extend the analysis to include any temporal flux variations.

We introduce the nondimensional variables:

$$\left.\begin{aligned} u &\equiv (T - T_o) \,/\, [(q_o'''/\mu)\ \kappa\omega/\rho cL] \\ \xi &\equiv x/L \\ \theta &\equiv \alpha t/L^2 \end{aligned}\right\} . \qquad (1.5)$$

In Eq. (1.5), the nondimensional temperature u is the ratio between the actual temperature rise and that obtained if the incident photons' energy were to be deposited uniformly and adiabatically. The Fourier number θ is the ratio between the actual time t and the time constant of the slab, L^2/α. In terms of these nondimensional variables, Eqs. (1.1-3) can be written as:

$$\frac{\partial^2 u}{\partial \xi^2} + Q(\xi)\ F(\theta) = \frac{\partial u}{\partial \theta} \qquad (1.1a)$$

$$\left.\begin{aligned} \frac{\partial u}{\partial \xi}(o,\theta) &= o \\ u(1,\theta) &= o \end{aligned}\right\} \qquad (1.2a)$$

$$u(\xi,o) = o\ . \qquad (1.3a)$$

The nondimensional heat generation function $Q(\xi)$ is given by:

$$\left.\begin{aligned} Q(\xi) &= A\, e^{-b\xi};\ 0 \leq \xi \leq 1\ , \\ A &\equiv b/\kappa\Omega\ , \\ b &\equiv \mu L\ , \\ \text{and} \\ \Omega &\equiv \alpha\omega/L^2 \end{aligned}\right\} \quad . \tag{1.6}$$

The on/off function $F(\theta)$ is shown in Fig. (1.1b).

The problem defined by Eqs. (1.1a-3a) is linear and nonhomogeneous. It can be solved by either superposition or variation of parameters techniques.[1,2] The latter method is outlined below.

The eigenfunctions, $\psi_n(\xi)$, to the corresponding homogeneous problem are:

$$\psi_n(\xi) = \cos\left(\frac{2n-1}{2}\right)\pi\xi;\ n = 1, 2, \ldots \tag{1.7}$$

Therefore, the solution to the $u(\xi,\theta)$ problem may be written as:[1,2]

$$u(\xi,\theta) = \sum_{n=1}^{\infty} C_n(\theta)\, \psi_n(\xi)\ . \tag{1.8}$$

Since the eigenfunctions $\psi_n(\xi)$ are orthogonal over the interval $0 \leq \xi \leq 1$, Eq. (1.8) can be multiplied by $\psi_m(\xi)$ and integrated over that region to yield:

$$C_n(\theta) = 2\int_0^1 u(\xi,\theta)\, \psi_n(\xi)\, d\xi\ . \tag{1.9}$$

Differentiating Eq. (1.9) with respect to θ and substituting for $\frac{\partial u}{\partial \theta}$ from Eq. (1.1a) we get:

$$\frac{dC_n}{d\theta} = \left(\frac{2n-1}{2}\pi\right)^2 C_n + 2I_n F(\theta) \qquad (1.10)$$

where,

$$I_n = \int_0^1 Q(\xi)\, \psi_n(\xi)\, d\xi \ ,$$

and

$$C_n(o) = o \ .$$

Equation (1.10) can be easily solved to determine $C_n(\theta)$ and hence $u(\xi,\theta)$. The resulting solution is:

$$u(\xi,\theta) = 2\sum_{n=1}^{\infty} \cos\left[\frac{(2n-1)}{2}\pi\xi\right] \left\{\frac{b^2}{b^2+\left(\frac{2n-1}{2}\pi\right)^2}\right\}$$

$$\left\{1 + \bar{e}^b \left(\frac{2n-1}{2b}\pi\right) \sin\left(\frac{2n-1}{2}\pi\right)\right\} \exp\left[-\left(\frac{2n-1}{2}\pi\right)^2 \delta\Omega\right]$$

$$\left\{\frac{\exp\left[\left(\frac{2n-1}{2}\pi\right)^2 \delta\Omega\right]-1}{\left(\frac{2n-1}{2}\pi\right)^2 \kappa\Omega} + \frac{\exp\left[\left(\frac{2n-1}{2}\pi\right)^2 \kappa\Omega\right]-1}{\left(\frac{2n-1}{2}\pi\right)^2 \kappa\Omega}\right.$$

$$\left.\frac{\left[1-\exp-\left(\frac{2n-1}{2}\pi\right)^2 N\Omega\right]}{\exp\left[\left(\frac{2n-1}{2}\pi\right)^2 \Omega\right]-1}\right\}$$

$$(o \leq \delta \leq \kappa) \qquad (1.11)$$

and

$$u(\xi,\theta) = 2\sum_{n=1}^{\infty} \cos\left[\frac{(2n-1)}{2}\pi\xi\right]\left\{\frac{b^2}{b^2+(\frac{2n-1}{2}\pi)^2}\right\}$$

$$\left\{1+\bar{e}^{b}\,(\frac{2n-1}{2b}\pi)\,\sin\,(\frac{2n-1}{2}\pi)\right\}\exp\,[-(\frac{2n-1}{2}\pi)^2\,\delta\Omega]$$

$$\left\{\frac{\exp\,[(\frac{2n-1}{2}\pi)^2\,\kappa\Omega]-1}{(\frac{2n-1}{2}\pi)^2\,\kappa\Omega}\right\}\left\{\frac{1-\exp-[(\frac{2n-1}{2}\pi)^2\,(N+1)\,\Omega]}{1-\exp-[(\frac{2n-1}{2}\pi)^2\,\Omega]}\right\}$$

$$(\kappa \leq \delta \leq 1)\ . \qquad (1.12)$$

In Eqs. (1.11) and (1.12), the integer N and the fraction δ are defined by: $\theta = (N + \delta)\,\Omega$. The above expressions for $u(\xi,\theta)$ can be simplified for $N \gg 1$ to yield the sustained transient solution $\tilde{u}(\xi,\theta)$:

$$\tilde{u}(\xi,\theta) = 2\sum_{n=1}^{\infty} \cos\,[(\frac{2n-1}{2})\,\pi\xi]\left\{\frac{b^2}{b^2+(\frac{2n-1}{2}\pi)^2}\right\}$$

$$\left\{1+\bar{e}^{b}\,(\frac{2n-1}{2b}\pi)\,\sin\,(\frac{2n-1}{2}\pi)\right\}\left\{\frac{\exp\,[-(\frac{2n-1}{2}\pi)^2\,\delta\Omega]}{(\frac{2n-1}{2}\pi)^2\,\kappa\Omega}\right\}$$

$$\left\{[\exp\,[(\frac{2n-1}{2}\pi)^2\,\delta\Omega]-1]+\frac{\exp\,[(\frac{2n-1}{2}\pi)^2\,\kappa\Omega]-1}{\exp\,[(\frac{2n-1}{2}\pi)^2\,\Omega]-1}\right\}$$

$$(o \leq \delta \leq \kappa) \qquad (1.11a)$$

and,

$$\tilde{u}(\xi,\theta) = 2\sum_{n=1}^{\infty} \cos\left[\left(\frac{2n-1}{2}\right)\pi\xi\right] \left\{\frac{b^2}{b^2+\left(\frac{2n-1}{2}\pi\right)^2}\right\}$$

$$\left\{1 + e^{-b}\left(\frac{2n-1}{2b}\pi\right)\sin\left(\frac{2n-1}{2}\pi\right)\right\} \left\{\frac{\exp\left[-\left(\frac{2n-1}{2}\pi\right)^2 \delta\Omega\right]}{\left(\frac{2n-1}{2}\pi\right)^2 \kappa\Omega}\right\}$$

$$\left\{\frac{\exp\left[\left(\frac{2n-1}{2}\pi\right)^2 \kappa\Omega\right]-1}{1-\exp-\left[\left(\frac{2n-1}{2}\pi\right)^2 \Omega\right]}\right\}$$

$$(\kappa \leq \delta \leq 1) \ . \qquad (1.12a)$$

Equations (1.11) and (1.12), or (1.11a) and (1.12a), can be used to determine the nondimensional transient temperature distribution in the liner resulting from the pulsating exponential heat deposition given by Eq. (1.4). After a large number of pulses, the temperature at any point within the liner will vary in a cyclic manner with a period ω. The nondimensional surface temperature (at $\xi = o$) will vary between a maximum value, u_{max}, at $\delta = \kappa$ and a minimum value, u_{min}, at $\delta = 1$. These temperature extremes are of particular significance when estimating the ablation rate and stress levels produced in the liner.

For small values of Ω, i.e. when the time constant of the liner is considerably larger than the time between pulses, u_{min} will depend only on the nondimensional absorption coefficient b, while u_{max} will depend on both b and the nondimensional pulse width κ. Plots of u_{min} and u_{max} as functions of b and κ for $\Omega = 0.01$ are shown in Fig. (1.2). These results are quite general inasmuch as they can be used for arbitrary

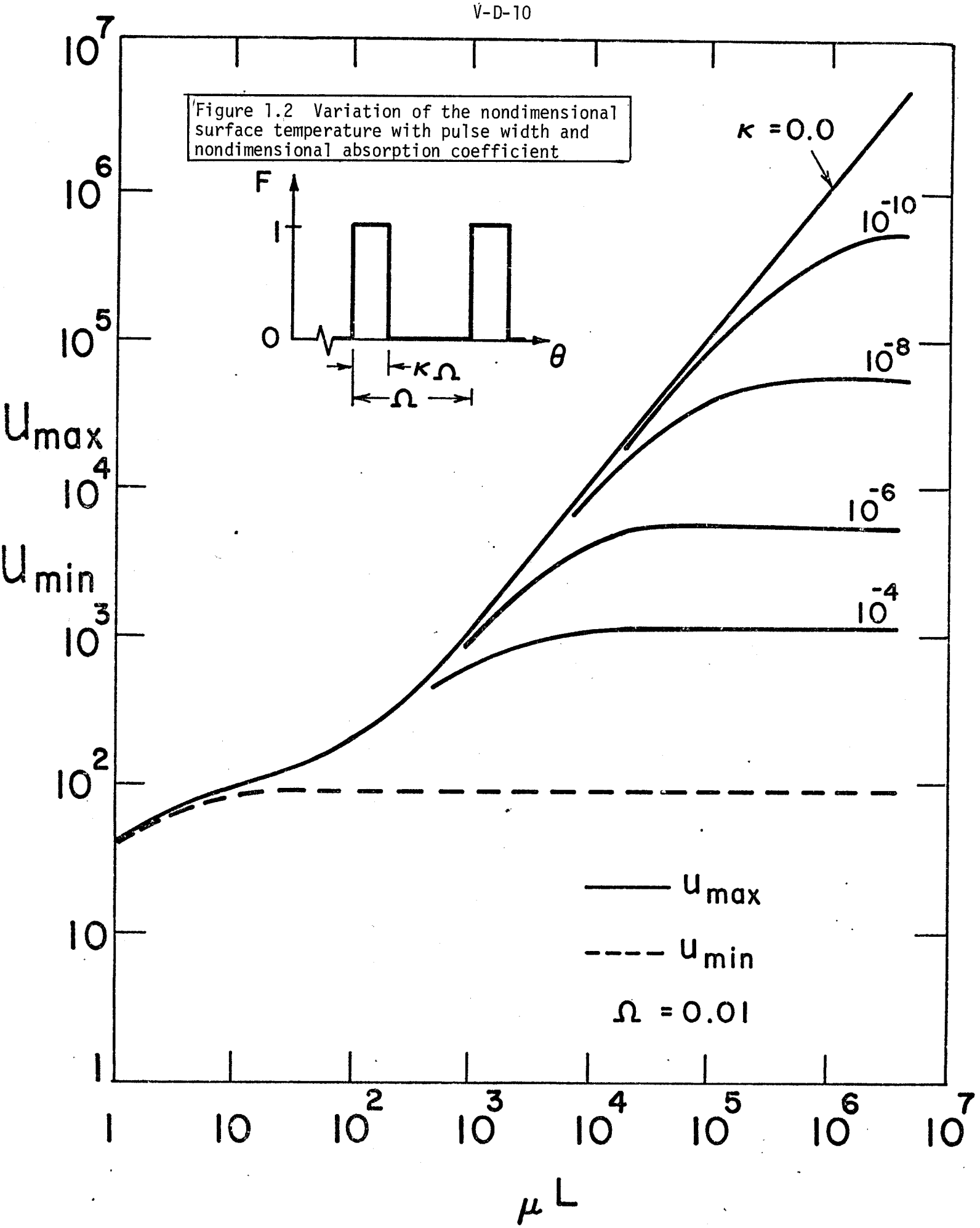
Figure 1.2 Variation of the nondimensional surface temperature with pulse width and nondimensional absorption coefficient
F
1
0
θ
κΩ
Ω
κ =0.0
10^-10
10^-8
10^-6
10^-4
u_max
u_min
Ω =0.01
10^7
10^6
10^5
10^4
10^3
10^2
10
1
1
10
10^2
10^3
10^4
10^5
10^6
10^7
μL

geometry, material, absorption coefficient (i.e. photon energy), repetition rate, wall loading, and pulse width. In the following we show how these results can be directly used to determine the surface temperature rise produced by the reflected laser light for different lasers and pellet "reflectivities." The results shown in Fig. (1.2) are also used, along with superposition techniques, to determine the surface temperature rise produced by a pulsating source of black body radiation.

(ii) Temperature Rise Produced by the Reflected Laser Light:

Fow low-energy photons incident on a homogeneous, isotropic medium, the attenuation coefficient μ in the exponential heat deposition curve of Eq. (1.4) may be estimated using the relation:[3,4] $\mu = 8\pi/\lambda$ where λ is the wavelength. Therefore, the results shown in Fig. (1.2) can be readily used to determine the surface temperature rise produced by the reflected laser light for a given system geometry and operating conditions.

A 1.5 cm thick graphite liner in a 10 m diameter cavity is considered. For a 1 MJ laser with a repetition rate of 30 sec^{-1} and a pellet "reflectivity" of 10%, the surface temperature rise is plotted in Figs. (1.3) and (1.4) for different laser wavelength and pulse width. These results can be easily used for other conditions since $\Delta T_{surface}$ is linearly proportional to the incident flux. It should be emphasized that the results shown in Figs. (1.3) and (1.4) do not account for any ablation which may take place at the liner surface. Efforts are currently underway to include phase-change processes into the analysis. Figures (1.3) and (1.4) are quite valuable inasmuch as they allow us to estimate the maximum tolerable pellet reflectivity corresponding to the onset of liner sublimation.

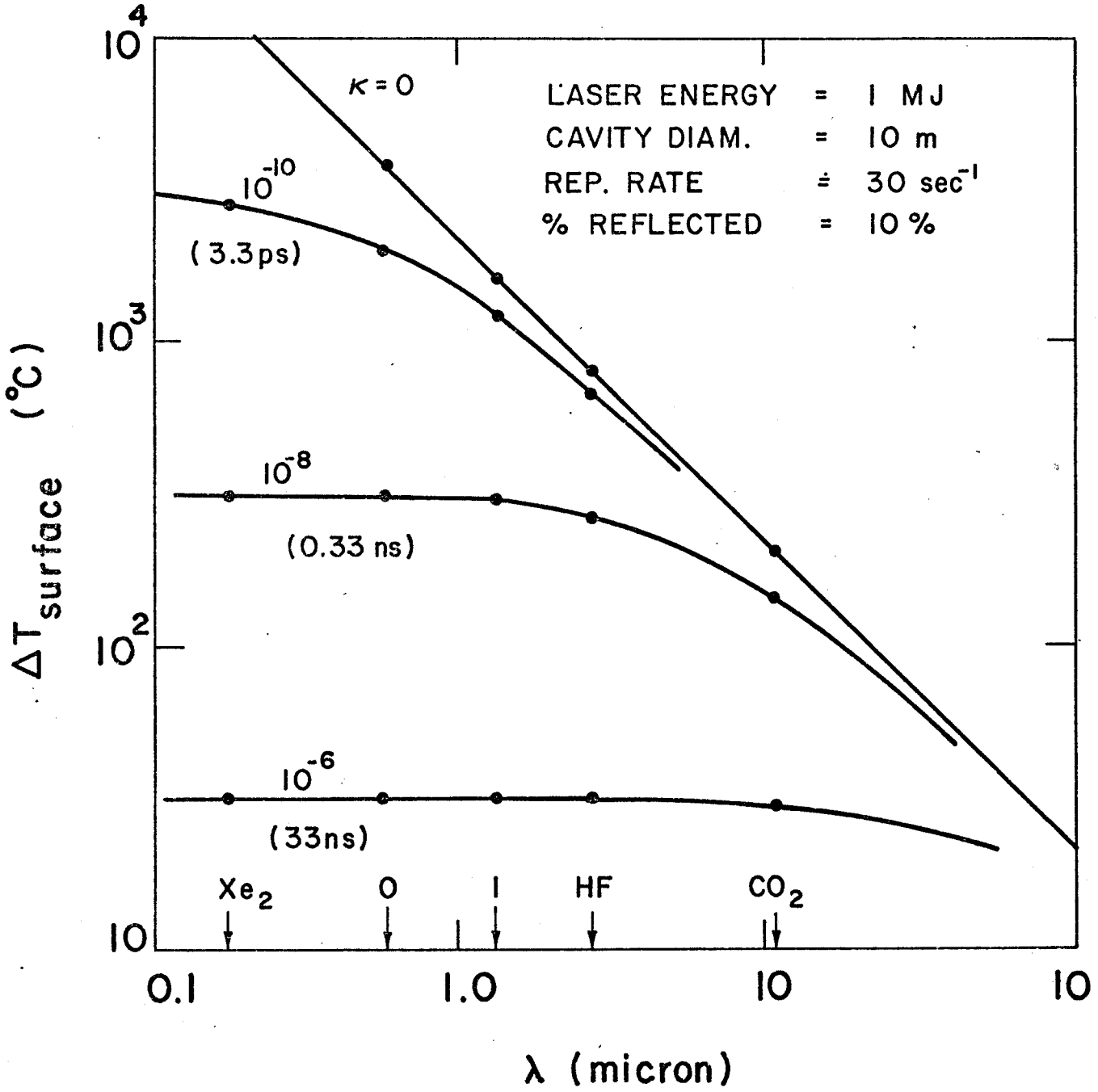

Figure 1.3

Variation of the surface temperature rise produced by the reflected laser light with laser wavelength and pulse duration (1.5 cm thick graphite liner)

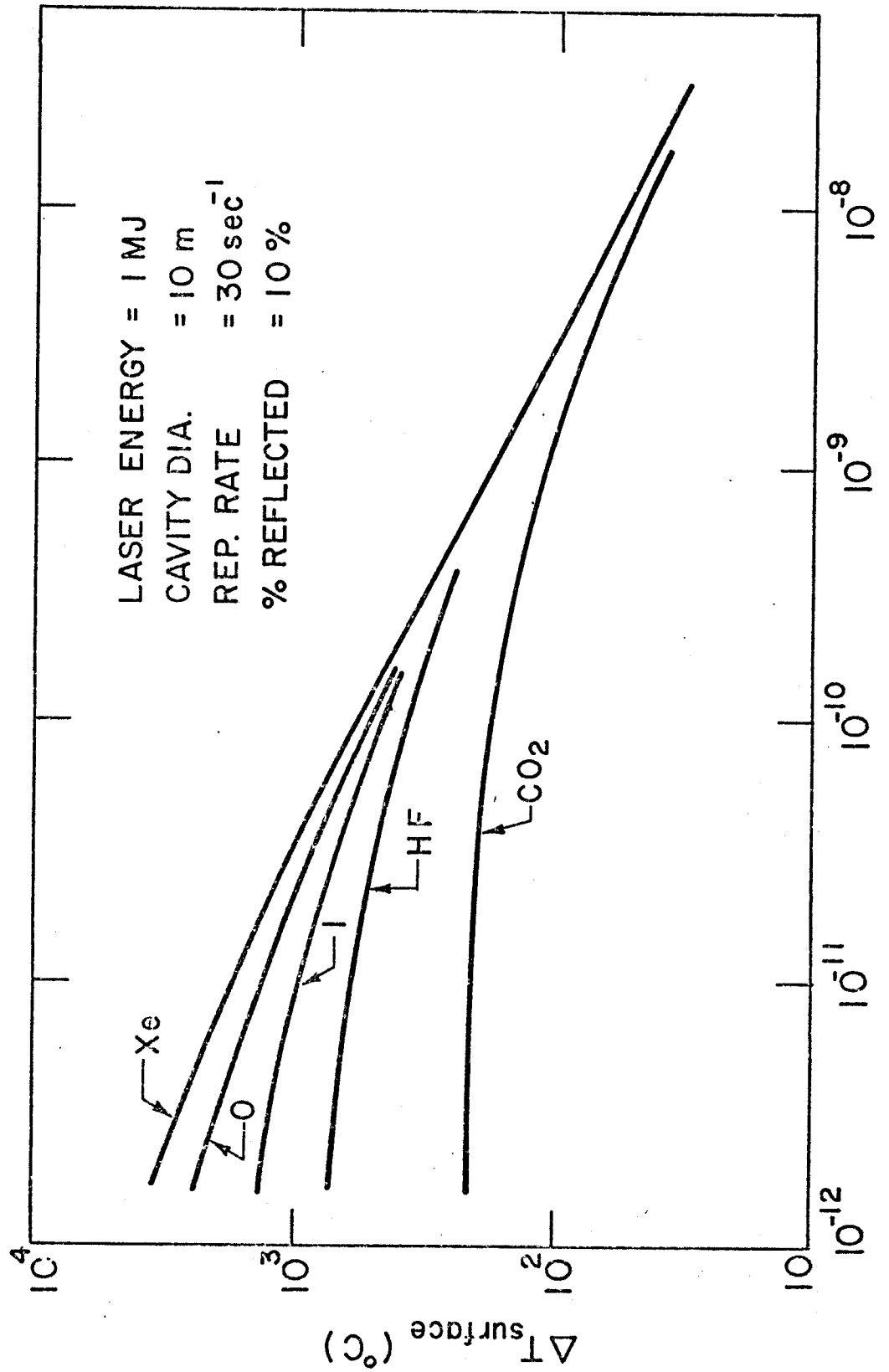

Figure 1.4

Variation of the surface temperature rise produced by the reflected laser light with pulse width for different lasers (1.5 cm thick graphite liner)

(iii) Temperature Rise Produced by the X-rays:

Calculations for the implosion of bare D-T pellets indicate that approximately 1% of the energy yield is in the form of X-rays.[5-7] Structured pellets produce higher X-ray fractions with considerably softer spectra.[8] Therefore, it is important to be able to determine the thermal response of the liner when subjected to a pulsating photon source with an arbitrary spectrum. This task can be readily accomplished by extending the solution for monoenergetic photons by means of superposition techniques. The X-ray spectra produced by the microexplosions are approximated by black-body radiations in the range 0.1-2.0 keV. This range is sufficiently wide to cover pellet designs of interest.

The spectrum is divided into M bands with average photon energies ε_i, i = 1, 2, . . ., M. Let ζ_i be the fraction of the incident energy within band i so that:

$$\sum_{i=1}^{M} \zeta_i = 1 \ . \tag{1.13}$$

The surface flux from the pulsating black-body source is given the symbol S so that the incident energy within a single pulse per unit surface area is equal to $S\kappa\omega$. We assume that the incident photons within the different bands will result in exponential heat deposition curves with absorption coefficients μ_i, i = 1, 2, . . ., M, so that the corresponding net heat generation rate $q'''(x,t)$ can be represented by:

$$q'''(x,t) = f(t)\ S \sum_{i=1}^{M} \zeta_i\ \mu_i\ \bar{e}^{\mu_i x} \ . \tag{1.14}$$

Similar to the case of monoenergetic photons, the nondimensional temperature $u(\xi,\theta)$ is defined by:

$$u(\xi,\theta) = (T - T_o) / (S\kappa\omega/\rho cL) \ . \tag{1.15}$$

Equations (1.1-3) can, therefore, be written as:

$$\frac{\partial^2 u}{\partial \xi^2} + F(\theta) \sum_{i=1}^{M} \zeta_i \, Q_i(\xi) = \frac{\partial u}{\partial \theta} \tag{1.1b}$$

$$\left.\begin{aligned} \frac{\partial u}{\partial \xi}(o,\theta) &= o \\ u(1,\theta) &= o \end{aligned}\right\} \tag{1.2b}$$

and

$$u(\xi,o) = o \tag{1.3b}$$

where,

$$\left.\begin{aligned} Q_i(\xi) &= A_i \, e^{-b_i \xi} \\ A_i &\equiv b_i/\kappa\Omega \\ b_i &\equiv \mu_i L \end{aligned}\right\} \ . \tag{1.6a}$$

Comparing Eqs. (1.1b-3b) with Eqs. (1.1a-3a), we can readily see that:

$$u(\xi,\theta) = \sum_{i=1}^{M} \zeta_i \, u_i(\xi,\theta) \tag{1.16}$$

where $u_i(\xi,\theta)$ is the solution to Eqs. (1.1a-3a) given by Eqs. (1.11) and (1.12), or (1.11a) and (1.12a), with b equal to b_i.

For a given black-body temperature, the spectrum is divided into 100 "equal-energy" bands (ζ_i = 0.01) and the corresponding average photon energies, and hence absorption coefficients μi, are obtained (Fig. 1.5). These are then used, along with the results presented earlier for monoenergetic photons (e.g. Fig. 1.2) and Eq. (1.16), to determine the liner's temperature response to the pulsating black body source.

For graphite, the absorption coefficients are curve fitted for five ranges of photon energies: (0.01-0.284 kev), (0.284-0.80 kev), (0.80-4.00 kev), (4.0-20.0 kev), and (20.0-100.0 kev) using relations of the form:

$$(\mu/\rho)\ (cm^2/g) = \sum_{j=1}^{4} a_j/\varepsilon_p^j \qquad (1.17)$$

where ε_p is the photon energy in kev. The constants a_j, j = 1 - 4 for the five ranges of photon energies are listed in Table (1.1).[9]

A 1.5 cm thick graphite liner in a 10 m diameter cavity is considered. For a pellet yield of 100 MJ, a repetition rate of 30 sec^{-1}, and an X-ray fraction of 1%, the periodic surface temperature rise is shown in Fig. (1.6) for different black-body temperatures and pulse durations. Obviously, softer spectra produce higher surface temperature jumps because of their shorter range. The case κ = o corresponds to instantaneous (delta-function) deposition of the X-ray energy into the liner; this produces the highest $\Delta T_{surface}$ since the energy is deposited

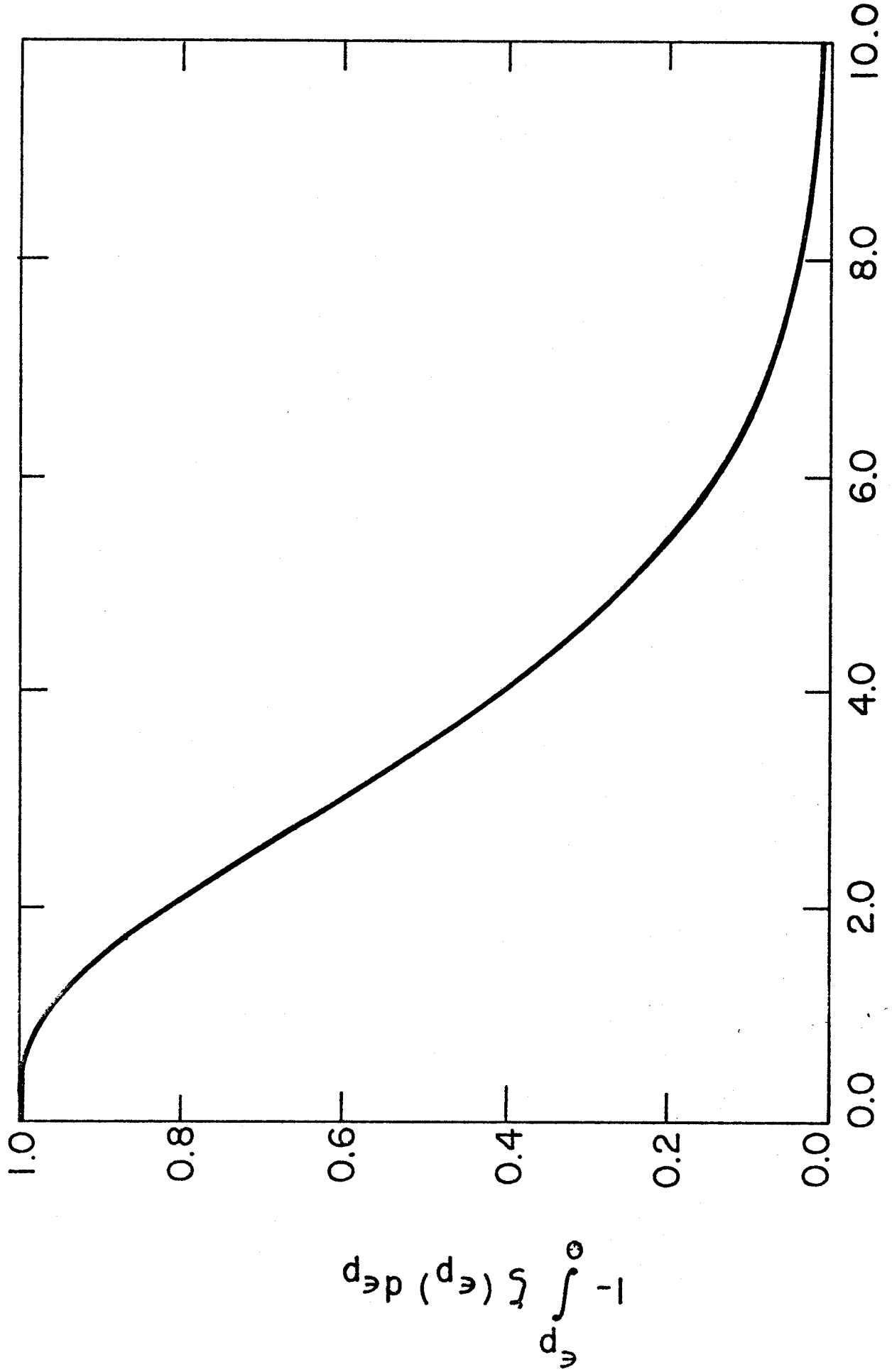

Figure 1.5 Variation of the nondimensional fraction of emissive power with the ratio between the photon energy ε_p (KeV) and the black body temperature ε_{bb} (KeV)

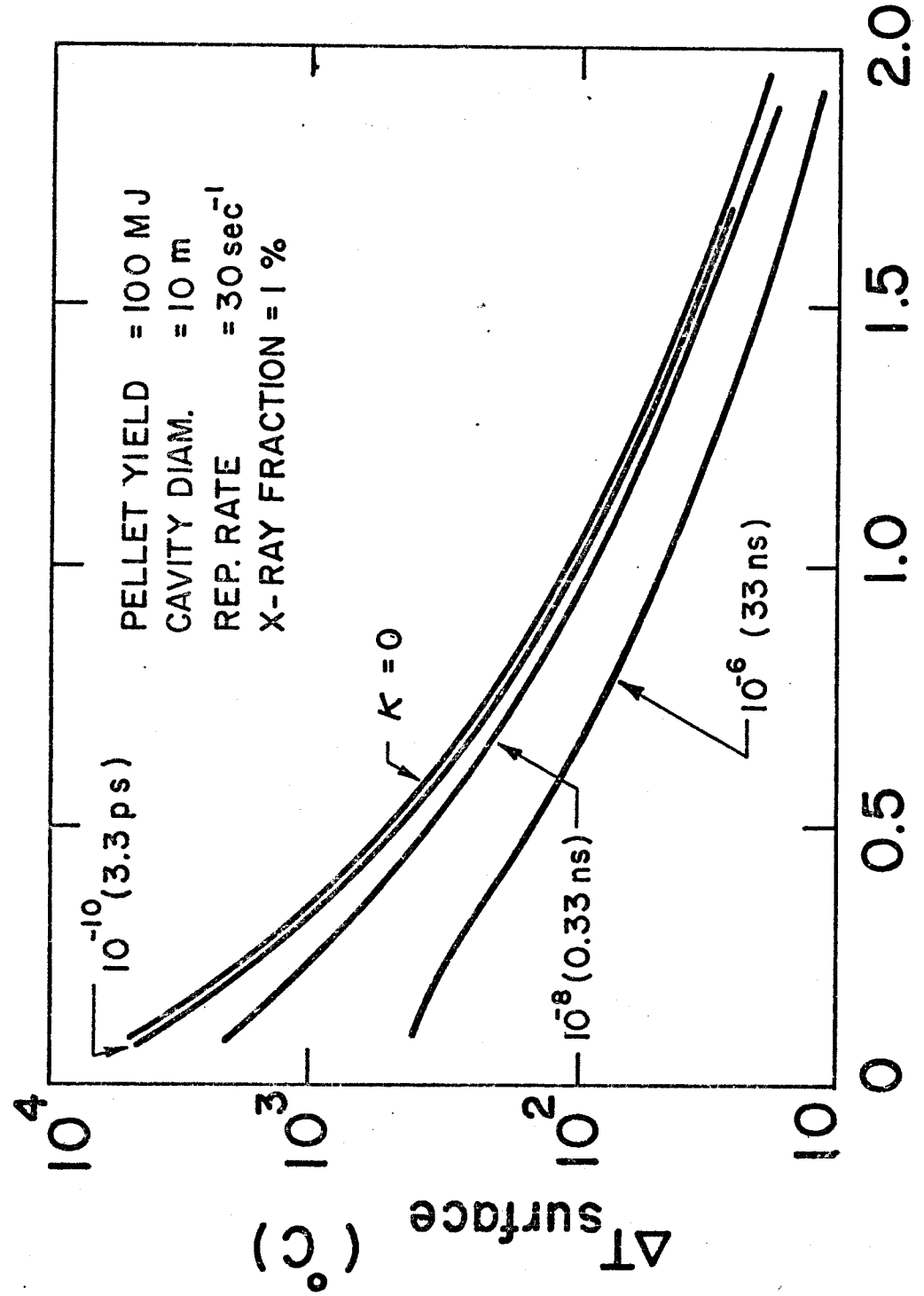

Figure 1.6 Variation of surface temperature rise produced by the X-rays with black body temperature and pulse duration

adiabatically. Figures (1.7) and (1.8) show the sustained surface temperature histories as functions of black body temperatures for a pulse width of zero and 33 ns respectively.

Again, it should be emphasized that the results shown in Figs. (1.6-8) do not account for any ablation which may take place at the liner surface. However, these results should help in determining the conditions corresponding to the onset of liner sublimation.

(i v) Thermal Response to Pulsed Ion Sources

A significant portion ($\sim$ 22%) of the energy yield from the micro-explosion is released in the form of energetic charged particles.[5,7] These particles eventually dissipate their energies in the cavity liner or, in the case of magnetic protection, on some collection surface. The thermal response of the collector plate materials to ion pulses can be determined upon knowledge of the spatial energy deposition as a function of particle energy and arrival time of each particle. A model has been developed whereby a given spectrum of particles is initiated at a point and each particle is allowed to propagate uncollided to the point of impact. The resulting particle arrival density is combined with their slowing-down characteristics to yield the spatial and temporal distribution of energy deposition. This, in turn, is used to determine the thermal response of the collector plate.

The particle energy loss is usually calculated as a function of its local kinetic energy. For electronic losses described by modified Lindhard slowing down, the rate of energy loss is given by[10]

$$\frac{dE}{dx} = - C \left(\frac{E}{E_o}\right)^{1/2} . \qquad (1.18)$$

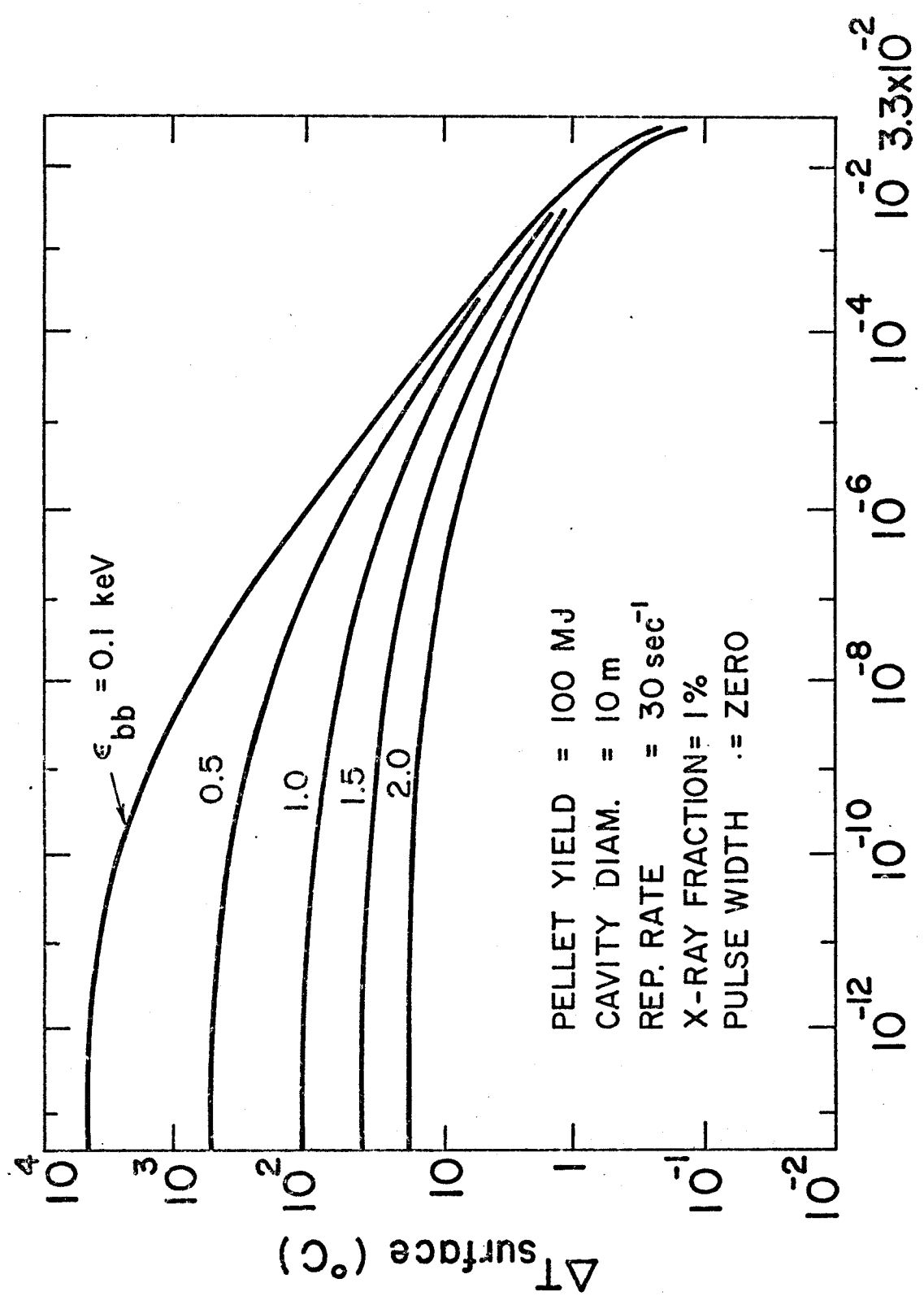

Figure 1.7 Variation of surface temperature history produced by the X-rays with black body temperature for instantaneous heat deposition in a 1.5 cm graphite liner

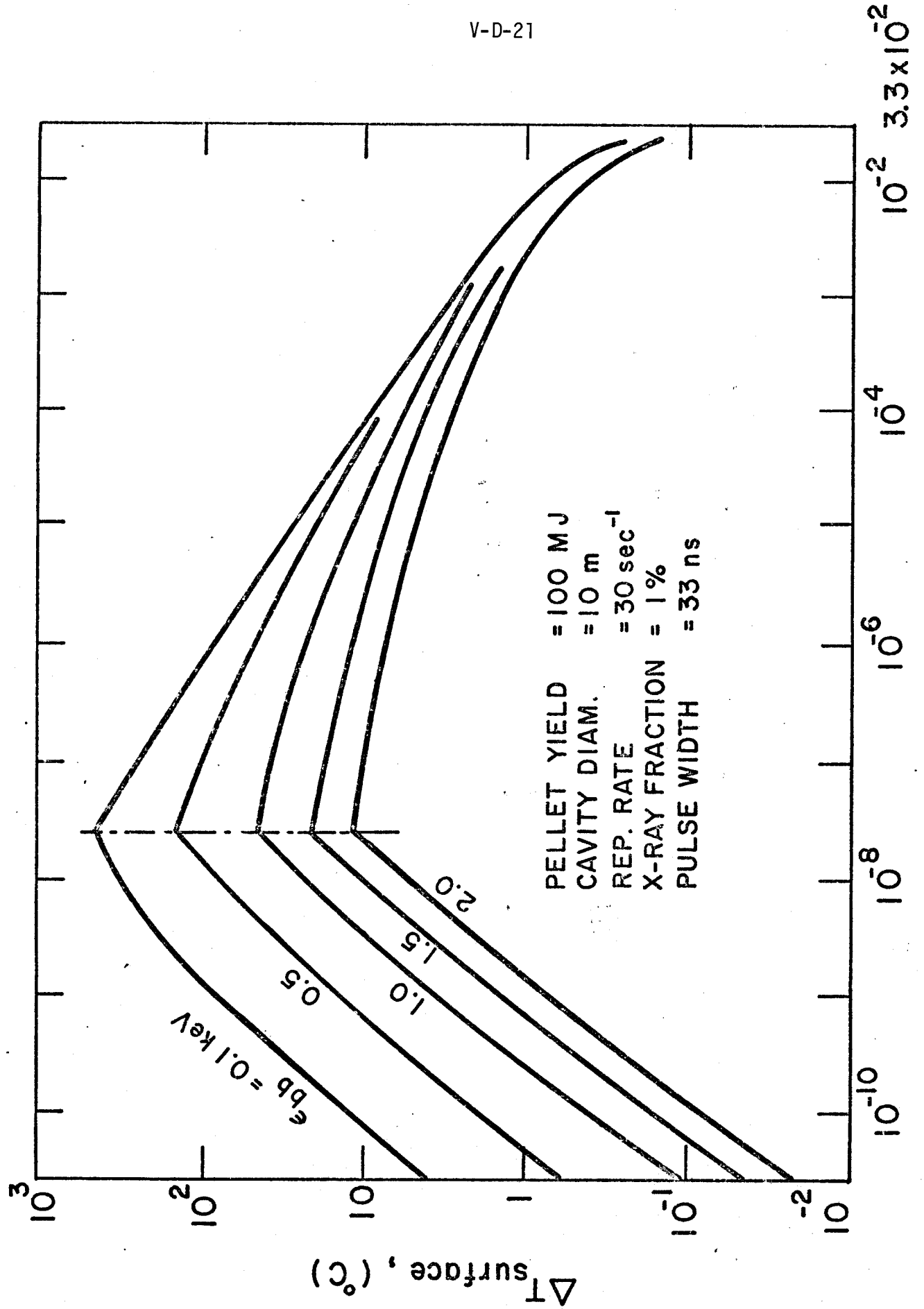

Figure 1.8 Variation of surface temperature history produced by the X-rays with black body temperature for a 1.5 cm graphite liner with a 33 nsec pulse duration

Table (1.1)

Parameters a_j for the Absorption Coefficients of Graphite Given by Eq. (17)[9]

Photon Energy (kev)	a_1	a_2	a_3	a_4
0.01-0.284	-6.531×10^{2}	3.748×10^{2}	-5.790	2.678×10^{-2}
0.284-0.80	-9.022×10^{2}	1.760×10^{3}	1.549×10^{3}	-2.280×10^{2}
0.80-4.0	-7.363	-1.537×10^{1}	2.672×10^{3}	-4.482×10^{2}
4.0-20.0	1.640	-9.428×10^{1}	2.872×10^{3}	-5.583×10^{2}
20.0-100.0	5.621×10^{-4}	-2.533	1.169×10^{3}	9.909×10^{3}

For a particle with incident energy E_1, Eq. (1.18) can be rearranged to give:

$$\frac{dE}{dx}(x) = \frac{xC^2}{2E_o} - C\left(\frac{E_1}{E_o}\right)^{1/2} . \tag{1.19}$$

The particle range, $x_m(E_1)$, is given by:

$$x_m(E_1) = \frac{2(E_o E_1)^{1/2}}{C} . \tag{1.20}$$

The particles from a pulsed source will arrive at a given location with an arrival density function f(t) given by:

$$\int_t f(t)\, dt = -\int_E S(E)\, dE . \tag{1.21}$$

Here, the integral is equal to the total number of incident particles per unit surface area, and S(E) is the particle energy spectrum at x = o. If the kinetic energy of the particles is primarily directed along the propagation axis (i.e. small thermal component), the arrival density would be given by:

$$f(t) = 2S(E)\, E^{3/2}/B \tag{1.22}$$

where,

$$B = 2.284 \times 10^{-6}\, RA^{1/2} .$$

Here, R is the distance travelled by the particles (i.e. cavity radius) in meters and A is the particle mass in amu.

The volumetric heating rate is related to the arrival density function by: $q'''(x,t) = f(t)\,\frac{dE}{dx}(x)$. Therefore,

$$\left.\begin{aligned} q'''(x,t) &= f(t)\left[\frac{A_1}{t} - A_2\,x\right]; \quad x < \frac{2BE^{1/2}}{Ct} \\ &= o \qquad\qquad\qquad\quad ; \quad x > \frac{2BE_o^{1/2}}{Ct} \end{aligned}\right\} \tag{1.23}$$

where

$$A_1 \equiv (CB/E_o^{1/2}),\ A_2 \equiv C^2/2E_o, \text{ and}$$

$$(B/\sqrt{E}_{max} < t < B/\sqrt{E}_{min})\ .$$

Here, E_{min} and E_{max} are the limits of the spectrum.

For a semi-infinite solid with an insulated boundary at $x = o$, and volumetric heat source $q'''(x,t)$, the transient temperature distribution is given by:[1]

$$T(x,t) = \iint_{tx} \frac{q'''(x',t')}{\rho c}\ G(x,t,x',t')\ dx'\ dt'$$

where G is green's function given by:

$$G(x,t,x',t') = \frac{1}{2\sqrt{\pi\alpha(t-t')}}\left\{\exp\left[-(x - x')^2/4\alpha\,(t - t')\right] + \exp\left[-(x + x')^2/4\alpha\,(t - t')\right]\right\}\ .$$

For the volumetric heat source given by Eq. (1.23), the above equation yields:

$$T(x,t) = \frac{1}{\rho c} \int_{t_{min}}^{t_{max}} f(t') \left\{ Q_1(t';t,x) + Q_2(t';t,x) + Q_3\ (t';t,x) \right\} dt' \quad (1.24)$$

where

$$Q_1(t';t,x) = \frac{A_1}{2t'} \left[\mathrm{erf}(F_1) + \mathrm{erf}(F_2) \right] ,$$

$$Q_2(t';t,x) = \frac{A_2 x}{2} \left[\mathrm{erf}(F_2) - \mathrm{erf}(F_1) - 2\,\mathrm{erf}(F_o) \right] ,$$

$$Q_3(t';t,x) = A_2 \sqrt{\frac{\alpha(t-t')}{\pi}} \left[\bar{e}^{F_2^2} + \bar{e}^{F_1^2} - 2\bar{e}^{F_o^2} \right] ,$$

$$F_o \equiv x/2\sqrt{\alpha(t-t')} , \quad (1.25)$$

$$F_1 = (x_m - x)/2\sqrt{2\alpha(t-t')} ,$$

$$F_2 = (x_m + x)/2\sqrt{2\alpha(t-t')} ,$$

and

$$x_m = 2BE_o^{1/2}/Ct' .$$

The above analysis has been performed for intermediate energy He ions (50 kev - 500 kev) for which the slowing down can be described by modified Lindhard theory. The time integral in Eq. (1.24) is performed numerically so that arbitrary spectra can be accommodated. Sample calculations have been made for Gaussian and Maxwellian spectra using appropriate slowing down parameters. Typical results for a 200 kev Maxwellian spectrum of ^{4}He ions in carbon are shown in Fig. (1.9). Figure (1.10) shows the variation of [$\rho c\ T(o,t)$] with time for different thermal diffusivities (α = o corresponds to the adiabatic case).

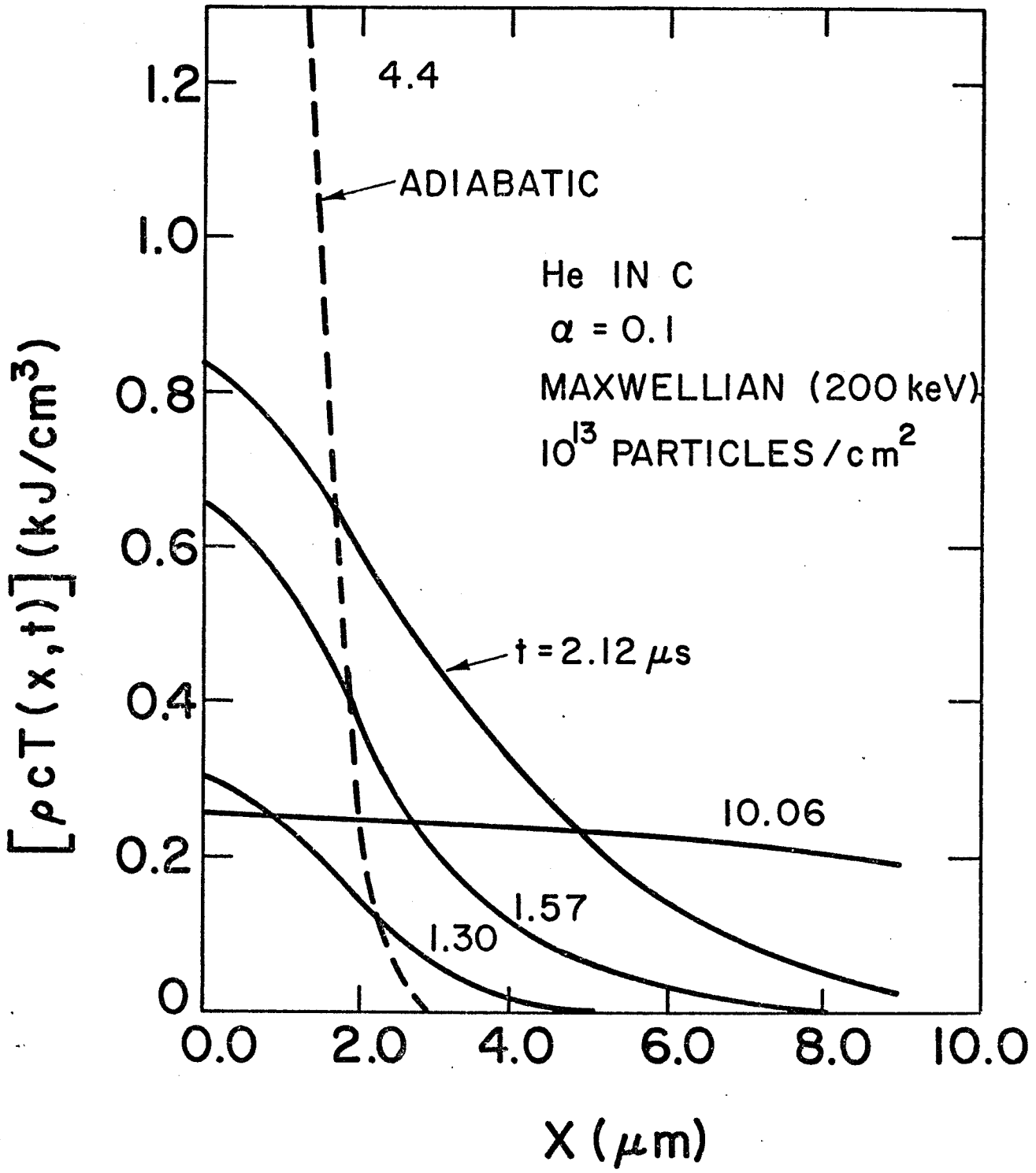

Figure 1.9 Variation of liner temperature with position and time for a 200 KeV Maxwellian spectrum of He in carbon

Figure 1.10
Variation of surface temperature with time for different material diffusivities

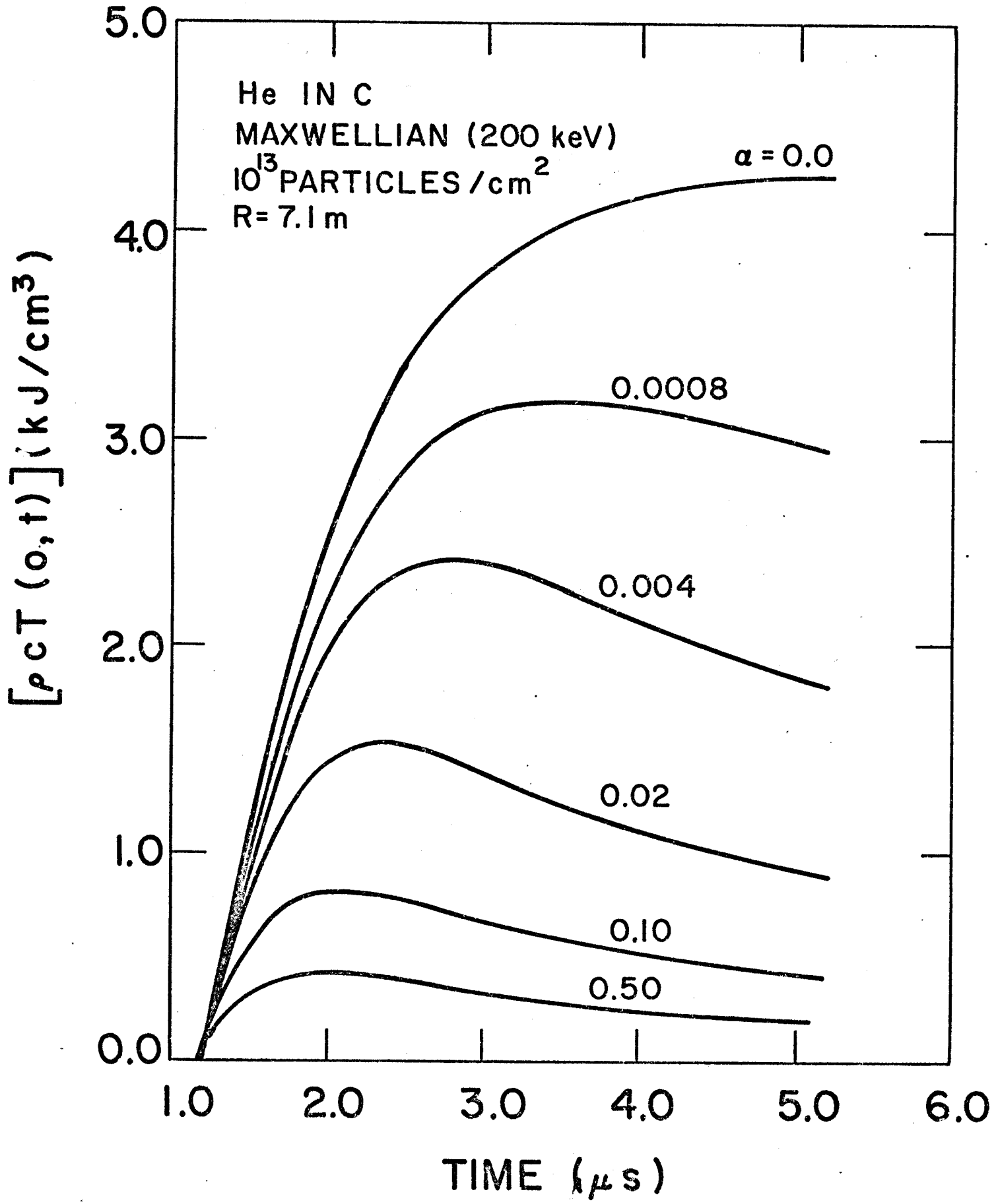

The model developed here is sufficiently general to include arbitrary spectra, cavity size, and material properties. It will be extended to include higher and lower energy particles as well as nuclear stopping.

V.D.2 Stress Analysis for the Liner

i. Impulsive Heat Deposition in a Semi-infinite Medium

Estimates of the stress levels produced in the liner can be made from solutions for impulsive energy deposition in an elastic half-space.[11] The volumetric heat generation rate is given by:

$$q'''(x,t) = q'''_0 e^{-x/\ell} [H(t) - H(t - t_0)] \tag{2.1}$$

where ℓ is the deposition length ($\ell \equiv 1/\mu$), t_0 is the deposition time, and H is the Heavyside step function. The heat conduction equation, boundary conditions, and initial condition are similar to these described in the previous section with T_0 = zero. When the deposition time approaches zero, the resulting temperature response becomes:

$$T(x,t) = T_s \exp(-x/\ell)\, H(t) \tag{2.2}$$

where $T_s = Q/\rho c_p \ell$ is the surface temperature rise and Q is the deposited energy.

For uniaxial motion, the equilibrium equation in terms of stress and temperature is:

$$\frac{\partial^2 \sigma}{\partial x^2} - \frac{1}{c^2}\frac{\partial^2 \sigma}{\partial t^2} = \frac{3\alpha K}{c^2}\frac{\partial^2 T}{\partial t^2} . \tag{2.3}$$

Here, σ is the normal stress in the x direction, K is the bulk modulus, c is the dilational wave speed ($c = (K + \frac{4}{3} G)/\rho$), α is the thermal expansion coefficient, G is the shear modulus, and ρ is the material density. In terms of the nondimensional variables: $\bar{x} \equiv x/\ell$, $\bar{t} \equiv tc/\ell$, and $\bar{\sigma} = \sigma/3\alpha T_s K$, the solution to Eq. (2.3) is:

$$\bar{\sigma} = \frac{-1}{2} \left\{ \exp\left[-(\bar{x} - \bar{t})\right] + \exp\left[-(\bar{x} + \bar{t})\right] \right\} H(t) + \cosh(\bar{t} - \bar{x})\, H(\bar{t} - \bar{x}) \; . \tag{2.4}$$

Initially, the wave is entirely compressive; however, the tensile component grows until in the limit for arbitrarily large values of time, the peak tensile and compressive stresses, $\bar{\sigma}_{max}$, are $\pm$ 0.50. The growth of the tensile component is very rapid, e.g. for $\bar{t} = 2$ when the front is at $\bar{x} = 2$, the maximum tensile stress $\bar{\sigma}$ is equal to 0.49. Therefore, the limiting fully-developed values can be used for estimates involving deposition in layers of finite thickness. With a reflection of the compressive stress from the outer free surface, the instantaneous maximum tensile stress is:

$$\sigma = 3\alpha T_s K = \alpha T_s E/(1 - 2\nu) \tag{2.5}$$

where E and ν are the elastic modulus and Poisson's ratio respectively. This result agrees with the quasi-static magnitude of $\alpha TE/(1 - k\nu)$ in which k = o, 1, and 2 for uniaxial, biaxial, and triaxial states respectively.

Results are shown in Fig. (2.1) for stainless steel and nearly-isotropic graphite. The fatigue limit for the graphite does not include temperature compensation and is based on a fraction of the instantaneous fracture strength.

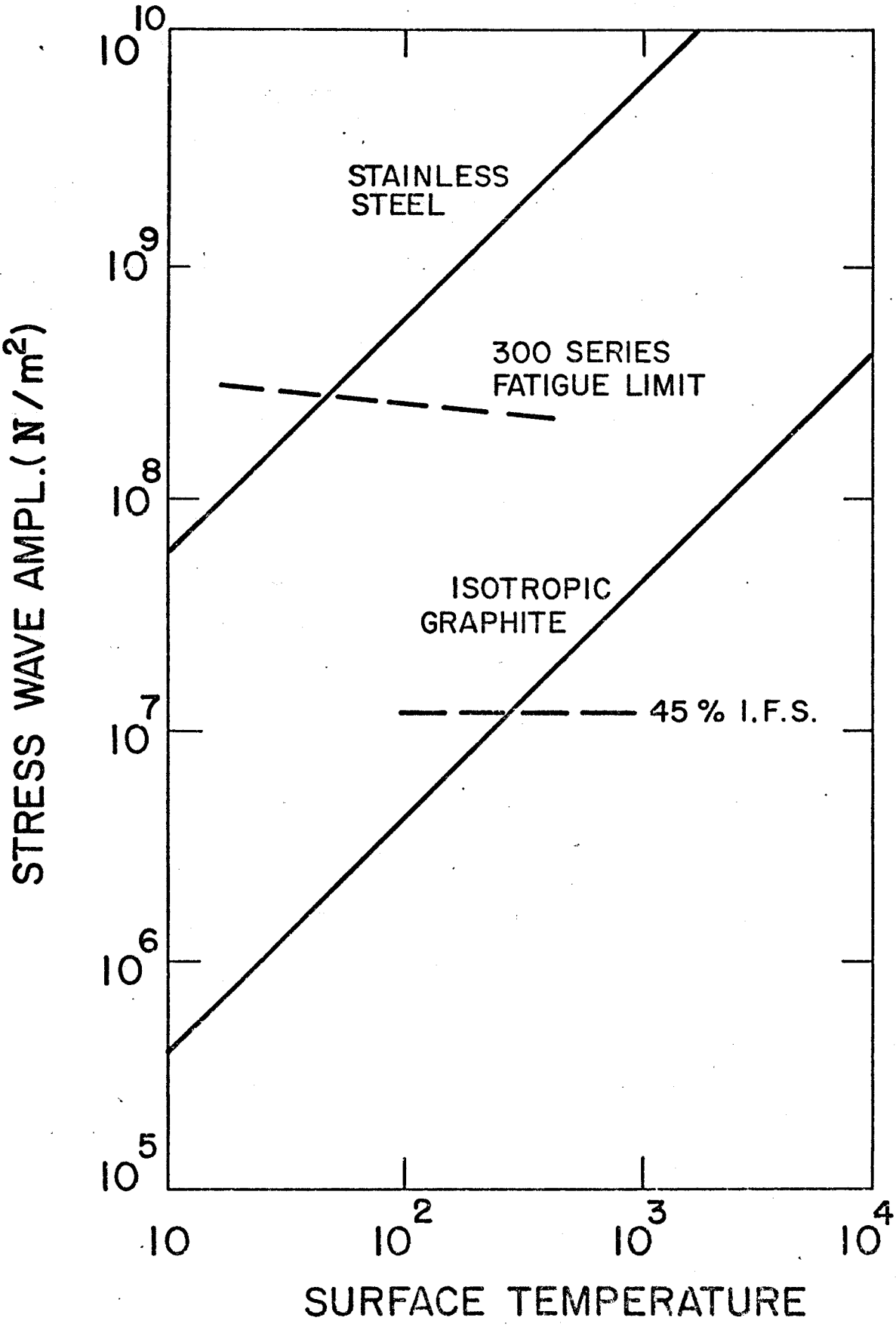

Figure 2.1 Typical variation of stress wave amplitude with surface temperature rise for stainless steel and isotropic graphite

ii. Energy Deposition in a Finite Elastic Layer

(a) Series Solution:

Here we consider a layer with finite thickness L as shown in Fig. (1.1a). The governing differential equation in terms of the x displacement component u(x,t) is:

$$c^2 \frac{\partial^2 u(x,t)}{\partial x^2} - \frac{\partial^2 u(x,t)}{\partial t^2} = a \frac{\partial T}{\partial x}(x,t) \tag{2.6}$$

where $a \equiv (1 + \nu)\, \alpha c^2/(1 - \nu)$. The boundary and initial conditions are:

$$\left.\begin{aligned} \sigma(o,t) = \quad \sigma(L,t) &= o \\ u(x,o) = \frac{\partial u}{\partial t}(x,o) &= o \end{aligned}\right\} . \tag{2.7}$$

Define:

$$\left.\begin{aligned} \overline{T}(x,t) &= T(x,t) \quad ; \quad o \leq x \leq L \\ &= -T(x,t) \quad ; \quad -L \leq x \leq o \end{aligned}\right\} . \tag{2.8}$$

Thus $\overline{T}(x,t)$ is an odd function of x which can be expressed as:

$$\overline{T}(x,t) = \sum_{n=o}^{\infty} T_n(t) \sin (n\pi x/L) \; ; \quad (-L \leq x \leq L) \tag{2.9}$$

and

$$T_n(t) = \frac{2}{L} \int_o^L T(x,t) \sin (n\pi x/L)\, dx \; .$$

The solution to Eq. (2.6) can be expressed as an infinite series:

$$u(x,t) = \sum_{n=o}^{\infty} u_n(t) \cos (n\pi x/L) \; . \tag{2.10}$$

Therefore,

$$u_n'' + \omega_n^2 u_n = - \omega_n sT_n \tag{2.11}$$

where, $\omega_n = n\pi c/L$ and $s = a/c$. The solution to Eq. (2.11) is:

$$u_n(t) = A \sin \omega_n t + B \cos \omega_n t - s \int_0^t T_n(\xi) \sin \omega_n (t - \xi) \, d\xi \, . \tag{2.12}$$

The initial conditions on displacement and velocity yield:

$A = B = o$. The resulting stress is given by:

$$\sigma(x,t) = \sum_{n=o}^{\infty} - [\rho c \omega_n u_n(t) + \rho a T_n(t)] \sin \frac{n\pi x}{L} \, . \tag{2.13}$$

Evaluation of $\sigma(x,t)$ from Eq. (2.13) is straightforward. For example, consider the case:

$$T(x,t) = T^* e^{ax} \quad (a < o, \; T^* > o)$$

$$T_n(t) = 2\omega_n T^* (1 - e^{aL} \cos n\pi) / cL \, [a^2 + (\omega n/c)^2] \, ,$$

and

$$u_n(t) = - (sT_n/\omega_n) (1 - \cos \omega_n t) \, .$$

Hence,

$$\sigma(x,t) = - \sum_{n=o}^{\infty} T_n \rho a \cos (\omega_n t) \sin (\omega_n x/c) \, . \tag{2.14}$$

This solution offers a relatively convenient means of determining the stress solution provided that the temperature gradient is not severe so that the summation can be truncated after a reasonable number of terms.

Under these conditions, the results given by Eq. (2.14) are in close agreement with those given by the half-space solution. However, if a severe temperature gradient exists, considerable error may result in the magnitude of the maximum stress and the shape of the wave profile unless an extremely large number of terms are taken in the summation.

b. Wave Solution:

In the following, an alternative solution to Eq. (2.6) subject to the boundary and initial conditions (2.7) is developed. The boundary conditions can be written as:

$$c^2 u_x (o,t) = a\, T(o,t) \tag{2.15}$$

and

$$c^2 u_x (L,t) = a\, T(L,t) \ . \tag{2.16}$$

If the temperature distribution does not change appreciably during wave generation, one can assume that $T_t = o$ and $T = T(x)$. Define:

$$\phi_x(x) = \frac{a}{c^2} T(x) \ , \tag{2.17}$$

and

$$V(x,t) = u(x,t) - \phi(x) \ . \tag{2.18}$$

Therefore,

$$u_{xx} = V_{xx} + \phi_{xx} = V_{xx} + \frac{a}{c^2} T_x \ . \tag{2.19}$$

Equation (2.6) can be written as:

$$c^2 \left(V_{xx} + \frac{aT_x}{c^2}\right) - V_{tt} = a\, T_x \tag{2.20}$$

or,

$$c^2\, V_{xx} - V_{tt} = o\ . \tag{2.21}$$

The initial conditions become:

$$V(x,o) = -\,\phi(x)\ , \tag{2.22}$$

and

$$V_t(x,o) = o\ . \tag{2.23}$$

The solution to Eq. (2.21) subject to (2.22) and (2.23) is:

$$v(x,t) = F(x + ct) + G(x - ct) \tag{2.24}$$

where,

$$V(x,o) = F(x) + G(x) = -\,\phi(x) \tag{2.22a}$$

and

$$V_t(x,o) = cF(x) - cG(x) = o\ . \tag{2.23a}$$

Thus,

$$F(x) = G(x) = -\,\frac{1}{2}\,\phi(x) \tag{2.25}$$

$$v(x,t) = -\,\frac{1}{2}\,[\phi(x + ct) + \phi(x - ct)] \tag{2.26}$$

$$u(x,t) = \phi(x) - \frac{1}{2}\,[\phi(x + ct) + \phi(x - ct)] \tag{2.27}$$

and the stress becomes:

$$\sigma(x,t) = - \frac{\alpha\rho c^2(1+\nu)}{2(1-\nu)} [T(x + ct) + T(x - ct)] . \qquad (2.28)$$

The stress boundary conditions require that: $T(ct) = - T(-ct)$ and $T(L + ct) = - T(L - ct)$. If $T = f(x)$, $(o \leq x \leq L)$, then the preceding conditions require that $T = - f(x)$, $- L \leq x \leq o$, and $T(x) = T(x + 2L)$.

Results for a typical example are shown in Fig. (2.2). The constants for steel are used and the stresses are given in lbs/in^2 per degree of temperature rise.

The preceeding wave solution can be extended to obtain a closed form solution for general temperature distributions of the form:

$$T(x,t) = (pt + q)\, f(x) + (mx + n)\, g(t) \qquad (2.29)$$

where p, q, m, and n are constants. The corresponding stress is given by:

$$\sigma(x,t) = \frac{\rho a}{2} \Big\{ q\, [f(x + ct) + f(x - ct)] + \frac{p}{c} [f(x + ct) - f(x - ct)] - (mx + n)\, g(t) \Big\} . \qquad (2.30)$$

Equation (2.30) is quite general and has not been previously reported in the literature.

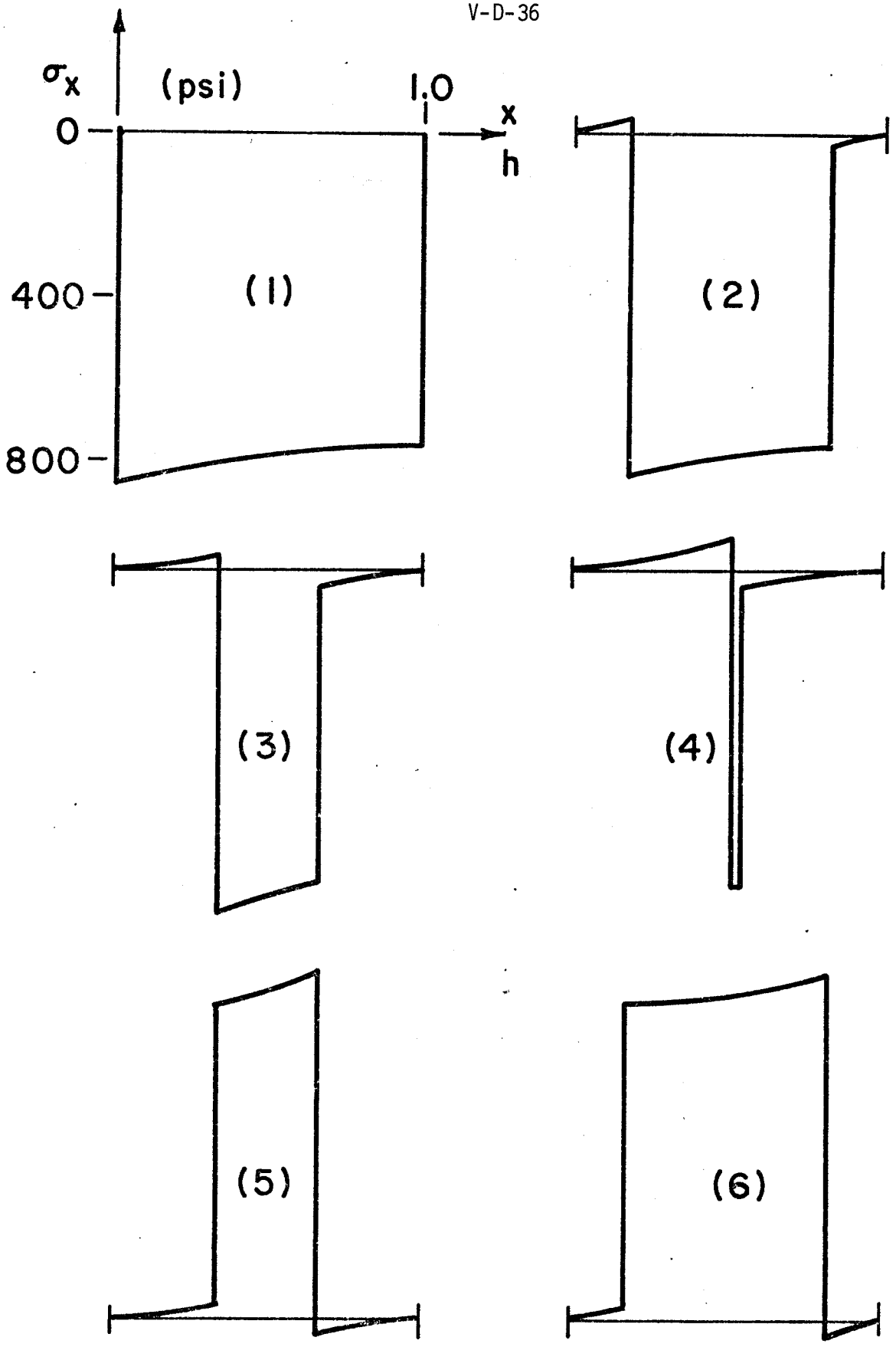

Figure 2.2

Typical stress wave profiles for different values of time (1.5 cm thick steel wall with temperature distribution given by $T = T_o e^{-x/10}$)

For $m = n = o$:

$$T(x,t) = (pt + q)\, f(x), \text{ and}$$

$$\sigma(x,t) = -\frac{\rho a}{2}\left[\left(q + \frac{p}{c}\right) f(x + ct)\right. \tag{2.31}$$

$$\left. + \left(q - \frac{p}{c}\right) f(x - ct)\right] .$$

The actual temperature distribution can be represented by piece-wise linear functions for which the above solution can be used. A computer program has been developed for this purpose.

References for Section V-D

[1] H. S. Carslaw and J. C. Jaeger, Conduction of Heat in Solids, Second Edition, Oxford University Press (1959).

[2] G. E. Myers, Analytical Methods in Conduction Heat Transfer, McGraw Hill (1971).

[3] J. Hovingh, "First Wall Studies of a Laser-Fusion Hybrid Reactor Design," Proc. 2nd Topical Meeting on the Technology of Controlled Nuclear Fusion, Richland, Washington (1976).

[4] M. Born and E. Wolf, Principles of Optics, Fifth Edition, Pergamon Press (1975).

[5] Lawrence Livermore Laboratory, "Laser Program Annual Report," A. E. Glass and K. L. Cummings, Editors (March 1976).

[6] L. A. Booth, "Central Station Power Generation by Laser-Driven Fusion," Los Alamos Scientific Laboratory report LA-4858-MS, Vol. I (Feb. 1972).

[7] J. M. Williams, et al., "A Conceptual Laser Controlled Thermonuclear Reactor Power Plant," Proc. 1st Topical Meeting on the Technology of Controlled Nuclear Fusion, San Diego, California (1974).

[8] T. G. Frank, et al., "Heat Transfer Problems Associated with Laser Fusion," Proc. 16th National Heat Transfer Conference, St. Louis, Missouri (1976).

[9] F. Biggs and R. Lighthill, "Analytical Approximations for X-ray Crossections II," SC-RR-71-0507, Sandia Laboratories (1971).

[10] J. Lindhard, M. Scharff and H. E. Schiott, Mat. Fys. Medd. Dan. Vid. Selsk, 33, 14 (1963).

[11] L. W. Morland, "Generation of Thermoelastic Stress Waves by Impulsive Electromagnetic Radiation," AIAA Journal, 6, 1063-1066 (1968).

V-E. Vacuum System Design and Requirements

V-E-1. General Description

The main function of the vacuum system in the laser cavity is to remove the products of the fusion reaction as well as the unburned fuel and to maintain the cavity at a prescribed pressure.The system also has to deliver the effluent to a processing center for separation and fuel recovery.

In general there are two basic methods for pumping the laser cell. The first is to seal the cavity completely from its containment building and to pump it internally. The second is to evacuate the containment building and to allow the cavity to be pumped through the ports provided for the laser beams. To decide which is the better way, one has to establish the criterion on whether or not the containment building has to be evacuated. There are some good arguments for an evacuated containment building among them being an inherent safety against an accidental tritium release.

For the present it will be assumed that the building will be evacuated and on this basis, the second method appears to have an advantage. The major advantages of this method are:

1 - No sealed windows are needed in the laser beam ports. Such windows would be subject to very high power density and a severe radiation environment. Although windows will ultimately have to be provided within the containment building, they will not be subjected to severe radiation and the power density will be lower.

2 - Mirror mounting is simplified. The mirror mounts can now be decoupled from the cavity and will therefore be more stable.

3 - No additional ports are needed for pumping. Any penetrations through the blanket provide leakage paths for neutrons and take valuable space from the blanket.

A disadvantage of this method is the possibility of depositing debris on the mirrors by the pumped gas. This, however, is a problem which will have to be addressed in any case, because debris from other sources could also be deposited on the mirrors.

V-E-2. Pump Selection

The prescribed operating pressure for the laser fusion cell is 0.1 torr. Although this pressure is readily achievable by many pumps, it does present a problem from the standpoint of tritium contamination.

The problem of tritium contamination is two fold. It is imperative to prevent tritium from combining with hydrocarbons from which it would be difficult to separate and which would finally have to be disposed of in an environmentally acceptable way. It is also equally important to prevent impurities from contaminating the effluent and thus further complicating the problem of fuel recovery.

Liquid helium cooled cryo-sorption pumps which are the cleanest of all the systems considered, operate very well below 10^{-3} torr, but experience "thermal runaway" at higher pressures. Nitrogen cooled cryo-sorption pumps are not very effective for hydrogen and are useless for pumping helium. Dry sealed mechanical pumps operate down to 10 torr but are inefficient at lower pressures. Similarly, turbo-molecular pumps, although clean, operate at 30% of rated capacity at 0.1 torr.

In this relatively high pressure range, positive displacement gas compressors are used successfully without the use of sealing oil. Such pumps are built with well balanced interleaving rotors and definite clearances between the moving parts so that operation at high rotational speeds is common practice. Roots blowers, sometimes called "mechanical booster pumps" operate at maximum capacity and efficiency in this pressure range, and are relatively contamination

free. It is recommended, however, that they operate at a compression ratio of about 10, which means that two compressors in series are needed if the effluent is to be delivered at 10 torr to whatever back up system is used. In the case of the laser cell, the back-up system will be an oil-less mechanical pump which will compress the gas to near atmospheric pressure for delivery to the isotope separation system.

V-E-3. Gas Throughput

The laser fusion cavity will burn about 145 mole atoms of D and T which comprises about 6% of the total injected fuel. This means that the total amount of D_2, T_2 and DT pumped out as unburned fuel at 600 K is:

$$\dot{Q}_{D_2,T_2,DT} = \left(\frac{145}{2}\right) \frac{\text{moles}}{\text{day}} (.06) \quad \frac{22.4 \text{ liters}}{\text{mole}} \quad \frac{760 \text{ torr}}{0.1 \text{ torr}} \quad \frac{600 \text{ K}}{300 \text{ K}}$$

$$= 4.11 \times 10^8 \text{ liters/day or } 4760 \text{ liters/sec.}$$

At 0.1 torr this amounts to

$$\dot{Q}_{D_2,T_2,\,DT} = 476 \text{ torr liters/sec.}$$

The helium gas production is figured similarly. For each DT reaction, an α particle is produced. Then the α particle production is:

$$\frac{72.5 \text{ moles}}{\text{day}} \quad \frac{6.02 \times 10^{23} \text{ atoms}}{\text{mole}} \quad \frac{\text{day}}{43{,}200 \text{ sec}} = 1.01 \times 10^{21} \ \alpha/\text{sec.}$$

Helium gas production is:

$$\frac{1.01 \times 10^{21} \ \alpha \text{ atom}}{\text{sec}} \quad \frac{1.03 \times 10^{-22} \text{ torr liters}}{\text{atom K}} \ 600 \text{ K} = 62.4 \ \frac{\text{torr liters}}{\text{sec.}}$$

Leakage from the helium carrier gas within the blanket into the cavity cell through the mechanical seals between the hemispherical head and the cylindrical portion is estimated at about 1.0×10^{-2} torr liters/ sec. cm. There is a total of ~ 100 meters of sealed surface on the cavity side, which will add 100 torr liters/sec of helium gas making the total helium gas throughput equal to

$$\dot{Q}_{He} \simeq 163 \text{ torr liters/sec.}$$

The conductance of a single laser beam port for viscous flow, when the product of pd > 0.5 torr cm is given by

$$\frac{1}{C} = \frac{8000\,\eta l}{\pi r^4 \phi\,(1333)} \quad \frac{\text{sec}}{\text{liter}}$$

where η is the viscosity of the gas in poise, l the length of the port, r its radius and p the pressure in torr. If we take l = 200 cm, r = 25 cm and η for hydrogen at 600 K as 138×10^{-6} poise, then

$$\frac{1}{C} = 1.35 \times 10^{-6} \quad \frac{\text{sec}}{\text{liter}}$$

$$C = 7.4 \times 10^5 \text{ liters/sec}$$

For eight ports at 0.1 torr, the total conductance is 5.9×10^5 torr liters/sec, which is far in excess of the estimated throughput.

If we assume the containment building to be 30 meters in diameter and 40 meters high, its volume will be $\sim 29 \times 10^6$ liters. A reasonable leak rate into such a building is ~ 200 torr liters/sec of essentially air.

Thus it appears that the total amount of gas that has to be exhausted by the vacuum system is about 840 torr liters/sec, consisting of about 57% D_2, T_2 and DT, 20% helium and 23% air.

V-E-4. Pump Capacity Requirements

The pumping capacity needed to maintain the laser cavity containment building at 0.1 torr is ~ 8400 liters/sec. Roots blowers of 6000 liters/sec capacity for air are readily available. Their capacity for hydrogen would be higher yet. Two sets of 6000 liter/sec roots blowers backed up by two sets of 600 liter/sec roots blowers will give the needed pumping capacity with a wide safety margin. A third set can be used as a standby and during building pumpdown.

The time required to evacuate the containment building from atmospheric pressure, if we assume a constant pumping speed is given by:

$t = \frac{V}{S} \ln \frac{\rho o}{p}$ where V is the volume and S, the pumping speed,

$$t = \frac{29 \times 10^6}{18 \times 10^3} \frac{\text{liters sec}}{\text{liters}} \text{Ln} \frac{760}{0.1} = 1.43 \times 10^4 \text{ sec}$$

$t \approx 4$ hours

VI. First Wall and Blanket Analyses

VI-A. Introduction

VI-A.1. Pedagogy

The blanket of a D-T fusion reactor is the zone where tritium is bred and where most of the nuclear reaction energy (~ 80%) is deposited. This energy must be removed and delivered to a power conversion unit. An efficient blanket cooling scheme at a relatively high temperature is therefore required in order to attain a reasonably high overall thermal efficiency for the plant. Such cooling scheme should be compatible with the tritium breeding and recovery processes. It would also be desirable to operate the blanket at relatively low pressures in order to reduce the structural materials requirements and simplify the overall design of the primary loop [1-3].

Various cooling-breeding schemes have been suggested for fusion reactor blankets. In all these schemes, the breeding material is either pure lithium or a lithium compound. The coolants most frequently used are lithium and helium. When a lithium compound is used, it usually serves the dual purpose of breeding and cooling, and thus the tritium recovery and heat removal loops are combined. Such a scheme greatly simplifies the blanket design since only one set of feed/discharge pipes and headers is required, which in turn reduces the effort needed to repair or replace part of the blanket [4]. On the other hand, when a lithium compound is used for cooling, the heat transfer problems encountered in the design process are less conventional and thus require additional effort during the design stage.

When a lithium compound is used as a coolant and breeding medium, it has to occupy a large fraction of the blanket volume (~95%) in order to maximize the breeding ratio. In such a design around 75% of the heat is deposited in the coolant while the remaining 25% are deposited in structural

materials. Thus, if the first wall is separately cooled, the blanket cooling process becomes a heat transport problem. Most of the efforts ordinarily devoted to obtaining high heat transfer coefficients and large cooling-surface areas are not needed in this case. The problem here is to select a good heat transport medium, viz one which would have a high value of (ρc_p/pumping power).

A gas-carried Li_2O blanket design has been suggested by Sze, et al. [4] for tokamak-type reactors. Such a design appears well suited for the geometrically-simple laser fusion reactors. It satisfies the different requirements for cooling/breeding materials and is expected to provide sufficiently high breeding ratios. Detailed description of the Li_2O blanket concept is given in the following section.

Several schemes for cooling the first walls of laser fusion reactors have been suggested. Three different approaches to the first wall design have been proposed (Section V-A & B): dry wall, wet wall and magnetically protected wall. In dry wall designs, a metallic wall which is independently cooled is used to separate the microexplosion cavity from the remainder of the reactor. This wall may be protected from the pulsating short-range photons and ions by a graphite liner which would absorb these radiations and radiate a relatively steady heat flux to the first wall. The wall is cooled by either helium, liquid metal, or boiling water. The latter is superior since the phase change process allows the wall to be operated at near-isothermal conditions (Section VI-C). Unprotected metallic walls on the other hand experience a pulsating surface heating load with an accompanying temperature rise and stresses (Section V.A).

For the wet wall concept, a thin liquid lithium film is used to protect the niobium first wall from the soft x-rays and charged particles emanating from the microexplosion. This design has several disadvantages among which

are: high vacuum pumping power requirements, limited rep rate capabilities and design complexity. These and other limitations are discussed in Section (V_B) of this report.

For magnetically protected walls the charged particles are diverted away from the first wall and deposited on some collection surface. The wall will still be subjected to the x-rays and reflected laser light, however, these can be accomodated with suitable liner design. Magnetically protected first walls coupled with nonmetallic cooling schemes offer distinct advantages over other designs.

The remainder of this section is concerned with the thermal hydraulic and mechanical design of the first wall and blanket. The advantages of the flowing Li_2O blanket concept are first discussed. The neutronic results used are presented in section VI-B while the main thermal hydraulic parameters are given in Section VI-C. Stress analysis and mechanical design considerations are presented in sections VI-D and E respectively.

VI.A.2 The Li_2O Blanket Concept

As indicated earlier, a lithium compound can be used to combine the blanket's heat removal and breeding functions. Here, a gravitational flow Li_2O blanket, originally proposed by Sze, et al. [4] for use in tokamak type reactors, is used. A schematic diagram of the cavity and blanket is shown in Fig (2.1).

Lithium oxide particles, 100-200 μ in diameter, enter the blanket at 450°C. While flowing through the blanket, energy is deposited in the particles and tritium is bred within them. Thus the Li_2O particles act as a heat transport medium. The particles flow by gravity through the two breeding zones of the blanket and exit at 550°C and 850°C respectively. The inner breeding zone is 35 cm thick while the outer zone is 6 cm thick. The hot Li_2O stream from the outer breeding zone flows to the tritium extraction cycle (Section IX) prior to joining the other stream on the way to the steam generator. After leaving

FIGURE (2.1)

U W LASER FUSION REACTOR CAVITY

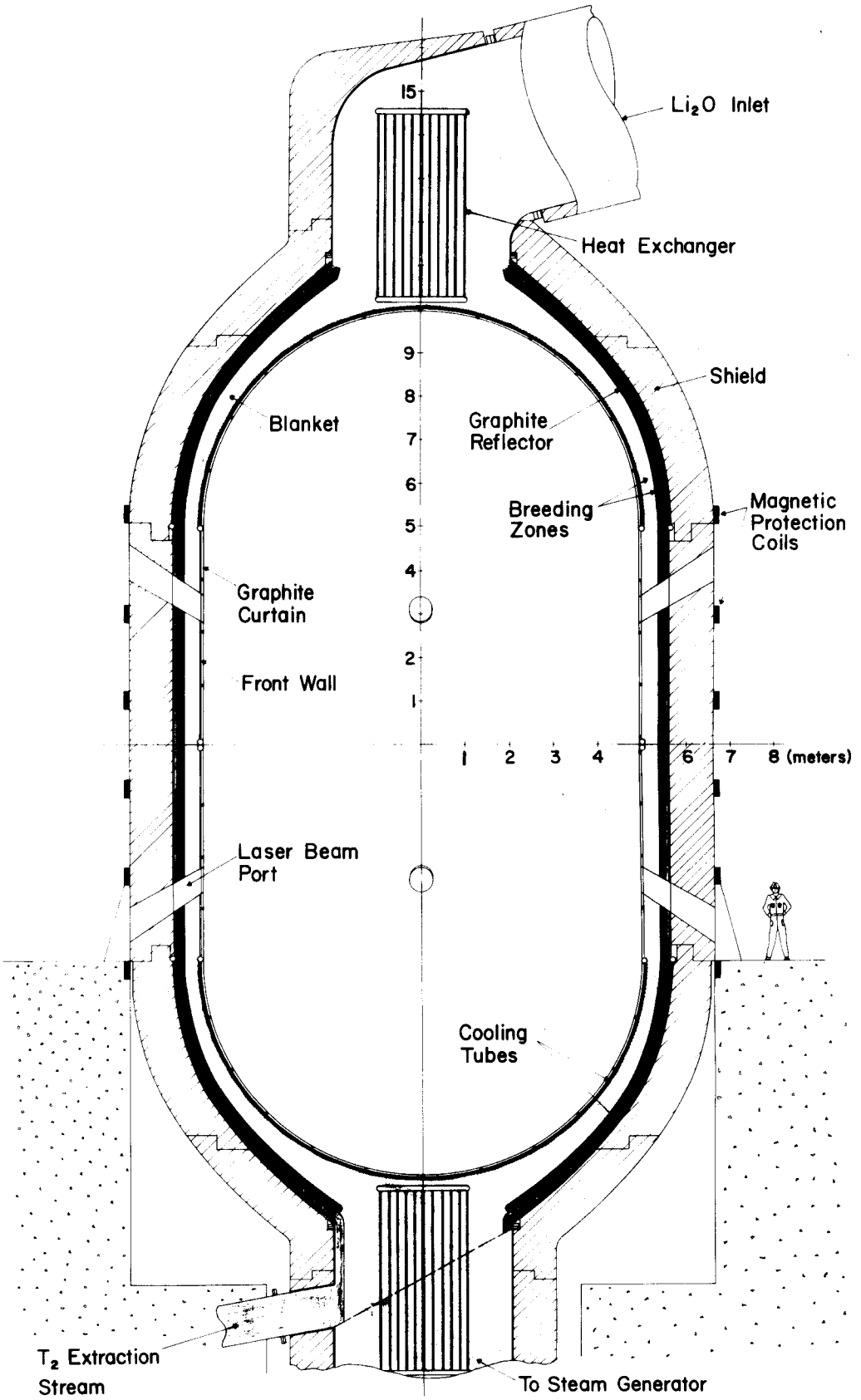

the steam generator, the particles are returned to the blanket either mechanically or penumatically.

The simple, and unique, blanket design described here has many attractions. The pressure inside the blanket is only 1 atm and, therefore, the structural materials requirements for the blanket will be quite small. Helium gas fills the gaps between the particles in the blanket and acts as a carrier gas in the pneumatic particle transport system. The void fraction in the blanket is only 40% which means that the required blanket thickness will not be large and that sufficiently high breeding ratios can be obtained. While the particles act as a good heat transport medium to remove the heat generated within the blanket, the rate of heat loss from the blanket to the first wall is relatively low because of the poor heat transfer coefficients associated with the low pressure gas-solid flow. Hence, the first wall can be maintained at temperatures well below those of the blanket without adversely affecting the overall thermal efficiency of the plant. The poor heat transfer coefficients in gas-solid flow allows the blanket's back wall to come in contact with the hot Li_2O stream in the outer breeding zone without fear of exceeding the maximum allowable temperature.

The Li_2O stream in the second breeding zone can be heated within the blanket to a sufficiently high temperature (850°C) compatible with tritium extraction. This allows a high degree of flexibility in designing the tritium extraction cycle since one can adjust the temperature and flow rate of the extraction stream. One controls the exit temperatures by merely adjusting the particles flow rate, i.e., residence time within the blanket. The fact that the heat deposition rate within the blanket drops as we move away from the first wall (Section VI-B) should not cause any difficulty. One can maintain relatively uniform exit temperatures by simply dividing the blanket into several subzones and adjusting the particles' flow rates within the different zones independently to match the local heat

generation rates. Flow channels orificing at the exit can be used to get the proper flow rates. Other, equally simple, schemes for obtaining a uniform exit temperature distribution can be surmised.

In this design, no intermediate heat exchanger is needed since the tritium diffusion through the primary system is sufficiently low. An Li_2O water reaction caused by a leak in the steam generator or first wall coolant channels is not hazardous. The elimination of the intermediate loop should have a significant impact on system economics. It will also allow for better steam conditions and hence a higher overall thermal efficiency.

The selected Li_2O particle size (100-200 μ) is a compromise between tritium diffusion, structural erosion, particle attrition, particle fabrication and material handling problems. Structural erosion does not appear to be a serious problem for particles of this size moving at $\sim$ 1m/sec [5]. Tritium recovery is possible if the solid particles are porous (Section IX).

Gravitational flow of the Li_2O particles through the blanket and steam generator will, of course, require corresponding material lifts to complete the flow path. Several particle transport schemes have been used in the chemical industry [6]; among these are mechanical transport, pneumatic mass lift, and pneumatic disperse phase flow. Selection of the best transport scheme will require further attention with the objectives of minimizing cost, circulation power, particle attrition and equipment maintenance.

Steam generators of the once-through or fluidized bed types can be used to extract the energy from the Li_2O stream. Fluidized bed heat exchangers have been extensively used in the chemical industry. However, with proper design and piping arrangement which allows for thorough mixing of the Li_2O particles, sufficiently high heat transfer coefficients can be obtained in a free-flow type heat exchanger. Selection among different heat exchanger designs will be dictated by economics, design simplicity and maintenance requirements.

In summary, the Li_2O blanket concept described here offers many attractions as evidenced by the simplicity of the heat removal and tritium extraction cycles.

References VI-A

[1]. B. Badger, et al., "UWMAK-I, A Toroidal Tokamak Power Reactor Design," UWFDM-68, Nuclear Eng. Dept., Univ. of Wisconsin (1974).

[2]. B. Badger, et al., "UWMAK-II, A Conceptual D-T Fueled, Helium Cooled, Tokamak Fusion Power Reactor Design, UWFDM-112, Nuclear Eng. Dept., Univ. of Wisconsin (1975).

[3]. B. Badger, et al., "UWMAK-III, An Advanced Noncircular Tokamak Power Reactor Design, UWFDM-150, Nuclear Eng. Dept., Univ. of Wisconsin (1976).

[4]. D. K. Sze, et al., "Gravity Circulated Solid Blanket Design For A Tokamak Fusion Reactor," Proc. 2nd Topical Meeting on the Technology of Controlled Nuclear Fusion, Richland (1976).

[5]. I. Finnie, "Erosion of Surfaces by Solid Particles," Wear, 3,87-103 (1960).

[6]. F. A. Fenz and D. F. Othmer, Fluidization and Fluid Particle Systems, Reinhold (1960).

VI-B Neutronic Results Used in Thermal Design

In this section, the neutronic results used in the thermal hydraulic design of the first wall and blanket are summarized. Additional details of the neutronic analyses and results may be found in Section VII of this report.

Figure 1 shows the volumetric heat generation profile in the Li_2O blanket. This information is needed for evaluating the particle velocities and temperature distribution within the blanket. The volumetric heating rate in the carbon liner, first wall, and first wall coolant are listed in Table 1. It should be indicated that these results pertain to the reactor midplane where the neutron wall loading is 7.65 MW/m^2. These results are modified to determine the heating rates at other locations where the wall loading is less than that at the midplane. The neutronic results from two-dimensional Monte Carlo calculations will be used in the future to refine the thermal hydraulic results presented here.

Table 1

Nuclear Heating Rates in the Carbon Liner, Stainless Steel, and Water Cooling Zones

(Based on 7.65 MW/m^2 Time-Averaged Neutron Wall Loading)

Zone No.	Composition	Neutron Heating[a]	Gamma Heating[a]	Total Heating
3	Carbon Liner	10.33	2.40	12.73
5	Stainless Steel (first wall)	20.59	29.43	51.02
6	16% Stainless Steel + 84% Water (40% dense) (first wall coolant)	19.13	5.85	24.98
7	Stainless Steel (back side of first wall coolant tubes)	19.02	29.50	48.52
13	Stainless Steel (blanket back wall)	0.47	3.35	3.82
14	16% Stainless Steel + 84% Water (steam) (back wall coolant)	0.07	0.45	0.52
15	Stainless Steel (back wall coolant tube)	0.41	2.73	3.14

a. in units of $watt/cm^3$

Figure 1

Volumetric heat generation profile in the Li_2O blanket

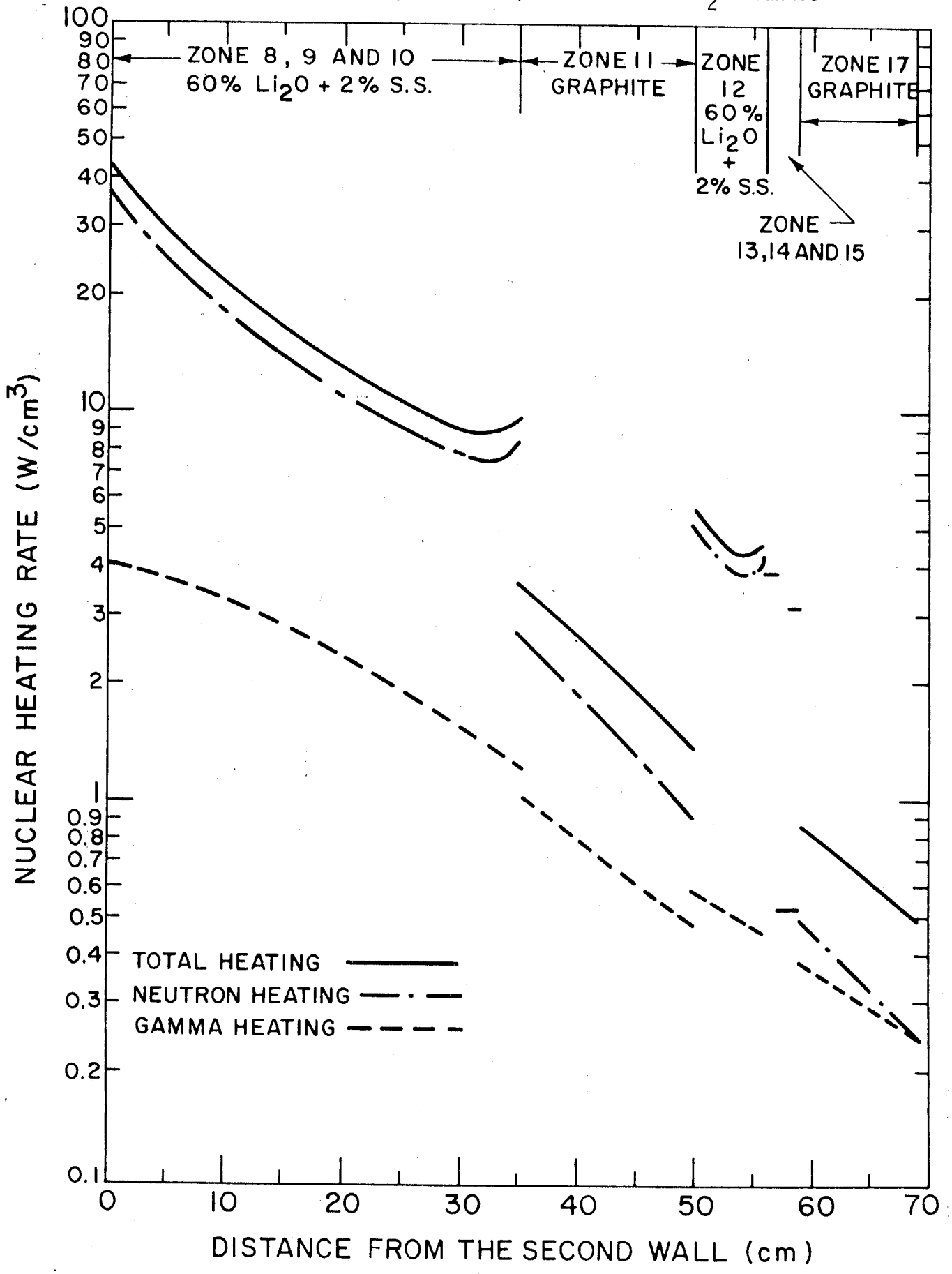

VI-C. Thermal Hydraulic Analyses

VI-C-1. First Wall Thermal Hydraulics

The first metallic wall in the reactor is a membrane type stainless steel structure with built-in coolant channels. Typical membrane wall designs are shown in Fig. 1.1. The design shown in Fig. 1.B has been developed and successfully used by Babcock & Wilcox in their modern high pressure fossil boilers.[1] Membrane walls can be easily manufactured; they have proven to be reliable, leak-free, and simple to install.

Boiling water is used to cool the first wall. The system is operated in a manner similar to recirculating boilers (see next section). Gaseous coolants were considered in great detail early on in the program and were abandoned in favor of the more efficient boiling mechanism. This is especially true in the end cap regions behind the collector plate of the charged particles where the heat flux is extremely high. The low-quality steam produced in the first wall is recirculated via a steam drum (Fig. 1.2). The saturated steam is used to cool the outer blanket surface where it is superheated before entering the intermediate pressure turbine.

In the following, the methods used in the thermal hydraulic design of the boiling-water cooled first wall are presented.

VI-C-1-i. Boiling Water Cooled First Wall

Nucleate boiling is an effective cooling mechanism for the expected high heat fluxes in the first walls of laser fusion reactors. In addition, it allows the first wall to be operated isothermally and, therefore, eliminates the thermal stresses which might have been produced by the axial temperature gradients in the wall. This is a desirable feature since neutronic considerations require these structures not to be massive.

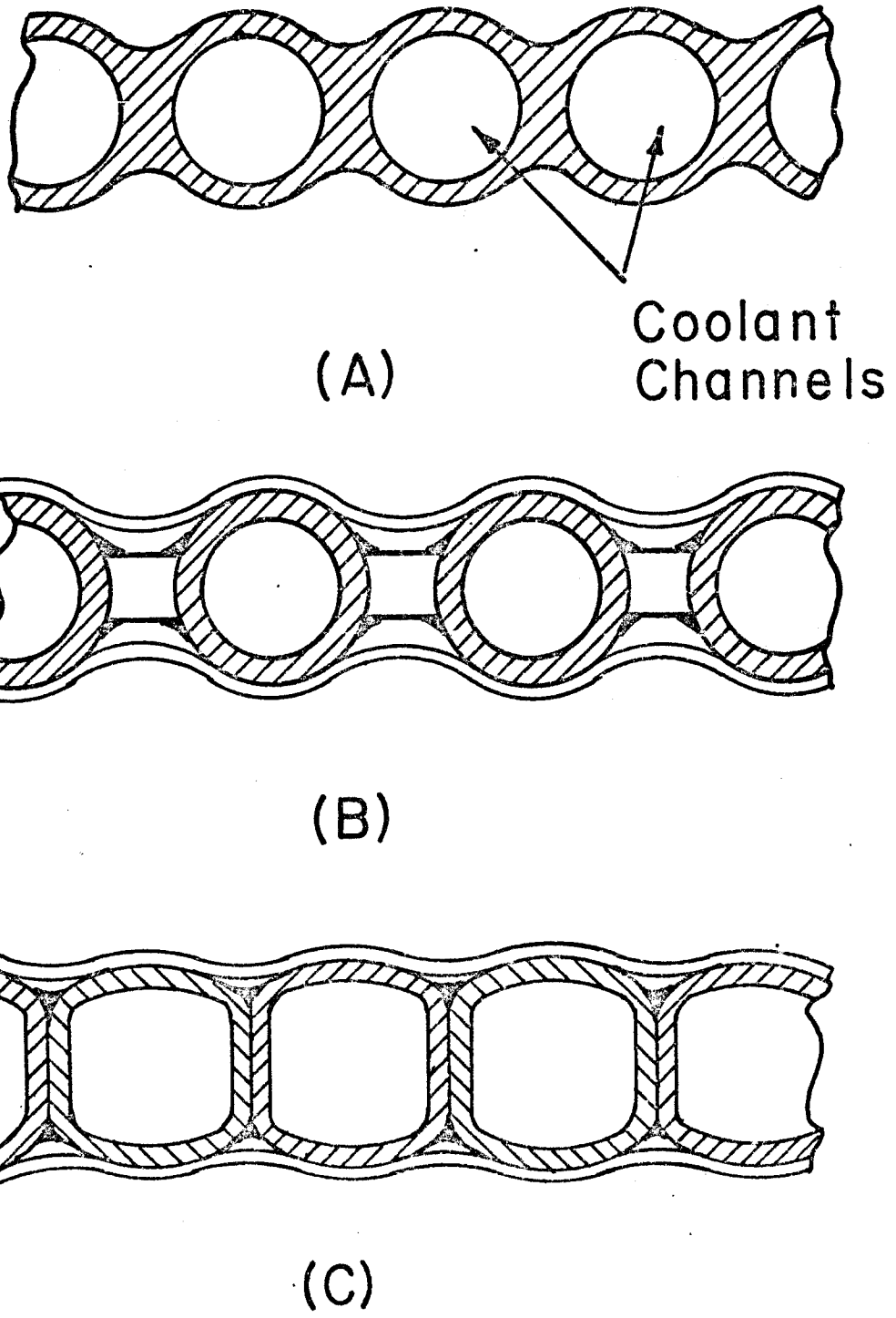

Figure 1.1 Typical membrane-wall designs for first wall construction.

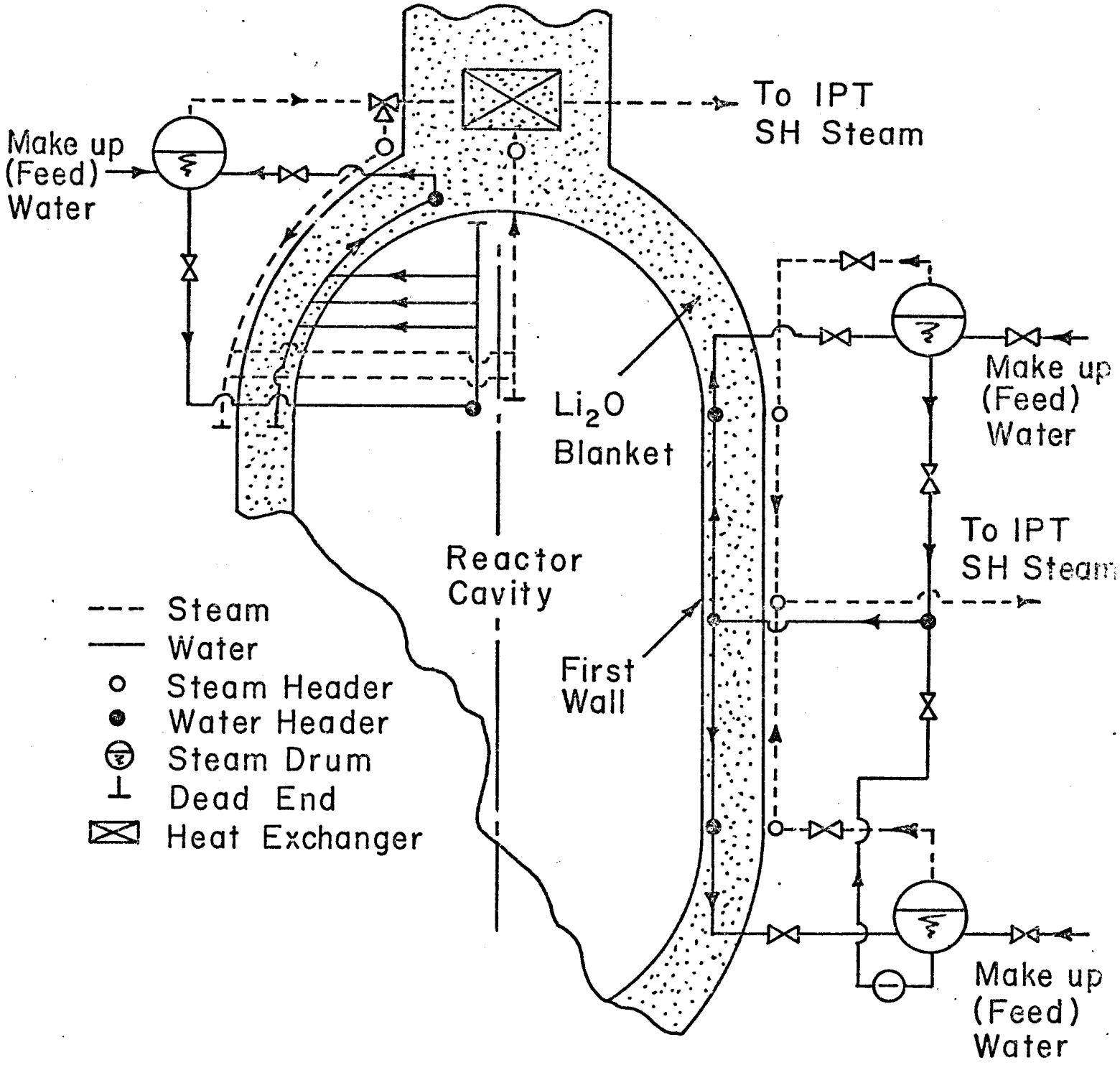

Figure 1.2 Schematic diagram showing coolant flow for the first wall and blanket back wall

A schematic diagram for the coolant flow arrangements in the first wall is shown in Fig. 1.2. For the cylindrical part of the cavity, saturated water enters the coolant channels of the membrane wall at the reactor's midplane. The two-phase mixture leaves the coolant channels at the junctures between the cylindrical part of the cavity and the two end caps. For the end caps of the cavity, the water flows in horizontal coolant channels between supply and exit headers arranged along four equally spaced meridians of these spherical surfaces (Fig. 1.2). The coolant flow rates are selected so that the exit quality of the two-phase mixture is less than 20%. This practical limit is dictated by water-chemistry considerations and is based on experience with recirculating-type fossil boilers.[2] The system pressure is selected such that the first wall can be kept at approximately 300°C which is the most suitable temperature from a radiation damage point of view (see Section VIII). The channel geometry and dimensions are selected such that the stresses are kept within design limits and the combined operational and initial costs are minimized.

A typical coolant channel with inside diameter D and thickness δ is shown in Fig. 1.3. The channel is subjected to the axially-varying heat fluxes $q''_L(Z)$ and $q''_B(Z)$; the first is radiated by the graphite liner while the latter is conducted from the Li_2O blanket. For the cylindrical part of the cavity, $q''_L(Z)$ consists of the time-averaged X-ray energy incident on the liner, and the neutron and gamma volumetric heating within it. In addition, for the end caps $q''_L(Z)$ includes the time-averaged ion energy incident on that part of the liner (collector plate). The heat flux $q''_B(Z)$ is proportional to the local temperature difference between the Li_2O and the coolant, and the overall heat transfer coefficient. In addition to $q''_L(Z)$ and $q''_B(Z)$, the coolant has to remove

Figure 1.3

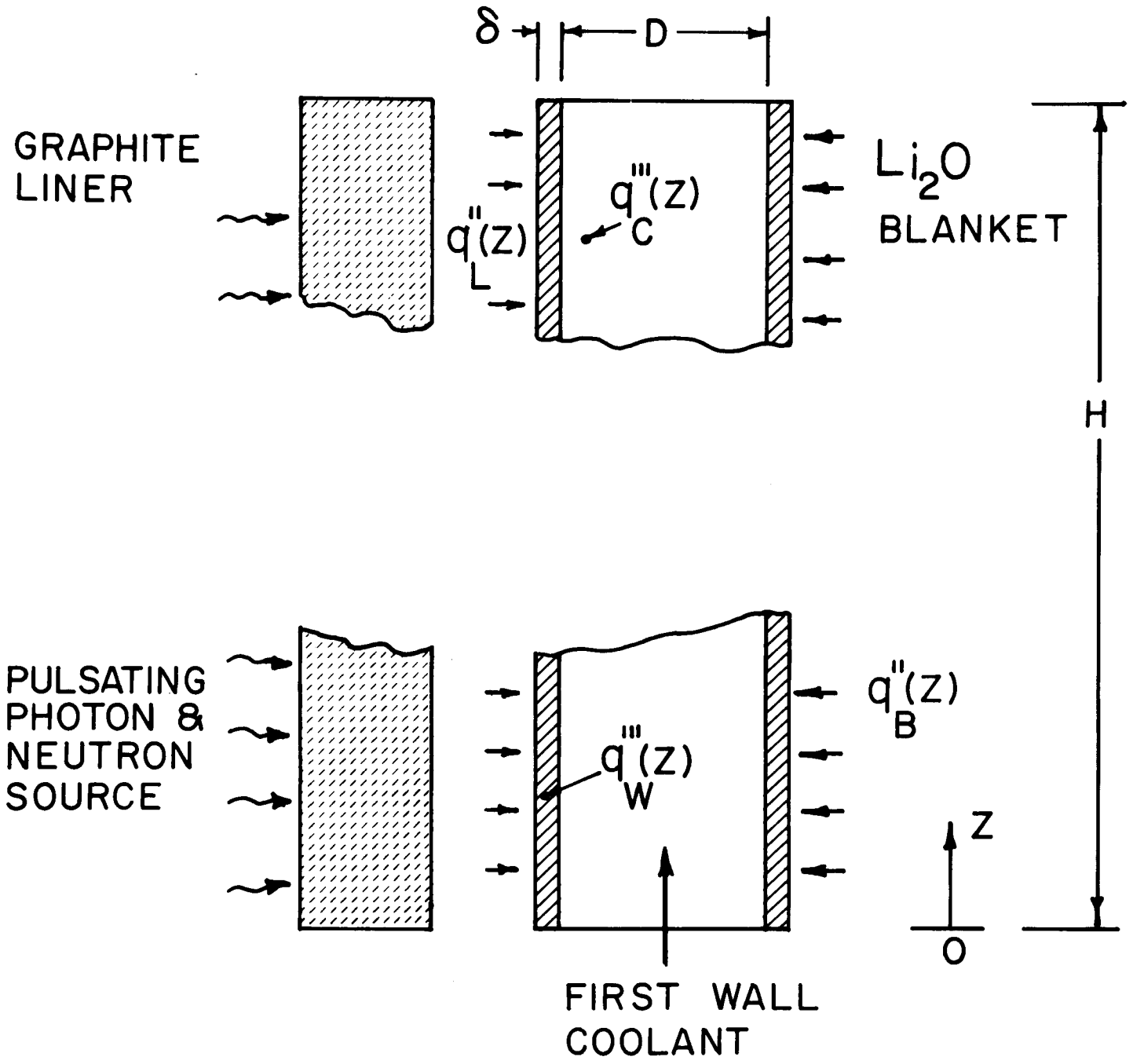

Schematic diagram of a typical coolant channel in the first wall.

the volumetric heat generated in the channel walls, $q_B'''(Z)$, and in the coolant itself, $q_c'''(Z)$.

For steady-state conditions, an energy balance for the system shown in Fig. 1.3 yields:

$$\dot{m}(h_Z - h_o) = \int_o^Z \{P_L\, q_L''(Z) + P_B\, q_B''(Z) + A_w\, q_W'''(Z) + A_c q_c'''(Z)\}dZ \qquad (1.1)$$

Here, $\dot{m}$ is the coolant flow rate, Z is the flow direction, h_Z is the local enthalpy, h_o is the inlet enthalpy, P_L is the heated perimeter on the liner side of the wall, P_B is the heated perimeter on the blanket side, A_w is the cross sectional area of the wall, and A_c is the flow area. For a given geometry, and inlet and exit conditions, Eq. 1.1 can be solved by trial and error to determine the necessary coolant flow rate $\dot{m}$ and hence the pressure drop in the channel. A trial and error solution is required since the heat generated within the coolant, $q_c'''(Z)$, depends on the local void fraction which depends indirectly on the flow rate.

As a first approximation, q_c''' is ignored and the corresponding coolant flow rate and quality distribution are determined. The latter is then used to determine the void fraction distribution by means of the von Glahn correlation[3] (Eq. 1.2) and hence, the volumetric heat generation in the coolant. The value of q_c''' is continually updated until the solution converges.

$$\frac{1}{X_Z} = 1 - \left(\frac{v_g}{v_f}\right)^{0.67}\left\{1 - \left(\frac{1}{\alpha_Z}\right)^{(v_g/v_f)^{0.1}}\right\} \qquad (1.2)$$

The pressure drop between the inlet section and any arbitrary location Z consists of the friction pressure drop Δp_f, the acceleration pressure drop Δp_a, and the static pressure difference Δp_s[4], where,

$$\Delta p_f = 2f \frac{(\dot{m}/A_c)^2}{\rho_f D} \int_o^Z \left\{\frac{1 - X_Z}{1 - \alpha_Z}\right\}^2 dZ, \qquad (1.3)$$

$$\Delta p_a(Z) = (\dot{m}/A_c)^2 \left\{\frac{(1 - X_Z)^2}{(1 - \alpha_Z)\rho_f} + \frac{X_Z^2}{\alpha_Z \rho_g} - \frac{1}{\rho_f}\right\}, \qquad (1.4)$$

and

$$\Delta p_s(Z) = \int_o^Z \{\rho_g \alpha_Z + \rho_f(1 - \alpha_Z)\} g \, dZ \qquad (1.5)$$

where f is the Fanning friction factor given by:[4]

$$\left.\begin{aligned} f &= (16/Re) && ; \quad Re < 2100 \\ &= 0.0791\ Re^{-0.25} && ; \quad 2100 < Re < 10^5 \\ &= 0.0460\ Re^{-0.2} && ; \quad Re > 10^5 \end{aligned}\right\} \qquad (1.6)$$

Here Re is Reynolds number ($Re = 4\dot{m}/\pi D\mu$). In the above equations, the saturated liquid density ρ_f and vapor density ρ_g are assumed to remain constant and equal to their value at the inlet pressure.

Knowing the mass flow rate and the quality and void fraction distributions, the above equations are used to determine the pressure drop in the channel and, hence, the pumping power.

The local heat transfer coefficient is determined using Jens-Lottes nucleate boiling correlation:[5]

$$\overline{h_Z} = 1.67 * 10^4 [10^{-6} q_L''(Z)]^{0.75} \exp(p/900) \qquad (1.7)$$

where $\overline{h_Z}$[=] Btu/hr-ft^2°F, q_L''[=] Btu/hr-ft^2, and p[=] psia. The inside wall surface temperature is then evaluated using the relation:

$$T_{in}(Z) = T_f + [q_L''(Z)/\overline{h_Z}] \qquad (1.8)$$

The outside wall temperature is given by[4]:

$$T_{out}(Z) = T_{in}(Z) + \left(\frac{q'''_w D_o^2}{8k} + \frac{q''_L D_o}{2k}\right) \ln\left(\frac{D_o}{D}\right) - \frac{q'''}{16\,k}\left(D_o^2 - D^2\right) \qquad (1.9)$$

where D_o is the outside tube diameter and k is the wall conductivity.

The critical heat flux is determined using the high-flow Macbeth correlation[6]

$$(q''_{CHF} * 10^{-6}) = A_1 - 0.25\, A_2 D(G*10^{-6})h_{fg}x \qquad (1.10)$$

where,

$$A_1 = a_o\, D^{a_1}\, (G * 10^{-6})^{a_2}$$
$$A_2 = a_3\, D^{a_4}\, (G * 10^{-6})^{a_4} \qquad (1.11)$$
$$G \equiv \dot{m}/A_c$$

The coefficients a_0, a_1 ..., a_4 are functions of pressure and are given in ref. 6. The local DNBR is determined by dividing q''_{CHF} by the local heat flux. Nowhere in the coolant channel does the DNBR drop below ~ 2.0.

Typical results are shown in Figs. 1.4 and 1.5 for the cylindrical portion of the cavity with coolant channel diameter of 1.8 cm and wall thicknesses of 1 mm. The cavity diameter is 10 m, the pellet yield is 100 MJ and the repetition rate is 30 sec^{-1}. The volumetric heating rates used in this analysis are presented in Section VI-B. For this case, the wall temperature varies between 290 and 310°C and the inlet pressure is 1000 psia. The main thermal hydraulic parameters for this example are listed in Table 1.1.

Figure 1.4

Variation of the different thermal hydraulic parameters in the first Wall Coolant Channel for up flow of boiling water (ID = 1.8 cm, δ = 0.1 cm)

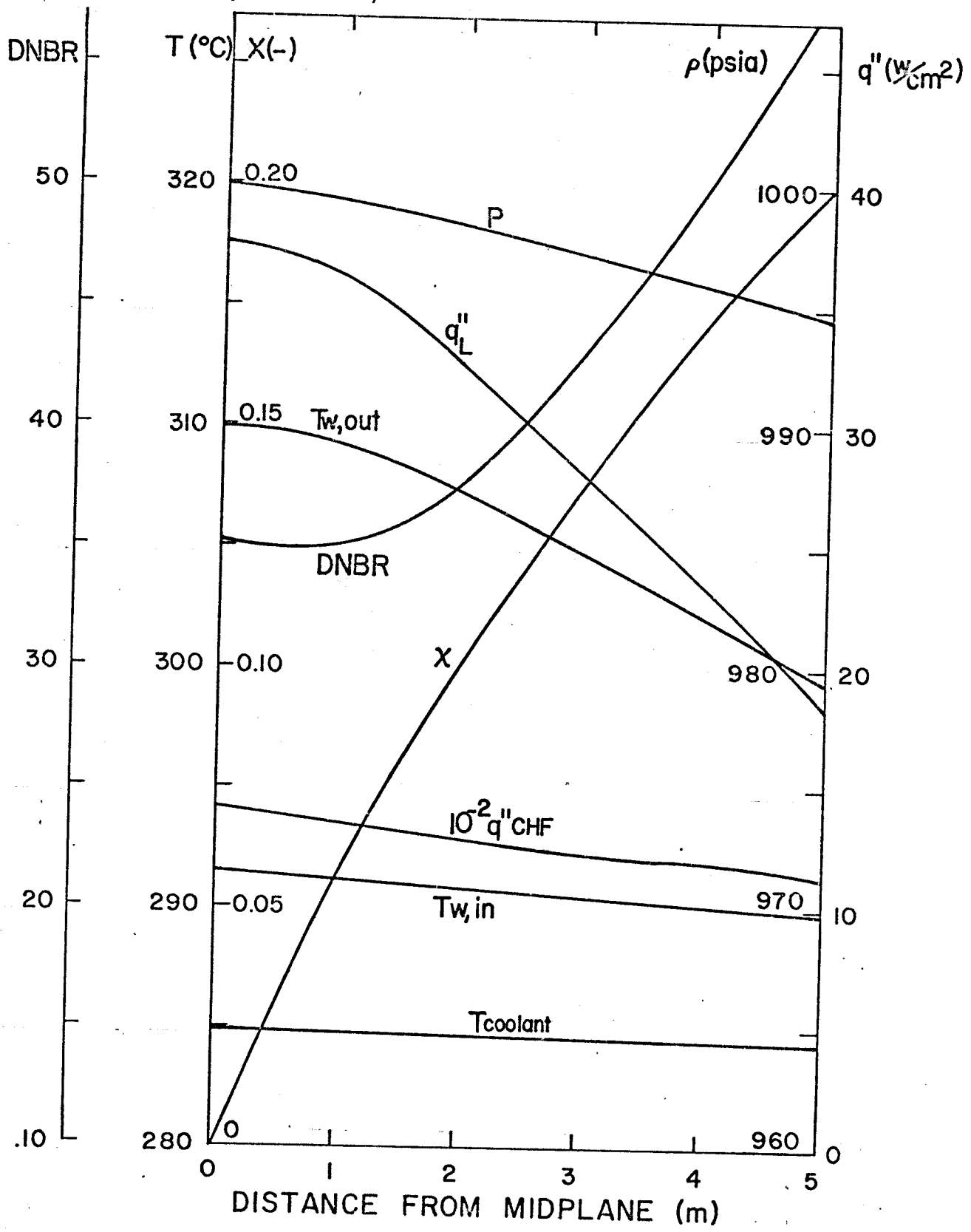

Figure 1.5
Variation of the different thermal hydraulic parameters in the first wall coolant channel for down flow of boiling water (ID = 1.8 cm, δ = 0.1 cm).

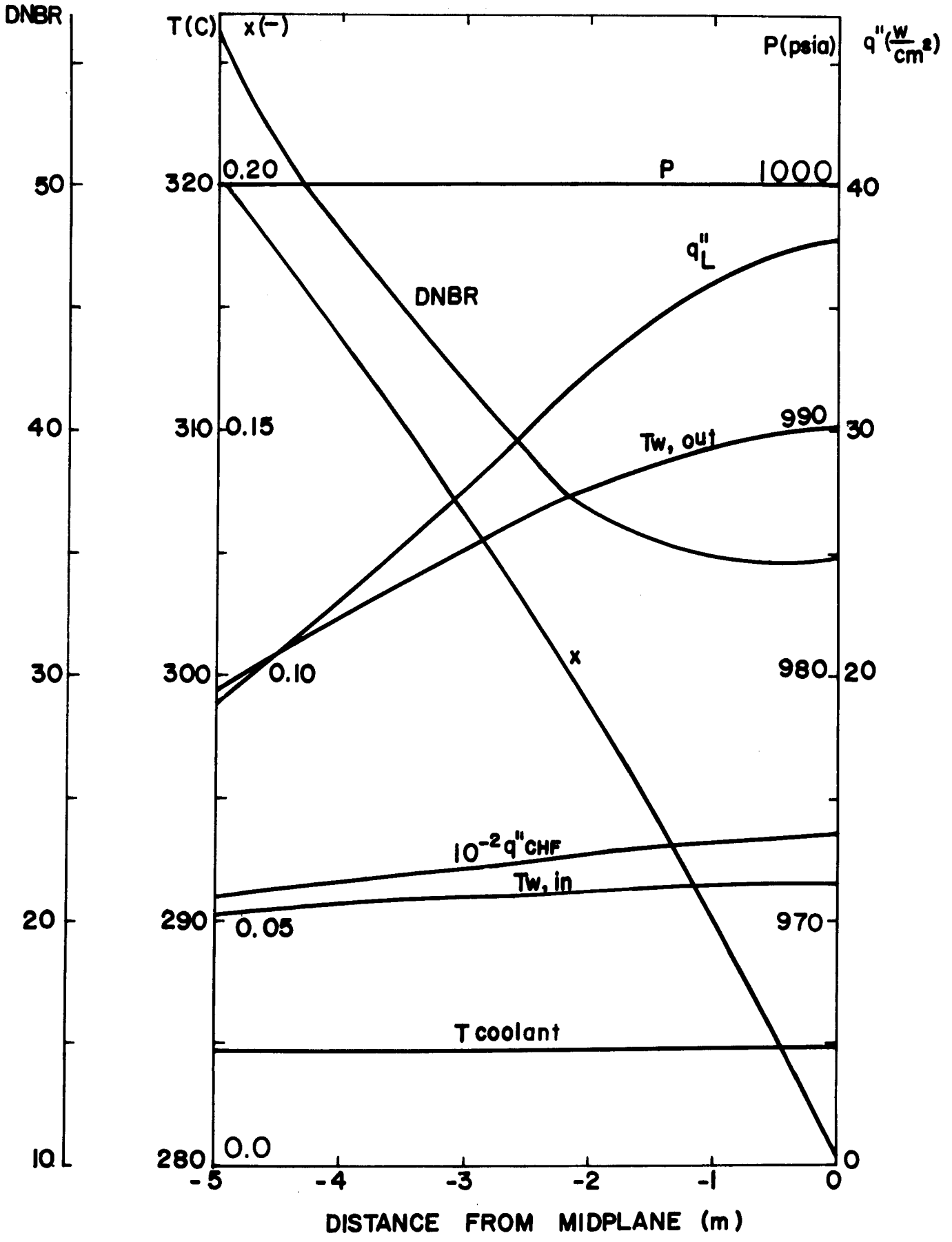

Table 1.1

Thermal Hydraulic Parameters for the Cylindrical Portion of the First Wall Under the Conditions Shown in Fig. 1-3,4

Parameter	Up Flow Section	Down Flow Section
Heat transfer rate from the liner (MW)	34.1	34.1
Heat transfer rate from the blanket (MW)	47.1	61.1
Heat generation rate in the coolant (MW)	23.9	24.6
Heat generation rate in the SS walls (MW)	18.3	18.3
Coolant flow rate (kg/sec)	411	458
Mass flux (kg/cm^2-sec)	0.103	0.115
Channel inside diameter (cm)	1.8	1.8
Wall thickness (cm)	0.1	0.1
Inlet pressure (psia)	1000	1000
Exit pressure (psia)	994.6	999.2
Exit quality	0.20	0.20
Exit void fraction	0.732	0.731
Maximum heat flux (W/cm^2)	39.4	39.4
Minimum DNBR	34.9	34.9
Pumping power (kw)	20.7	3.6
Thermal stress (ksi)	7.45	7.45
Hoop stress (ksi)	10.00	10.0

Similar calculations have been performed for the hemispherical segment of the first wall. Here, the heat flux is considerably higher than that for the cylindrical portion because of the increased q_L'' resulting from the charged particle energy deposited in the liner. However, the operating conditions have been selected so that the minimum DNBR is nearly 2.0. The coolant channel length depends on its latitude on the hemispherical surface. The channel diameter is varied with latitude so that the pressure drop between headers and exit quality in all channels remain the same. Typical results showing the variation of pressure drop with tube diameter and length are shown in Fig. 1.6. The thermal hydraulic parameters for a 8 m long (zero latitude), and 2 cm OD tube on the hemispherical part of the first wall are listed in Table 1.2.

A general computer program for evaluating the different thermal hydraulic parameters in a boiling-water cooled first wall has been developed. This program is currently used to perform parametric studies on the effect of channel geometry and operating conditions on the pumping and initial costs of the first wall. These results will then be used to determine the optimum operating conditions for the cooling system.

Figure 1.6

Variation of pressure drop with tube diameter and flow length for the hemispherical portion of the first wall

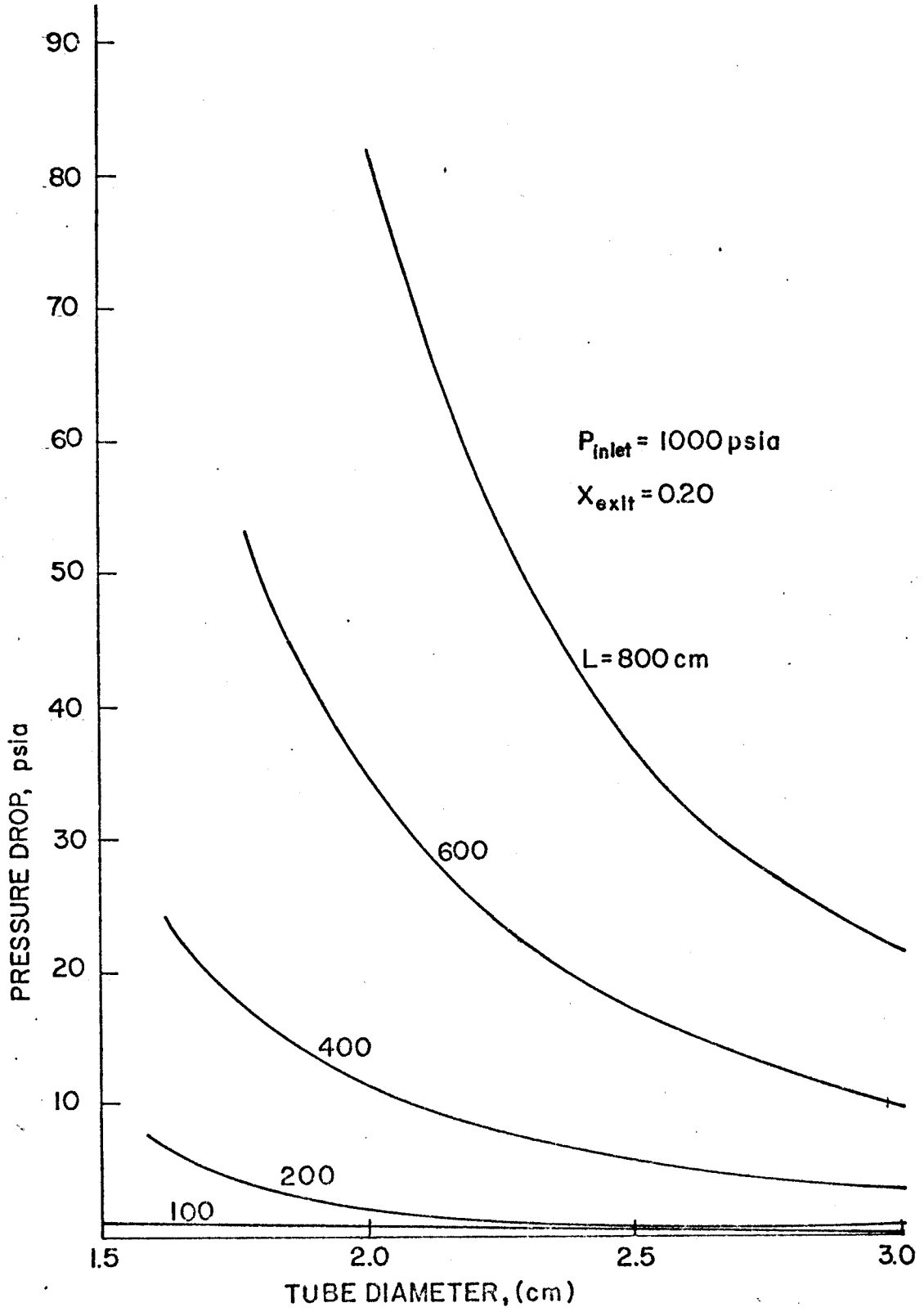

Table 1.2

Thermal Hydraulic Parameters for a Typical Coolant Channel on the Hemispherical Portion of the First Wall

Channel inside diameter	(cm)	1.8
Wall thickness	(cm)	0.1
Distance between headers	(m)	8.0
Latitude		0
Inlet pressure	(psia)	1000
Exit pressure	(psia)	918.2
Coolant mass flux	(kg/cm^2-sec)	0.638
Exit quality		0.20
Exit void fraction		0.628
Maximum heat flux	(w/cm^2)	221.5
Minimum DNBR		2.11
Thermal Stress	(ksi)	44.5
Hoop Stress	(ksi)	10.0

References VI-C-1.

1. D. E. James and M. W. Peterson, "Suspension Type Gasifiers," Proc. AIChE 68th Annual Meeting, Los Angeles (Nov. 1975).

2. D. C. Schluderberg, Private Communication (1976).

3. U. H. von Glahn, "An Empirical Relation for Predicting Void Fraction with Steam-Water Flow," NASA Tech. Note, D-1189 (Jan. 1962).

4. M. M. El-Wakil, Nuclear Heat Transport, Intext (1971).

5. W. H. Jens and D. A. Lottes, "Analysis of Heat Transfer, Burnout, Pressure Drop and Density Data for High Pressure Water, ANL-4627, Argonne National Laboratory (1951).

6. W. M. Rohsenow, Developments in Heat Transfer, MIT Press (1964).

VI-C-2. Blanket Thermal Hydraulics

A gravitational-flow lithium oxide blanket is used in our design. The merits of such a design for use in tokamak type reactors have been discussed by Sze, et al. [1]. Here, approximately 75% of the total thermal power of the reactor is deposited in the blanket. The Li_2O microspheres serve the dual purpose of tritium breeding and heat transport. The particles enter the blanket from the top at 450°C. The stream is then divided into two breeding zones separated by a graphite reflector (Section VI.B). Approximately 98% of the Li_2O flows through the first breeding zone and leaves the blanket at an average temperature of 550°C. The remaining 2% flow through the second zone and are heated to 850°C; this high-temperature stream is used in the tritium extraction cycle (Section IX).

The pressure within the blanket is kept at 1 atm; such low pressure allows the use of relatively thin structures to construct the blanket. Another advantage of this type of blanket is that Li_2O is a poor heat transfer medium. This allows the first wall to be operated at considerably lower temperatures than the Li_2O stream without transferring (i.e. degrading) too much heat to the first wall coolant. It also allows the steam-cooled back wall of the blanket to come in contact with the 850°C Li_2O in the second breeding zone without fear of the stainless steel wall ever exceeding the maximum safe temperature of 650°C.

The lithium oxide leaving the blanket is transported to the steam generator and back to the blanket. A gas-solid transport system is used to circulate the particles between the different components of the system.

The particle velocity distribution within the blanket is tailored to match the radial heat deposition curve; faster flow is provided near the first wall where the volumetric heating is high (see section VII.B). Higher velocities are also required near the graphite reflector to remove the heat generated

within the graphite which is radiated and conducted to the Li_2O stream. The shaping of the velocity profile is accomplished by subdividing the blanket into different zones and maintaining the proper velocity within each zone by means of adjustable baffles at the exit. Other schemes for velocity shaping can be surmised.

A summary of the main thermal-hydraulic parameters of the blanket is given in table 2.1. The velocity distribution within the blanket and the corresponding residence times are shown in Fig. (2.1). For the subregion immediately adjacent to the first wall, a trial and error solution is required to determine the necessary coolant velocity since the rate of heat transfer from that zone to the first wall coolant is dependent on the "effective" Reynolds number of the Li_2O stream. A viscosity of 1.5 cp is used to calculate Re for an equivalent continuum on the particles' side [1]. The Dittus-Boelter correlation (Eq. 2.1) is used to determine the equivalent Nusselt number on the Li_2O side.

$$Nu = 0.023\ Re^{0.8}\ Pr^{0.4} \qquad (2.1)$$

The method of Deissler and Beogli [2] is used to determine the effective thermal conductivity of the particles' stream and, hence, the heat transfer coefficient. Similar procedure is used to determine the rate of heat transfer from the second breeding zone to the steam-cooled back wall of the blanket. Heat transfer coefficients of 1.78 and 0.23 $kw/m^2\ ^oK$ are obtained at the front and back walls respectively.

References VI-C-2

[1] D. K. Sze, et al., "Gravity Circulated Blanket Design for a Tokamak Fusion Reaction," Proc. 2nd Topical Meeting on the Technology of Controlled Nuclear Fusion, Richland (1976).

[2] R. G. Deissler and J. S. Boegli, "An Investigation of Effective Thermal Conductivities of Powders in Various Gases," ASME Trans. (October 1958).

Table (2.1)

Blanket Thermal Hydraulic Parameters

Parameter	1st Breeding Zone	2nd Breeding Zone
Inlet temperature (^{o}C)	450	450
Exit temperature (^{o}C)	550	850
Max first wall temperature (^{o}C)	320	---
Max back wall temperature (^{o}C)	---	525
Pressure (atm)	1	1
Flow rate (kg/hr)	3.34×10^{7}	0.685×10^{6}
Average velocity (cm/sec)	67	7.5
Void fraction	0.40	
Specific heat ($cal/g^{o}C$)	0.431	
Equivalent density (g/cm^{3})	1.20	

Figure (2.1)

Particle velocity distribution in the blanket (numbers in parenthesis indicate average residence times in seconds)

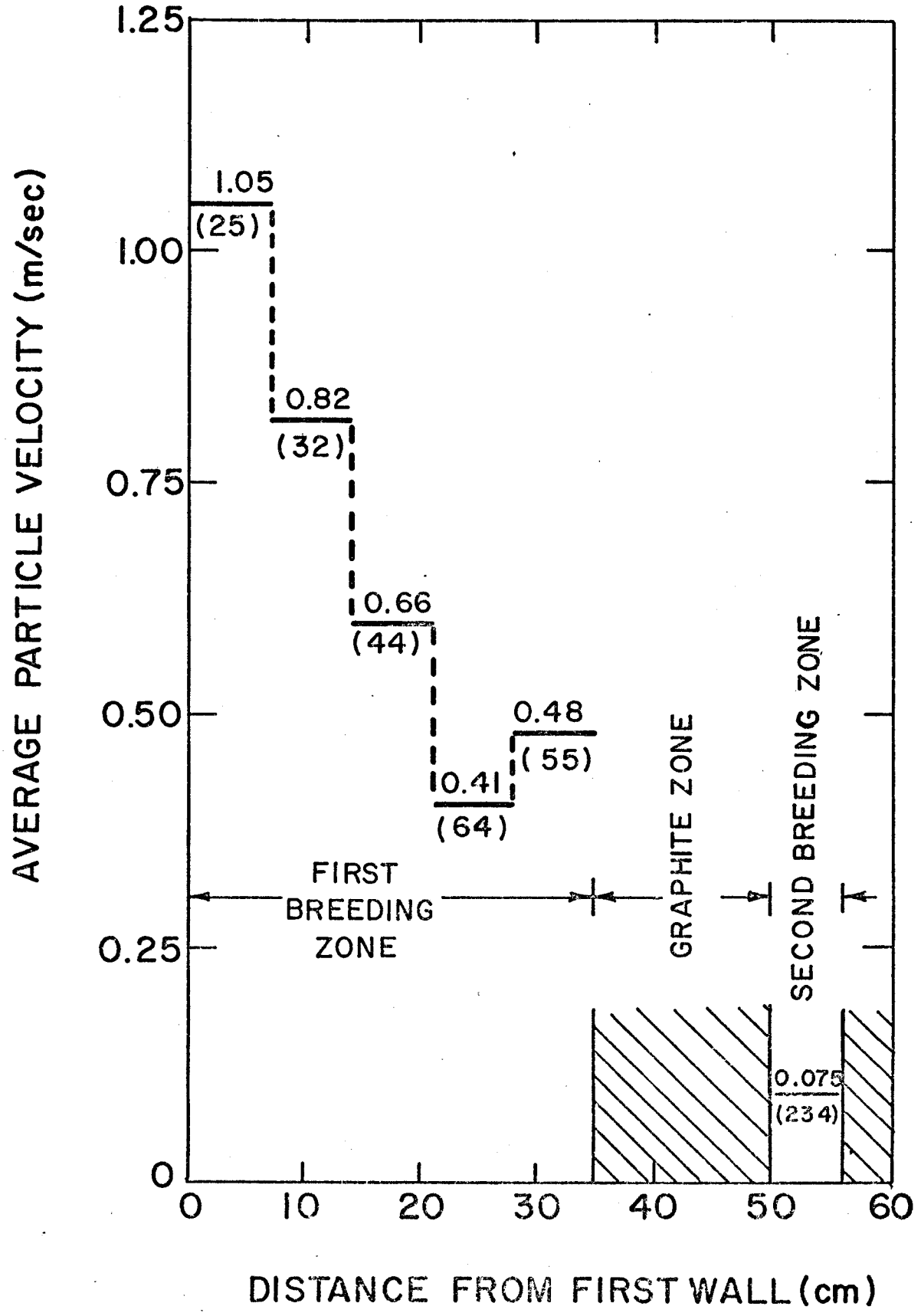

VI-D Stress Analysis

VI-D-1 The First Wall

Aside from the hoop stresses produced by the coolant pressure and the thermal stresses resulting from the temperature gradients within the first wall, it is also subjected to a pulsating load produced by the expanding plasma against the magnetic field. The methods used to estimate the stresses produced by this dynamic loading mode are described.

The first wall, considered as a cylindrical shell with its wall made up of small interconnected coolant tubes, is an effective structure for carrying axisymmetric radial pressure distributions by its membrane action. This advantage, however, is lost if the shell is segmented. In such a case the cylindrical panels must resist the radial pressure by flexural action. The support from the partitioning structure will then be primarily radial and shear with the support moment reactions being negligible (Fig 1-1a). The curvature of the panel is less significant in the absence of circumferential normal force. Neglection of the curvature will not appreciably affect the result; however, the tangential flexural stiffness will be underestimated. The flat panel model considered here is shown in Fig 1-1b.

Since the loading is now to be taken in flexure, the bending rigidity about longitudinal axes must be increased; this can be accomplished by any of the three membrane wall designs shown in section VI-C-1. The important contribution to the unit moment of inertia now comes from the corrugated outer layer (Fig 1-2). An additional simplification in the model can be made by replacing these layers by equivalent flat plates located at the centroid position of the corrugation. The resulting isotropic sandwich plate structure is an approximation of the original orthotropic structure where the cross webs are neglected. This approximation will provide conservative estimates of the stresses produced in the first wall.

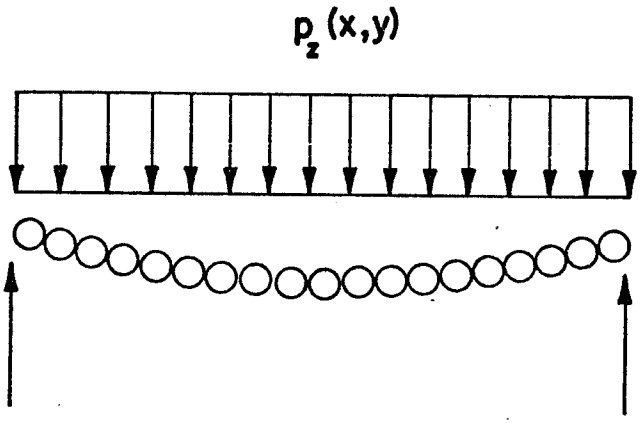

Figure 1-1a

First-wall cylindrical panel

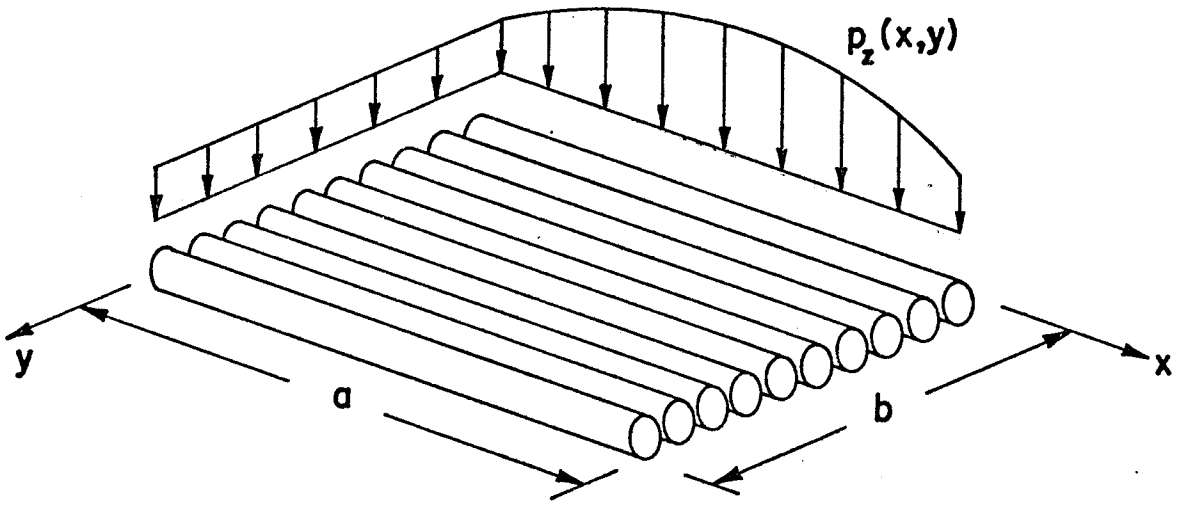

Figure 1-1b

Equivalent flat panel

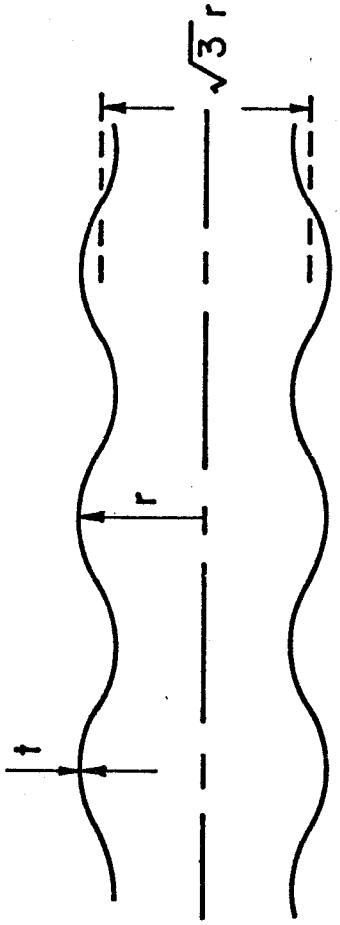

Sandwich plate model

Figure 1-2

VI-D-1-i Static Loading

Referring to the coordinate system in Fig (1-1b), the pressure distribution can be expressed as

$$\left.\begin{aligned} p(x,y) &= \sum_{m=1}^{\infty}\sum_{m=1}^{\infty} P_{mn} \sin\frac{m\pi x}{a} \sin\frac{n\pi y}{a} \\ \text{with } P_{mn} &= \frac{4}{ab}\int_o^a\int_o^b p(x,y) \sin\frac{m\pi x}{a} \sin\frac{n\pi y}{b}\, dx\, dy \end{aligned}\right\} \quad (1\text{-}1)$$

The pressure is uniform-circumferentially (y direction). As a first approximation, consider a single series component in the x direction, i.e.,

$$\left.\begin{aligned} p(x,y) &= po \sin \pi x/a \\ P_{mn} &= 4\ po/n\pi,\ m = 1,\ n = 1, 3, 5, \ldots \\ p(x,y) &= \sum_{n=1,3,5,\ldots}^{\infty} \frac{4\ po}{n\pi} \sin\frac{\pi x}{a} \sin\frac{n\pi y}{b} \end{aligned}\right\} \quad (1\text{-}2)$$

If the edges are considered to be simply supported with negligible flexural reaction, the transverse displacement component is

$$w(x,y) = \sum_{m=1}^{\infty}\sum_{m=1}^{\infty} W_{mn} \sin\frac{m\pi x}{a} \sin\frac{n\pi y}{b} \quad (1\text{-}3)$$

with

$$W_{mn} = \frac{Pmn}{D\pi^4\left(\frac{m^2}{a^2} + \frac{n^2}{b^2}\right)^2} \quad (1\text{-}4)$$

For the current example, this general expression reduces to

$$W_{mn} = \frac{4\ po/n\pi}{D\pi^4\left(\frac{1}{a^2} + \frac{n^2}{b^2}\right)^2} \quad (1\text{-}5)$$

in which D is the flexural stiffness,

$$D = 3\ tE\ r^2/2\ (1 - \nu^2)$$

where E and ν are the elastic modulus and Poisson's ratio, respectively. The displacement component is necessary for calculating the flexural moment per unit length; for an edge parallel to the x axis this is given by:

$$M_y = -D\left[\frac{\partial^2 w}{\partial y^2} + \nu \frac{\partial^2 w}{\partial x^2}\right]$$

$$= \frac{1}{\pi^2} \sum_{m=1}^{\infty} \sum_{m=1}^{\infty} \left(\frac{n^2}{b^2} + \nu\frac{m^2}{a^2}\right) \frac{P_{mn} a^4}{(m^2b^2 + n^2a^2)^2} \sin\frac{m\pi x}{a} \sin\frac{n\pi y}{b} \qquad (1\text{-}6)$$

and the corresponding flexural stress is:

$$\sigma_y = M_y \, Z/I^* \qquad (1\text{-}7)$$

where I* denotes the moment of inertia per unit length, $3t\, r^2/2$.

The maximum moment occurs at the center (a/2, b/2),

$$(M_y)_{MAX} = \frac{4p_o a^2}{\pi^3} \left\{ (\nu + \frac{a^2}{b^2})/(1 + \frac{a^2}{b^2})^2 - (\nu + \frac{9a^2}{b^2})/3(1 + \frac{9a^2}{b^2})^2 + \ldots \right\} \qquad (1\text{-}8)$$

For n = 3,5 ..., the corresponding terms in the series are of order $1/n^3(a/b)^2$ and can be neglected for $(a/b) >> 1$. Thus

$$(\sigma_y)_{max} = [4\sqrt{3}\, p_o a^2/3\pi^3\, tr]\, (\nu + a^2/b^2)/(1 + a^2/b^2)^2 \qquad (1\text{-}9)$$

This stress is displayed in Figures (1-3) and (1-4) as a function of the plate aspect ratio a/b and the slenderness ratio of the tubes, $a/\sqrt{tr}$. Similar expressions can be developed for the other coordinate direction.

VI-D-1-ii Dynamic Loading

The preceeding static stresses can be used with an appropriate dynamic load factor to obtain estimates of dynamic stresses. The determination of the dynamic coefficient (C_d) is based upon a reduction of the plate response in its fundamental mode to an equivalent simple harmonic oscillator. For this purpose, the static transverse deflection can be expressed as:

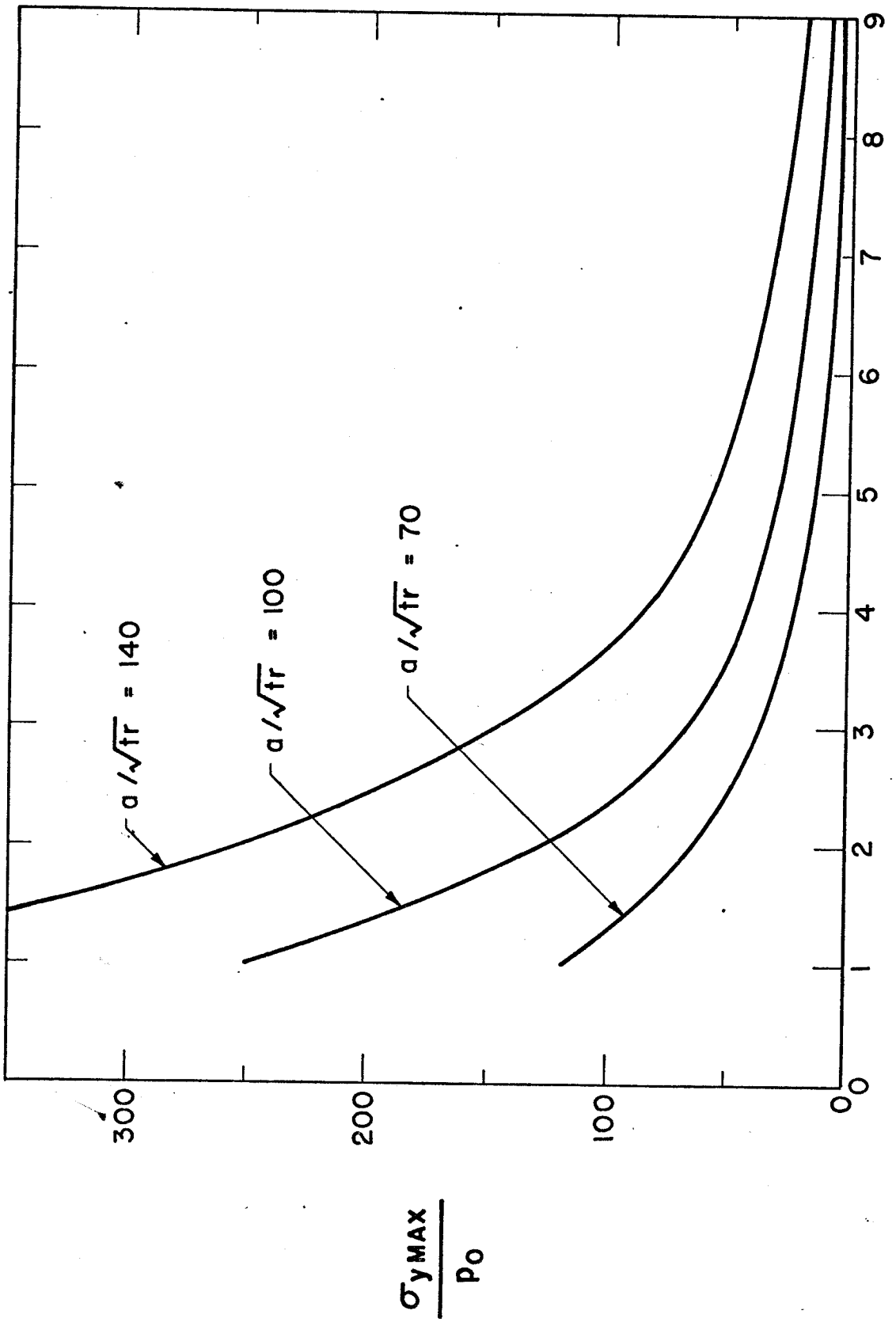

Figure 1-3 Static Flexural stress as a function of plate aspect ratio

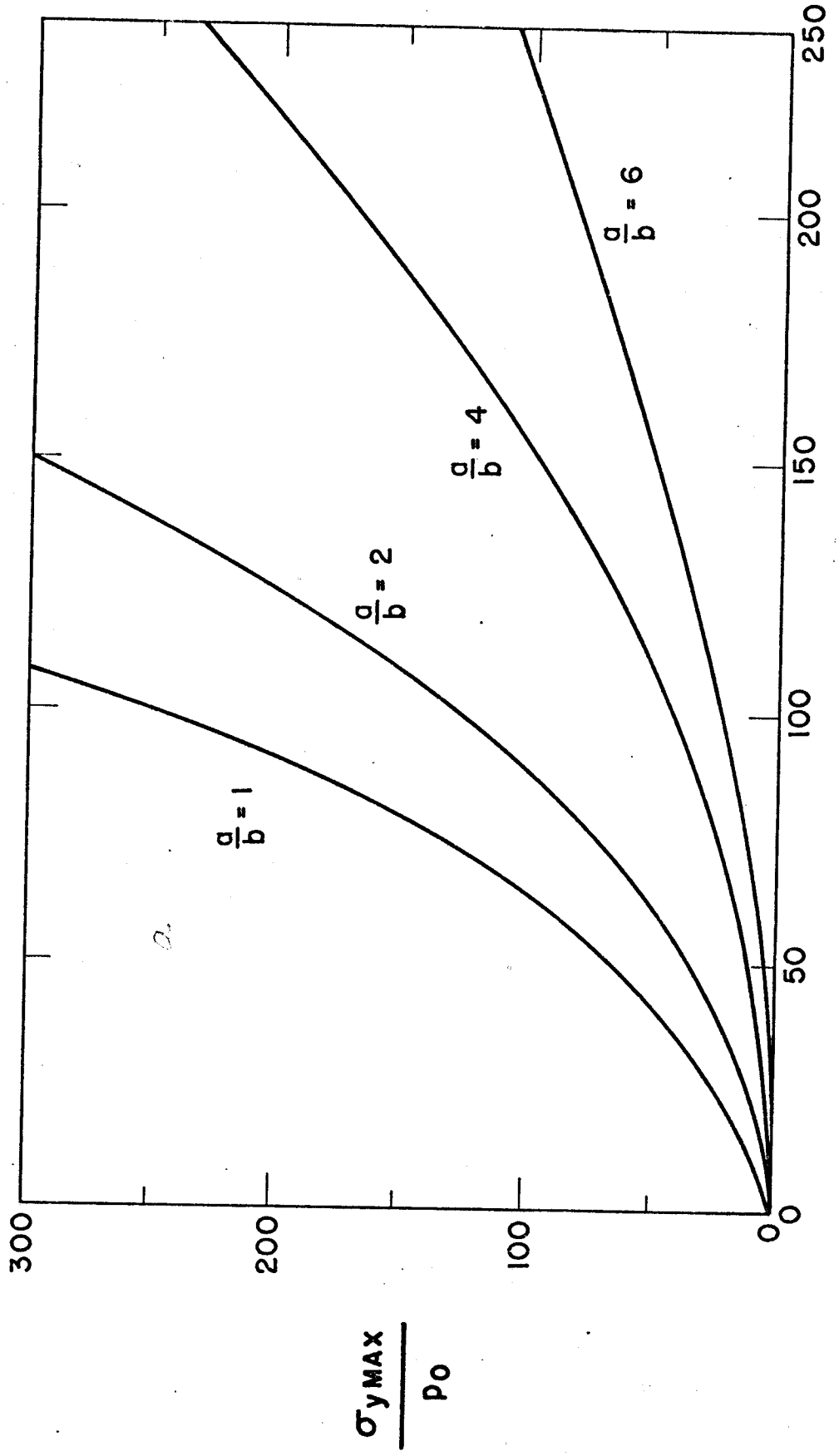

Figure 1-4 Static flexural stress as a function of tube slenderness

$$\left.\begin{aligned} w(x,y)_{static} &= {}^{w}max\ \phi(x,y) \\ p(x,y) &= p_o \sin \pi x/a \end{aligned}\right\} \tag{1-10}$$

The load and mass factors C_L and C_m are:

$$C_L = \frac{\int_o^a \int_o^b \phi(x,y)\ p(x,y)\ dy\ dx}{\int_o^a \int_o^b p(x,y)\ dy\ dx} = 1/2 \tag{1-11}$$

$$C_m = \frac{\int_o^a \int_o^b \bar{m}\ \phi^2(x,y)\ dy\ dx}{\int_o^a \int_o^b \bar{m}\ dy\ dx} = \frac{1}{4} \tag{1-12}$$

where $\bar{m}$ is the mass per unit area.

The spring constant of the plate is the ratio between the total force and the maximum deflection:

$$K = \int_o^a \int_o^b p(x,y)\ dy\ dx/[4\ p_o a^4 b^4/D\pi^5\ (a^2 + b^2)^2]$$

$$= D\pi^4\ (a^2 + b^2)^2/2\ a^3 b^3 \tag{1-13}$$

and the equivalent spring factor C_K is

$$C_K = k_e/K \tag{1-14}$$

where k_e is the equivalent spring constant. It can be shown that $C_K = C_L$. The forcing function is the product

$$P(t) = [\int p(x,y)\ dA]\ \Theta\ (t)$$

$$= (2\ p_o ab/\pi)\ \Theta\ (t) \tag{1-15}$$

where $\Theta(t)$ is a rectangular step function. Thus for the single degree of freedom model, the equivalent spring constant, mass and forcing function are:

$$\left.\begin{aligned} k_e &= C_k\ K = D\pi^4\ (a^2 + b^2)^2/4\ a^3b^3 \\ m_e &= c_m\ \bar{m}_T = \frac{1}{4}\ \bar{m}\ ab \\ P_e(t) &= C_L\ P_T(t) = (p_o\ ab/\pi)\ \theta(t) \end{aligned}\right\} \qquad (1\text{-}16)$$

The equivalent fundamental frequency is given by:

$$\omega_1 = (k_e/m_e)^{1/2} = [\pi^2(a^2 + b^2)/a^2b^2]\ (D/\bar{m})^{1/2} \qquad (1\text{-}17)$$

For a simple harmonic oscillator subjected to a rectangular pulse of intensity q_o (force per unit mass) with a duration τ, considerably less than the fundamental period, the response is:

$$\frac{2q_o}{\omega^2} \sin \frac{\omega\tau}{2} \sin \omega(t - \tau/2) \cong \frac{q_o\tau}{\omega} \sin \omega(t - \tau/2) \qquad (1\text{-}18)$$

Thus the ratio of dynamic to static deflections (and dynamic to static stress) is simply:

$$\begin{aligned} C_d &= \omega_e\tau \\ &= \tau\ \frac{\pi^2\ (a^2 + b^2)}{a^2\ b^2}\ \sqrt{D/\bar{m}} \end{aligned} \qquad (1\text{-}19)$$

Using $D = 3t\ E\ r^2/2\ (1 - \nu^2)$, and $\bar{m} = 4\ \pi t\ \rho/3$, where ρ is the mass density,

$$C_d = \frac{3\ r\ \tau\ \pi^2\ (a^2 + b^2)}{a^2\ b^2}\ [E/8\pi\ \rho(1 - \nu^2)]^{1/2} \qquad (1\text{-}20)$$

The dynamic stress is obtained as the product of the static stress and the coefficient C_d. Typical results are shown in Figs. (1-5, 6, and 7) for plates of different aspect ratios. For dynamic stresses, the aspect ratio is not an important parameter; the results depend primarily upon pulse width and tube thickness. It can be seen that the stresses are well within acceptable limits for the practical range of these parameters.

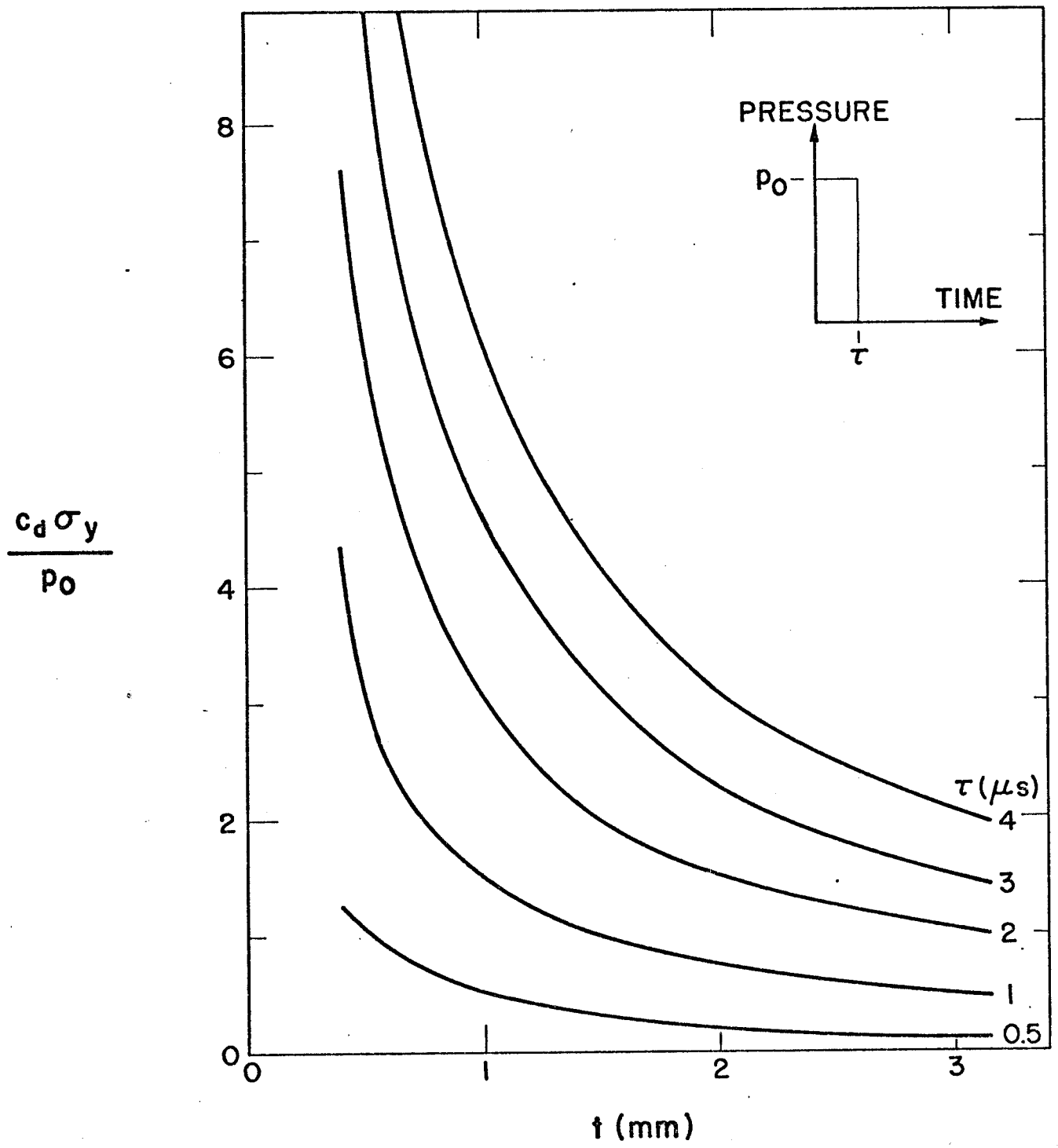

Figure 1-5

Dynamic flexural stress vs. tube thickness, a/b = 0.5; various pulse widths.

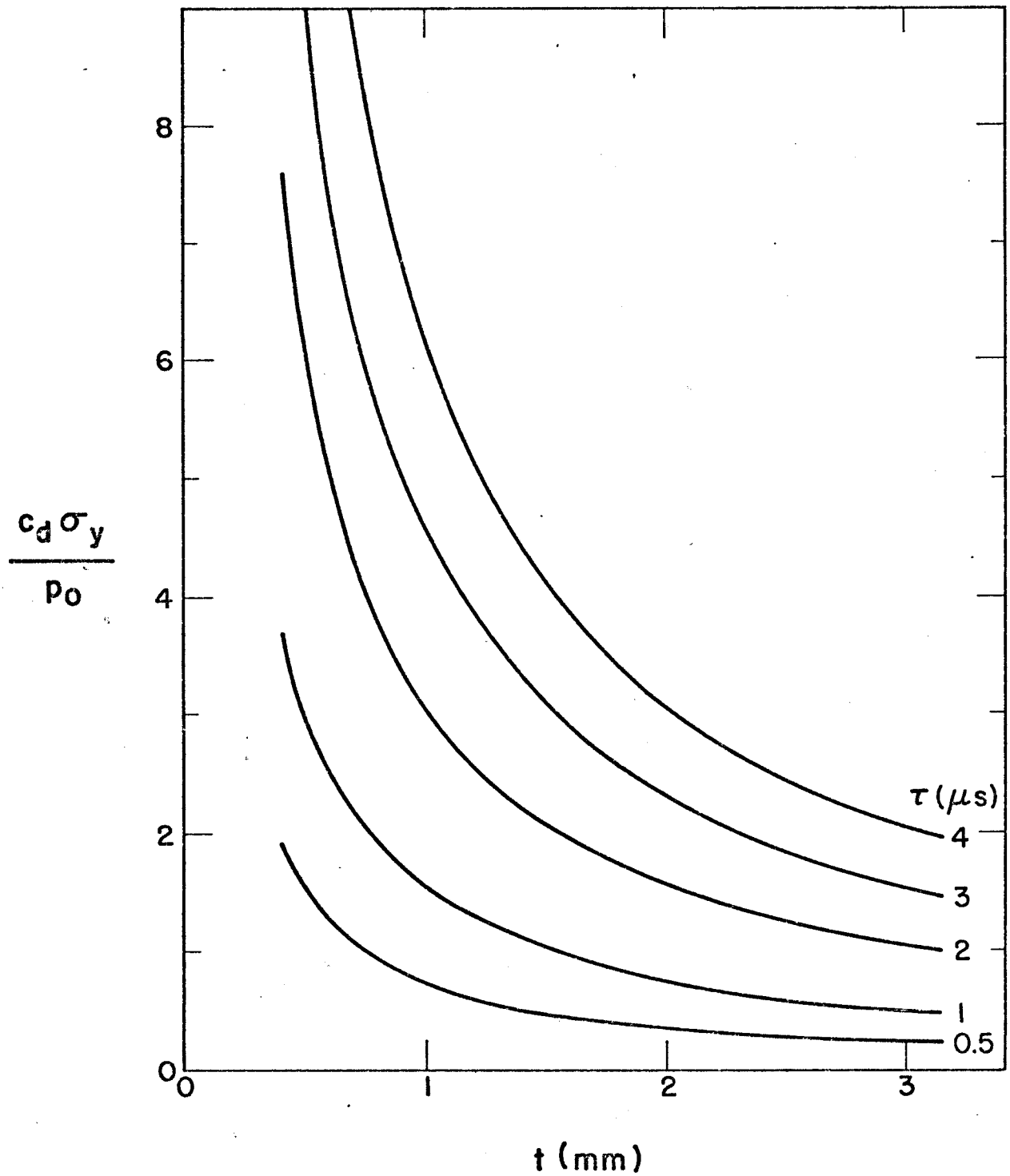

Figure 1-6

Dynamic flexural stress vs. tube thickness, a/b = 1.0; various pulse widths.

Figure 1-7

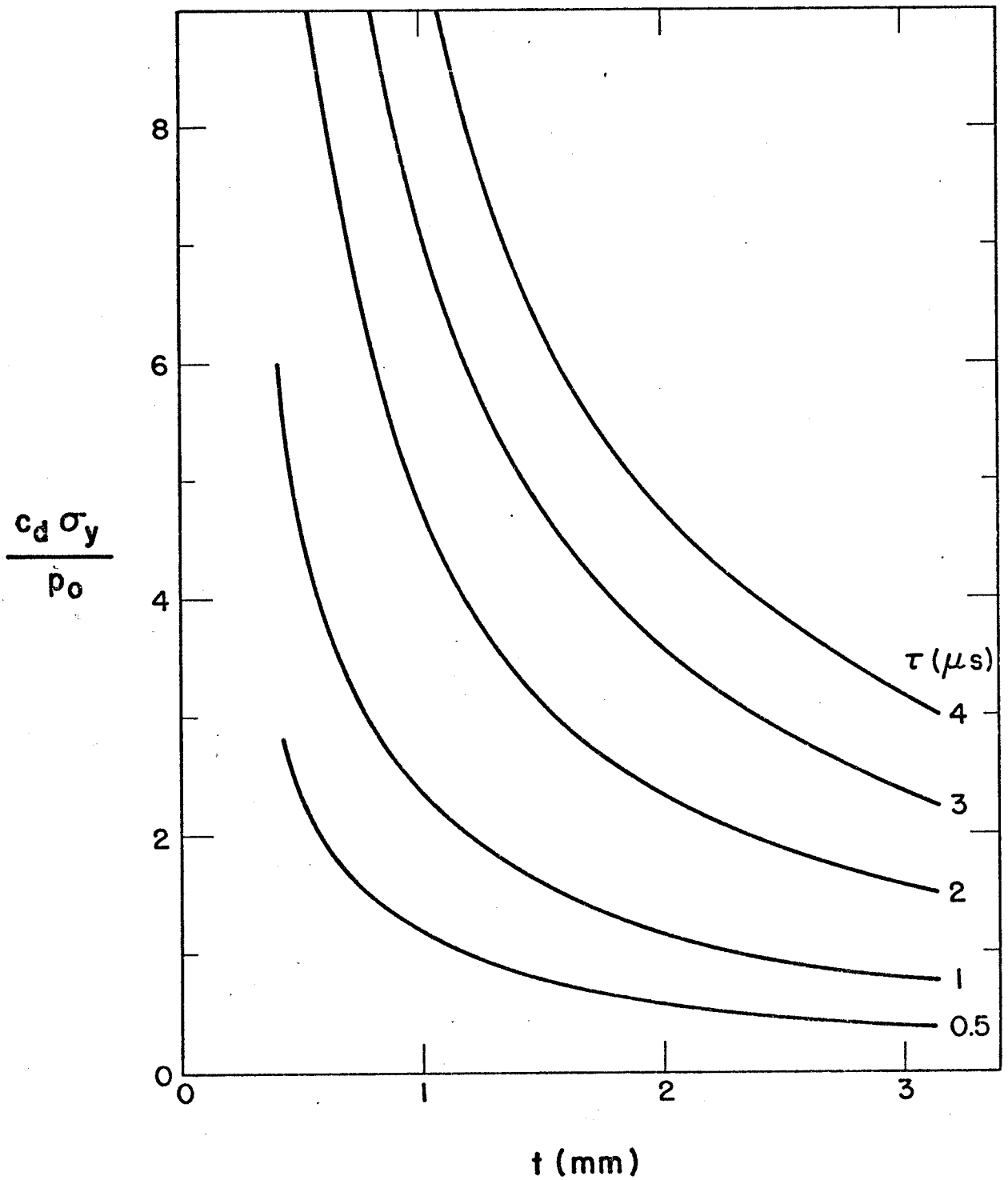

Dynamic flexural stress vs. tube thickness, a/b = 10; various pulse widths.

VI-D-2 Thermal Buckling of the Outer Blanket Wall

The outer blanket wall is subjected to higher temperatures than the first wall and may, therefore, buckle. For a conservative estimate of this action, the ends of the cylindrical segment of the cavity are assumed to be completely constrained. Under direct compression, the axial buckling stress σ_c is given by:

$$\sigma_c = \pi^2 D\, k/\ell^2 h \qquad (2\text{-}1)$$

Here h is the wall thickness, ℓ is the height, D is the flexural rigidity ($D = E\, h^3/12(1 - \nu^2)$), and k is a coefficient which depends on the aspect ratio Z of the shell:

$$Z = \ell^2\, (1 - \nu^2)^{1/2}/a\, h \qquad (2\text{-}2)$$

where a is the wall radius. The variation of k with Z is shown in Fig (2-1).

The temperature rise T necessary for shell instability is given by:

$$T = \pi^2\, h^2\, k/12\alpha\, \ell^2\, (1 - \nu^2) \qquad (2\text{-}3)$$

where α is the coefficient of thermal expansion.

Typical results are shown in Fig (2-2). The elastic constants of steel are used in these calculations. These results do not change appreciably with changes in ℓ/a.

Simple unstiffened walls without additional support are likely to exhibit instability. If stiffeners are used, external stringers will raise the buckling load (i.e. temperature) higher than internal stringers. Additional support of the wall and some axial expansion will exist. However, these results indicate the limiting situation for the problem.

Figure 2-1

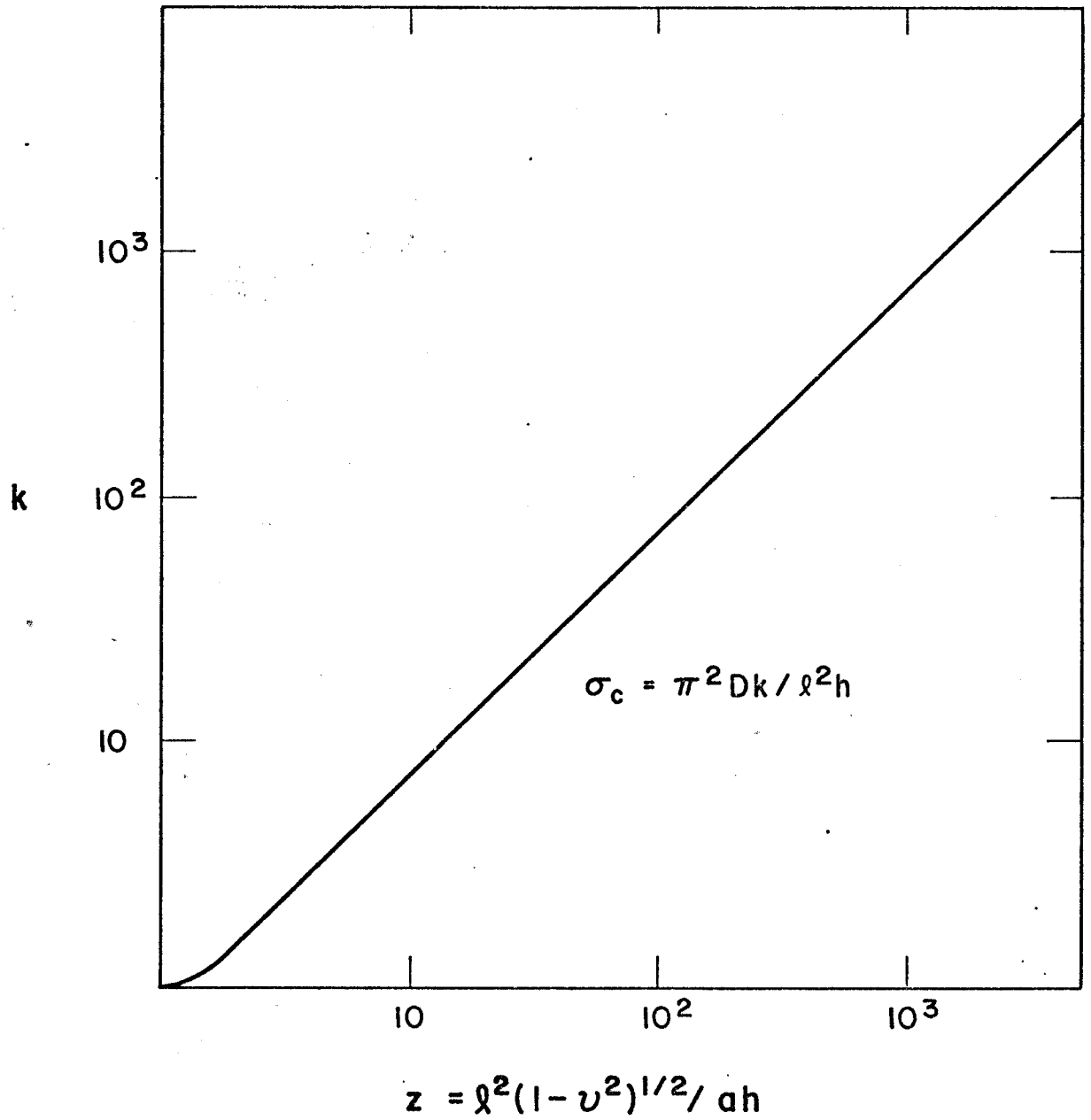

Buckling coeff. vs. slenderness ratio

Figure 2-2

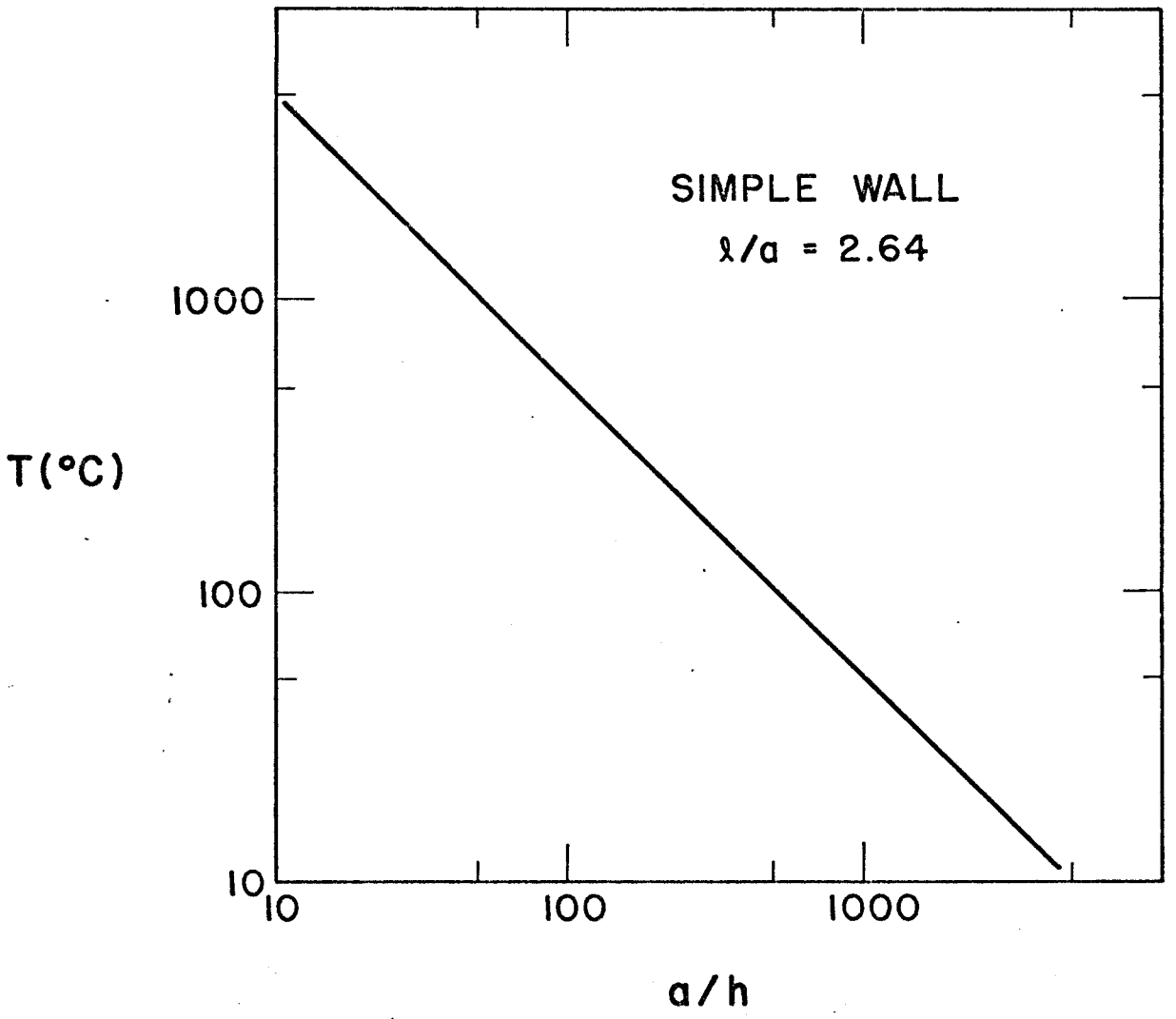

Buckling temperature vs. radius to thickness ratio

VI-E. Mechanical Design

1. General Description

The dimensions and shape of the laser fusion cavity have only been recently decided on after several earlier attempts. For this reason the details of the mechanical design have not yet been developed. In this section we will describe in a very general way some of the design considerations that we feel can be adopted.

The shape of the cavity is that of a right cylinder with hemispherical ends as shown in Fig.1-1. Its inside diameter is 10 meters and the height is 20 meters. A 1.5 cm woven graphite curtain, made of three or more pieces will cover the whole inside wall of the cavity with the exception of the laser beam ports and the pellet injection port. It will be attached to the front wall of the blanket by means of graphite studs which will engage into graphite mating receptacles fixed to the front wall.

The front wall of the blanket consists of a bank of cooling tubes joined together to form a continuous structure. Some possible designs are shown in Section VI-C. The rest of the blanket is divided into two breeding zones separated by a 15 cm graphite layer, followed by another bank of cooling tubes which will comprise the back wall of the blanket. Further details of the blanket are given in the thermal hydraulics section.

It is contemplated that the hemispherical portion of the blanket will be single monolithic structures while the cylindrical portion will be divided into four sections. The sections will have to be shaped such that they can be taken out internally from within the cylindrical shield.

Access to the inside of the cavity is provided by removing the top hemispherical head. This means that seals have to be provided between the hemispherical and cylindrical portions of the blanket. Although welding

Figure I-1

UW LASER FUSION REACTOR CAVITY

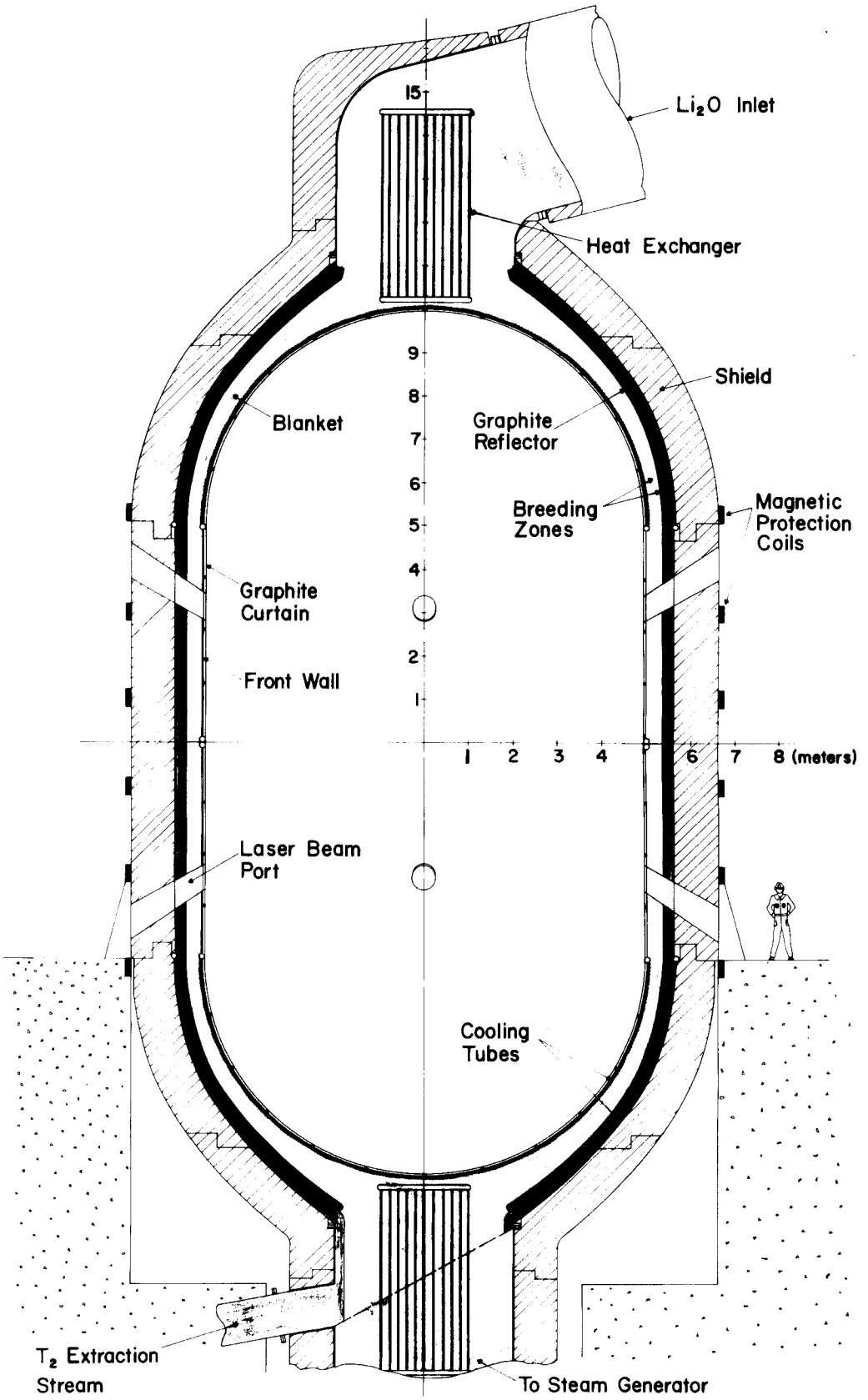

here would have been desirable, it does not appear that access can be provided, especially if all the operations are to be performed outside the cavity by remote control. It seems reasonable to use a mechanical seal here with clamping provided on the outside of the cavity. The seal can be in the form of a metal "O" ring or some other available form. The pressure in the blanket is about one atmosphere, and some leakage of the helium carrier gas can be tolerated, as discussed in the vacuum section. Flow continuity for the breeding material within the blanket must be provided across the joint between the blanket zones at the top and bottom. The whole problem of seals and blanket continuity will require careful thought.

Since the cooling system for the hemispherical head is essentially independent of the cylindrical blanket cooling system, as shown in Section VI-C the only connections that have to be broken in order to remove the upper head are those connecting it to its own water supply and steam return lines. These are high pressure lines and are accessible on the outside of the cavity making weldments possible.

The breeding material enters the blanket at the top and flows through it by gravity. The velocity is controlled by adjustable louvers on the bottom. The 4 meter diameter breeding material supply and return lines are connected to the cavity by means of flanges which can either be welded or mechanically seated. At least a portion of the supply line will have to be removed in order to provide access for removal of the top hemispherical head.

The Li_2O breeding material will be in the form of microspheres 100-200 μ in diameter. Gravity flow through the blanket and steam generator will require corresponding material lifts in order to complete the cycle.

Both pneumatic and mechanical systems are under consideration. Further study with the objective of minimizing cost, pumping power, particle attrition, etc., will be required to determine the best choice.

As in the UWMAK series of Tokamak fusion reactors, the shield for the laser cavity will consist of discrete zones of materials such as stainless steel, lead, boron carbide and possibly tungsten, with cooling channels provided for heat removal. Its construction will be in the form of wide flange I beams oriented in the axial direction of the cavity. Welding the flanges together will provide the compartments into which the shield material can be placed. In the case of lead and boron carbide, the material can be cast in place and in the case of tungsten or stainless steel, it can be in the form of slabs on in powder mixed with a suitable binder. The orientation of the structural material will have to be such as to provide the strength and rigidity needed to support the heavy shielding material. As in the blanket, the shield will also have penetrations in it,such as laser beam ports.

Little thought has been devoted to the support of optical elements, in particular the last mirrors. It would make sense to support the last mirrors independently from the shield, in order to uncouple the vibrations of the cavity from the optics.

As mentioned in the vacuum section, the laser cavity will be contained within an evacuated building, which means that the last mirrors will not have to be sealed within a separate cavity vacuum. This should considerably simplify the design of the optics.

In general it is thought that the optics supports might be made of a material such as Invar which is essentially insensitive to thermal variations with respect to expansion. Techniques such as automatic motorized adjustments of the mirrors may also be employed.

2. Support of the Blanket and Shield

The shield is the heaviest and bulkiest component of the laser cavity and therefore should not be handled and moved unnecessarily. It makes sense to make the shield the anchor to which other components, like the blanket,can be attached to and supported on.

In the present design, the shield which surrounds the cylindrical portion of the cavity and weighs about 3500 tonnes will be considered semi-permanently fixed and all the other components will be supported on it. The hemispherical ends will be shielded by sections of shield which can be taken apart as shown in Fig. (1-1). The total weight of each hemispherical shield is ~ 2000 tonnes and will most likely be divided into 20 sections of about 100 tonnes each. These sections will have to be disassembled prior to the removal of the top hemispherical end to provide access to the inside of the cavity.

As shown in Fig. (1-1) the cylindrical shield is supported on a heavily reinforced concrete foundation with the bottom hemispherical end contained within a pit. Since the total load supported is on the order of 8500 tonnes, eight or more support ledges, about 80 cm x 200 cm will be required producing a compression stress on the concrete of ~ 70 Kg/cm^2 (~ 1000 psi).

The total weight of a loaded blanket is ~ 650 tonnes consisting of 50% Li_2O, 45% graphite and 5% structural stainless steel. This weight will be distributed evenly on the cylindrical shield. The supports will be designed to accomodate expansion of the blanket modules as they are heated from room temperature to operating temperature.

3. Cavity Access and Maintenance

Periodic replacement of the graphite curtain, and eventually the blanket section will be needed due to sputtering and radiation damage. Access to the inside of the cavity has to be provided.

As mentioned earlier, only the top hemispherical head has to be removed to provide the needed access. To do this, the following operations have to be performed:

1 - The blanket and adjacent supply and return lines have to be emptied of all breeding material. Cooling lines have to be drained.

2 - Shield sections covering the top hemispherical head have to be disassembled and removed.

3 - The section of breeding material supply header immediately above the cavity has to be disconnected and removed.

4 - The mechanical seal between the top hemispherical and cylindrical blanket sections is released, allowing the removal of the head.

5 - The graphite curtain can now be removed and a new one installed.

6 - The reactor cavity can then be closed up, the piping connections made and the shield sections replaced.

In order to replace blanket sections, further disassembly of the cavity will be needed. The cylindrical blanket sections have to be uncoupled from the support shield and removed from above. This would make it possible for the bottom hemispherical head to be removed through the top. These operations will have to be performed by a crane capable of handling rather bulky sections weighing the order of 100 tonnes.

VII. Neutron and Gamma Transport Analysis of Cavity and Blanket Design

VII-A. Introduction

The neutronics analysis of laser fusion reactor systems requires both time dependent and steady state methods of analysis. Steady state, or more accurately, time integrated neutronics are useful in providing integral parameters such as the tritium breeding ratio and the total energy produced per fusion neutron. Such an approach is also valuable for shield design and the analysis of leakage through ports in the system. On the other hand, effects that are rate dependent require a time dependent analysis of this basically pulsed neutron problem. This is especially true for materials radiation damage where displacement per atom rates can be the order of 1-10 dpa/s compared to 10^{-4} to 10^{-6} dpa/s in steady state magnetic confinement fusion devices and in fission reactors. In the sections to follow, we present the results of both steady state and time dependent neutronics analysis.

VII-B. Time Integrated (Steady State) Neutronics Studies

1. Calculational Method

If the time-dependent flux $\phi(\underline{r}, \underline{\Omega}, E, t)$ is solved, the (time) overall spatial nuclear response, R(r), can be estimated as

$$R(r) = \int d\underline{\Omega} \int\int \Sigma_R(\underline{r}, E)\phi(\underline{r}, \underline{\Omega}, E, t)dtdE$$

However, the time-dependent transport equation can be transformed into a time-independent form by integrating over certain (time) period to the equation itself. Let us define

$$\Phi(\underline{r}, \underline{\Omega}, E) = \int \phi(\underline{r}, \underline{\Omega}, E, t)dt$$

and

$$S(\underline{r}, \underline{\Omega}, E) = \int s(\underline{r}, \underline{\Omega}, E, t)dt,$$

the time-dependent (time integrated) form becomes

$$L(\underline{r}, \underline{\Omega}, E)\Phi(\underline{r}, \underline{\Omega}, E) = S(\underline{r}, \underline{\Omega}, E),$$

which is equivalent to a steady-state transport form, and the (time) overall nuclear response can be evaluated from the simple relation

$$R(\underline{r}) = \int \Sigma_R(\underline{r}, E) \int \Phi(\underline{r}, \underline{\Omega}, E)\, d\underline{\Omega} dE.$$

In the following, the time-integrated angular flux $\Phi(\underline{r}, \underline{\Omega}, E)$ will be solved numerically using the widely used steady-state transport code, ANISN[1]. The neutron source introduced here corresponds to the neutron density produced in the single laser induced fusion event. The neutronics calculations have been performed using the P_3-S_8 approximation in spherical geometry.

The total number of neutrons produced in laser fusion explosions in a time period of one second is $\sim 1.07 \times 10^{21}$ assuming an energy of 3×10^3 MJ is released in this period. The equivalent time-averaged neutron wall loading at the midplane of the blanket is ~ 7.65 MW/m^2. The nuclear data used is given elsewhere[2], and has been collapsed into coupled neutron-gamma cross section sets with 25 neutron and 21 gamma energy groups. The new neutron and gamma energy group structures are given in Tables 1 and 2 respectively.

2. Blanket Model and Nuclear Analysis

The schematic of the one-dimensional blanket model is shown in Table 3. It consists of a 1.5 cm (50% dense) carbon liner (zone 3) two stainless steel walls of 0.1 cm each (zone 5 and 7) with a 1.8 cm thick, homogenized zone of 16% (volume) stainless steel and 84% (volume, 40% dense) water (zone 6) between a 35 cm cooling-breeding zone (zone 8, 9 and 10), a 15 cm graphite reflector (zone 11), and a 6 cm cooling-breeding zone (zone 12). The stainless steel zones are to approximate the water cooling tubes between the carbon liner and the first breeding zone as well as the second breeding zone and the graphite zone (zone 17). The cooling-breeding zones consist of Li_2O particles with 60% (volume) packing fraction and 2% (volume) stainless steel structure. The nuclide density for those elements which compose the material in each zone is tabulated on Table 4.

The neutronic results are tabulated on Table 5. Note that the tritium breeding ratio in this design is 1.24. The tritium breeding ratio as a function of the first breeding zone thickness is plotted in Fig. 1. Two other design considerations are compared here. One is that the blanket is designed with a 20 cm graphite reflector and with no second breeding zone. The other is that the blanket is designed with no second graphite zone (zone 17). The basic design criterion is to reduce the reactor size which will then decrease the

cost for the material components. For a marginal value of tritium breeding ratio, ~1.10[1], the first breeding zone can be decreased to approximately 25 cm, with a total blanket thickness of 46 cm, compared with a thickness of 55 cm for the other two designs. A summary of the tritium produced in the breeding regions is given in Table 6. It is seen from this table that the contribution to the tritium breeding ratio from the second breeding zone (zone 12) is approximately 8%.

The total nuclear heating and energy deposition in the breeding zones are in general not sensitive to the above design variations. The total nuclear heating per incoming 14.1 MeV neutron in the blanket is ~15 MeV, of which ~18% is contributed from the gamma-ray heating. About 84% of the total nuclear energy is deposited in the cooling-breeding zones and most of that is carried by the solid particles.[3] The average nuclear energy deposition rate in the carbon liner, stainless steel walls, and in the breeding zones and graphite reflectors are tabulated and depicted in Table 7 and Fig. 2, respectively. These values are important input for the blanket heat transfer analysis. Finally, the nuclear energy deposition rates in each zone are summarized in Table 8.

1. ~ 10% of the uncertainty from the neutron cross section data is considered here.

Table 1

Neutron 25 Energy Group Structure in eV

Group	Group Limits E(Top)	E(Low)	E(Mid Point)
1	1.4918 (+7)	1.3499 (+7)	1.4208 (+7)
2	1.3499 (+7)	1.2214 (+7)	1.2856 (+7)
3	1.2214 (+7)	1.1052 (+7)	1.1633 (+7)
4	1.1052 (+7)	1.0000 (+7)	1.0526 (+7)
5	1.0000 (+7)	9.0484 (+6)	9.5242 (+6)
6	9.0484 (+6)	8.1873 (+6)	8.6178 (+6)
7	8.1873 (+6)	7.4082 (+6)	7.7979 (+6)
8	7.4082 (+6)	6.7032 (+6)	7.0557 (+6)
9	6.7032 (+6)	6.0653 (+6)	6.3843 (+6)
10	6.0653 (+6)	5.4881 (+6)	5.7787 (+6)
11	5.4881 (+6)	4.4933 (+6)	4.9907 (+6)
12	4.4933 (+6)	3.6788 (+6)	4.0860 (+6)
13	3.6788 (+6)	3.0119 (+6)	3.3453 (+6)
14	3.0119 (+6)	2.4660 (+6)	2.7390 (+6)
15	2.4660 (+6)	1.3534 (+6)	1.9097 (+6)
16	1.3534 (+6)	7.4274 (+5)	1.0481 (+6)
17	7.4274 (+5)	4.0762 (+5)	5.7518 (+5)
18	4.0762 (+5)	1.6573 (+5)	2.8667 (+5)
19	1.6573 (+5)	3.1828 (+4)	9.8779 (+4)
20	3.1828 (+4)	3.3546 (+3)	1.7591 (+4)
21	3.3546 (+3)	3.5358 (+2)	1.8541 (+3)
22	3.5358 (+2)	3.7267 (+1)	1.9542 (+2)
23	3.7267 (+1)	3.9279 (+0)	2.0597 (+1)
24	3.9279 (+0)	4.1399 (-1)	2.1718 (+0)
25	4.1399 (-1)	2.200 (-2)	2.1800 (-1)

Table 2

Gamma-Ray 21 Energy Group Structure in MeV

Group	Group Limits E(Top)	E(Low)	E(Mid Point)
1	14.00	12.00	13.00
2	12.00	10.00	11.00
3	10.00	8.00	9.00
4	8.00	7.50	7.75
5	7.50	7.00	7.25
6	7.00	6.50	6.75
7	6.50	6.00	6.25
8	6.00	5.75	5.875
9	5.75	5.00	5.375
10	5.00	4.50	4.75
11	4.50	4.00	4.25
12	4.00	3.50	3.75
13	3.50	3.00	3.25
14	3.00	2.50	2.75
15	2.50	2.00	2.25
16	2.00	1.50	1.75
17	1.50	1.00	1.25
18	1.00	0.40	0.70
19	0.40	0.20	0.30
20	0.20	0.10	0.15
21	0.10	0.001	0.0505

Table 3

Neutronics Analysis - Material Composition

Zone Number	Thickness (cm)	Material Composition
1	0.1	Vacuum (Neutron Source)
2	499.9	Vacuum
3	1.5	Carbon Liner (50% dense)
4	1.0	Vacuum
5	0.1	Stainless Steel
6	1.8	16% Stainless Steel + 84% (40% dense) Water
7	0.1	Stainless Steel
8	15	60% Li_2O
9	10	+
10	10	2% Stainless Steel
11	15	Graphite
12	6	60% Li_2O + 2% Stainless Steel
13	1	Stainless Steel
14	1.8	16% Stainless Steel + 84% Water (Steam)
15	0.1	Stainless Steel
16	1	Vacuum
17	10	Graphite

Table 4

Nuclide Concentrations Employed in Calculations

Zone No.	Material Composition	Nuclide	Concentration(10^{24} atoms/cm^3)
3	Carbon Liner (50% dense)	C	0.0402
5	Stainless Steel	Cr	0.01450
		Ni	0.00938
		Fe	0.06141
6	16% Stainless Steel + 84% (40% dense) water	Cr	0.00232
		Ni	0. 0150
		Fe	0.00982
		H	0.02248
		O	0.01124
7	Stainless Steel	Cr	0.01450
		Ni	0.00938
		Fe	0.06141
8, 9, 10	60% Li_2O + 2% Stainless Steel	^6Li	0.0036507
		^7Li	0.0455493
		O	0.0246000
		Cr	0.000290
		Ni	0.0001876
		Fe	0.0012282
11	Graphite	C	0.0804
12	60% Li_2O + 2% Stainless Steel	^6Li	0.0036507
		^7Li	0.0455493
		O	0.0246000
		Cr	0.0002900
		Ni	0.0001876
		Fe	0.0012282
13	Stainless Steel	Cr	0.0145
		Ni	0.00938
		Fe	0.06141
14	16% Stainless Steel + 84% (Steam) Water	Cr	0.00232
		Ni	0.00150
		Fe	0.00982
15	Stainless Steel	Cr	0.01450
		Ni	0.00938
		Fe	0.06141
17	Graphite	C	0.0804

Table 5

Summary of Tritium Breeding, Radiation Damage Parameters and Nuclear Heating in the Laser Fusion Blanket

Tritium Breeding	
Tritium Production from $^{6}Li(n,\alpha)$	0.8228
Tritium Production from $^{7}Li(n,n'\alpha)$	0.4126
Tritium Breeding Ratio	1.2354
Atomic Displacement[a]	
Carbon Liner	1.2848×10^{-6}
Stainless Steel Wall	1.4580×10^{-6}
Helium Production[b]	
Carbon Liner	3.1164×10^{-4}
Stainless Steel Wall	2.9695×10^{-5}
Hydrogen Production[b]	
Stainless Steel Wall	8.2616×10^{-5}
Nuclear Heating[c]	
Neutron Heating	12.35
Gamma Heating	2.72
Total Heating	15.07

a. dpa per unit time interval (total number of neutrons produced equivalent to a fusion energy of 3×10^{3} MJ)

b. appm per unit time interval (total number of neutrons produced equivalent to a fusion energy of 3×10^{3} MJ)

c. in units of MeV per incoming 14.1 MeV neutron

Table 6

Summary of Tritium Breeding in the Cooling/Breeding Zones

Zone No.	T_6[a]	T_7[b]	$T_6 + T_7$
8	0.3973	0.2619	0.6592
9	0.1577	0.0933	0.2510
10	0.1722	0.0512	0.2234
12	0.0956	0.0062	0.1018
Sum	0.8228	0.4216	1.2354

a. Tritium Production from $^{6}Li(n,\alpha)$

b. Tritium Production from $^{7}Li(n,n'\alpha)$

Table 7

Nuclear Heating Rates in the Carbon Liner, Stainless Steel and Water Cooling Zones

(Based on 7.65 MW/m^2 Time-Averaged Neutron Wall Loading)

Zone No.	Composition	Neutron Heating[a]	Gamma Heating[a]	Total Heating
3	Carbon Liner	10.33	2.40	12.73
5	Stainless Steel	20.59	29.43	51.02
6	16% Stainless Steel + 84% Water (40% dense)	19.13	5.85	24.98
7	Stainless Steel	19.02	29.50	48.52
13	Stainless Steel	0.47	3.35	3.82
14	16% Stainless Steel + 84% Water (Steam)	0.07	0.45	0.52
15	Stainless Steel	0.41	2.73	3.14

a. in units of $watt/cm^3$

Table 8

Nuclear Energy Deposition in the Blanket

Zone No.	Composition	Neutron Heating[a]	Gamma Heating[a]	Total Heating[a]
3	Carbon Liner	0.2861	0.0663	0.3524
5	Stainless Steel	0.0380	0.0543	0.0923
6	16% Stainless Steel + 84% Water (40% dense)	0.6366	0.1949	0.8315
7	Stainless Steel	0.0352	0.0546	0.0898
8	60% Li_2O	6.1781	0.9945	7.1726
9	+	2.2953	0.4707	2.7660
10	2% Stainless Steel	1.6887	0.3248	2.0135
11	Graphite	0.5292	0.3268	0.8560
12	60% Li_2O + 2% SS	0.5699	0.0703	0.6402
13	Stainless Steel	0.0096	0.0693	0.0789
14	16% Stainless Steel + 84% Water (Steam)	0.0025	0.0169	0.0194
15	Stainless Steel	0.0008	0.0057	0.0065
17	Graphite	0.0826	0.0727	0.1553
Summation Over the Blanket		12.3526	2.7218	15.0744
Nuclear Energy Leakage to the Shield		0.0939	0.1054	0.1993

a. in units of MeV per incoming 14.1 MeV neutron

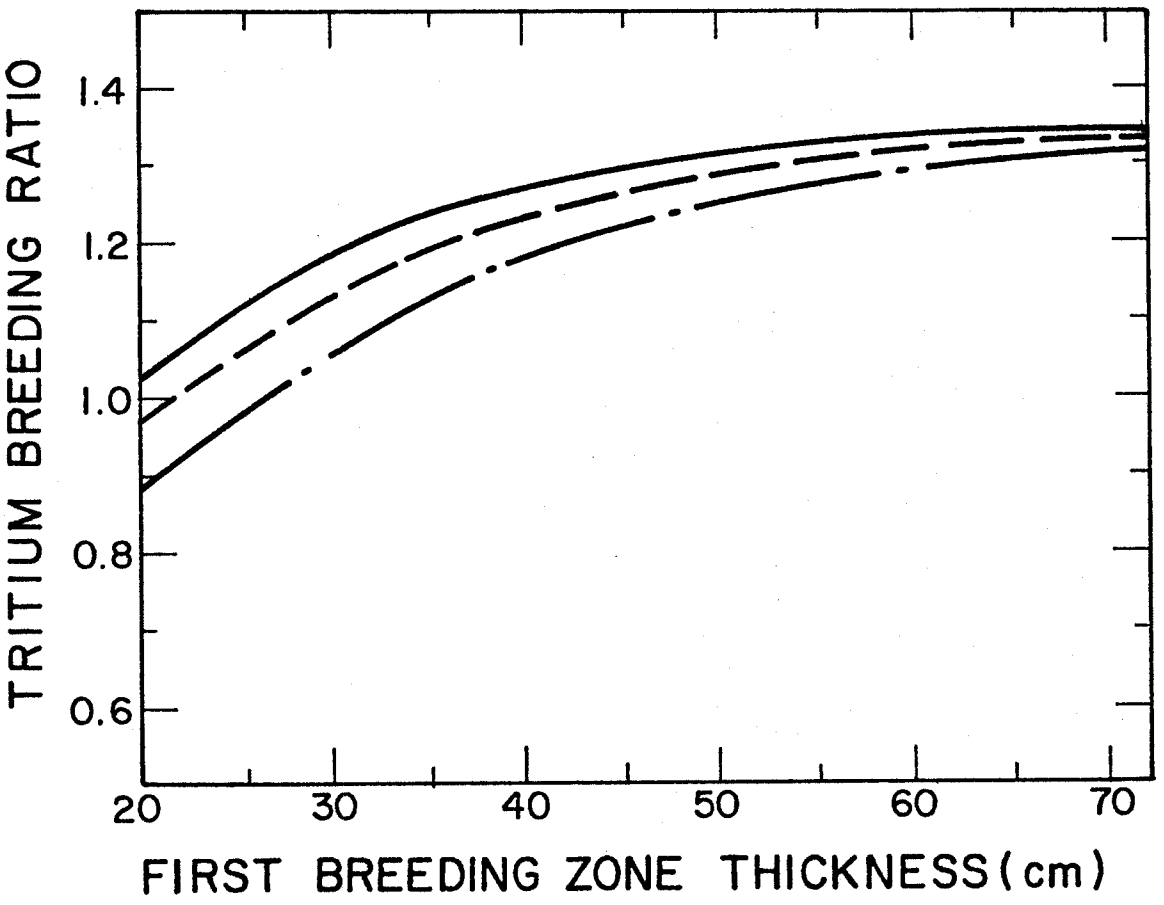

Figure 1. Tritium breeding ratio as a function of first breeding zone thickness for three blanket design considerations.

——blanket with second breeding zone and second graphite reflector

----blanket with second breeding zone only

– – –blanket with first breeding zone only (20 cm graphite reflector)

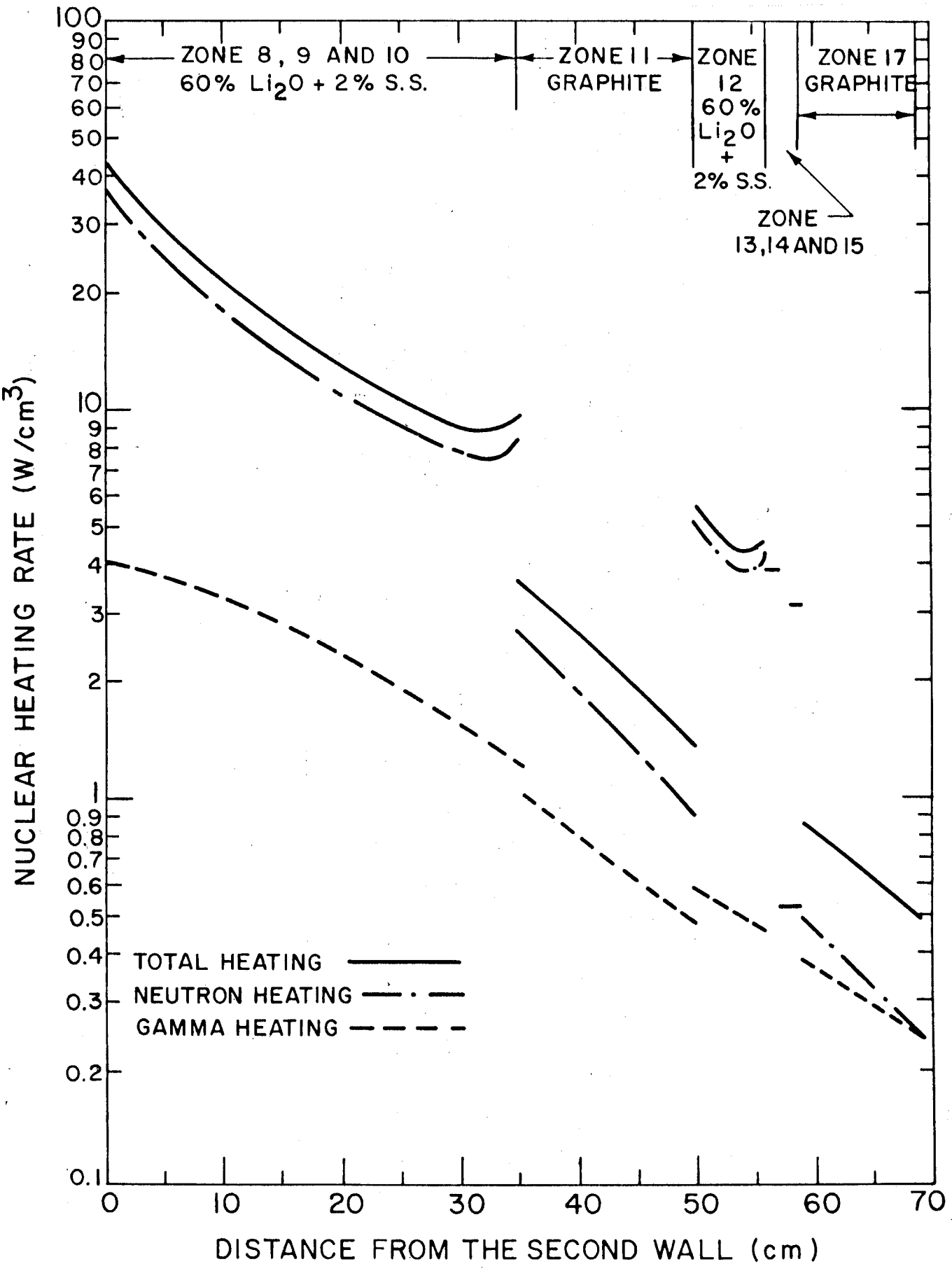
ZONE 8, 9 AND 10
60% Li_2O + 2% S.S.
ZONE 11
GRAPHITE
ZONE 12
60% Li_2O + 2% S.S.
ZONE 17
GRAPHITE
ZONE 13,14 AND 15
NUCLEAR HEATING RATE (W/cm^3)
TOTAL HEATING
NEUTRON HEATING
GAMMA HEATING
DISTANCE FROM THE SECOND WALL (cm)

FIGURE 2

3. Comparative Monte Carlo-Discrete Ordinates Neutronics and Photonics Analysis

Although one-dimensional calculations are practical for initial blanket and shield optimization studies, two and three-dimensional studies are necessary at more advanced stages of the designs. Asymmetries affect the tritium breeding, nuclear heating and primary neutron damage, as well as particle leakage through the laser beams system, which will be required for detailed investigation at a later stage. Two-dimensional discrete ordinates can treat asymmetry effects but they cannot treat the effects of penetrations without major approximations. Monte Carlo calculations are the best candidate for such investigations because of the ability to treat complex geometries.

Forseeing this future application, a comparative analysis between Monte Carlo and discrete ordinates was carried by Ragheb, Cheng and Conn.[4] The objective of the analysis was to assess the capabilities of Monte Carlo for blanket and shield studies compared to discrete ordinates, and to test the reliability of the used version of the Monte Carlo code.

A one-dimensional spherical lithium oxide blanket reactor model was chosen for the investigation. The blanket consists of a 1.5 cm thick carbon liner, two 0.1 cm thick stainless steel walls with a 0.8 cm (30% dense) stainless steel zone between them to simulate the front wall tubing, a 50 cm thick cooling-breeding zone and a 20 cm thick graphite reflector. A shield was included in some of the studied models.

Using the same coupled neutron-gamma cross section sets, the nuclear parameters were calculated by discrete ordinates using the code ANISN[1], and by Monte Carlo using a modified version of the MORSE multigroup code.[5] Several models were used for the Monte Carlo Calculations as discussed in reference 4. Table 9 displays a summary of the results of the investigation for one of the treated models for tritium breeding, radiation damage parameters

and nuclear heating. Details of the nuclear energy deposition in the different blanket zones are further tabulated in Table 10.

The analysis suggests that adequate results can be obtained by Monte Carlo, even for a small number of treated particles, in the blanket part of the system. The reliability of this version of the Monte Carlo code has been established by the satisfactory agreement between the Monte Carlo and discrete ordinate results. It was even found that Monte Carlo can compete favorably in terms of computation costs with discrete ordinates for one-dimensional blanket studies.

It is recommended that the Monte Carlo method be used for future two and three dimensional studies of the contemplated design. Due to its moderate cost when treating the blanket, parametric studies can easily be undertaken. The design of the shield will require the processing of a large number of particles if Monte Carlo is used, so that one-dimensional discrete ordinates must be still relied upon for that part of the analysis. Monte Carlo can treat asymmetry effects on the nuclear parameters, shielding of the cryogenic pellet injection system, leakage through the laser beam ports, and other problems of a two or three-dimensional nature.

Table 9

Summaries of Tritium Breeding, Radiation Damage Parameters and Nuclear Heating for MORSE and ANISN Calculations

	MORSE(P_3, 1000 histories)	ANISN (P_3S_8)
Tritium Breeding		
Tritium Production from $^{6}Li(n,\alpha)$	0.8103 ± 0.0159	0.8104
Tritium Production from $^{7}Li(n,n'\alpha)$	0.4477 ± 0.0096	0.4430
Tritium Breeding Ratio	1.2580 ± 0.0186	1.2534
Atomic Displacement[a]		
Carbon Liner	$(1.5637 \pm 0.0625) \times 10^{-6}$	1.56×10^{-6}
Stainless Steel Walls	$(1.5058 \pm 0.5019) \times 10^{-6}$	1.56×10^{-6}
Helium Production[b]		
Carbon Liner	$(3.1248 \pm 0.2427) \times 10^{-4}$	3.38×10^{-4}
Stainless Steel Walls	$(2.6817 \pm 0.5157) \times 10^{-5}$	2.92×10^{-5}
Hydrogen Production[b]		
Stainless Steel Walls	$(7.8465 \pm 1.4060) \times 10^{-5}$	8.42×10^{-5}
Nuclear Heating[c]		
Neutron Heating	12.3520 ±0.690	12.280
Gamma Heating	2.7597 ± 0.0532	2.717
Total Heating	15.1117 ± 0.1772	14.997

a. dpa per unit time interval (total number of neutrons produced equivalent to a fusion energy of 3×10^3 MJ)

b. appm per unit time interval (total number of neutrons produced equivalent to a fusion energy of 3×10^3 MJ)

c. in units of MeV per incoming 14.1 MeV neutron

Table 10

Nuclear Energy Deposition in the Studied Blanket for MORSE and ANISN Calculations[a]

Zone Number	Material Composition	MORSE (P_3 1000 histories)			ANISN (P_3S_8)		
		Neutron	Gamma	Total	Neutron	Gamma	Total
3	Carbon Liner	0.5810±0.0336	0.1246±0.1025	0.7056±0.0358	0.592	0.133	0.725
5	Stainless Steel	0.0351±0.0061	0.0582±0.0079	0.0932±0.0100	0.038	0.055	0.093
6	30% Stainless Steel	0.1097±0.0142	0.1306±0.0115	0.2404+0.0183	0.088	0.131	0.219
7	Stainless Steel	0.0408±0.0060	0.0652±0.0079	0.1060±0.0001	0.042	0.055	0.097
8 9 10	60% Li_2O + 2% Stainless Steel	11.3424±0.1629	2.1494±0.0476	13.4918±0.0280	11.286	2.113	13.399
11	Graphite	0.2430±0.0252	0.2318±0.0122	0.4748±0.0280	0.234	0.230	0.464
TOTAL		12.35	2.577	14.93	12.28	2.717	15.00

a. in Units of MeV/14.1 MeV neutron.

References

[1] W. W. Engle, Jr., "A User's Manual for ANISN," K-1693, Union Carbide Corporation, (1967)

[2] B. Badger et al., "A Wisconsin Toroidal Fusion Reactor Design," Vol. 1 UWFDM-68, University of Wisconsin Fusion Feasibility Study Group (November 1973).

[3] E. T. Cheng, T. Y. Sung and D. K. Sze, "Neutronics Studies of the Gas-Carried Li_2O Cooling/Breeding Fusion Reactor Blanket and Shield," UWFDM-187, University of Wisconsin Fusion Technology Program (February 1976).

[4] M. M. H. Ragheb, E. T. Cheng and R. W. Conn, "Comparative One-Dimensional Monte Carlo and Discrete Ordinates Neutronics and Photonics Analysis for a Laser Fusion Reactor Blanket with Gravitational Flowing Li_2O Particles as Coolant and Breeder," To be published as a UWFDM in 1977.

[5] RSIC Code Package CCC-203, "MORSE-CG," Radiation Shielding Information Center, ORNL, September 1976.

VII-C. Time Dependent Neutronics

The analysis of the blanket is carried out using the multigroup discrete ordinates computer code Time Dependent ANISN (TDA).[1] This code was chosen over one employing a Monte Carlo technique since a simple one-dimensional geometry is used and the main reason for using a Monte Carlo code is its capability of handling complex or multidimensional geometries. A spherical geometry is used to simulate the midplane of the cylindrical vessel which is the region receiving the highest flux thus incurring the most damage. A sphere also allows the use of a point source. This is the most realistic source for this calculation since the flux from a pellet explosions falls as $1/r^2$ as it approaches the wall. If a cylindrical geometry was chosen, a line source must be used which falls as $1/r$.

The details of the blanket structure as simulated in the calculation are seen in Figure 1. It consists of a spherical shell with an inner diameter of 10 m. The innermost portion of the shell contains a 1.5 cm carbon liner of normal density. This is supported such that the back of the liner is 1 cm from the first wall which is comprised of a bank of stainless steel pipes (O.D. = 1 cm; I.D. = .8 cm). This can be represented for neutronics purposes by homogenizing the zone creating a 1 cm region of stainless steel with a density factor of 0.36 (metal volume/total volume). This wall is followed by a breeding zone of Li_2O, He and a small amount of structure. The thickness of this zone being 22 cm should not be mistaken for the actual design width. Since the time dependent study is interested in damage rates to the liner and first wall, extending the breeding zone any further would only serve to increase the cost of the analysis with no accompanying increase in the accuracy of the results. Any backscattering which would occur from the missing part of the blanket is approximated by appropriate albedos at the

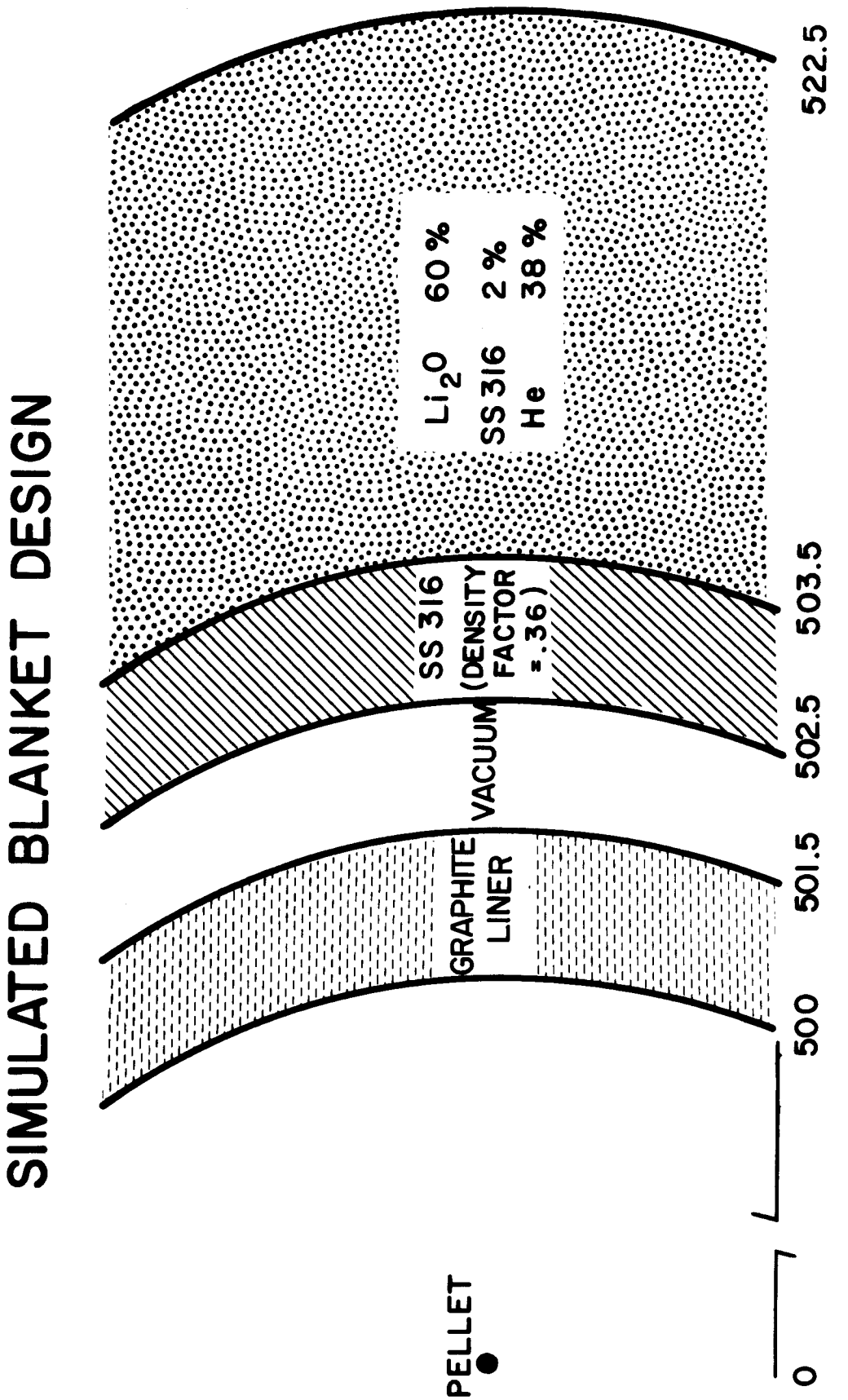
SIMULATED BLANKET DESIGN
PELLET
0
500
501.5
502.5
503.5
522.5
GRAPHITE LINER
VACUUM
SS 316 (DENSITY FACTOR = .36)
Li_2O 60 %
SS 316 2 %
He 38 %

FIGURE 1

right boundary. The steady state work which calculated the breeding ratio, energy deposition and energy leakage in this region included the entire zone and a reflector.

A major problem with the analysis arose when large negative fluxes appeared in the zones through which the pulse had recently passed. This resulted in a long investigation to determine the cause. The source of the problem was discovered to lie in the treatment of the neutron cross sections.

Traditionally, the angular dependence of neutron differential elastic scattering cross sections has been accounted for by a spherical harmonic expansion which, in cases involving azimuthal symmetry, can be reduced to Legendre polynomials. An infinite number of polynomials accompanied by an infinite set of expansion coefficients exactly fits the true cross section at all points. However, if the code is required to handle very large numbers of polynomials and coefficients then there is no benefit gained over handling the exact pointwise cross sections. Therefore, the cross section data sets commonly used today, which were originally compiled with fission research in mind, use four coefficients (P_3 approximation) to describe the fit. In fission work, however, the highest neutron energy contemplated was on the order of 2 MeV. The treatment of anisotropic scattering is important at these energies but is more so at fusion neutron energies of 14 MeV. When dealing with cross sections in this energy range, the data files still use a P_3 expansion even though the degree of anisotropy has increased to a point where one can see by inspection that at the very least a higher order P_N expansion is required. However, it can be shown that even a traditional P_9 expansion for cross sections which fits the data very well, is not always compatible with a discrete ordinates code which requires only cross sections for scattering through certain specified angles. There is no guarantee

that the P_3 or higher P_N expansion will produce the correct value for these particular cross sections even if the Gauss quadrature set is used. As a matter of fact, it would be a very fortuitous expansion that would result in any true values. The upshot of the poor fitting is that cross sections for scattering through particular angles can be substantially negative.

There is another related problem that is very difficult to notice from analyzing the computer results as there are no blatantly erroneous values such as negative fluxes. One can easily show by mere kinematics arguments that there is only a definite range of angles through which a neutron can elastically scatter off of a nucleus of a given mass and still be in a particular energy group. The cross sections, then, for scattering through all other angles and remaining in that energy group are identically equal to zero. Thus a fit to an isolated peak over a small angular range with a P_3 expansion over the entire range $-1 \leq \mu \leq 1$ (where μ is the cosine of the angle through which a neutron scatters) must be attempted. Due to the oscillatory nature of the Legendre polynomials, this expansion results in positive values of the cross sections through angles which are physically impossible. This effect is particularly important for light nuclides because of their small allowable angular range of scattering from any particular group to another. Direct backscattering of 14 MeV neutrons which remain at 14 MeV has been noticed in graphite.

The most significant part of the problem arises from the external source which is incident normal to the inner surface of the shell. Since neutrons can travel only in specified directions, the sources in these directions must be computed. This is accomplished using the expansion coefficients for the ingroup scattering cross section corresponding to the energy group of the source. This is where the large negative fluxes originate and likewise the

"impossible" positive backscattered fluxes. Other erroneous fluxes are produced by scattering between the various discrete angles but they are smaller factors than the source effect.

A method has now been developed to correct this problem which stays within the framework of a Legendre expansion so no alteration of the code is necessary. The expansion coefficients for cross sections are presently calculated using the orthogonality properties of the polynomials with the result being that the first N moments of the true cross section are preserved by N coefficients. The new technique does not preserve integral moments (other than the zeroth moment) but preserves the true cross sections for scattering from a normal direction to all the discrete quadrature points. Therefore, the sources in all directions are physically correct. This change was performed for the materials used in the blanket for the first group (14 MeV) in-group scattering cross section. The result was a three order of magnitude reduction in the negative fluxes and backscattered component. Negative fluxes still were present because of the incorrect handling of the angle to angle scattering where the angles were other than $\mu = \pm 1$.

Another important aspect of this analysis was the calculation of the neutron source for the microexplosion. A zeroth order approximation is that the burn is 10 ps and the neutrons are all emitted at 14.1 MeV thus resulting in a pulse incident on the liner of 10 ps width since there will be no spreading of arrival times if all neutrons are the same energy. This guess is adequate for calculating steady state quantities since they depend only on the total number of neutrons. However, for transient calculations, this approximation is not accurate and would greatly overestimate the reaction rates. The neutron energy is actually 14 MeV in the center of mass system. In order to obtain the neutron energy in the lab frame, two effects must be considered:

(1) the random velocity distribution of the deuterium and tritium as characterized by their temperature; and (2) the directed motion of the fuel due to the explosion. The inclusion of these effects results in an energy spectrum of 1.7 MeV fwhm about an average of 14 MeV (Figure 2). In a steady state multigroup neutronics calculation, the energy spread has little effect since the majority (~70%) of the neutrons are still in the first group and the remainder are in the second. However, for time dependent work the energy distribution produces a time-of-flight spreading of arrival times resulting in a pulse of 10 ns width arriving at the liner 5 m from the explosion instead of a 10 ps pulse. This effect alone reduces calculated reaction rates by three order of magnitude. Thus, since the damage rate is inversely proportional to the pulse width, it is important to have a good representation of the source. The source is also dependent on pellet design and burn dynamics so the source calculation must be redone if pellet designs are changed.

It is important to note that the only way to simulate time-of-flight spreading of the pulse in a multigroup calculation is by allowing the neutrons to be artifically born over a longer time interval than the actual burn. This is because, as indicated before, all neutrons in a particular energy group will stream with the same velocity and won't spread in time. Therefore, the simulated neutron birth time is dependent on the velocity of the neutrons and the radius of the sphere and the spectrum will be correct only at that radius. If damage rates were also desired at a zone deeper in the blanket, a different calculation must be run since the pulse shape will never be exact at different radii.

The above treatment of the source does not include any effect due to neutron-fuel or neutron-fusion product interaction. In a low ρR pellet, this is a small effect.

Figure 2

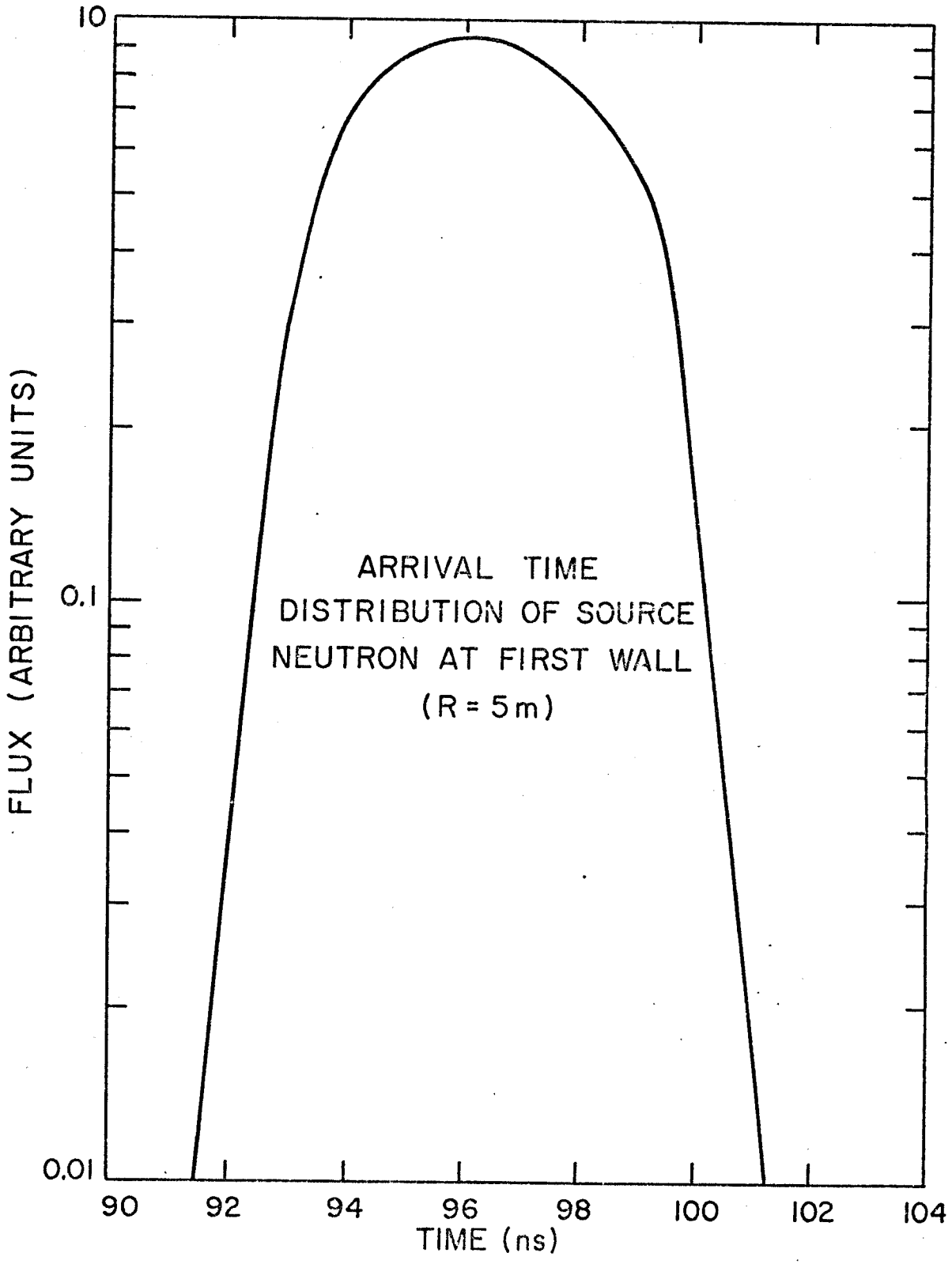
10
0.1
0.01
FLUX (ARBITRARY UNITS)
ARRIVAL TIME
DISTRIBUTION OF SOURCE
NEUTRON AT FIRST WALL
(R = 5 m)
90
92
94
96
98
100
102
104
TIME (ns)

The results of the damage rate and time integrated damage calculations are shown in Figures 3-12. The values correspond to a 100 MJ microexplosion and a peak neutron wall loading of .255 MJ/m^2/pulse. The damage rates initially follow the shape of the pulse which is to be expected since this is the highest flux the region receives. An interesting result is that although the peak displacement rate for SS316 is about 4.5 dpa/sec and that in graphite is 2.7 dpa/sec, the total number of displacements per pulse is about the same. This is because the displacement cross sections for stainless steel at high energies are almost twice as high as those for graphite while in the intermediate range of energies the graphite displacement cross sections are higher. This can also be seen from the time integrated curves. The stainless steel region receives 50% of its total number of displacements within 10 ns after the leading edge of the pulse strikes the graphite liner while it takes the graphite 100 ns to reach half of its maximum value. The gas production reaches 90% of its maximum value in all cases within 10 ns. This is accounted for by the fact that gas production is a threshold reaction with a lower energy limit in the several MeV range. Thus, in a very short time there are no high energy neutrons and no gas production. The detailed effect of these damage rates is discussed in Section VIII of this report.

Energy deposition rates were also calculated and found to be insignificant in comparison with the heating by X-rays. Thus, no shock effect of any consequence will be produced by the neutrons. The total energy deposition of the neutrons and gammas is important, however, and is discussed in Section VII-B.

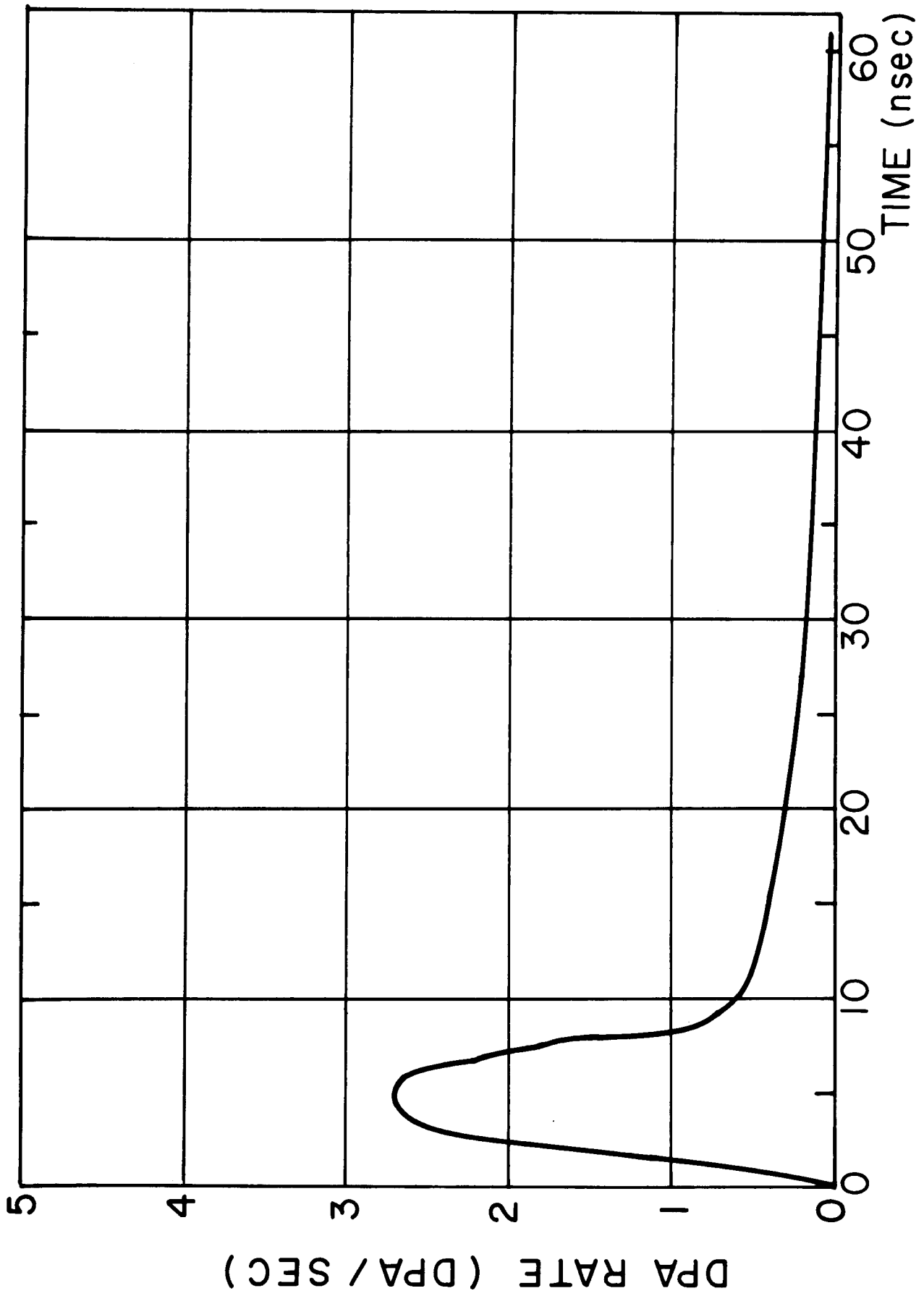

DPA RATE IN GRAPHITE VS TIME
FOR UWICTR

Figure 3

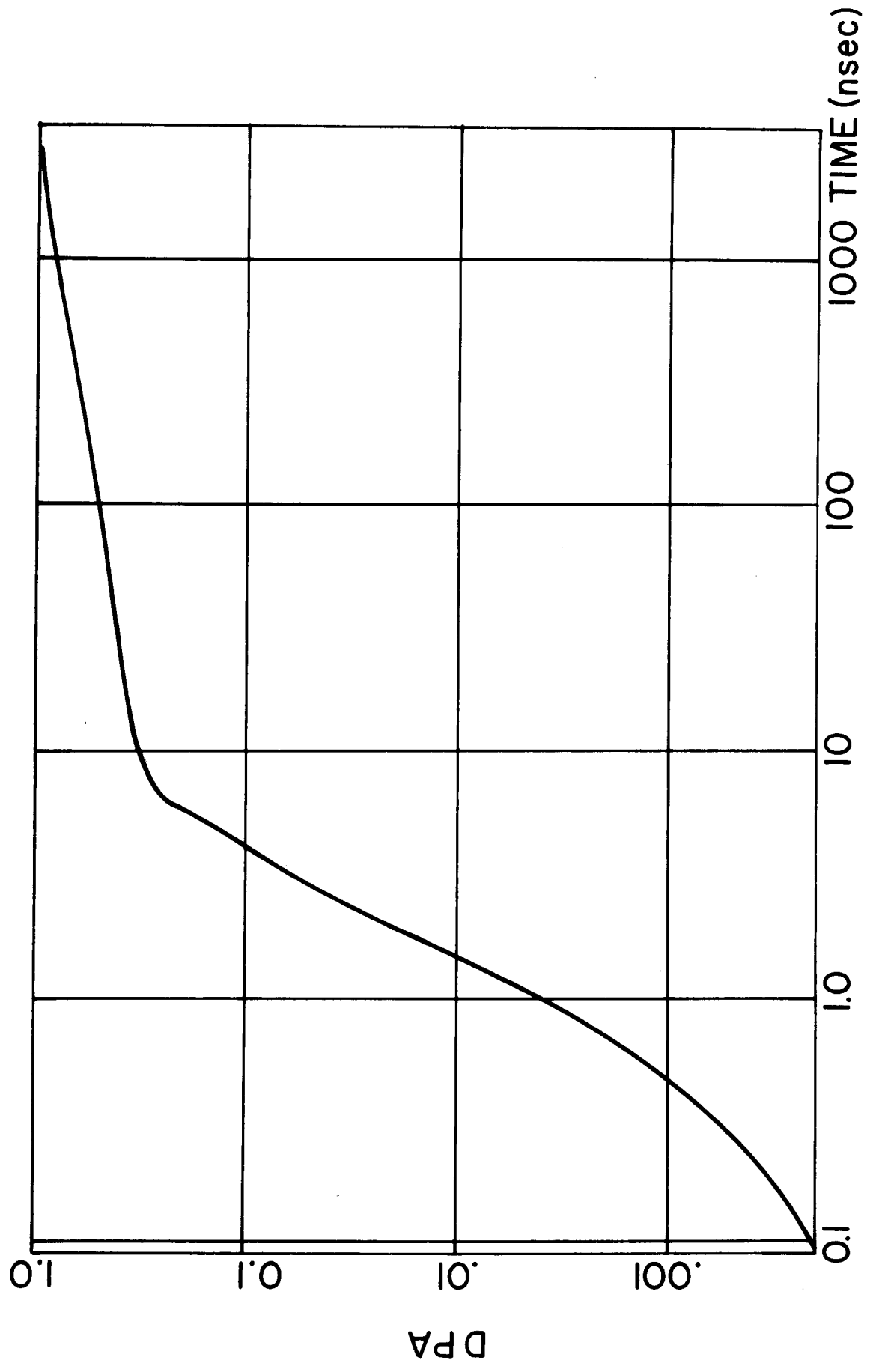
CUMULATIVE DPA IN GRAPHITE VS TIME
NORMALIZED TO TOTAL OF 5.19 x 10^-8
DPA
0.1
1.0
10
100
1000 TIME (nsec)
0.1
1.0
10.
100.

Figure 4

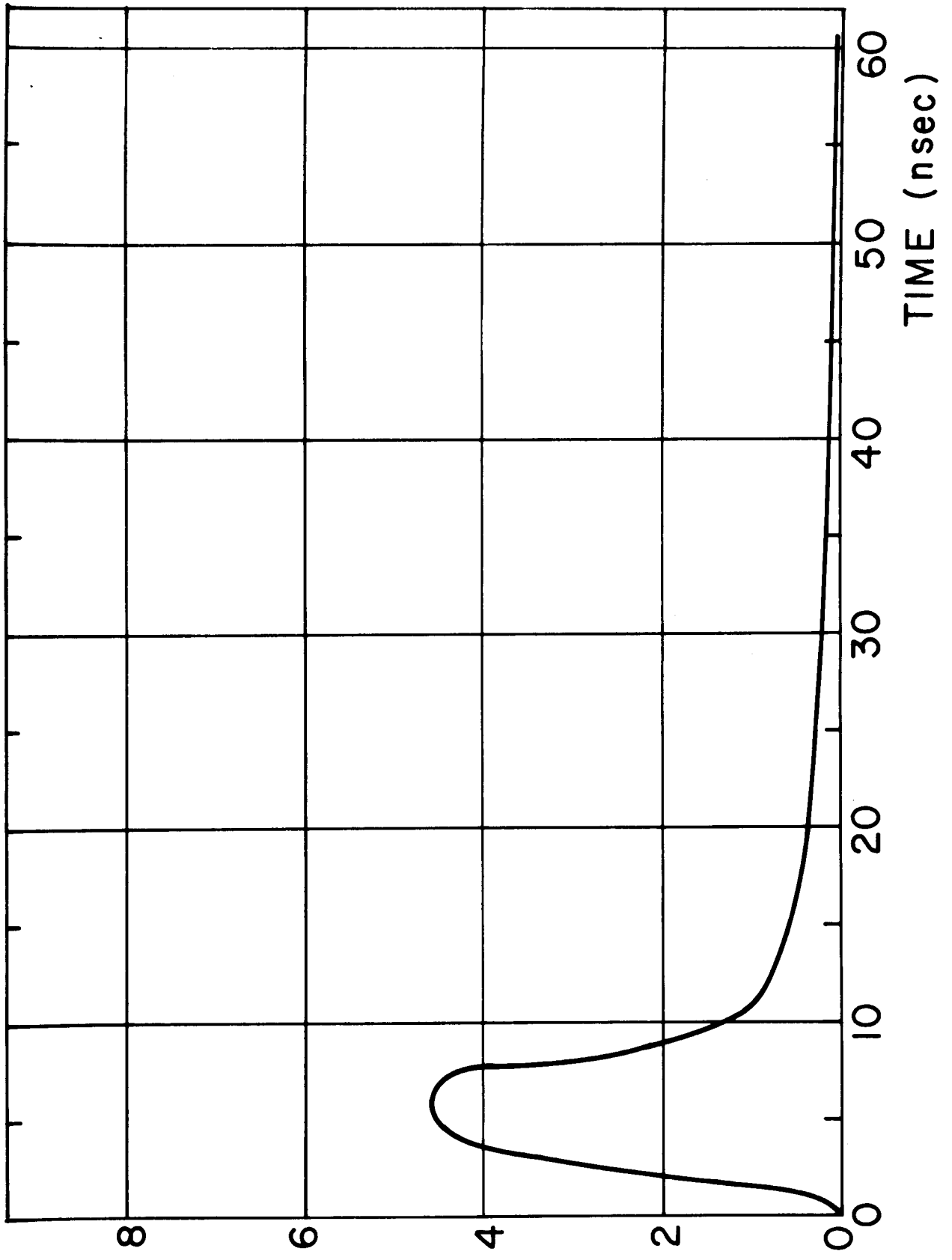

DPA RATE IN 316 SS VS TIME
FOR UWICTR

Figure 5

HELIUM PRODUCTION RATE IN GRAPHITE
VS. TIME FOR UWICTR

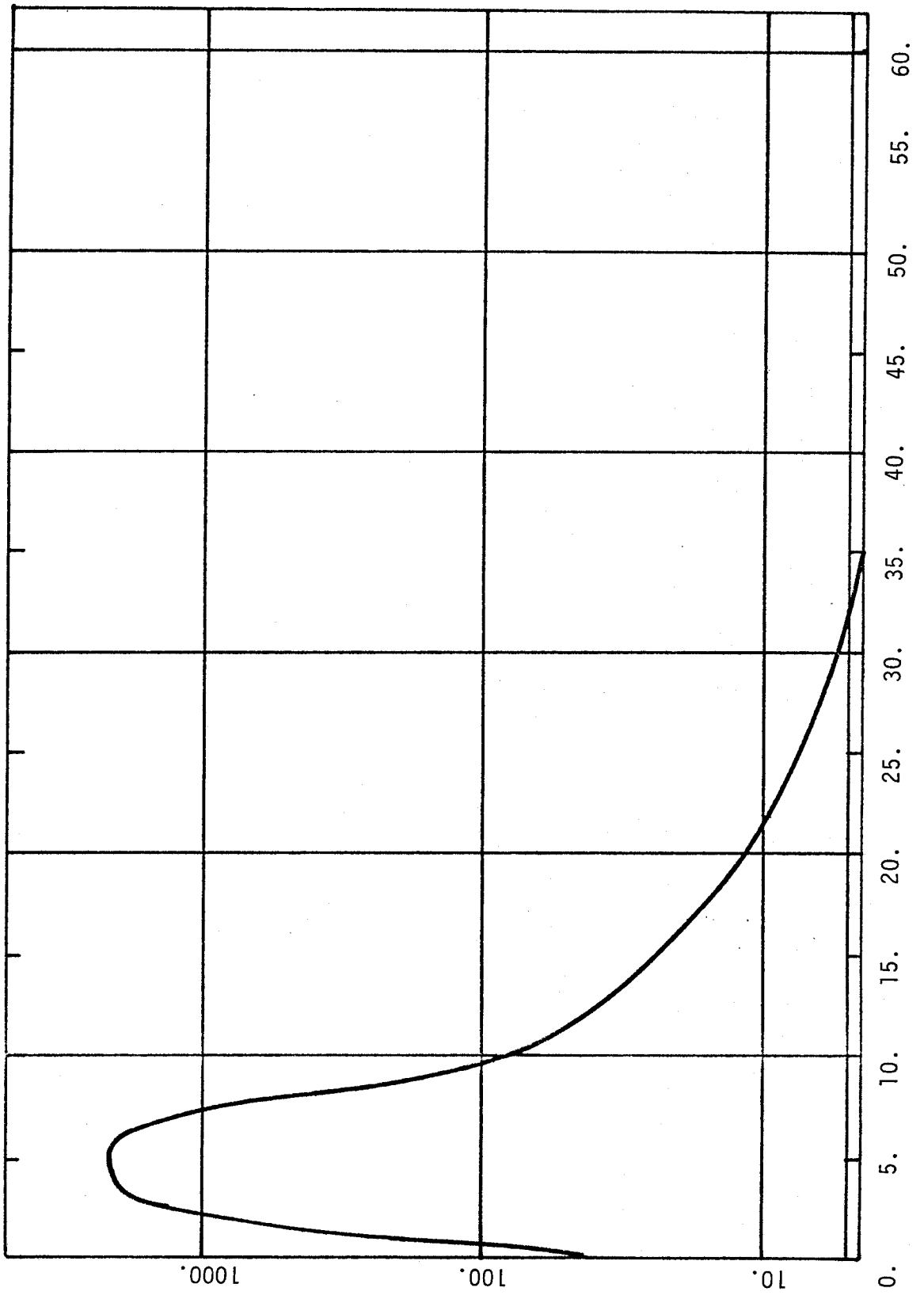

Figure 7

CUMULATIVE HELIUM PRODUCTION IN GRAPHITE
VS. TIME NORMALIZED TO
1.126×10^{-5} APPM

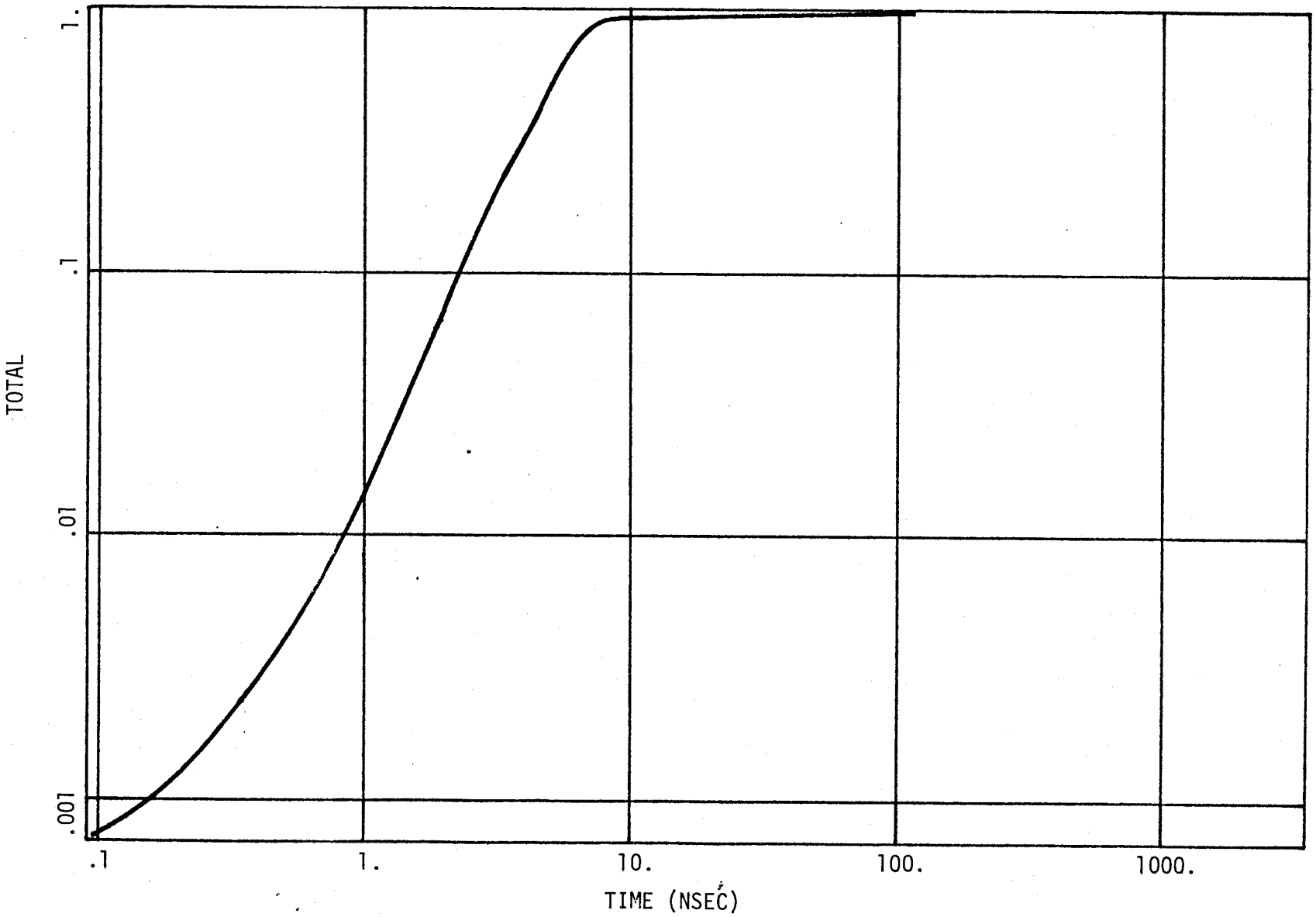

Figure 8

HYDROGEN PRODUCTION RATE IN SS 316
VS. TIME FOR UWICTR

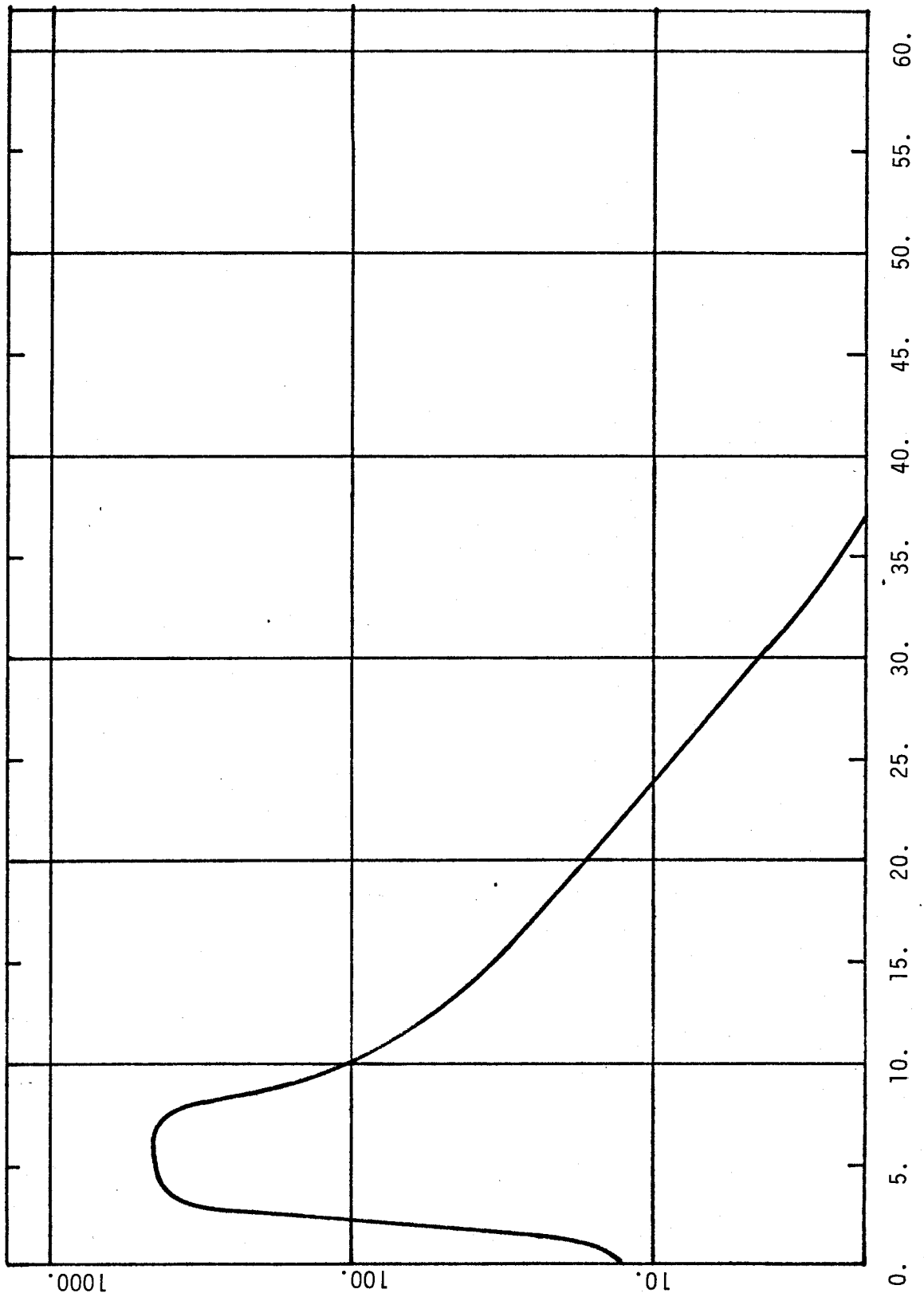

Figure 9

CUMULATIVE HELIUM PRODUCTION IN SS 316
VS. TIME NORMALIZED TO
9.73×10^{-7} APPM

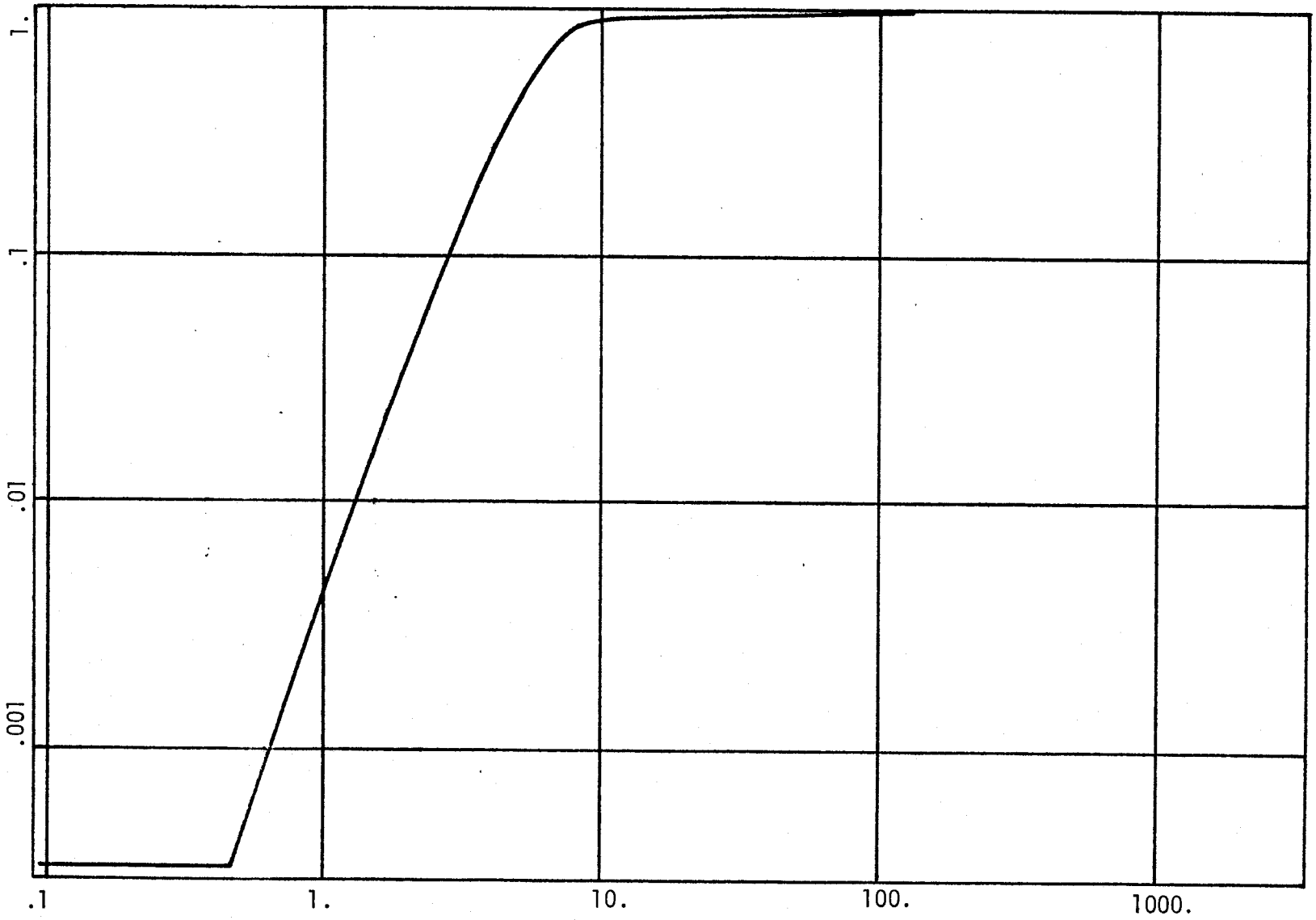

Figure 10

HELIUM PRODUCTION RATE IN SS 316
VS. TIME FOR UWICTR

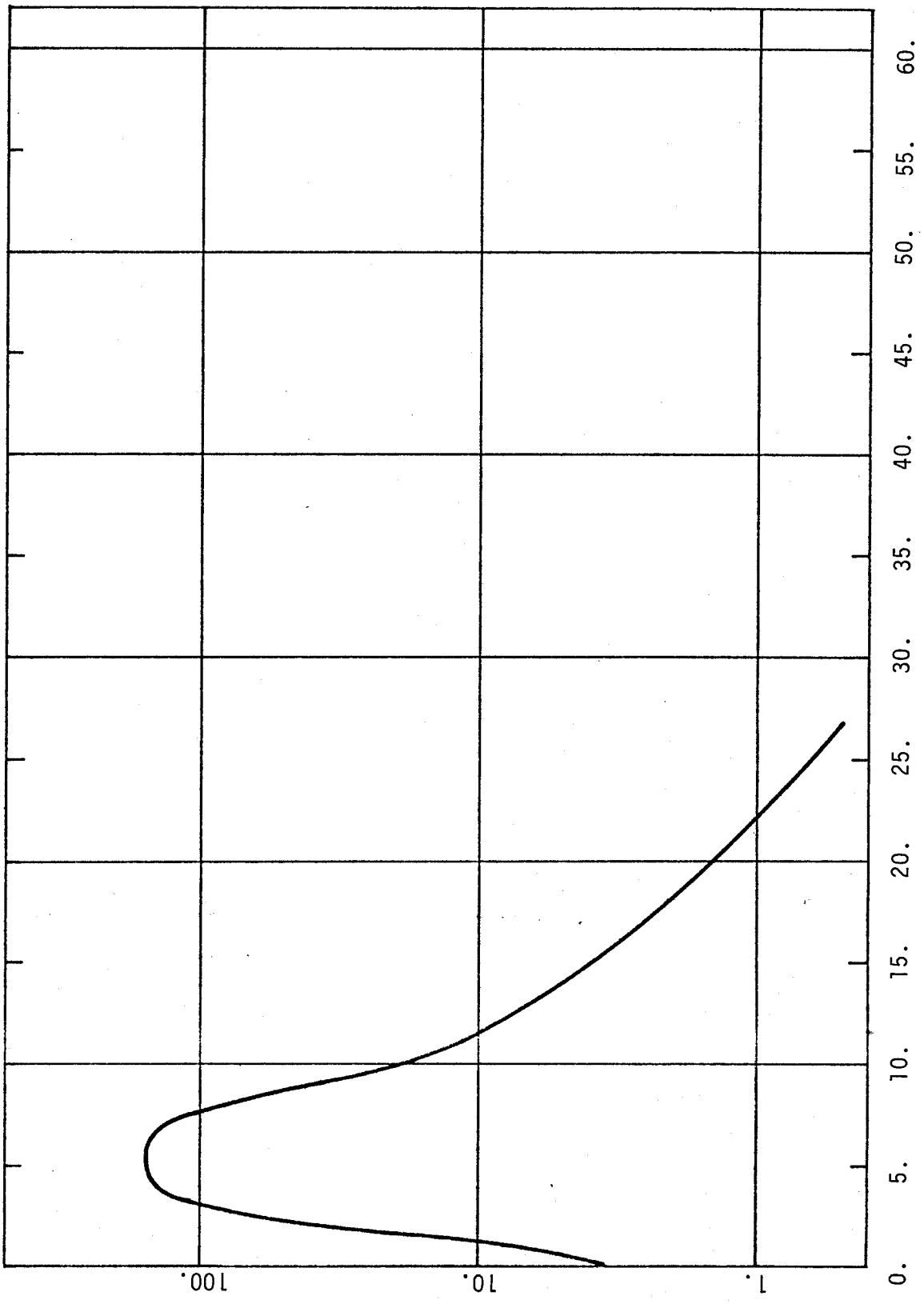

Figure 11

CUMULATIVE HYDROGEN PRODUCTION IN SS 316
VS. TIME NORMALIZED TO
2.81×10^{-6} APPM

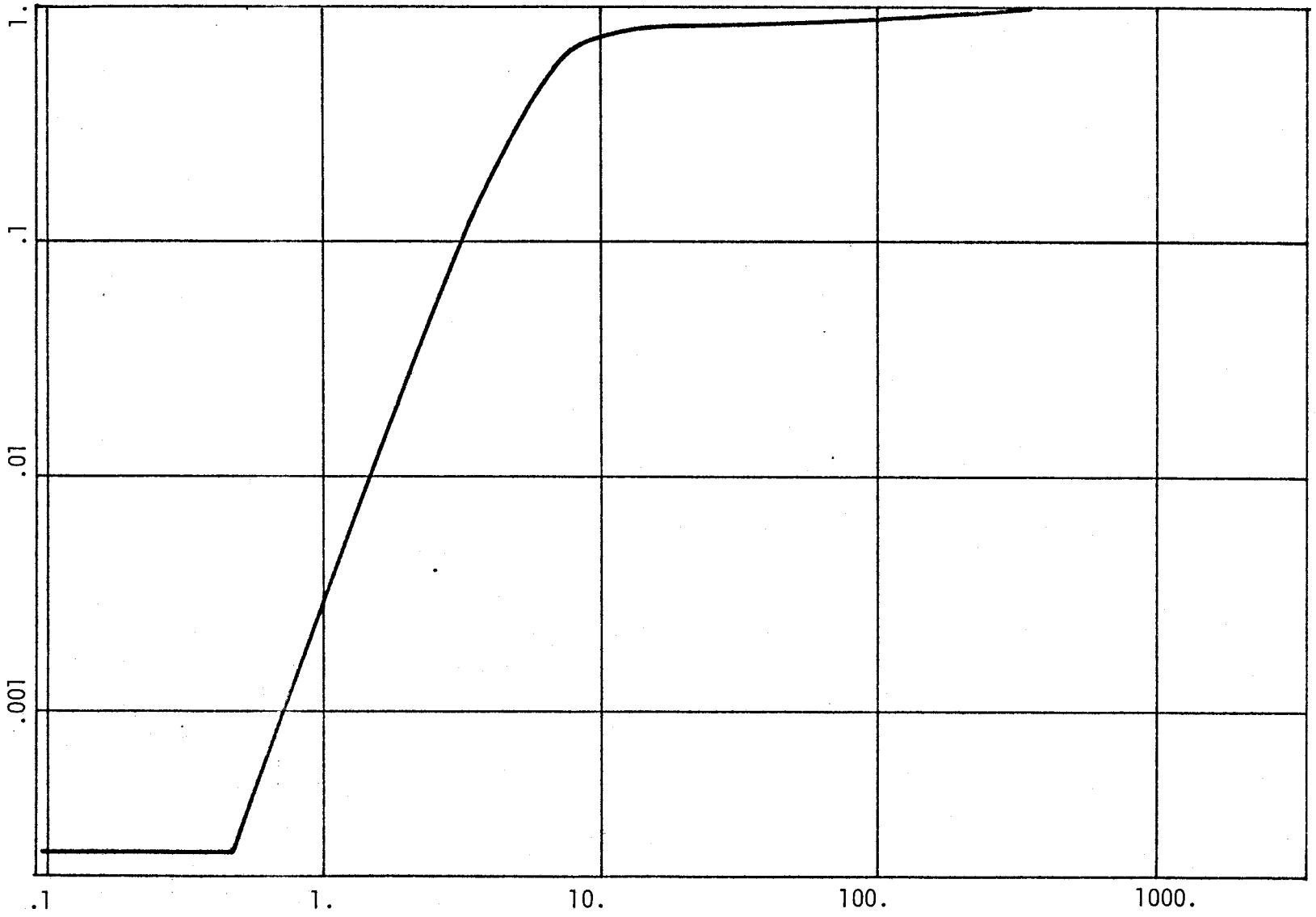

Figure 12

References for Section VII-C

1. S. A. Dupree et al., "Time Dependent Neutron and Photon Transport Calculations Using the Method of Discrete Ordinates," Joint Los Alamos Scientific Laboratory - Oak Ridge National Laboratory Report LA-4557 (ORNL-4662) (1971).

VIII. Radiation Damage and Materials Consideration

VIII-A. Pedagogy

VIII-A-1. Nature of Radiation Effect Problems

The neutron radiation environment for the first wall and all other structural materials between the liner and the blanket differs in two distinct ways from the neutron radiation in fission reactors: a major part of the neutron spectrum consists of 14 MeV neutrons, and this component is pulsed. Therefore, during a very short time interval of 10 nsec, displacements are produced at a very fast rate, i.e., 4.53 dpa/sec in the first wall. The form of the damage produced by 14 MeV neutrons consists of larger cascades compared to those generated by fast neutrons in a breeder reactor. Furthermore, the gas production rate via (n,α) reactions is also substantially higher than in a breeder reactor.

Since there is no data available at this time on irradiation effects of pulsed 14 MeV neutrons, a theoretical assessment of possible radiation effect was made in conjunction with experimental data which covers some aspect of this particular irradiation environment. It should be noted at the outset that we have an incomplete understanding and only a sketchy theoretical description of the radiation damage even for steady-state neutron irradiations in fission reactors. The various attempts described here to assess the radiation effects in inertially confined fusion reactors only delineate the possibilities and limitations that may exist for the design of these future reactors. Futhermore, the various attempts were not designed to be mutually consistent, but rather to approach the problems from different viewpoints.

VIII-A-2. Nature of Microscopic Damage Structure

The displacement damage fast neutrons produce in metals is in the form of collision cascades. Direct collision of neutrons generate primary knock-on atoms which in turn create the collision cascade. For 14 MeV neutrons, the

average energy of the primary knock-on atoms in stainless steel is about 490 keV. Using a displacement energy of 40 eV and a displacement efficiency of 0.5 to account for electronic energy losses, one finds that the average number of displacements in one cascade is 3050. The time-dependent neutronics calculation described in Section VII-C gives a displacement damage of 4.6×10^{-8} dpa per pulse. Hence, it follows that during each pulse there are generated 2.7×10^{5} displacements per cm^3 or 8.9×10^{11} cascades/cm^3. We estimated that the average spatial extent of one cascade is around 500 Å which is still small compared with the average distance of simultaneously produced cascades, i.e. $(8.9 \times 10^{11})^{-1/3} \cong 10^{-4}$ cm. Therefore, there exists a small overlap probability of only 5% for cascades produced by the same pulse, and in this respect there is little difference between steady state neutron irradiations or even ion bombardment experiments. However, cascades may be overlapping those from previous pulses. To consider this possibility, the average migration distances were computed for interstitials and vacancies for the two time intervals during one pulse and between consecutive pulses.

The average migration distance of a point defect during the time interval Δt is given by

$$\Delta L = 1/2\sqrt{D\Delta t} \ ,$$

where D is the diffusion coefficient given by

$$D = D^{\circ} \exp(-E^{m}/kT).$$

The activation energy E^{m} and the preexponential factor are given in Table 1 for interstitials and vacancies in nickel. These values are also appropriate for stainless steels.

Table 1

Point Defect Parameters for Nickel

	$D°[cm^2/sec]$	$E^m[ev]$
Interstitial	0.01	0.20
Vacancy	0.07	1.38

Values of $\Delta L/b$, where b = 2.57 Å is the elementary jump distance, are listed in Table 2. The number of jumps necessary to migrate the distance between cascades, 10^{-4}cm, is equal to 3.9×10^4. A smaller number of jumps, 5000, must be made by the point defects to reach sinks, such as dislocations. It is obvious from Table 2 that not even the interstitials have made many jumps during the pulse. However, before the next pulse occurs, the interstitials have migrated a sufficient distance to either recombine with vacancies in their own cascade, with vacancies of neighboring cascades, reacted with other interstitials to form interstitial clusters, or migrated to sinks. Therefore, the interstitial component of the cascades disappears before the next pulse arrives. The same is not true for the vacancy component or the depleted zone. It survives, whatever remains after recombination with interstitials, so that depleted zones accumulate over long time periods, and they represent additional sinks for the interstitials of subsequent collision cascades. The conclusion from this simple qualitative picture is that there exists little difference in defect production between pulsed and continuous irradiation except perhaps for the very early state of irradiation.

In the above discussion, we did not mention the stability of secondary defect, such as voids and dislocation loops, during pulsed irradiation. At temperatures above 0.5 Tm (Tm is the melting point in °K), these secondary defects can anneal. Under irradiation, their stability is determined by the balance between

Table 2

Number of Atomic Jumps of Interstitials and Vacancies During the Pulse and Between Pulses

Time, Δt (sec)	Temp. T (°C)	Interstitial Jumps	Vacancy Jumps
10^{-8}	200	17	2.3×10^{-5}
	300	26	4.4×10^{-4}
	400	35	3.5×10^{-3}
	500	43	1.6×10^{-2}
	600	51	5.3×10^{-2}
	700	59	1.4×10^{-1}
0.033	200	3.0×10^{4}	0.04
	300	4.7×10^{4}	0.82
	400	6.3×10^{4}	6.4
	500	7.9×10^{4}	29
	600	9.0×10^{4}	97
	700	1.1×10^{5}	251

bias driven growth and shrinkage due to annealing. A detailed analysis of void stability under pulsed irradiation was carried out by Ghoniem and Kulcinski[1] and a summary of this work is described in the section below.

VIII-B. Swelling

VIII-B-1. Void Growth under Pulsed Irradiation

A somewhat different approach to the defect production rate was adopted for this study. It was assumed, in accordance with the conjecture of Bullough et al.[2] that a portion of the vacancies in the core of the cascade collapse into a dislocation loop and that the remainder is uniformly distributed throughout the solid. The vacancy loops were treated as sinks and the production rate for the uniformly distributed interstitials and vacancies was assumed to follow the time-dependent displacement rate. Using a modified rate theory the concentrations of vacancies and interstitials was computed. From these time-dependent point defect concentrations, the growth rate of a void with 40 Å diameter was evaluated. The number of gas atoms in the void was held constant and assumed to be ten. Results of these computations are shown in the Figures 1, 2, and 3. During the pulse, the uniformly distributed vacancies and interstitials build up almost linearly with time. At the end of the pulse, the interstitials diffuse rapidly to the sinks, and the void shrinks. Due to the lower mobility, the vacancies arrive at the sinks much later, and the void starts to grow again. Because of the preferential attraction of interstitials to dislocations, however, more vacancies than interstitials eventually arrive at the void, and there is a net gain in its radius. After the uniformly distributed point defects have migrated to sinks, the void shrinks again by slowly emitting vacancies. This process constitutes the annealing, and it is a strong function of time for the three irradiation temperatures

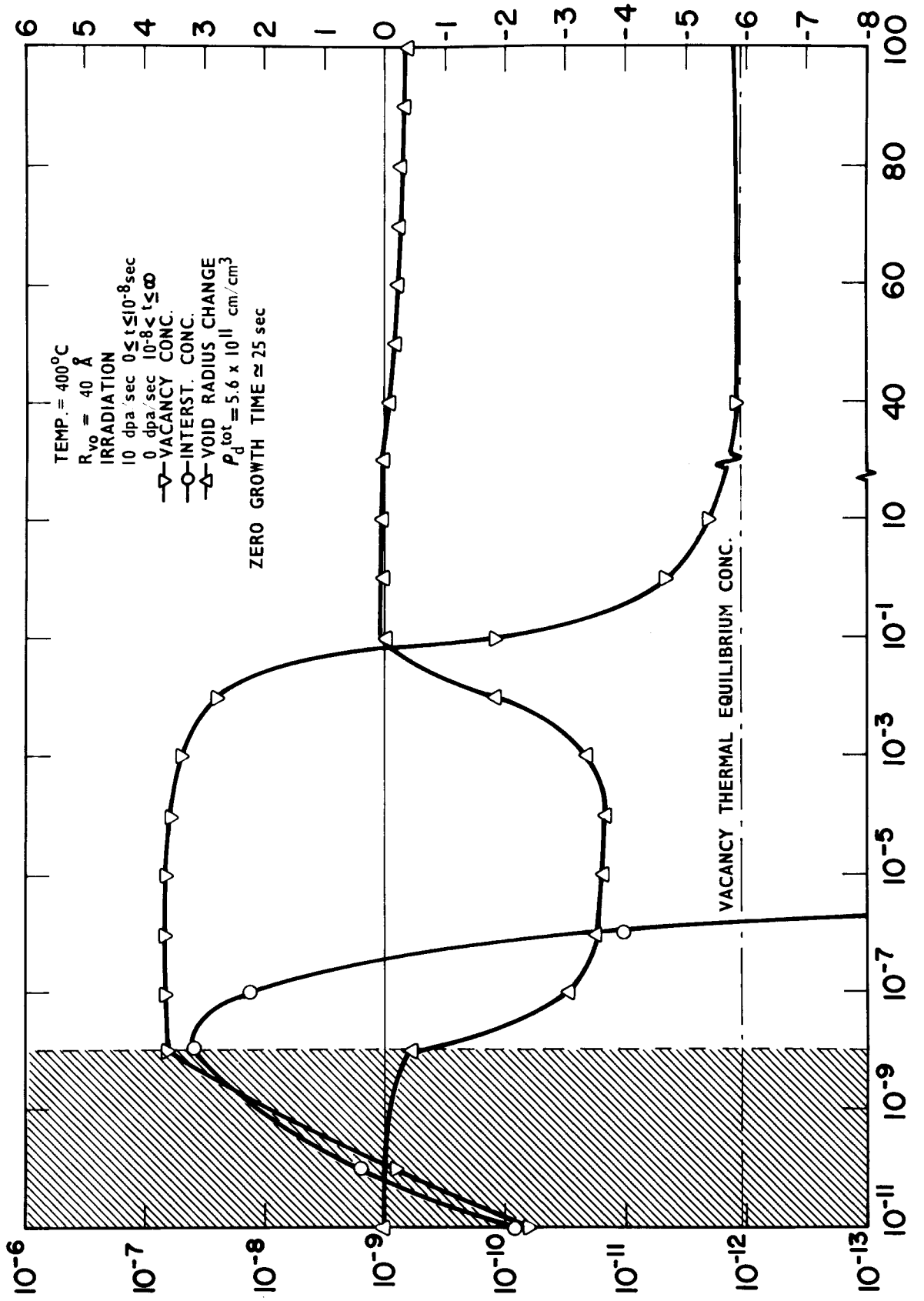

Fig.(1) POINT DEFECT CONCENTRATIONS AND CHANGE IN VOID RADIUS AS A FUNCTION OF TIME DURING AND AFTER AN IRRADIATION PULSE AT 400 °C FOR S.T. 316 S.S.

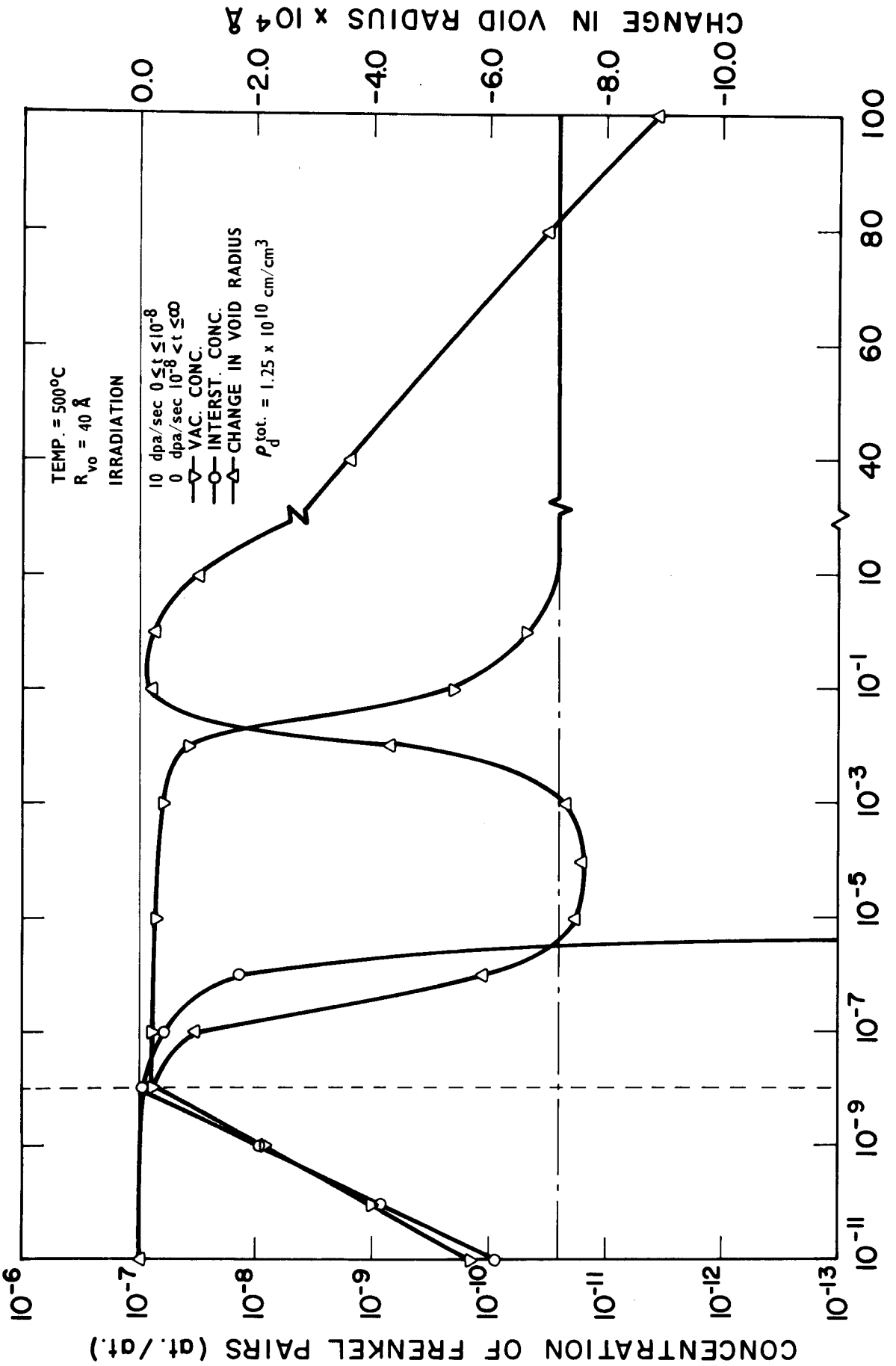
CONCENTRATION OF FRENKEL PAIRS (αt./αt)
CHANGE IN VOID RADIUS x 10⁴ Å
TIME, sec.
TEMP. = 500°C
R_vo = 40 Å
IRRADIATION
10 dpa/sec 0≤t≤10⁻⁸
0 dpa/sec 10⁻⁸<t≤∞
VAC. CONC.
INTERST. CONC.
CHANGE IN VOID RADIUS
ρ_d^tot. = 1.25 x 10¹⁰ cm/cm³

Fig. (2)

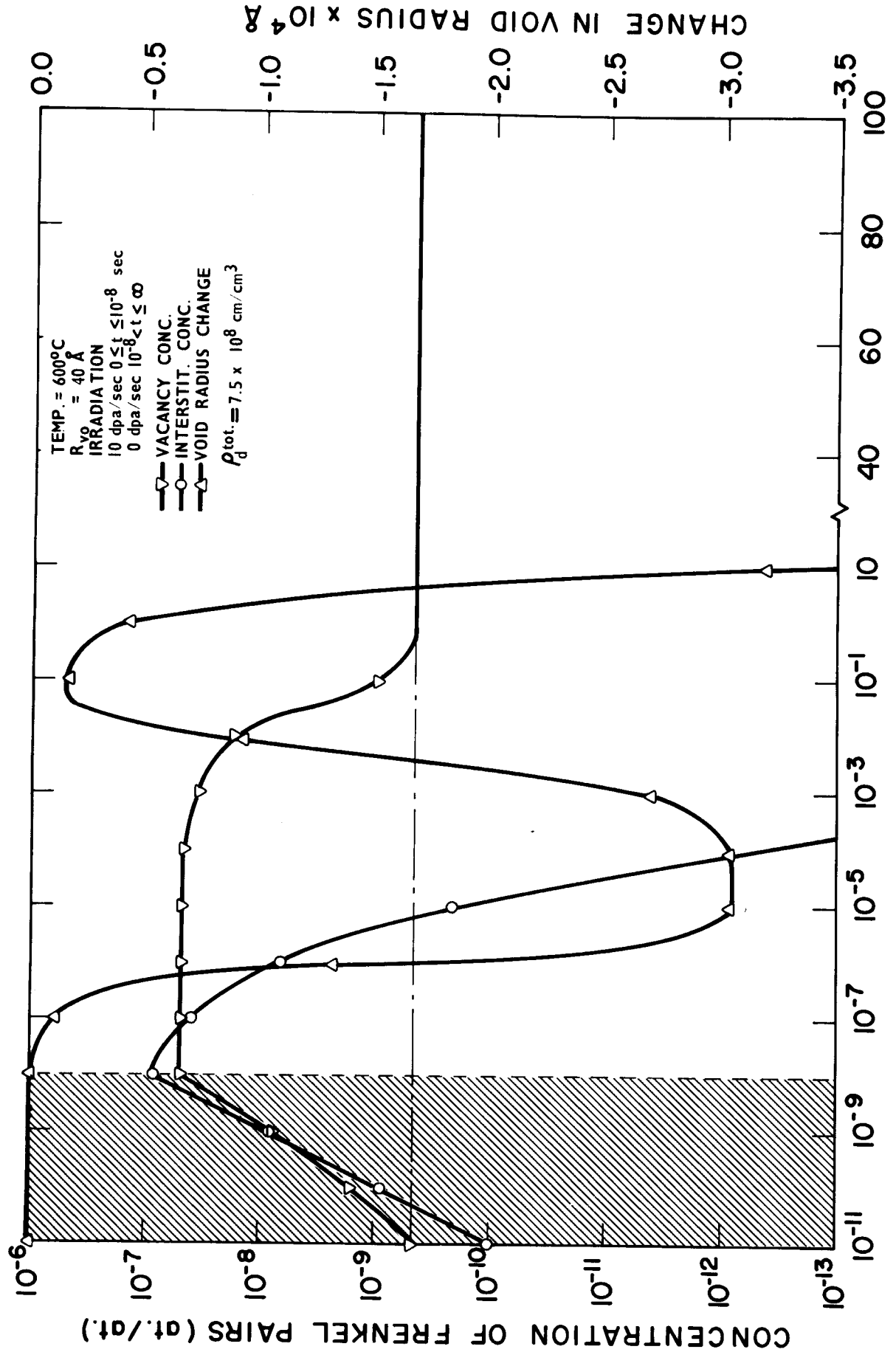

Fig. (3) POINT DEFECT CONCENTRATION AND CHANGE IN VOID RADIUS AS A FUNCTION OF TIME DURING AND AFTER AN IRRADIATION PULSE AT 600 °C FOR S.T. 316 S.S.

of 400, 500 and 600°C, respectively. Depending on the pulse repetition rate and temperature, the void may on the average grow or shrink. In fact, for each temperature there exists a critical pulse rate or minimum time between pulses so that no net change occurs of the void radius. This minimum time interval is shown in Fig. 4. It is seen that the annealing rate above a temperature of 550°C is sufficiently large to suggest that no net void growth may take place for a repetition rate of 10 to 20 pulses/sec. However, it is important to consider the high helium generation rate, and the gradual gas build-up in voids. As the gas pressure increases in the void, the annealing rate is decreased. Therefore, the void growth at temperatures above 550°C in stainless steel should be controlled by the gas production rate. This conclusion is in agreement with the swelling data obtained recently from irradiation experiments on type 316 stainless steels in HFIR. As shown in Fig. 5, the excessively large swelling at temperatures above 550°C is in marked contrast to the low swelling below this temperature. This phenomenon of break-away swelling can be induced by either the gas pressure or by tensile hydrostatic loads on the irradiated metal. Due to the high gas generation rate in fusion reactors, it is essential to operate all structural materials at irradiation temperatures below about 0.5 Tm. The same conclusion is derived from ductility considerations discussed below.

VIII-B-2. Comparison of Radiation Damage by Fission and Fusion Neutrons

The displacement damage initially created by the primary recoil atoms from neutrons of different energies can be computed with a reasonable degree of reliability. But even if radiation-induced property changes are correlated with the displacement dose rather than the neutron flux, there remains differences between irradiation with fission and fusion neutrons.

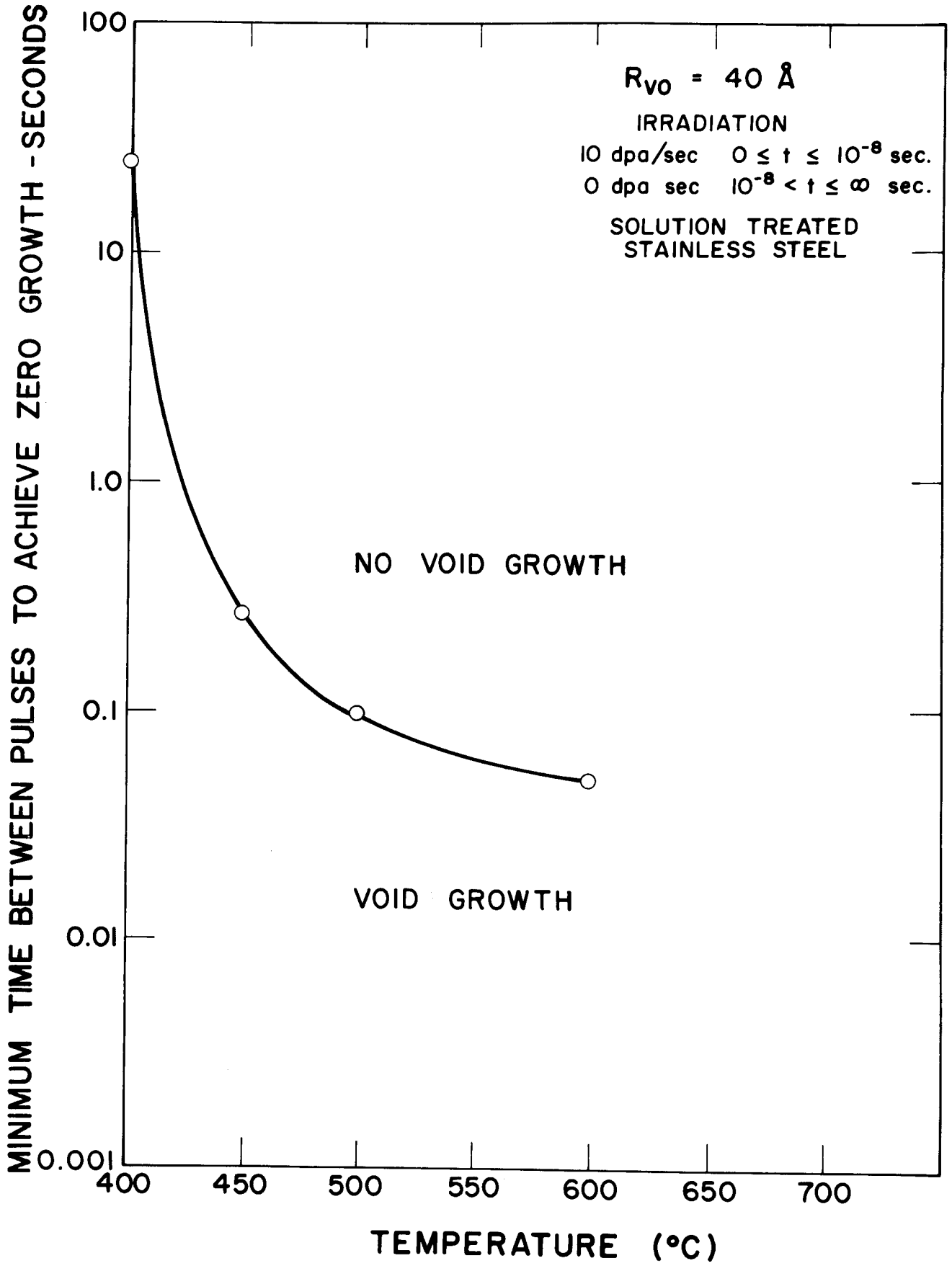
MINIMUM TIME BETWEEN PULSES TO ACHIEVE ZERO GROWTH - SECONDS
100
10
1.0
0.1
0.01
0.001
400
450
500
550
600
650
700
TEMPERATURE (°C)
R_{VO} = 40 Å
IRRADIATION
10 dpa/sec $0 \leq t \leq 10^{-8}$ sec.
0 dpa sec $10^{-8} < t \leq \infty$ sec.
SOLUTION TREATED
STAINLESS STEEL
NO VOID GROWTH
VOID GROWTH

Fig. (4)

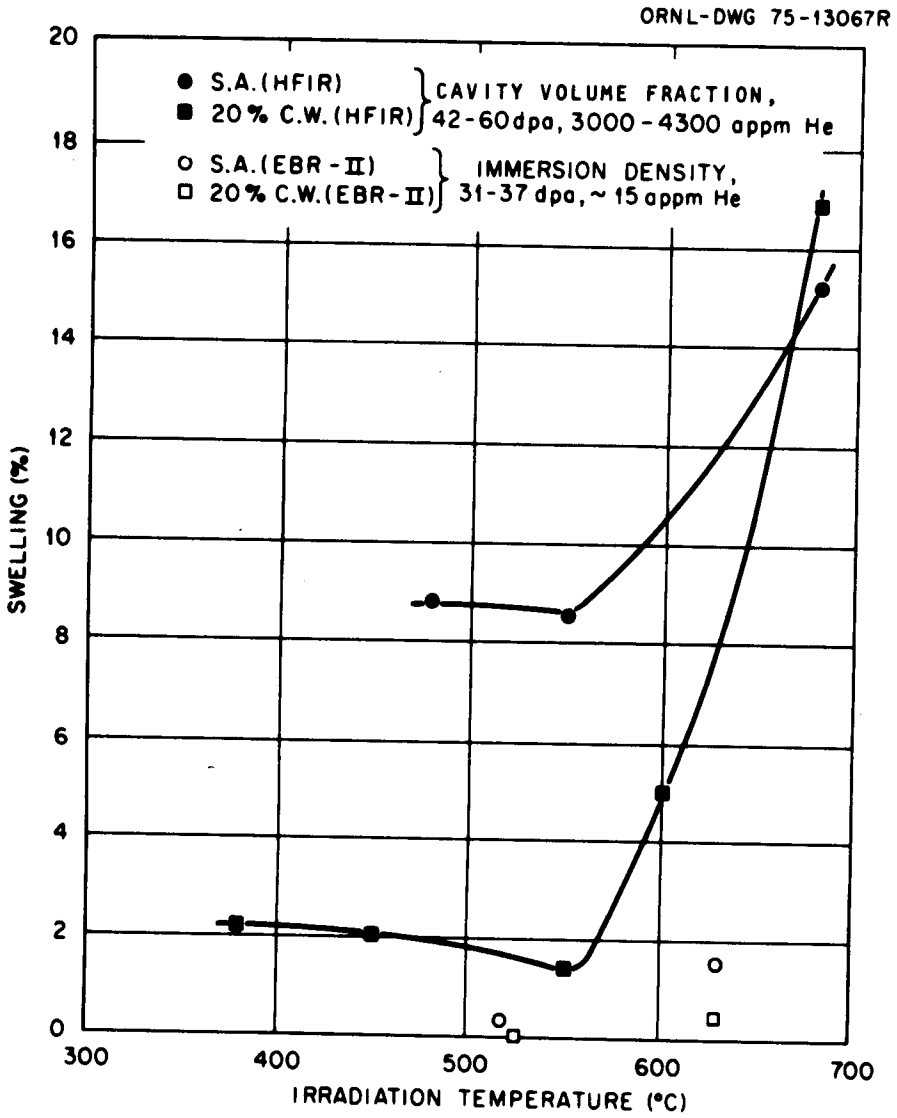

Figure 5

Variation in Swelling as a Function of Temperature for Both 20% Cold Worked and Annealed Type 316 Stainless Steel Samples Irradiated in the HFIR. In addition, points from the same heat of steel irradiated in EBR-II are plotted for reference at low helium content.

The experiments by Brimhall et al.[3] on Mo illustrate this point. When property changes were correlated with displacement dose, the electric resistivity changes agreed for fission neutrons and 14 MeV neutron irradiations. However, the change in the lattice parameter indicated that 14 MeV neutrons were more effective by a factor of 4 to 5 compared to fission neutrons. Since a change in lattice parameter reveals in particular the clustering of interstitials, whereas resistivity changes are insensitive to it, the difference suggests that 14 MeV neutrons produce defect clusters at a smaller equivalent dose. At low temperatures (below the peak swelling temperature) the radiation-hardening by 14 MeV neutrons is expected to take place at a dose level lower by a factor of 4 to 5 when compared with fission neutron results. Irradiation creep, which is related to the loop structure at low temperatures, is also expected to proceed at a faster rate initially.

However, it is not clear at present whether swelling would also commence at a smaller dose just because of the difference in interstitial clustering. Perhaps, more effective in initiating void nucleation is the large He production rate. Again, the HFIR results when compared to EBR-II irradiations on the identical material suggest that He promotes void nucleation and thereby reduces the incubation dose for swelling.

VIII-B-3. Assessment of Low Temperature Swelling

Based on the discussions of Section A-2, the release of vacancies from the cascades is so slow that one should not expect any difference in pulsed or steady-state irradiations for processes which are controlled by the vacancy kinetics. The swelling rate when averaged over many pulses is then expected to be very similar to steady state irradiations. Accordingly, we adopted the viewpoint with regard to swelling at low temperatures ($T < 550°C$), that its rate is independent of the pulsed nature and the gas production rate and determined only by the average point defect production rate, P, and the irradiation temperature,

T. However, the incubation dose for swelling is strongly dependent upon the gas production rate. This viewpoint is suggested also by the extensive observations on the variability in the swelling behavior of type 316 stainless steel. Differences in heat treatment and cold-working, in the reactor environment and even in the irradiation source,mainly affect the incubation dose for swelling. However, the steady-state swelling rate is changed little by these variables. It has also been observed that the microstructure (i.e., in particular the dislocation density) becomes very similar in the steady-state swelling regime although it may have been different initially. The steady-state density of the microstructure is a strong function of the temperature. Based on the observations of Brager and Straalsund,[4] the total sink density (i.e. dislocations, loops, and voids) was assumed to be given by

$$L[cm^{-2}] = \{1.35 \times 10^{-9} \exp(-E_1/kT) + 6.67 \times 10^{-3} \exp(-E_v^m/kT)\}^{-1} \quad (1)$$

where E_1 = 0.3 eV and E_v^m = 1.4 eV is the vacancy migration energy. Fig. 6 shows the total sink density L as a function of temperature.

If N_o is the void concentration and r the average radius, then the swelling rate is given by

$$4\pi N_o r^2 \frac{dr}{dt} = \Omega\left(\frac{1}{4\pi N_o r} + \frac{1}{\rho}\right)^{-1} \{\delta Z \underline{\psi} - D_v(C_v^o - C_v^{eq})\} . \quad (2)$$

Here, ρ is the dislocation density (including loops),

$$L = 4\pi N_o r + \rho, \quad (3)$$

$$C_v^o = C_v^{eq} \exp\{\left(\frac{2\gamma}{r} - p_g\right) \frac{\Omega}{kT}\} \quad (4)$$

is the vacancy concentration in equilibrium with the voids (γ is the surface energy, p_g the gas pressure, Ω the atomic volume), δZ the bias,

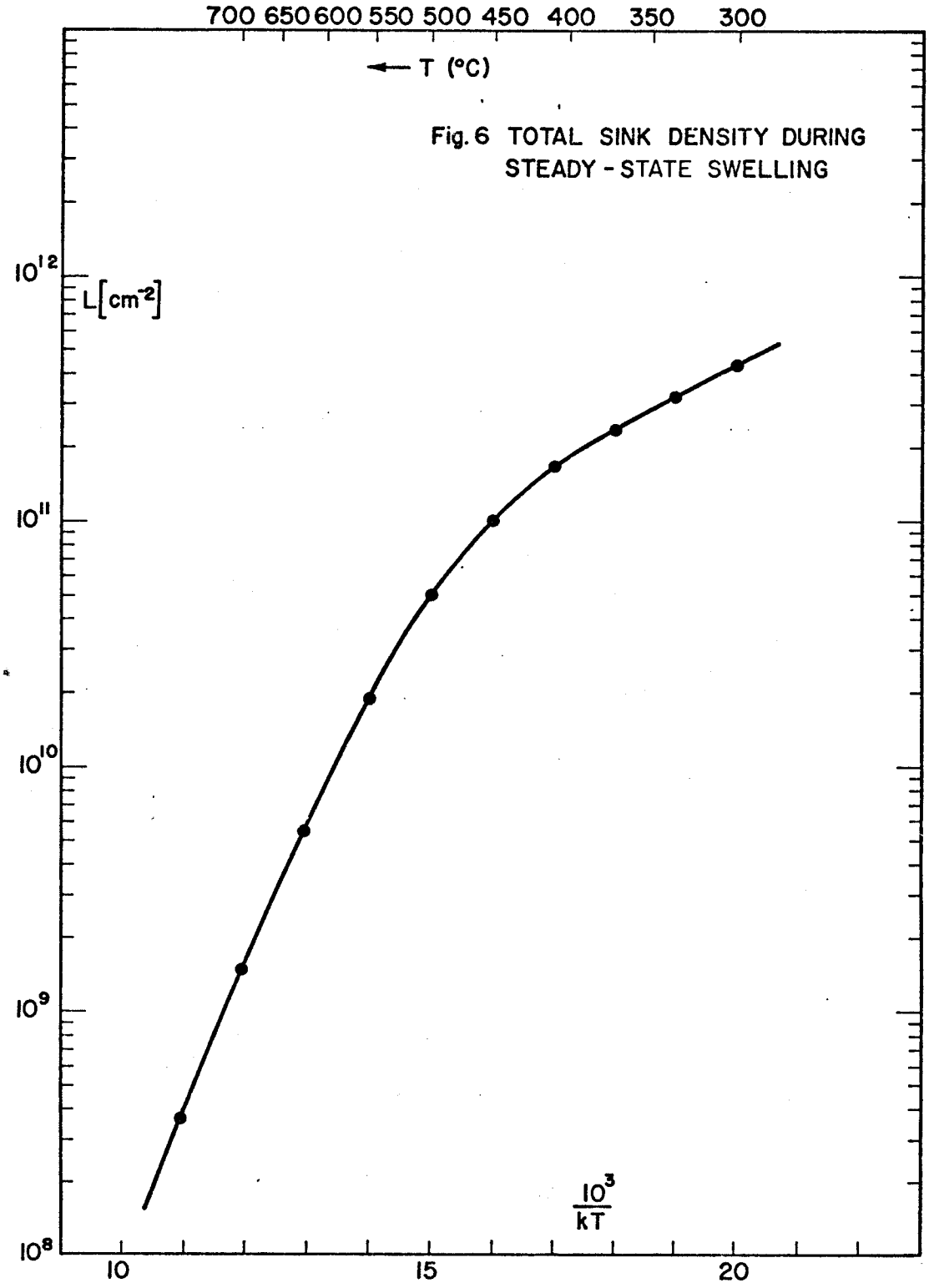

Fig. 6 TOTAL SINK DENSITY DURING STEADY-STATE SWELLING

$$\Psi = \frac{L}{2K}\{[(1 + \frac{K}{L} D_v C_v^{eq})^2 + 4P\frac{K}{L^2}]^{1/2} = (1 + \frac{K}{L} D_v C_v^{eq})\} , \qquad (5)$$

and

$$K = 10^3 \Omega^{-2/3}/D_v. \qquad (6)$$

is the recombination coefficient.

To fix the bias, δZ, and the void density, N_o, we assumed that $4\pi N_o\ r = 10^{10} cm^{-2}$ at T = 500°C when steady-state swelling is reached. The steady state swelling rate of SA 316 in EBR-II at this temperature is about 1% per $\phi t = 10^{22} n/cm^2/sec$. The point defect production rate was estimated to be $P = 10^{16}$ Frenkel pairs/cm^3/sec or 5.6×10^{-7} dpa/sec. At this temperature we may neglect the annealing term in Eq. (2). Then δZ was determined to be 0.033 or 3.3%.

Next, we assumed that $4\pi N_o\ r$ remained the same for steady state swelling at all temperatures and computed the swelling rate for T below 500°C.

The results are given in the second column of Table 3, and the rates are in good agreement with the observed rates for CW 316 stainless steels irradiated in EBR-II. In fact, the selection of the temperature dependence of L was made so as to achieve this agreement over the temperature range from about 370°C up to 550°C, where sufficient data are available. This particular fitting of a swelling rate model to the data was adopted in order to predict swelling at temperatures below 370°C. It was felt that the uncritical use of the swelling correlation used for fast reactors was inappropriate here, since the incubation dose for swelling in EBR-II is rather large, i.e. around 40 dpa. However, the irradiation results from HFIR give substantial swelling already at 40 to 50 dpa. Indeed, in order to predict the swelling of 20% CW 316 at T = 380°C as observed in HFIR based on the rates listed in the second column of Table 3, a zero incubation dose must be assumed. However, the irradiation

Table 3

Swelling Rates in %/dpa

	In EBR-II		In Solase	
T (°C)	nominal	maximum	nominal	maximum
250	0.003	0.016	0.0017	0.0095
300	0.010	0.035	0.0063	0.0205
350	0.027	0.066	0.0182	0.0392
400	0.059	0.113	0.0424	0.0666
450	0.109	0.167	0.0844	0.0994
500	0.195	0.212	0.1248	0.1576

Table 4

Swelling in %/yr in Solase

T (°C)	nominal	maximum
250	0.086	0.484
300	0.323	1.040
350	0.925	1.994
400	2.156	3.389
450	4.297	5.061
500	6.352	8.024

results at 450°C in HFIR indicate that an incubation dose of 40 dpa is needed just as in EBR-II. It should be noted that this is coincidental since the particular materials used in HFIR irradiations has a much larger incubation dose if irradiated in EBR-II.

A rather pessimistic estimate of the swelling rate at low temperatures can be made by assuming that the void sink density, $4\pi N_o r$, is always equal to the dislocation density ρ. It is easy to show that Eq. 2 gives the maximum swelling rate, i.e.

$$\dot{S} \leq \frac{\Omega L}{4} \delta Z \psi$$

Although this condition may prevail at the temperature for peak swelling (~500°C), it is usually not observed at lower temperatures for 316 stainless steel. Nevertheless, using this assumption and Eq. (1) for L, swelling rates as listed in the third column of Table 3 were computed.

In the forth and fifth column are listed the estimated nominal and maximum swelling rate for the midplane of the first wall in SOLASE. Note, that the EBR-II damage rate is 5.6×10^{-7} dpa/sec, whereas the dose rate here is 1.64×10^{-6} dpa/sec; therefore, the recombination is higher for a larger dose rate and the swelling rate per dpa correspondingly lower.

The swelling in % per year for the midplane of the first wall is given in Table 4 computed from the swelling rates. It was assumed that no incubation period exists and that swelling is linear with dose. For a first-wall temperature of 300°C, the nominal swelling is expected to be around 10% for a plant-life of 30 years. The maximum swelling could be expected to reach 30%. Since the maximum wall loading is 7.65 MW/m^2, this would correspond to a material lifetime of about 230 MW-yr/m^2, an obviously very large value. Note however that earlier estimates made at Wisconsin and elsewhere of wall lifetimes of 2-6 MW-yr/m^2 were for operating temperatures of 500°C and above. The results shown in Table 4 are consistent with these earlier measurements and show the strong motivation to operate components in high fluxes at low temperatures.

VIII-B-4. Swelling Due to Helium in Solution

The large amounts of helium atoms produced by the fusion neutrons raises the possibility that helium alone could lead to large volume changes even if it were not contained in gas bubbles, but instead be incorporated in the crystalline lattice. The distortion of the lattice around the helium atoms changes the lattice parameter and hence the volume of the crystal.

To evaluate this, we used the recent calculations by Johnson et al.[5] on the relaxation volume of helium atoms in bcc metals. Their results are summarized in Table 5.

Table 5

Volume Changes for He Atoms in bcc Metals in Units of the Atomic Volume of the Host Metal

Metal	V	Fe	Mo	Ta	W
Substitutional	0.88	1.21	0.93	0.74	0.85
Interstitial	0.39	0.93	0.46	0.44	0.56

The helium production in the first wall is equal to 7.82×10^{-4} He atoms/year/host atom. Assuming that all He atoms are in substitutional positions and that each occupies the volume of 1.21 host atoms, the volumetric expansion rate is

$$\frac{d}{dt}(\Delta V/V)_{SHe} = 9.46 \times 10^{-4}/\text{year}$$

For a 30 year operation time with a plant availability of 75%, we obtain

$$(\Delta V/V)_{SHe} = 2.13\%$$

It should be noted that although a helium concentration of 1.76% is large, it is still an order of magnitude lower than the critical concentration at which blistering takes place in He-ion bombardments of metals. There, a critical He fluence of 10^{18} He/cm^2 is needed before blistering or gas-release is observed. For an ion energy of 300 keV, the penetration depth is about 10^{-4}cm.

Hence, the critical concentration of He in the bombarded layer is of the order of 10^{22} He atoms/cm^3 or about one helium atom for every ten target atoms. As a result, it appears that even over 30 years at 7.65 MW/m^2, the swelling due to He buildup for steel operating at 300°C will be about 2% and less than that due to displacement damage. Thus, the results on extended wall life remain strikingly positive. Clearly, more experimental work on low temperature irradiation is needed to confirm this analysis.

VIII-C. Ductility and Fracture Toughness

VIII-C-1. General Considerations

The secondary defects such as dislocation loops produced during irradiation damage change the mechanical properties. In annealed materials, the yield strength is increased whereas in cold-worked materials the yield strength may drop somewhat. This trend suggests that after a sufficiently large dose, the yield strength becomes independent of the initial dislocation structure.

Materials with high yield strength fracture usually at small strains, and the benefit rendered by the high strength may be cancelled by the possibility of failure with very small or zero plastic strain. In order to avoid brittle fracture, a small residual ductility is necessary so that elastic stress concentrations at the tips of small cracks can be relieved by local plastic deformation. In this regard, the first 1/2% yielding is considered the most useful, and yielding of 1.3% relieves, in most cases, the stress concentrations at the tip of cracks.

Failure without yielding (i.e. plastic deformation) can occur if one of the following conditions exists:

(a) The yield stress, σ_y, is greater than the decohesion stress, σ_f^*, where σ_f^* is the lower of the fracture stresses for separation of bonds within the grain or bonds across grain boundaries, respectively.

(b) The yield stress, σ_y, is greater or equal to the ultimate stress, σ_u, of the material.

Case (a) explains the brittle fracture of bcc metals below a certain transition temperature where the flow stress for dislocation motion exceeds the decohesion stress within the grain. The transition temperatures increases with increasing

radiation hardening, and hence, the applicability of bcc materials for the first wall at temperatures below the swelling range is in question. However, there may exist a narrow window between the transition temperature and the temperature for the onset of swelling which depends on the material and the dose.

In principle, the flow stress for dislocation motion in fcc materials is always smaller than the decohesion stress within the grain. Therefore, fcc materials are intrinsicly ductile. Nevertheless, they may still fail by the mechanism (a) if the flow stress exceeds the grain boundary strength. Such a situation occurs in stainless steels if hydrogen or helium accumulates along grain boundaries and forms small gas bubbles.

Under stress and for small deformation rates, the grain boundary bubbles grow and coalesce, and failure takes place by intergranular fracture. Bubble growth requires self-diffusion, and hence, this failure mechanism becomes important in stainless steels at and above a temperature of 550°C. The complete loss of ductility due to this mechanism is well illustrated by the results of HFIR irradiations[6] on solution annealed and cold-worked stainless steel as shown in Fig. 7.

At low temperatures where grain boundary bubbles do not grow, loss of ductility in fcc metals is due to mechanism (b). For this case, the material exhibits a plastic instability. Although plastic deformation takes place, it is highly localized so that the measurable macroscopic fracture strain is again small. However, it is important to emphasize the fact that the local strains in the plastic instability regions are very large and the failure along the plastic zones is then a ductile mode, in contrast to the complete brittle failure without any local plastic deformation in bcc metals below the transition

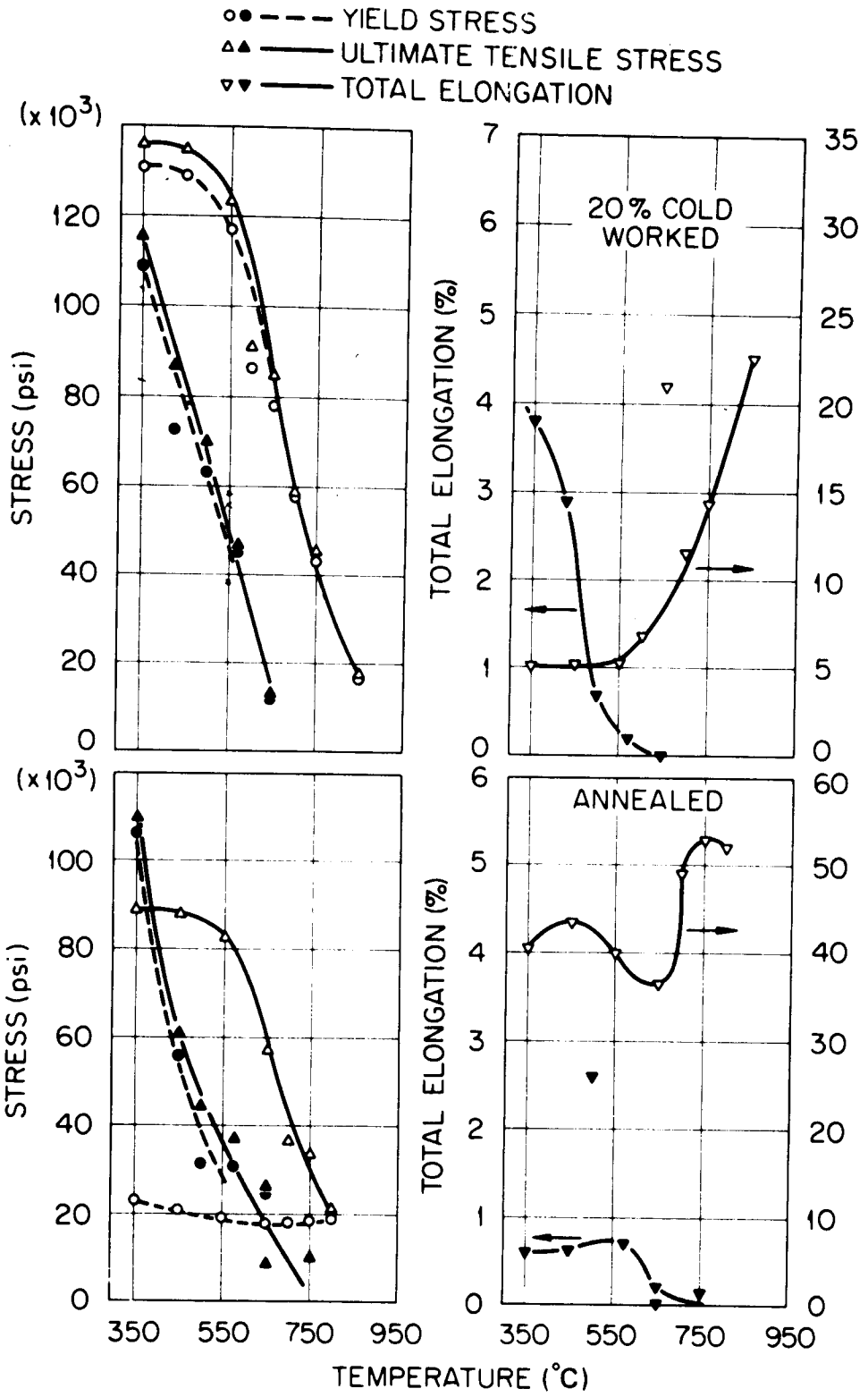

Figure 7 Tensile properties of 20% cold-worked (upper figures) and annealed (lower figures) Type 316 stainless steel. Open symbols are for unirradiated material and filled symbols are for HFIR-irradiated samples (5.6 to 8.7 X 10^{26} n/m^2). Samples were irradiated near the test temperature to 40 to 60 dpa and 3000 to 4300 appm helium.

temperature. Consequently, fracture by plastic instability does not necessarily imply low fracture toughness or excessive notch sensitivity.

VIII-C-2. Ductility of Irradiated Stainless Steels

The results of Fig. 7 for the tensile properties and for the total elongation of cold worked and solution annealed 316 stainless steel indicate that the uniform elongation in both cases is sufficient for temperatures below 550°C and for doses of about 50 dpa. This corresponds to the dose accumulated in the first wall on the reactor midplane during one year. The concentration of He in the HFIR irradiated samples corresponds to about 4 years in SOLASE at the reactor midplane location. An extrapolation of these data to 30 times greater fluences or about 8 times greater He concentrations in very difficult. However, the present experience with the microstructural changes in stainless steels indicate that it stabilizes eventually and little changes are expected to occur at doses above 50 dpa. The increase in He concentration, may, however, still increase the yield strength somewhat, and thereby reduce the small difference already observed between yield and ultimate strength to practically zero. Therefore, the macroscopic fracture strain may further be reduced, and fracture and fracture toughness is likely to be controlled by the degree to which plastic flow is localized.

VIII-C-3. Fracture Toughness Considerations

The microscopic observations of the fracture surface of stainless steels irradiated and tested at low temperatures indicates that plastic deformation is restricted to narrow channels following certain crystallographic directions. The fracture follows these deformation channels. With this fracture mode, the fracture toughness is very sensitive to the channel width.

In order to estimate the critical fracture toughness parameter, K_{Ic}, a model by Malkin and Tetelman[7] was used. In this model, the critical fracture toughness for plane strain bending is given by

$$K_{Ic} = 2.89\ \sigma_y\{\exp[\frac{\sigma_f^*}{\sigma_y} - 1] - 1\}^{1/2}\sqrt{\rho_o}\ [\text{psi}\sqrt{\text{inch}}] \qquad (7)$$

where ρ_o is the minimum notch radius. The formula is based on the concept that the stress concentration factor is determined by the size of the plastic region at the crack tip and by the stress σ_f^* to cause rupture in this plastic zone.

The decohesion stress, σ_f^*, is approximately independent of the microstructure. Hence, it can be evaluated for unirradiated material by measuring K_{Ic} and the yield stress σ_y.

In a dynamic tear test, the energy absorbed per unit fracture surface for type 304 stainless steel in the annealed condition was found to be

$$G_{Ic}^{\circ} = 2.2 \times 10^4 \text{ in. lb./in.}^2$$

The fracture toughness parameter in plane strain is then given by

$$K_{Ic}^{\circ} = [\frac{E\ G_{Ic}^{\circ}}{(1-\nu^2)}]^{1/2} = 7.2 \times 10^5 \text{ psi } \sqrt{\text{in}}\ .$$

where the elastic modulus is $E = 21 \times 10^6$ psi and the Poisson's ratio is $\nu = 0.3$.

Using an unirradiated yield stress of $\sigma_y^{\circ} = 20$ ksi, and a minimum notch radius of $\rho_o = 0.002$ typical for most annealed material we find from Eq. (7) that

$$\sigma_f^* \cong 235 \text{ ksi}$$

We assumed that the decohesion stress is the same for 316 stainless steel and not dependent on the microstructure. Hence, we can use it also for irradiated

materials. Yield strength values were taken from Fig. 7 and extrapolated to lower temperatures. They are listed in Table 6 together with values for K_{Ic} for the minimum notch radius of ρ_o = 1000 Å. The latter value is of the order of the width of the plastic channels observed in fractured specimens.

Table 6

Estimates of the Critical Fracture Toughness Parameter

T (°C)	σ_y (ksi)	$K_{Ic}/\sqrt{\rho_o}$ (ksi)	K_{Ic} (ksi$\sqrt{in}$)
250	120	440	0.872
300	115	451	0.894
350	110	462	0.917
400	90	521	1.033
450	62	700	1.390

Let us assume that a longitudinal crack is inside one of the cylindrical channels of the first wall. The depth of the crack is equal to a. The stress-intensity K_I is related to the fluid pressure p and the inner radius r_1 and the outer radius r_2 by

$$K_I = p\sqrt{\pi a}\left[1.12\,\frac{r_1^2 + r_2^2}{r_2^2 - r_1^2} + 1.13\right] .$$

With r_1 = 0.9 cm and r_2 = 1.0 cm,

$$K_I = 11.8\ p\sqrt{\pi a} = 20.9\ p\sqrt{a} \quad .$$

To prevent failure of the tubes, $K_I \leq K_{Ic}$ or

$$\sqrt{\frac{a}{\rho_o}} \leq \frac{K_{Ic}}{\sqrt{\rho_o}}\,\frac{1}{20.9p[\text{ksi}]}$$

This requires that $\sqrt{a/\rho_o} \leq 21.6$ at 300°C and for a fluid pressure of 1 ksi. Hence, the crack penetration, a, must satisfy the criterion

$$a \leq 466\ \rho_o \quad .$$

If the plastic channel width is indeed as small at 1000 Å, then the surface cracks inside the tube must not exceed a depth of 4.6×10^{-3}cm or 46 microns.

It appears from this analysis that it is of great importance to investigate the fracture mechanism of irradiated material at higher doses and helium concentrations.

It should be noted, however, that stress relaxation will take place during irradiation due to irradiation creep, and that this deformation process is not localized but extends throughout the material.

This deformation mechanism has the effect of enlarging ρ_o and improving fracture toughness. Nevertheless, the first wall material will have a low fracture toughness when loaded while the reactor is not producing power.

Note Added in Proof:

The assumption that plastic relaxation of stresses at a crack tip occurs by the formation of only one plastic channel is not borne out by the experimental findings.

An accidental fracture of an irradiated duct was produced[9] by handling in a hot cell. Subsequent investigations of the material in the vicinity of the fracture surface revealed that many plastic channels criss-crossed the grains, and plastic channels were found up to 3/16 of an inch from the fracture surface. Hence, the conclusion can be drawn that the localization of plastic flow at the crack tip is at least as large as the grain size, i.e., ρ_o is as large as in unirradiated material. Therefore, if ρ_o is taken

to be 0.002 inch, then the predicted fracture toughness is as given in Table 6a.

Table 6a

T(°C)	σ_y(ksi)	K_{Ic}(ksi$\sqrt{in}$)
250	120	19.7
300	115	20.2
350	110	20.7
400	90	23.3
450	62	31.3

The critical crack depth in the coolant tubes at a temperature of 300°C is now

$$a = 466\ \rho_0 = 0.932 \text{ inch},$$

i.e., greater than the wall thickness of the tubes.

We can conclude from this more realistic estimate that the fracture toughness is still sufficiently large to prevent failure of the coolant tubes. In this case, the lifetime of the coolant tubes is probably limited by stress corrosion.

Nevertheless, it must be emphasized that the application of Tetelman's model to highly irradiated materials is perhaps questionable, and the discussion here clearly demonstrates the need for measurements on fracture toughness and for a better understanding of the fracture mechanism in irradiated materials. It should also be noted that the channel deformation is not unique for stainless steels, since radiation hardening is expected in most structural materials.

VIII-D. Irradiation Creep

Irradiation creep at temperatures below 550°C is the predominant creep mechanism. In contrast to swelling, it takes place at all temperatures. Nevertheless, it has been recognized recently that it is not independent of temperature, and that it is influenced by the dislocation structure produced during irradiation.

The empirical equation developed by Gilbert and Bates[8] on 20% CW type 316 stainless steel incorporates these effects, and it is given by

$$\varepsilon_\theta/\sigma_\theta = 10^{-8}\, B(P - 1.3\, B \tanh \frac{P}{2B}), \tag{8}$$

where

$$B = 0.6 + 2.7 \times 10^{6} \exp\{-12{,}000/T\}, \tag{9}$$

T is the absolute temperature, P the displacements per atom, σ_θ the hoop stress in psi, and ε_θ is the hoop strain.

Eq. (1) was used to compute the diametral expansion of the coolant tubes assuming that each tube can be considered isolated so that interactions with neighboring tubes can be neglected. The diametral expansions, ε_θ, on the reactor midplane are listed in Table 7. The hoop stress taken was σ_θ = 10 ksi.

Table 7

Diametral Expansion of Coolant Tubes Due to Irradiation Creep

T(°C)	$\frac{\varepsilon_\theta}{\sigma_\theta}[yr^{-1}\ psi^{-1}]\times 10^{7}$	ε_θ for 10 yrs. (%)	ε_θ for 30 yrs. (%)
250	3.01	3.05	9.16
300	3.02	3.06	9.17
350	3.06	3.10	9.31
400	3.22	3.27	9.82
450	3.74	3.81	11.45
500	5.17	5.29	15.90
550	8.48	8.83	26.60

It is seen from these results that irradiation creep at a temperature of 550°C would be almost a factor of 3 larger than irradiation creep at 300°C. For 30 years of operation, the diametral expansion of the coolant tubes due to irradiation creep would be about 10% at 300°C. Together with the swelling estimate the nominal diametral expansion of the first wall is about 20% on the midplane. These distortions of the first wall decrease with the distance from the midplane. At the location where the cylindrical part of the first wall joins the hemispherical part the dose is smaller by a factor of 2, and hence the total expansion is reduced to about 10%.

A detailed analysis of the deformation and stress due to the differential swelling and irradiation creep will be performed in the near future.

References for Section VIII

1. N. M. Ghoniem and G. L. Kulcinski, "Fully Dynamic Rate Theory (FDRT) Simulation of Radiation Induced Swelling in Metals," UWFDM-180, University of Wisconsin, October 1976.

2. R. Bullough, B. L. Eyre and R. Krishan, Proc. Roy. Soc. London, A346, 81 (1975).

3. J. L. Brimhall, L. A. Charlot and H. E. Kissinger, Rad. Effects 28, 115 (1976).

4. H. R. Brager and J. L. Straalsund, J. Nucl. Mat. 46 , 136 (1973).

5. R. A. Johnson, C. L. Bisson and W. D. Wilson, Rad. Effects 25, 155 (1975).

6. E. E. Bloom, F. W. Wiffen, P. J. Maziasz, and J. O. Stiegler, Nucl. Tech. 31, 115 (1976).

7. J. Malkin and A. S. Tetelman, Engineering Fracture Mechanics 3, 151 (1971).

8. E. R. Gilbert and J. F. Bates, Trans. ANS 22, 183 (1975).

9. J. E. Flinn et al., "Evaluation of Ex-Reactor Loading Event on High-Fluence EBR-II Control-Rod Thimble 5E3", ANL/EBR-068, February 1973.

IX. The Tritium Cycle in ICTRS

IX-A. Introduction

This section deals with the pathways of tritium (Figure 1) in the entire plant, tritium breeding, extraction, recycle and loss to the environment. This study differs from preceeding UWMAK designs (1,2) in that Li_2O particles (60%, Li_2O, 40% He) carried in a helium gas stream (3,4) constitute the breeding blanket as well as the heat transport agent for steam generation.

IX-B. The Deuterium-Tritium Fuel Cycle

The exact construction of the D-T pellet and its method of insertion into the reactor with the required accuracy and frequency is unknown at this time. The data in Table I on the deuterium and tritium mass requirements for fueling this plant are based on an energy yield/pellet of 100×10^6 joules and an energy yield/fusion event of 2.93×10^{-12} joules (18.3 mev). The number of fusion events/pellet is then 7.6×10^{19} and since the D and T are consumed one for one, this is also the number of D and T atoms consumed per shot. The masses of fuel atoms consumed and recycled per day are based on a rep rate of 30/sec and a fusion efficiency of 6%. These calculations do not take into account misfirings which would add to the recycle burden and the total mass of D and T fabricated as pellets/day.

Table I

Deuterium-Tritium Fuel Requirements

	D	T
Moles consumed/day	145	145
kg consumed/day	0.290	0.435
kg recycled/day	4.83	7.25
kg fabricated/day	5.12	7.685

The exhaust from the reactor will first have to be scrubbed free of non-hydrogenic impurities. (Details of the pumping may be found in Sec. V-E). The impurities will consist of the non-hydrogen components of the pellets, ablated material from the carbon liner and side walls, helium generated in the reaction and protium generated in nuclear reactions. We have no estimate of these impurities. We would expect condensable gasses to be trapped at low temperature and particles larger than 5 microns to be trapped on filters. The helium and hydrogen isotopes can be separated from any volatile impurities by passing through a silver-palladium diffuser. The hydrogen isotopes can then be collected in cryoabsorption pumps and the non-condensable helium vented. As in previous systems (1) the pumps will work in tandem and in four hour cycles. During a four hour cycle about 0.8 kg of D and 1.21 kg of T will accumulate. As one set of pumps is regenerated, the gasses will go directly to the pellet-making system or to a hydrogen isotope fractionator.

If the pellet initially contains D and T in a 1:1 mole ratio, then the exhaust gases will also contain D and T in a 1:1 mole ratio and no isotope fractionation will be necessary for this part of the cycle unless the amount of protium produced is at an unacceptable level. The 0.435 kg of tritium consumed each day will be bred in the reactor and, after recovery and isotope separation, will be merged with the recycle fuel stream. The 0.290 kg of deuterium consumed each day will be obtained from an external supplier.

IX-C. Tritium Breeding and Extraction

IX-C-1. Li_2O Inventory

The amounts of lithium oxide present on a steady state basis in the reactor, steam generators, reheater and the rest of the lithium oxide handling equipment are given in Table II. The means of transporting the lithium oxide through piping has not been established.

IX-C-2. Tritium Breeding

From preceeding calculations we know that we must breed and extract a minimum of 435 g of tritium each day. It has been shown that with Li_2O containing natural lithium, a breeding ratio of 1.25 is attainable for this kind of a blanket. On this basis we would produce 0.544 kg T/day in the blanket which is in excess of that consumed but we will base our calculations on this latter quantity. The balance between tritium production, consumption and losses can be adjusted at a later date.

Table II

Li_2O and Tritium Parameters

Li_2O Inventory

Item	kg
Reheater (15 B & W size, 34.2 mwt each)	38,632
Steam Generator (188.84 mwt each)	234,904
Reactor (60% density 271 m^3)	325,000
Tritium Extractor, Li_2O conveyor, piping, etc.	401,464
	1,000,000

Blanket Parameters

Li_2O flow rate (98% stream) Channel 1	3.34×10^7 kg/hr
Li_2O flow rate (2% stream) Channel 2	6.85×10^5 kg/hr
Li_2O temperature-entrance	450°C
Li_2O temperature-exit-Channel 1	550°C
Li_2O temperature-exit-Channel 2	850°C
Breeding ratio (combined channels)	1.25
Average tritium production	0.544 kg T/day
	6.3×10^{-3} gmsT/sec
	6.8×10^{-7} gmsT/kg Li_2O

The breeding process results in the loss of one lithium for each tritium bred. This can be expressed by the following equation

$$Li O_3^6 Li + {}_0^1 n \rightarrow Li O_1^3 T + {}_2^4 He$$

It is assumed that the tritium to be bred is present in the Li_2O as LiOT and thus the design of the tritium recovery process must be based on the separation of low concentrations of LiOT from a large mass of Li_2O.

IX-C-3. Tritium Separation Processes

A likely separation process is based on the dehydration reaction for LiOT

$$2LiOT_{(soln)} \rightarrow Li_2O_{(s)} + T_2O_{(g)}$$

Thermodynamic data are available for the equivalent hydrogen system although in the temperature range 400-800°C there are large discrepancies in the values reported by different authors. We have taken data from the JANAF tables[5] for the purposes of the calculations which follow. We also make the assumption that the LiOT will be present in Li_2O as an ideal solid solution rather than as a pure phase and therefore the tritium species vapor pressures will be dependent upon the mole fraction of the tritium present and the temperature of the lithium oxide.

IX-C-3-i. Plan 1

Let us first examine the condition in which the tritium species in the solid and gas phase are in constant equilibrium and the vapor phase concentration is not dependent on the rate of diffusion of the tritium species through the solid phase to the surface of the lithium oxide particle. Several alternate schemes suggest themselves based on these assumptions.

In principle, we could devise a system in which the tritium generated during the transit time of the lithium oxide through the reactor was completely removed so that non-tritium bearing Li_2O could be transported around the energy loop.

A simple calculation based on the quantities given in Table II shows that the average tritium production would be 6.8×10^{-7} gmsT/kg Li_2O or a mole fraction of LiOT equivalent to 6.8×10^{-9}. At this concentration the T_2O vapor pressure would be very small at any reasonable temperature. It is not a promising extraction procedure.

A more reasonable approach would be to allow the total tritium inventory to grow to a significant concentration before entering the extraction system. The equilibrium vapor pressures of tritium species above anhydrous lithium oxide have been calculated using JANAF data[5] for the corresponding protium species for 1 ppm and 10 ppm tritium over the temperature range 500 to 1700°K. These data are plotted in Figure 2. A 1 ppm level (1×10^{-5} mole fraction LiOT) would be attained in about 2 days after which a small side stream (2%) could be diverted to separate the gas phase containing tritium mainly as T_2O. A straightforward calculation using the data in Table II and Figure 2 quickly shows that the total gas volume and equilibrium T_2O vapor pressure are such at any reasonable temperature, that the total amount of tritium in the gas phase will be only a small fraction of the tritium daily requirement. Even though the vapor pressure of T_2O in the case of the 10 kg T inventory is 10^2 larger than in the 1 kg T case at the same temperature, we cannot simply recover sufficient tritium from the gas phase alone to cover our daily requirements.

The above schemes are based on anhydrous lithium oxide. In fact, it is very difficult to completely dehydrate lithium oxide so some water will be present. This suggests that it may be advantageous to maintain a certain mole fraction of water in the lithium oxide and use the vapor phase H_2O as a carrier for the tritium species. The vapor pressure data in Figure 3 are calculated on the assumption that a water content of 0.1% by weight is maintained in the solid phase and that LiOH and Li_2O form ideal solid solutions. Under these circumstances

the concentration of the HTO, H_2O, T_2O species will be proportional to the mole fraction of each component in the solid phase and the temperature of the lithium oxide. It is clear from Figure 3 that HTO will now be the most important tritium species in the gas phase, with a vapor pressure at 850°C (1123°K) of 9×10^{-5} torr (1.2×10^{-7} atmospheres.) However, at a flow rate of only 0.685×10^9 gms Li_2O at 60% density (40% He), the total gaseous volume available per hour is only 2.3×10^5 l/hr. The moles of HTO available in the gas phase/day is calculated to be only 0.072, a tiny fraction of the required amount. Even at a 10 Kg T inventory the gas phase inventory is only 0.72 moles HTO/day.

It is clear from this analysis that there is no way to extract the tritium from the solid phase Li_2O without considering diffusion of the tritium species in the solid phase and the residence time in the extractor. The presence of a small quantity of H_2O as a carrier still has its advantages and will be retained. For the purpose of the analysis which follows it will be assumed that equilibrium has been established between the tritium species in the gas phase and solid phases, but upon entering the reactor the tritium species in the gas phase is instantaneously condensed on a cold surface. The tritium concentration on the surface of the lithium oxide is zero and remains zero during the transit time so that all the tritium which diffuses to the surface of the solid phase is instantaneously transported and condensed out on a cold surface of the extractor.

IX-C-3-ii. Plan 2

The lithium oxide in the laser fusion reactor is in the form of a suspension of spherical Li_2O particles of radius 100 microns (10^{-2} cm) in helium gas. The suspension consists of 60% Li_2O and 40% He gas by volume. The volume of each Li_2O particle is 4.19×10^{-6} cm^3 and the weight of each Li_2O particle is

8.42×10^{-6} g based on a density of 2.01 g/cc. Since the total inventory of Li_2O in the reactor is estimated to be 10^9 g, the total number of Li_2O particles in the system is 1.19×10^{14} particles. Assuming a 1 kg T inventory (1 ppm T), the grams of T present in each Li_2O particle is 8.42×10^{-12} g. Then the number of atoms of T present in each Li_2O particle is

$$8.42 \times 10^{-12} \frac{\text{g T}}{\text{Li}_2\text{O particle}} \times \frac{1 \text{ mole T}}{3 \text{ g T}} \times \frac{6.023 \times 10^{23} \text{atoms T}}{1 \text{ mole T}} = 1.69 \times 10^{12} \text{ atoms}$$

If 0.544 kg of T is produced per day, it will be necessary to extract 0.544 kg of T per day to maintain a 1 kg T inventory. This is equivalent to extracting 6.30×10^{-3} g of T per second. So the number of atoms that need to be extracted from the system per second is

$$6.30 \times 10^{-3} \frac{\text{g T}}{\text{sec}} \times \frac{1 \text{ mole T}}{3 \text{ g T}} \times \frac{6.023 \times 10^{23} \text{ atoms T}}{1 \text{ mole T}} = 1.26 \times 10^{21} \text{ atoms}$$

To extract the T, a fraction of the stream is diverted through a tritium recovery system. In the tritium recovery system the Li_2O particles are heated and the T species diffuses out of the particles. It should be pointed out that the effective diffusion path length is not necessarily the macroscopic particle radius. Rather, the nature of the pore path in the solid may be the determining factor. Since Li_2O is prepared by the thermal decomposition of the peroxide, carbonate, or hydroxide with the evolution of a gas, it is expected to be quite

porous, so that diffusion path lengths of ~ 0.1 μ should be attainable. The diffusivity of the T in Li_2O is assumed to follow the data for T_2O in BeO. At 850°C, the diffusivity of T_2O through BeO is extrapolated to be 1×10^{-17} $\frac{cm^2}{sec}$. (Figure 4) Then if a 300 second residence time for the Li_2O particles in the tritium recovery system is assumed, the percent of the stream that must be diverted to the tritium recovery system may be calculated using the non-steady state solution to Fick's Law of diffusion. It can be solved, given the following boundary conditions:

1. The concentration at t = 0, C_o, is uniform throughout the sphere.
2. The concentration at the surface is zero.

The approximate solution is

$$-\ln C/C_o = \frac{\pi^2 Dt}{r^2}$$

where C = concentration of T at time t

D = diffusivity in $\frac{cm^2}{sec} = 1 \times 10^{-17}$ $\frac{cm^2}{sec}$

t = residence time = 300 sec

r = radius of sphere or effective diffusion path length (cm) = 0.1 μ (10^{-5} cm)

Solving the above equation yields $C/C_o = 0.9997$. Therefore the fraction of T that diffuses out of each Li_2O particle is 3×10^{-4} of the total T present in each particle. The number of atoms of T that diffuse to the surface of each Li_2O particle and are subsequently recovered during the 300 seconds the Li_2O is in the extractor is $3 \times 10^{-4} \times 1.69 \times 10^{12}$ $\frac{\text{atoms T}}{\text{particle}} = 5.07 \times 10^8$ atoms

Then the number of particles of Li_2O that are needed in the side stream in order to recover 1.26×10^{21} atoms of T per sec (6.3×10^{-3} $\frac{g\ T}{sec}$) is

$$1.26 \times 10^{21} \frac{\text{atoms T}}{\text{sec}} \times \frac{Li_2O \text{ particle}}{5.07 \times 10^8 \text{ atoms T}} = 2.49 \times 10^{12} \text{ particles}$$

Since there are 1.19×10^{14} particles of Li_2O in the entire system,

$$\frac{2.49 \times 10^{12}}{1.19 \times 10^{14}} \times 100 = 2\%$$

of the stream must be diverted to the T recovery system.

The tritium recovery system has not been designed but a simple calculation can be made to arrive at some idea of the size requirement. The above calculation was based on the assumption that as soon as the tritium species reached the surface of a Li_2O particle, it is immediately cold trapped. This would be true only in the case of a monolayer of Li_2O particles which would be an unreal 2-dimensional system. For the purposes of calculation, though, it is assumed the T extractor is cubic in nature. If the flow rate of Li_2O is $3.34 \times 10^7 \frac{kg}{hr}$, a 2% side stream flow rate will be $0.685 \times 10^6 \frac{kg}{hr}$ which is $1.90 \times 10^2 \frac{kg}{sec}$. For a 300 second residence time, the T recovery system must contain 5.70×10^4 kg of Li_2O. The volume the Li_2O occupies is $2.84 \times 10^7 cm^3$ and the volume of the accompanying helium is 1.87×10^7 cm^3 for a total of 4.73×10^7 cm^3 or 47.3 m^3. In terms of a cubic figure, this would be an object 3.6 meters on edge. The shape undoubtedly would be designed to accomodate the flow rate of Li_2O in the system and the required residence time of 300 secs. Whether the temperature of 850°C can be maintained during this five minute period without supplementary heating seems problematical. A potential problem with the preceeding description of the extractor is its large size. The need for a tritium recovery system that must contain 47.3 m^3 of material is directly related to the residence time of 300 sec. A decrease in the residence time will cause a proportional decrease in the volume of the extractor. One method of decreasing the residence time is to increase the T from a 1 kg inventory to a 10 kg inventory. This would decrease the residence time by a factor of 10 to 30 sec.

The total volume of the extractor would now be 4.73 m^3. In terms of a cubic figure, this would be an object 1.68 m on edge. Whether a 10 kg tritium inventory in the lithium oxide is acceptable may be debatable. In any event, the apparatus will have to be constructed in such a way that the gas phase is separated from the solid phase by a membrane with a pore size of less than 100 microns so the Li_2O solid is not transported into the gas phase. The condensables in the gas phase are cold trapped and the helium carrier gas recycled.

The condensables, consisting of H_2O, HTO, T_2O, LiOH and LiOT are electrolyzed to produce tritium, deuterium and protium gaseous species which are in turn sent to an isotope separation facility designed on the basis of the work of Wilkes[6], and then returned to the fueling cycle. Problems related to the high β activity of tritium in the condensate have not been considered.

IX-D. Tritium Containment and Emergency Tritium Recovery System

These problems have not been considered here. For a suitable analysis, more information is required on the size of the building, the piping requirements, and the total tritium inventory. It can be assumed, however, that these sytems will be similar to those designed for UWMAK-I, II and III[1,2,3,7]

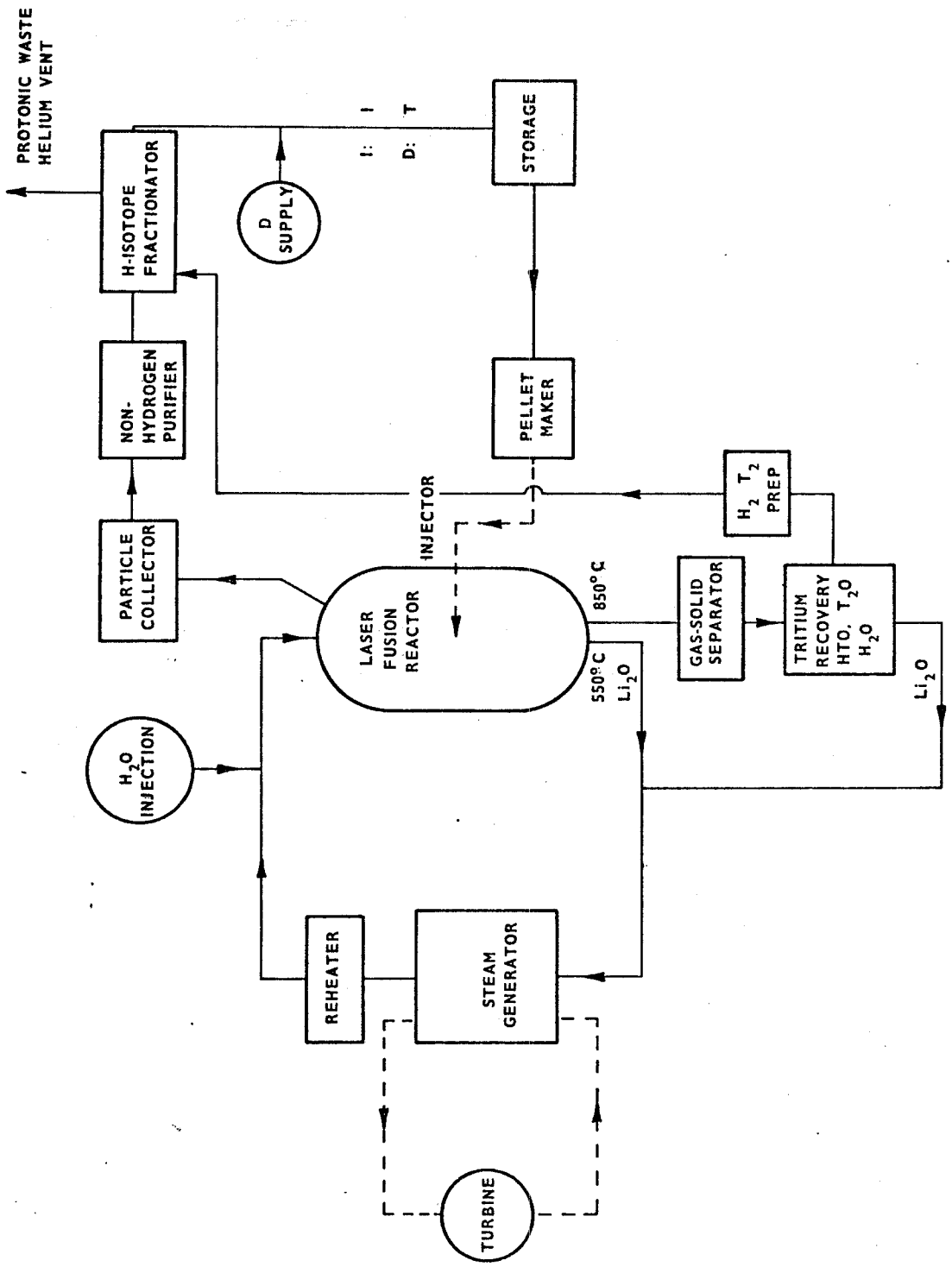

FIGURE I - TRITIUM PATHWAYS IN LASER FUSION PLANT

Figure 2

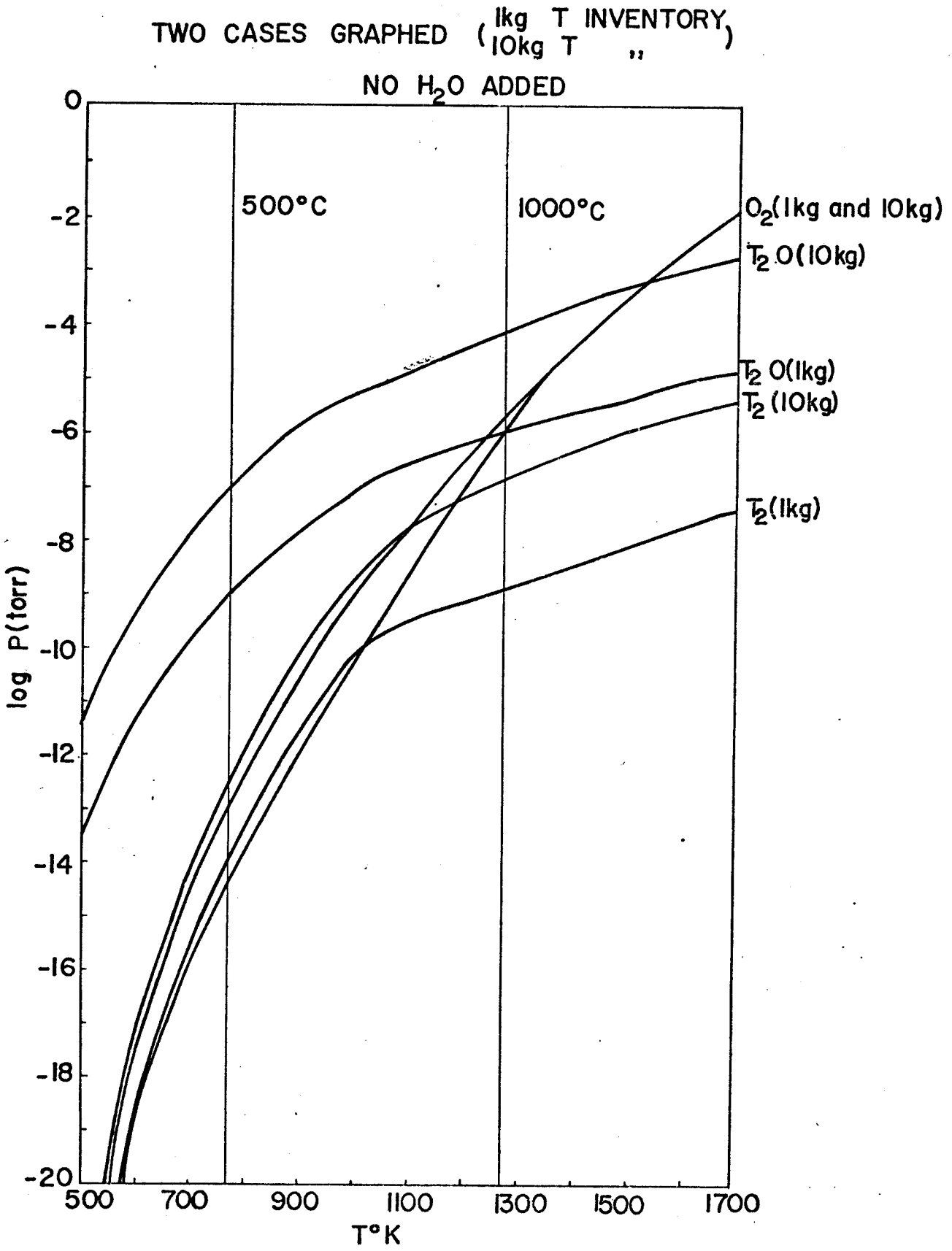

Variation of Partial Pressure of the different species with temperature when no H_2O is added.

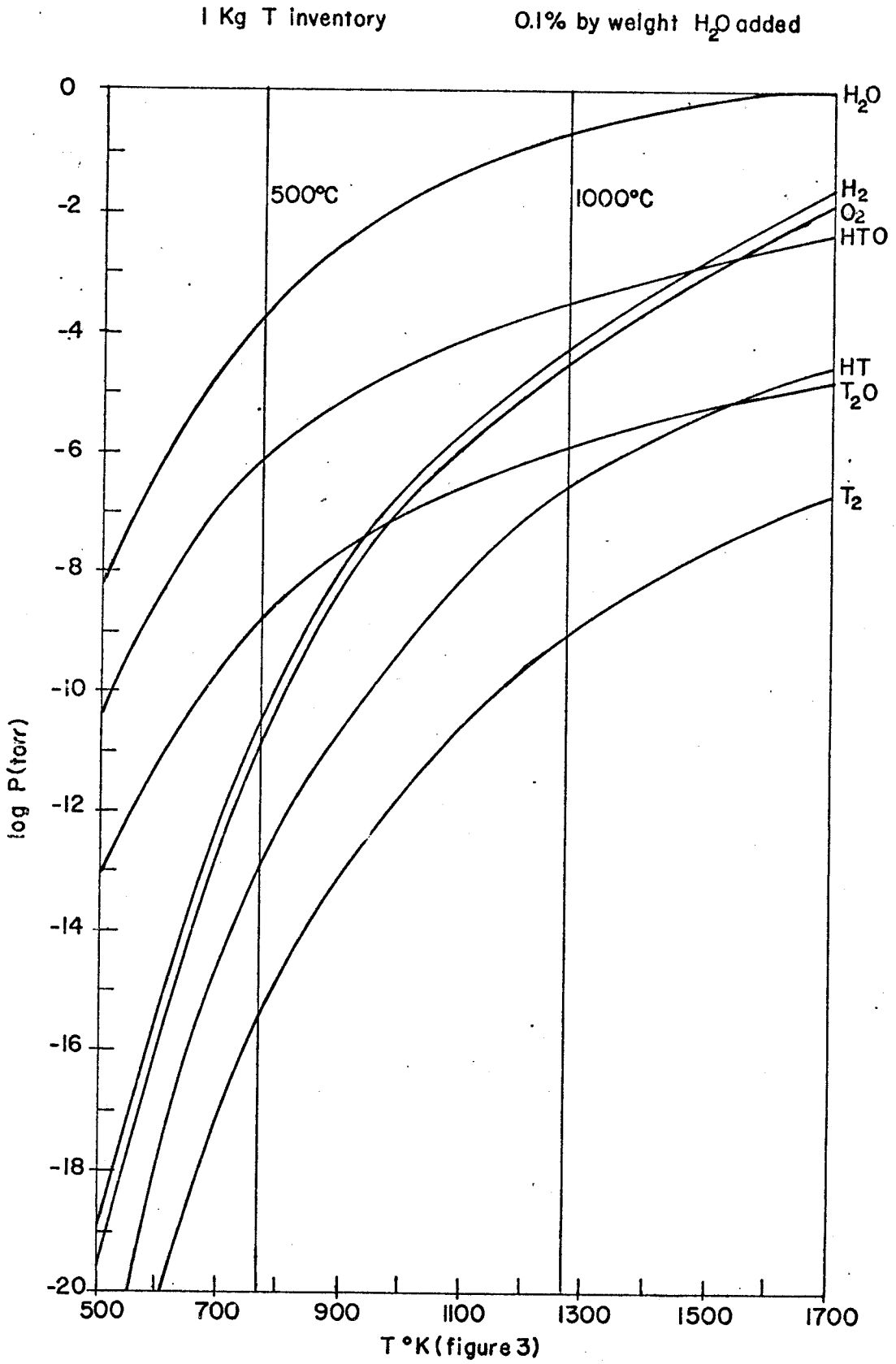

Variation of the Partial Pressures of the different species with temperature when 0.1% water is added.

DIFFUSION OF TRITIUM OR HYDROGEN
IN CERAMIC MATERIALS

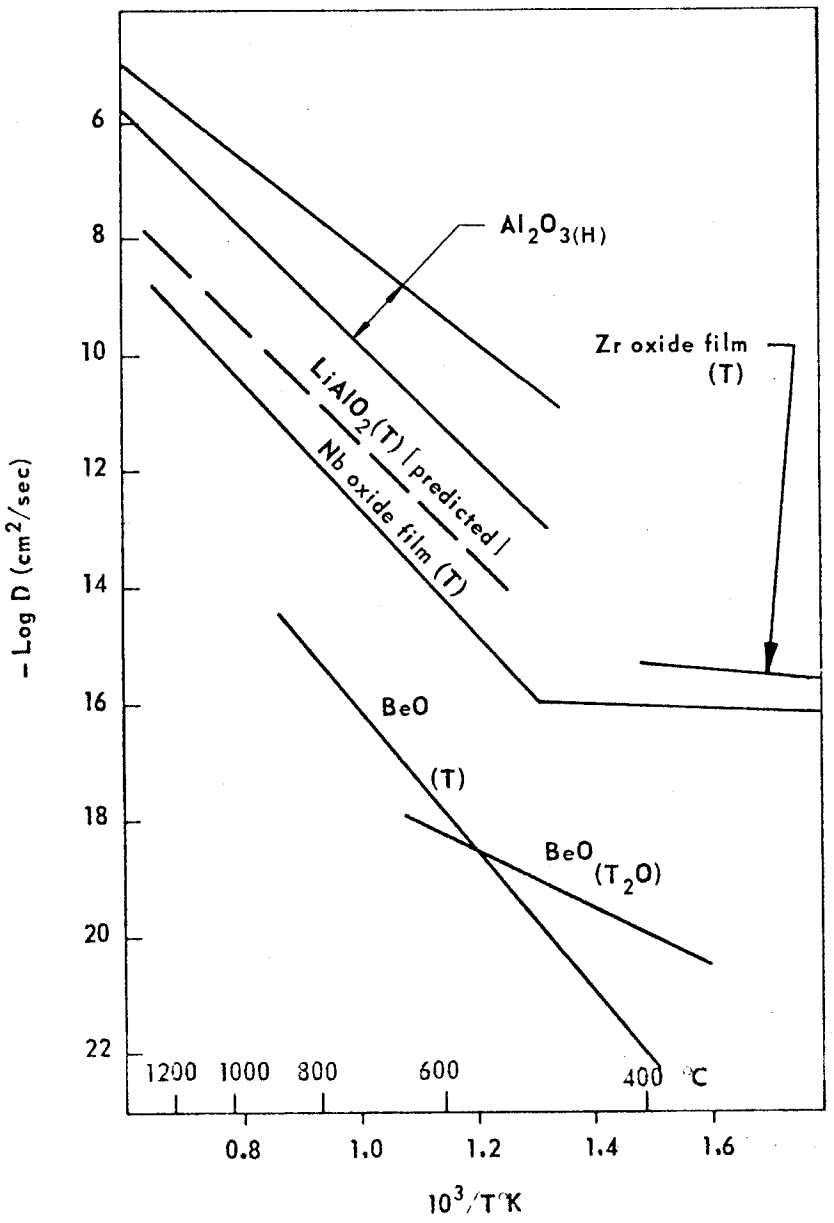

FIGURE 4

Bibliography

1. B. Badger, et al. Fusion Feasibility Study Group, "UWMAK-II, A Conceptual Tokamak Fusion Reactor Design," Nuclear Engineering Dept. Report UWFDM-112, University of Wisconsin (November 1975).

2. R. G. Clemmer, E. M. Larsen and L. J. Wittenberg, Nucl. Eng. Design 39(1), 85-98 (1976).

3. D. K. Sze, E. M. Larsen, E. T. Cheng and R. G. Clemmer, Trans. Am. Nucl. Soc. 22, 21 (1975).

4. E. M. Larsen, R. G. Clemmer and D. K. Sze Trans. Am. Nucl. Soc. 23, 56 (1976).

5. JANAF THEROCHEMICAL Tables, D. R. Stull et al., The Dow Chemical Company, Midland, Michigan, March 1964.

6. W. R. Wilkes "Hydrogen Isotope Distillation in a Fusion Reactor System," Trans. Am. Nucl. Soc. 19,20 (1974).

7. L. J. Wittenberg, et al., "Evaluation Study of the Experimental Power Reactor," Mound Laboratory, Monsanto Research Corporation, Miamsburg, Ohio Report MIM-2259, November 1975.

X. Power Cycle Considerations

In this section, a preliminary description of the power cycle to be used is given. The main distinguishing features of this system are: (1) Lithium oxide is the primary heat transport medium requiring special circulating system and steam generator design, (2) An intermediate coolant loop is not required (Section IX), and (3) Multiple heat sources at different temperatures are available (first wall, blanket back wall, and Li_2O).

Steam is generated in the boiling-water cooled first wall and in the Li_2O steam generator. A schematic diagram of the first wall cooling system is shown in Fig. 1. Saturated water at 1000 psia enters the coolant channels of the cylindrical membrane wall at the reactor's midplane. The coolant pressure is selected so that the maximum first wall temperature is ~300°C (Section VIII). The low-quality (x=20%) two phase mixture leaving the cylindrical portion of the first wall is recirculated via a steam drum. The saturated steam withdrawn from the steam drum is used to cool the back wall of the blanket where it is superheated to approximately 400°C. The superheated steam (1000 psia, 400°C) produced in the cylindrical portion of the blanket's back wall flows to the second stage of the high pressure turbine (Fig. 2).

For the hemispherical end caps of the cavity, the boiling water coolant flows in horizontal channels between supply and exit headers arranged along four equally-spaced meridians (Fig. 1). The coolant pressure at inlet is 350 psia. The lower pressure is necessitated by the high heat flux in these regions and the requirement that the maximum wall temperature be kept at ~300°C. Similar to the cylindrical portion of the cavity, the low-quality two phase mixture leaving the coolant channels is recirculated via a steam

drum. The coolant flow rate here is considerably higher than that for the cylindrical section because of the higher heat flux produced by the ion energy deposited in the end caps' liner. The large amount of steam produced in these regions can not be sufficiently superheated in the blanket's back wall cooling channels. Therefore, a significant fraction of this steam is superheated by passing it through two heat exchangers placed in the inlet and exit Li_2O streams (Fig. 1). The superheated steam produced in these heat exchangers (350 psia, 400°C) is combined with that produced in the back wall of the hemispheres before entering the intermediate pressure turbine (Fig. 2). The main design parameters for these heat exchangers are given in Table 1.

The steam generator is a fluidized bed heat exchanger with lithium oxide particles entering at ~550°C and leaving at ~450°C. Fluidized bed heat exchangers are routinely used in the chemical industry with particle flow rates comparable to those used here. The fluidization technique has been used for operations involving solid/fluid contacting whenever high rates of heat and mass transfer between the solid and fluid are required. The main advantages of the technique are [1]: (1) the extremely large contact area between the solid and fluid allows for high heat and mass transfer rates (1 m^3 of 100 μm particles has a surface area greater than 30,000 m^2), (2) the comparative ease with which fluidized solids can be handled, (3) the temperature gradients within the bed are considerably reduced as a result of the high degree of solids mixing, i.e., a very high effective internal thermal conductivity, (4) high rates of heat transfer between the fluidized solids and an immersed surface, (5) high thermal inertia of the solids, and (6) gas-fluidized systems approximate a fluid with a low vapor pressure; as a thermodynamic fluid it has roughly between gases and liquids.

Inherent within the fluidization technique are some limitations: (1) the process demands the expenditure of power for fluidization, (2) attrition or agglomeration of the particles may occur; the latter may result in agglomerated particles too large to fluidize, (3) there is a limit on the size of particles which may fluidize (few μm - ~6500 μm); this limit depends on fluid viscosity, particle'fluid density ratio, and fluid flow rate, and (4) the dynamics of fluidized systems are not well understood to permit confident scale-up to large units from small scale test data.

A common operational difficulty of fluidized beds is that of maintaining a stable particle size distribution. The size distribution can change through the production of fines by attrition or through agglomeration. This may necessitate periodical variation of the fluid flow rate to assure satisfactory operation.

A list of the main design parameters for the steam generators is given in Table 2. Efforts are currently underway to produce detailed steam generator and particle transport system designs.

A schematic diagram of the steam cycle is shown in Fig. 2. The three steam supplies from the steam generator (1800 psi and 500°C), the back wall coolant (1000 spi and 400°C), and heat exchangers (350 psi and 400°C) are integrated into the cycle. The cycle has an overall thermal efficiency of 38%. The main pressure, temperature, and flow parameters are given in Fig. 2.

References

[1] J. S. Botterill, Fluid-Bed Heat Transfer, Academic Press (1975).

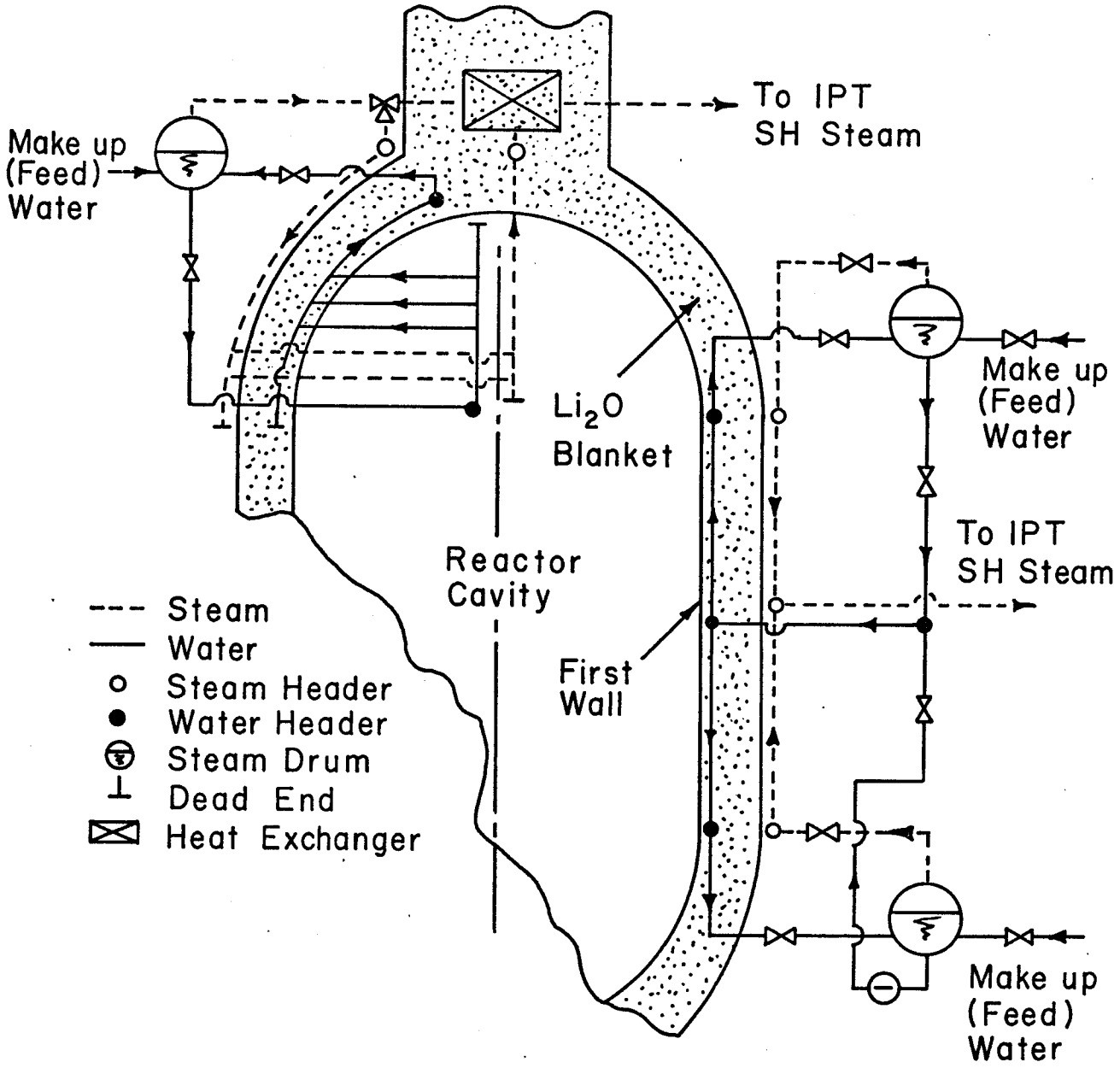

Figure 1

Schematic diagram showing coolant flow for the first wall and blanket back wall, and top heat exchanger

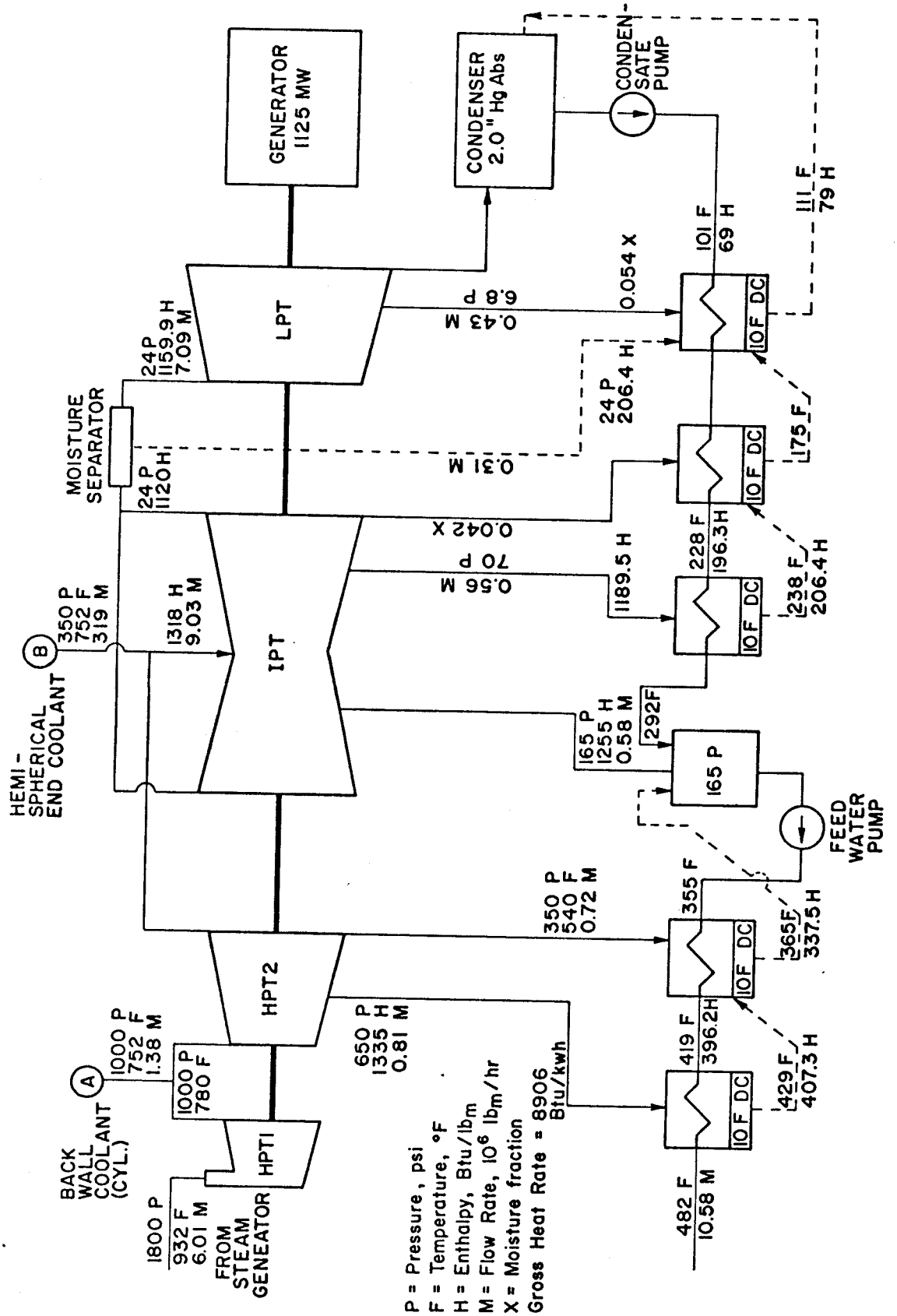

Figure 2 - Schematic Diagram of the Steam Cycle

TABLE 1

HEAT EXCHANGERS' PARAMETERS

	Top Exchanger	Bottom Exchanger
Inlet Conditions:		
Steam	350 psi (sat)	350 psi (sat)
Li_2O	450°C	554°C
Exit Conditions:		
Steam	345 psi (400°C)	345 psi (400°C)
Li_2O	445°C	550°C
Flow Rates: (kg/hr)		
Steam	5.2×10^5	9.3×10^5
Li_2O	3.34×10^7	3.34×10^7
Effectiveness:	0.78	0.54
NTU:	1.50	0.78
H/T Area: (m^2)	1.97×10^3	1.97×10^3
# of Tubes:	8250	8250
Tube Size:	3/4" OD, 1/32" thick, 13.1' long	
Arrangement:	1-1/4" triangular pitch	

TABLE 2

STEAM GENERATOR PARAMETERS

	Water	Li_2O
Inlet Conditions:	250°C (1810 psia)	550°C
Exit Conditions:	500°C (1800 psi)	450°C
Flow Rate (kg/hr):	2.73×10^6	3.41×10^7
Effectiveness	0.833	
NTU	2.75	
MWT	1710 *	(combined)
H/T Area (m^2):	3.58×10^4	(")
# of Tubes:	9.81×10^4	(")
Tube Size:	3/4" OD, 1/32" thick, 20' long	
Arrangement:	1-1/4" triangular pitch	

*Five steam generators are used; these are 7 m long with a 4 m diameter shell.